VOL.29 NO.4
APRIL
2026

AJSTR
of Scientific and Technological Reports



ASEAN JOURNAL

of Scientific and Technological Report

ISSN 2773-8752 (online)



ASEAN
Journal of Scientific and Technological Reports
Online ISSN:2773-8752

ASEAN Journal of Scientific and Technological Reports (AJSTR)

Name ASEAN Journal of Scientific and Technological Reports (AJSTR)

Owner Thaksin University

Advisory Board Assoc. Prof. Dr. Nathapong Chitniratna
(President of Thaksin University, Thailand)
Assoc. Prof. Dr. Samak Kaewsuksaeng
(Vice President for Reserach and Innovation, Thaksin University, Thailand)
Assoc. Prof. Dr. Samak Kaewsuksaeng
(Acting Director of Reserach and Innovation, Thaksin University, Thailand)

Editor-in-Chief Assoc. Prof. Dr. Sompong O-Thong, Mahidol University, Thailand

Associate Editor

1. Prof. Dr. Jompob Waewsak, Thaksin University, Thailand
2. Assoc. Prof. Dr. Samak Kaewsuksaeng, Thaksin University, Thailand

Session Editors

1. Prof. Dr. Rattana Jariyaboon, Prince of Songkla University, Thailand
2. Assoc. Prof. Dr. Jakkree Boonlakhorn, Thaksin University, Thailand
3. Assoc. Prof. Dr. Supawadee Thawaro, Nakhon Si Thammarat Rajabhat University, Thailand
4. Assoc. Prof. Dr. Surapon Boonlue, King Mongkut's University of Technology Thonburi, Thailand
5. Assoc. Prof. Dr. Warangkana Jutidamrongphan, Prince of Songkla University, Thailand
6. Asst. Prof. Dr. Aungkana Jattamart, Rajamangala University of Technology Rattanakosin, Thailand
7. Asst. Prof. Dr. Suphada Kiriratnikom, Thaksin University, Thailand
8. Dr. Pawadee Hamtanon, Thaksin University, Thailand

Editor Board

1. Amir Sada Khan, American University of Sharjah, United Arab Emirates
2. Chart Chiemchaisri, Kasetsart University,Thailand
3. Chen-Yeon Chu, Feng Chia University, Taiwan
4. Dariusz Jakobczak, National University, Pakistan
5. Ganjar Samudro, Universitas Diponegoro, Indonesia
6. Ghulam Murtaza, Government College University Lahore, Pakistan
7. Hidenari Yasui, University of Kitakyushu, Japan
8. Jatuporn Kaew-On, Thaksin University, Thailand
9. José Antonio Álvarez-Bermejo, University of Almeria, Spain
10. Jutamas Kumchai, Chiang Mai University, Thailand
11. Karun Thongprajukaew, Prince of Songkla University, Thailand
12. Marchee T. Picardal, Cebu Normal University, Philippines
13. Nares Chimres, Thaksin University, Thailand
14. Nasser Ahmed, Kyushu University, Japan
15. Noppamas Pukkhem, Thaksin University, Thailand
16. Peer Mohamed Abdul, Universiti Kebangsaan Malaysia, Malaysia
17. Prasong Kessaratikoon, Thaksin University, Thailand
18. Prawit Kongjan, Prince of Songkla University, Thailand
19. Sappasith Klomklao, Thaksin University, Thailand
20. Shahrul Isamail, Universiti Malaysia Terengganu, Malaysia
21. Supawadee Theerathammakorn, Sukhothai Thammatirat Open University, Thailand
22. Tharith Sriv, Royal University of Phnom Penh, Cambodia
23. Tjokorda Gde Tirta Nindhia, Udayana University in Bali, Indonesia
24. Tsuyoshi Imai, Yamaguchi University, Japan
25. Visit Boonchom, Thaksin University, Thailand
26. Win Win Myo, University of Information Technology, Myanmar
27. Yves Gagnon, University of Moncton, Canada
28. Zairi Ismael Rizman, Universiti Teknologi MARA, Malaysia

Staff: Journal Management Division

Miss Kanyanat Liadrak, Thaksin University, Thailand

Contact Us Institute of Research and Innovation, Thaksin University
222 M. 2 Ban-Prao sub-district, Pa-Pra-Yom district, Phaᵒhalung province, Thailand
Tel. 0 7460 9600 # 7258, 09 1070 0916, 08 1540 7304, E-mail: aseanjstr@tsu.ac.th

List of Contents

Application of YOLOv8 Improved Model Incorporating Attentional Mechanism in Weed Identification **e260523**
Zhanwei Feng, Adisak Sangsongfa, and Noppadol Amdee

Improving Drying Efficiency for Red Chili Peppers Using Ventilated Solar Technology **e261032**
Tanawat Srirugsa, Supachai Kaewpoung, Wiwat Su-hren, Kansinee Panwanitdumrong, and Tawat Chuchit

Technology Transfer Assessment of Amino Acid Block Fertilizer Production from Salted Egg White Waste for Coconut Farming in Paktrae, Songkhla Province **e261099**
Saowanee Lekbangpong, Prisana Wonglom, Niramol Juntarachat, and Thidarat Juthong

Orbital Period Change of the Binary Star System V829 Aql **e258435**
Supat Sairattanain, Torik Hengpiya, and Wiraporn Maithong

AI-Based Detection of Leaf Diseases in Durian (*Durio zibethinus*) Using Convolutional Neural Networks: Model Development and Performance Evaluation **e261309**
Supreeya Thepparak, Prisana Wonglom, Samak Kaewsuksaeng, and Anurag Sunpapao

Work-related Musculoskeletal Disorders among Rubber Tappers in Phatthalung Province, Thailand **e262782**
Sutee Inraksa, Angoon Sungkhapong, Supapan Chaiprapat, and Klangduan Pochana

SUMO-Based Optimization of Intersection Performance under Heterogeneous Traffic **e261278**
Md. Emtiaz Kabir, Mehruba Akter Sara, Md. Ibrahim Islam Ifty, and Zaber Ahmed

Production of Fermented Vinegar Drink From Hang Rice With Pineapple Peel Syrup **e262439**
Nisa Romsomsa, Nithiphon Tiapasert, Karid Jittimanee, Chaiwat Paungkrathok, Nutthawut Meesilp, and Numphon Thaiwong

Comparison of Color Space Performance for Colorimetric Detection of Heavy Metals in Drinking Water Using Image Processing and Convolutional Neural Networks **e260866**
Atthapol Phongsuwan, Nadh Ditcharoen, and Sompong Valuvanathorn

Effects of Cassava Tails and Stalk and Superabsorbent Polymer on Soil Properties, Growth, and Yield of Cassava in Sandy Loam and Clay Loam Soils **e260726**
Prinda Kongyinghan, Sodchol Wonprasaid, Wimonsiri Pingthaisong, and Thitiporn Machikowa

The Influence of Managerial and Operational Characteristics on Food Waste Reduction Practices Among the Restaurants Along the Andaman Coast of Thailand **e261801**
Mumtas Meraman, and Morakot Ditta-Apichai

Comparative Analysis of Rubberwood, Plywood, and Wood-Plastic Composites for Safe Elderly Toy Applications **e260685**
Pruttipong Pantamanatsopa, Chainarong Srivabut, Chatree Homkhiew, Worapong Boonchouytan, Surasit Rawangwong, and Apichon Thongmung Kamnerdwam

The Preparation and Characterisation of a Bioplastic Film from Acrylated Epoxidized Soybean Oil (AESBO) **e261617**
Apatsara Uchupap, Suppachai Sattayanurak, Ismail Ibrahim, Mohd Hafiz Zainol, Tulyapong Tulyapitak, Anuwat Saetung, and Weerawut Naebpetch

List of Contents

Evaluation of the Nutritional, Mineral, and Estimated Metabolizable Energy Values of Agricultural Biomass Raw Materials Used for the Development of Concentrated Fermented Feed for Beef Cattle in Mukdahan Province, Northeast Thailand **e262452**
Nathaporn Jirawattanasomkul, Wuttichai Roschat, Tappagorn Leelatam, Sasithon Phanphli, Watanya Chaipikun, Aekkaphon Thammayod, Noppharat Khotsuno, Permsak Yeemin, Nattapong Wongma, and Sunti Phewphong

Effects of Hydroponic Cultivation Systems on Growth Performance and Yield of Pakchoi (*Brassica rapa* var. *chinensis*) **e261311**
Pakamas Thaenkaew, Ronnarit Khuengphukhiao, Sirawat Surachotivet, and Khitaphat Khongthaen

A Framework for a Geospatial Predictive Decision Support System for Hazard Risk Profiling **e261475**
Anna Monica Paculaba, and Thelma Palaoag

Design and Development of a Smart Automated System for Poultry Farm Management Using Internet of Things (IOT) **e260601**
Jaiinder Preet Singh, Piyush Gulati, Vikas Sharma, Hemant Kumar, Prakash Mahto, and Ashish Choudhary

Histology and Histochemistry of the Digestive Tract of Transverse-bar Barb, *Hampala macrolepidota* Kuhl & Van Hasselt, 1823 **e263072**
Akapon Vaniksampanna, Sonchai Intachai, Wankuson Chanasit, Sakorn Khongsud, and Akkanee Pewhom

Optimizing Brown Rice Drying With Modified LSU Systems For Energy Efficiency, Carbon Reduction, and 2AP Preservation **e260421**
Sompot Khomkaew, Nattapong Suksabai, Tanawat Srirugsa, Tawat Chuchit, Wiwat Su-hren, and Supachai Kaewpoung

A Hybrid Facial Expression Recognition System Based on Machine Learning and Deep Learning Models **e261424**
Akkapop Prasompon, Prompong Sugunnasi, and Atigorn Sanguansri



ASEAN
Journal of Scientific and Technological Reports
Online ISSN:2773-8752

ASEAN
Journal of Scientific and Technological Reports
Online ISSN:2773-8752

Research article

Application of YOLOv8 Improved Model Incorporating Attentional Mechanism in Weed Identification

Zhanwei Feng[1], Adisak Sangsongfa[1*], and Noppadol Amdee[1]

[1] Faculty of Industrial Technology, Muban Chombueng Rajabhat University, 70150, Thailand
* Correspondence:adisaksan@mcru.ac.th

Citation:
Feng, Z.; Sangsongfa, A.; Amm-Dee, N. Application of YOLOv8 improved model incorporation attentional mechanism in weed identification. *ASEAN J. Sci. Tech. Report.* **2026**, *29*(4), e260523. https://doi.org/10.55164/ajstr.v29i4.260523

Article history:
Received: July 26, 2025
Revised: December 23, 2025
Accepted: January 11, 2026
Available online: March 24, 2026

Publisher's Note:
This article is published and distributed under the terms of the Thaksin University.

Abstract: Accurate identification of weeds plays a pivotal role in precision agriculture, as it supports targeted herbicide application and enhances crop productivity. This paper presents an improved YOLOv8-based object detection framework that integrates a global attention mechanism to strengthen weed recognition performance. Although YOLOv8 demonstrates strong baseline accuracy and speed, it lacks sufficient global contextual modeling, which constrains its ability to capture fine-grained features in visually complex or dense field scenarios. To overcome this limitation, we incorporate a Global Attention Module (GAM) after each C2f block in the backbone, enabling the network to capture long-range dependencies and highlight semantically relevant regions. Experiments on a custom weed dataset indicate that the attention-enhanced model considerably surpasses the baseline YOLOv8 in precision, recall, and mean Average Precision (mAP), especially under challenging conditions with small-scale or overlapping targets. Furthermore, the proposed method attains a favorable trade-off between detection accuracy and computational efficiency, making it suitable for real-time smart farming applications.

Keywords: Global attention; object detection; precision agriculture; weed detection; YOLOv8

1. Introduction

Weed infestation poses a critical challenge in contemporary agriculture, significantly reducing crop yields and increasing production costs [1–3]. Accurate and timely weed identification is essential for precision management, enabling selective application of herbicides to targeted areas [4-5]. Conventional identification approaches are often inefficient, labor-intensive, and susceptible to human error, particularly in large-scale field conditions [6–7]. As a result, the adoption of automated, robust, and real-time weed-detection technologies has become an urgent requirement for smart farming practices [8–9]. Driven by the rapid progress in deep learning, the YOLO (You Only Look Once) series has gained considerable popularity for its balance of detection accuracy and speed [10-11]. In particular, YOLOv8 achieves promising results by introducing several architectural improvements, such as the C2f module and anchor-free detection heads [12-13]. However, a critical research gap persists in current agricultural object detection: standard lightweight frameworks often struggle to maintain discriminative precision when confronted with cluttered backgrounds, overlapping plant structures, and small-scale targets [14-16]. Although existing studies have attempted to incorporate attention mechanisms such as CBAM or

SE, these modules are predominantly local in nature and often fail to capture the long-range cross-dimensional dependencies required to distinguish morphologically similar species in unconstrained environments [17-18]. To address these identified limitations, we propose an improved YOLOv8-based model that innovatively integrates a Global Attention Module (GAM) into the backbone network [19-20]. The primary technical contribution of this work lies in the strategic transition from local feature processing to multi-dimensional global dependency modeling by embedding GAM layers directly after each C2f block. This architectural synergy facilitates enhanced semantic feature propagation without significantly increasing model complexity, thereby boosting performance for small, hard-to-identify weed instances [21-22]. To validate our approach, experiments were conducted using a specifically constructed dataset featuring four species: Carpetweeds, Eclipta, Goosegrass, and Prickly Sida (Figure 1).



Carpetweeds Eclipta Goosegrass Prickly Sida

Figure 1. Representative examples of the weed types used in this study: Carpetweeds, Eclipta, Goosegrass, and Prickly Sida.

Beyond technical refinement, this study contributes to broader agricultural impacts. By preserving fine-grained morphological cues often overlooked by conventional detectors, our proposed framework bridges the gap between high-precision recognition and real-time edge deployment. Such advancement enables highly targeted herbicide application, thereby directly minimizing environmental chemical exposure and optimizing operational efficiency in precision agriculture. By incorporating global attention, this research provides a robust, field-ready solution that highlights semantically relevant weed features under complex field conditions, even when targets are partially occluded or densely overlapping. The following sections detail the proposed model's structure, the experimental setup, and a comprehensive analysis of the results.

2. The Method Described

2.1 Integration of Global Attention Module (GAM)

Although YOLOv8 offers a solid foundation for real-time object detection, its ability to capture long-range contextual relationships remains limited, particularly in complex agricultural environments with densely distributed or visually similar weeds [23-24]. To overcome this drawback, we embed a Global Attention Module (GAM) [25-26] within the YOLOv8 backbone, thereby improving the model's representational capacity by capturing global dependencies across both spatial and channel dimensions. The structural design of GAM is depicted in Figure 2. It is composed of two sequential components: a Channel Attention mechanism that emphasizes "what" information is critical, and a Spatial Attention mechanism that focuses on "where" the emphasis should be placed. Together, these attention branches refine the feature representations and yield an attention-guided output.

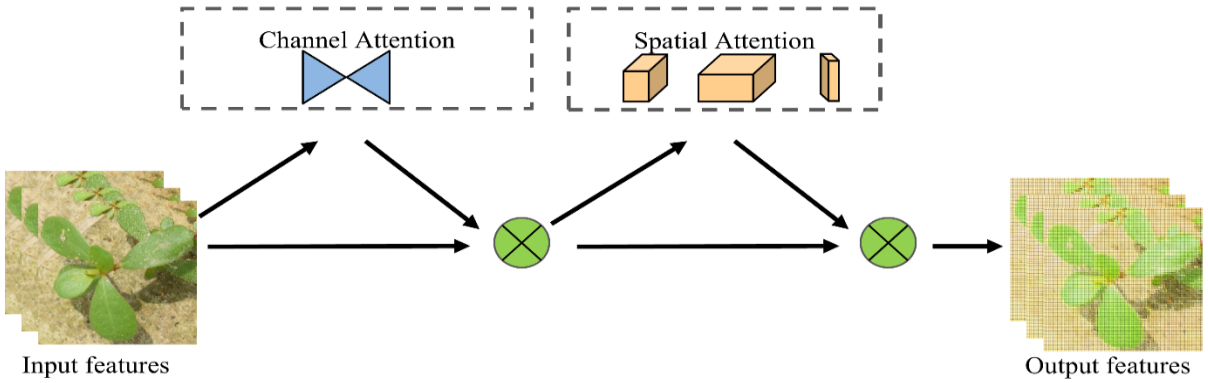


Figure 2. The Global Attention Module (GAM) comprises channel and spatial attention mechanisms. The module adaptively re-weights features to enhance relevant semantic information and suppress background noise.

Let the input feature map be denoted as X ∈ ℝ^{C×H×W}, where C, H, and W represent the number of channels, height, and width, respectively. To compute channel attention, global average pooling (GAP) is first applied to X, followed by two fully connected layers with ReLU activations and a sigmoid activation. This process generates the attention weights Ac ∈ ℝ^C, formulated as:

$$\mathbf{A}_c = \sigma(W_2 \cdot \delta(W_1 \cdot \mathrm{GAP}(X))) \quad (1)$$

where W1 ∈ ℝ^{C/r×C} and W2 ∈ ℝ^{C×C/r} are the weight matrices of two fully connected layers, r is the channel reduction ratio (typically set to 16), δ(·) denotes the ReLU activation, and σ(·) is the sigmoid function. The resulting attention weights are then applied to the input feature map by channel-wise multiplication to produce the intermediate output X':

$$X' = \mathbf{A}_c \otimes X \quad (2)$$

Next, spatial attention is applied to emphasize informative regions across spatial locations. This is achieved by performing both average and max pooling along the channel axis, concatenating the results, and passing the concatenated results through a convolutional layer with a 7×7 kernel, followed by a sigmoid activation. The resulting spatial attention map As ∈ ℝ^{1×H×W} is computed as:

$$\mathrm{As} = \sigma(\mathrm{Conv}_{7\times7}([\mathrm{AvgPool}(X'); \mathrm{MaxPool}(X')])) \quad (3)$$

where [·; ·] indicates channel-wise concatenation, and $\mathrm{Conv}_{7\times7}$ represents the convolution operation. The final output is obtained by applying spatial attention to X':

$$X'' = \mathrm{As} \otimes X' \quad (4)$$

Through this two-stage refinement, the Global Attention Module adaptively re-weights feature responses in both channel and spatial dimensions, enabling the model to capture better contextual and structural cues essential for accurate weed detection.

2.2 Proposed Method: YOLOv8 with Integrated GAM Modules

To address YOLOv8's limitation in capturing global semantic context, we introduce a novel modification by embedding the Global Attention Module (GAM) into its backbone. The schematic layout of the proposed model is presented in Figure 3. In this framework, GAM modules are strategically positioned after each C2f block within the backbone. These modules refine feature maps by successively applying spatial and channel attention mechanisms. The channel attention mechanism adjusts the relative weights of each channel based on global contextual cues, while the spatial attention mechanism emphasizes the most informative regions within the feature maps. This dual refinement enables the network to better concentrate on weed targets and suppress background noise. By integrating GAM directly into the feature-extraction hierarchy, the model progressively strengthens its semantic representation throughout the forward pass. Consequently, the network

achieves improved localization and classification accuracy, particularly for small or visually ambiguous weed instances. Notably, although introducing GAM modules incurs a modest computational cost, it retains the lightweight structure and real-time efficiency of the YOLOv8n baseline.

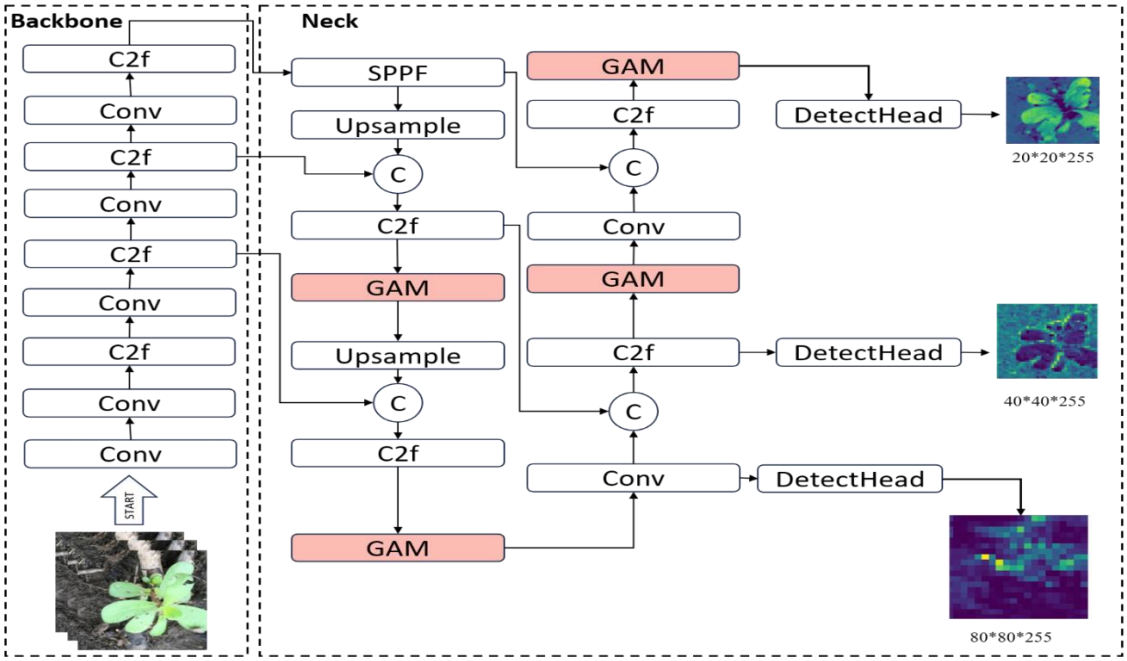


Figure 3. Architecture of the proposed GAM-enhanced YOLOv8 model. GAM modules are inserted after C2f blocks in the backbone to enrich feature representations. The output features exhibit enhanced semantic focus, especially on weed regions.

Compared to conventional attention mechanisms, such as the Convolutional Block Attention Module (CBAM), integrating GAM into our proposed model offers distinct advantages for capturing complex agricultural features. While CBAM sequentially infers attention maps along two separate dimensions (channel and spatial), it often suppresses significant cross-dimension interactions by using a simple pooling-based reduction. In contrast, the GAM employed in this study adopts a sequential channel-spatial attention structure that preserves information across multiple dimensions without drastic reduction. By utilizing a 3D-permutation-based technique and a multi-layer perceptron (MLP) within the channel submodule, and using two convolutional layers in the spatial submodule, GAM effectively mitigates the loss of fine-grained details. This characteristic is particularly vital for weed identification in dense field environments, where subtle morphological differences between crops and weeds require preserving rich spatial-channel dependencies that traditional mechanisms might overlook.

3. Results

This section presents the experimental outcomes, their interpretation, and the derived conclusions. Where appropriate, the results are organized into sub-sections to enhance clarity. The discussion focuses on how the findings align with or diverge from previous studies and their implications for the research hypotheses. Broader contextual relevance is also considered, and potential directions for future investigations are briefly outlined.

3.1 experimental design

To assess the performance of the proposed YOLOv8n + GAM framework, experiments were performed on a weed dataset containing 11,232 annotated images distributed across four categories: Carpetweeds, Eclipta, Goosegrass, and Prickly Sida. The images were primarily captured from a top-down perspective to ensure a consistent field of view for detection. To enhance the model's robustness to

environmental variability, the data collection spanned different times of day, encompassing diverse lighting conditions and weather (e.g., sunny and overcast). The dataset was partitioned into training, validation, and independent test sets at 70:20:10 (8,004 for training, 2,152 for validation, and 1,076 for final performance testing). The class distribution is detailed in Table 1, showing a relatively balanced representation to prevent model bias. To further improve generalization and prevent overfitting, offline data augmentation was applied to the training set, including horizontal flipping, random rotation (±15°), and brightness adjustment. All images were then standardized to a resolution of 640×640 pixels for consistent model input. For the training phase, we configured the Adam optimizer with a learning rate of 0.001 and processed 16-image batches across 300 epochs. To refine detection results during inference, we implemented Non-Maximum Suppression (NMS) to eliminate overlapping predictions, using a confidence cutoff of 0.25 and an IoU threshold of 0.45 for optimal box selection. The generalizability of the proposed method was subsequently verified on the test partition by measuring standard benchmarks, specifically mAP@0.5, mAP@0.5:0.95, Recall, and Precision.

Table 1. Ablation study results of GAM integration

Weed Category	Training	Validation	Test	Total Instances
Carpetweeds	2010	540	270	2820
Eclipta	1995	536	268	2799
Goosegrass	2004	541	271	2816
Prickly Sida	1995	535	267	2797
Total	8004	2152	1076	11232

3.2 Ablation Study

To examine the impact of the Global Attention Module (GAM), an ablation study was performed by comparing the baseline YOLOv8n model with the proposed YOLOv8n + GAM variant. Both models were trained under the same experimental conditions to ensure a fair comparison. A summary of the results is provided in Table 2.

Table 2. Ablation study results of GAM integration.

Method	GFLOPS	mAP@0.5	FPS
YOLOv8n (baseline)	8.2	0.86	60
YOLOv8n + GAM(our)	8.2	0.90	70

According to Table 2, the YOLOv8n + GAM model achieves a 4% improvement in mAP@0.5, increasing from 0.86 to 0.90. Notably, this accuracy gain comes without any increase in computational complexity, as both models share the same GFLOPs value of 8.2. Moreover, the inference speed of the GAM-enhanced model improves slightly, reaching 70 FPS compared to 60 FPS for the baseline.

Although attention mechanisms often entail additional computational overhead, the observed acceleration can be attributed to more discriminative feature representations produced by GAM. By effectively suppressing background noise and emphasizing informative spatial regions, the model reduces the number of redundant low-confidence predictions during inference. This refinement alleviates the computational burden of the Non-Maximum Suppression stage, which is commonly a bottleneck in object detection pipelines. Furthermore, the parallel-friendly design of the GAM module enables efficient execution on modern GPUs, such as the NVIDIA RTX 4090, thereby offsetting the nominal increase in internal operations and improving real-time detection performance. Overall, these experimental findings verify the efficacy of incorporating GAM into the YOLOv8n framework. The enhanced model effectively addresses challenges such as dense weed distribution, small-scale targets, and complex agricultural backgrounds—scenarios where conventional detectors often struggle. Moreover, the improvement in both accuracy and speed underscores the practicality of the proposed method for deployment in real-time, resource-constrained agricultural environments. This makes YOLOv8n + GAM a compelling solution for intelligent weed monitoring and precision farming applications.

Overall, these experimental findings verify the efficacy of incorporating GAM into the YOLOv8n framework. The enhanced model effectively addresses challenges such as dense weed distribution, small-scale

targets, and complex agricultural backgrounds—scenarios where conventional detectors often struggle. Moreover, the improvement in both accuracy and speed underscores the practicality of the proposed method for deployment in real-time, resource-constrained agricultural environments. This makes YOLOv8n + GAM a compelling solution for intelligent weed monitoring and precision farming applications.

3.3 Comparative Evaluation

To provide additional verification of the proposed approach, we conducted a comparative study between YOLOv8n + GAM and several widely adopted lightweight object detection models, including Faster R-CNN, SSD, YOLOv8n + CBAM, and an experimental version of YOLOv11. All models were trained and evaluated on the identical weed dataset under uniform conditions to guarantee fairness. A summary of the results is reported in Table 3.

According to Table 3, the YOLOv8n + GAM model reaches the highest mAP@0.5 (0.90) among all compared methods, surpassing both conventional and modern lightweight detectors. Notably, this improvement is achieved with a computational demand of 8.2 GFLOPs, which is considerably lower than that of heavier architectures such as Faster R-CNN, which achieves only 0.70 mAP@0.5 at the cost of 170 GFLOPs and 12 FPS. Although SSD offers a more balanced trade-off between accuracy and speed (35 GFLOPs and 36 FPS), its detection accuracy (0.76) is lower than that of the GAM-augmented YOLOv8n. Furthermore, when compared with the YOLOv8n + CBAM model, a commonly adopted attention-based baseline, the GAM-integrated model achieves an additional 2% improvement in mAP@0.5. This gain can be attributed to the GAM module's ability to model richer cross-dimensional feature interactions via a 3D permutation mechanism, whereas CBAM's sequential channel and spatial attention may limit global dependency modeling. Importantly, this accuracy enhancement is achieved without increasing computational complexity, as the model maintains a low cost of 8.2 GFLOPs while achieving a higher inference speed of 70 FPS, exceeding the 65 FPS of the CBAM-based variant. These results collectively confirm the effectiveness and efficiency of the proposed GAM-enhanced YOLOv8n for real-time weed detection in complex agricultural environments.

Table 3. Comparative Evaluation results of GAM integration.

Method	GFLOPS	mAP@0.5	FPS
YOLOv8n (baseline)	8.2	0.86	60
Faster-rcnn[27]	170	0.70	12
SSD[28]	35	0.76	36
YOLOv11[29]	12.5	0.80	52
YOLOv8n + CBAM[30]	8.3	0.88	65
YOLOv8n + GAM(our)	8.2	0.90	70

The experimental YOLOv11 model, although more efficient than Faster R-CNN and SSD in both GFLOPs and speed, still falls short in both accuracy (0.80 mAP@0.5) and FPS (52) compared to YOLOv8n + GAM. In contrast, our method achieves the best performance in both accuracy and inference speed (70 FPS), highlighting the effectiveness of the integrated Global Attention Module in improving feature discrimination without compromising real-time performance. These results strongly suggest that including GAM enables the detector to more effectively capture spatial and semantic context, particularly for small or overlapping weeds commonly found in real-world agricultural environments. By enhancing inter-channel and spatial interactions within feature maps, the attention mechanism enables the model to focus more precisely on weed regions while suppressing irrelevant background noise. The high mAP of 0.90 achieved by YOLOv8n+GAM is attributed to the Global Attention Module's ability to generate more distinct and non-redundant feature maps. This reduces the density of low-quality candidate proposals, allowing the NMS process to accurately select the most representative bounding box for each weed instance, thereby significantly reducing false positives. In conclusion, YOLOv8n + GAM offers a superior balance of accuracy, computational efficiency, and inference speed, making it well-suited for real-time deployment in precision agriculture applications such as autonomous weeding, field surveillance, and intelligent spraying systems. To intuitively demonstrate the

practical effectiveness of the proposed YOLOv8n + GAM model, we present several qualitative detection results on the validation set, as shown in Figure 4.



Figure 4. Qualitative detection results using the proposed YOLOv8n + GAM model. The model shows high confidence and accurate bounding boxes across different weed species and visual conditions.

From the visualizations, it is evident that the model successfully identifies and localizes various weed instances, including Carpetweeds, Eclipta, Goosegrass, and Prickly Sida, with high confidence scores and tight bounding boxes. The results remain stable even under challenging scenarios such as complex textures, partial occlusions, or intra-class shape variability. The visual clarity and localization precision in these examples further support the quantitative results reported earlier. Specifically, the use of the Global Attention Module enhances the model's ability to suppress background interference while focusing on the most informative regions of the image, resulting in more robust detection. These results affirm the model's suitability for deployment in real-world agricultural environments, where weed species often exhibit inconsistent appearances and grow under noisy, uncontrolled conditions. The proposed framework not only improves detection accuracy but also supports real-time, image-based weed monitoring solutions in precision farming systems.

4. Discussion of Results

Experimental validation on a custom weed dataset revealed that the YOLOv8n + GAM configuration consistently surpasses the baseline across multiple evaluation metrics. The enhanced model demonstrated marked improvements in precision, recall, and mAP, particularly when processing images containing small-scale weeds, overlapping instances, or dense spatial arrangements. Notably, these performance gains were achieved without introducing additional computational overhead, thereby maintaining the model's viability for deployment on resource-constrained edge devices commonly used in agricultural settings. The results confirm that attention-based mechanisms can effectively complement lightweight detection architectures, providing a practical pathway toward more accurate field-level weed-monitoring systems. Despite the promising outcomes, several limitations warrant acknowledgment. The current evaluation was conducted on a dataset collected under relatively controlled lighting and weather conditions, which may not fully represent the variability encountered across different growing seasons or geographic regions. Additionally, while GAM enhances global context modeling, the framework does not explicitly address challenges posed by extreme occlusion or severe background interference, scenarios that occasionally arise in densely planted fields. Furthermore, the study focused exclusively on RGB imagery; incorporating additional spectral bands (such as near-infrared) could potentially yield further performance improvements, but remains unexplored in this work. Several avenues exist for extending this research. Adaptive attention mechanisms that dynamically

adjust their receptive fields based on input characteristics could be investigated to improve robustness across diverse environmental conditions. Beyond this, integrating multi-modal data sources—combining RGB with thermal or hyperspectral imagery—may enable more comprehensive weed characterization and discrimination between weed species and crop plants. Expanding the evaluation to encompass multiple crop types and weed species under varied field conditions would further strengthen the generalizability of the proposed approach. Finally, exploring model compression techniques and knowledge distillation strategies could reduce computational requirements, facilitating deployment on low-power agricultural robots and drones. This research demonstrates that incorporating attention mechanisms into real-time object detectors represents a viable strategy for advancing precision agriculture applications. The proposed framework establishes a foundation for developing intelligent, autonomous crop management systems that support sustainable farming practices by enabling efficient, accurate weed identification.

5. Conclusions

This study introduced an enhanced weed detection framework by integrating a Global Attention Module (GAM) into the YOLOv8 architecture. The baseline YOLOv8, despite its robust real-time detection capabilities, exhibits limited ability to model global contextual information, which restricts its effectiveness in complex agricultural scenes characterized by visual clutter and irregular weed distribution patterns. By strategically inserting GAM blocks after each C2f module within the backbone network, our approach enables the model to establish long-range feature dependencies and selectively emphasize semantically important weed regions.

6. Acknowledgements

The authors gratefully acknowledge the insightful discussions and support of colleagues and peers throughout this work. We also thank those who assisted with data collection and experimental procedures. Finally, we appreciate the constructive feedback provided by the anonymous reviewers, which greatly enhanced the manuscript.

Funding: This research received no external funding.

Conflicts of Interest: The authors declare no conflict of interest.

References

[1] Paul, A.; Ghosh, S.; Mandal, A.; Dutta, S.; Banerjee, S.; Das, S. Smart Solutions for Capsicum Harvesting: Unleashing the Power of YOLO for Detection, Segmentation, Growth Stage Classification, Counting, and Real-Time Mobile Identification. *Comput. Electron. Agric.* **2024**, *219*, 108832. https://doi.org/10.1016/j.compag.2024.108832

[2] Badgujar, C. M.; Poulose, A.; Gan, H. Agricultural Object Detection with You Only Look Once (YOLO) Algorithm: A Bibliometric and Systematic Literature Review. *Comput. Electron. Agric.* **2024**, *223*, 109090. https://doi.org/10.1016/j.compag.2024.109090

[3] Gerhards, R.; Andújar, D.; Hamouz, P.; Peteinatos, G. G.; Christensen, S.; Fernandez-Quintanilla, C. Advances in Site-Specific Weed Management in Agriculture—A Review. *Weed Res.* **2022**, *62*, 123–133. https://doi.org/10.1111/wre.12526

[4] Singh, P.; Zhao, B.; Shi, Y. Computer Vision for Site-Specific Weed Management in Precision Agriculture: A Review. *Agriculture* **2025**, *15*(21), 2296. https://doi.org/10.3390/agriculture15212296

[5] Guo, Z.; Cai, D.; Bai, J.; Xu, T.; Yu, F. Intelligent Rice Field Weed Control in Precision Agriculture: From Weed Recognition to Variable Rate Spraying. *Agronomy* **2024**, *14*, 1702. https://doi.org/10.3390/agronomy14081702

[6] Hasan, A. S. M.; Sohel, F.; Diepeveen, D.; Laga, H.; Jones, M. G. K. A Survey of Deep Learning Techniques for Weed Detection from Images. *Comput. Electron. Agric.* **2021**, *184*, 106067. https://doi.org/10.1016/j.compag.2021.106067

[7] Wang, A.; Zhang, W.; Wei, X. A Review on Weed Detection Using Ground-Based Machine Vision and Image Processing Techniques. *Comput. Electron. Agric.* **2019**, *158*, 226–240. https://doi.org/10.1016/j.compag.2019.02.005

[8] Ji, X.; Yue, Z.; Yang, H.; Zhang, Z. Infrared Image Classification and Detection Algorithm for Power Equipment Based on Improved YOLOv10. *IEEE Access* **2024**, *12*, 184976–184988. https://doi.org/10.1109/ACCESS.2024.3514103

[9] Lippi, M.; Bonucci, N.; Carpio, R. F.; Contarini, M.; Speranza, S.; Gasparri, A. A YOLO-Based Pest Detection System for Precision Agriculture. In *Proc. 29th Mediterr. Conf. Control Autom. (MED)*; **2021**; pp 342–347. https://doi.org/10.1109/MED51440.2021.9480344

[10] Tang, Z.; Chen, Z.; Qi, F.; Zhang, L.; Chen, S. Pest-YOLO: Deep Image Mining and Multi-Feature Fusion for Real-Time Agriculture Pest Detection. In *Proc. IEEE Int. Conf. Data Mining (ICDM)*; **2021**; pp 1348–1353. https://doi.org/10.1109/ICDM51629.2021.00169

[11] Pulipalupula, M.; Patlola, S.; Nayaki, M.; Yadlapati, M.; Das, J.; Reddy, B. R. S. Object Detection Using You Only Look Once (YOLO) Algorithm in Convolution Neural Network (CNN). In *Proc. IEEE 8th Int. Conf. Convergence in Technology (I2CT)*; **2023**; pp 1–4. https://doi.org/10.1109/I2CT57861.2023.10126213

[12] Li, M.; Zhang, Z.; Lei, L.; Wang, X.; Guo, X. Agricultural Greenhouses Detection in High-Resolution Satellite Images Based on Convolutional Neural Networks: Comparison of Faster R-CNN, YOLOv3 and SSD. *Sensors* **2020**, *20*, 4938. https://doi.org/10.3390/s20174938

[13] Liu, Y.; Zeng, F.; Diao, H.; Zhu, J.; Ji, D.; Liao, X.; Zhao, Z. YOLOv8 Model for Weed Detection in Wheat Fields Based on a Visual Converter and Multi-Scale Feature Fusion. *Sensors* **2024**, *24*, 4379. https://doi.org/10.3390/s24134379

[14] Kumar, Y.; Kumar, P. Comparative Study of YOLOv8 and YOLO-NAS for Agriculture Application. In *Proc. 11th Int. Conf. Signal Process. Integr. Networks (SPIN)*; **2024**; pp 72–77. https://doi.org/10.1109/SPIN60856.2024.10511673

[15] Liu, Q.; Lv, J.; Zhang, C. MAE-YOLOv8-Based Small Object Detection of Green Crisp Plum in Real Complex Orchard Environments. *Comput. Electron. Agric.* **2024**, *226*, 109458. https://doi.org/10.1016/j.compag.2024.109458

[16] Huang, J.; Xia, X.; Diao, Z.; Li, X.; Zhao, S.; Zhang, J.; Zhang, B.; Li, G. A Lightweight Model for Weed Detection Based on the Improved YOLOv8s Network in Maize Fields. *Agronomy* **2024**, *14*(12), 3062. https://doi.org/10.3390/agronomy14123062

[17] Wang, X.; Girshick, R.; Gupta, A.; He, K. Non-Local Neural Networks. In *Proc. IEEE/CVF Conf. Comput. Vis. Pattern Recognit. (CVPR)*; **2018**; pp 7794–7803. https://doi.org/10.1109/CVPR.2018.00813

[18] Cao, Y.; Xu, J.; Lin, S.; Wei, F.; Hu, H. GCNet: Non-Local Networks Meet Squeeze-Excitation Networks and Beyond. In *Proc. IEEE/CVF Int. Conf. Comput. Vis. Workshops (ICCVW)*; **2019**; pp 1971–1980. https://doi.org/10.1109/ICCVW.2019.00246

[19] Ji, X.; Yue, Z.; Yang, H.; Li, M.; Han, H. SCAD-DETR: An Infrared Image Detection Method for Switchgear Equipment. *IEEE Internet Things J.* **2025**, in press. https://doi.org/10.1109/JIOT.2025.3571499

[20] Liu, J.; Yu, E.; Li, Y.; Zhao, Y.; Mao, B. YOLO-DCPG: A Lightweight Architecture with Dual-Channel Pooling Gated Attention for Intensive Small-Target Agricultural Pest Detection. *Front. Plant Sci.* **2025**, in press. https://doi.org/10.3389/fpls.2025.1716703

[21] Morbekar, A.; Parihar, A.; Jadhav, R. Crop Disease Detection Using YOLO. In *Proc. Int. Conf. Emerging Technol. (INCET)*; **2020**; pp 1–5. https://doi.org/10.1109/INCET49848.2020.9153986

[22] Marvin-DiPasquale, M.; Windham-Myers, L.; Agee, J. L.; Kakouros, E.; Kieu, L. H.; Fleck, J. A.; Alpers, C. N.; Stricker, C. A. Methylmercury Production in Sediment from Agricultural and Non-Agricultural Wetlands in the Yolo Bypass, California, USA. *Sci. Total Environ.* **2014**, *484*, 288–299. https://doi.org/10.1016/j.scitotenv.2013.09.098

[23] Guo, A.; Jia, Z.; Wang, J.; Zhou, G.; Ge, B.; Chen, W. A Lightweight Weed Detection Model with Global Contextual Joint Features. *Eng. Appl. Artif. Intell.* **2024**, *136*, 108903. https://doi.org/10.1016/j.engappai.2024.108903

[24] Alhawsawi, A. N.; Khan, S. D.; Rehman, F. U. Enhanced YOLOv8-Based Model with Context Enrichment Module for Crowd Counting in Complex Drone Imagery. *Remote Sens.* **2024**, *16*, 4175. https://doi.org/10.3390/rs16224175

[25] Liu, Y.; Shao, Z.; Hoffmann, N. Global Attention Mechanism: Retain Information to Enhance Channel–Spatial Interactions. *arXiv Preprint* **2021**, arXiv:2112.05561. https://doi.org/10.48550/arXiv.2112.05561

[26] Ni, Z.-Y.; Wang, J.-C. A Global Attention Mechanism-Based EfficientNet Model for Road Pavement-Type Identification. *Int. J. Comput. Intell. Syst.* **2025**, *18*, 1–18. https://doi.org/10.1007/s44196-025-00842-3

[27] Sun, X.; Wu, P.; Hoi, S. C. H. Face Detection Using Deep Learning: An Improved Faster R-CNN Approach. *Neurocomputing* **2018**, *299*, 42–50. https://doi.org/10.1016/j.neucom.2018.03.030

[28] Liu, W.; Anguelov, D.; Erhan, D.; Szegedy, C.; Reed, S.; Fu, C.-Y.; Berg, A. C. SSD: Single Shot Multibox Detector. In *Proc. Eur. Conf. Comput. Vis. (ECCV)*; **2016**; pp 21–37. https://doi.org/10.1007/978-3-319-46448-0_2

[29] Khanam, R.; Hussain, M. YOLOv11: An Overview of the Key Architectural Enhancements. *arXiv Preprint* **2024**, arXiv:2410.17725. https://doi.org/10.48550/arXiv.2410.17725

[30] Lai, Y. CBAM-Enhanced YOLOv8: An Attention-Based Approach for Tomato Disease Detection. In *Proc. 2nd Int. Symp. Agric. Eng. Biol. (ISAEB)*; **2025**; pp 337–346. https://doi.org/10.2991/978-94-6463-910-0_36

ASEAN
Journal of Scientific and Technological Reports
Online ISSN:2773-8752

Research article

Improving Drying Efficiency for Red Chili Peppers Using Ventilated Solar Technology

Tanawat Srirugsa[1, 3], Supachai Kaewpoung[1, 3], Wiwat Su-hren[1] , Kansinee Panwanitdumrong[2], and Tawat Chuchit[1, 3*]

[1] Faculty of Engineering, Thaksin University, Phatthalung, 93210, Thailand
[2] Faculty of Science and Fisheries Technology, Rajamangala University of Technology Srivijaya, Trang, 92150, Thailand
[3] Center of Excellence for Agricultural Innovation and Bioproducts of Thaksin University, Thaksin University, Phatthalung, 93210, Thailand
* Correspondence: tawat.c@tsu.ac.th

Citation:
Srirugsa, T., Kaewpoung, S., Su-hren, W., Panwanitdumrong, K., Chuchit, T., Improving drying efficiency for red chili peppers using ventilated solar technology. *ASEAN J. Sci. Tech. Report.* **2026**, *29*(4), e261032. https://doi.org/10.55164/ajstr.v29i4.261032

Article history:
Received: August 28, 2025
Revised: January 30, 2026
Accepted: February 7, 2026
Available online: March 24, 2026

Publisher's Note:
This article is published and distributed under the terms of the Thaksin University.

Abstract: This study compares three drying methods for Jinda red chili peppers: open sun drying (OSD), conventional solar drying (SD), and ventilated solar drying (VSD). Fresh chilies with an initial moisture content of 80% were dried to achieve the industry standard of ≤13.5% final moisture content. Temperature monitoring showed that SD reached the highest peak temperature (75°C), followed by VSD (56°C) and OSD (52°C). Significant differences in drying time were observed: VSD reached appropriate moisture levels in under 17 hours, SD in 34 hours, and OSD in 45 hours. Compared with the first day of SD and OSD, which had drying rates of 49.5% and 55.5%, respectively, VSD showed the highest drying rate, reducing the moisture content to 34.6%. By the second day, VSD had a moisture content of 12.5%, while SD and OSD retained 33.7% and 37.3%, respectively. The enhanced efficiency of VSD is attributed to the combined effects of elevated temperature and mechanical ventilation, which accelerated moisture removal despite the lower chamber temperature than in SD. While solar dryers require greater initial investment than traditional methods, they offer significant advantages in processing time, product quality, contamination prevention, and labor requirements, potentially yielding faster returns on investment. These findings suggest that VSD is optimal for commercial chili drying operations in Thailand's agricultural sector.

Keywords: Red chili peppers; sun drying; solar drying; drying rate

1. Introduction

Red chili peppers (Capsicum annuum L.) originated in Central and South America and have been used in culinary traditions for over 7,000 years. Their global dissemination, driven by European maritime trade networks in the sixteenth century, led to their introduction into Southeast Asia, including Thailand, during the Ayutthaya period, especially from the sixteenth century onward [1], [2]. This adoption significantly transformed Thai cuisine, establishing spiciness as a hallmark of its flavor profile and fostering widespread cultural and culinary integration. Today, chili peppers are a critical economic crop in Thailand, with annual production surpassing 200,000 metric tons, highlighting their agricultural and commercial significance. Domestic consumption accounts for the bulk of Thailand's red chili pepper utilization, with the surplus processed for export markets as dried chilies. There are 3 main uses of Red chili peppers: 1) Use as food. Most Thai food has chili as an ingredient, whether fresh, dried, or ground. 2) Use in the food industry, such as chili paste, curry paste, chili sauce, and canned fish. 3) Medical use because chili

contains Capsaicin, which is spicy and can be used as an ingredient in various oral and topical medicines, treating various pains such as colic, back pain, gout, paralysis, and rashes. Thailand's chili pepper industry is dominated by two main varieties: the highly pungent bird's eye chili (Capsicum frutescens L.) and the moderately spicy Jinda chili (Capsicum annuum L.), both widely cultivated in the Northeast, North, East, and Central regions. These red chili peppers are particularly favored in Thai markets for their vibrant color, which enhances their visual appeal in both fresh and dried forms. When dried, Jinda red chilies retain a crisp texture, easy grindability, and high seed content, making them ideal for culinary and industrial applications. Their dense structure, mild aroma, and rich pigmentation further enhance their commercial value, as they can be easily incorporated into various dishes without overpowering other flavors. These superior physicochemical properties explain why these cultivars remain staples in Thai cuisine and key agricultural exports. Thailand's chili pepper export market predominantly comprises dried products, accounting for approximately 50% of total exports with an annual value exceeding 4 billion THB (approximately 123 million USD). This variety's dominance in international markets stems from its reliable processing performance and alignment with global culinary standards for spice ingredients. The substantial export volume of dried Jinda red chili underscores Thailand's competitive advantage in value-added agricultural products within the global spice trade. Due to favorable climatic conditions and consistent sunlight exposure, Thailand predominantly relies on sun-drying for chili processing. However, this traditional method presents multiple challenges that compromise product quality. The open-air drying process requires human labor while remaining susceptible to environmental contaminants, including dust, rainfall, and animal intrusion. These uncontrolled conditions frequently lead to undesirable outcomes such as microbial contamination, inconsistent color, and reduced quality [3]. Solar drying technology has been increasingly adopted for chili processing in Thailand to overcome these limitations. This method produces higher-quality dried chilies than traditional sun-drying. For Jinda red chilies, the process successfully reduces moisture content from approximately 80% in fresh chilies to no more than 13.5% in the final dried product. The controlled conditions of solar drying help maintain product quality while addressing the challenges associated with conventional drying methods. Comparative studies have demonstrated significant differences in processing duration, with sun drying requiring approximately 40 hours versus 24 hours for oven drying to achieve optimal moisture reduction [4]. During nighttime or periods of insufficient sunlight, supplementary measures such as UV irradiation or auxiliary heating systems may be required to prevent mold growth in Jinda chili. However, these introduce additional capital and maintenance costs. A critical consideration in implementing such drying technologies is the production cost, as evidenced by the Khon Kaen Agricultural Engineering Research Center [5], which demonstrated that conventional drying cabinets require approximately 2 years to recover costs [6].

This study therefore focuses on comparing traditional sun drying with solar drying. These systems are selected due to their low initial investment requirements and operational simplicity for household and SME applications.

2. Materials and Methods

2.1 Jinda red chili peppers

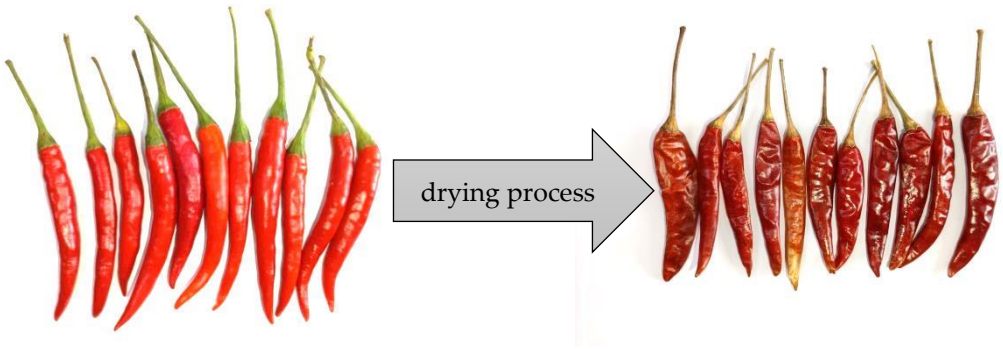


Figure 1. Jinda red chili peppers.

Jinda red chili peppers (Figure 1) were obtained from local markets for 55 THB/kg (approximately 1.7 USD/kg, based on a 32.5 THB/USD exchange rate). The initial moisture content was determined according to AOAC International standard methods [7]. Five replicate samples (200 g each) were dried in an oven maintained at 110 ± 2°C until constant weight was achieved (no further weight change was observed between consecutive measurements). The mean moisture content of fresh Jinda red chili peppers was 80.2% (wet basis). The wet basis moisture content (M_{wb}) can be calculated using equation 1 [4], [8], [9].

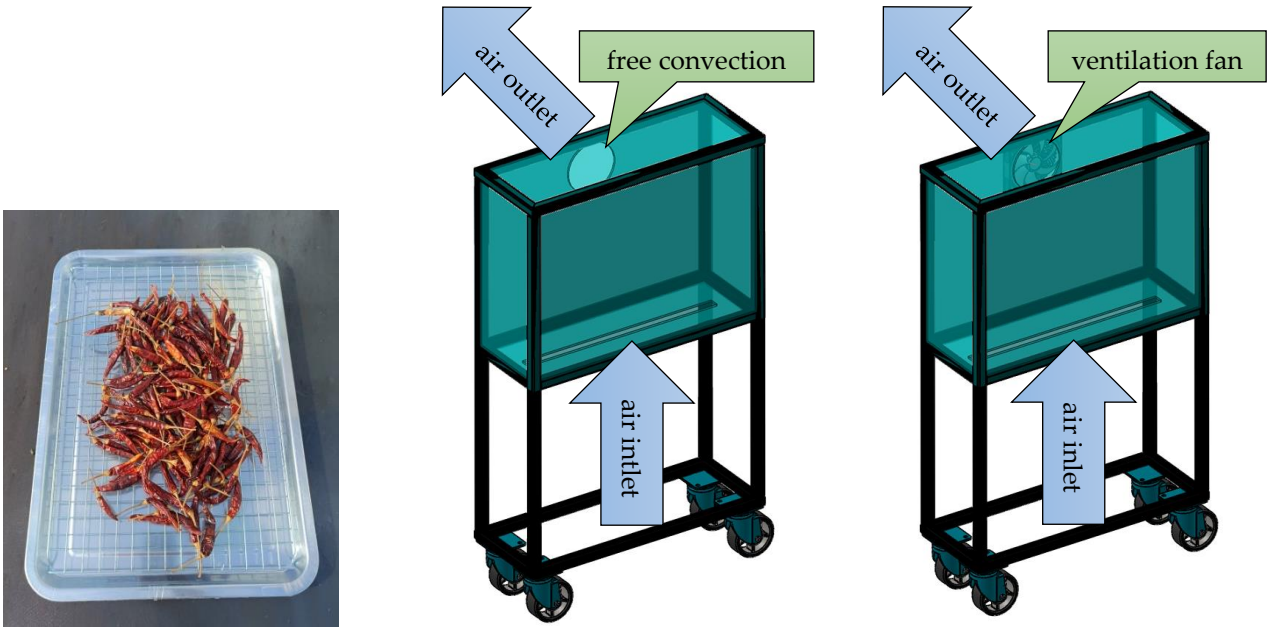
$$M_{wb} = \frac{M_w - M_d}{M_w} \times 100 \quad (1)$$

Where,

M_{wb} = the grain moisture content (wet basis)
M_w = the mass of the wet sample (g)
M_d = the mass of dry sample (g)

2.2 Solar dryer

The solar dryers employed in this study were classified into two distinct configurations based on their ventilation mechanisms: 1) a passive natural ventilation design and 2) an active forced ventilation system incorporating an electric fan. Both dryer types featured identical black-painted steel frames with dimensions of 800 mm (width) × 600 mm (length) × 600 mm (height) (shown in figure 2.1). The enclosures were fully insulated with polyurethane sheathing on all six surfaces. Airflow was facilitated through strategically positioned intake vents at the base of the drying chamber, with moist air being expelled through a rear exhaust port. In the forced-ventilation variant, an 8-inch, 10-blade axial fan (12V DC, 80W) was integrated to enhance convective heat transfer. Operational control was automated using a timer relay, maintaining consistent drying conditions daily from 07:00 to 18:00 to align with solar irradiation periods.



2(a) open sun drying (OSD) 2(b) solar dryer (SD) 2(c) ventilated solar dryer (VSD)

Figure 2. Three drying methods for Jinda red chili peppers.

2.3 Experiment

The study evaluated three drying methods: open-sun drying (OSD), a conventional solar dryer (SD), and a ventilated solar dryer (VSD). For each condition, 200 g of red chili peppers were placed on five mesh grids. Type K thermocouples (±1.5°C) were installed on the OSD sample surface and inside the SD/VSD chambers, with data recorded every 5 minutes using a data logger. Sample weight was measured hourly using an electronic balance (E-Scale KD-KC-1000, 1000 g capacity, ±0.1 g accuracy) until reaching approximately 13.5% (wet basis) moisture content. The experiment was repeated five times for each method. The wet basis moisture content (M_{wb}) can be calculated using equation 1.

2.4 Drying rate (D_R)

The drying rate (D_R) of water from Jinda res chili peppers is defined as the ratio of the weight loss of the material at a particular time interval to the difference in the time period. The drying rate (DR) of the sample was determined using equation 2 [10].

$$D_R = \frac{\Delta M}{\Delta t \times W_2} \tag{2}$$

Where,

D_R = drying rate (g water/g dry matter/h)
$\triangle M$ = weight loss at any time (g)
$\triangle t$ = time difference (hour)
W_2 = weight of sample after drying (g)

2.5 Drying efficiency (η)

System drying efficiency is defined as the ratio of the energy required for moisture evaporation to the heat supplied to the dryer. For solar collectors, this refers to incident solar radiation; for forced-convection dryers, the energy consumed by the fan or blower must also be included in the VSD condition [10], [11].

$$\eta = \frac{Q_{THD}}{Q_{SA} + Q_{EF}} \times 100 \tag{3}$$

Where,

Q_{THD} = total quantity of heat utilized for drying (J)
= $[M \times C_P \times (T_d - T_a)] + [M_W \times \lambda]$
Q_{SA} = heat from solar energy (J)
= $A \times I \times t$
Q_{EF} = electric fan energy (J)
= $W \times s$
M = mass of the product (kg)
C_P = specific heat of wet product (kJ/kg °K)
T_d = temperature of the drying air (°K)
T_a = temperature of the inlet/ambient air (°K)
W_W = mass of water to be removed during drying (kg)
λ = latent heat of vaporization of water (kJ/kg)
η = efficiency of the drying system
A = collector area (m^2)
I = solar insolation (W/m^2)
T = time for which dryer is exposed to solar radiation (s)
W = watt of ventilation system (W)
s = second (s)

3. Results and Discussion

3.1 Temperature profiles across different drying methods

The temperature profiles for the three drying methods—open sun drying (OSD), conventional solar drying (SD), and ventilated solar drying (VSD)—exhibited distinct patterns throughout the daily drying cycle, as shown in Table 1. In all three conditions, temperatures began rising at approximately 8:00, reaching their respective peaks at 13:00, and subsequently declining toward the initial values by 18:00. The SD method consistently demonstrated the highest temperature readings, reaching a maximum of 75°C at 13:00. This elevated temperature can be attributed to the greenhouse effect created within the enclosed drying chamber, where solar radiation is trapped. Heat accumulation occurs due to limited air exchange [4]. The VSD method achieved a moderate peak temperature of 56°C, while OSD recorded the lowest maximum temperature at 52°C. Interestingly, although it had lower peak temperatures than SD, the VSD method demonstrated superior drying efficiency. This phenomenon aligns with findings from [4], who noted that effective moisture removal is influenced by temperature and air circulation rates. Integrating a fan in the VSD setup facilitated continuous moisture evacuation from the drying chamber, preventing humidity saturation that would otherwise impede evaporation. The temperature differential between the drying methods directly impacts the moisture migration rate from the product interior to the surface. Previous research has shown that, in many applications, the temperature inside a solar drying chamber is typically 20-25°C higher than the ambient temperature [12]. Our findings showed a narrower gap of approximately 23°C between the SD and OSD methods at peak conditions, within the expected range for subtropical climates. The optimal drying temperature range for red chili peppers is generally 45-60°C [6]. Temperatures below this range prolong drying time, potentially allowing microbial growth, while temperatures above 60°C may cause case hardening and undesirable color changes. The SD and VSD methods maintained temperatures within or above this optimal range for 5-7 hours daily, whereas the OSD method only briefly reached the lower threshold of this range during peak sunlight hours (shown in Table 1 and Figure 3).

Table 1. Temperature Comparison Across Drying Methods

Time (hr)	Open Sun Drying (OSD) Temperature (°C)	Solar Drying (SD) Temperature (°C)	Ventilated Solar Drying (VSD) Temperature (°C)
7:00	25	25	25
8:00	32	35	33
9:00	35	45	40
10:00	38	53	45
11:00	42	62	48
12:00	45	70	51
13:00	**52**	**75**	**56**
14:00	49	72	52
15:00	46	65	49
16:00	45	56	45
17:00	39	45	40
18:00	35	38	37

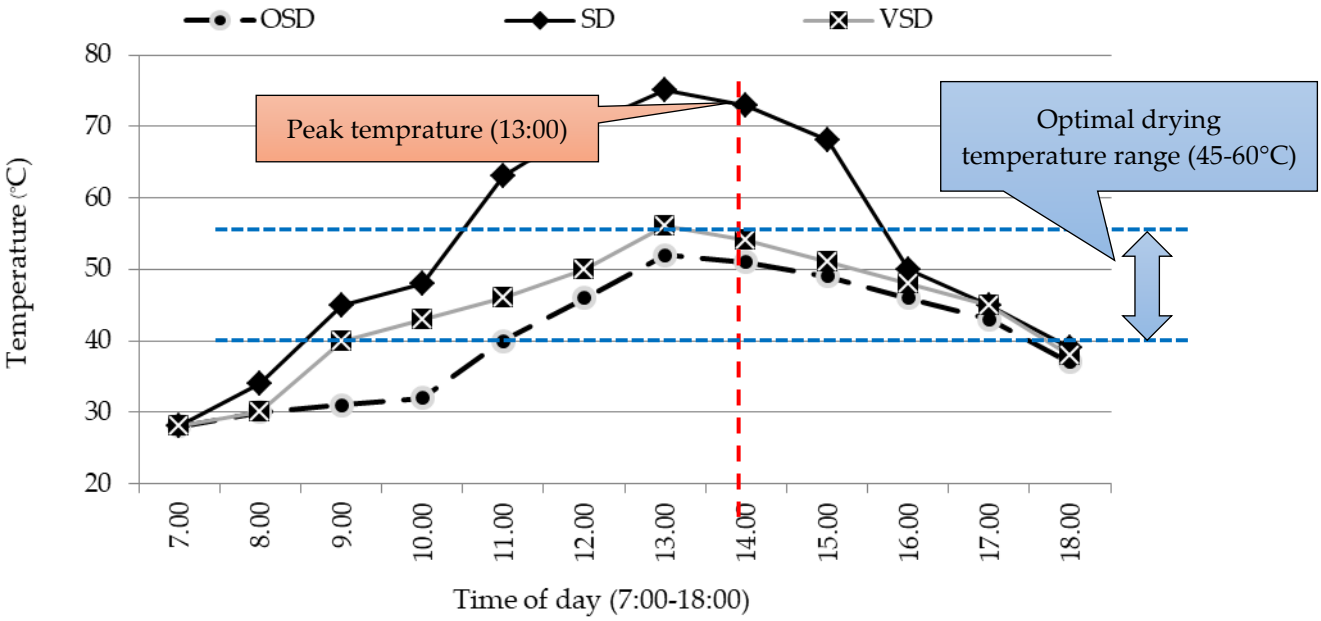


Figure 3. Comparison of temperature profiles for Open Sun Drying (OSD), Solar Drying (SD), and Ventilated Solar Drying (VSD) methods over a 12-hour drying period.

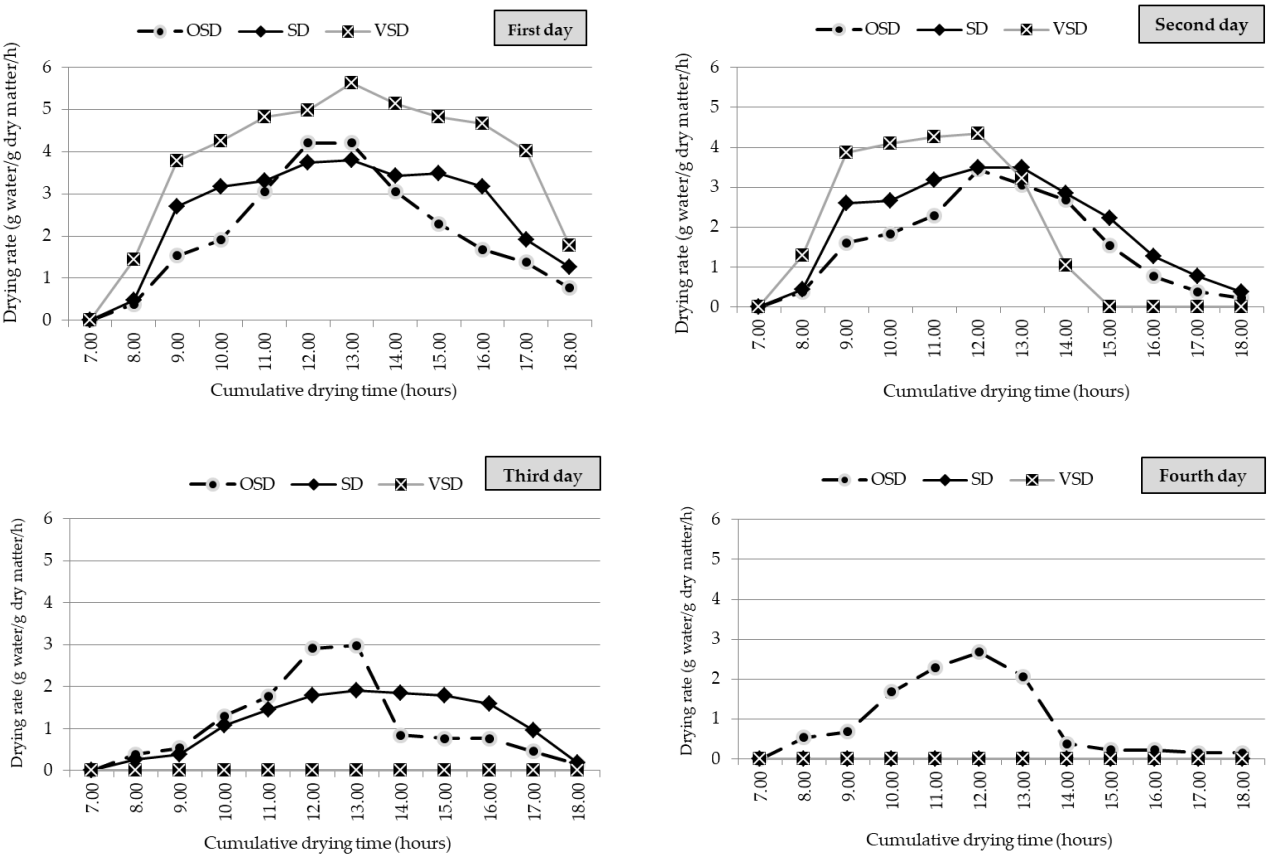


Figure 4. Drying rates for Open Sun Drying (OSD), Solar Drying (SD), and Ventilated Solar Drying (VSD) methods.

3.2 Drying rates and moisture reduction patterns

Analysis of drying kinetics across the three methods revealed significant differences in moisture reduction rates, as illustrated in Figure 4. The ventilated solar drying (VSD) method consistently outperformed, achieving the industry-standard moisture content of <13.5% in just 17 hours. This was followed by conventional solar drying (SD) at 34 hours and open sun drying (OSD) at 45 hours. During the initial drying phase (0-6 hours), all three methods exhibited their highest drying rates, with VSD at 5.6 g water/g dry matter/h, SD at 3.8 g water/g dry matter/h, and OSD at 4.2 g water/g dry matter/h. The initial drying process is characterized by a rapid, constant-rate evaporation phase, followed by a decreasing, falling-rate evaporation phase [13]. The higher initial drying rate in VSD can be attributed to the combined effect of elevated temperature and forced convection, which enhances mass transfer coefficients at the product surface. As drying progressed (6-20 hours), all methods exhibited a characteristic decline in drying rates, entering the falling-rate period [8]. However, VSD maintained significantly higher rates throughout this period, with values approximately 1.5-2 times those of SD and 3-4 times those of OSD. Ventilation drying systems sustain a higher drying rate during the falling-rate period by continuously removing humidified air from the drying chamber. [4]. The moisture content reduction followed an expected exponential decay pattern across all methods. After the first day (12 hours of active drying), VSD reduced the moisture content from 80% to 34.6%, while SD and OSD achieved reductions to 49.5% and 55.5%, respectively (shown in Table 2). This differential performance became more pronounced on the second day, with VSD reaching the target moisture content by hour 17, while SD required an additional 17 hours and OSD needed 28 more hours beyond that point. The superior performance of VSD, despite its lower peak temperature compared to SD (as discussed in Section 3.1), aligns with the findings of Selvaraja et al. [14], suggesting that effective moisture removal in agricultural products depends more on the combination of moderate heat and adequate ventilation than on temperature alone. The fan in the VSD system created a pressure differential that facilitated vapor-pressure-driven moisture migration from the interior of the chili peppers to the surface and, subsequently, to the surrounding air. Interestingly, during the final stages of drying (moisture content <20%), the OSD method demonstrated a slight increase in drying rate (hours 40-45). This phenomenon, also observed by [15], may be attributed to the direct exposure of the product to solar radiation, which becomes more impactful when the moisture content is low and internal resistance to moisture migration is the limiting factor.

Table 2. Daily Moisture Content Reduction Across Drying Methods

Day	Time	Moisture Content (%)		
		OSD	**SD**	**VSD**
1	7:00	80.0	80.0	80.0
1	13:00	64.7	62.8	55.1
1	18:00	55.5	49.5	34.6
2	7:00	55.5	49.5	34.6
2	13:00	42.9	32.1	13.6
2	18:00	37.3	33.7	12.5 [Complete]
3	7:00	37.3	26.2	[Complete]
3	13:00	27.4	19.3	[Complete]
3	18:00	24.5	13.0 [Complete]	[Complete]
4	7:00	24.5	[Complete]	[Complete]
4	13:00	14.5	[Complete]	[Complete]
4	18:00	13.4 [Complete]	[Complete]	[Complete]

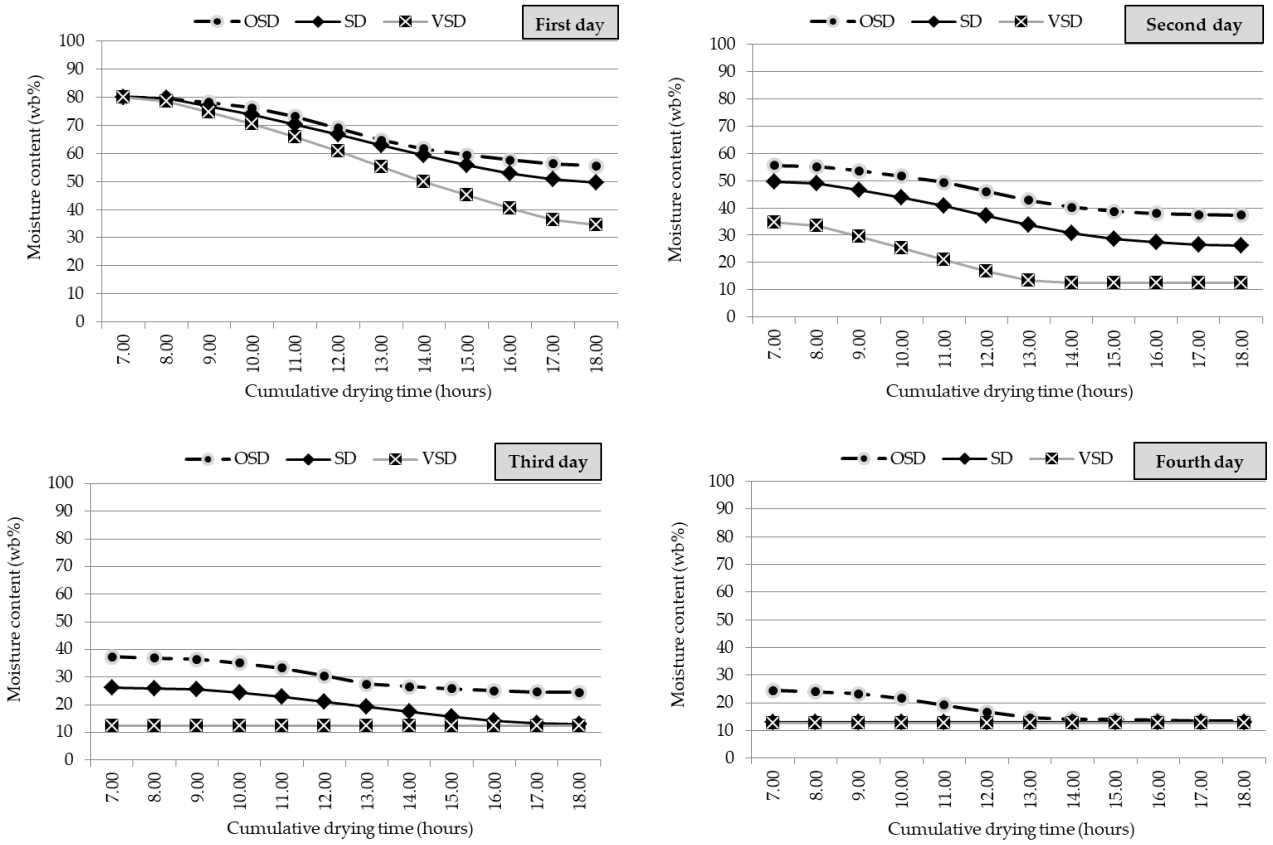


Figure 5. Moisture content reduction for Open Sun Drying (OSD), Solar Drying (SD), and Ventilated Solar Drying (VSD) methods

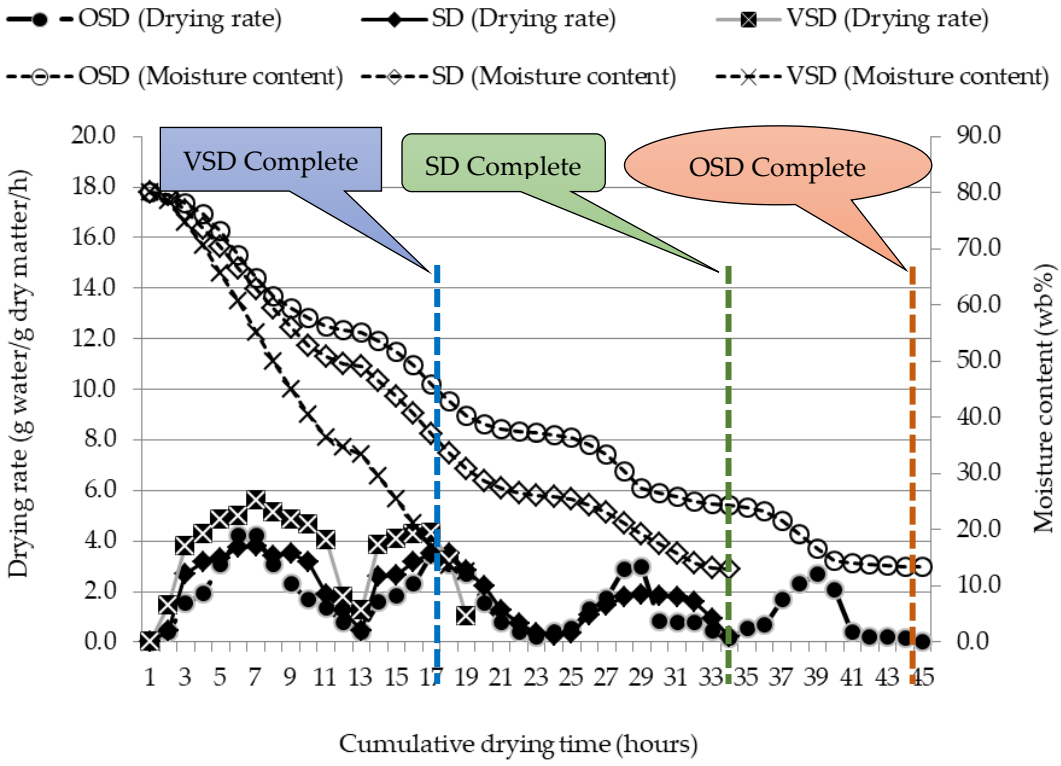


Figure 6. Drying rate and moisture content comparison across methods

3.3 Comparison of drying duration (45 hours for OSD, 34 hours for SD, 17 hours for VSD)

The total drying duration required to reach the industry-standard moisture content of <13.5% varied significantly across the three methods, as illustrated in Figure 3. Ventilated solar drying (VSD) demonstrated superior efficiency, requiring only 17 hours of active drying spread across two days. The conventional solar drying (SD) method required 34 hours (three days), while open-sun drying (OSD) required 45 hours (four days) to achieve comparable results. The reduced drying time for VSD represents a 50% improvement over SD and a 62% improvement over OSD. This substantial time reduction aligns with findings from [8], who reported 30-50% time savings when comparing ventilated solar drying systems to conventional methods for Capsicum annuum. The efficiency advantage of VSD (41.6%) over SD (22.7%) and OSD (17.0%) further demonstrates the effectiveness of forced convection in accelerating drying. The combination of moderate heating and forced air circulation creates an optimal environment for dehumidification by sustaining a favorable vapor pressure gradient between the product and the surrounding air [16]. This principle explains VSD's superior performance despite its lower peak temperature than SD. While SD reached higher temperatures (75°C vs. 56°C), the absence of forced air circulation resulted in localized humidity saturation, creating a barrier to further moisture removal. The practical implications of these duration differences are significant for commercial operations. Reducing the drying time directly enhances productivity, minimizes labor costs, and mitigates the risk of product spoilage [17]. Based on the estimated labor hours required for each method (16, 12, and 8 hours for OSD, SD, and VSD, respectively), VSD offers substantial operational advantages despite the additional energy consumption for fan operation (80 Wh). The economic impact of these efficiency differences is particularly relevant for Thailand's chili processing industry, which handles approximately 200,000 metric tons annually [18], [19]. Khon Kaen Agricultural Engineering Research Center [5] estimated that upgrading from traditional drying methods to more efficient technologies could reduce processing costs by 25-30% while improving product quality and consistency. Our findings suggest that implementing VSD systems would yield returns on investment within approximately two harvesting seasons for medium-scale operations, primarily through labor savings and increased processing capacity. Interestingly, the relationship between drying method sophistication and efficiency appears nearly linear (Figure 3), suggesting that incremental improvements to the drying system produce proportional benefits in processing time. This trend corresponds with observations from [6], who noted that technological enhancements in agricultural processing systems typically yield diminishing returns after reaching certain efficiency thresholds.

Table 3. Performance Comparison of Different Drying Methods for Red Chili Peppers

Parameter	OSD	SD	VSD
Total drying time (hours)	45	34	17
Days required	4	3	2
Peak temperature (°C)	52	75	56
Average drying rate (g water/g dry matter/h)	1.5	2.0	3.7
Energy consumption (fan) (Wh)	0	0	80
Estimated labor hours	16	12	8
Final moisture content (%)	13.4	13.0	12.5

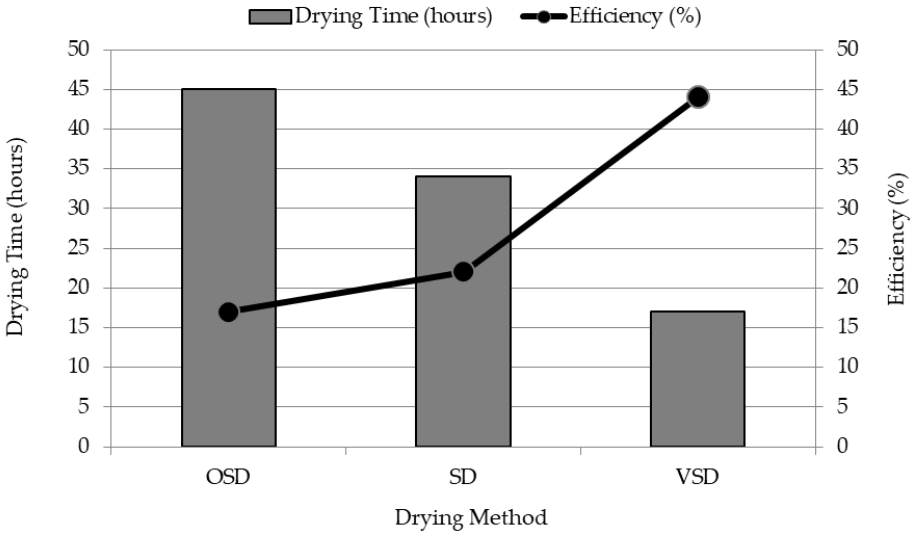


Figure 7. Comparative drying time and efficiency

4. Economic and Practical Implications

The initial capital investment required for each drying method varies considerably, with important implications for adoption by small-scale farmers and processors. As shown in Table 4, open sun drying (OSD) requires minimal equipment investment (approximately 500 THB or 15.4 USD), consisting primarily of drying mats and basic handling tools. Although sun drying has a lower initial cost, it entails significant disadvantages, notably extensive space requirements and the risk of weather dependence and product contamination. These drawbacks can lead to hidden costs, such as increased labor expenses or product loss [15]. The conventional solar dryer (SD) requires a moderate investment of approximately 5,500 THB (169.3 USD), primarily for construction materials, including the frame structure, transparent covering, and insulation. According to the Khon Kaen Agricultural Engineering Research Center [5], such systems can be constructed using locally available materials, reducing costs while significantly improving upon traditional methods. The design simplicity allows for local fabrication and maintenance, an essential consideration for rural implementation [4]. The ventilated solar dryer (VSD) has the highest initial investment at approximately 8,500 THB (261.6 USD), with additional costs for the fan, controller components, and electrical integration. Despite representing a 42% higher investment than conventional solar dryers, the components contribute significantly to increased efficiency and reliability [14]. Modular design enables manufacturers to begin with a basic solar drying system. To achieve higher efficiency, the system's ventilation must be enhanced, often by adding appropriately sized ventilation fans to the drying chamber [6].

Labor requirements account for a significant portion of operational costs in agricultural processing, particularly for labor-intensive crops such as chili peppers. For a standard 10 kg batch of fresh red chili peppers, our analysis indicated labor requirements of 23, 17, and 9 hours for OSD, SD, and VSD methods, respectively. These differences translate directly to operational costs, with labor expenses of 1,044 THB (32.2 USD), 696 THB (21.4 USD), and 348 THB (10.7 USD) per batch based on current agricultural wages in Thailand. Beyond direct labor costs, several operational efficiency factors favor advanced drying systems. Specifically, the VSD method demonstrated the lowest spoilage rate at 3%, compared to 5% for SD and 12% for OSD, representing significant product conservation [17]. The reduction in product spoilage in a controlled drying environment is attributed to consistent moisture removal and minimal exposure to environmental contaminants [12]. The processing capacity also varied substantially, with monthly throughput potential of 70 kg, 100 kg, and 150 kg for OSD, SD, and VSD, respectively. This increased production capacity enables processors to manage seasonal harvest volumes more efficiently, thereby reducing post-harvest losses that often occur when existing capacity limits are exceeded [18]. Furthermore, improvements in product quality consistency associated with controlled drying conditions often command premium pricing in domestic and export markets [16].

Despite higher initial investments in solar drying technologies, their economic advantages become evident through return-on-investment analysis. Based on operational savings relative to traditional methods, the payback periods for SD and VSD systems were calculated at 4.5 and 2.5 months, respectively, assuming consistent production volumes. These remarkably short payback periods align with observations from [13], who reported rapid investment recovery for solar drying technologies applied to high-value agricultural products. The annual return on investment percentages of 46.6% for SD and 74.6% for VSD underscore the exceptional economic efficiency of these technologies. These returns primarily derive from reduced labor costs, increased processing capacity, and improved product quality. Cooperative operations could further reduce individual investment burdens while simultaneously maintaining access to improved processing capacity [15]. Beyond direct financial returns, several long-term economic benefits favor advanced drying systems that are not captured in traditional ROI calculations, notably reduced dependency on favorable weather, enhanced production scheduling, and improved market access via consistent product quality [20]. These factors contribute to business resilience and sustainability, essential considerations in Thailand's increasingly variable climate conditions.

Table 4. Economic Comparison of Red Chili Pepper Drying Methods

Parameter	OSD	SD	VSD
Initial Investment			
Equipment cost (THB)	500	5,500	8,500
Set up labor (hours)	4	8	10
Estimated useful life (years)	1	5	5
Operational Costs			
Labor hours per 10 kg batch	23	17	9
Labor cost per batch (THB)	1,044	696	348
Energy cost per batch (THB/month)	0	0	5
Spoilage rate (%)	12	5	3
Production Capacity			
Batches per month	7	10	15
Processing capacity (kg/month)	70	100	150
Product quality consistency	Low	Medium	High
Financial Analysis			
Monthly operational savings vs. OSD (THB)	-	1,260	3,360
Payback period (months)	-	4.5	2.5
Annual return on investment (%)	-	46.6	74.6

4. Conclusions

This study evaluated the performance of three drying methods for Jinda red chili peppers: open sun drying (OSD), conventional solar drying (SD), and ventilated solar drying (VSD). The findings revealed substantial differences in efficiency, with drying durations of 45, 34, and 17 hours for OSD, SD, and VSD, respectively, all achieving the industry-standard final moisture content below 13.5%. The superior performance of VSD can be attributed to the synergistic effect of elevated temperature and forced air circulation, which maintained optimal drying conditions throughout the process. While SD achieved higher peak temperatures (75°C versus 56°C for VSD), the absence of mechanical ventilation led to humidity saturation in the drying chamber, limiting moisture removal rates. Conversely, the fan in the VSD system continuously evacuated moisture-laden air, sustaining favorable vapor pressure gradients despite lower operating temperatures. Temperature profiles and drying rates demonstrated distinct patterns across all

methods, with the highest drying rates occurring during the initial 6-8 hours, followed by a characteristic falling-rate period. The VSD method maintained significantly higher drying rates throughout all phases, achieving complete drying in 2 days compared to 3 and 4 days for SD and OSD, respectively. Economic analysis revealed compelling advantages of advanced drying technologies despite higher initial investment costs. The VSD system offered substantial labor savings, reduced processing time, lower spoilage rates, and increased throughput capacity, which resulted in a remarkably short payback period of less than one month under typical production conditions. These economic benefits make VSD particularly appealing for small-scale producers and SMEs seeking to improve production efficiency and product quality. Beyond economic considerations, the controlled environment of solar drying systems mitigates contamination risks and weather dependencies inherent in traditional methods. For Thailand's chili production sector, widespread adoption of improved drying technologies could significantly enhance processing capacity, product quality, and market competitiveness while reducing post-harvest losses. Future research should explore optimizing ventilation parameters, integrating renewable energy sources for fan operation, and scaling up for commercial implementation.

5. Acknowledgements

We are grateful to the Faculty of Engineering, Thaksin University, Phatthalung Campus, for allowing the use of the location for this research experiment.

Author Contributions: The following are the contributions of each author in this research: Conceptualization: Tanawat Srirugsa and Tawat Chuchit; Methodology: Tanawat Srirugsa and Kansinee Panwanitdumrong; Software: Wiwat Su-hren and Supachai Kaewpoung; Writing—review and editing: Tawat Chuchit and Wiwat Su-hren; Project administration: Tanawat Srirugsa.

Funding: This research received no external funding.

Conflicts of Interest: The authors of this study hereby state that they have no conflicts of interest.

References

[1] Anderson, H. A. *Chillies: A Global History*; Reaktion Books: London, 2016.

[2] Andrews, J. *The Pepper Trail: History & Recipes from around the World*; 1999.

[3] Hasan, M. U.; Malik, A. U.; Ali, S.; Imtiaz, A.; Munir, A.; Amjad, W.; Anwar, R. Modern Drying Techniques in Fruits and Vegetables to Overcome Postharvest Losses: A Review. *J. Food Process. Preserv.* **2019**, *43* (12), e14280. https://doi.org/10.1111/jfpp.14280

[4] Wongbubpa, N.; Treeamnuk, K.; Treeamnuk, T. Influence of Drying Air Velocity Characteristics on Paddy Drying. *RMUTP Res. J.* **2022**, *16*, 165–176.

[5] Research Center. *Research and Development of Technology and Machines for Chili*; Department of Agriculture, Ministry of Agriculture and Cooperatives: Khon Kaen, Thailand, 2009.

[6] Cruz-Domínguez, O.; Carrera-Escobedo, J. L.; Guzman-Valdivia, C. H.; Ortiz-Rivera, A.; García-Ruiz, M.; Duran-Muñoz, H. A.; Vidales-Basurto, C. A.; Castaño, V. M. A Novel Method for Dried Chili Pepper Classification Using Artificial Intelligence. *J. Agric. Food Res.* **2021**, *3*, 100099. https://doi.org/10.1016/j.jafr.2021.100099

[7] AOAC International. *Official Methods of Analysis of AOAC International*, 17th ed.; AOAC International: Gaithersburg, MD, 2000.

[8] Fudholi, A.; Othman, M. Y.; Ruslan, M. H.; Sopian, K. Drying of Malaysian *Capsicum annuum* L. (Red Chili) Dried by Open and Solar Drying. *Int. J. Photoenergy* **2013**, *2013*, 167895. https://doi.org/10.1155/2013/167895

[9] Benyoucef, M.; Panigrahi, S. S. Fluidization-Bed Drying and Microwave Radiation Effects on Drying Rate, Fatty Acid, Protein and Germination of Rapeseed. *J. Food Compos. Anal.* **2025**, *142*, 107562. https://doi.org/10.1016/j.jfca.2025.107562

[10] Jain, R.; Paul, A. S.; Sharma, D.; Panwar, N. L. Enhancement in Thermal Performance of Solar Dryer through Conduction Mode for Drying of Agricultural Produces. *Energy Nexus* **2023**, *9*, 100182. https://doi.org/10.1016/j.nexus.2023.100182

[11] Korbuakaew, K.; Phoosomma, P. The Approach for Boosting the Drying Chamber's Temperature by Pulse Copper Pipes to Conduct Heat. *ASEAN J. Sci. Technol. Rep.* **2025**, *28* (3), e254983. https://doi.org/10.55164/ajstr.v28i3.254983

[12] Meghwar, B. L.; Khan, A.; Lakhiar, I. A.; Mirani, A. A.; Daper, M. S.; Kalroo, M. W. Comparison between Solar Tunnel, Solar-Cum Gas Dryer, and Open Sun Drying Methods for Drying Red Chilies. *Pak. J. Agric. Res.* **2023**, *36*, 63–70. https://doi.org/10.17582/journal.pjar/2022/36.1.63.70

[13] Nimrothama, C.; Songprakorpa, R.; Thepa, S.; Monyakul, V. Experimental Research of Drying Red Chili by Two Methods: Solar Drying and Low-Temperature System Drying. *Energy Procedia* **2017**, *138*, 512–517. https://doi.org/10.1016/j.egypro.2017.10.237

[14] Selvaraja, M.; Sadagopan, P.; Vijayan, S. Investigation of the Thermal Performance of an Indirect Forced Convection Solar Dryer for Tapioca Chips Drying. *Desalin. Water Treat.* **2021**, *230*, 430–441. https://doi.org/10.5004/dwt.2021.27214

[15] Jeentada, W.; Niyomvas, B.; Thailul, A. Experimental Study on Drying Conditions of Solar Fish Dryer with Temperature Controlled by Open–Closed Ventilation System. *J. KMITNB* **2018**, *28*, 525–536.

[16] Dussan, E. D.; Uribe, J. R.; Banout, J. Design and Evaluation of a Hybrid Solar Dryer for Postharvesting Processing of Parchment Coffee. *Renew. Energy* **2023**, *215*, 118961. https://doi.org/10.1016/j.renene.2023.118961

[17] Krabch, H.; Tadili, R.; Idrissi, A. Design, Realization and Comparison of Three Passive Solar Dryers: Orange Drying Application for the Rabat Site (Morocco). *Results Eng.* **2022**, *15*, 100532. https://doi.org/10.1016/j.rineng.2022.100532

[18] Purika, S.; Aunaudomvana, N.; Panyoyai, N. Pretreatment Techniques of Dehydrated Red Spur Chilli Peppers for Compliant Thai Agricultural and Community Food Standards. *Sci. Technol. Community* **2023**, *1*, 1–18.

[19] Lakshmi, D. V. N.; Palanisamy, M. Design and Development of Mixed Mode Forced Convection Solar Dryer for Drying of *Curcuma zedoaria*. In *Proc. Int. Conf. Therm. Eng. (ICTEA)*; **2019**.

[20] Nukulwar, M. R.; Tungikar, V. B. A Review on Performance Evaluation of Solar Dryer and Its Material for Drying Agricultural Products. *Mater. Today: Proc.* **2021**, *46*, 345–349. https://doi.org/10.1016/j.matpr.2020.08.354

ASEAN
Journal of Scientific and Technological Reports
Online ISSN:2773-8752

Research article

Technology Transfer Assessment of Amino Acid Block Fertilizer Production from Salted Egg White Waste for Coconut Farming in Paktrae, Songkhla Province

Saowanee Lekbangpong[1*], Prisana Wonglom[1], Niramol Juntarachat[2], and Thidarat Juthong[3]

[1] Faculty of Agriculture, Thaksin University, Phatthalung, 93210, Thailand
[2] Faculty of Engineering, Thaksin University, Phatthalung, 93210, Thailand
[3] Faculty of Agro and Bio Industry, Thaksin University, Phatthalung, 93210, Thailand
* Correspondence: saowanee.l@tsu.ac.th

Citation:
Lekbangpong, S. ; Wonglom, P.; Juntarachat, N.; Juthong, T. Technology transfer assessment of amino acid block fertilizer production from salted egg white waste for coconut farming in paktrae, Songkhla Province. *ASEAN J. Sci. Tech. Report.* **2026**, *29*(4) , e261099. https://doi.org/10.55164/ajstr.v29i4.261099

Article history:
Received: September 1, 2025
Revised: January 23, 2026
Accepted: February 7, 2026
Available online: March 24, 2026

Publisher's Note:
This article is published and distributed under the terms of the Thaksin University.

Abstract: This study aimed to investigate farmers' knowledge of Good Manufacturing Practice (GMP)-compliant production of salted egg products, evaluate the technology transfer process, and assess user satisfaction with the application of amino acid block fertilizer derived from salted egg white waste for coconut cultivation. The study sample comprised 25 salted egg producers from Paktrae Subdistrict, Ranot District, Songkhla Province, Thailand. Data were collected using structured questionnaires and analyzed using descriptive statistics, including percentages, mean, and standard deviation, as well as a paired t-test. The results indicated that before the technology transfer, farmers exhibited a low level of knowledge, with a mean score of 5. After the technology transfer, knowledge increased significantly, with a mean score of 14, and the difference was statistically significant at the 0.01 level. The technology transfer process for amino acid block production from salted egg white waste was implemented through a participatory approach, including GMP training, technology introduction, hands-on practice, participatory discussions on product labeling, and the development **of** user manuals and infographic-based labels. Overall satisfaction with the technology transfer was at the highest level, with a mean score of 4.30. The highest satisfaction ratings were associated with lecturers (4.66), staff services (4.65), and knowledge and understanding gained from the training (4.48), followed by knowledge application (4.32) and training location (4.15). These findings suggest that participatory technology transfer can effectively enhance farmers' knowledge and satisfaction. Continuous monitoring and sustained technology support are recommended to ensure effective adoption and long-term utilization of the transferred technology among target communities.

Keywords: Evaluation; technology transfer; satisfaction; amino acid block fertilizer

1. Introduction

Technology transfer is essential for applying scientific knowledge and innovation in practical contexts, particularly in agriculture. It supports the adoption of appropriate technologies that enhance productivity, add value to local resources, and promote sustainable community development [1]. Effective technology transfer requires clear communication from the knowledge provider to the recipient. Currently, agriculture places great importance on technology to improve efficiency, and technology plays a significant role in Thailand's

agricultural sector [2]. The application of knowledge and technology resulting from research serves as a catalyst for community development by fostering management innovations that solve local problems and promote change through an area-based approach. This empowers local communities to create sustainable livelihoods and incomes, thereby enhancing the stability of the grassroots economy and improving quality of life, which is a key component of national development in response to ongoing societal changes [3].

The Paktrae Salted Egg Production Group, located in Paktrae Subdistrict, Ranot District, Songkhla Province, produces salted eggs using free-range duck eggs. These ducks are raised on rice farms in the Ranot District and surrounding areas. Their products include salted eggs and salted egg yolks, with the latter especially popular for its versatility in a variety of dishes, both sweet and savory, such as Chinese pastries, mooncakes, bun fillings, and spicy salads served in restaurants. Salted egg yolks are produced by separating the yolks from eggs that have been cured in salt for 21 days, then vacuum-sealing them in bags. With its 10 members, the group has a production capacity of 45,000 salted eggs and salted egg yolks per month, which does not fully meet current market demand. The production process generates by-products, including approximately 2,250 kilograms of eggshells and 13,500 kilograms of salted egg whites each month. Initially, the group managed this waste by producing a fermented liquid, mixing eggshells with soil, and selling the resulting material as a raw ingredient for animal feed. However, more than 70% of the salted egg whites and eggshells remained unused, leading to unpleasant odors. These materials still hold potential for value creation, particularly through the development of processes that utilize salted egg whites.

Salted eggs are widely used as ingredients in food processing, particularly in bakery and confectionery products, where only the egg yolk is typically utilized. As a result, substantial quantities of by-products, including salted egg shells and salted egg whites, are generated and often discarded into the environment. However, these by-products possess potential value, as both egg shells and egg whites contain nutrients and minerals beneficial to plant growth. Therefore, they can be reutilized by incorporating them with other agricultural residues to produce organic fertilizers. This approach represents an effective strategy for waste valorization, contributing to environmental sustainability and the efficient use of resources. The production of amino acid block fertilizer from salted egg white waste represents an innovative approach that supports sustainable agriculture and the circular economy. Salted egg white is a by-product of the food processing industry that is often discarded in large quantities, potentially causing environmental pollution due to its high organic content. Transforming this waste into value-added fertilizer not only reduces environmental burdens but also promotes efficient resource utilization [4].

Amino acids play a crucial role in plant growth and development, as they are directly involved in protein synthesis, enzyme activation, and metabolic processes. The application of amino acid–based fertilizers has been reported to enhance nutrient uptake, stimulate root development, and improve plant tolerance to abiotic stresses such as salinity and drought [5]. These properties are particularly important for perennial crops that require continuous nutrient availability. Coconut is an economically important crop that requires adequate, balanced nutrition to support vegetative growth, flowering, and fruit development. The use of amino acid block fertilizer can provide a slow-release source of organic nutrients, improving fertilizer use efficiency and supporting sustained growth in coconut plantations. Moreover, amino acids can act as chelating agents, facilitating the absorption of essential nutrients and enhancing overall plant productivity [6].

Community-based participatory technology transfer is a learning process that emphasizes the active involvement of recipients through hands-on practice, experience sharing, and collaborative learning between technology providers and the community. This approach enhances understanding and enables the appropriate application of technology within the local context, increasing the likelihood of technology adoption, bridging the gap between academic knowledge and practical use, and strengthening community self-reliance [7]. Based on the above, the researchers recognize the importance of knowledge related to the production of salted egg products under GMP standards, as well as the transfer of amino acid block technology derived from salted egg white waste for application in coconut production. This is essential for the development and advancement of the Paktrae salted egg group and its network.

The objectives of the study were to investigate the level of knowledge related to GMP-compliant salted egg production, evaluate the technology transfer process, and assess satisfaction with the transfer of amino

block technology for use in coconut production. The results of this study can serve as guidelines for developing knowledge-based groups and networks. They also provide a framework for creating alternative careers and additional sources of income to help address poverty among farmers in a manner that is both appropriate and aligned with established standards. Furthermore, the findings can support the expansion of knowledge transfer to other farmer groups.

2. Materials and Methods

Study area

Salted egg farmers in Paktrae, Ranot District, Songkhla Province, are registered under the Paktrae Group as producers of OTOP salted egg products. The group comprises 25 members, including local farmers and unemployed individuals who are interested in increasing their income in Paktrae Subdistrict. Therefore, purposive sampling was applied to include all members of the group, ensuring a comprehensive representation of the community's problems and potential. Data collection and statistical analyses. This study was reviewed and approved by the Institutional Ethics Committee. All participants were informed about the objectives, procedures, potential benefits, and possible risks of the study, and written informed consent was obtained before participation.

Data collection.

This study employed a structured questionnaire to gather data on the transfer of amino acid block fertilizer production from salted egg white waste for coconut farming, divided into five parts, as follows:

Part 1: Basic farmer information.

Part 2: Assessment of knowledge on GMP-compliant production of Paktrae salted eggs in Paktrae Subdistrict, Songkhla Province, conducted before and after the technology transfer. The assessment consisted of closed-ended questions with four response options (A, B, C, and D). Each correct answer was scored as 1 point, while incorrect answers received 0 points. The mean knowledge scores were interpreted using a three-level criterion, as follows:

A score of 5 or fewer points indicates a low level of knowledge.

A score of 6–10 points indicates a moderate level of knowledge.

A score of 11–15 points represents a high level of knowledge.

Part 3: Transfer of technology for amino acid block fertilizer production from salted egg white waste for coconut farming. The technology transfer process for amino acid block fertilizer derived from salted egg white waste for application in coconut production employed a community-based participatory approach, with collaborative activities. It was divided into five key technology transfer activities, as follows:

Activity I: Provision of knowledge on GMP-compliant production of salted egg products;

Activity II: Introduction of amino acid block fertilizer technology;

Activity III: Demonstration and hands-on practice;

Activity IV: Participatory discussion and feedback on product label design;

Activity V: Summary of outcomes through the development of a manual and infographic-based product labels.

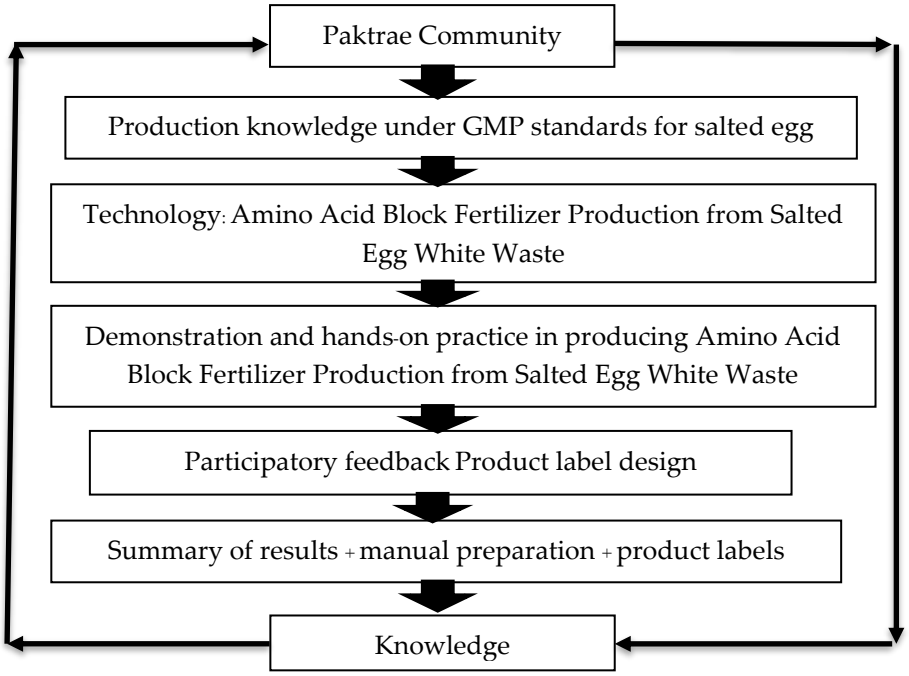


Figure 1. The process of transfer of technology for Amino Acid Block Fertilizer Production from Salted Egg White Waste for Coconut Farming in Paktrae, Songkhla Province

Part 4: Satisfaction with the technology transfer of amino acid block fertilizer production from salted egg white waste for coconut farming in Paktrae Subdistrict, Songkhla Province. Questionnaires comprising both closed- and open-ended questions were used to collect basic personal data and assess farmers' satisfaction with the technology transfer for amino acid block fertilizer production. The questionnaire used a five-point Likert scale, consisting of least satisfaction (1), low satisfaction (2), moderate satisfaction (3), high satisfaction (4), and highest satisfaction (5).To interpret the respondents' mean scores, a five-level criterion scale was applied, as follows:

Mean score of 4.21–5.00: Most satisfied
Mean score of 3.41–4.20: Very satisfied
Mean score of 2.61–3.40: Moderately satisfied
Mean score of 1.81–2.60: Slightly satisfied
Mean score of 1.00–1.80: Least satisfied

To ensure questionnaire quality, content validity was evaluated by three experts, who assessed the congruence between the questionnaire items, their content, and alignment with the research objectives using the Item–Objective Congruence (IOC) index. The revised questionnaire was subsequently pilot-tested with 30 non-sample farmers. Its reliability was assessed using Cronbach's alpha, yielding an alpha of 0.94 for the entire instrument. Data analysis was conducted using IBM SPSS statistical software. Descriptive statistics were employed, including frequency distributions, percentages, means, and standard deviations. The results were presented in frequency distribution tables, including minimum and maximum values for each variable.

3. Results and Discussion

3.1 Farmers' Basic Demographic Information

An analysis of the basic characteristics of farmers in Paktrae Subdistrict, Ranot District, Songkhla Province, indicated that the majority were female (66.67%), with an average age of 61.36 years. Most respondents had attained lower secondary education (76.00%), followed by upper secondary education (16.00%), while the smallest proportion held a bachelor's degree (8.00%). In terms of marital status, 86.67%

were married, while 13.33% were divorced. The most common occupation was agriculture (53.33%), followed by general labor (26.67%), with the smallest proportion employed as private company employees (6.67%) (Table 1).

Table 1. Farmers' Basic Demographic Information

Farmers' Basic Demographic Information	Frequency	Percentage
Gender		
Male	8	32.00
Female	7	68.00
Age		
Less than 41 years	4	16.00
42 year – 50 year	3	12.00
51 years – 59 years	5	20.00
60 years – 68 years	6	24.00
More than 69 years	7	28.00
Education Level		
Junior high school	19	76.00
Senior high school	4	16.00
Associate's degree	0	0.00
Bachelor's degree	2	8.00
Marital status		
Marital status	22	88.000
Divorced	**3**	12.00
Occupation		
Government service	1	4.00
Personal business	1	4.00
General labor	7	28.00
Private company employees	2	8.00
Agriculture	14	56.00

3.2 Assessment of knowledge on GMP-compliant production of Paktrae salted egg products

The assessment of farmers' knowledge regarding GMP-compliant production of Paktrae salted egg products indicated that, before the technology transfer, farmers demonstrated low (56.00%), moderate (40.00%), and high (4.00%) levels of knowledge. After the technology transfer, the assessment showed that 92.00% of farmers demonstrated a high level of knowledge, while 8.00% had a moderate level. Notably, no farmers remained in the low knowledge category after the technology transfer (Table 2).

Table 2. Knowledge before and after knowledge transfer training about the production of Paktrae salted egg products under GMP standards

Test Scores	Before knowledge transfer		After knowledge transfer	
	Numbers	Percentage	Numbers	Percentage
Low (0-5 score)	14	56.00	0	0.00
Moderate (6-10 score)	10	40.00	2	8.00
High (11-15 score)	1	4.00	23	92.00
Mean ± S.D	5 ± 2.22		14 ± 1.28	
Min	4		10	
Max	10		15	

A comparison of farmers' knowledge before and after the transfer of GMP-compliant production practices for Paktrae salted egg products, using a paired t-test, revealed a statistically significant difference at $\alpha = 0.01$. The farmers' knowledge after the transfer was significantly higher than at the beginning of the training. Before training, the farmers had an average score of 5 points, which increased to 14 points after the technology transfer. This indicates a significant improvement in their knowledge of GMP-compliant

production of Paktrae salted egg products. This improvement can be attributed to a clear and systematic technology transfer process that emphasized hands- on learning. This approach helped farmers better understand the principles of Good Manufacturing Practices (GMP), including production site hygiene, raw material quality, production processes, and product quality control. The results of the knowledge assessment further indicated that farmers answered 11 questions correctly at a rate of 80.00% or higher, whereas four questions had a correct response rate of less than 79.00% (Table 3).

Table 3. Comparative knowledge before and after the technology transfer of amino acid block fertilizer production from salted egg white waste for coconut farming in Paktrae, Songkhla Province

Items	Pre-test Post-test	Correct answers	Mean± S.D.	t	p value
1. How long is a community product standard certificate valid?	Pre-test	19	0.76 ± 0.43	-1.445	0.161
	Post-test	23	0.92 ± 0.27		
2. Which ministry certifies the Community Product Standard (CPS)?	Pre-test	9	0.36 ± 0.48	-3.098	0.005**
	Post-test	19	0.76 ± 0.43		
3. This mark represents which of the following product certifications?	Pre-test	5	0.20 ± 0.40	-3.934	0.001**
	Post-test	19	0.76 ± 0.43		
4. To what food group do raw salted eggs belong?	Pre-test	23	0.92 ± 0.27	-1.445	0.161
	Post-test	25	1.00 ± 0.00		
5. Where should I contact to apply for Community Product Standard (CPS) certification?	Pre-test	9	0.36 ± 0.48	-1.541	0.136
	Post-test	15	0.60 ± 0.50		
6. What is the application period for Community Product Standards (CPS) certification?	Pre-test	7	0.28 ± 0.45	-7.856	0.000**
	Post-test	25	1.00 ± 0.00		
07. How many digits are in a food registration number (FDA number)?	Pre-test	7	0.28 ± 0.45	-7.856	0.000**
	Post-test	25	1.00 ± 0.00		
8. Which of the following are the first two digits of the FDA registration number for a manufacturing facility in Songkhla province?	Pre-test	6	0.24 ± 0.43	-8.718	0.000**
	Post-test	25	1.00 ± 0.00		
9. Benefits of applying for community product certification.	Pre-test	6	0.24 ± 0.43	-8.718	0.000**
	Post-test	25	1.00 ± 0.00		
10. What is the minimum height of a table from the floor?	Pre-test	11	0.44 ± 0.50	-5.527	0.000**
	Post-test	25	1.00 ± 0.00		
11. What types of microorganisms serve as indicators of personal hygiene?	Pre-test	17	0.68 ± 0.47	-2.009	0.056*
	Post-test	23	0.92 ± 0.27		
12. Which of the following is the most correct approach for applying for an FDA registration number?	Pre-test	14	0.56 ± 0.50	-1.732	0.096
	Post-test	19	0.76 ± 0.43		
13. What GMP (Good Manufacturing Practice) regulations are currently in place for obtaining certification of a manufacturing facility?	Pre-test	13	0.52 ± 0.50	-4.707	0.000**
	Post-test	25	1.00 ± 0.00		
14. Which of the following is NOT a basic requirement of GMP (Good Manufacturing Practice) for obtaining certification of a manufacturing facility?	Pre-test	12	0.48 ± 0.50	-5.099	0.000**
	Post-test	25	1.00 ± 0.00		
15. Which production facilities are classified as factories?	Pre-test	5	0.20 ± 0.40	-9.798	0.000**
	Post-test	25	1.00 ± 0.00		

Remark: * Statistically different at probability level 0.05 ** Statistically different at probability level 0.01

3.3 Technology transfer of amino acid block fertilizer production from salted egg white waste for coconut farming in Paktrae, Songkhla Province

The production of salted eggs is a food processing method that requires careful consideration of consumer safety, as eggs are raw materials highly susceptible to contamination by pathogenic microorganisms. Therefore, the application of Good Manufacturing Practice (GMP) in food production is crucial for controlling product quality and ensuring food safety throughout the manufacturing process. Accordingly, training and technology transfer for salted egg production in accordance with GMP standards are essential to improve production standards in Paktrae Subdistrict. An increasing awareness and commitment among farmers to enhance product quality in compliance with established standards were observed, particularly among small-scale entrepreneurs and community enterprises. This contributes to the production of safe, high-quality food and enhances sustainable commercial competitiveness, consistent with previous findings [8]. Previous studies comprehensively evaluated the mechanisms underlying the formation of quality in salted eggs, including water and salt mass transfer, protein conformational changes, and the synthesis of small molecules. In addition, various pickling-assisted physical technologies and chemical additives have been developed and assessed to improve processing efficiency and product quality, as well as potential value-added applications of salted eggshells, salted egg whites (SEW), and salted egg yolks (SEY).

This context led to the initiation of efforts to expand knowledge on the production of amino acid block fertilizer derived from salted egg white waste for coconut cultivation. Amino acid–based fertilizers have been reported to enhance nutrient use efficiency and crop productivity by promoting root development and stimulating beneficial soil microbial activity. Such principles can be effectively applied to coconut production, particularly through the integration of biofertilizers and organic compounds, such as humic substances and amino acids, thereby increasing productivity and sustainability in agricultural systems [9]. Furthermore, studies on organic fertilization strategies in coconut farming indicate that incorporating biologically derived nutrient sources, including materials rich in amino acids, supports long-term soil health and productivity in coconut plantations [10].

The technology transfer of amino acid block fertilizer production from salted egg white waste for coconut farming was systematically designed to strengthen conceptual understanding, technical competence, and practical skills among the target group, within a participatory, knowledge-driven framework. The process was grounded in established theories of technology transfer, experiential learning, and adult education, integrating both theoretical instruction and applied practice to facilitate effective knowledge internalization and skill acquisition.

The transfer activities comprised structured academic lectures, hands-on training sessions, and on-site demonstrations conducted in an open learning environment that encouraged scholarly discussion, critical reflection, and knowledge exchange. The implementation commenced with a comprehensive introduction to the scientific background, objectives, and anticipated benefits of the technology, to establish a shared understanding of the problem context, the technology transfer model, and the chemical and nutritional characteristics of the amino acid block fertilizer. Subsequently, the production process was systematically and reproducibly presented, covering raw material selection, equipment requirements, and step-by-step manufacturing procedures, all under quality control principles. Particular emphasis was placed on the scientific rationale underlying each production stage to enhance participants' analytical understanding. In parallel, guidelines for fertilizer application in coconut cultivation were provided based on principles of plant physiology, nutrient management, and sustainable agricultural practices.

In addition, academic knowledge related to product development, value addition, and market planning was incorporated to support effective technology utilization at the community level. The practical training component was carefully structured with defined learning outcomes, enabling participants to translate theoretical knowledge into practice, critically evaluate the technology, and adapt it to local conditions. This academically oriented technology transfer approach contributed to the effective adoption, contextualization, and potential dissemination of the innovation within the target community.

The research team transferred the amino acid block technology to the salted egg production group in Paktrae through collaborative efforts involving Thaksin University, the Ranot District Administration Office,

and the Ranot District Community Development Office. These organizations jointly promoted the utilization of waste generated from salted egg yolk production by developing value-added products from unused egg whites through technology transfer. The knowledge transfer was conducted through practical training activities combining theoretical instruction and hands-on experience, which were subsequently applied in coconut production practices. The project results demonstrated that farmers reduced production costs and improved product quality and safety, benefiting both producers and consumers. In addition, the approach's environmental friendliness highlights its potential for sustainable technology development at the community level. This finding is consistent with [11], which emphasized that effective innovation transfer requires a clear understanding of recipients' living conditions, lifestyles, and knowledge levels to select appropriate delivery formats and communication methods. Aligning transfer strategies with the characteristics of each target group enhances learning outcomes and supports long-term sustainability.



Figure 2. Production of amino acid blocks from salted egg white powder

Following the completion of amino acid block product development, subsequent efforts focused on marketing extension, with an emphasis on establishing a distinct product identity through strategic branding. The research team facilitated consultative discussions among key stakeholders, including farmer groups, relevant government agencies, and local community representatives, to generate ideas collaboratively and reach consensus on product branding. As a result, the product was officially named "Paktrae Salted Egg White Amino Salt," a designation intended to reflect both the geographical origin and the distinctive characteristics of the raw materials utilized in its production. In addition, product label design and development were undertaken to reinforce the producer group's identity and enhance consumer trust. This effort aimed to strengthen the product's market competitiveness and address the absence of an official label during the initial stage of product development, a critical limitation that affects value creation and market positioning.

The label development process was therefore considered a strategic intervention to enhance product value and promote the sustainability of community-based products. The labels were designed to meet marketing requirements by incorporating visually appealing, distinctive elements that clearly reflect the product's characteristics, explicitly communicate the origin of the raw materials (Paktrae salted eggs), and emphasize the role of local wisdom in the production process. The labeling strategy aimed to establish and reinforce brand recognition for "Paktrae Salted Egg White Amino Salt," attract the attention of the target consumer segment, and stimulate initial purchase decisions. Furthermore, the labels were intended to support long-term customer engagement by fostering brand loyalty and encouraging repeat purchases.

Group members actively contributed their perspectives on marketing communication strategies. Based on a synthesis of these inputs, the message "Amino Egg White, Sweet Coconut Water (Paktrae)" was identified as an appropriate and effective communication theme for advertising and public relations across multiple online platforms. This message was formulated to convey the product's uniqueness while supporting the objective of generating sustainable, long-term income for the community.

This finding is consistent with previous research [12], which reported that major challenges in product packaging development stem from entrepreneurs' limited knowledge and understanding of packaging design. Although many producers have established brands, these brands often lack market recognition, and

the packaging materials are frequently unsuitable for use as souvenir products. In addition, product labels commonly fail to comply with labeling standards, resulting in incomplete or unclear information for consumers.

In response to these challenges, the packaging design was systematically improved to enhance product visibility and strengthen brand recognition through the use of modern design elements and illustrative graphics. The revised packaging includes complete, standardized product information and accessible contact channels to facilitate consumer engagement. Furthermore, the packaging was redesigned to support convenient handling and consumption, while ensuring durability and effective preservation of product quality. These improvements enhance market appeal and align the product with contemporary consumer expectations.



Figure 3. Product label

3.4 Satisfaction with the technology transfer of amino acid block fertilizer production from salted egg white waste for coconut farming in Paktrae, Songkhla Province

Farmers who participated in the technology transfer reported the highest overall satisfaction, with a mean score of 4.45. When considering each aspect, farmers reported the highest levels of satisfaction with the trainers (mean 4.66) and the services provided by officials (mean 4.65). In terms of knowledge and understanding, farmers expressed a high level of satisfaction (mean 4.48). Satisfaction with the training location was also high (mean 4.15), followed by knowledge and understanding, which was rated at a moderately high level, and application of knowledge, which was rated at a high level (mean 4.32). The study results are summarized below.

1) Trainers*:* Farmers reported the highest overall satisfaction in this category, with a mean score of 4.66. Among the specific aspects evaluated, the trainers' preparation and readiness received the highest rating (mean 4.81). Their ability to explain content clearly and concisely, using appropriate, easy-to-understand language, also received a high satisfaction score (mean 4.71). The delivery of lectures was rated at the highest level (mean 4.67), as was their responsiveness to questions (mean 4.57). In addition, the appropriateness of lecture materials received a high rating (mean 4.48). This finding is consistent with [13], who reported that effective lecturers should be able to create a positive learning atmosphere and communicate content clearly to trainees.

2*)* Training location*:* Farmers expressed a high overall level of satisfaction with the training location (mean 4.15). Among the evaluated aspects, the training duration was rated as the most appropriate (mean 4.38). The availability of audiovisual equipment and food services was rated as very appropriate (mean 4.19), while the cleanliness and suitability of the venue were also rated as appropriate (mean 3.86). The training schedule was designed to align with farmers' availability, and equipment and facilities were adequately prepared. The venue's cleanliness and organization contributed to a comfortable learning environment that encouraged active participation.

3) Services provided by officials*:* Farmers expressed the highest overall satisfaction with the services provided by officials (mean 4.65). Specifically, staff service quality received the highest rating (mean 4.71).

Project coordination and facilitation by staff were also rated at the highest level (mean 4.67), as were staff members' advice and responsiveness to questions (mean 4.57). The professionalism, attentiveness, and effective coordination of the staff contributed to farmers' confidence and sense of support throughout the technology transfer process.

4) Knowledge and understanding*:* Farmers expressed a high overall level of satisfaction with their knowledge and understanding (mean 4.48). After the training, their overall understanding was rated at the highest level (mean 4.67). Farmers were able to clearly explain the benefits of amino acid block development (mean 4.57) and the details of the production process (mean 4.48). Their ability to organize and apply knowledge systematically to work development was also rated at a high level (mean 4.05).

5) Knowledge application*:* Farmers expressed a high level of overall satisfaction with knowledge application (mean 4.32). They demonstrated the highest ability to disseminate and transfer knowledge to the community (mean 4.48). In addition, they were able to apply the acquired knowledge in their work and provide guidance to coworkers (mean 4.29), while also showing strong confidence and capability in applying the knowledge independently (mean 4.24). This finding is consistent with [14], which emphasized that agricultural technology and innovation transfer enable farmers to apply knowledge to improve their livelihoods and those of their families (Table 4).

Table 4. Satisfaction with the technology transfer of amino acid block fertilizer production from salted egg white waste for coconut farming in Paktrae, Songkhla Province

Satisfaction	Mean	S.D.	Level
Trainers	**4.66**	**0.46**	**Highest**
1. The trainers' preparation and readiness	4.81	0.39	Highest
2. Explain the content clearly and concisely	4.71	0.45	Highest
3. Using appropriate and easy-to-understand language	4.71	0.45	Highest
4. Delivery of the lectures	4.67	0.47	Highest
5. Responsiveness to questions	4.57	0.49	Highest
6. Appropriateness of the lecture materials	4.48	0.50	Highest
Location	**4.15**	**0.66**	**High**
1. Training duration	4.38	0.49	Highest
2. Availability of audiovisual equipment	4.19	0.59	High
3. Availability of food	4.19	0.73	High
4. Cleanliness and suitability of the venue	3.86	0.83	High
Service Provided by Officials	**4.65**	**0.47**	**Highest**
1. The staff's service quality	4.71	0.45	Highest
2. Project staff coordination	4.67	0.47	Highest
3. Project staff facilitation	4.67	0.47	Highest
4. The staff's advice and responsiveness to questions	4.57	0.49	Highest
Knowledge and Understanding	**4.48**	**0.51**	**High**
1. After training, knowledge and understanding	4.67	0.47	Highest
2. The benefits of developing amino acid blocks from salted egg white powder for application in coconut production can be explained.	4.57	0.49	Highest
3. The advantages of developing amino blocks from salted egg white powder for application in coconut production can be explained.	4.57	0.49	Highest
4. The development of amino blocks, a salt substitute from salted egg white powder, can be described in detail for application in coconut production	4.48	0.50	Highest
5. Can organize/process ideas into systematic work development.	4.05	0.58	High

Table 4. Satisfaction with the technology transfer of amino acid block fertilizer production from salted egg white waste for coconut farming in Paktrae, Songkhla Province (Continue)

Satisfaction	Mean	S.D.	Level
Knowledge Application	**4.32**	**0.64**	**Highest**
1. Disseminate and transmit knowledge to the community	4.48	0.50	Highest
2. Demonstrated the ability to apply the knowledge gained in their work	4.29	0.63	Highest
3. Provide advice to coworkers to a great extent	4.29	0.63	Highest
4. Farmers showed strong confidence and capability in applying the knowledge acquired	4.24	0.81	Highest
Total	**4.45**	**0.55**	**Highest**

Remark: Levels

Average 4.21 - 5.00 Most Satisfied
Average 3.41 - 4.20 Very Satisfied
Average 2.61 - 3.40 Moderately Satisfied
Average 1.81 - 2.60 Slightly Satisfied
Average 1.00 - 1.80 Least Satisfied

4. Conclusions

The findings revealed that farmers had significantly higher knowledge levels regarding GMP-compliant production of Paktrae salted egg products following the technology transfer. The difference in knowledge levels before and after the transfer was statistically significant, at $\alpha = 0.01$, indicating the effective implementation of the technology transfer process. The transfer of amino acid block fertilizer production technology derived from salted egg white waste is a key strategy to promote waste management and value addition within the salted egg production process, with an emphasis on sustainable development. This approach enables the community to utilize unused salted egg whites effectively. Previously regarded as waste from salted egg yolk production, salted egg whites have been developed into value-added products that benefit both the agricultural sector and community-based enterprises. This innovation is community-based, fostering new business opportunities, generating additional employment, increasing household income, and reducing waste from the production process. It reflects efficient resource use, promotes environmental sustainability, and contributes to resilient, sustainable community development. The evaluation of satisfaction with the transfer of amino acid block fertilizer technology revealed the highest overall satisfaction, particularly with respect to the lecturers and the services provided by project staff. In terms of knowledge application, training location, and overall understanding, satisfaction was high. The activities were organized with an emphasis on participatory learning and hands-on training. Lecturers, as subject matter experts, clearly and effectively communicated the content. Staff provided efficient coordination and support, while the training venue was appropriate, accessible, and conducive to learning. The content was practical, easy to understand, and applicable to real-world situations.

5. Acknowledgements

The authors would like to express their sincere gratitude to the community leaders for providing valuable information and supporting coordination within the study area. Special thanks are extended to the farmers in Paktrae Subdistrict, Ranot District, Songkhla Province, for their kind cooperation and willingness to participate in and support this study. This study was conducted under the human research ethics approval code SCOHYLIRB-2568/360, which was approved before the commencement of the study.

Author Contributions: Conceptualization, P.W. and N.J.; data collection, S.L.; formal analysis and writing—review, S.L.; review and editing, T.J.; supervision, S.L. All authors have read and agreed to the published version of the manuscript.

Funding: This research was supported by the Academic Service Fund Project under the Academic Service and Innovation Fund, Thaksin University, Thailand, for the fiscal year 2024.

Conflicts of Interest: The authors declare no conflicts of interest.

References

[1] Food and Agriculture Organization of the United Nations (FAO). *Agricultural Extension and Advisory Services*; FAO: Rome, 2017.

[2] Malisuwan, S.; Kaewphanuekrungsi, W.; Milindavanij, D. Digital Divide in Thailand: Analysis and Recommendations. *Int. J. Adv. Res. Eng. Technol.* **2016**, *7*(1), 41–46. https://doi.org/10.34218/IJIERD.7.2.2016.004

[3] Kuntongjan, S. Relationships between Globalization and Basic Values of Thai Society. *J. Human Soc. Sci.* **2016**, *7*(1), 160–185 (in Thai).

[4] Chalermsan, N.; Navanukraha, B.; Kitiyanupab, J.; Moun-Wang, S.; Montatham, S. The Use of Moringa Leaf Meal in Laying Quail Diets. *Rajamangala Univ. Technol. Srivijaya Res. J.* **2016**, *8*(2), 137–146 (in Thai).

[5] Khan, W.; Rayirath, U. P.; Subramanian, S.; et al. Seaweed Extracts as Biostimulants of Plant Growth and Development. *J. Plant Growth Regul.* **2019**, *28*(4), 386–399. https://doi.org/10.1007/s00344-009-9103-x

[6] Du Jardin, P. Plant Biostimulants: Definition, Concept, Main Categories and Regulation. *Sci. Hortic.* **2015**, *196*, 3–14. https://doi.org/10.1016/j.scienta.2015.09.021

[7] Rogers, E. M. *Diffusion of Innovations*, 5th ed.; Free Press: New York, NY, 2003.

[8] Wang, X.; Zhang, J.; Vidyarthi, S. K.; Xu, M.; Liu, Z.; Zhang, C.; Xiao, H. A Comprehensive Review on Salted Eggs: Quality Formation Mechanisms, Innovative Pickling Technologies and Value-Added Applications. *Sustainable Food Technol.* **2024**, *2*, 1409–1427. https://doi.org/10.1039/D4FB00129J

[9] Wang, X.; Zhang, Y.; Xu, W.; Cheng, J.; Liu, J.; Pei, W.; Wang, J.; Chuang, S. Amino Acid Fertilizers Strengthen Crop Yield and Quality by Recruiting Beneficial Rhizosphere Microbes. *J. Sci. Food Agric.* **2023**, *103* (12), 5970–5980. https://doi.org/10.1002/jsfa.12667

[10] Atapattu, A. J.; Nuwarapaksha, T. D.; Udumann, S. S.; Dissanayaka, N. S. Integrating Organic Fertilizers in Coconut Farming: Best Practices and Application Techniques. *Crops* **2025**, *5*(2), 17. https://doi.org/10.3390/crops5020017

[11] Pittayapitak, T.; Vicheanpant, T. Innovation Diffusion: Concept and Model. *J. Libr. Inf. Sci. Srinakharinwirot Univ.* **2012**, *5*(1), 107–118 (in Thai).

[12] Underwood, R. L. The Communicative Power of Product Packaging: Creating Brand Identity via Lived and Mediated Experience. *J. Mark. Theory Pract.* **2003**, *11*(1), 62–76. https://doi.org/10.1080/10696679.2003.11501933

[13] Wanzer, M. B.; Frymier, A. B.; Irwin, J. An Explanation of the Relationship between Instructor Humor and Student Learning: Instructional Humor Processing Theory. *Commun. Educ.* **2010**, *59*(1), 1–18. https://doi.org/10.1080/03634520903367238

[14] Bulan, K. Personal Media and Agriculture 4.0 Promotion. *Veridian E-Journal, Silpakorn Univ.* **2017**, *10*(3), 2440–2454 (in Thai).

ASEAN
Journal of Scientific and Technological Reports
Online ISSN:2773-8752

Research article

Orbital Period Change of the Binary Star System V829 Aql

Supat Sairattanain[1], Torik Hengpiya[2], and Wiraporn Maithong[3*]

[1] Faculty of Education and Human Development, Sisaket Rajabhat University, Sisaket, 33000, Thailand
[2] National Astronomical Research Institute of Thailand (Public Organization), Songkhla, 90000, Thailand
[3] Faculty of Science and Technology, Chiang Mai Rajabhat University, Chiang Mai, 50300, Thailand
* wiraporn_mai@cmru.ac.th

Citation:
Sairattanain, Supat.; Hengpia, Torik.; Maithong, Wiraporn. Orbital period change of the binary star system V829 Aql. *ASEAN J. Sci. Tech. Report.* **2026**, *29*(4), e258435. https://doi.org/10.55164/ajstr.v29i4.258435

Article history:
Received: March 24, 2025
Revised: December 25, 2025
Accepted: February 7, 2026
Available online: March 24, 2026

Publisher's Note:
This article is published and distributed under the terms of the Thaksin University.

Abstract: A variable star, V829 Aql, is considered one of the binary stars providing invaluable insights into the process of stellar evolution. The purpose of this research study is to calculate the orbital period change of the binary star system V829 Aql using a telescope at the Regional Observatory for the Public, Songkhla, National Astronomical Research Institute of Thailand (Public Organization). Images in the *B* and *V* wavelength range will be taken on the night of July 1-2, 2021, from 9:00 p.m. to 5:00 a.m., and subsequently examined. It was discovered that the brightness value pattern adhered to an equation (relationship): the orbital period equals the lowest brightness when it does. The orbital period change is growing, as indicated by the equation $O\text{-}C = (4.82878 \times 10^{-13})$ Epoch^2 - (1.5221×10^{-7}) Epoch – 0.01052, which gives a rate of change in orbital period of 1.05×10^{-4} seconds/year. This means that stars continue to separate, which explains the evolution of the TRO theory.

Keywords: V829 Aql; orbital period change; TRO

1. Introduction

The Moon, Mars, Mercury, Jupiter, Venus, and Saturn are the only six celestial objects in the night sky that are not stars. Binary stars, or systems of two stars with the same barycenter, make up the majority of stars in our sky. Astronomers learned about the evolution of stars by analyzing data from binary star systems. Periodically brilliant binary systems are known as eclipsing binaries [1]. When one is behind the other, their light curves are smaller. Some of their attributes were calculated using the light curve and the photometry approach. The V829 Aql was reported to be a pulsating star in 1997 [1] and 1998 [2]. In the present time, according to the SIMBAD Astronomical Database [3], the V829 Aql is an eclipsing binary star with R.A. 19 h 46 m 57.282 s and Dec. +03° 30' 28.482". The duration of the orbit is 0.211401 days [4]. To understand the evolution, we examine the period changes of V829 Aql in this paper. The binary is compatible with the Thermal Relaxation Oscillation (TRO) theory if the change is growing [5]. On the other hand, the binary is equivalent to the Angular Momentum Loss (AML) theory if the period change is decreasing [6-7].

This study's goal is to examine how the V829 Aql period has changed. The light curve used in this paper comes from photometric analysis in the *B* and *V* wavelength bands.

2. Materials and Methods

On July 1, 2021, UT, the V829 Aql was observed at the Regional Observatory for the Public located in Songkhla, Thailand. Utilized was the 0.7-meter reflecting telescope and CCD equipped with the UBV system's blue *(B)* and visual *(V)* filters. The observation was conducted under a nearly clear sky with partial cloud cover. V829 Aql was observed with B and V filters, with an exposure time of 30 seconds per frame. A total of 129 images were obtained in the *B* filter and 118 images in the *V* filter. The example of the V829 Aql photograph and the fundamental data are shown in Figure 1 and Table 1, respectively.

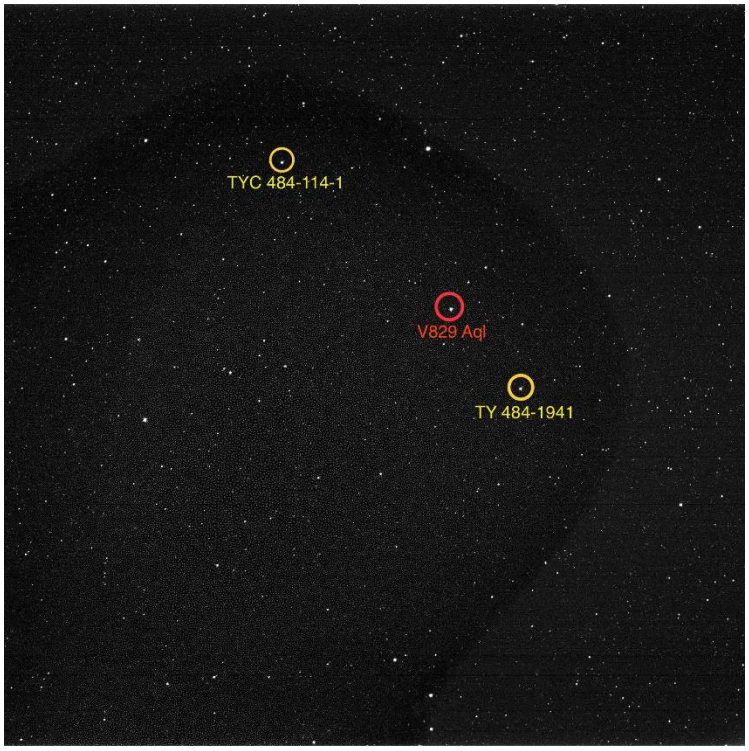


Figure 1. Photograph of the V829 Aql

Table 1. Information on the V829 Aql

Star	R.A. (h m s)	Dec (° ′ ″)	Magnitude *V*
V829 Aql	19 46 57.281	+03 30 28.481	10.06
TYC 484-194-1 (comparison)	19 46 51.094	+03 26 50.201	10.83
TYC 484-114-1 (check)	19 47 14.563	+03 37 37.662	10.77

The photometric analysis was performed using MaxIm DL6 software [8]. As the first step of noise reduction, the bias and dark frames were subtracted, and the flat-field correction was applied [9], as expressed in equation (1). Subsequently, the stellar flux was analyzed, and the results are presented in Figure 2.

$$\text{Reduction Image} = \frac{\text{Raw - bias - dark}}{\text{Flat}} \quad (1)$$

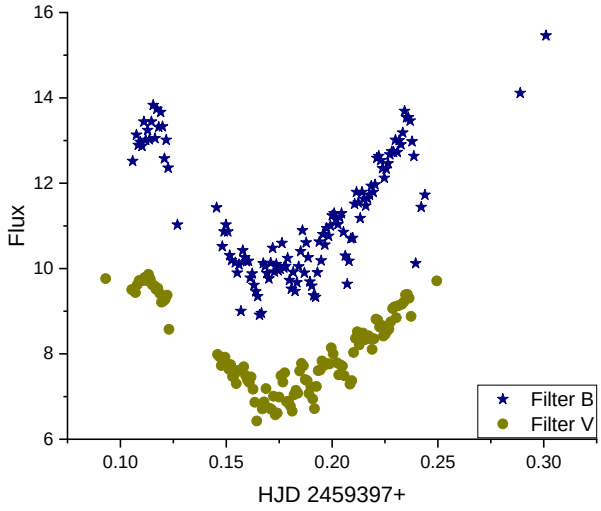
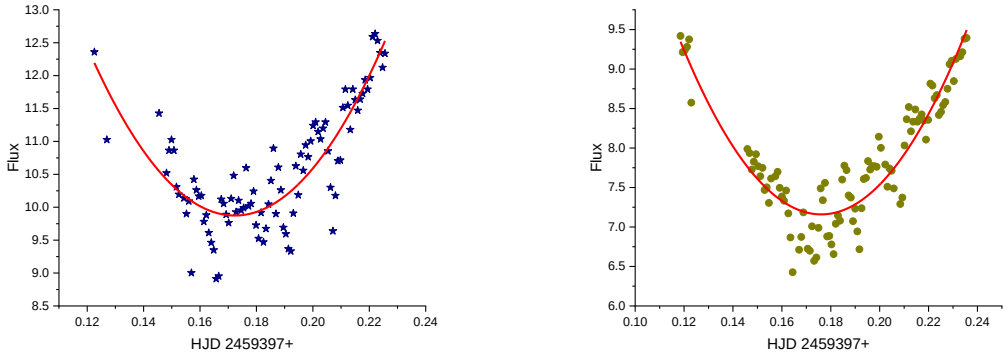


Figure 2. The light curve of V829 Aql in *the B* (blue dots) and *V* (green dots) filter.

3. Results and Discussion

The times of minimum light computation in this work were obtained from ordinary differential equation (ODE) theory [10]. The minimum-light areas in the B and V filters were selected for calculation, as shown in Figures 3(a) and 3(b), respectively.



(a) (b)

Figure 3. The ODE fits show the minimum eclipse depths obtained from the observation with *B* (a) and *V* (b) filters, respectively.

To determine the *O-C* data for all the moments of minimum light, Bob Nelson's database of eclipsing binary O-C data was used [5].

$$\text{HJD Min} = 2443061.404+0.2114012E \quad (2)$$

The times of V829 Aql's minimum brightness were determined throughout the investigation, as shown in Table 2.

Table 2. The *O-C* data of V829 Aql

Time of Minimum	Epoch	*O-C*	Source
2429794.379	-107407.5	0.011389	AC 39.5
2429823.283	-107270.5	-0.0465754	AC 39.5
2429875.167	-107025.5	0.0441306	AC 39.5
2430929.277	-102039	0.0020468	AC 39.5
2430939.267	-101991.5	-0.0495102	AC 39.5
2430995.148	-101727.5	0.021573	AC 39.5
2431236.367	-100586.5	0.0318038	AC 39.5
2431265.344	-100449.5	0.0468394	AC 39.5
2431287.315	-100345.5	0.0321146	AC 39.5
2442621.464	-46731	0.0114772	BBS 34
2442632.34	-46679.5	0.0003154	BBS 34
2442633.5	-46674	-0.0023912	BBS 34
2442740.26	-46169	2.8E-06	BBS 34
2442993.382	-44971.5	-0.0309342	BBS 34
2443016.378	-44863	0.0280356	BBS 34
2443360.421	-43235.5	0.0155826	BBS 34
2443431.29	-42900	-0.04052	BBS 35
2443434.32	-42886	0.0298632	BBS 35
2444793.498	-36456.5	0.0038478	BBS 56
2444821.398	-36324.5	-0.0011106	BBS 56
2448127.371	-20686	-0.0257768	BBS 96
2448167.313	-20497	-0.0386036	BBS 96
2448534.308	-18761	-0.0360868	BBS 99
2449549.456	-13959	-0.0366492	BBS 107
2449600.339	-13718.5	0.0043622	BBS 107
2449933.493	-12142.5	-0.009929	BBS 110
2452500.442	0	0	vis
2453981.993	7008	0.0514904	VSB 45
2454297.54	8501	-0.0232012	BAVM 193
2455324.242	13357.5	0.007971	VSB 51
2455438.031	13896	-0.0417752	VSB 51
2459397.174	32624	-0.0205488	This work

The quadratic polynomial fitting method was used to fit the *O-C* data from this study, in combination with values from Bob Nelson and the AASVO database. The outcome is displayed in Figure 4.

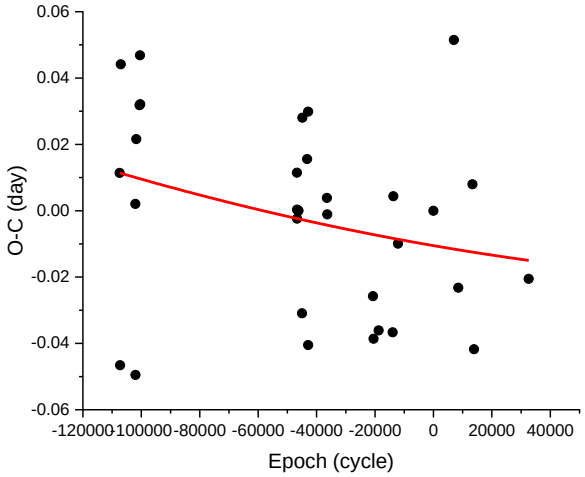


Figure 4. The *O*−*C* diagram of V829 Aql.

The relevant equation for the quadratic fitting method in Figure 3 (red line) is as follows.

$$O-C = (4.82878 \times 10^{-13})\, E^2 - (1.5221 \times 10^{-7})\, E - 0.01052 \quad (3)$$

The value of dP/dE was obtained by comparing it with the *O*-*C* quadratic equation (3) as follows:

$$dP/dE = 2 \times (4.82878 \times 10^{-13}) = 9.65756 \times 10^{-13} \text{ days/cycle} \quad (4)$$

The rate of increment in the V829 Aql period is 9.65756 (10^{-13} days/cycle) or 1.05 (10^{-4} seconds/year). The increase in the period indicated that, in accordance with Thermal Relaxation Oscillation (TRO), the distance between the stars had increased [11].

4. Conclusions

On July 1, 2021, UT, the eclipsing binary system V829 Aql was spotted at the Regional Observatory for the Public in Songkhla, Thailand, and photometry analysis was performed. The V829 Aql light curve indicated that HJD 2459397.1742 was the minimum light time of V829 Aql. The binary system V829 Aql's period change (dP/dE) is evident from both the diagram and the solution, and it is $2 \times (4.82878 \times 10^{-13})$ days/cycle or roughly 1.05×10^{-4} seconds/year. It indicates a greater separation between the two stars. Ultimately, the double stars will evolve align with the TRO theory. It explained that the binary star system will transfer its energy. In the condition that mass and angular momentum are conserved, the distance is far apart. That means the orbital period is increased. The steadily increasing orbital period indicates that the two stars are gradually moving farther apart.

5. Acknowledgements

The author would like to thank the National Astronomical Research Institute of Thailand (Public Organization) for this observation.

Author Contributions: Conceptualization, methodology, investigation, formal analysis, S.S. and W.M., writing—original draft preparation, S.S.; Observation, T.H., writing—review and editing, and project administration, W.M.

Funding: This research received no external funding.

Conflicts of Interest: The authors declare no conflict of interest.

References

[1] Diethelm, R. V829 Aquilae is a Pulsating Star with a Variable Light Curve. *Commissions 27 and 42 of the IAU Information Bulletin on Variable Stars*. **1997**, *4530*, 1-2.

[2] Diethelm, R. V829 Aquilae Is a Pulsating Star with a Variable Light Curve. *Inf. Bull. Var. Stars* **1997**, *4530*, 1–2.

[3] Handler, G.; Pikall, H.; Diethelm, R. The Nature of A829 Aql: A Triple-Mode Radially Pulsating Post-Main-Sequence Delta Scuti Star. *Inf. Bull. Var. Stars* **1998**, *4549*, 1–4.

[4] Prša, A. *Modeling and Analysis of Eclipsing Binary Stars: The Theory and Design Principles of PHOEBE*; IOP Publishing, 2018. https://doi.org/10.1088/978-0-7503-1287-5

[5] SIMBAD Astronomical Database—CDS (Strasbourg). http://simbad.u-strasbg.fr/simbad/ (accessed 2022-10-22).

[6] American Association of Variable Star Observers (AAVSO). Bob Nelson's Database of Eclipsing Binary O–C Files. https://www.aavso.org/bob-nelsons-o-c-files (accessed 2022-10-22).

[7] Lucy, L. B.; Wilson, R. E. Observational Tests of Theories of Contact Binaries. *Astrophys. J.* **1979**, *231*, 502–513. https://doi.org/10.1086/157212

[8] Rahunen, T. The Evolution of Contact Binaries: A New Approach. *Astron. Astrophys.* **1981**, *97*(2), 406–409.

[9] Qian, S. Orbital Period Changes of Contact Binary Systems: Direct Evidence for Thermal Relaxation Oscillation Theory. *Mon. Not. R. Astron. Soc.* **2001**, *328*, 914–924. https://doi.org/10.1046/j.1365-8711.2001.04921.x

[10] Diffraction Limited. *MaxIm DL* Software. https://diffractionlimited.com/maxim-dl/ (accessed 2022-10-22).

[11] Romanishin, W. *An Introduction to Astronomical Photometry Using CCDs*; University of Oklahoma, 2002.

[12] Pancharoen, W.; Maithong, W. The First Study of a Period Change of the V1851 Orion Eclipsing Binary System. *ASEAN J. Sci. Technol. Rep.* **2021**, *24*(3), 9–14. https://doi.org/10.55164/ajstr.v24i3.243575

ASEAN
Journal of Scientific and Technological Reports
Online ISSN:2773-8752

Research article

AI-Based Detection of Leaf Diseases in Durian (*Durio zibethinus*) Using Convolutional Neural Networks: Model Development and Performance Evaluation

Supreeya Thepparak[1], Prisana Wonglom[1], Samak Kaewsuksaeng[1], and Anurag Sunpapao[2*]

[1] Faculty of Agriculture, Thaksin University, Phatthalung Campus, Phatthalung, 93210, Thailand
[2] Faculty of Natural Resources, Prince of Songkla University, Songkhla, 90110, Thailand
* Correspondence: anurag.s@psu.ac.th

Citation:
Thepparak, S.; Wonglom, P.; Kaewsuksaeng, S.; Sunpapao, A. AI-Based detection of leaf diseases in durian (*Durio zibethinus*) using convolutional neural networks: model development and performance evaluation. *ASEAN J. Sci. Tech. Report.* **2026**, *29*(4), e261309. https://doi.org/10.55164/ajstr.v29i4.261309

Article history:
Received: September 16, 2025
Revised: January 26, 2026
Accepted: February 7, 2026
Available online: March 24, 2026

Publisher's Note:
This article is published and distributed under the terms of the Thaksin University.

Abstract: Early detection of durian leaf diseases using artificial intelligence (AI) plays an important role in supporting effective plant disease management within digital agriculture systems. This study aimed to develop an AI-based system for the preliminary detection and classification of common durian leaf diseases using image analysis. Diseased leaf samples were collected from durian orchards in Pa Phayom District, Phatthalung Province, and Chang Klang District, Nakhon Si Thammarat Province, southern Thailand. Associated microorganisms were isolated using the tissue transplanting technique, and morphological characteristics indicated the presence of *Colletotrichum* spp. in leaf spot samples and *Fusarium* spp. in leaf blight samples. In contrast, the algal leaf spot pathogen could not be cultured on standard fungal media. A Convolutional Neural Network (CNN) was employed to classify three disease categories: leaf spot, leaf blight, and algal leaf spot. The image dataset was divided into training, validation, and testing sets, and the model was trained and evaluated accordingly. The results demonstrated that the proposed AI model effectively classified durian leaf disease images, particularly leaf spot and leaf blight. However, this study used a relatively limited dataset, and the proposed system should therefore be considered a preliminary disease-detection tool. The developed AI-based system shows potential for deployment on mobile devices or online platforms to support early disease recognition and decision-making by farmers, thereby improving disease management strategies in durian cultivation.

Keywords: Artificial intelligence; durian leaf disease; image processing; neural networks

1. Introduction

Durian (*Durio zibethinus*) is one of Thailand's most economically significant fruit crops, often referred to as the "King of Fruits." Thailand is the world's largest exporter of durian, with major markets in China, Malaysia, and Hong Kong. Fruit plays a vital role in Thailand's agricultural economy, supporting thousands of farmers, traders, and exporters. Besides its economic value, durian is also culturally significant, often featured in festivals and local markets. However, durian cultivation faces challenges, including pest infestations and fungal diseases, which can significantly affect yield and fruit quality. One of the major challenges affecting durian production and quality is plant diseases, particularly foliar diseases that impact tree growth and fruit

development. Common leaf diseases in durian include leaf spot, leaf blight, Rhizoctonia leaf blight, and algal leaf spot [1–3]. Traditionally, diagnosing these diseases relies on visual observation of symptoms or laboratory analysis, which is time-consuming and requires expert knowledge.

In recent years, artificial intelligence (AI) technology has played a crucial role in digital agriculture, particularly in the classification and diagnosis of plant diseases through image processing and machine learning [4]. This technology helps overcome the limitations of traditional disease diagnosis by accurately and rapidly detecting disease characteristics from plant leaf images. The application of lightweight AI for durian leaf disease classification offers a practical approach for the agricultural sector, especially for farmers who lack expertise in plant pathology and need user-friendly, accessible tools. The application of artificial intelligence (AI), particularly deep learning and convolutional neural networks (CNNs), to plant disease diagnosis has attracted substantial attention in recent years [5]. Numerous studies have demonstrated the effectiveness of image-based models for automated disease classification, including the detection of *Phytophthora* blight [6], classification of foliar diseases in various crops [7], and rice disease identification systems [8]. However, research on AI applications for durian disease classification remains limited. Developing an AI system capable of accurately identifying durian leaf diseases is an essential step toward enhancing plant disease management efficiency and reducing unnecessary chemical use in disease control.

This study aims to develop a simple AI-based system for classifying durian leaf diseases using image analysis, enabling farmers to identify diseases and implement appropriate preventive measures quickly. The proposed system utilizes fundamental machine learning techniques, specifically Convolutional Neural Networks (CNN), trained on a dataset of durian leaf images affected by various diseases [9]. Designed for compatibility with mobile devices and online platforms, the system enables practical, real-time field application. This research introduces an approach to developing a lightweight AI system for durian leaf disease classification based on image analysis. The system's performance was evaluated using accuracy, sensitivity, and specificity metrics. The findings will be valuable to both farmers and researchers in developing an accurate and practical AI-based diagnostic tool.

2. Materials and Methods

2.1 Collection of Durian Leaf Disease Samples

Durian leaves exhibiting disease symptoms were collected from Moo 6, Pa Phayom Subdistrict, Pa Phayom District, Phatthalung Province, and Chang Klang District, Nakhon Si Thammarat, Thailand. The collected samples were then brought to the Plant Science Laboratory, Faculty of Agriculture, Thaksin University, Phatthalung Campus, for further analysis.

2.2 Isolation of Pathogenic Fungi and Preliminary Morphological Study

Fungal pathogens were isolated using the tissue-transplanting method as previously described by Daengsuwan et al. [10]. Infected leaf samples were cut into small sections (3 × 3 mm), surface-disinfected with 1% sodium hypochlorite (NaOCl), and rinsed three times with sterilized distilled water to remove excess NaOCl for 1 minute each. The samples were then blotted dry with sterile filter paper before being placed onto 17% water agar (WA, 17% agar and distilled water) medium and incubated at room temperature (28±2°C) for three days. Following incubation, hyphal tips emerging from the samples were cut and transferred to potato dextrose agar (PDA, HiMedia, Mumbai, India). The fungal isolates were then examined under a Leica S8AP0 stereomicroscope (Leica Microsystems, Wetzlar, Germany) and a Leica DM750 compound microscope (Leica Microsystems, Wetzlar, Germany) to assess their preliminary morphological characteristics.

2.3 Preparation of Plant Disease Dataset

In this study, a dataset of 1,600 red-green-blue images of durian leaves affected by different leaf diseases was collected from a smartphone (iPhone 16, iOS version 18.6) with a resolution of 8,064 × 6,048 pixels. The digital images were taken using a photography box (40 cm wide × 40 cm deep × 40 cm high) with a light-emitting diode, with the object-to-camera distance about 45 cm. The image processing technique was coded in Python on Google Colaboratory (Google, California, USA). The images were categorized into four district groups (four classes): healthy leaf, leaf spot, leaf blight, and algal leaf spot, with 400 images per class. Sixty

percent (60%) of the dataset was allocated for training the model, ensuring that it learned patterns and disease characteristics effectively. Twenty percent (20%) of the data was set aside for validation, which was used to fine-tune the model's parameters and prevent overfitting. The remaining 20% was reserved as a test set, allowing an unbiased evaluation of the model's performance in classifying durian leaf diseases (Figure 1).

2.4 Development of the AI Model for Durian Leaf Disease Classification

The image processing technique and AI model were implemented in Python on Google Colaboratory (Google, California, USA). The image was resized to 224 x 224 pixels before being input to the model. Image augmentation, such as horizontal flipping, 90-degree rotation, brightness, and hue adjustment, was used to generate additional training examples to alleviate overfitting. This study employed a Convolutional Neural Network (CNN) to develop an AI model using a transfer-learning architecture based on MobileNetV2 for disease diagnosis. Model development began by defining the CNN architecture, consisting of three convolutional layers with 32 filters and a stride of 2, using the ReLU activation function. Additionally, average pooling layers were incorporated to reduce data size and computational complexity, thereby improving efficiency. The extracted features were then passed through a fully connected layer with 256 neurons. A 0.5 dropout rate was used to prevent overfitting, and the final classification was performed using a Softmax function that categorized the input images into different disease classes. The model was trained on the prepared dataset using Categorical Cross-Entropy as the loss function, which is well-suited to multi-class classification. The Adam optimizer was selected to efficiently optimize the model parameters. The training process was configured to run for 200 epochs with a batch size of 4 and a learning rate of 0.001, ensuring stable learning while minimizing the risk of overfitting (Figure 1). The first training period lasted about 26 seconds, and each of the next two to three epochs lasted about 2 to 3 seconds. This amounts to about 6–7 minutes in total across 200 epochs.

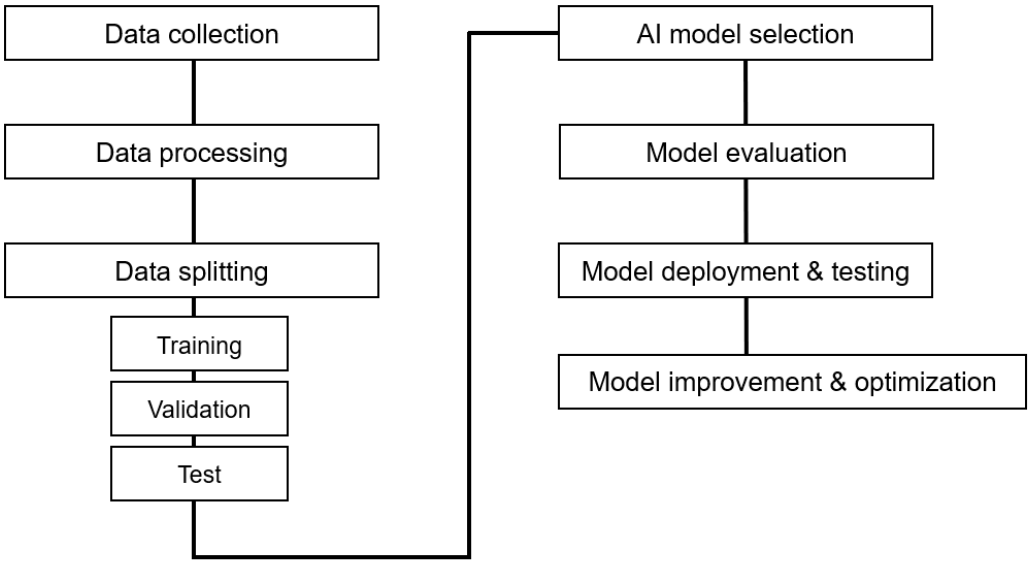


Figure 1. The schematic represents the preparation of the plant disease dataset and the development of the AI model for dirian leaf disease classification.

2.5 AI Model Test with Real Sample from the Fields

Unknown durian leaf disease samples were used to test the model's accuracy. The entire evaluation procedure was performed, and the results were expressed to assess the consistency of model performance. The model's accuracy was expressed as a percentage for each sample.

3. Results and Discussion

A survey of durian leaf diseases in Pa Phayom District, Phatthalung Province, and Chang Klang District, Nakhon Si Thammarat, revealed that the most commonly observed diseases were leaf spot, leaf blight, and algal leaf spot. Leaf samples exhibiting disease symptoms were collected and subjected to fungal isolation in the laboratory using the tissue transplanting technique. Preliminary morphological studies of the isolated fungi indicated that *Colletotrichum* sp. was isolated from leaf spot samples, while *Fusarium* sp. was isolated from leaf blight samples (Figure 2). These fungal genera have been previously reported in association with various durian diseases, including foliar diseases such as leaf spot and anthracnose, as well as non-foliar diseases such as twig dieback [11,12]. *Fusarium* species have been widely reported as important pathogens of durian, particularly associated with dieback and canker diseases [11]. For algal leaf spots, fungal cultures could not be established on standard fungal growth media. This finding aligns with the biological characteristics of algae, which typically require specific environmental conditions for growth [13]. Algae must be cultivated on specialized media, such as Bold's Basal Medium [14,15]. Although precise identification of fungal pathogens requires several methods, pathogen isolation and pathogenicity tests are needed to fulfill Koch's postulates, along with morphological characteristics and molecular identification [16,17]. However, this study did not conduct pathogenicity tests or molecular identification of the isolated fungi. Instead, it focused on documenting disease symptoms and identifying the fungal isolates at a preliminary level to support the development of a lightweight AI system for the initial classification of durian leaf diseases.

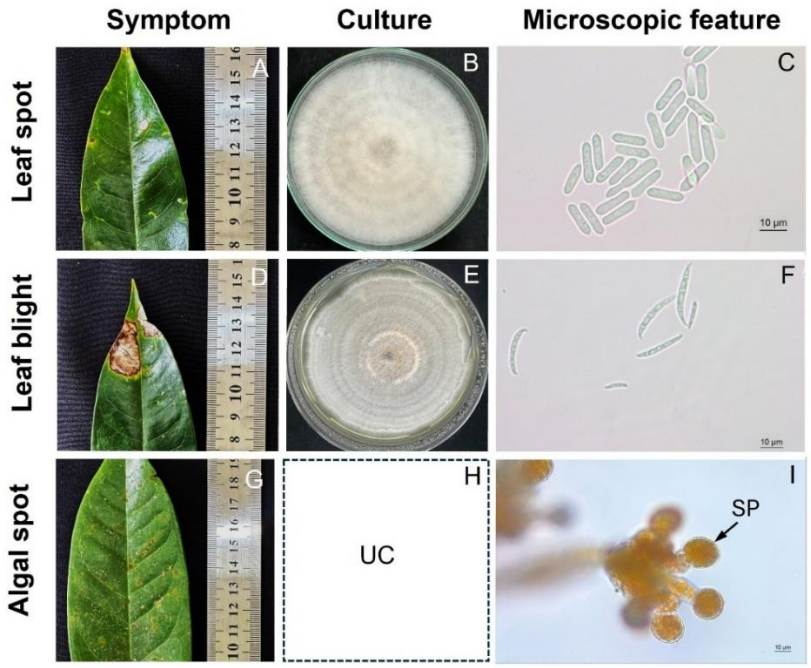


Figure 2. Symptom development of durian leaf disease and culture on potato dextrose agar (PDA), and microscopic features observed by a compound microscope. Durain leaf spot (A), colony of *Colletotrichum* on PDA (B), conidial mass (C), durian leaf blight (D), colony of *Fusarium* sp. on PDA (E), and conidial mass (F), durain algal leaf spot represent orange thalli (G), unculturable (UC) on PDA (H) and struccture of parasitic algae (I). The arrow indicates zoosporangia of the plant-parasitic alga *Cephaleuros*., SP = sporangia.

To develop an AI model for classifying durian leaf diseases, the dataset was split into three subsets: training (60%), validation (20%), and test (20%). This division ensures that the model can effectively learn patterns from the training data while being evaluated on separate validation and test sets. The model was developed using a Convolutional Neural Network (CNN), a deep learning technique widely used for image classification tasks. After training the model, its accuracy was analyzed using the model accuracy graph (Figure 3). The graph's X-axis shows the number of training iterations (epochs), while the Y-axis shows the

model's accuracy. The training accuracy curve shows a rapid increase in accuracy during the initial epoch, demonstrating that the model quickly learned distinguishable features of durian leaf diseases. As training progressed, accuracy continued to improve, eventually stabilizing between 98% and 100% in the later epoch. This stabilization suggests that the model effectively captured the dataset's key characteristics and achieved high classification accuracy.

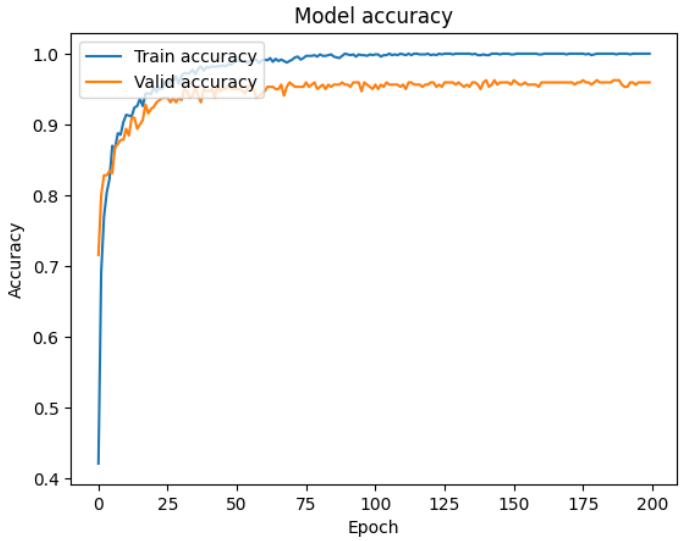


Figure 3. The learning curve from the training and validation datasets shows accuracy (Training accuracy: 1.00; Validation accuracy: 0.96). Training accuracy of the model across different epochs. The x-axis represents the number of epochs, and the y-axis shows the model's accuracy.

However, one critical aspect to consider in training deep learning models is overfitting. Suppose the model's accuracy on the training set is significantly higher than on the validation or test sets. In that case, it may indicate that the model has overfit the training data and struggles to generalize to new, unseen data. Without validation accuracy as a reference, there is a risk that the model may overfit the training data. To ensure the model's generalizability, it is essential to monitor validation accuracy and validation loss throughout training. These metrics help assess whether the model effectively classifies new data rather than memorizing the training dataset.

The model loss graph provides valuable insights into the AI model's learning process. This graph shows the loss values across different training epochs, helping assess whether the model is improving over time (Figure 4). The X-axis (Epochs) represents the number of training iterations, where each epoch refers to a complete pass through the training dataset. The Y-axis (Loss) indicates how far the model's predictions deviate from the expected values, with lower loss values suggesting better learning. The train loss curve shows a continuous decline as the number of epochs increases, indicating that the model is progressively learning from the data and reducing errors. The learning curve from the training and validation datasets shows a loss of 0.002 (Training loss) and 0.10 (Validation loss). This steady downward trend suggests that the model effectively captures the patterns in the dataset. Additionally, the absence of significant fluctuations in the graph indicates that the learning process is stable and free from erratic changes. If the loss continues to decrease without sudden increases, it implies that the model is learning efficiently and has not yet overfitted to the training data. However, to ensure optimal model performance, it is crucial to monitor both the validation and training losses. If the validation loss decreases alongside the training loss, it suggests the model is generalizing well. Conversely, if the validation loss begins to rise while the training loss continues to decline, this may indicate overfitting, where the model memorizes the training data but fails to perform well on new, unseen data (Figure 4).

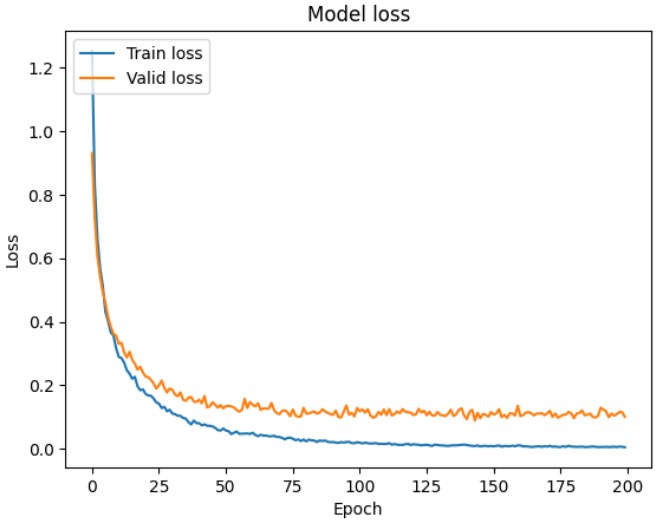


Figure 4. The learning curve from the training and validation datasets represents the loss. (Training loss 0.002, and Validation loss 0.10)Training loss of the model across different epochs. The x-axis represents the number of epochs, and the y-axis shows the loss.

Table 1 presents the performance of the proposed AI-based model for durian leaf disease classification, comparing predicted results with expert observations across four classes: healthy leaf, algal leaf spot, leaf blight, and leaf spot. The evaluation metrics include precision, recall, and F1-score, which provide a comprehensive assessment of the model's classification capability for each disease class. The model demonstrated strong performance across all classes, with precision values ranging from 0.96 to 0.98. The healthy leaf class achieved a precision of 0.96 and a recall of 0.98, indicating that the model accurately distinguished healthy leaves from diseased ones with minimal misclassification. Similarly, the algal leaf spot class achieved the best performance, with a precision of 0.98 and perfect recall of 1.00, resulting in an F1-score of 0.99. This suggests that the model was highly effective in identifying algal leaf spot symptoms. For the leaf blight class, the model achieved a precision of 0.96 and a recall of 0.97, yielding an F1-score of 0.96, indicating balanced and reliable classification performance. The leaf spot class exhibited slightly lower recall (0.91) compared to other classes, which may be attributed to visual similarities with other disease symptoms. Nevertheless, the precision remained high at 0.96, and the F1-score reached 0.94, reflecting satisfactory predictive capability. Overall, the macro-averaged F1-score of 0.96 and an overall accuracy of 0.97 confirm that the proposed model performs consistently well across all disease categories. These results demonstrate the model's robustness and its potential for practical durian leaf disease diagnosis in real-world agricultural settings.

Table 1. The comparison of leaf diseases in durian between the observer and the predictive model.

		Predicted leaf disease						
		Healthy leaf	**Algal leaf spot**	**Leaf blight**	**Leaf spot**	**Precision**	**Recall**	**F1-score**
Observers	Healthy leaf	82	0	0	2	0.96	0.98	0.97
	Algal leaf spot	0	86	0	0	0.98	1.00	0.99
	Leaf blight	0	1	68	1	0.96	0.97	0.96
	Leaf spot	3	1	3	73	0.96	0.91	0.94
Macro F1-score						0.96		
Accuracy						0.97		

To further evaluate the model's performance, it was tested for classifying three durian leaf diseases: leaf spot, leaf blight, and algal leaf spot in unknown samples. Figure 5 shows the predictions of the trained AI model on unseen durian leaf images. For each input image, the model outputs the probability distribution across four classes: healthy leaf, algal leaf spot, leaf blight, and leaf spot. For the image "Unknown1.jpg", the model classified the leaf as an algal leaf spot with a confidence of 100%, while assigning 0% probability to the healthy leaf, leaf blight, and leaf spot classes. This result indicates highly confident, correct classification, demonstrating the model's strong ability to recognize algal leaf spot symptoms. Similarly, for the image "Unknown2.jpg", the model again predicted algal leaf spot with 100% probability, with no confusion observed among the remaining disease classes. This further confirms the model's consistency and robustness in identifying algal leaf spot under different visual conditions. For the image "Unknown3.jpg", the model predicted algal leaf spot with a probability of 98.70%, assigning small probabilities to leaf blight (1.29%) and leaf spot (0.01%). Although minor confusion was observed between algal leaf spot and leaf blight, the dominant prediction remained correct, indicating that the model can effectively distinguish algal leaf spot even when visual features overlap with those of other disease symptoms. Overall, these results demonstrate that the proposed model provides high-confidence predictions and exhibits strong discriminatory power among durian leaf disease classes. The probability output also provides transparency into model decision-making, which is particularly valuable for practical applications, as users can assess prediction confidence when diagnosing diseases in real-world conditions.

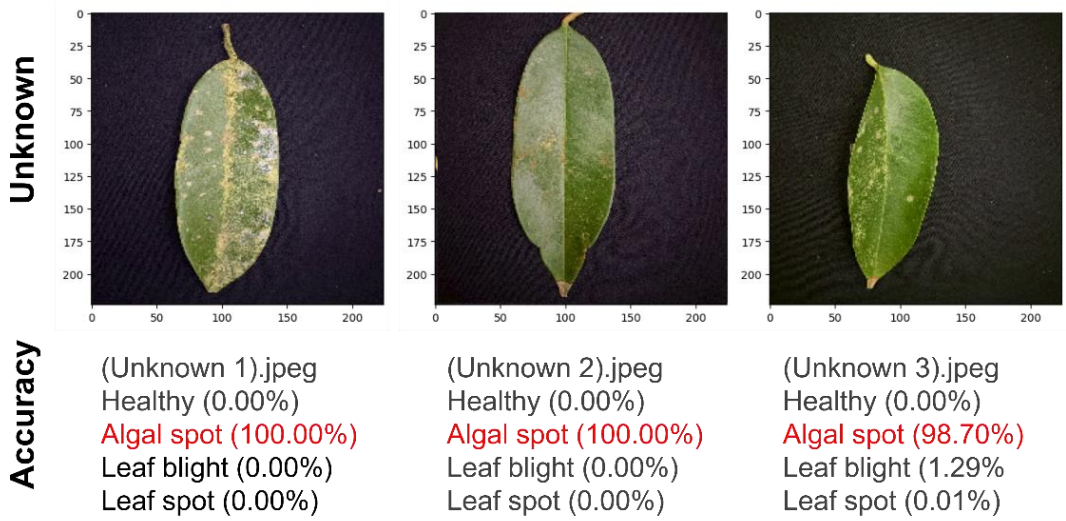


Figure 5. Classification results of durian leaf diseases using an artificial intelligence-based system. The left panel displays the predicted disease class and its associated probability for each test image.

The loss values significantly decreased after 200 epochs, further indicating that the model was well-trained and capable of distinguishing between different disease types with high reliability (Figure 5). The experimental results demonstrate that the CNN model effectively classifies durian leaf diseases with high accuracy, particularly for leaf spot and leaf blight. This aligns with previous studies on the application of CNNs in plant disease classification [18,19]. For example, Mohanty et al. [20] reported that CNN models could achieve up to 99% accuracy in identifying plant diseases from images. However, the classification accuracy for algal leaf spot was lower than that for the other two diseases. This may be attributed to unclear disease characteristics or to the visual similarity between infected and non-infected leaves, which makes classification more challenging [21]. Several factors could influence the model's performance, including dataset quality and data augmentation techniques used to enhance image diversity. Since deep learning models require large datasets to reduce the risk of overfitting, the effectiveness of data augmentation is crucial for improving model generalization [22]. Additionally, hyperparameter selection, such as learning

rate and batch size, significantly affects the training speed and model efficiency. Further optimization of these parameters may be required to achieve even better classification performance.

Although the developed system effectively classifies durian leaf diseases, it cannot identify the exact causal pathogens. For accurate pathogen identification, morphological characterization is required to distinguish algal species [23,24], while both morphological and multi-locus DNA analyses are necessary for fungal species identification [17,25]. The current system serves as a preliminary plant disease classification tool, but its real-world application requires consideration of external factors, such as lighting conditions and camera angles during image capture. This finding would help farmers manage their durian fields early using appropriate methods, such as chemical control [26], biological control [27], or integrated pest management [28]. Additionally, integrating the system into mobile devices or online platforms would enhance accessibility for farmers, making disease diagnosis more practical in the field. Future research should focus on expanding the model's ability to classify a broader range of durian diseases and on enhancing real-time disease analysis via mobile applications. These improvements would contribute to more efficient, user-friendly disease-detection systems for agricultural use.

In this study, a CNN-based model was developed to demonstrate the feasibility of image-based preliminary detection of durian leaf diseases. The primary focus was on model development and performance evaluation within a cloud-based environment (Google Colab), rather than on deployment-level optimization or hardware-specific benchmarking. Consequently, inference time, memory consumption, and computational efficiency on mobile devices were not directly evaluated in this study. The Google Colab environment is designed for model training and validation and does not support direct measurement of real-time inference performance on mobile hardware. Evaluating mobile deployment performance would require exporting the trained model and testing it on actual mobile devices under specific hardware conditions, which was beyond the scope of this study. Nevertheless, the proposed model demonstrates potential for future integration into mobile or web-based platforms to support field-level disease detection. Further work will focus on optimizing the model architecture, comparing it with established lightweight networks (e.g., MobileNet or EfficientNet), and benchmarking performance on mobile devices to enable practical, efficient deployment for real-world agricultural applications.

4. Conclusions

This study successfully developed an AI-based system using Convolutional Neural Networks (CNNs) for the preliminary detection and classification of common durian leaf diseases, namely leaf spot, leaf blight, and algal leaf spot, based on image analysis. The model demonstrated strong classification performance, particularly for leaf spot and leaf blight, consistent with previous studies highlighting the effectiveness of CNNs for image-based plant disease detection. The relatively lower accuracy observed for algal leaf spot may be attributed to the disease's subtle visual characteristics and its similarity to other leaf symptoms. It is important to note that the proposed system is intended as an initial screening tool rather than a definitive diagnostic method. Future work should focus on expanding the range of durian diseases included in the model, optimizing its deployment efficiency, and evaluating its performance under field conditions. These advancements would support early disease recognition and informed decision-making, ultimately contributing to more effective disease management and improved durian production.

5. Acknowledgements

We want to thank Durian Orchard, Moo 6, Pa Phayom Subdistrict, Pa Phayom District, Phatthalung Province, Thailand, for providing a sample site and durian leaf disease samples for this study. We want to thank Generative AI via ChatGPT for improving the academic English in this manuscript. This research was also supported by the Thaksin University, and partially supported by the Prince of Songkla University.

Author Contributions: Conceptualization, S.P., P.W. and A.S.; methodology, A.S.; software, S.T.; validation, P.W., S.T. and A.S.; formal analysis, S.T.; investigation, A.S.; resources, P.W., S.K.; data curation, S.T.; writing—original draft preparation, A.S.; writing—review and editing, P.W., S.K. and S.T.; visualization, A.S.;

supervision, P.W; project administration, P.W.; funding acquisition, A.S. and P.W. All authors have read and agreed to the published version of the manuscript.

Funding: This research was funded by Thaksin University and Prince of Songkla University.

Conflicts of Interest: The authors declare no conflict of interest.

References

[1] Thuan, T. T. M.; Tho, N.; Tuyen, B. C. First Report of *Rhizoctonia solani* Subgroup AG 1-ID Causing Leaf Blight on Durian in Vietnam. *Plant Dis.* **2008**, *92*(4), 648. https://doi.org/10.1094/PDIS-92-4-0648B

[2] Pitaloka, M. K.; Petcharat, V.; Sunpapao, A. *Cephaleuros solutus* Karsten as a Causal Agent of Durian (*Durio zibethinus* Murray) Algal Leaf Spot Disease in Thailand. *Khon Kaen Agric. J.* **2014**, *42* (Suppl. 3), 644–648.

[3] Tongsri, V.; Songkumarn, P.; Sangchote, S. Leaf Spot Characteristics of *Phomopsis durionis* on Durian (*Durio zibethinus* Murray) and Latent Infection of the Pathogen. *Acta Univ. Agric. Silvic. Mendel. Brun.* **2016**, *64*(1), 185–193. https://doi.org/10.11118/actaun201664010185

[4] Li, X.; Zhang, S.; Wang, X.; Wang, W. Applications of Artificial Intelligence in Plant Protection: A Review. *Front. Plant Sci.* **2022**, *13*, 845134.

[5] Pan, Y. Leaf Disease Detection and Classification with a CNN–LSTM Hybrid Model. *Appl. Comput. Eng.* **2024**, *104*, 7–20. https://doi.org/10.54254/2755-2721/104/20240902

[6] Duan, Z.; Li, H.; Li, C.; Zhang, J.; Zhang, D.; Fan, X.; Chen, X. A CNN Model for Early Detection of Pepper *Phytophthora* Blight Using Multispectral Imaging Integrating Spectral and Textural Information. *Plant Methods* **2024**, *20*(1), 115. https://doi.org/10.1186/s13007-024-01239-7

[7] Thanjaivadivel, M.; Gobinath, C.; Vellingiri, J.; Kaliraj, S.; Femilda Josephin, J. S. EnConv: Enhanced CNN for Leaf Disease Classification. *J. Plant Dis. Prot.* **2025**, *132*(1), 32. https://doi.org/10.1007/s41348-024-01033-6

[8] Pai, P.; Amutha, S.; Basthikodi, M.; Ahamed Shafeeq, B. M.; Chaitra, K. M.; Gurpur, A. P. A Twin CNN-Based Framework for Optimized Rice Leaf Disease Classification with Feature Fusion. *J. Big Data* **2025**, *12*(1), 89. https://doi.org/10.1186/s40537-025-01148-z

[9] Chen, J.; Wang, Y.; Liu, H.; Zhang, D. Deep Learning-Based Plant Disease Detection: Recent Trends and Future Perspectives. *Comput. Electron. Agric.* **2023**, *205*, 107586.

[10] Daengsuwan, W.; Wonglom, P.; Arikit, S.; Sunpapao, A. Morphological and Molecular Identification of *Neopestalotiopsis clavispora* Causing Flower Blight on *Anthurium andraeanum* in Thailand. *Hortic. Plant J.* **2021**, *7*(6), 573–578. https://doi.org/10.1016/j.hpj.2020.10.004

[11] Pongpisutta, R.; Keawmanee, P.; Sanguansub, S.; Dokchan, P.; Bincader, S.; Phuntumart, V.; Rattanakreetakul, C. Comprehensive Investigation of Die-Back Disease Caused by *Fusarium* in Durian. *Plants* **2023**, *12*, 3045. https://doi.org/10.3390/plants12173045

[12] Xu, H.; Zhang, Z.; Zhou, Z.; West, J. S.; Wang, J.; Cao, X. *Colletotrichum* Species Associated with Durian (*Durio zibethinus* Murray) in Hainan, China. *Crop Prot.* **2025**, *188*, 107034. https://doi.org/10.1016/j.cropro.2024.107034

[13] Wonglom, P.; Thithuan, N.; Sunpapao, A. Occurrence and Seasonal Development of Plant Parasitic Algae *Cephaleuros* (Chlorophyta, Ulvophyceae) in Southern Thailand. *Chiang Mai J. Sci.* **2026**, *53*(1), e2026013. https://doi.org/10.12982/CMJS.2026.013

[14] Agrawal, S. C.; Sarma, Y. S. R. K. Effects of Nutrients Present in Bold's Basal Medium on the Green Alga *Stigeoclonium pascheri*. *Folia Microbiol.* **1982**, *27*, 131–137. https://doi.org/10.1007/BF02879772

[15] Bunjongsiri, P.; Sunpapao, A. Optimal Growth Conditions for *In Vitro* Cultures of Plant Parasitic Algae *Cephaleuros*. *Philipp. Agric. Sci.* **2018**, *101*(1), 45–50. https://doi.org/10.62550/PB4550

[16] Sunpapao, A.; Suwannarach, N.; Kumla, J.; Dumhai, R.; Riangwong, K.; Sanguansub, S.; Wancahan, S.; Arikit, S. Morphological and Molecular Identification of Plant Pathogenic Fungi Associated with Dirty Panicle Disease in Coconuts (*Cocos nucifera*) in Thailand. *J. Fungi* **2022**, *8*(4), 335. https://doi.org/10.3390/jof8040335

[17] Daengsuwan, W.; Wonglom, P.; Sunpapao, A. First Report of *Lasiodiplodia theobromae* Causing Spadix Rot in *Anthurium andraeanum*. *J. Phytopathol.* **2020**, *168*(2), 129–133. https://doi.org/10.1111/jph.12877

[18] Boulent, J.; Foucher, S.; Théau, J.; St-Charles, P. L. Convolutional Neural Networks for the Automatic Identification of Plant Diseases. *Front. Plant Sci.* **2019**, *10*, 941. https://doi.org/10.3389/fpls.2019.00941

[19] Abade, A.; Ferreira, P. A.; de Barros Vidal, F. Plant Diseases Recognition on Images Using Convolutional Neural Networks: A Systematic Review. *Comput. Electron. Agric.* **2021**, *185*, 106125. https://doi.org/10.1016/j.compag.2021.106125

[20] Mohanty, S. P.; Hughes, D. P.; Salathé, M. Using Deep Learning for Image-Based Plant Disease Detection. *Front. Plant Sci.* **2016**, *7*, 1419. https://doi.org/10.3389/fpls.2016.01419

[21] Lu, J.; Hu, J.; Zhao, G.; Mei, F.; Zhang, C. A Combination of K-Means and Convolutional Neural Network for Automatic Fruit Segmentation and Identification in Natural Environments. *Comput. Electron. Agric.* **2017**, *142*, 338–350. https://doi.org/10.1016/j.compag.2017.09.012

[22] Shorten, C.; Khoshgoftaar, T. M. A Survey on Image Data Augmentation for Deep Learning. *J. Big Data* **2019**, *6*(1), 60. https://doi.org/10.1186/s40537-019-0197-0

[23] Thompson, R. H.; Wujek, D. E. *Trentepohliales, Cephaleuros, Phycopeltis and Stomatochroon: Morphology, Taxonomy and Ecology*; Enfield Publishing and Distribution: USA, 1997.

[24] Wonglom, P. Occurrence and Morphospecies Study of Plant-Parasitic Algae *Cephaleuros* on Betel Vine (*Piper betle*) in Southern Thailand. *Agrisc. Soc. J.* **2025**, *1*(2), 37–41.

[25] Chairin, T.; Pornsuriya, C.; Thaochan, N.; Sunpapao, A. *Corynespora cassiicola* Causes Leaf Spot Disease on Lettuce (*Lactuca sativa*) Cultivated in Hydroponic Systems in Thailand. *Australas. Plant Dis. Notes* **2017**, *12*, 1–3. https://doi.org/10.1007/s13314-017-0241-x

[26] Thaochan, N.; Pornsuriya, C.; Chairin, T.; Sunpapao, A. Roles of Systemic Fungicide in Antifungal Activity and Induced Defense Responses in Rubber Tree (*Hevea brasiliensis*) against Leaf Fall Disease Caused by *Neopestalotiopsis cubana*. *Physiol. Mol. Plant Pathol.* **2020**, *111*, 101511. https://doi.org/10.1016/j.pmpp.2020.101511

[27] Intana, W.; Kumla, J.; Suwannarach, N.; Sunpapao, A. Biological Control Potential of a Soil Fungus *Trichoderma asperellum* K1-02 against *Neoscytalidium dimidiatum* Causing Stem Canker of Dragon Fruit. *Physiol. Mol. Plant Pathol.* **2023**, *128*, 102151. https://doi.org/10.1016/j.pmpp.2023.102151

[28] Stenberg, J. A. A Conceptual Framework for Integrated Pest Management. *Trends Plant Sci.* **2017**, *22*(9), 759–769. https://doi.org/10.1016/j.tplants.2017.06.010

ASEAN
Journal of Scientific and Technological Reports
Online ISSN:2773-8752

Research article

Work-related Musculoskeletal Disorders among Rubber Tappers in Phatthalung Province, Thailand

Sutee Inraksa[1*], Angoon Sungkhapong[1], Supapan Chaiprapat[2], and Klangduan Pochana[2]

[1] Faculty of Engineering, Prince of Songkla University, Songkhla, 90110, Thailand
[2] Smart Industry Research Center, Department of Industrial and Manufacturing Engineering, Faculty of Engineering, Prince of Songkla University, Songkhla, 90110, Thailand
* Correspondence: juk007@hotmail.com

Citation:
Inraksa, S.; Sungkhapong, A.; Chaiprapat, S.; Pochana K. Work-related musculoseletal disorders among rubber tappers in Phatthalung province, Thailand. **2026**, *29*(4), e262782. https://doi.org/10.55164/ajstr.v29i4.262782.

Article history:
Received: December 12, 2025
Revised: February 5, 2026
Accepted: February 7, 2026
Available online: March 24, 2026

Publisher's Note:
This article is published and distributed under the terms of the Thaksin University.

Abstract: This cross-sectional study presents the prevalence of Work-related Musculoskeletal Disorders (MSDs) among rubber tappers in Pa Phayom District, Phatthalung Province, Thailand. The results were assessed using descriptive statistics and binary logistic regression at the 95% confidence interval, with consideration of variables influencing MSDs. The results showed that most participants (51.90%) were female, with a sample mean age of 43.95 ± 10.77 years, an average work experience of 13.68 ± 8.87 years, and a working time per day of 3.75 ± 1.52 hr. The physical work characteristics of the sample group revealed that the rubber plantations were on flat land (87.01%), more than 500 rubber trees were tapped per day (62.99%), the tapping height was below waist level (61.04%), and the rubber trees were older than 10 years (73.38%). The results for the severity of musculoskeletal disorders at the unbearable level showed that the lower back had the highest incidence (9.1%), followed by the upper back (2.6%). At the severe level, the lower back (26.6%) had the highest incidence, followed by the shoulder (7.8%) and the upper back (7.1%). When considering overall pain levels across different body parts, the hand/wrist was the most common (87.7%), followed by the neck (83.1%) and the lower back (82.5%). Factors associated with MSD symptoms among rubber farmers include the age of the trees and exercise. The reported acute MSD in their lower backs throughout the one-month study duration. Therefore, ergonomic knowledge should be promoted to help rubber farmers improve their working posture and reduce injuries.

Keywords: Musculoskeletal disorders; rubber tappers; ergonomics; rubber farmers

1. Introduction

Rubber tapping is a primary source of income for smallholder farmers across Southeast Asia, but the work is hazardous, exposing rubber tappers to multiple occupational hazards that can adversely affect health and productivity. Rubber tappers perform repetitive actions, such as cutting, forward bending, and trunk twisting, during prolonged standing—movements strongly associated with musculoskeletal disorders (MSDs). Studies in Thailand and neighboring countries reported high prevalence of lower back pain, shoulder pain, and upper-limb disorders among rubber farmers [1–3]. Rubber tappers are also vulnerable to injuries from knives, slipping on wet terrain, and encounters with insects or wildlife [4]. Many plantations use agrochemicals for weed and pest control, increasing chemical exposure linked to reduced quality of life and other chronic health effects among rubber farmers [5]. Assessment of

musculoskeletal disorders is therefore critical for estimating their severity and developing targeted preventive measures. Previous community-based studies in Southern Thailand have reported that musculoskeletal diseases (MSDs) are a concern among rubber tappers. Rubber tappers are more likely to experience lower back pain if they use improper ergonomics. It is necessary to implement preventive measures to reduce this issue in the future [1]. Current rubber tapping practices lack adequate health safeguards and pose significant health risks, including musculoskeletal injuries. Therefore, it is crucial to survey rubber tapping injuries to gather data for prevention, health promotion, and the development of activities to reduce work-related injuries [6,7]. In Pa Phayom District, Phatthalung Province, rubber farming is economically significant, but work-related musculoskeletal disorders have not been adequately documented. Therefore, a systematic investigation of musculoskeletal injuries in this local context is crucial to identify key causes, understand contributing factors, and propose concrete solutions to meet the needs of farmers. This study surveyed the musculoskeletal injuries and factors associated with MSD symptoms of rubber tappers in Pa Phayom District, Phatthalung Province. This study aims to present appropriate rubber tapping practices that reduce injuries and promote sustainable livelihoods among rubber farmers in southern Thailand.

2. Materials and Methods

This descriptive cross-sectional study evaluated the ergonomics of MSDs among rubber tappers in Phatthalung Province. A structured questionnaire and in-person interviews were used to gather data. The research was carried out between January 1, 2024, and September 30, 2025. The posture of rubber tapping is shown in Figure 1.



Figure 1. Rubber tapping posture of a rubber farmer (waist level)

2.1 Sample size

Phatthalung Province, Pa Phayom District has 256 registered rubber tappers. A simple sampling method [8] was employed to select 154 rubber tappers. The inclusion criteria included over one year of work experience, voluntary participation, and proficiency in Thai communication and comprehension. Rubber tappers with a history of MSDs or congenital diseases and ensuing musculoskeletal conditions such as gout, rheumatoid arthritis, or renal disease, as well as a history of injuries and conditions affecting the skeletal system and muscles, were excluded.

Sample Size Calculation

The sample size was calculated using the Krejcie and Morgan equation (1970), as shown in Equation 1, with a population of 256 members of a farmer group in Pa Phayom District (Phatthalung Provincial Agricultural and Cooperative Office, 2023).

$$n = \frac{x^2 Np(1-p)}{e^2(N-1)+x^2 p(1-p)} \quad (1)$$

n = Sample size
N = Population size
e = Acceptable sample error (e=0.05)
x^2 = Chi-square value at df = 1 and 95% confidence level (x^2 = 3.841)
p = Proportion of the characteristic of interest in the population (p = 0.5)

Substituting the values into the Krejcie-Morgan equation yields a sample size of 154.

2.2 Ethical approval

The Thaksin University Ethics Committee approved this study (COA No. TSU 2024_070 REC No. 0174). All the participants were informed of the study's purpose and signed informed consent forms before data collection.

2.3 Questionnaire

The research used a structural questionnaire adapted from Meksawi S. [1]. The three components comprising the questionnaire were 1) The demographic questionnaire includes gender, age, work experience, work time per day, marital status, religion, smoking, and drinking., 2), The physical work characteristics questionnaire consists of 9 questions: plantation ground level, trees tapped per day, tapping light, handedness, break time, standing posture, ages of trees, tapping height, and exercise., and 3) The MSDs assessment tool is adapted from the Nordic Musculoskeletal Disorder Questionnaire[9] and evaluates 12 body parts: lower back, upper back, hip/thigh, shoulder, hand/wrist, upper arm, foot, lower arm, calves, neck, knee, and elbow. The severity of the symptoms is categorized into four levels: 1) slight, 2) moderate, 3) severe, and 4) unbearable.

2.4 Statistical analysis

A statistical program was used to analyze the data. Frequency, percentage, mean, and standard deviation (SD) were calculated for physical work characteristics and demographic traits using descriptive statistics. Factors associated with MSD were identified using binary logistic regression, with ORs set at the 0.05 significance level. The prevalence of MSDs for every body part was recorded throughout the one-month study period.

3. Results and Discussion

3.1. Demographic data

Personal characteristics of a sample of 154 rubber farmers in Phatthalung province revealed that the majority were female (51.90%), with an average age of 43.95 ± 10.77 years. A quarter of the subjects were non-smokers, and one-third were teetotalers. Most participants were Buddhists (81.17%), and 69.48% were married. The sample group had relatively high work experience (13.68 ± 8.87) and rubber tapping time per day (3.75 ± 1.52). (Table 1).

3.2. Physical work characteristics

The tapping light was sufficient (89.60%) on the plantation ground level, which was mainly flat (87.01%), with tapping height below waist level (61.04%). Most rubber tappers balance standing posture (88.30%) and right-handedness (87.00%). The majority of the sample tapped rubber at a height below the waist (61.04%), and most rubber trees were older than 10 years (73.38%). Most rubber farmers take breaks between rubber tapping sessions (53.20%). It was also found that the majority of rubber farmers exercise (64.30%). (Table 2).

Table 1. Demographic characteristic (n =154).

Characteristic	n (%)
Age (mean± SD) yrs = 43.95 ± 10.77	
Work experience (mean ± SD) yrs = 13.68 ± 8.87	
Work time per day (mean ± SD) hr = 3.75 ± 1.52	
Gender	
Male	74(48.10)
Female	80(51.90)
Status	
Single	29(18.83)
Marry	107(69.48)
Widow/Divorced	18(11.69)
Religion	
Buddha	125(81.17)
Islam	29(18.83)
Smoking	
No	118(76.62)
Yes	36(23.38)
Drinking	
No	109(70.78)
Yes	45(29.22)

Table 2. Physical work characteristics (n =154).

Characteristics	n (%)
Plantation ground level	
Flat	134(87.01)
Slope	20(12.99)
Trees tapped per day	
≤ 500	57(37.01)
>500	97(62.99)
Tapping light	
Sufficient	138(89.60)
Insufficient	16(10.40)
Handedness	
Right	134(87.00)
Left	20(13.00)
Break time	
Yes	82(53.20)
No	72(46.80)
Standing posture	
Balance	136(88.30)
Not balance	18(11.70)

Table 2. Physical work characteristics (n =154). (Continue)

Characteristics	n (%)
Ages of trees	
≤ 10 yrs	41(26.62)
>10 yrs	113(73.38)
Tapping height	
Below waist	94(61.04)
Above waist	60(38.96)
Exercise	
No	55(35.70)
Yes	99(64.30)

3.3. Musculoskeletal disorders (MSDs)

The severity of musculoskeletal disorders, categorized by body part over the past month, has been reported as follows: Moderate discomfort was most commonly reported in the lower back (39.6%), hands and wrists (35.1%), and knees (30.5%), followed by the hip/thigh (26.6%) and neck regions. (26.0%) regions. and upper back (26.0%) regions. Severe to intolerable symptoms were recorded in the lower back (26.6%), shoulder (7.8%), and upper back (7.1%). In addition, it was found that at the unbearable level, the body parts with the highest values are the lower back (9.1%) and the upper back (2.6%) (Table 3 and Figure 2).

Table 3. Number and percentage of rubber tappers with levels of musculoskeletal discomfort, classified by body part (n =154).

Body Part	Discomfort Level				
	Not Discomfort	Slight	Moderate	Severe	Unbearable
Lower back	27(17.5)	11(7.1)	61(39.6)	41(26.6)	14(9.1)
Upper back	31(20.1)	68(44.2)	40(26.0)	11(7.1)	4(2.6)
Hip/ Thigh	62(40.3)	43(27.9)	41(26.6)	8(5.2)	0
Shoulder	29(18.8)	83(53.9)	29(18.8)	12(7.8)	1(0.6)
Hand /wrist	19(12.3)	70(45.5)	54(35.1)	10(6.5)	1(0.6)
Upper arm	71(46.1)	58(37.7)	16(10.4)	8(5.2)	1(0.6)
Foot	29(18.8)	81(52.6)	35(22.7)	8(5.2)	1(0.6)
Lower arm	54(35.1)	66(42.9)	29(18.8)	5(3.2)	0
Calves	53(34.4)	60(39.0)	35(22.7)	5(3.2)	1(0.6)
Neck	26(16.9)	84(54.5)	40(26.0)	3(1.0)	1(0.6)
Knee	38(24.7)	66(42.9)	47(30.5)	2(1.3)	1(0.6)
Elbow	84(54.5)	55(35.7)	13(8.4)	2(1.3)	0

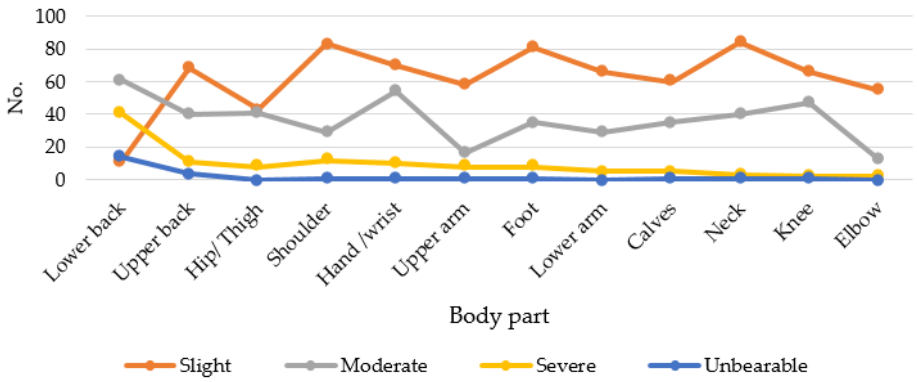


Figure 2. The graph shows levels of musculoskeletal discomfort, classified by body part.

3.4 The MSDs are classified as pain or no pain

The analysis of MSD symptoms, categorized by the presence or absence of pain, showed that most participants reported pain in the hand/wrist (87.7%), neck (83.1%), lower back (82.5%), and shoulder and foot (81.2%). Furthermore, the pain-free body parts were the elbow (54.5%), upper arm (46.1%), hip/thigh (40.3%), and lower arm (35.1%). (Table 4)

Table 4. The MSD results are classified according to whether or not the individual is in pain. (n = 154).

Body part	MSDs			
	Pain		No pain	
	Number	Percentage	Number	Percentage
Lower back	127	82.5	27	17.5
Upper back	123	79.9	31	20.1
Hip/ Thigh	92	59.7	62	40.3
Shoulder	125	81.2	29	18.8
Hand /wrist	135	87.7	19	12.3
Upper arm	83	53.9	71	46.1
Foot	125	81.2	29	18.8
Lower arm	100	64.9	54	35.1
Calves	101	65.6	53	34.4
Neck	128	83.1	26	16.9
Knee	116	75.3	38	24.7
Elbow	70	45.5	84	54.5

3.5 Factors associated with MSD symptoms in rubber farmers.

The results of the binary logistic regression analysis of the relationship between factors affecting MSDs are as follows: Ages of trees (OR=0.12, 95%CI=0.02-0.58) and Exercise (OR=0.15, 95%CI=0.03-0.79). Furthermore, other factors were found not to affect MSD symptoms (This analysis focuses only on the unbearable level) (Table 5).

Table 5. Factors associated with MSDs using binary logistic regression analysis. (n = 154).

Factors	OR	95%CI	P-value
Plantation ground level	0.56	0.05, 5.77	0.626
Trees tapped per day	1.15	0.27, 4.87	0.848
Tapping light	1.27	0.19, 8.30	0.802
Handedness	1.40	1.17,11.45	0.751
Break time	0.32	0.05, 1.76	0.192
Standing posture	4.67	0.72, 30.09	0.105
Ages of trees	0.12	0.02, 0.58	0.008*
Tapping height	0.44	0.10, 1.85	0.265
Exercise	0.15	0.03, 0.79	0.026*

*Statistics significant at *p-value* < 0.05

3.6 Discussion

The rubber tappers numbered more females than males, with those aged 20 to 60, consistent with findings by Meksawi S. [1] and M. Umar H.Y.[10], but different from Chow li Shan [11], S. Arphorn [12], and Chaigliang S. [13] for the age group between 41 and 60 years, because rubber plantations are most extensive in southern Thailand, leading many family members across different age groups to take up rubber tapping as their occupation. Participants who smoked numbered 23.38%, with more men than women, consistent with Shan C. L. [11] smokers being mostly males. The average working time per day was 3.75 hours, corresponding to < 5 hours by Shan C. L. [11] and Chaigliang S. [13], but different from Meksawi S. [1] at 6.2 hours. In Phatthalung, most households have small rubber plantations, so tapping time is shorter than in large rubber

plantations. The majority of rubber plantation areas are flat (87.01%), resulting in a balanced posture for rubber tapping (88.30%). The majority of the sample group is right-handed, consistent with Chaigliang S. [13]. The majority of rubber farmers are right-handed (71.84%). This aligns with the fact that the majority of the population is right-handed, so rubber-tapping knives are also manufactured for right-handed people. Most rubber farmers tap more than 500 trees per day (62.99%), which is inconsistent with Stankevitz's report [4]. This may be because rubber plantations in Sri Lanka are smaller than those in Thailand. The highest prevalence of severe-to-intolerable MSD discomfort occurred in the lower back, followed by the upper back. This result was consistent with previous research reports [1, 7, 11-13], as the posture for tapping rubber trees involves bending, twisting, or squatting below the knees. MSD pain, across all levels, is most commonly found in the hand/wrist, consistent with research reports [14], due to the repetitive hand and wrist movements required in the rubber tapping process. The highest MSD injury rate was recorded in the lower back because the rubber tapping process involves repetitive movements, and tapping below the waist requires continued bending. The analysis of factors related to MSD using binary logistic regression in this study found that exercise was the only significant factor ($p = 0.026$). Exercise helps strengthen the body and reduce injuries from rubber tapping, consistent with the research report by Chaigliang S. [7]. Hand-grip strength has a statistically significant effect on the risk of MSD. Furthermore, it was found that older rubber trees (>10 years) had higher MSD during rubber tapping ($p = 0.008$). Older rubber trees are larger, which helps reduce wrist bending and body twisting during tapping.

4. Conclusions

The study found that rubber farmers experienced MSD in all parts of the body after tapping rubber for 1 month, particularly in the lower and upper back. Furthermore, an analysis of MSD pain levels showed that the hand/wrist pain was the most severe. Factors associated with MSD included tapping light, break time, standing posture, age of trees, and exercise, all of which were statistically significant. The nature of rubber tapping involves twisting and bending the body, repeatedly twisting and jerking the wrists. Furthermore, ergonomically incorrect working postures involving excessive bending and straightening of the body can also lead to injuries. Therefore, ergonomic work postures should be improved, appropriate tools for rubber tapping should be designed, suitable rest periods should be planned, and occupational health and safety should be promoted among rubber farmers to ensure better working conditions and improved health.

5. Acknowledgements

The investigator would like to express gratitude. All of the advisers who consistently give up their precious time to offer thoughtful, considerate guidance, edit, and support until the researcher is finished with their work.

Author Contributions: Conceptualization: Inraksa S.; Methodology: Inraksa S., Chaiprapat S., Pochana K., and Sungkhapong A.; Validation, formal analysis: Chaiprapat S. and Pochana K.; Writing—original draft preparation, review, and editing: Inraksa S., Chaiprapat S., Pochana K., and Sungkhapong A. All authors have read and agreed to the published version of the manuscript.

Funding: This research received no external funding

Conflicts of Interest: The authors declare no conflict of interest

References

[1] Meksawi, S.; Tangtrakulwanich, B.; Chongsuvivatwong, V. Musculoskeletal Problems and Ergonomic Risk Assessment in Rubber Tappers: A Community-Based Study in Southern Thailand. *Int. J. Ind. Ergon.* **2012**, *42*(1), 129–135. https://doi.org/10.1016/j.ergon.2011.08.006

[2] Chokprasit, P.; Yimthiang, S.; Veerasakul, S. Predictors of Low Back Pain Risk among Rubber Harvesters. *Int. J. Environ. Res. Public Health* **2022**, *19*(17), 10492. https://doi.org/10.3390/ijerph191710492

[3] Varghese, V.; Panicker, V. V. Effect of MSDs and Scope of Ergonomic Interventions among Rubber Processing Workers: A Systematic Review. *Med. Lav.* **2022**, *113*(4), e2022032. https://doi.org/10.23749/mdl.v113i4.12826

[4] Stankevitz, K.; et al. Prevalence of Occupational Injury and Its Contributing Factors among Rubber Tappers in Galle, Sri Lanka. *Int. J. Occup. Environ. Health* **2016**, *22*(4), 333–340. https://doi.org/10.1080/10773525.2016.1247026

[5] Nippanon, P.; et al. Chemical Pesticide Use and Quality of Life of Rubber Farmers in the Northeast of Thailand. *Kathmandu Univ. Med. J.* **2019**, *17*(65), 3–8.

[6] Inraksa, S.; Sungkhapong, A.; Pochana, K. Risk Assessment of Rubber Tapping a Case Study: Pa Phayom District, Phatthalung Province, Thailand. *ASEAN J. Sci. Technol. Rep.* **2024**, *27*(5), e254127. https://doi.org/10.55164/ajstr.v27i5.254127

[7] Chaigliang, S.; Khanaphan, K.; Suggaravetsiri, P. Factors correlated with risk levels of musculoskeletal disorders among rubber planters. *J. Med. Tech. Phys. Ther.* **2020**, *32*(1), 82–94 (in Thai).

[8] Krejcie, R. V.; Morgan, D. W. Determining Sample Size for Research Activities. *Educ. Psychol. Meas.* **1970**, *30*(3), 607–610. https://doi.org/10.1177/001316447003000308

[9] Kuorinka, I.; et al. Standardised Nordic Questionnaires for the Analysis of Musculoskeletal Symptoms. *Appl. Ergon.* **1987**, *18*(3), 233–237. DOI: 10.1016/0003-6870(87)90010-x

[10] Hy, M. U.; Agbonaye, O.; Uwumarongie, A.; Eboigbe, G. Impact analysis of occupational hazard on the productivity of Rubber tappers in Rubber Research Institute of Nigeria, Iyanomo, Benin City. *Research Report* **2016**.

[11] Shan, C. L.; Adon, M. Y. B.; Rahman, A. B. A.; Hassan, S. T. S.; Ismail, K. B. Prevalence of Neck Pain and Associated Factors with Personal Charateristics, Physical Workloads and Pyschosocial among Male Rubber Workers in FELDA Settlement Malaysia. *Global J. Health Sci.* **2011**, *4*(1). https://doi.org/10.5539/gjhs.v4n1p94

[12] Arphorn, S.; Chaonesuan, P.; Pruktharathikul, V.; Singhakajen, V.; Chaikittiporn, C. A Program for Thai Rubber Tappers to Improve the Cost of Occupational Health and Safety. *Ind. Health* **2010**, *48*(3), 275–282. https://doi.org/10.2486/indhealth.48.275.

[13] Chaigliang, S. Occupational health risk assessment of musculoskeletal disorders on exposure to working ergonomic factors in para rubber plant farmers. *KKU J. Public Health Res.* **2019**, *14*(2), 32–44 (in Thai).

[14] Khanaphan, K.; Suggaravetsiri, P.; Chaigliang, S. Ergonomics risk and muscle fitness among rubber planters in Ubon Ratchatani Province. *UBRU J. Public Health Res.* **2019**, *8*(2), 21–31 (in Thai).

ASEAN
Journal of Scientific and Technological Reports
Online ISSN:2773-8752

Research article

SUMO-Based Optimization of Intersection Performance under Heterogeneous Traffic

Md. Emtiaz Kabir[1], Mehruba Akter Sara[2], Md. Ibrahim Islam Ifty[3], and Zaber Ahmed[4*]

[1] Department of Civil Engineering, Atish Dipankar University of Science & Technology, Uttara, Dhaka-1230
* Correspondence: zaber_ce@adust.edu.bd

Citation:
Kabir, E.M.; Sara, A.M.; Ifty, I.I.M.; Ahmed, Z. SUMO-Based optimization of intersection performance under heterogeneous traffic. *ASEAN J. Sci. Tech. Report.* **2026**, *29*(4), e261278. https://doi.org/10.55164/ajstr.v29i4.261278

Article history:
Received: September 15, 2025
Revised: January 24, 2026
Accepted: January 25, 2026
Available online: March 24, 2026

Publisher's Note:
This article is published and distributed under the terms of the Thaksin University.

Abstract: Traffic congestion is one of the most critical challenges in metropolitan cities, where intersections often experience long queues, high delays, and increased emissions due to mixed traffic and reliance on manual police control. This study examined how geometric improvements and signal timing optimization can improve the performance of a busy four-arm intersection in Uttara, Dhaka. Traffic data were collected through field surveys during peak hours and used to build a detailed microsimulation model in SUMO, which was calibrated against local driving behavior. Three scenarios were tested: the existing manual police control, channelization of turning lanes with current timings, and channelization with optimized fixed-time signals using Webster's method. Results showed that under current conditions, delays and queues were extremely high, corresponding to the lowest service level. Channelization alone reduced delays by up to 40% and improved overall flow. In contrast, the combination of channelization and optimized signals achieved the best outcomes, cutting delays to less than 40 seconds per vehicle, reducing queues by more than 70%, and improving the level of service to stable and acceptable conditions. An environmental analysis confirmed that the optimized scenario reduced fuel consumption and carbon emissions by 25–35% compared to current operations. These findings demonstrate that integrating physical improvements with evidence-based signal control can substantially enhance traffic efficiency, reduce energy use, and improve air quality in rapidly growing cities. The study provides practical insights for policymakers and planners seeking sustainable, low-cost solutions to congestion in Dhaka and other megacities facing similar challenges.

Keywords: Heterogeneous traffic; intersection performance; traffic signal optimization; SUMO microsimulation; urban traffic management

1. Introduction

Traffic congestion has become one of the most pressing urban challenges in Dhaka, Bangladesh, a megacity characterized by rapid urbanization, high population density, and increasing motorization [1]. According to recent studies, Dhaka consistently ranks among the most congested cities in the world, with travel speeds dropping sharply during peak periods, resulting in high economic, social, and environmental costs [2, 3]. Intersections, as the primary points of conflict and delay in road networks, are widely recognized as critical bottlenecks contributing to this chronic congestion problem [4].

A key feature of Dhaka's traffic environment is its diverse composition, including motorized vehicles such as buses, cars, trucks, motorcycles, and CNG three-wheelers alongside non-motorized rickshaws. The lack of lane discipline and weak enforcement further complicates traffic management at intersections. In many areas, traffic police rely on manual signal control, using hand signals to regulate traffic. While this approach offers flexibility during irregular traffic conditions, it often results in inconsistent green time allocation, reduced intersection efficiency, and significant delays during peak hours [5].

Globally, two strategies are commonly used to improve intersection performance: geometric channelization and traffic signal optimization. Channelization, which involves designating separate lanes for left-turn, right-turn, and through movements, reduces turning conflicts and increases discharge capacity. However, without coordinated signal control, its full potential remains limited. Signal optimization, on the other hand, ensures green times are allocated based on demand. Classical methods like Webster's are still popular in developing regions because of their simplicity and proven ability to decrease delays at intersections. Combining these two approaches — geometric improvements and optimized control — offers significant potential for sustainable congestion reduction, although this remains underexplored in Dhaka.

Recent advances in traffic microsimulation provide an opportunity to evaluate such integrated strategies under heterogeneous traffic conditions rigorously [6]. Simulation platforms such as VISSIM [7], AIMSUN [8], and SUMO [9] have been applied worldwide to assess intersection performance in complex traffic environments [10]. Among these, SUMO (Simulation of Urban Mobility) has proven particularly effective for developing cities due to its flexibility in modeling diverse vehicle classes, driver behaviors, and control schemes [11]. Several studies from India, Bangladesh, and Vietnam have shown that SUMO can realistically replicate mixed traffic dynamics when properly calibrated with local data [18-20]. Beyond operational efficiency, simulation-based studies also highlight the environmental benefits of improved traffic management, with optimized signals and channelization reducing fuel consumption and CO_2 emissions by 20–30% [15-17]. Despite this growing body of research, a clear gap remains in the Dhaka context. While some studies have examined either signal timing or geometric improvements in isolation [23, 24], very few have assessed their combined impact under heterogeneous traffic. Moreover, limited work has explored both operational and environmental implications, which are critical for a city facing both severe congestion and worsening air pollution.

To address this gap, the present study investigates the effectiveness of channelization and signal timing optimization at a major four-arm intersection in Uttara, Dhaka, using a calibrated SUMO microsimulation framework. A key contribution of this research is the rigorous calibration of the SUMO model using the Krauß car-following model, with locally observed traffic and driver-behavior parameters, explicitly tailored to Dhaka's heterogeneous, weakly lane-disciplined traffic conditions. Field-collected data were used to calibrate class-specific parameters for motorcycles, rickshaws, CNG three-wheelers, private cars, buses, trucks, and covered vans, and the model was validated against observed queue lengths and vehicle delays. This calibration-focused approach ensures that the simulated traffic dynamics closely represent real-world conditions, distinguishing the present study from generic microsimulation applications that rely on default parameter settings. Three operational scenarios were then analyzed: (i) the existing manual police control, (ii) channelization with observed signal timings, and (iii) channelization with optimized fixed-time signal control based on Webster's method. Performance was evaluated using multiple indicators, including delay, queue length, fuel consumption, CO_2 emissions, and level of service.

2. Methodology

The overall research methodology followed in this study is illustrated in Figure 1, which summarizes the sequential steps from data collection to model calibration, simulation, and performance evaluation. This framework ensured a systematic, reproducible approach to assessing intersection improvement strategies.

2.1 Study Area

The study was conducted at a four-arm intersection located in Uttara, Dhaka, one of the busiest sub-centers of the city, shown in Figure 2, where recurrent congestion is observed during peak hours. The selected

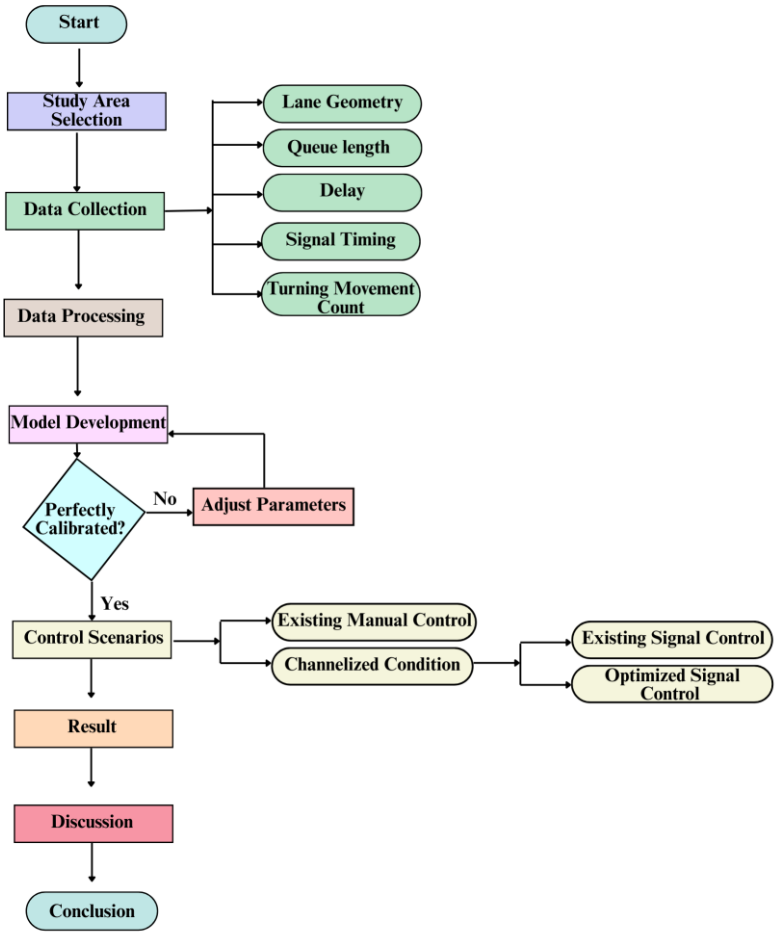


Figure 1. Research methodological framework outlining sequential steps from traffic data collection to model calibration, simulation, and performance evaluation.

Site experiences a heterogeneous traffic mix comprising buses, private cars, motorcycles, trucks, covered vans, CNG three-wheelers, and non-motorized rickshaws, typical of Dhaka's traffic environment. The intersection currently operates under manual signal control, with traffic police regulating movements for turning and through traffic. The geometric details of the intersection, including the number of lanes and lane widths, were measured in the field and are summarized in Table 1.



Figure 2. Study intersection at Zam Zam Tower, Uttara, Dhaka, showing approach lanes and geometric layout.

Table 1. Geometric characteristics of the study intersection

Approach	Number of Lanes	Lane Width (m)
NBD	2	3.5
SBD	2	3.5
EBD	3	3.5
WBD	3	3.5

2.2 Data Collection

Traffic data were collected using camera-based observation and manual counting across two peak periods: the weekday morning (08:00–09:00) and the evening (17:00–18:00) on Wednesday, 16th July, 2025. The selected day exhibited atypical dry day but realistic peak-period traffic patterns, capturing pronounced congestion conditions during both time windows. The surveys recorded detailed counts of turning movements for all approaches, disaggregated by vehicle class. Vehicles were counted manually from video footage to ensure accurate classification and movement tracking. In addition, average queue lengths (m) and average vehicle delays (s/veh) were manually measured on-site from direct field observations, while discharge rates were determined by observing the number of vehicles clearing the intersection during green phases under police control. The processed traffic data were converted into PCU using standard conversion factors [20], which are presented in Table 2 with vehicle dimensions [12]. The resulting total PCU values for each lane under different conditions are summarized in Table 3.

Table 2. Passenger Car Unit (PCU) equivalency factors and vehicle dimensions for heterogeneous traffic categories.

Category of Vehicles	Attribute	Equivalent PCU Factors		Dimensions	
		5%	10% and above	Length	Width
Two-wheeler (Motorcycle/Scooter)		0.5	0.75	1.9	0.6
Bus		2.2	3.7	10.6	2.5
Passenger Car		1.0	1.0	4.6	1.7
Rickshaw		1.2	2.0	2.3	1.5
Truck		2.2	3.7	7.5	2.5
CNG		1.2	2.0	2.9	1.8
Covered Van		1.4	2.0	5.5	2

2.3 Car-Following Model

In this study, the Krauß car-following model was implemented in SUMO to simulate longitudinal vehicle interactions. This model captures how a following vehicle adjusts its speed in response to the leading vehicle's behavior, accounting for driver reaction time, acceleration/deceleration limits, and stochastic imperfections.

The basic formulation is expressed as:

$$\frac{dv_i(t)}{dt} = \frac{v_n(t) - v_{n-1}(t)}{\tau} \tag{1}$$

where $v_n(t)$ is the speed of the leading vehicle, $v_{n-1}(t)$ is the speed of the following vehicle, $v_i(t)$ denotes the instantaneous speed of vehicle i. and τ is the driver's reaction time.

The safe velocity is calculated as:

$$v_{\text{safe}}(t) = v_l(t) + \frac{g(t) - g_{\text{des}}(t)}{\tau_b + \tau} \tag{2}$$

Table 3. PCU flows by vehicle type and approach during weekday morning and evening peak periods.

Vehicle Type	Source Lane	NBD	WBD	SBD	EBD	NBD	WBD	SBD	EBD
		Morning Peak				Evening Peak			
Bus	EBD	0	11	0	–	0	46.2	0	–
Private Car		18	218	34	–	34	206	33	–
CNG		2.4	39.6	3.6	–	21.6	58.8	14.4	–
Motorcycle		2.25	35.25	2.25	–	13.5	51.75	18	–
Truck		0	8.8	4.4	–	4.4	26.4	6.6	–
Covered Van		2.8	28	8.4	–	4.4	44	13.2	–
Rickshaw		248	336	164	–	44	300	160	–
Bus	SBD	0	0	–	0	0	0	–	0
Private Car		30	181	–	47	27	168	–	40
CNG		4.8	13.2	–	8.4	6	19.2	–	9.6
Motorcycle		7.5	23.25	–	20.25	6.75	18.75	–	13.5
Truck		0	4.4	–	0	4.4	4.4	–	0
Covered Van		7	8.4	–	9.8	8.4	16.8	–	30.8
Rickshaw		116	264	–	116	224	224	–	140
Bus	WBD	0	–	13.2	0	0	–	35.2	0
Private Car		37	–	159	23	38	–	121	38
CNG		1.2	–	16.8	1.2	12	–	46.8	8.4
Motorcycle		4.5	–	64.5	9	9	–	50.25	13.5
Truck		4.4	–	17.6	0	13.2	–	30.8	13.2
Covered Van		4.2	–	8.4	2.8	2.8	–	21	9.8
Rickshaw		108	–	288	194	204	–	362	272
Bus	NBD	–	0	0	0	–	0	0	0
Private Car		–	20	155	25	–	18	350	223
CNG		–	6	9.6	2.4	–	4.8	8.4	2.4
Motorcycle		–	7.5	12.75	7.5	–	6.75	11.25	6.75
Truck		–	4.4	13.2	11	–	4.4	11	8.8
Covered Van		–	4.2	9.8	2.8	–	4.2	8.4	2.8
Rickshaw		–	148	260	182	–	134	234	274

where $v_l(t)$ is the speed of the leader, g(t) is the actual spacing between vehicles, $g_{\text{des}}(t)$ is the desired gap, and τ_b represents the braking reaction time. The spacing is given by:

$$g(t) = x_l - x_f - l \tag{3}$$

with $x_l(t)$ and $x_f(t)$ denoting the positions of the leader and follower, respectively, and l the vehicle length.

The desired velocity is

$$v_{des} = min[\, v_{max}, v_t + a(v)\Delta t, v_{safe}(t)] \tag{4}$$

where v_{des} is the desired velocity, v_{max} is the maximum allowable speed, v_t is the current speed, a(v) is the acceleration function, Δt is the simulation time step, and v_{safe} is the safe speed.

Finally, the updated vehicle velocity with stochastic variation is:

$$v(t + \Delta t) = \max\{0,\ v_{\text{des}}(t) - \eta\} \tag{5}$$

where η is a random noise term representing driver imperfection.

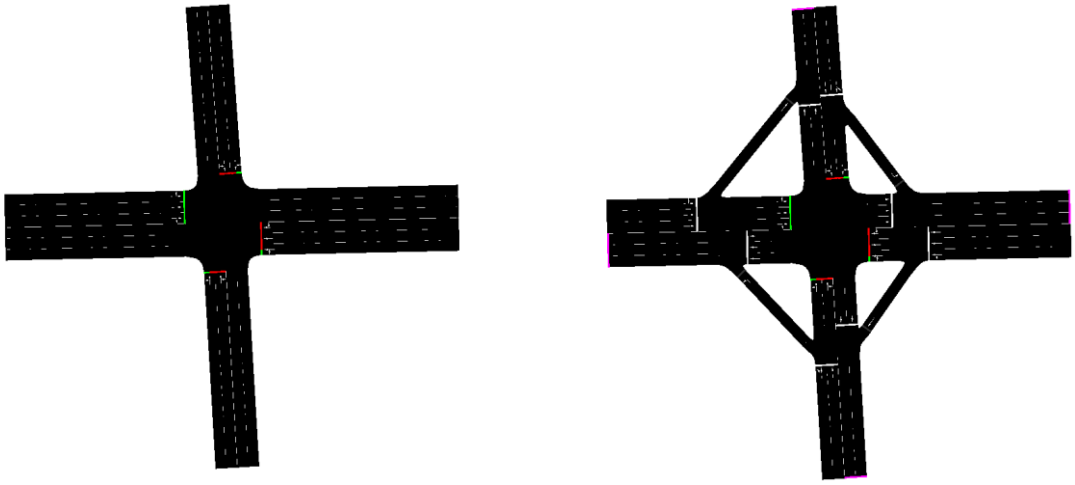


Figure 3. Network development in SUMO illustrating baseline (non-channelized) and channelized control strategies.

2.4 Network Development in SUMO

The intersection was modeled in SUMO using NetEdit, incorporating the exact geometric details such as lane widths, approach lengths, and turning connections. Vehicle flows were generated in the .rou.xml file based on observed turning counts, while multiple vehicle classes were defined with specific parameters for length, acceleration, deceleration, and maximum speed to represent the heterogeneous traffic conditions of Dhaka realistically. Figure 3 shows the developed network with baseline and channelized control strategies.

2.5 Model Calibration and Validation

The SUMO microsimulation was calibrated to replicate the field-observed traffic dynamics of the study intersection, with emphasis on queue formation and per-vehicle delay as the primary performance indicators. The model incorporated the heterogeneous vehicle fleet (motorcycles, cars, CNG three-wheelers, rickshaws, covered vans, buses, and trucks), and class-specific attributes were assigned based on field observations and regional literature [12]. The calibration and validation process is described below.

2.5.1 Representation of Vehicle Classes

Each vehicle class was explicitly represented with parameters for length, acceleration, deceleration, and desired speed to reflect local traffic characteristics. For example, rickshaws and CNGs were modeled with shorter lengths and lower speeds, while buses and trucks were assigned lower acceleration/deceleration envelopes.

2.5.2 Calibration Parameters

Model calibration was treated as a central component of this study rather than a routine preprocessing step, given the complexity of heterogeneous traffic and weak lane discipline observed at the study intersection. Calibration focused on car-following and lane-changing parameters, as they significantly influence mixed-traffic dynamics in Dhaka. The explored parameter ranges and the corresponding calibrated values are summarized in Table 4. The following aspects were systematically adjusted:

Car-following (tau, sigma): Time-headway (τ) was varied within class-specific ranges (motorcycles: 0.7–0.9 s, rickshaws: 0.6–0.8 s, cars: 1.0–1.2 s, covered-vans: 1.2–1.5 s, buses/trucks: 1.5–2.0 s). Driver randomness (σ) was explored between 0.5 and 0.8 to capture weak lane discipline.

Lane-changing (minGap, aggressiveness): Minimum gaps for lane-change checks were reduced (0.3–0.7 m), while strategic aggressiveness was modestly increased (+10–30%) to reproduce opportunistic weaving.

Speed & Dynamics (vType): Desired speeds were set — Motorcycle (9.7 m/s), Rickshaw (3.3 m/s), Car (6.9 m/s), Covered Van (5.6 m/s), Bus (5.0 m/s), and Truck (4.2 m/s) — with uniform acceleration (2.8 m/s^2) and deceleration (1.9 m/s^2) applied across all vehicle types to ensure consistent calibration of movement dynamics [12].

Table 4. Calibrated SUMO model parameters for different vehicle classes with explored ranges and final selected values.

Parameter (SUMO name)	Vehicle class	Explored range	Final calibrated value
tau (s)	Motorcycle	0.7 – 0.9	0.8
	Rickshaw	0.6 – 0.8	0.7
	Car	1.0 – 1.2	1.1
	Covered van	1.2 – 1.5	1.3
	Bus & Truck	1.5 – 2.0	1.6
sigma (driver imperfection)	All classes	0.5 – 0.8	0.65
minGap (m)	All classes	0.3 – 0.7	0.45

Vehicle lengths: Adjusted to reflect the local fleet, with motorcycles, rickshaws, and CNGs shorter than cars, and Cavad vans intermediate, shown in Table 2.

2.5.3 Calibration Procedure

Calibration followed an iterative and structured process in which one parameter family (e.g., car-following) was varied at a time, and the resulting model outputs in terms of average queue length and delay were compared against field data. Parameter sets that improved fit across approaches were retained, and the process was repeated until the simulated queue lengths (m) and delays (s/veh) closely matched observed values. Goodness-of-fit was evaluated using the Root Mean Square Error (RMSE) for queue length and the Mean Absolute Percentage Error (MAPE) for delay. Calibration was deemed satisfactory once both metrics fell below the accepted microsimulation threshold of ≤15%.

$$\text{RMSE} = \sqrt{\frac{1}{n}\sum_{i=1}^{n}(\text{Simulated}_i - \text{Observed}_i)^2} \tag{6}$$

$$\text{MAPE} = \frac{100}{n}\sum_{i=1}^{n}\frac{|\text{Simulated}_i - \text{Observed}_i|}{\text{Observed}_i} \tag{7}$$

2.5.4 Validation

To prevent overfitting, validation was performed using hold-out field data. A one-traffic-phase segment from each peak-hour observation, excluded during calibration, was used for model validation. Multiple stochastic replications confirmed robustness. The model's ability to reproduce average queue lengths and delays at each approach was assessed and summarized in Table 5.

Table 5. Validation results comparing observed and simulated average queue lengths and vehicle delays for each intersection approach.

Approach	Average Queue Length			Average Delay		
	Observed (m)	Simulated (m)	% Error	Observed (s/veh)	Simulated (s/veh)	% Error
Northbound	38	42	10.53%	106	112	5.66%
Southbound	35.3	38	7.65%	87	92	5.75%
Eastbound	34.8	36	3.45%	83	88	6.02%
Westbound	31.2	34	8.97%	74	79	6.76%

Additionally, sensitivity tests were conducted by varying τ and σ by ±10%. The qualitative ranking of the three strategies (baseline, channelised, Webster) remained unchanged, confirming stability of results under plausible behavioral uncertainty.

The validation results indicate that the simulation model reasonably replicates observed traffic conditions, with an RMSE of 2.24 m for queue lengths and 4.1 s/veh for vehicle delays, and MAPE of 7.15 % and 6.05 % for queues and delays, respectively.

2.5.5 Emission modeling in SUMO

CO_2 emissions were estimated using SUMO's HBEFA-based emission model, which calculates instantaneous emissions as a function of vehicle speed and acceleration. Each heterogeneous vehicle class was mapped to an appropriate HBEFA emission category based on its size and operating characteristics. Emission outputs were generated directly from SUMO using the .emission.xml output file, which records per-vehicle emission rates at each simulation step. The reported CO_2 values (mg/s) represent average emission rates aggregated across all vehicles and simulation replications for each control scenario and peak period.

2.6 Control Scenarios

To ensure a consistent and transparent evaluation, three traffic control conditions were developed and tested in SUMO. Each scenario reflects a different level of intervention, ranging from the current observed operation to proposed engineering and signalization strategies.

2.6.1 Existing Manual Control (Baseline)

Field observations confirmed that the intersection is operated manually by police officers, without any fixed cycle length. Green time allocations varied according to the officer's discretion, traffic volume, and congestion levels. However, to simulate this condition in SUMO, the observed timings were averaged for each approach and used as a representative baseline signal plan, as shown in Table 6.

Table 6. Average observed green times under manual police control for each intersection approach.

Approach	Avg. Green (s)	Range Observed (s)
Northbound Direction(NBD)	55	30–120
Southbound Direction (SBD)	60	40–110
Eastbound Direction (EBD)	50	35–100
Westbound Direction (WBD)	65	45–115

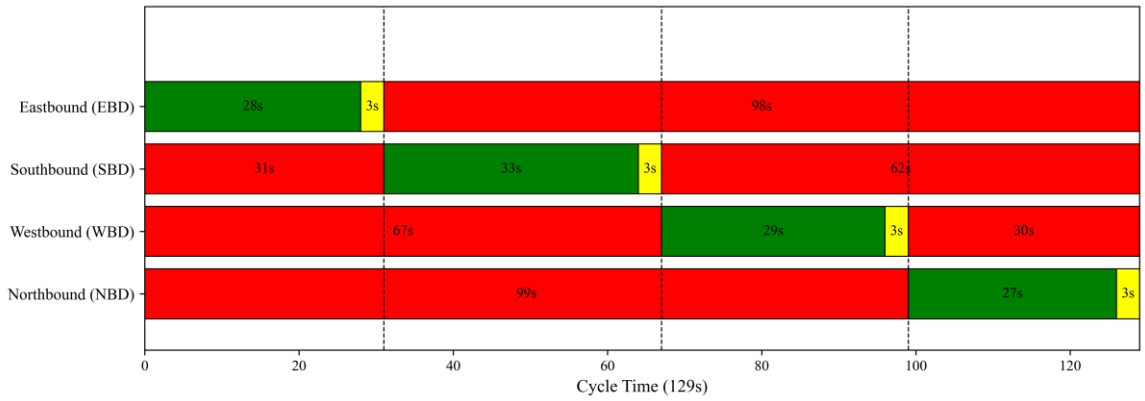


Figure 4. Optimized fixed-time signal plan for the study intersection, designed using Webster's method.

The baseline simulation was configured in SUMO using the average green splits observed in the field, without applying any fixed cycle optimization. All turning and through movements were allowed within the same green phase, as no channelization was introduced. This setup was designed to replicate the irregular and discretionary nature of manual police control while providing a consistent and reproducible baseline against which alternative signal control strategies could be evaluated.

2.6.2 Channelized Condition

In this scenario, geometric improvements were implemented without altering the overall control type. Dedicated lanes were introduced for left-turn and through movements on each approach, reducing blocking conflicts and enhancing lane discharge capacity. Channelization improved lane discipline and ensured more efficient utilization of the available green time. Two signal control strategies were tested under the channelized configuration:

Existing Signal Control: The same average observed green times (Table 6) were applied to replicate the manual officer-based control. This setup allowed the assessment of benefits achieved solely through geometric improvements, without altering the signal timing plan.

Optimized Signal Control (Webster's Method): A fixed-time signal plan was designed using Webster's formula:

$$C = \frac{1.5L + 5}{1 - \sum y} \quad (8)$$

where L represents the total lost time per cycle (s), and ∑y is the sum of critical flow ratios. The resulting optimal cycle length was then allocated into green splits proportional to the critical lane-group flows. A multiphase plan was developed to ensure safe sequencing of turning and through traffic movements, as illustrated in Figure 4. This condition represents a fully engineered traffic signalization strategy aimed at minimizing average delay and maximizing overall intersection efficiency.

Table 7. Intermediate parameters and phase-wise signal timing obtained using Webster's method for the optimized channelized intersection.

Phase	Approach	Lanes	Saturation Flow (PCU/h/lane)	yi	Effective Green (s)	Lost time (s)	Adopted cycle length (s)
1	Eastbound (EBD)	3	1890	0.20	28	3	129
2	Southbound (SBD)	2	1890	0.24	33	3	
3	Westbound (WBD)	3	1890	0.20	29	3	
4	Northbound (NBD)	2	1890	0.18	27	3	

Table 7 summarizes the key parameters and results of the signal timing optimization for the channelized intersection. It presents the saturation flow rates assumed for each approach, the corresponding critical flow ratios (yi), and the effective green times allocated to each phase based on demand. A uniform lost time of 3 s per phase is assumed, yielding an optimized common cycle length of 129 s. The distribution of effective green times reflects the relative traffic demand of each approach: the southbound approach receives the highest green time due to its larger critical flow ratio. In contrast, the remaining approaches are allocated comparable green times consistent with their respective yi values.

Table 8. Level of Service (LOS) classification based on average vehicle control delay according to HCM standards.

LOS	Average Control Delay (s/veh)	Description
A	≤ 10	Free flow; very little delay, high comfort.
B	> 10 – 20	Stable flow; short delays, acceptable operations.
C	> 20 – 35	Stable flow; noticeable delays, satisfactory operations.
D	> 35 – 55	Approaching unstable flow; longer delays, tolerable for short periods.
E	> 55 – 80	Unstable flow; very long delays, operating near capacity.
F	> 80	Forced/unacceptable flow; breakdown conditions with excessive delays.

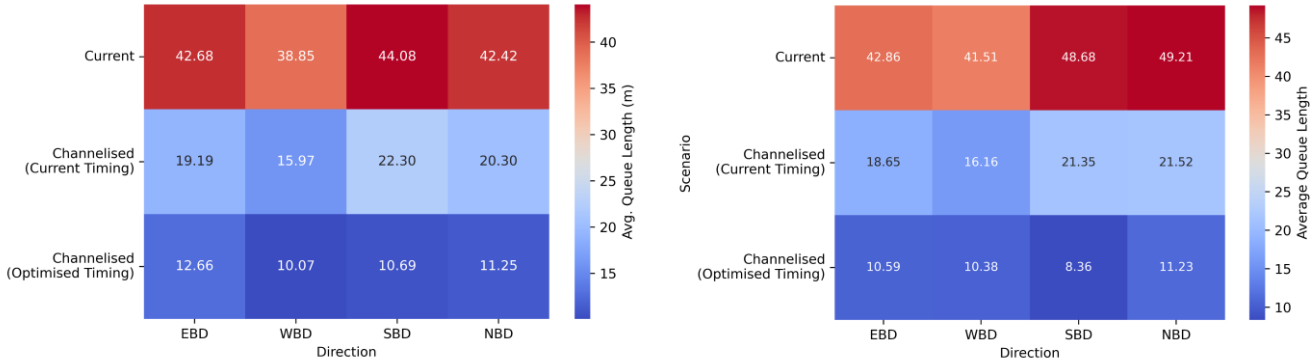
2.7 Simulation Experiments

Simulations were run for each control strategy across the four defined traffic periods, with multiple replications to minimize stochastic variability and ensure reliable results. The evaluation was based on key performance indicators, including average queue length (m), average vehicle delay (s/veh), fuel consumption (mg/veh), and CO_2 emissions (mg/veh). These performance measures enabled a comprehensive assessment of the intersection's operational efficiency and environmental impacts under different management strategies. Later, the Level of Service (LOS) was evaluated from the Average Vehicle delay [21]. The standard chart for finding LOS is given in Table 8.

3. Results

3.1 Average Queue Length

The simulation results reveal notable variations in queue lengths across the three operational scenarios, as illustrated in Figure 5. During the morning peak, the Current scenario exhibits severe congestion, with the Southbound (44.08 m), Eastbound (42.68 m), and Northbound (42.42 m) approaches



(a) Morning Peak hour (b) Evening Peak hour

Figure 5. Average queue length across four approaches under three control strategies

experiencing the longest queues. Introducing channelization under existing timings substantially alleviates congestion, reducing queues to within 15–22 m. The greatest improvement, however, is observed under the Channelized with Optimized Timing scenario, where all approaches fall below 13 m, with Eastbound achieving the minimum at 12.66 m.

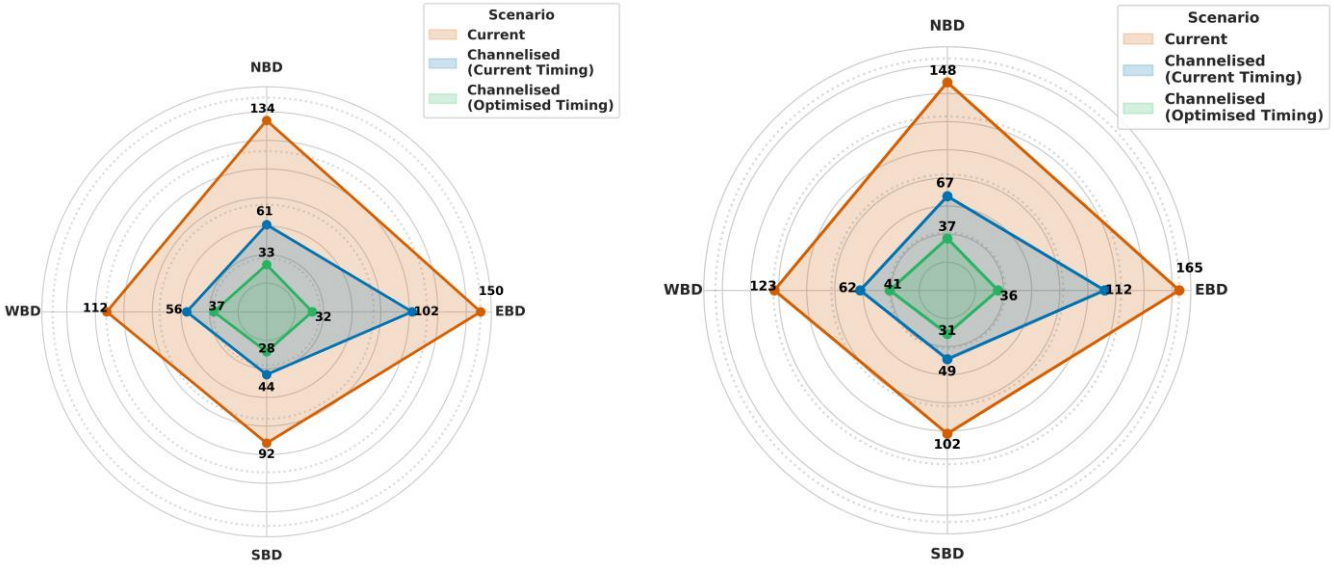
Evening peak conditions demonstrate heightened traffic demand, leading to longer queues overall. Under the Current scenario, Northbound (49.21 m) and Southbound (48.68 m) approaches display critical bottlenecks. Channelization moderates these queues to a range of 16–22 m, while optimization reduces them further to 8.36–11.23 m, the Southbound approach recording the lowest. Comparatively, queues are consistently higher in the evening; nevertheless, the combined effect of channelization and optimized timings delivers reductions exceeding 70% relative to the baseline, underscoring the role of integrated strategies in enhancing operational efficiency.

3.2 Average Vehicle Delay

The analysis of average vehicle delays further reinforces the trends observed in queue length performance, as illustrated in Figure 6. During the morning peak period, the Current scenario exhibits excessive delays across all approaches, particularly severe impacts on Eastbound and Northbound movements, with average delays of approximately 150 s and 134 s, respectively. The introduction of geometric channelization while retaining existing signal timings results in measurable performance improvements, most notably on the Eastbound approach, where average delay is reduced to about 102 s. However, residual congestion persists on several approaches, indicating that geometric improvements alone are insufficient to address operational inefficiencies fully. The application of optimized signal timing in conjunction with channelization yields substantial additional benefits, reducing average delays on all approaches to below 40 s. This improvement reflects a more balanced allocation of green time that better matches approach-specific demand, resulting in smoother traffic progression and reduced intersection delay during the morning peak.

During the evening peak period, traffic demand increases considerably, leading to more pronounced congestion and systematically higher delays than in the morning. Under the Current scenario, delays reach critical levels, with eastbound traffic experiencing an average delay of approximately 165 s and northbound traffic around 148 s. Although channelization under existing timings provides partial relief, it does not fully mitigate the intensified congestion or eliminate the performance gap between morning and evening conditions. In contrast, the optimized signal timing strategy remains highly effective under heavier demand, reducing average delays to a narrow range of 31–41 s across all approaches. Overall, the findings indicate that

while evening peak conditions inherently impose greater operational stress on the intersection, the combined implementation of channelization and optimized signal timing consistently delivers substantial delay reductions. This demonstrates the robustness of the proposed strategy and its ability to maintain acceptable service levels even under high-demand, heterogeneous traffic conditions.



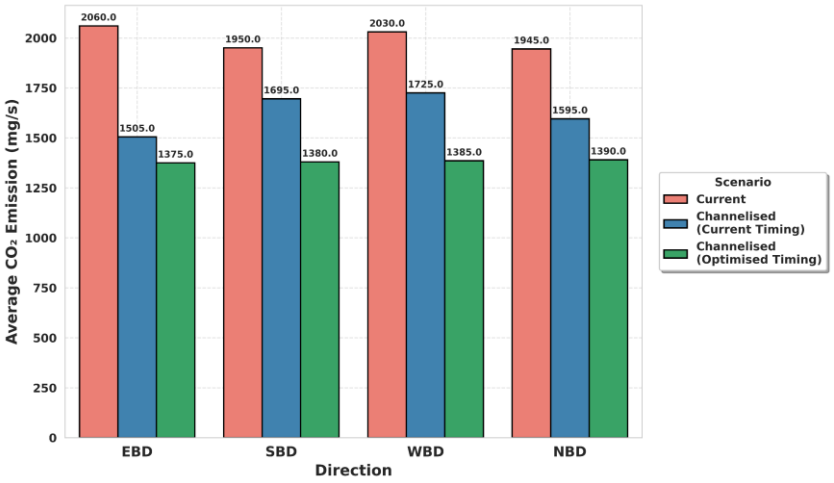
(a) Morning Peak hour (b) Evening Peak hour

Figure 6. Average vehicle delay (s) across four approaches under different control strategies

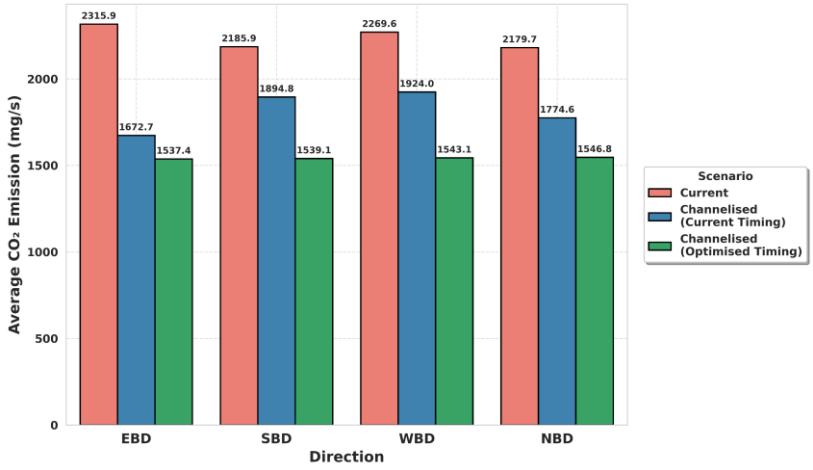
3.3 Carbon Dioxide Emissions

The analysis of average CO_2 emissions, illustrated in Figure 7, further highlights the efficiency gains achieved through the combined application of geometric and signal-control improvements. Under the Current scenario, emissions remain consistently high, exceeding 2,100 mg/s across all approaches, with the Eastbound approach reaching a peak value of 2,315.89 mg/s, reflecting prolonged idling, frequent stops, and inefficient queue discharge. The introduction of channelization reduces emissions to a range between 1,672.65 mg/s on the Eastbound approach and 1,924.01 mg/s on the Westbound approach, indicating that geometric reconfiguration alone can partially mitigate unnecessary idling and improve vehicle progression. These reductions are consistent with the observed decreases in queue lengths and delays, confirming the strong linkage between operational efficiency and emission performance. However, the remaining emission levels suggest that further improvements require complementary signal optimization to fully exploit the benefits of geometric interventions under heterogeneous traffic conditions.

The most substantial reductions are achieved in the Channelized with Optimized Timing scenario, where emissions converge to a narrow band of 1,537–1,547 mg/s across all directions. This outcome reflects the synergistic effect of smooth traffic progression and reduced stop-and-go operations. Although evening peaks generate slightly higher emissions than morning peaks, consistent with longer delays and queues, the optimized channelization scenario reduces emissions by 25–35% relative to the Current scenario. These findings confirm the dual benefits of traffic management strategies: improving operational efficiency while reducing environmental impacts.



(a) Morning Peak hour

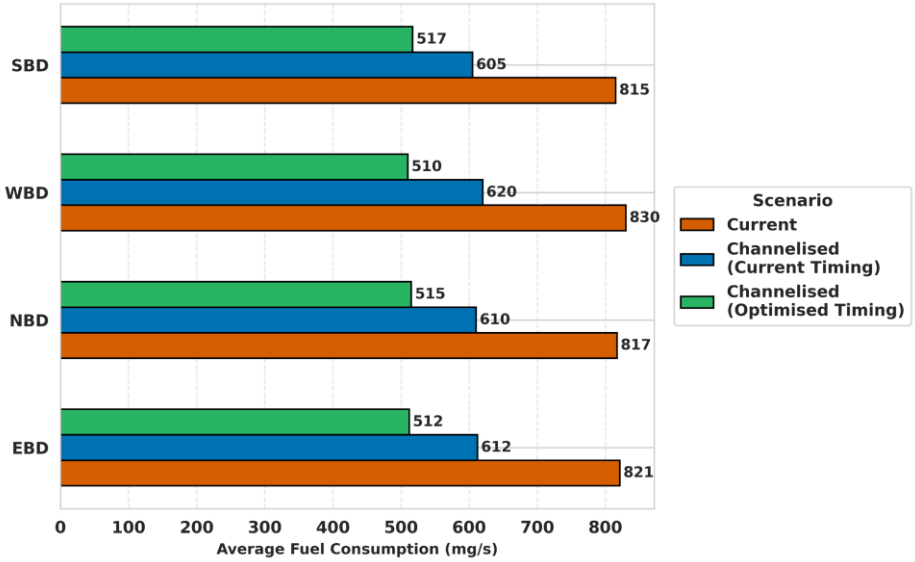


(b) Evening Peak hour

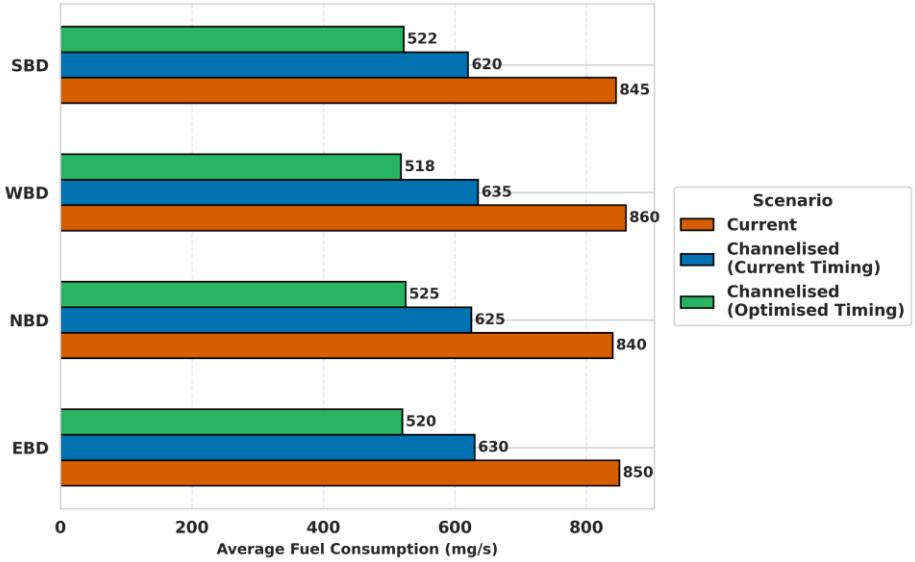
Figure 7. Average CO_2 emissions by approach for each control strategy

3.4 Fuel Consumption

Fuel consumption patterns mirror those of delay and emissions. In both the morning and evening peaks, the Current scenario yields the highest consumption, with all approaches exceeding 815 mg/s in the morning and rising to 860 mg/s in the evening, as shown in Figure 8. Channelization under existing timings reduces these values by approximately 200–220 mg/s, while the addition of optimized timings contributes a further reduction of 90–110 mg/s. Evening conditions consistently lead to higher fuel consumption, attributable to higher traffic volumes and longer idling times. For example, the Westbound approach records 830 mg/s in the morning under the Current scenario, increasing to 860 mg/s in the evening. Similar differences are evident across other approaches. Despite this, the optimized channelization strategy consistently outperforms alternatives, minimizing idling and smoothing discharge flows. These results underline the importance of combining physical and control measures not only for congestion relief but also for reducing energy consumption at urban intersections.



(a) Morning Peak hour



(b) Evening Peak hour

Figure 8. Average fuel consumption across four approaches under three control strategies

3.5 Comparative performance and statistical significance

Table 9 compares the performance of the three control strategies under repeated simulation runs for both morning and evening peak hours. The results show a clear and consistent reduction in average delay, queue length, CO_2 emissions, and fuel consumption as the control strategy progresses from the current manual operation to channelization and finally to channelization with optimized signal timing.

During the morning peak, average delay decreases from 128.6 s/veh under current control to 89.3 s/veh with channelization, and further to 32.4 s/veh under optimized control. A similar pattern is observed for queue length, which reduces from 42.9 m to 18.7 m and then to 12.1 m. Environmental indicators follow the same trend, with CO_2 emissions and fuel consumption dropping steadily across the three scenarios. Evening peak conditions show higher absolute values due to increased demand; however, the relative improvements remain consistent, with optimized control producing the lowest delays (35.7 s/veh), the shortest queues (10.4 m), and the lowest emission and fuel consumption levels. The values in Table 9 are reported as mean ± standard

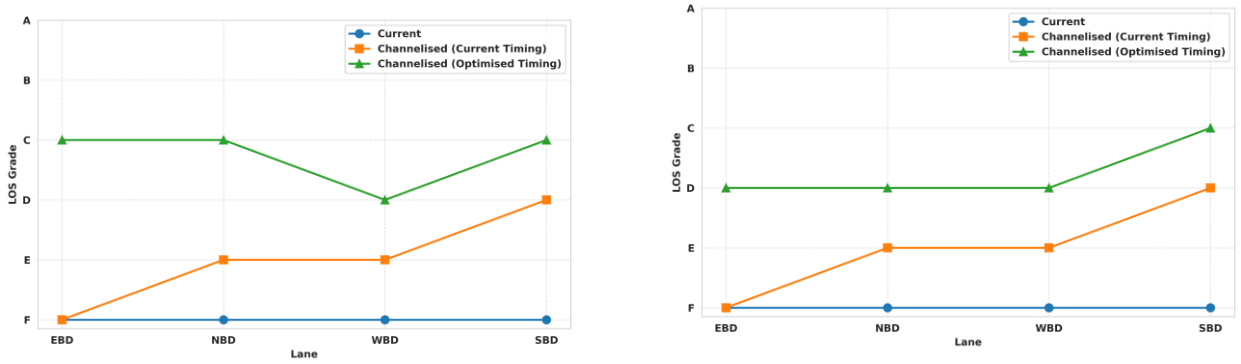
deviation, based on 10 independent simulation replications, which capture the inherent stochastic variability of microsimulation. To verify that the observed differences between scenarios are not due to random effects, a one-way ANOVA was applied separately for each performance indicator and peak period. The resulting p-values (< 0.001 for all cases) indicate that the differences in operational and environmental performance between the control strategies are statistically significant. This confirms that the improvements achieved through channelization and optimized signal timing are systematic and reproducible rather than incidental.

Table 9. Statistical comparison of delay, queue length, emissions, and fuel consumption across control scenarios for morning and evening peak hours.

Duration	Performance Indicator	Current Control (Mean ± SD)	Channelized (Mean ± SD)	Channelized + Optimized (Mean ± SD)	ANOVA (p-value)
Morning peak hour	Average Delay (s/veh)	128.6 ± 7.2	89.3 ± 5.8	32.4 ± 4.9	< 0.001
	Average Queue Length (m)	42.9 ± 3.0	18.7 ± 2.2	12.1 ± 1.8	< 0.001
	CO_2 Emissions (mg/s)	2148 ± 81	1769 ± 69	1568 ± 58	< 0.001
	Fuel Consumption (mg/s)	818 ± 49	602 ± 38	521 ± 34	< 0.001
Evening peak hour	Average Delay (s/veh)	154.3 ± 7.8	102.4 ± 6.1	35.7 ± 5.3	< 0.001
	Average Queue Length (m)	48.6 ± 3.2	19.8 ± 2.4	10.4 ± 1.9	< 0.001
	CO_2 Emissions (mg/s)	2315 ± 88	1821 ± 72	1542 ± 61	< 0.001
	Fuel Consumption (mg/s)	862 ± 54	648 ± 41	512 ± 36	< 0.001

4. Discussion

The simulation results clearly demonstrate the impact of channelization and signal timing optimization on intersection performance. In the Current scenario, the average queue lengths and vehicle delays were unacceptably high, particularly during the evening peak, where Northbound and Southbound queues reached 49.21 m and 48.68 m, respectively, and delays exceeded 160 s/vehicle. According to the HCM methodology, these conditions correspond to Level of Service (LOS) F, as shown in Figure 9, indicating unstable traffic flow, frequent stop-and-go conditions, and extreme driver discomfort. Such performance highlights the limitations of unstructured traffic management and manual signal control.



(a) Morning Peak hour (b) Evening Peak hour

Figure 9. Intersection Level of Service (LOS) classification for under alternative scenarios.

Introducing channelization with existing timings substantially improved operational efficiency. Queues were reduced to 15–22 m in the morning and 16–22 m in the evening, and delays decreased by approximately 30–40%. These improvements generally correspond to LOS D, reflecting stable flow with occasional delays. Although this scenario shows clear benefits over the baseline, it remains sensitive to peak-period demand, particularly in the evening, suggesting that physical modifications alone cannot fully alleviate congestion.

The Channelized with Optimized Timing scenario produced the most significant gains. Average queue lengths fell below 13 m in the morning and to 8–11 m in the evening, while delays were limited to 31–41 s across approaches. From an LOS perspective, these outcomes correspond to LOS C, indicating stable flow, acceptable driver comfort, and manageable delays even during high-demand periods. This confirms that combining geometric channelization with evidence-based signal optimization can dramatically enhance intersection performance and sustain acceptable operational conditions under varying traffic volumes.

Environmental and energy efficiency benefits were also observed. Under the Current scenario, CO_2 emissions exceeded 2,100 mg/s and fuel consumption was above 815 mg/s in the morning, rising further during the evening peak. Channelization alone reduced emissions by 10–20%, and optimized signal timings further lowered CO_2 emissions and fuel consumption by 25–35% relative to the baseline. These reductions highlight that improvements in traffic flow directly translate into environmental gains, as smoother vehicle progression reduces idling and stop-and-go operations. The comparative analysis between morning and evening peaks reveals that the evening consistently experiences higher queues, delays, and emissions, a consequence of increased traffic demand. Nevertheless, the optimized scenario maintained robust performance, demonstrating its effectiveness under heavier congestion. This indicates that the integrated approach is not only efficient under typical conditions but also resilient to peak-period stress.

To place the observed improvements in a broader regional context, it is useful to compare the magnitude of delay and queue reductions with those reported in other microsimulation studies conducted under heterogeneous traffic conditions in developing countries. For example, an intersection microsimulation study in Dhaka that combined video data analysis and optimized signal timing reported significant reductions in queue length (around 40 %) and corresponding decreases in delay through data-driven signal adjustments and expert-tuned scenarios. However, the reductions were more moderate than those observed here [22]. In another study from Pakistan, geometric and signal improvements modelled with microsimulation yielded nearly 40 % reduction in delay and fuel consumption, demonstrating substantial performance gains, albeit below the ~70 % delay reduction achieved in this work [6]. Similarly, research on heterogeneous traffic using calibrated simulation in Indian urban settings shows improved intersection performance, though exact quantitative improvements (e.g., in average delay or queue length) tend to vary between 20 % and 60 % depending on local context and modelling assumptions [13], [23]. By comparison, the more than 70% reduction in average delay observed in the present study suggests that the combination of channelization and optimized fixed-time signal control, when applied within a rigorously calibrated SUMO model, delivers performance improvements at the higher end of reported outcomes in similar contexts. In summary, the discussion of queue lengths, delays, emissions, and fuel consumption in conjunction with LOS evaluation demonstrates the multi-dimensional benefits of combining channelization with optimized signal control. While channelization alone provides notable operational improvements, only the combined application achieves a balance of acceptable service levels, reduced environmental impact, and efficient fuel usage. These findings provide strong evidence for urban traffic management strategies that integrate geometric modifications with adaptive signal optimization to enhance both performance and sustainability.

5. Limitations and Future Work

While the results indicate notable operational and environmental improvements from channelization and optimized signal timing, certain limitations should be recognized. Traffic data were collected during peak periods on a single representative weekday; therefore, the results primarily reflect peak-hour conditions and may not fully capture day-to-day, seasonal, or weather-related variability. Incorporating multi-day and multi-season observations would enhance the robustness of future analyses. Although SUMO is well-suited for modeling heterogeneous traffic, some locally prevalent behaviors, such as informal lane usage and non-lane-based movements, can only be approximated through calibration rather than explicitly modeled. Despite satisfactory agreement with observed queues and delays, this may influence the detailed representation of highly irregular traffic interactions. The signal timings were optimized using a fixed-time Webster-based approach, which assumes relatively stable demand within the analysis period. While this method is practical and easy to implement, it does not account for short-term demand fluctuations; future studies could compare

adaptive or real-time control strategies. Finally, the analysis was limited to a single isolated intersection, and corridor-level or network-wide interactions were not considered. Extending the framework to multi-intersection systems would provide broader insights into cumulative traffic performance.

Overall, these limitations do not undermine the validity of the findings but rather highlight opportunities for extending the methodology in future research.

6. Conclusion

Using field data and a calibrated SUMO microsimulation, this study evaluated three scenarios: the current manual police control, channelization with existing timings, and channelization with optimized fixed-time signals to examine intersection performance in Dhaka, a city burdened by chronic congestion and mixed traffic. A key methodological contribution of this research is the rigorous calibration of the SUMO model using the Krauß car-following framework, with locally observed traffic composition and driver-behavior parameters, enabling a realistic representation of Dhaka's heterogeneous, weakly lane-disciplined traffic conditions. The findings clearly demonstrate that while channelization alone alleviates delays and reduces queue lengths, the greatest improvements occur when it is coupled with optimized signal control. Together, these interventions reduced average delays by more than 70%, lowered fuel consumption and CO_2 emissions by up to 35%, and improved the level of service from failing to stable conditions. The reliability of these performance gains is strengthened by the validated calibration process, which ensured close agreement between simulated and observed queue lengths and vehicle delays. Beyond operational efficiency, the results underscore the environmental and energy-saving benefits of integrated traffic management strategies, offering a dual advantage for both mobility and sustainability. For rapidly urbanizing cities like Dhaka, where resources for large-scale infrastructure expansion are limited, low-cost, evidence-based measures such as channelization and optimized signalization offer practical, immediate solutions to congestion. The calibrated SUMO modeling framework developed in this study is transferable and can be applied to other South Asian cities with similar heterogeneous traffic characteristics. Looking ahead, policymakers and urban planners should prioritize adopting data-driven signal control and incremental geometric improvements at critical intersections. Integrating such strategies into a broader smart mobility framework will not only ease congestion but also contribute to cleaner air, reduced fuel dependency, and improved quality of urban life. In doing so, Dhaka can move toward a more resilient, efficient, and sustainable transport future.

7. Acknowledgements

The authors would like to express their sincere gratitude to the Department of Civil Engineering, Atish Dipankar University of Science & Technology (ADUST), for providing continuous support, academic guidance, and necessary facilities to carry out this research.

Author Contributions: M.E.K.: Conceptualization, Methodology, Software, Validation, Formal analysis, Investigation, Resources, Data curation, Writing—original draft, Visualization. M.A.S.: Writing—original draft, Validation**.** M.I.I.I.: Validation, Writing—review and editing, Supervision. Z.A.: Writing—review and editing, Supervision, Funding acquisition, Project administration.

Funding: This research received no external funding.

Conflicts of Interest: The authors declare no conflict of interest.

References

[1] Subree, M. I. H.; Hasan, M. R.; Sayma, M. H. Design and Implementation of an Unreal Engine 4-Based Smart Traffic Control System for Smart City Applications. *Int. J. Adv. Comput. Sci. Appl.* **2022**, *13*(12). https://doi.org/10.14569/IJACSA.2022.01312100

[2] Rahman, M. M.; Jahan, J.; Zhou, Y. Alleviating Traffic Congestion by the Strategy of Modal Shift from Private Cars to Public Transports: A Case of Dhaka City, Bangladesh. In *Proc. Conf. Comput. Soc. Sci.*

Soc. Am.; Carmichael, T., Yang, Z., Eds.; Springer: Cham, 2020; pp 101–115. https://doi.org/10.1007/978-3-030-35902-7_7

[3] Arif, T.; Muhammad Mussa, A. S.; Rahman, M.; Joarder, M. A. Vision-Based Real-Time Traffic Flow Monitoring System for Road Intersections in Dhaka City. *Appl. Intell.* **2025**, *55*(11), 800. https://doi.org/10.1007/s10489-025-06631-x

[4] Klobučar, M.; Deluka-Tibljaš, A.; Šurdonja, S.; Ištoka Otković, I. A Theoretical Model for Optimizing Signalized Intersection and Roundabout Distance Using Microsimulations. *Future Transp.* **2025**, *5*(1), 28. https://doi.org/10.3390/futuretransp5010028

[5] El Mokhi, C.; Erguig, H.; Hmina, N.; Hachimi, H. Intelligent Traffic Management Systems: A Literature Review on AI-Based Traffic Light Control. In *The Future of Urban Living: Smart Cities and Sustainable Infrastructure Technologies*; El Mokhi, C., Hachimi, H., Nayyar, A., Eds.; Springer Nature Switzerland: Cham, 2025; pp 154–171. https://doi.org/10.1007/978-3-031-98334-4_15

[6] Riaz, M. S.; et al. Strategic Utilization of Microsimulation for Sustainable Traffic Analysis and Intersection Improvement. *Open Transp. J.* **2023**, *17*(1), e26671212281061. https://doi.org/10.2174/0126671212281061231123113624

[7] Hassan, S. A.; Hamzani, I. N. S.; Sabli, A. R.; Sukor, N. S. A. Bus Rapid Transit System Introduction in Johor Bahru: A Simulation-Based Assessment. *Sustainability* **2021**, *13*(8), 4437. https://doi.org/10.3390/su13084437

[8] Abedian, S.; Mirsanjari, M. M.; Salmanmahiny, A. Investigating the Effect of Suburban Buses on Traffic Flow and Carbon Monoxide Emission by Aimsun Simulation Software. *J. Indian Soc. Remote Sens.* **2021**, *49*(6), 1319–1330. https://doi.org/10.1007/s12524-020-01289-z

[9] Vertegaal, A. C. O. Signalling Mechanisms and Cellular Functions of SUMO. *Nat. Rev. Mol. Cell Biol.* **2022**, *23*(11), 715–731. https://doi.org/10.1038/s41580-022-00500-y

[10] Hassan, M.; et al. Mapping the Machine Learning Landscape in Autonomous Vehicles: A Scientometric Review of Research Trends, Applications, Challenges, and Future Directions. *IEEE Access* **2025**, *13*, 182036–182077. https://doi.org/10.1109/ACCESS.2025.3620637

[11] Modi, R. N.; Patel, C. G. Data-Driven Microscopic Simulation for Analyzing Traffic Volume, Road Geometry, and Speed: A Case Study of Palanpur Aroma Circle. In *Recent Advancements in Sustainable and Safe Transportation Infrastructure*; Jain, U., Srinivasan, V., Anjaneyulu, M. V. L. R., Parida, M., Eds.; Springer Nature: Singapore, 2025; Vol. 622; pp 285–297. https://doi.org/10.1007/978-981-96-1988-7_21

[12] Chowdhury, M. M. H.; Chakraborty, T. Calibration of SUMO Microscopic Simulation for Heterogeneous Traffic Condition: The Case of the City of Khulna, Bangladesh. *Transp. Eng.* **2024**, *18*, 100281. https://doi.org/10.1016/j.treng.2024.100281

[13] Bodkhe, U.; Tanwar, S. Indian SUMO Traffic Scenario-Based Misbehaviour Detection Dataset for Connected Vehicles. *Multimodal Transp.* **2025**, *4*(1), 100148. https://doi.org/10.1016/j.multra.2024.100148

[14] Phan, T. C.; Le, V. D.; Nguyen, T. Application of Dueling Double Deep Q-Network for Dynamic Traffic Signal Optimization: A Case Study in Danang City, Vietnam. *Mach. Learn. Knowl. Extr.* **2025**, *7*(3), 65. https://doi.org/10.3390/make7030065

[15] Mutambik, I. IoT-Enabled Adaptive Traffic Management: A Multiagent Framework for Urban Mobility Optimisation. *Sensors* **2025**, *25*(13), 4126. https://doi.org/10.3390/s25134126

[16] Skoropad, V. N.; et al. Dynamic Traffic Flow Optimization Using Reinforcement Learning and Predictive Analytics: A Sustainable Approach to Improving Urban Mobility in the City of Belgrade. *Sustainability* **2025**, *17*(8), 3383. https://doi.org/10.3390/su17083383

[17] Hassan, M.; Kabir, M. E.; Jusoh, M.; An, H. K.; Negnevitsky, M.; Li, C. Large Language Models in Transportation: A Comprehensive Bibliometric Analysis of Emerging Trends, Challenges, and Future Research. *IEEE Access* **2025**, *13*, 132547–132598. https://doi.org/10.1109/ACCESS.2025.3589319

[18] Yaibok, C.; Suwanno, P.; Pornbunyanon, T.; Kanjanakul, C.; Luathep, P.; Fukuda, A. Improving Urban Intersection Safety: Insights from Simulation Analysis. *IATSS Res.* **2024**, *48*(4), 523–536. https://doi.org/10.1016/j.iatssr.2024.10.005

[19] Bindzar, P.; Marasova, D.; Brodny, J.; Tutak, M.; Ulewicz, R.; Sliva, A. Modeling the Impact of Intersection Design Configurations on Traffic Flow during Peak Hour in Smart Cities: A Case Study on Urban Roads in Slovakia. *IEEE Access* **2024**, *12*, 83072–83090. https://doi.org/10.1109/ACCESS.2024.3412709

[20] Rahimi, M. R.; Vala, M.; Patel, B. N. Evaluation of Capacity and Level of Service for Selected Urban Arterial Roads—A Case Study of Rajkot City. In *Recent Advances in Traffic Engineering*; Arkatkar, S. S., Velmurugan, S., Verma, A., Eds.; Springer: Singapore, 2020; Vol. 69; pp 23–41. https://doi.org/10.1007/978-981-15-3742-4_2

[21] Saldivar-Carranza, E.; Li, H.; Mathew, J.; Hunter, M.; Sturdevant, J.; Bullock, D. M. Deriving Operational Traffic Signal Performance Measures from Vehicle Trajectory Data. *Transp. Res. Rec.* **2021**, *2675*(9), 1250–1264. https://doi.org/10.1177/03611981211006725

[22] Labib, S. M.; Mohiuddin, H.; Hasib, I. M. A.; Sabuj, S. H.; Hira, S. Integrating Data Mining and Microsimulation Modelling to Reduce Traffic Congestion: A Case Study of Signalized Intersections in Dhaka, Bangladesh. *Urban Sci.* **2019**, *3*(2), 41. https://doi.org/10.3390/urbansci3020041

[23] Gunarathne, D.; Amarasingha, N.; Wickramasighe, V. Traffic Signal Controller Optimization through VISSIM to Minimize Traffic Congestion, CO and NOx Emissions, and Fuel Consumption. *Sci. Eng. Technol.* **2023**, *3*(1). https://doi.org/10.54327/set2023/v3.i1.56

ASEAN
Journal of Scientific and Technological Reports
Online ISSN:2773-8752

Research article

Production of Fermented Vinegar Drink From Hang Rice With Pineapple Peel Syrup

Nisa Romsomsa[1*], Nithiphon Tiapasert[1], Karid Jittimanee[1], Chaiwat Paungkrathok[1], Nutthawut Meesilp[1], and Numphon Thaiwong[2]

[1] Faculty of Sciences and Liberal Arts, Rajamangala University of Technology Isan, Nakhon Ratchasima, 30000, Thailand
[2] Faculty of Agricultural Innovation and Technology, Rajamangala University of Technology Isan, Nakhon Ratchasima, 30000, Thailand
* Correspondence: nisa_romsomsa@hotmail.com

Citation:
Romsomsa, N.; Tiapasert, N.; Jittimanee, K.; Paungkrathok, C.; Meesilp, N.; Thaiwong, N. Production of fermented vinegar drink from hang rice with pineapple peel syrup. *ASEAN J. Sci. Tech. Report.* **2026**, *29*(4), e261278. https://doi.org/10.55164/ajstr.v29i4.262439

Article history:
Received: November 20, 2025
Revised: February 8, 2026
Accepted: February 17, 2026
Available online: March 24, 2026

Publisher's Note:
This article is published and distributed under the terms of the Thaksin University.

Abstract: This study aimed to develop fermented vinegar beverages produced from Hang rice combined with pineapple peel syrup through traditional fermentation. The fermentation process was carried out under ambient conditions for 30 days using a traditional method to monitor changes in acetic acid bacteria and yeast populations, as well as acetic acid production. Consumer preference for the final product was also assessed. The microbial populations of both acetic acid bacteria and yeast showed a sharp increase during the first 14 days, reaching their peaks at 7.92 ± 0.24 log CFU/mL and 7.06 ± 0.28 log CFU/mL, respectively, after 30 days. The final vinegar exhibited 4.44 ± 0.31% acetic acid, a pH of 3.6, and showed no detectable alcohol. Three formulations were prepared by varying the ratio of Hang rice vinegar to pineapple peel syrup—Formula 1 (60:40), Formula 2 (50:50), and Formula 3 (40:60). Among them, Formula 3 demonstrated the highest DPPH radical scavenging activity (503.70 ± 24.42 μg Trolox/mL) and the greatest total phenolic content (97.24 ± 4.36 μgGAE/mL). Sensory analysis revealed comparable acceptability scores across all samples, ranging from "like slightly" to "like moderately". These findings suggest that Hang rice vinegar supplemented with pineapple peel syrup represents a novel beverage with significant in vitro antioxidant capacity, adding value to germinated brown rice and promoting the utilization of pineapple peel waste.

Keywords: Vinegar; hang rice; pineapple peel syrup; acetic acid bacteria; antioxidant activity

1. Introduction

Vinegar is a naturally fermented product obtained through two sequential processes—alcoholic and acetic acid fermentation. Traditionally used as a sour condiment, preservative, and functional beverage, vinegar has recently gained attention for its potential health-promoting properties. Vinegar contains a wide range of bioactive compounds, including organic acids, phenolic acids, flavonoids, anthocyanins, melanoidins, tetramethylpyrazine, carotenoids, alkaloids, phytosterols, and vitamins, which have been associated with antioxidant, antimicrobial, anti-inflammatory, antidiabetic, anti-obesity, antihypertensive, and cholesterol-lowering effects [1–4]. Among various types of vinegar, cereal-based vinegars produced from grains such as rice, barley, wheat, sorghum, and corn are particularly rich in bioactive compounds, including γ-oryzanol, γ-aminobutyric acid (GABA), and tetramethylpyrazine

[2]. Rice vinegar, widely consumed in Asian countries, especially China and Japan, has been extensively studied for its fermentation processes, bioactive composition, antioxidant and antibacterial activities, enzyme-inhibitory properties, and sensory characteristics [5–9]. Hang rice, a traditional product of northeastern Thailand, is derived from the local rice varieties Hom Mali 105 and glutinous RD6, through a process involving soaking, steaming, drying, and dehusking [10]. Germination enhances the nutritional profile of Hang rice by increasing the levels of γ-aminobutyric acid (GABA), phenolic compounds, γ-oryzanol, vitamin E, and other phytochemicals [11–14]. It is nutritionally rich in vitamin E, folate, pantothenic acid, B-group vitamins, niacin, and minerals such as magnesium, selenium, and calcium [15]. Pineapple peel, which accounts for approximately 35% of the total fruit weight, is a major by-product of the fruit processing industry and poses environmental concerns when discarded. Nevertheless, pineapple peel is rich in carbohydrates, dietary fiber, minerals, and phenolic antioxidants, making it a promising low-cost functional ingredient for sustainable food applications [16, 17].

Despite extensive studies on rice- and fruit-based vinegars, no previous research has reported the development of a fermented vinegar beverage derived from Hang rice. Moreover, the utilization of pineapple peel as a functional ingredient in vinegar beverages remains limited. This study, therefore, addresses this research gap by developing a novel functional fermented vinegar drink made from Hang rice and pineapple peel syrup. The objectives of this study were to optimize the formulation ratio between Hang rice vinegar and pineapple peel syrup, investigate the population dynamics of yeast and acetic acid bacteria during fermentation, and evaluate the total phenolic content, antioxidant activity, and sensory acceptability of the developed product.

2. Materials and Methods

2.1 Materials

The Hang rice variety used in this study was Khao Dawk Mali 105, obtained from the Ban Samran Suk Hang Rice Homemakers Community Enterprise, Nong Bua Lam Phu Province, Thailand. Pineapple peels were collected from a local fruit market in Chokchai, Nakhon Ratchasima, and *Loog-pang* (a traditional starter culture) was purchased from a Thai SME located in Mueang District, Maha Sarakham Province.

2.1.1 Production of Hang rice vinegar

Hang rice was washed, soaked overnight in water, drained, and steamed for 30 min. After cooling to room temperature, the steamed rice was inoculated with 1.0% (w/w) Loog-pang and transferred to a 3 L glass jar for saccharification at 30–35 °C for 10 days. The liquid fraction obtained after saccharification was filtered and adjusted to 18 °Brix. Alcoholic fermentation was initiated by adding 200 mL of sterile water. The glass jar was loosely covered with sterile cheesecloth and a lid to prevent contamination while allowing limited gas exchange. Fermentation was carried out at ambient room temperature (30 ± 2 °C) for 4 days, resulting in a total fermentation period of 14 days. After alcoholic fermentation, the rice wine was pasteurized at 60 °C for 15 min, and the ethanol concentration was standardized to 8% (v/v) using distilled water to ensure consistent initial conditions for acetic acid fermentation. The acetic acid fermentation was then conducted under aerobic conditions for 16 days, bringing the total fermentation period to 30 days. Samples were collected at defined intervals to determine ethanol content, total acidity, pH, and microbial populations, and to evaluate the fermentation kinetics throughout the process. The growth of acetic acid bacteria (AAB) and yeasts was monitored over the 30-day fermentation period using the spread plate method to determine viable cell counts. Briefly, 100 µL aliquots from appropriate serial dilutions were spread onto Glucose Yeast Calcium Carbonate (GYC) agar for enumeration of AAB and onto yeast extract peptone dextrose (YEPD) agar for yeast counts. All samples were plated in triplicate and incubated at 30 °C for 24–48 h for AAB and 48 h for yeasts.

2.1.2 Analysis of physicochemical properties

The vinegar samples were analyzed for pH, total soluble solids (TSS), alcohol content, and acetic acid concentration. All samples were analyzed in triplicate. pH values were determined using a pH meter (AB15, Hampton, USA), while TSS was measured with a refractometer (RHB-32ATC, Yago Technology, China). Alcohol content was assessed using an ebulliometer (Alla France, France) by measuring the difference in

boiling points between water and the sample solution. The total acidity of the vinegar samples was determined by titration using AOAC Official Method 930.35 [18]. A 10 mL aliquot of the sample was diluted with distilled water and titrated against a standardized 1N NaOH solution using phenolphthalein as an indicator. The total acidity was calculated and expressed as grams of acetic acid per 100 mL of sample (%, w/v), calculated as follows (Equation 1):

$$\text{Acetic acid (g/100 mL)} = \frac{C \times V \times MW \times 100}{1{,}000 \times 10} \quad (1)$$

Where C is the NaOH concentration, V is the titration volume, and MW is the molar mass of acetic acid.

2.2 Production of fermented vinegar drink from Hang rice with pineapple peel syrup

2.2.1 Preparation of pineapple peel syrup

Pineapple peels were washed, trimmed, and cut into thin pieces. The peels (250 g) were combined with brown sugar (200 g), two cinnamon sticks (5 g), lemon juice (20 mL), and water (250 mL). The mixture was boiled, then simmered for 20 minutes while gently crushing the fruit until thickened. The syrup was filtered through muslin cloth, cooled, and stored at 4 ± 1 °C.

2.2.2 Formulation of Fermented Vinegar Drink

Three formulations were prepared by blending fermented Hang rice vinegar with pineapple peel syrup at ratios of 60:40 (Formula 1), 50:50 (Formula 2), and 40:60 (Formula 3). The mixtures were filtered, bottled (250 mL glass bottles), sealed, and stored at 4 ± 1 °C for antioxidant and sensory analyses.

2.3 Sensory evaluation of fermented Hang rice vinegar drink with pineapple peel syrup

The fermented Hang rice vinegar drink with pineapple peel syrup was evaluated on a 9-point hedonic scale. Thirty untrained panelists evaluated six attributes: appearance, color, aroma, taste, and overall acceptability. On this scale, a value of 9 represented 'like extremely,' 5 represented 'neither like nor dislike,' and 1 represented 'dislike extremely.

2.4 Antioxidant activity analyses of the fermented Hang Rice vinegar drink with pineapple peel syrup

2.4.1 Determination of Total Phenolic Content

The total phenolic content of the fermented Hang rice vinegar drink with pineapple peel syrup was determined using the Folin-Ciocalteu reagent. Briefly, 50 µL of each sample was diluted with distilled water, then mixed with 100 µL of Folin-Ciocalteu reagent and 2 mL of 2% Na_2CO_3 solution. After a 30-minute incubation at room temperature, the absorbance was measured at 750 nm using a UV-Vis spectrophotometer (Genesys 10S UV-Vis, Thermo Scientific, USA). The results were expressed as micrograms of gallic acid equivalents per 1 mL of sample (µg GAE/mL).

2.4.2 Determination of DPPH Radical Scavenging Activity

The antioxidant activity of the fermented Hang rice vinegar drink with pineapple peel syrup was evaluated using the DPPH radical assay, where the DPPH radical served as a stable radical. In brief, 50 µL of each sample was added to 1.950 mL of a 40 mg/L DPPH radical solution prepared in ethanol. The mixture was then incubated for 30 minutes at room temperature in the dark. After the incubation period, the absorbance was measured at 515 nm using a UV-Vis spectrophotometer, and the scavenging activity was calculated using Equation 2.

$$\text{scavenging activity (\%)} = ((A_{DPPH} - A_{sample})/A_{DPPH}) \quad (2)$$

where A_{DPPH} and A_{sample} denote the absorbance of the control and sample, respectively.

The antioxidant activity was calculated from a standard curve of Trolox, and the results were expressed as milligrams of Trolox equivalents per milliliter of sample µg TE/mL).

2.5 Microbiological Safety Assessment

The microbiological safety of the fermented Hang rice vinegar drink was evaluated according to the BAM (Bacteriological Analytical Manual) standard methods. Samples from the optimal formulation were analyzed for Total Plate Count (TPC), Coliforms, yeasts and molds, and the presence of pathogenic microorganisms (Escherichia coli and Salmonella spp.). Ten milliliters of each sample were serially diluted in 0.1% peptone water. TPC and yeast/mold counts were determined using Plate Count Agar (PCA) and Potato Dextrose Agar (PDA), respectively, after incubation at 35°C for 48 hours and 25°C for 5 days. The results were expressed as colony-forming units per milliliter (CFU/mL). All tests were performed in triplicate.

2.6 Statistical Analysis

All analyses were carried out in triplicate, and results were expressed as mean ± standard deviation (SD). Data were subjected to one-way analysis of variance (ANOVA). Statistical differences among treatments were determined by Duncan's multiple range test at a significance level of $p \leq 0.05$.

3. Results and Discussion

3.1 Changes in chemical and microbiological parameters during fermentation of Hang rice vinegar

The traditional static fermentation of Hang rice vinegar for 30 days is illustrated in Figure 1. Cooked Hang rice can be fermented into Khao Mak within 24 hours. After the first day of fermentation, the sample developed a pale yellowish-white color and a pleasant aroma with mild alcoholic notes, accompanied by a small amount of clear exudate (*Nam-toy*). Subsequently, during fermentation, the alcohol content slowly increased until day 21. At the end of fermentation (30 days), the vinegar exhibited a clear to light yellow appearance and a slightly pungent smell, attributed to the presence of acetic acid (Figure 1).

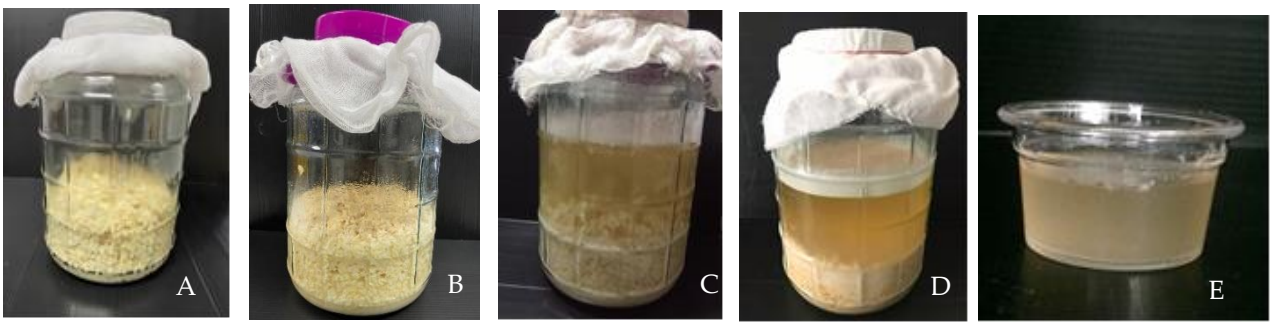


Figure 1. Appearance of Hang rice vinegar during traditional static fermentation; (A) beginning of fermentation; (B) 10 days (before alcoholic fermentation); (C) 21 days; (D) 30 days; (E) the final Hang rice vinegar product obtained after 30 days of fermentation.

The dynamic changes in microbial populations, ethanol and acetic acid production, and pH during fermentation are shown in Figure 2. Both yeast and acetic acid bacteria (AAB) populations increased markedly within the first 14 days of fermentation. Maximum cell densities of AAB (7.92 ± 0.24 log CFU/mL) and yeasts (7.06 ± 0.28 log CFU/mL) were observed at day 30, indicating sustained microbial activity throughout the fermentation process. Ethanol concentration increased significantly during the early fermentation stage, reaching a maximum of 9.5 ± 0.4% (v/v) after 14 days, reflecting the efficient conversion of fermentable sugars into ethanol by yeast cells. The relatively high ethanol yield during this period can be attributed to the starch-rich nature of Hang rice, combined with continuous saccharification within the fermentation system. Given the high starch content of Hang rice, saccharification represents a critical prerequisite for effective alcoholic fermentation [19, 20]. This process generates fermentable sugars, including glucose and oligosaccharides, through the action of α-amylase and related enzymes, which are subsequently metabolized by yeasts into ethanol and later oxidized into acetic acid during vinegar fermentation [21, 22]. Traditional starter cultures such as *Loog-pang* harbor diverse fungal and yeast communities capable of producing amylolytic enzymes that hydrolyze complex starch into fermentable sugars, thereby ensuring a sustained supply of substrates to support yeast metabolism during rice-based alcoholic fermentation. This process is mediated by the complex microbial consortium present in *Loog-pang*, which includes molds (e.g., *Aspergillus*, *Amylomyces*, *Rhizopus*, and

Mucor spp.), yeasts (e.g., *Saccharomyces cerevisiae* and *Candida* spp.), and associated bacteria that collectively secrete amylolytic enzymes, facilitating starch degradation and sustained alcohol formation [23–26]. Following the alcoholic fermentation stage, ethanol concentration declined significantly to 6.2 ± 0.3% (v/v) and became undetectable by day 30. In contrast, acetic acid concentration increased sharply, reaching 4.44 ± 0.31% (w/v) by day 21, accompanied by a decrease in pH from 6.5 to 3.6. These results comply with the Codex Alimentarius standard for fermented vinegar (CXS 162-1987), which specifies a minimum acetic acid content of 4% (w/v), residual ethanol levels below 0.5% (v/v), and a typical pH range of 2.5–3.5 [27]. The inverse relationship between ethanol depletion and acetic acid accumulation reflects AAB's metabolic activity, which oxidizes ethanol to acetic acid under aerobic conditions. Vinegar production involves two distinct yet interrelated fermentation stages. During the initial alcoholic fermentation, yeasts—predominantly *Saccharomyces cerevisiae*—convert fermentable sugars into ethanol [28, 29]. In addition to ethanol production, yeast metabolism releases amino acids, vitamins, and autolysis-derived compounds that stimulate the growth and metabolic activity of AAB [30]. Subsequently, acetic acid fermentation is driven mainly by *Acetobacter* spp., which oxidize ethanol to acetic acid via the sequential action of membrane-bound alcohol dehydrogenase (ADH) and aldehyde dehydrogenase (ALDH) enzymes [29, 31]. In this study, spontaneous fermentation was employed to exploit the indigenous microbiota naturally associated with Hang rice and pineapple peels, thereby promoting microbial interactions and metabolic synergy. This approach results in a more complex metabolic profile and distinctive sensory characteristics compared with pure-culture inoculation [32–34]. Such microbial interactions are often associated with enhanced production of bioactive compounds and increased antioxidant potential [19]. Moreover, spontaneous fermentation aligns with traditional artisanal vinegar production practices, where diverse microbial communities play a crucial role in developing unique functional and sensory attributes [34]. From a practical perspective, this strategy also supports a cost-effective and sustainable production model by reducing reliance on commercial starter cultures, thereby improving accessibility for small-scale producers and local communities [35, 36].

Colony morphology of isolated yeast and AAB from Hang rice vinegar after 30 days of fermentation is shown in Figure 3. The yeast isolates exhibited white, powdery, rough colonies with raised elevation and undulated margins, which are commonly associated with yeast involved in alcoholic fermentation, as reported in previous studies [37–39]. In the literature, various yeast species, including *Saccharomycopsis fibuligera*, *Pichia* spp., *Issatchenkia* spp., *Candida* spp., and *Torulaspora* spp., have been reported in traditional rice-based starters such as Loog-pang and Medombae [40, 41]. These references are provided for comparative context, as species-level identification was not performed in the present study. AAB colonies exhibited small, creamy-white circular forms with convex elevation and clear zones around colonies, which are characteristic features of acetic acid–producing bacteria. Consistently, *Acetobacter* species have been reported to form beige, circular colonies on glucose, yeast extract, and peptone agar [42]. Microbial identification in this study was based on culture-dependent methods, including plate counts and colony morphology, which provide presumptive identification of yeast and acetic acid bacteria. These approaches are commonly applied in vinegar fermentation studies and are suitable for evaluating overall microbial population trends during fermentation. However, they do not provide precise taxonomic resolution. Therefore, the observed microbial dynamics should be interpreted as indicative population trends. Future studies employing molecular identification techniques, such as 16S rRNA gene or ITS sequencing, would further strengthen microbial characterization.

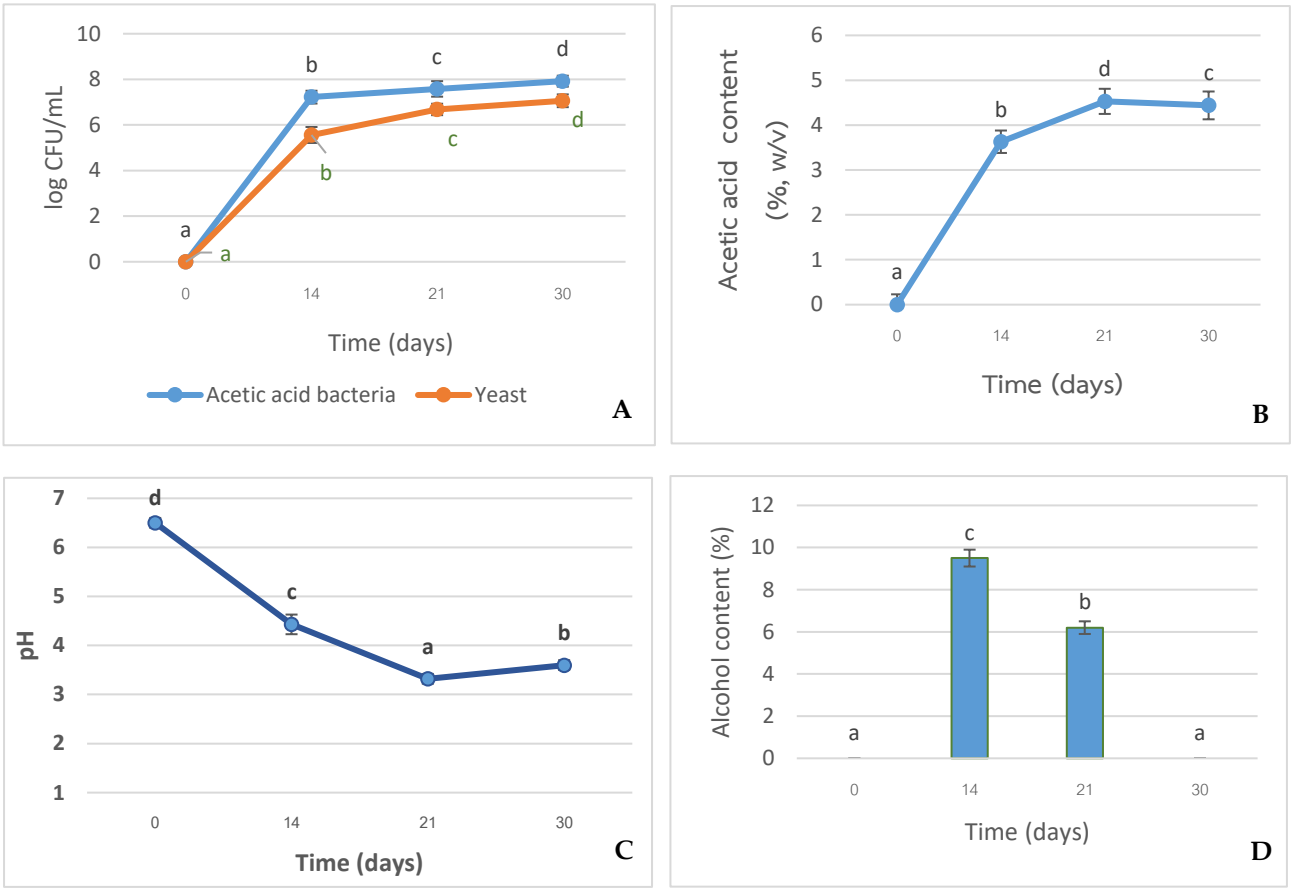


Figure 2. Dynamic changes in microbial populations (AAB and Yeast) (A), acetic acid content (% w/v) (B), pH (C), and alcohol content (% v/v) (D), during the 30-day traditional static fermentation of Hang rice vinegar. Each data point represents the mean ± standard deviation (n=3). Significant differences ($p < 0.05$). Different letters show significant differences ($p \leq 0.05$) among vinegar samples during the fermentation period.

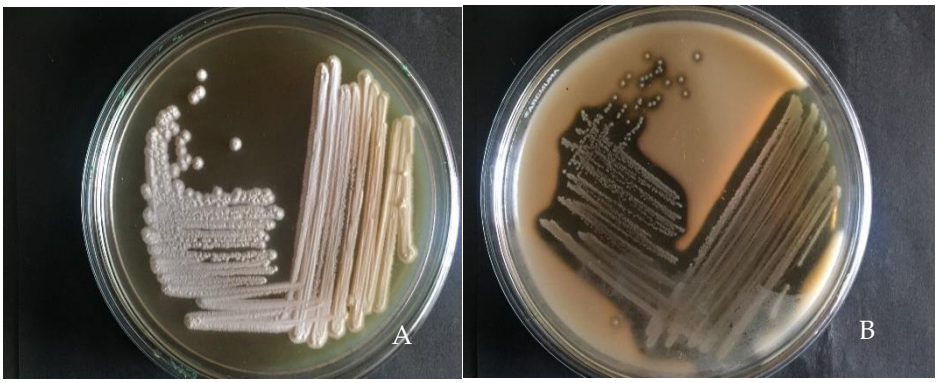


Figure 3. Colony morphology of isolated yeast from Hang rice vinegar on YEPD agar (B), isolated acetic acid bacteria from Hang rice vinegar showing formation of a halo zone surrounding their colonies grown on GYC agar.

3.3 Production of fermented Hang rice vinegar drink with pineapple peel syrup

The pineapple peel syrup exhibited an amber-brown, viscous, and slightly turbid appearance with a distinctive fruity, sweet, and spicy aroma (Figure 4). The syrup had total soluble solids of 16°Brix and a pH of 5.4. The final vinegar drink formulations (Figure 5) showed distinct color variations: Formulas 1 and 2 displayed an amber-yellow hue with slight turbidity, while Formula 3 showed a bronze-orange tone.



Figure 4. Preparation process of pineapple peel syrup (A) and the final pineapple peel syrup product (B).

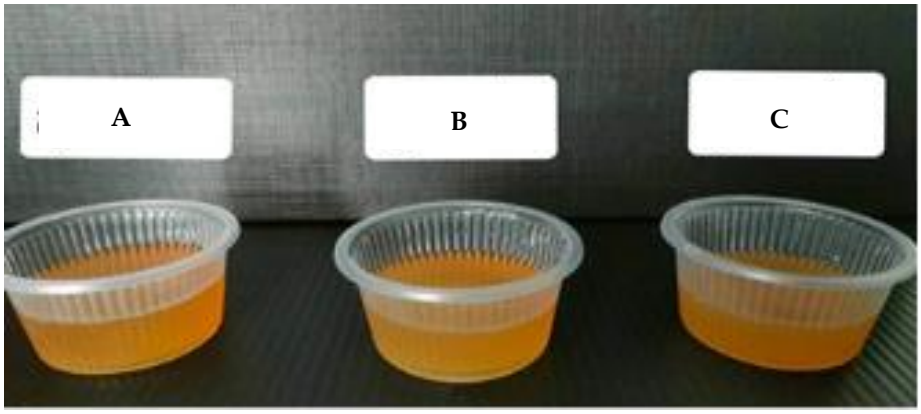


Figure 5. The appearance of three fermented Hang rice vinegar drink formulations, prepared with Hang rice vinegar and pineapple peel syrup in *different ratios:* (A) formula 1(60:40); (B) formula 2 (50:50), and formula 3 (40:60).

3.3 Sensory evaluation of Hang rice vinegar drink with pineapple peel syrup

The sensory characteristics of the three Hang rice vinegar drink formulations are presented in Figure 6. All three samples achieved moderate consumer acceptability, with mean scores ranging from 5.4 to 7.0. No significant differences were observed among formulations in appearance, with ratings classified as "like slightly" (6.43 ± 1.29–6.63 ± 1.29). In terms of color, Formula 1 obtained the highest score ("like moderately"; 6.83 ± 1.26), comparable to Formula 2, while Formula 3 received a lower rating (6.10 ± 1.26), possibly due to its darker, brownish hue compared with the brighter tone of Formula 1. Aroma scores also showed no significant difference among the samples, ranging between "neither like nor dislike" and "like slightly" (5.40 ± 1.88 – 6.10 ± 1.88). Similarly, taste scores did not differ significantly, ranging within the "like slightly" category (6.10 ± 1.52–6.70 ± 1.52). The overall acceptability of all three vinegar drinks did not differ significantly either, ranging from "like slightly" to "like moderately" (6.76 ± 1.56–7.00 ± 2.34). These findings align with those of Saithong et al. [43], who reported overall acceptability scores of 7.05-7.18 for rice vinegars produced from various Thai rice varieties, including Khao Dawk Mali 105, Sangyod, and Hom Nil. Vinegar coloration depends primarily on raw material pigments and the chemical transformations that occur during fermentation and storage, including the Maillard reaction and enzymatic browning [44]. Likewise, the aroma and flavor profiles of vinegar are shaped by multiple factors, including substrate composition, fermentation conditions, and the presence of volatile organic compounds. Earlier studies have identified acetic acid and other short-chain organic acids (e.g., propionic, tartaric, and butyric acids), as well as esters and alcohols, as the major contributors to vinegar's characteristic aroma and taste [45]. Acetic acid imparts the characteristic sourness, pungent aroma, and sharp flavor typical of vinegar products [46–48]. Esters, produced during alcoholic and acetic acid fermentation or during aging, provide pleasant floral and fruity notes typical of fruit vinegars [49, 50].

Alcohols, mainly generated during alcoholic fermentation, add additional fruity, fatty, and fragrant characteristics [51]. Therefore, these findings suggest that Hang rice vinegar blended with pineapple peel syrup can be developed into a novel functional beverage that combines favorable sensory qualities with potential nutritional and health benefits.

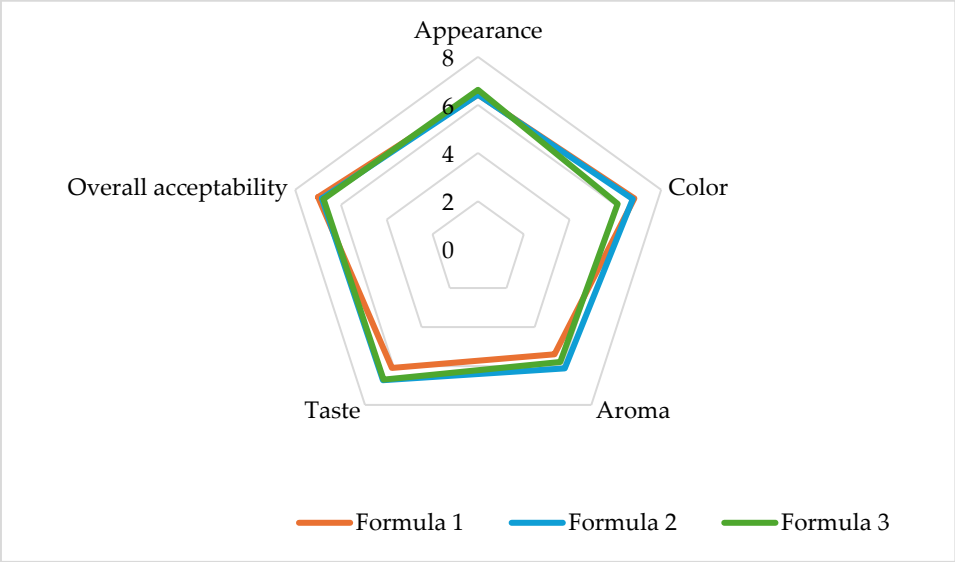


Figure 6. Sensory evaluation radar chart of three Hang rice vinegar drinks with pineapple peel syrup formulation.

3.4 Antioxidant Activity of Hang rice vinegar drink with pineapple peel syrup

3.4.1 Scavenging activity towards DPPH free radicals

The antioxidant capacity of three Hang rice vinegar drink formulations supplemented with pineapple peel syrup is illustrated in Figure 7. Among the tested samples, Formula 3 exhibited the highest scavenging activity (503.70 ± 24.42 μg Trolox/mL), followed by Formula 1 (465.58 ± 8.90 μg Trolox/mL) and Formula 2 (413.64 ± 21.78 μg Trolox/mL). The superior antioxidant performance of Formula 3 is likely attributed to the higher contribution of Hang rice vinegar, which is rich in bioactive compounds such as phenolics, flavonoids, γ-oryzanol, tocopherols, and tocotrienols [52]. These findings are consistent with Suwannawong et al. [53], who reported Hang rice extract showed DPPH radical scavenging activity with an IC_{50} of 594.625 μg/mL, while Phattayakorn et al. [54] observed 73.6% DPPH inhibition in germinated Hang rice (jasmine KDML105). Moreover, rice vinegars such as Hom Nil, Sangyod, and Riceberry have been shown to exhibit antioxidant activity ranging from 49.27% to 74.95% [43, 55]. Meanwhile, pineapple peel contains high levels of natural antioxidants, including phenolic compounds, flavonoids, and vitamin C [56]. Lourenço et al. [57] reported antioxidant activity of 91.79 ± 1.98 μmol Trolox/g dry extract for pineapple peel using the DPPH assay. In addition to antioxidant activity, pineapple peel extracts exhibit anti-inflammatory, antiviral, antiparasitic, antifungal [58], and antimicrobial effects against common foodborne pathogens [59].

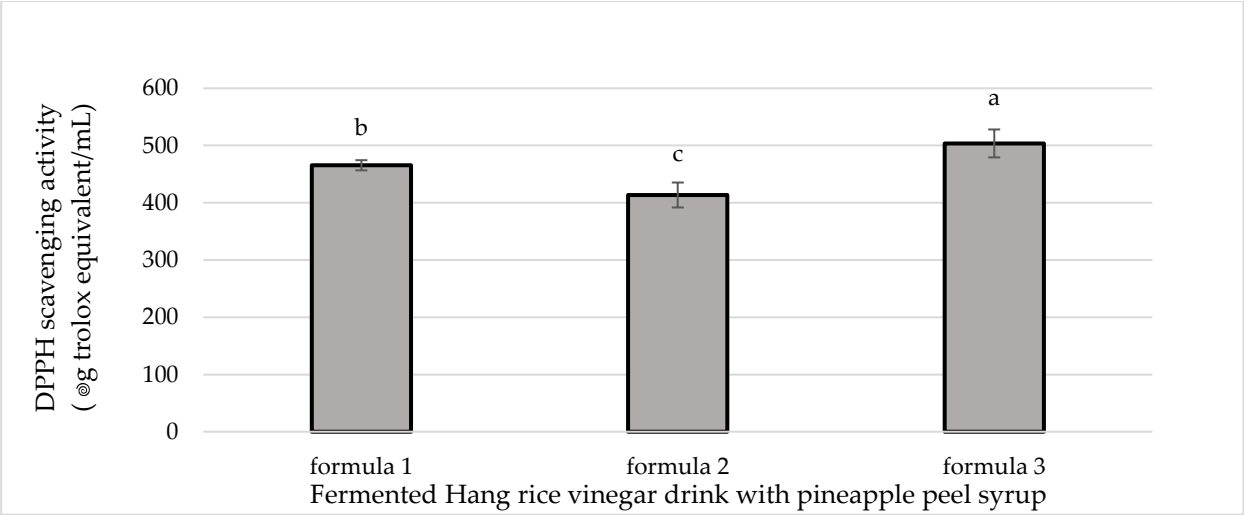


Figure 7. DPPH radical scavenging activity of Hang rice vinegar drink with pineapple peel syrup. Different letters show significant differences ($p \leq 0.05$) among fermented vinegar drink formulations.

3.4.2 Total phenolic contents of Hang rice vinegar drink with pineapple peel syrup

As shown in Figure 8, Formula 3 recorded the highest total phenolic content (97.24 ± 4.36 µg GAE/mL), followed by Formula 1 (84 ± 3.15 µg GAE/mL) and Formula 2 (78.16 ± 2.59 µg GAE/mL). These variations may result from differences in the proportions of Hang rice vinegar and pineapple peel syrup. Phenolic compounds are abundant in both rice and pineapple peels and function as major antioxidants [60, 61]. In rice, phenolic acids, anthocyanins, and proanthocyanidins represent the predominant bioactive constituents [62]. Specifically, ferulic, p-coumaric, sinapic, and vanillic acids are highly concentrated in whole grains and germinated brown rice [63]. These are also the primary bioactive components in Hang rice, as their levels are further enriched by the unique germination and hydrothermal treatment processes (soaking, steaming, drying, and dehusking). These traditional preparation stages significantly enhance the bioavailability of phenolics, γ-oryzanol, vitamin E, and GABA [64-66]. Furthermore, during vinegar fermentation, these compounds undergo microbial biotransformations catalyzed by yeast and acetic acid bacteria (AAB), which may enhance their antioxidant potential and health-related properties [24, 33, 67]. Consequently, these transformed compounds exhibit diverse biological activities, including antioxidant [68], antimutagenic, anticancer, anti-allergic, and cholesterol-lowering effects [69–71]. Previous reports have indicated that Hang rice contains higher phenolic content than brown rice, reaching up to 17.857 mg GAE/g [60], and germinated Hang rice (KDML105) as high as 437.16 mg GAE/g [72]. Pineapple peel also contains diverse phenolic constituents, including flavonoids and acids such as gallic, catechin, epicatechin, ferulic, salicylic, myricetin, trans-cinnamic, tannic, and p-coumaric acids [67, 68]. Campos et al. [73] and Lourenço et al. [57] confirmed that pineapple peel extract possesses higher phenolic levels than stem extract, with 11.10 ± 0.01 mg GAE/g dry extract. During acetic acid fermentation, phenolic composition may change due to oxidation and hydrolysis reactions [74-77]. Previous reports confirmed that rice vinegar generally exhibits substantial phenolic content and antioxidant capacity. Pokkakaw and Manangsatit [78] found that Riceberry and Kao Luem Pua vinegars contained 17.5 ± 0.27 and 9.75 ± 0.33 mg GAE/100 mL, respectively, while Taweekasemsombut et al. [79] reported 133.68 mg GAE/100 mL for Black glutinous rice vinegar. Similarly, Saithong et al. [43] observed 428.47 ± 4.04 GAE/mL in Hom Nil vinegar, and another study [80] reported 50.7 ± 2.8 mg GAE/mL for germinated brown rice vinegar. These findings collectively confirm that Hang rice vinegar combined with pineapple peel syrup exhibits strong antioxidant potential, primarily due to the synergistic effects of the phenolic compounds and other bioactive constituents present in both substrates. Furthermore, the antioxidant capacity of the developed Hang rice vinegar drink was within the reported range for various commercial fruit vinegars, such as pineapple and rosehip. Similarly, the total phenolic content observed in this study (97.24 ± 4.36 µg GAE/mL) aligned with the values reported for other commercial fruit vinegar beverages, which typically range from

96.21 to 4,441.25 mg GAE/L [81]. This comparison confirms that the developed formulation is competitive with established commercial products in terms of functional properties.

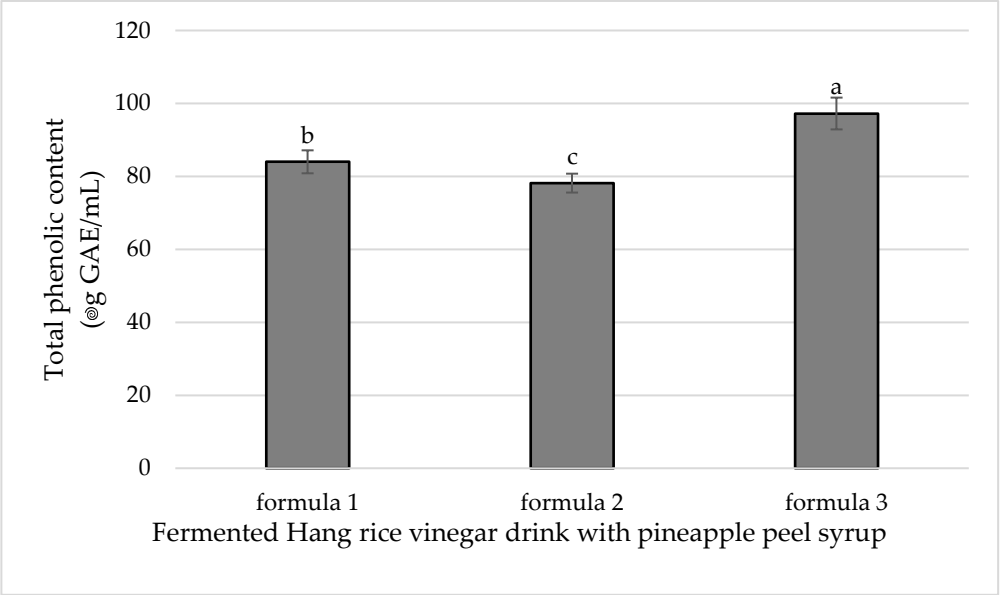


Figure 8. The total phenolic content of Hang rice vinegar drink with pineapple peel syrup. Different letters show significant differences ($p \leq 0.05$) among fermented vinegar drink formulations.

In addition, the microbiological quality of the Hang rice vinegar drink was evaluated using Total Plate Count (TPC) and coliform analysis. The results showed that the total viable count of the fermented vinegar drink was below the countable range (< 30 CFU/mL), while the coliform count was below 1.1 MPN/100 mL. No pathogenic microorganisms were detected under the analytical conditions employed, as shown in Table 1. These microbiological parameters were within the acceptable limits specified by the Thai Community Product Standard for Vinegar Drink (TIS No. 1287/2550), indicating that the Hang rice vinegar drink met the microbiological quality requirements for fermented beverages.

Table 1. Microbiological safety assessment of Hang rice vinegar drink supplemented with pineapple peel syrup.

Microorganisms	Testing results
Total viable count, CFU/mL	Not detected (<30 CFU/mL)
Coliforms, MPN/100 mL	< 1.1
Yeast and Mold, CFU/mL	Not detected
Escherichia coli	Not detected
Salmonella spp.	Not detected

4. Conclusions

This study demonstrated the successful development of a novel functional vinegar beverage from Hang rice combined with pineapple peel syrup. During 30 days of fermentation, the populations of acetic acid bacteria and yeast reached 7.92 log CFU/mL and 7.06 log CFU/mL, respectively, while the final vinegar contained 4.44% acetic acid, exhibited a pH of 3.6, and had no detectable alcohol. Among the three tested formulations, Formula 3 (Hang rice vinegar to pineapple peel syrup ratio of 40:60) was identified as the most suitable. This formulation exhibited the highest antioxidant activity (503.70 ± 24.42 μg Trolox/mL) and the greatest total phenolic content (97.24 ± 4.36 GAE/mL), along with a favorable sensory score of 6.70 ± 1.52 for overall acceptability. These results suggest that Formula 3 is the optimal formulation for a functional Hang rice vinegar drink enriched with pineapple peel syrup, offering promising in vitro antioxidant properties and demonstrating high consumer preference. Although this work demonstrates the successful development of

the vinegar drink, the findings are considered preliminary regarding consumer safety. Further studies are required to evaluate the product's shelf-life stability over an extended storage period.

5. Acknowledgements

The authors would like to acknowledge the Department of Applied Biology, Faculty of Sciences and Liberal Arts, Rajamangala University of Technology Isan, for kindly providing research locations and equipment.

Author Contributions: Nisa Romsomsa conceptualization, designed research, analyzed data, and wrote the paper; Nithiphon Tiapasert, Karid Jittimanee, and Chaiwat Paungkrathok performed research; Nutthawut Meesilp coordinated research; and Numphon Thaiwong contributed new reagents/analytic tools. All authors have read and agreed to the published version of the manuscript.

Funding: The research was funded by the Plant Genetic Conservation Project initiated by Her Royal Highness Princess Maha Chakri Sirindhorn, RMUTI Coordination Center, Rajamangala University of Technology Isan, Nong Rawiang Subdistrict, Mueang District, Nakhon Ratchasima, Thailand (Grant Number 65-1214-1-4-005-00).

Conflicts of Interest: The authors declare that they have no conflicts of interest.

References

[1] Xia, T.; Zhang, B.; Duan, W.; Zhang, J.; Wang, M. Nutrients and Bioactive Components from Vinegar: A Fermented and Functional Food. *J. Funct. Foods* **2020**, *64*, 103681. https://doi.org/10.1016/j.jff.2019.103681

[2] Kandylis, P.; Bekatorou, A.; Dimitrellou, D.; Plioni, I.; Giannopoulou, K. Health Promoting Properties of Cereal Vinegars. *Foods* **2021**, *10*, 344. https://doi.org/10.3390/foods10020344

[3] Hindi, N. K. K. In Vitro Antibacterial Activity of Aquatic Garlic Extract, Apple Vinegar and Apple Vinegar–Garlic Extract Combination. *AJPCT* **2013**, *1*, 42–51.

[4] Baba, N.; Higashi, Y.; Kanekura, T. Japanese Black Vinegar "Izumi" Inhibits the Proliferation of Human Squamous Cell Carcinoma Cells via Necroptosis. *Nutr. Cancer* **2013**, *65*(7), 1093–1097. https://doi.org/10.1080/01635581.2013.815234

[5] Shi, G. Talk about Chinese Vinegar. *China Brewing* **1999**, *63*, 9–40

[6] Taweekasemsombut, S.; Tinoi, J.; Mungkornasawakul, P.; Chandet, N. Thai Rice Vinegars: Production and Biological Properties. *Appl. Sci.* **2021**, *11*, 5929. https://doi.org/10.3390/app11135929

[7] Tudpor, K.; Jirasatid, S.; Srinukoon, K.; Srisuk, N. Vinegar Production from Thai Rice Varieties with Emphasis on the Biological Properties of Sangyod Rice Vinegar. *Res. Square* **2025**. https://doi.org/10.21203/rs.3.rs-7050140/v1

[8] Boonsupa, W.; Tongdonpriang, K.; Seehabuntong, K.; Soongpon, W.; Kinboran, W.; Chumduang, N.; Janngam, W.; Thongdee, A.; Pase, U.; Saksriboondee, P. Chemical Properties, Antioxidant Activity and Sensory Evaluation of Fermented Vinegar from Three Rice Cultivars. *RMUTI J. Sci. Technol.* **2019**, *12*(2), 52–61

[9] Saithong, P.; Permpool, J.; Nitipan, S. Antioxidant and Anthocyanin-Rich Vinegar Fermented from Thai Colored Rice Varieties. *Trends Sci.* **2023**, *21*(6), 7532. https://doi.org/10.48048/tis.2024.7532

[10] Prommakool, A. Comparison of Chemical Compositions and Bioactive Compounds of Non-Germinated and Germinated Black Hang Rice. In *Proc. Int. Conf. Starch Technol.*; Bangkok, Thailand, 2013

[11] Moongngarm, A.; Saetung, N. Comparison of Chemical Compositions and Bioactive Compounds of Germinated Rough Rice and Brown Rice. *Food Chem.* **2010**, *122*, 782–788. https://doi.org/10.1016/j.foodchem.2010.03.053

[12] Lin, P. Y.; Lai, H. M. Bioactive Compounds in Rice during Grain Development. *Food Chem.* **2011**, *127*, 86–93. https://doi.org/10.1016/j.foodchem.2010.12.092

[13] Kim, H. Y.; Hwang, I. G.; Kim, T. M.; Woo, K. S.; Park, D. S.; Kim, J. H.; Kim, D. J.; Lee, J.; Lee, Y. R.; Jeong, H. S. Chemical and Functional Components in Different Parts of Rough Rice (Oryza sativa L.) before and after Germination. *Food Chem.* **2012**, *134*(1), 288–293. https://doi.org/10.1016/j.foodchem.2012.02.138

[14] Chunthanom, P.; Tsai, P. J. Qualities of Hang Rice in Northeast Thailand. In *Proc. KU-KPS Natl. Conf.*; Kasetsart University: Nakhon Pathom, Thailand, 2014
[15] Kerdpiboon, S.; Puttongsiri, T. Characteristics of Hang Rice and Its Cooking. *KKU Res. J.* **2015**, *20*(1), 26–33. https://doi.org/10.14456/KKURJ.2015.3
[16] Cornelia, M.; Kristyanti, T. Utilization of Pineapple Peel Waste as Raw Material in Cider Making. In *Proc. Int. Conf. Comput. Environ. Agric. Soc. Sci. Eng. Technol.*; Medan, Indonesia, 2018. https://doi.org/10.5220/0010041402580263
[17] Roda, A.; Lambri, M. Food Uses of Pineapple Waste and By-Products: A Review. *Int. J. Food Sci. Technol.* **2019**. https://doi.org/10.1111/ijfs.14128
[18] AOAC International. *Official Methods of Analysis*, 21st ed.; AOAC: Gaithersburg, MD, 2019
[19] Xia, T.; Zhang, B.; Duan, W.; Zhang, J.; Wang, M. Nutrients and Bioactive Compounds in Traditional Rice Vinegars: A Review. *Food Chem.* **2020**, *310*, 125835. https://doi.org/10.1016/j.foodchem.2019.125835
[20] Tamaruay, C.; Boonkerd, N.; Tantratian, S.; Panyachariwat, A. Quality of Germinated Brown Rice Vinegar Fermented by Different Strains of *Acetobacter aceti*. *J. Appl. Sci.* **2017**, *16*(1), 1–13
[21] Klaudia, M.; Karolina, J. Chemical Profiles and Antioxidant Properties of Fruit and Vegetable Vinegars Available on the Polish Market. *Foods* **2024**, *13*, 1488. https://doi.org/10.3390/foods13101488
[22] Manosroi, A.; Ruksiriwanich, W.; Kietthanakorn, B.; Manosroi, W.; Manosroi, J. Relationship between Biological Activities and Bioactive Compounds in Fermented Rice Sap. *Food Res. Int.* **2011**, *44*, 2757–2765. https://doi.org/10.1016/j.foodres.2011.06.010
[23] Taechavasonyoo, A.; Thaniyavarn, J.; Yompakdee, C. Identification of Molds and Yeasts in Loogpang Starter. *Asian J. Food Agro-Ind.* **2013**, *6*, 24–38
[24] Tochampa, W.; Jittrepotch, N.; Kongbangkerd, T.; Kraboun, K.; Rojsuntornkitti, K. Microwave Heating Effects on Sweet Fermented Glutinous Rice. *Int. J. Food Sci. Technol.* **2011**, *18*, 239–248
[25] Isham, N. K. M.; Mokhtar, N.; Fazry, S.; Lim, S. J. Development of an Alternative Fermentation Model for Vinegar Production. *LWT* **2019**, *100*, 322–327. https://doi.org/10.1016/j.lwt.2018.10.065
[26] Codex Alimentarius Commission. *Standard for Vinegar (CXS 162-1987)*; FAO/WHO, 1987
[27] Bhat, S. V.; Akhtar, R.; Amin, T. Biological Production of Vinegar: An Overview. *Int. J. Food Sci. Technol.* **2014**, *3*, 139
[28] Mota, J.; Vilela, A. Aged to Perfection: The Science behind Vinegar and Acetic Acid Bacteria. *Fermentation* **2024**, *10*, 200. https://doi.org/10.3390/fermentation10040200
[29] Tran, T.; Grandvalet, C.; Verdier, F.; Martin, A.; Alexandre, H.; Tourdot-Maréchal, R. Microbial Dynamics in Kombucha Fermentation. *Foods* **2020**, *9*, 963. https://doi.org/10.3390/foods9070963
[30] Vilela, A. Microbial Dynamics in Wine Vinegar. *Appl. Sci.* **2023**, *13*, 7366. https://doi.org/10.3390/app13137366
[31] Vilela, A. Microbial dynamics in sour–sweet wine vinegar: Impacts on chemical and sensory composition. *Appl. Sci.* **2023**, *13*, 7366. https://doi.org/10.3390/app13137366.
[32] Wu, J. J.; Ma, Y. K.; Zhang, F. F.; Chen, F. S. Biodiversity of yeasts, lactic acid bacteria and acetic acid bacteria in the traditional fermentation of Shanxi aged vinegar. *Food Microbiol.* **2012**, *30*(2), 289–297. https://doi.org/10.1016/j.fm.2011.08.010
[33] Santos, R. C.; Pires, L. S. O.; Barbosa, H. C. P.; Uetanabaro, A. P. T.; Assis, S. A.; Ramos, C. L.; Schwan, R. F. Spontaneous and induced fermentation of pineapple vinegar: Physicochemical and sensory profiles. *Int. J. Food Sci. Technol.* **2022**, *57*(1), 45–56. https://doi.org/10.1111/ijfs.15174
[34] Roda, A.; Lambri, M.; De Faveri, D. M. Vinegar production from pineapple wastes: An overview. *J. Food Process. Preserv.* **2017**, *41*(5), e13173.
[35] Antoniewicz, P.; Satora, P.; Pielech-Przybylska, K. Microbiological and chemical profile of vinegars produced by spontaneous fermentation. *Appl. Sci.* **2021**, *11*(13), 5929. https://doi.org/10.3390/app11135929
[36] Jayus, J.; Setiawan, R.; Giyarto, G. Chemical and sensory properties of spontaneous fermented red rice vinegar. In *Proceedings of the 3rd International Conference on Food and Agriculture (ICFA)*; Politeknik Negeri Jember (Polije): Jember, Indonesia, 2020.

[37] Talukder, A. A.; Easmin, F.; Mahmud, S. A.; Yamada, M. Thermotolerant yeasts capable of producing bioethanol: Isolation from natural fermented sources, identification and characterization. *Biotechnol. Biotechnol. Equip.* **2016**, *30*(6), 1106–1114. https://doi.org/10.1080/13102818.2016.1228477

[38] Choi, D. H.; Park, E. H.; Kim, M. D. Isolation of thermotolerant yeast *Pichia kudriavzevii* from nuruk. *Food Sci. Biotechnol.* **2017**, *26*, 1357–1362. https://doi.org/10.1007/s10068-017-0155-6

[39] Aouine, M.; Elalami, D.; Koraichi, S. I.; Haggoud, A.; Barakat, A. Exploring natural fermented foods as a source for new efficient thermotolerant yeasts for the production of second-generation bioethanol. *Energies* **2022**, *15*(14), 4954. https://doi.org/10.3390/en15144954

[40] Cheenacharoen, S.; Juntachai, W. Diversity and genetic relationship of ethanol tolerant yeasts isolated from rice wine starters (Loog-Pang) in Chiang Mai province. *TJST* **2018**, 478–489. https://doi.org /10.14456/jstel.2022.23

[41] Chay, C.; Dizon, E. I.; Elegado, F. B.; Norng, C.; Hurtada, W. A.; Raymundo, L. C. Isolation and identification of mold and yeast in medombae, a rice wine starter culture from Kompong Cham Province, Cambodia. *Food Res.* **2017**, *6*, 213–220. https://doi.org/10.26656/fr.2017.6.101

[42] Gullo, M.; Giudici, P. Acetic acid bacteria in traditional balsamic vinegar: Phenotypic traits relevant for starter cultures selection. *Int. J. Food Sci. Technol.* **2018**, *125*(1), 46–53. https://doi.org/10.1016 /j.ijfoodmicro.2007.11.076

[43] Saithong, P.; Permpool, J.; Nitipan, S. Antioxidant and anthocyanin-rich vinegar fermented from Thai colored rice varieties. *TiS* **2023**, *21*(6), 7532. https://doi.org/10.48048/tis.2024.7532

[44] Ezemba, A. S.; Osuala, O. J.; Orji, M. U.; Ezemba, C. C.; Anaukwu, C. Production and comparative physicochemical analysis of vinegar from locally grown fruits in Nigeria and industrial produced vinegar. *Am. J. Microbiol. Res.* **2021**, *9*(1), 25–33. https://doi.org/10.12691/ajmr-9-1-4

[45] Pan, D. D.; Wu, Z.; Peng, T.; Zeng, X. Q.; Li, H. Volatile organic compounds profile during milk fermentation by *Lactobacillus pentosus* and correlations between volatile flavor and carbohydrate metabolism. *J. Dairy Sci.* **2014**, *97*, 624–631. https://doi.org/10.3168/jds.2013-7131

[46] Su, M. S.; Chien, P. J. Aroma impact components of rabbiteye blueberry (*Vaccinium ashei*) vinegars. *Food Chem.* **2010**, *119*, 923–928. https://doi.org/10.1016/j.foodchem.2009.07.053

[47] Umaru, F. F.; Esedafe, W. K.; Obidah, J. S.; Akinwotu, O.; Danba, E. Production of vinegar from pineapple peel wine using *Acetobacter* species. In *Proceedings of the 3rd International Conference on Biological, Chemical and Environmental Sciences*; Kuala Lumpur, Malaysia, 2015.

[48] Tesfaye, W.; García-Parrilla, M.; Troncoso, A. Sensory evaluation of sherry wine vinegar. *J. Sens. Stud.* **2002**, *17*, 133–144. https://doi.org/10.1111/j.1745-459X.2002.tb00338.x

[49] Lu, S.; Cao, Y.; Yang, Y.; Jin, Z.; Luo, X. Effect of fermentation modes on nutritional and volatile compounds of Huyou vinegar. *J. Food Sci. Technol.* **2018**, *55*, 2631–2640. https://doi.org/10.1007/s13197-018-3184-0

[50] Al-Dalali, S.; Zheng, F. P.; Xu, B. C.; Abughoush, M.; Li, L. H.; Sun, B. G. Processing technologies and flavor analysis of Chinese cereal vinegar: A comprehensive review. *Food Anal. Methods* **2023**, *16*(1), 29–29. https://doi.org/10.1007/s12161-022-02328-w

[51] Zhou, Z.; Liu, S.; Kong, X.; Ji, Z.; Han, X.; Wu, J.; Mao, J. Elucidation of the aroma compositions of Zhenjiang aromatic vinegar using comprehensive two-dimensional gas chromatography coupled to time-of-flight mass spectrometry and gas chromatography-olfactometry. *J. Chromatogr. A* **2017**, *1487*, 218–226. https://doi.org/10.1016/j.chroma.2017.01.014

[52] Chotimarkorn, C.; Benjakul, S.; Silalai, N. Antioxidant components and properties of five long-grained rice bran extracts from commercially available cultivars in Thailand. *Food Chem.* **2008**, *111*, 636–641. https://doi.org/10.1016/j.foodchem.2008.04.031

[53] Suwannawong, P.; Waratchareeyakul, W.; Chasvised, S.; Yuenyongcharoendee, K.; Pangnole, S.; Yusorn, A.; Apinansawat, N. Brown rice and Hang rice of Lai Pla Thong variety: Antioxidant activity and consumer acceptance. *J. Sci. Technol. Rajabhat Maha Sarakham Univ.* **2023**, *6*(1), 1–13.

[54] Phattayakorn, K.; Pajanyor, P.; Wongtecha, S.; Prommakool, A.; Saveboworn, W. Effect of germination on total phenolic content and antioxidant properties of Hang rice. *Int. Food Res. J.* **2016**, *23*(1), 406–409.

[55] Boonsupa, W.; Tongdonpriang, K.; Seehabuntong, K.; Soongpon, W.; Kinboran, W.; Chumduang, N.; Janngam, W.; Thongdee, A.; Pase, U.; Saksriboondee, P. Chemical properties, antioxidant activity and sensory evaluation of fermented vinegar from three rice cultivars. *RMUTI J. Sci. Technol.* **2019**, *12*(2), 52–61.

[56] Liu, S. H.; Liu, Y. G.; Zhang, X. M. Extraction conditions and antioxidant activities of pineapple peel extracts by ultrasonic method. *IOP Conf. Ser.: Earth Environ. Sci.* **2018**, *186*, 012038. https://doi.org/10.1088/1755-1315/186/4/012038

[57] Lourenço, S. C.; Campos, D. A.; Gómez-García, R.; Pintado, M.; Oliveira, M. C.; Santos, D. I.; Corrêa-Filho, L. C.; Moldão-Martins, M.; Alves, V. D. Optimization of natural antioxidants extraction from pineapple peel and their stabilization by spray drying. *Foods* **2021**, *10*, 1255. https://doi.org/10.3390/foods10061255

[58] Dabesor, A. P.; Asowata-Ayodele, A. M.; Umoiette, P. Phytochemical compositions and antimicrobial activities of *Ananas comosus* peel and *Cocos nucifera* kernel. *Am. J. Plant Sci.* **2017**, *2*, 73–76. https://doi.org/10.11648/j.ajpb.20170202.15

[59] Punbusayakul, N.; Samart, S.; Sudmee, W. Antimicrobial activity of pineapple peel extract. In *Proceedings of the Innovation of Functional Foods in Asia Conference*; University of Phayao: Phayao, Thailand, 2017.

[60] Li, T.; Shen, P.; Liu, W.; Liu, C.; Liang, R.; Yan, N.; Chen, J. Major polyphenolics in pineapple peels and their antioxidant activities. *Food Chem.* **2014**, *154*, 112–118. https://doi.org/10.1016/j.foodchem.2013.12.110

[61] Shao, Y.; Bao, J. Polyphenols in Whole Rice Grain: Genetic Diversity and Health-Promoting Effect. *Food Chem.* **2015**, *59* (1), 31–54. https://doi.org/10.1016/j.foodchem.2015.02.027

[62] Goufo, P.; Trindade, H. Rice Antioxidants: Phenolic Acids, Flavonoids, Anthocyanins, Proanthocyanidins, Tocopherols, Tocotrienols, γ-Oryzanol, and Phytic Acid. *Food Sci. Nutr.* **2014**, *2*(2), 75–104. https://doi.org/10.1002/fsn3.86

[63] Tian, S.; Nakamura, K.; Kayahara, H. Analysis of Phenolic Compounds in White Rice, Brown Rice, and Germinated Brown Rice. *J. Agric. Food Chem.* **2004**, *52*, 4808–4813. https://doi.org/10.1021/jf049446v.

[64] Prommakool, A.; Tinchan, P. Effect of Steaming on GABA and Physico-Chemical Properties of Hang Rice. In *Proceedings of the 16th Food Innovation Asia Conference 2014: Science and Innovation for Quality of Life*; Bangkok, Thailand, June 12–13, 2014.

[65] Moongngarm, A.; Saetung, N. Comparison of Chemical Compositions and Bioactive Compounds of Germinated Rough Rice and Brown Rice. *Food Chem.* **2010**, *122*, 782–788. https://doi.org/10.1016/j.foodchem.2010.03.053

[66] Kim, H. Y.; Hwang, I. G.; Kim, T. M.; Woo, K. S.; Park, D. S.; Kim, J. H.; Kim, D. J.; Lee, J.; Lee, Y. R.; Jeong, H. S. Chemical and Functional Components in Different Parts of Rough Rice (*Oryza sativa* L.) before and after Germination. *Food Chem.* **2012**, *134*(1), 288–293. https://doi.org/10.1016/j.foodchem.2012.02.138

[67] Lynch, K. M.; Zannini, E.; Coffey, A.; Arendt, E. K. The Role of Microbial Biotransformation in the Development of Healthy Fermented Foods. *Curr. Opin. Food Sci.* **2018**, *22*, 75–82. https://doi.org/10.1016/j.cofs.2018.01.002

[68] Soobrattee, M. A.; Neergheen, V. S.; Luximon-Ramma, A.; Aruoma, O. I.; Bahorun, T. Phenolics as Potential Antioxidant Therapeutic Agents: Mechanism and Actions. *Mutat. Res., Fundam. Mol. Mech. Mutagen.* **2005**, *579* (1–2), 200–213. https://doi.org/10.1016/j.mrfmmm.2005.03.023

[69] Zawistowski, J.; Kopec, A.; Kitts, D. D. Effects of a Black Rice Extract (*Oryza sativa* L. indica) on Cholesterol Levels and Plasma Lipid Parameters in Wistar Kyoto Rats. *J. Funct. Foods* **2009**, *1*, 50–56. https://doi.org/10.1016/j.jff.2008.09.008

[70] Pengkumsri, N.; Chaiyasut, C.; Saenjum, C.; Sirilun, S.; Peerajan, S.; Suwannalert, P.; Sirisattha, S.; Sivamaruthi, B. S. Physicochemical and Antioxidative Properties of Black, Brown and Red Rice Varieties of Northern Thailand. *Food Sci. Technol.* **2015**, *35*, 331–338. https://doi.org/10.1590/1678-457X.6573

[71] Tananuwong, K.; Tewaruth, W. Extraction and Application of Antioxidants from Black Glutinous Rice. *LWT--Food Sci. Technol.* **2010**, *43*, 476–481. https://doi.org/10.1016/j.lwt.2009.09.014

[72] Larrauri, J. A.; Rupérez, P.; Saura-Calixto, F. Pineapple Shell as a Source of Dietary Fiber with Associated Polyphenols. *J. Agric. Food Chem.* **1997**, *45*(10), 4028–4031. https://doi.org/10.1021/jf970450j.

[73] Campos, D. A.; Ribeiro, T. B.; Teixeira, J. A.; Pastrana, L.; Pintado, M. M. Integral Valorization of Pineapple (*Ananas comosus* L.) By-Products through a Green Chemistry Approach towards Added Value Ingredients. *Foods* **2020**, *9*(1), 60. https://doi.org/10.3390/foods9010060

[74] Dávalos, A.; Bartolomé, B.; Gómez-Cordovés, C. Antioxidant Properties of Commercial Grape Juices and Vinegars. *Food Chem.* **2005**, *93*, 325–330. https://doi.org/10.1016/j.foodchem.2004.09.030

[75] Chen, S.; Su, J.; Liu, C.; Zhang, H. Y.; Heng, Y. W.; Liu, Y. B. Analysis of Contents of Total Phenolic Compounds and Total Flavones and DPPH Radical Scavenging Activity during Overmature Vinegar Production. *Food Sci.* **2009**, *17*, 159–162.

[76] Li, Y.-L.; Hu, J.-J.; Li, H.-M.; Shan, F.; Bian, J.-S.; Sun, Q.-Y. Study on Variations of Main Functional Ingredients in the Tartary Buckwheat Vinegar Fermentation Process with Uncooked Material. *Sci. Technol. Food Ind.* **2011**, *12*, 55.

[77] Wang, A.; Zhang, J.; Li, Z. Correlation of Volatile and Nonvolatile Components with the Total Antioxidant Capacity of Tartary Buckwheat Vinegar: Influence of the Thermal Processing. *Food Res. Int.* **2012**, *49*, 65–71. https://doi.org/10.1016/j.foodres.2012.07.020

[78] Pokkakaw, R.; Manangsatit, P. The Comparison of Two Rice Varieties on Quality of Rice Vinegar. In *Proceedings of the 20th Food Innovation Asia Conference 2018 (FIAC 2018): Creative Food for Future and Sustainability*; Bangkok, Thailand, June 14–16, 2018.

[79] Taweekasemsombut, S.; Tinoi, J.; Mungkornasawakul, P.; Chandet, N. Thai Rice Vinegars: Production and Biological Properties. *Appl. Sci.* **2021**, *11*, 5929. https://doi.org/10.3390/app11135929

[80] Sriphochanart, W.; Krusong, W.; Surayot, U.; Mekkerdchoo, O.; Sriprom, P. Germinated Brown Rice Preparation for Value Added Material for Healthy Brewed Vinegar. *Curr. Appl. Sci. Technol.* **2021**, *22*(3). https://doi.org/10.55003/cast.2022.03.22.007

[81] Topuz Türker, S.; Bayram, M. Determination of Total Phenolic Compound, Antioxidant Activity, and Some Physicochemical Properties of Different Commercial Fruit Vinegars. *Gida* **2025**, *50*(4), 606–619. https://doi.org/10.15237/gida.GD25063

ASEAN
Journal of Scientific and Technological Reports
Online ISSN:2773-8752

Research article

Comparison of Color Space Performance for Colorimetric Detection of Heavy Metals in Drinking Water Using Image Processing and Convolutional Neural Networks

Atthapol Phongsuwan[1], Nadh Ditcharoen[1*], and Sompong Valuvanathorn[1]

[1] Faculty of Science, Ubon Ratchathani University, Ubon Ratchathani, 34190, Thailand
* Correspondence: nadh.d@ubu.ac.th

Citation:
Phongsuwan, A.; Ditcharoen, N.; Valuvanathorn, S. Comparison of color space performance for colorimetric detection of heavy metals in drinking water using image processing and convolutional neural networks. *ASEAN J. Sci. Tech. Report.* **2026**, *29*(4), e260866. https://doi.org/10.55164/ajstr.v29i4.260866

Article history:
Received: August 16, 2025
Revised: February 11, 2026
Accepted: February 22, 2026
Available online: March 24, 2026

Publisher's Note:
This article is published and distributed under the terms of the Thaksin University.

Abstract: Heavy metal contamination in drinking water, including arsenic, lead, cadmium, iron, copper, and manganese, is an environmental issue that adversely affects human health and ecosystems. Although standard laboratory methods provide high accuracy, they are limited by cost, time, and operational complexity. This study aimed to develop and compare the performance of eight color spaces (RGB, RGBA, Grayscale, GrayscaleA, CIE LAB, CIE LABA, HSV, HSVA) for classifying heavy metal concentration levels from microplate images using image processing techniques combined with a Convolutional Neural Network (CNN), and to select the optimal color space using the Weighted Sum Model. The dataset comprised images of six types of heavy metals, with 368,000 images after preprocessing and data augmentation. The model was trained using K-Fold Cross Validation (K=5). Experimental results showed that the HSVA color space achieved the best performance (Accuracy 99.65%, Loss 0.01382, Training Time 1,606 seconds). When tested on a separate set of 920 images, the model maintained an accuracy of 99.0%, indicating stability and strong practical applicability. The findings confirm that selecting an appropriate color space in conjunction with a CNN significantly improves the accuracy of heavy metal analysis on test datasets and has strong potential for further development into a portable, low-cost analytical tool for field applications.

Keywords: Heavy metals; image processing; color spaces; nvolutional neural network; colorimetric measurement

1. Introduction

Heavy metal contamination in drinking water—such as arsenic (As), lead (Pb), cadmium (Cd), iron (Fe), copper (Cu), and manganese (Mn)—poses a serious environmental threat with profound impacts on human health and ecosystems. Bioaccumulation of these metals can lead to neurological disorders, kidney dysfunction, cardiovascular diseases, and gastrointestinal complications [1, 2]. Current detection of heavy metals predominantly relies on laboratory-based standard methods, such as Atomic Absorption Spectrometry (AAS) and Inductively Coupled Plasma Mass Spectrometry (ICP-MS), which, although highly accurate, are limited by high operational costs, bulky instrumentation, and complex procedures, making them unsuitable for field deployment [3, 4]. To address these limitations, portable, low-cost colorimetric techniques have been explored, often using smartphones or digital cameras to capture color changes resulting from chemical reactions with heavy metals. Such methods

offer low cost, portability, and practical applicability in on-site testing [5, 6]. However, the accuracy of this approach depends critically on image quality and the choice of a suitable color space for chemical classification.

Previous studies have investigated the influence of color space transformations on the performance of Convolutional Neural Networks (CNNs) across various domains, including plant disease diagnosis, smoke detection, and medical image analysis [7 – 15]. Findings indicate that certain color spaces—such as HSV and CIE LAB—can significantly improve classification accuracy. Although prior studies have demonstrated that color space transformations can improve CNN performance across various domains, there remains a lack of a systematic investigation focused specifically on colorimetric heavy metal detection in drinking water. In particular, no prior study has comprehensively compared multiple conventional and alpha-channel color spaces within a single experimental framework. This gap limits the development of robust, field-deployable colorimetric detection systems.

Therefore, this study aims to compare the performance of eight color spaces—RGB, RGBA, Grayscale, GrayscaleA, CIE LAB, CIE LABA, HSV, and HSVA—in classifying heavy metal concentration levels from microplate images using image processing techniques combined with CNNs. The Weighted Sum Model (WSM) [16, 17] is employed to identify the optimal color space that achieves high classification accuracy while balancing processing time and loss. The results are intended to serve as a guideline for developing low-cost, portable heavy metal analysis tools for effective field applications.

2. Research Objectives

2.1 To develop a convolutional neural network model for classifying and analyzing heavy metal concentration levels in drinking water from microplate images.

2.2 To compare the performance of eight color spaces — RGB, RGBA, Grayscale, GrayscaleA, CIE LAB, CIE LABA, HSV, and HSVA — using accuracy, loss, and training time as evaluation metrics.

2.3 To identify the optimal color space using the weighted sum model and evaluate the model's performance on a previously unseen test dataset.

3. Materials and Methods

This research used Python 3.8, OpenCV, TensorFlow, and Keras to develop and evaluate CNN models. The methodology consisted of 4 steps, illustrated in Figure 1 and detailed as follows.

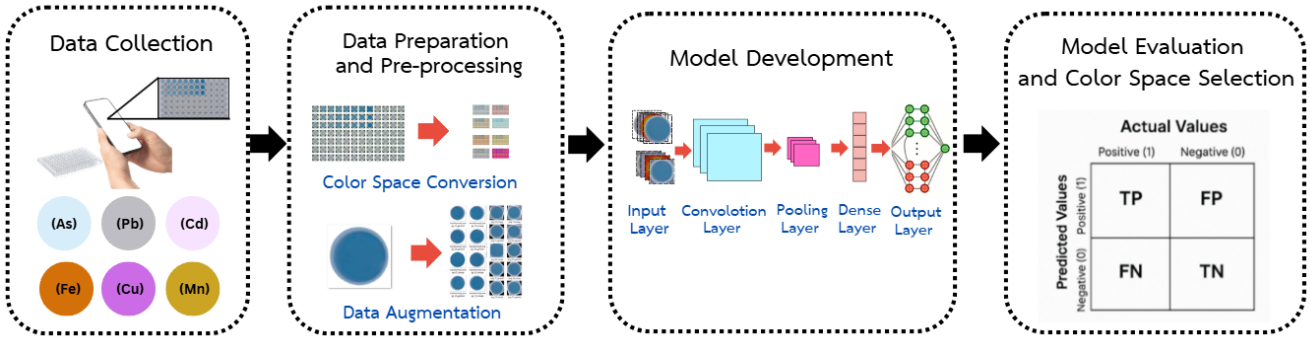


Figure 1. Research methodology.

3.1 Data Collection

The image data used in this study were obtained from Chunta [18], originating from laboratory analyses using a simple heavy metal test kit applied to drinking water samples. Tests were conducted on six types of heavy metals across 46 concentration levels, as shown in Table 1. Images were captured from a 96-well microplate using a Samsung SM-A515F smartphone with a resolution of 3,000 × 4,000 pixels, a 5 mm focal length lens (equivalent to 25 mm in 35 mm format), an aperture of f/2, a shutter speed of 1/365 s, and ISO-32. No flash was used, and the center-weighted average metering mode was applied. The camera was positioned

at 0° directly above the microplate, with constant lighting and fixed camera settings to ensure high-quality, consistent images, as illustrated in Figure 2.

Table 1. Details of the dataset [18].

Heavy Metal	Detection Range (mg/L)	# of Concentration Level (Class)
Arsenic (As)	0.007 – 4.00	10
Cadmium (Cd)	0.0002 – 0.05	9
Copper (Cu)	0.35 – 6.00	6
Iron (Fe)	0.10 – 100.00	9
Lead (Pb)	0.007 – 0.10	5
Manganese (Mn)	0.006 – 0.10	7

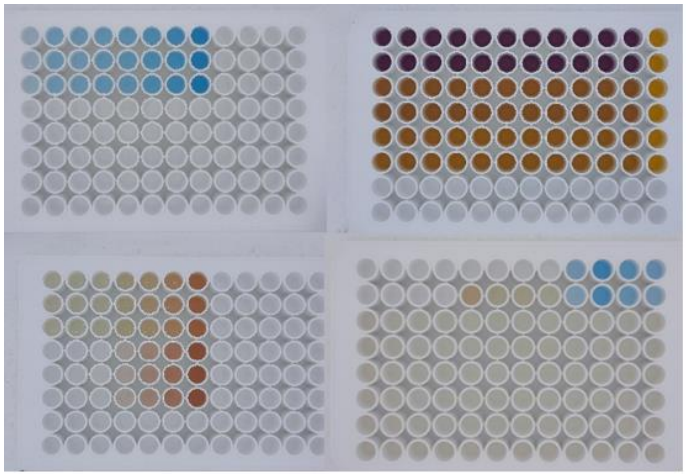
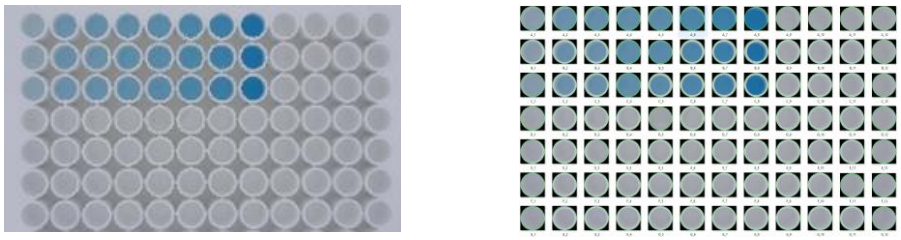


Figure 2. Example of heavy metal testing images using a 96-well microplate test kit [18].

3.2 Data Preparation and Pre-processing

3.2.1 Image Segmentation

The collected images were segmented by detecting and cropping the boundaries of the microplate wells using the Hough Circle Transform function (https://docs.opencv.org) [5]. The cropped images were then resized to 100×100 pixels. To enhance the CNN's learning capability, an alpha channel was created to make the area outside the circle transparent, and the images were saved as PNG files for further processing. Figure 3 presents examples of the images before and after pre-processing.



(A) (B)

Figure 3. Example of the images (A) before image segmentation and (B) after image segmentation.

3.2.2 Color Space Conversion

Each cropped image was converted into eight color spaces (RGB, RGBA, Grayscale, GrayscaleA, CIE LAB, CIE LABA, HSV, HSVA), as illustrated in Figure 4. Before being input into the CNN model, the pixel values were normalized to the range 0–1 to reduce data variability.

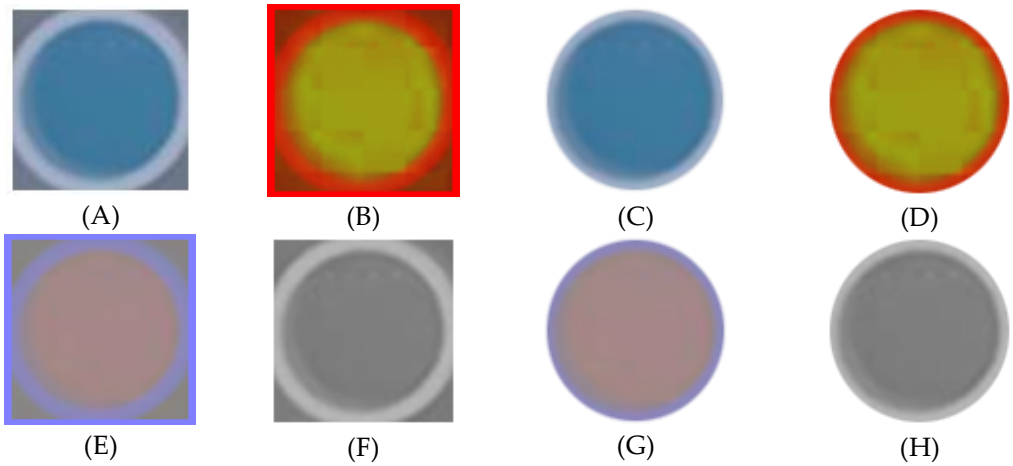


Figure 4. Example of the images after color space conversion (A) RGB, (B) HSV, (C) RGBA, (D) HSVA, (E) CIE LAB, (F) Grayscale, (G) CIE LABA, (H) GrayscaleA.

3.2.3 Data Augmentation

Data augmentation was applied to increase the size and diversity of the training dataset [19] by generating new images from the original images at a 9:1 ratio per class. The augmentation techniques included rotation, flipping, noise addition, brightness and contrast adjustment, and mix-up augmentation, as illustrated in Figure 5.

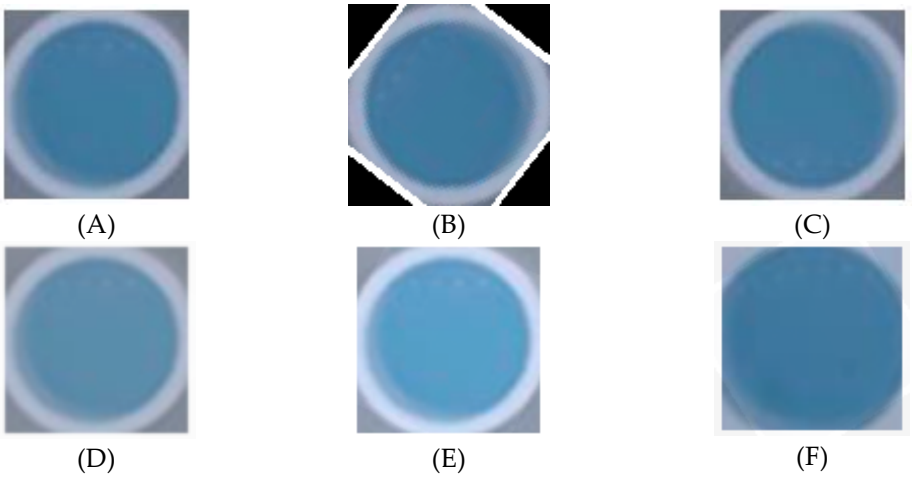


Figure 5. Example of the images after data augmentation (A) original image, (B) rotated image, (C) flipped image, (D) noise added image, (E) brightness and contrast adjustment image, (F) mix-up image.

3.2.4 Dataset Splitting

Each original image was augmented to produce nine additional images, resulting in 1,000 images per class (concentration level) when combined with the original. This yielded 46,000 images for each color space. For each color space dataset, the images were randomly split at an 80:20 ratio into a training set of 36,800 images and a validation set of 9,200 images. In this study, experiments were conducted across eight color spaces, yielding a total of 368,000 images used for training and validation.

3.3 Model Development

The CNN model was designed to support all 8 color spaces and comprised convolutional layers, max pooling layers, fully connected layers, and a dropout layer (rate = 0.5) before the final dense output layer with 46 nodes. The model used categorical cross entropy as the loss function, the Adam optimizer (learning rate = 0.001), and a batch size of 32. Training was conducted using K-fold cross-validation (K = 5) with early stopping (patience = 3). Details are provided in Table 2 and illustrated in Figure 6.

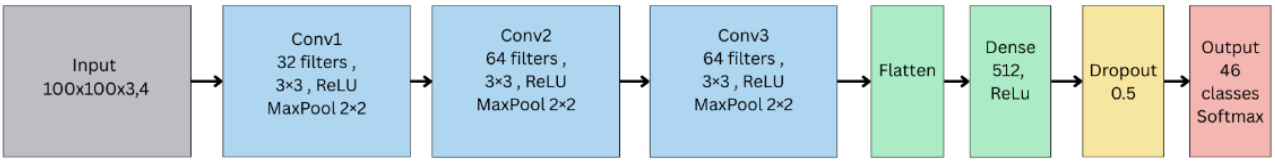


Figure 6. Structure and parameters of the convolutional neural network.

Table 2. Details of the convolutional neural network model.

Layer (Type)	Output	# of Parameters
Input	(100, 100, 3)	-
Conv2D (filters=32, kernel_size=(3,3), padding='same',activation='relu')	(98, 98, 32)	896
MaxPooling2D (pool_size=(2,2))	(49, 49, 32)	0
Conv2D (filters=64, kernel_size=(3,3), padding='same', activation='relu')	(47, 47, 64)	18,496
MaxPooling2D (pool_size=(2,2))	(23, 23, 64)	0
Conv2D (filters=128, kernel_size=(3,3), padding='same', activation='relu')	(21, 21, 128)	73,856
MaxPooling2D (pool_size=(2,2))	(10, 10, 128)	0
Flatten	12,800	0
Dense (activation='relu')	512	6,554,112
Dropout (rate=0.5)	512	0
Dense (activation='softmax')	46	23,598

3.4 Model Evaluation and Color Space Selection

The evaluation of color space performance and the selection of the optimal color space in this study comprised the following steps:

3.4.1 Train and test a separate CNN model for each of the eight color spaces using K-Fold Cross Validation (K = 5), recording key metrics including validation accuracy, validation loss, and training time for each color space.

3.4.2 Normalize the recorded metrics using Min–Max normalization to scale all values to the range of 0–1, enabling direct comparison.

3.4.3 Calculate the weighted sum score (Weighted Sum Model: WSM), as defined in Equation (1), by assigning weights to the metrics—accuracy = 0.5, loss = 0.3, and training time = 0.2—multiplying each normalized value by its corresponding weight, and summing the results to obtain a total score for each color space.

$$S_i = \sum_{j=1}^{n} w_j \times x_{ij} \quad (1)$$

where S_i is the weighted sum score for the i-th alternative, w_j is the weight assigned to the j-th criterion, x_{ij} is the normalized value of the i-th alternative for the j-th criterion, and n is the total number of criteria.

The weighting scheme was designed to reflect practical deployment priorities. Classification accuracy was assigned the highest weight (0.5) due to its direct impact on detection reliability. Validation loss (0.3) reflects model stability and convergence behavior, while training time (0.2) represents computational efficiency, which is important for future scalability but secondary to predictive performance.

3.4.4 Select the optimal color space by ranking all color spaces based on their WSM scores and choosing the one with the highest score.

3.4.5 Test the model trained on the selected color space using a testing set that was not included in the training process. Evaluate the results using a confusion matrix, which includes true positives (TP), false positives (FP), true negatives (TN), and false negatives (FN), along with the metrics accuracy, precision, recall, and F1-score, as illustrated in Figure 7 and defined in Equation (2) - (5) [19], to confirm stability and practical applicability, as defined in the following equations.

$$Accuracy = \frac{TP+TN}{TP+TN+FP+FN} \quad (2)$$

$$Precision = \frac{TP}{TP+FP} \tag{3}$$

$$Recall = \frac{TP}{TP+FN} \tag{4}$$

$$F1\text{-}score = \frac{2\times Precision\times Recall}{Precision+Recall} \tag{5}$$

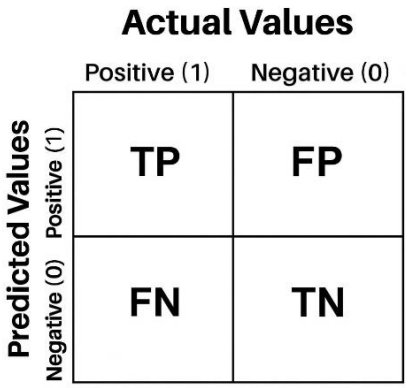


Figure 7. Confusion matrix and equations for evaluating model performance.

4. Results

4.1 Model Performance Evaluation

The CNN models were trained on eight different color spaces, and the HSVA color space achieved the best results, with the highest average accuracy (99.65%), the lowest loss (0.01382), and a training time of 1,606 seconds. This demonstrates a balance between classification accuracy and computational efficiency. The HSV and CIE LAB color spaces ranked second and third, respectively, while GrayscaleA recorded the lowest performance across both accuracy and loss. Results of average accuracy, loss, and training time for each color space are provided in Table 3. The low standard deviation across folds indicates stable model performance and minimal sensitivity to data partitioning.

Table 3. Results of average accuracy, loss, and training time for each color space.

Color Space	Validation Accuracy	Validation Loss	Training Time (s)
HSVA	**99.65 ± 0.25%**	**0.01382**	1606
HSV	99.32 ± 0.67%	0.02740	1318
CIE LABA	98.71 ± 1.11%	0.05510	1822
CIE LAB	99.43 ± 0.25%	0.01992	2090
RGBA	98.61 ± 1.24%	0.02554	1661
RGB	97.62 ± 1.10%	0.04800	**1176**
Grayscale	98.56 ± 0.89%	0.07150	1840
GrayscaleA	98.16 ± 1.40%	0.05210	2039

4.2 Weighted Sum Model (WSM) Analysis

By combining the normalized scores of accuracy, loss, and training time, HSVA achieved the highest weighted score (0.8819), followed by HSV (0.8662) and CIE LABA (0.8309). This confirms HSVA's balanced performance across all evaluation metrics. The normalized metrics and WSM analysis for each color space are provided in Table 4.

Table 4. Results of normalized metrics for each color space.

Color Space	Normalized Accuracy	Normalized Loss	Normalized Time	WSM
HSVA	1	0.8067	0.2316	**0.8819**
HSV	0.9967	0.6168	0.3694	0.8662
CIE LABA	0.9906	0.2294	0.1282	0.8309
CIE LAB	0.9978	0.7214	0	0.7430
RGBA	0.9896	0.6428	0.2053	0.7434
RGB	0.9796	0.3287	0.4373	0.7452
Grayscale	0.9891	0	0.1196	0.6155
GrayscaleA	0.985	0.2713	0.0244	0.4959

4.3 Performance Evaluation of the HSVA-based CNN Model on the Test Image Dataset

The HSVA-based CNN model was tested on 920 images (20 per class) that were not used during training. The model achieved accuracy, precision, recall, and F1-score values of 0.99. Errors occurred only minimally in classes with similar colors, as shown in the confusion matrix in Figure 8. Misclassifications mainly occur between adjacent concentration levels with similar color intensity.

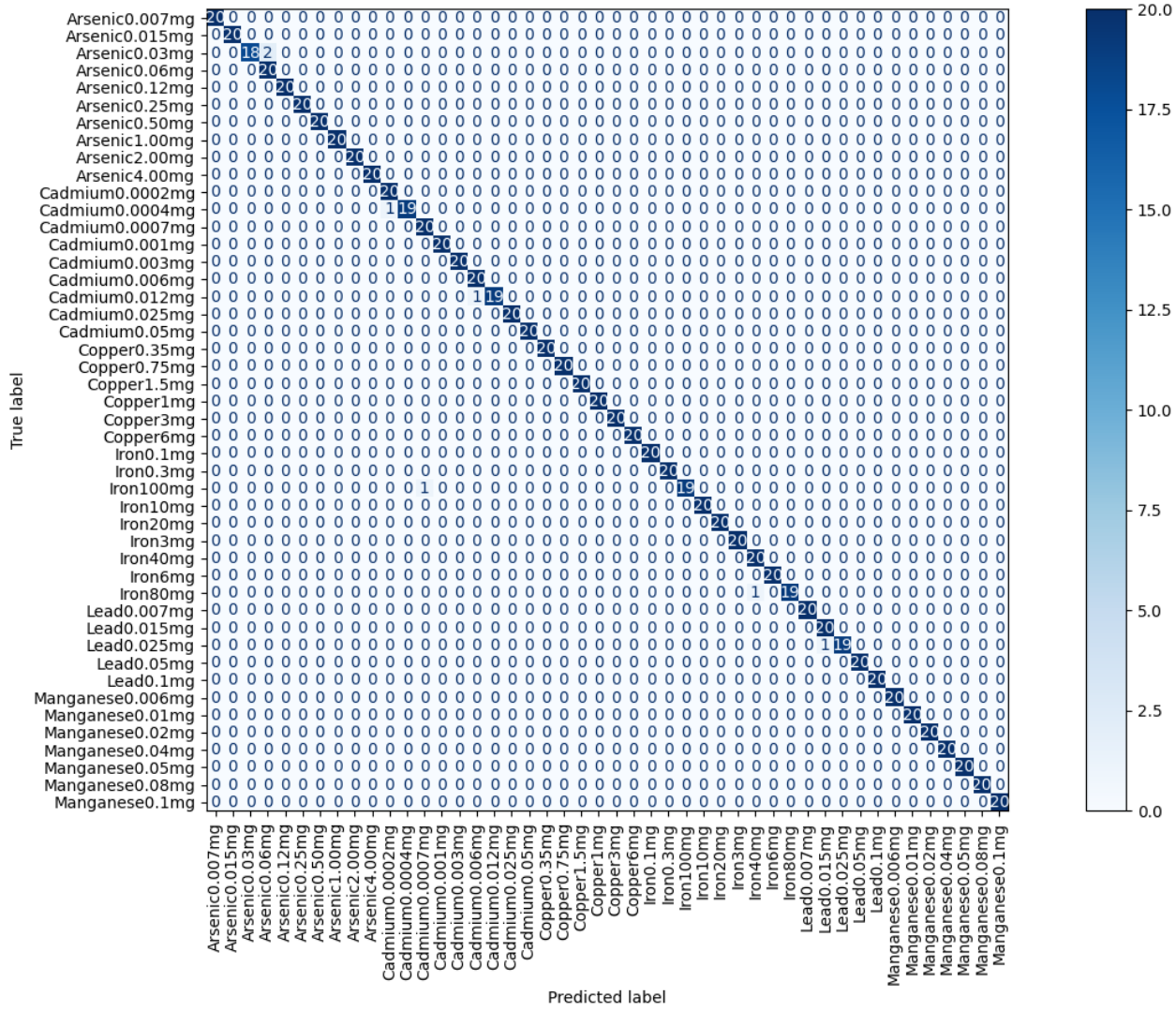


Figure 8. Confusion matrix of the HSVA-based CNN model on the test image dataset.

4.4 Key Findings

HSVA delivered the highest classification accuracy and demonstrated a balanced trade-off between accuracy, loss, and training time. Real-world testing confirmed the model's applicability and robustness in practical scenarios. Including the alpha channel in HSVA enabled the model to focus solely on the chemical reaction area, reducing background noise and improving classification accuracy.

5. Discussion

The results indicate that the HSVA color space achieved the highest performance in terms of accuracy, loss, and training time compared to other color spaces. Preserving the alpha channel enabled the model to focus solely on the chemical reaction area, reducing background noise and improving classification accuracy. This finding is consistent with Taithong *et al.* [5] and Xian *et al*. [12], who reported that using color spaces with fine color differentiation, combined with region-of-interest (ROI) masking, significantly improves CNN performance. Moreover, the application of data augmentation techniques—such as rotation, flipping, brightness and contrast adjustment, and mix-up augmentation—played a crucial role in reducing overfitting and improving the model's ability to process diverse real-world images. This observation aligns with Haikal *et al*. [9] and Liu [10], who emphasized that increasing the diversity of training data enhances model generalization. However, this study has certain limitations. The image dataset was collected under fixed lighting and camera angles, which may not fully represent all real-world scenarios. Expanding the experiments to include varying lighting conditions and image-acquisition settings could further improve the model's robustness and applicability in practical environments.

6. Conclusions

This study successfully achieved its objectives: developing a CNN model for classifying and analyzing heavy metal concentrations from microplate images; comparing eight color spaces; and selecting the optimal color space using the WSM approach. The HSVA color space was identified as the best performer, offering a balanced trade-off among accuracy, loss, and training time. Testing with real-world images confirmed the model's stability and practical potential. The proposed HSVA-based CNN framework can be directly extended to smartphone-assisted water quality monitoring, on-site screening in rural communities, and rapid preliminary assessment before laboratory confirmation. With further validation under varying lighting conditions, the method has potential for integration into portable diagnostic platforms and decision-support systems for environmental health monitoring.

7. Acknowledgements

The authors would like to express their gratitude to Assoc. Prof. Dr. Suthicha Chunta for kindly providing the dataset used in this research, and to Assoc. Prof. Dr. Purim Jarujamrus for valuable suggestions and guidance throughout the course of this study.

Author Contributions: Conceptualization, N.D. and S.V.; methodology, N.D., A.P., and S.V.; software, A.P.; validation, N.D., A.P., and S.V.; formal analysis, N.D. and A.P.; investigation, N.D.; resources, N.D. and A.P.; data curation, A.P.; writing—original draft preparation, N.D.; writing—review and editing, N.D., A.P., and S.V.; visualization, A.P.; supervision, N.D. and S.V.; project administration, N.D. All authors have read and agreed to the published version of the manuscript.

Funding: This research received no external funding.

Conflicts of Interest: The authors declare no conflict of interest.

References

[1] Yang, Y.; Li, Y.; Wang, X.; Li, J.; Chen, W. The Gut Microbiota and Chronic Inflammation Induced by Heavy Metals: A Review. *Ecotoxicol. Environ. Saf.* **2023**, *254*, 114720. https://doi.org/10.1016/j.ecoenv.2023.114720

[2] Jaishankar, M.; Tseten, T.; Anbalagan, N.; Mathew, B. B.; Beeregowda, K. N. Toxicity, Mechanism and Health Effects of Some Heavy Metals. *Interdiscip. Toxicol.* **2014**, *7*(2), 60–72. https://doi.org/10.2478/intox-2014-0009

[3] Bansod, B. K.; Kumar, T.; Thakur, R.; Rana, S.; Singh, I. A Review on Various Electrochemical Techniques for Heavy Metal Ions Detection with Different Sensing Platforms. *Microchem. J.* **2017**, *133*, 502–512. https://doi.org/10.1016/j.microc.2017.03.025

[4] Fakayode, S. O.; Walgama, C.; Fernand Narcisse, V. E.; Grant, C. Electrochemical and Colorimetric Nanosensors for Detection of Heavy Metal Ions: A Review. *Sensors* **2023**, *23*(22), 9080. https://doi.org/10.3390/s23229080

[5] Taithong, P.; Wichai, S.; Waranusast, R.; Riyamongkol, P. Image-Based Automatic Counting of *Bacillus cereus* Colonies Using Smartphone. *Int. J. Adv. Comput. Sci. Appl.* **2022**, *13*(2), 627–634. http://dx.doi.org/10.14569/IJACSA.2022.0130274

[6] Chunta, S.; Phongthai, S.; Jarujamrus, P. Simple Colorimetric Assay Using Pectin Hydrogel Reagent Coupled with Camera-Based Photometry for Trace Arsenic Determination. *Anal. Bioanal. Chem.* **2023**, *415*, 4603–4614. https://doi.org/10.1007/s00216-023-04762-z

[7] Ahmad, N.; Singh, S.; AlAjmi, M. F.; Hussain, A.; Raza, K. CropGCNN: Color Space-Based Crop Disease Classification Using Group Convolutional Neural Network. *PeerJ Comput. Sci.* **2024**, *10*, e2136. https://doi.org/10.7717/peerj-cs.2136

[8] Aydın Atasoy, N.; Kura, İ. Classification of X-ray and CT Images in Different Color Spaces Using Robust CNN. *J. Eng. Sci. Des.* **2024**, *12*(3), 505–516. https://doi.org/10.21923/jesd.1415150

[9] Haikal, A. L. A.; Yudistira, N.; Ridok, A. Comprehensive Mixed-Based Data Augmentation for Detection of Rice Leaf Disease in the Wild. *SSRN* **2024**. https://doi.org/10.2139/ssrn.4705403

[10] Liu, X. *Evaluating the Impact of Data Augmentation on Explainable AI in Medical Image Analysis*; Master's Thesis, Eindhoven University of Technology, Eindhoven, The Netherlands, 2024.

[11] Taha, M.; Safaa, M. Impact of Colour Space Transformation on Smoke Detection Accuracy Using ResNet50. *Infotech Spectrum: Iraqi J. Data Sci.* **2025**, *2*(1), 37–49.

[12] Xian, Z.; Huang, R.; Towey, D.; Yue, C. Convolutional Neural Network Image Classification Based on Different Color Spaces. *Tsinghua Sci. Technol.* **2025**, *30*(1), 402–417. https://doi.org/10.26599/TST.2024.9010001

[13] Satrya, G. B.; Ramatryana, I. N. A.; Shin, S. Y. Compressive Sensing of Medical Images Based on HSV Color Space. *Sensors* **2023**, *23*, 2616. https://doi.org/10.3390/s23052616.

[14] Frincu, R. M. Artificial Intelligence in Water Quality Monitoring: A Review of Water Quality Assessment Applications. *Water Qual. Res. J.* **2025**, *60*(1), 164–176. https://doi.org/10.2166/wqrj.2024.049

[15] Olawade, D. B.; Wada, O. Z.; Ige, A. O.; Egbewole, B. I.; Olojo, A.; Oladapo, B. I. Artificial Intelligence in Environmental Monitoring: Advancements, Challenges, and Future Directions. *Hyg. Environ. Health Adv.* **2024**, *12*, 100114. https://doi.org/10.1016/j.heha.2024.100114

[16] Budiharjo; Windarto, A. P.; Muhammad, A. Comparison of Weighted Sum Model and Multi Attribute Decision Making Weighted Product Methods in Selecting the Best Elementary School in Indonesia. *Int. J. Softw. Eng. Its Appl.* **2017**, *11*(4), 69–90. http://dx.doi.org/10.14257/ijseia.2017.11.4.06.

[17] Ouchra, H.; Belangour, A. Object Detection Approaches in Images: A Weighted Scoring Model Based Comparative Study. *Int. J. Adv. Comput. Sci. Appl.* **2021**, *12*(8), 268–275. http://dx.doi.org/10.14569/IJACSA.2021.0120831

[18] Chunta, S. *Development of the Hydrogel-Based Reagent Field Test Kit for Screening Heavy Metal in Water Coupled with Smartphone-Based Colorimetric Analyzer*; Research Report, Agricultural Research Development Agency (Public Organization): Bangkok, Thailand, 2021.

[19] Nasritha, K.; Kerdprasop, K.; Kerdprasop, N. Comparison of Sampling Techniques for Imbalanced Data Classification. *J. Appl. Inform. Technol.* **2018**, *1*(1), 20–37. https://doi.org/10.14456/jait.2018.2

ASEAN
Journal of Scientific and Technological Reports
Online ISSN:2773-8752

Research article

Effects of Cassava Tails and Stalk and Superabsorbent Polymer on Soil Properties, Growth, and Yield of Cassava in Sandy Loam and Clay Loam Soils

Prinda Kongyinghan[1], Sodchol Wonprasaid[2], Wimonsiri Pingthaisong[3], and Thitiporn Machikowa[4*]

[1] School of Crop Production Technology, Suranaree University of Technology, Nakhon Ratchasima, 30000, Thailand
[*] Correspondence: machiko@sut.ac.th

Citation:
Kongyinghan, P.; Wonprasaid, S.; Machikowa, T. Effects of soil amendment and superabsorbent polymer on soil properties, growth, and yield of cassava. *ASEAN J. Sci. Tech. Report.* **2026**, *29*(4), e260726. https://doi.org/10.55164/ajstr.v29i4.260726.

Article history:
Received: August 6, 2025
Revised: March 9, 2026
Accepted: March 11, 2026
Available online: March 24, 2026

Publisher's Note:
This article is published and distributed under the terms of the Thaksin University.

Abstract: The objective of this study was to evaluate the effects of cassava tails and stalk (CTS) and superabsorbent polymer (SAP) on soil properties, as well as on cassava growth and yield in sandy loam and clay loam soils. The research employed a randomized complete block design with three treatments, including unamended soil (control, T1) , 8,000 kg/rai of fresh weight CTS (T2), and 0.25% (w/w) of SAP (T3) with four replications. In sandy loam soil, the SAP application showed a significant decrease in soil bulk density (BD) and increase in soil particle density (PD) and soil porosity (PO). Both soil amendment treatments increased organic matter (OM) (0.58%) compared with the control (0.51%). The SAP application showed the highest content of P and K (9 and 69 ppm, respectively), while CTS showed the highest content of Ca (411 ppm). In clay loam soil , the SAP application resulted in the lowest BD (1.36 g/cm^3), while the CTS application resulted in the highest soil PO (50.11%). Both treatments increased OM (~1.00%) and the content of Ca and Mg (~2,000 ppm and ~220 ppm, respectively) compared with the control (0.73%, 1,559 ppm, and 182 ppm, respectively). The SAP application showed a better leaf water potential and stomatal conductance, which led to the highest plant height, leaf area, and stem diameter of cassava. In addition, the SAP application resulted in the highest cassava yield (7.83 and 6.20 tons/rai) in both soils and starch content (21.44%) in sandy loam soil. Therefore, both SAP and CTS applications improved soil properties and promoted cassava growth, resulting in higher yields; however, their effectiveness was strongly dependent on soil texture.

Keywords: *Manihot esculenta*; organic amendments; synthetic polymers; bulk density

1. Introduction

Cassava (*Manihot esculenta* (L.) Crantz) is an important economic crop in Thailand. In 2024, Thailand exported cassava products valued at 3,133.4 million USD (110,276 million baht) to major markets such as China, Japan, Indonesia, Taiwan, and Malaysia [1]. However, cassava production still faces limitations related to soil properties and moisture, especially in the Northeast, a major cassava-producing region of the country. The soils in this area are mostly coarse-textured, such as sandy soil, sandy loam, and loamy sand, with poor soil structure, high water permeability, and low water retention capacity [2]. These problems are exacerbated by climate change, continuous monoculture, herbicide use, and improper soil management, leading to soil degradation and reduced fertility, which in turn affect cassava production [3]. Physical and chemical soil

properties such as soil porosity (PO), bulk density (BD), organic matter content (OM), and nutrient fertility directly influence cassava growth and yield. It has been found that OM, phosphorus (P), and calcium (Ca) are key factors determining the variability of cassava tuber yield.

The application of organic soil amendments, such as cow manure, chicken manure, cassava pulp, and cassava processing plant residues, has been reported to significantly increase cassava root yield and starch content [4-5]. When applied at appropriate rates in combination with chemical fertilizers, these amendments result in high cassava yields. They also increase OM, P, K, Ca, and Mg, contributing to long-term soil fertility and nutrient balance [6]. Beyond improving soil fertility, these amendments enhance soil structure and physical properties, including PO, BD, aggregate stability, and water holding capacity [7-9]. Research showed that combining a sugarcane filter with biochar enhances PO and pore size distribution. It reduces large pores in sandy soils while increasing small pores, thereby reducing water loss [10]. Integrating green manure, chicken manure, and biofertilizers with chemical fertilizers promotes plant growth and yield. Green manure increases soil organic matter, pore space, and N and P levels compared with unfertilized conditions [11]. Cassava tails and stalk (CTS) are an agricultural by-product produced during the initial stage of cassava starch processing. It contains soil particles, root fragments, and other impurities removed through mechanical shaking [12]. Approximately 100-200 kg of CTS is generated per ton of fresh cassava processed [13]. Previous studies have shown that the combined application of CTS and chicken manure increases plant nutrient accumulation in plant tissues and enhances fresh root yield [14]. Moreover, CTS combined with bentonite at a rate of 25+5 tons/ha significantly increased fresh tuber yield and starch content compared with untreated soil [14]. Superabsorbent polymers (SAP) can absorb water up to approximately 1,000 times their own weight and gradually release it, thereby maintaining soil moisture and supporting crop growth under water-limited conditions [15]. Their swelling-shrinking behavior also improves soil pore distribution and aggregate stability [16], promoting root development and more efficient water uptake. This is essential for cassava growth, as it allows for better root development and water uptake. In addition to SAP, soil amendments play a crucial role in enhancing soil properties and improving cassava yield. The application of these amendments can increase production efficiency and ensure long-term food security. Effective soil management practices, including the management of macro and micronutrients, as well as efficient water use, are crucial for enhancing cassava productivity. By evaluating the effects of soil amendments and SAP on soil properties, cassava growth, and yield, sustainable soil management strategies can be identified. This can help improve cassava production, ensuring food security and reducing the environmental impact of farming practices. Overall, the use of SAP and soil amendments has the potential to significantly improve cassava yield, particularly in regions with limited water availability. The objective of this study was to evaluate the effects of CTS and SAP on soil properties, as well as on cassava growth and yield in sandy loam and clay loam soils.

2. Materials and Methods

The study on the effects of CTS and SAP on soil properties, cassava growth, and yield used the Rayong 72 cassava variety. The CTS was sourced from a cassava starch manufacturing plant in Nakhonratchasima, which still contained moisture, and SAP was obtained from a commercial supplier in Thailand. The experiment took place from June 2024 to May 2025 at Suranaree University of Technology in Nakhon Ratchasima, Thailand.

2.1 Experimental design

The experiment was conducted on two soil textures: sandy loam and clay loam. The research employed a randomized complete block design with three treatments: unamended soil (control, T1), soil amended with 8,000 kg/rai of fresh weight CTS (T2), and soil amended with 0.25% (w/w) SAP (T3), across four replications. Each sampling plot size measured 60 m^2 with a spacing of 1.2 x 0.8 m (Figure 1). CTS was broadcast over the field and incorporated into the soil, whereas SAP was applied along the ridge line at a depth of 30 cm.

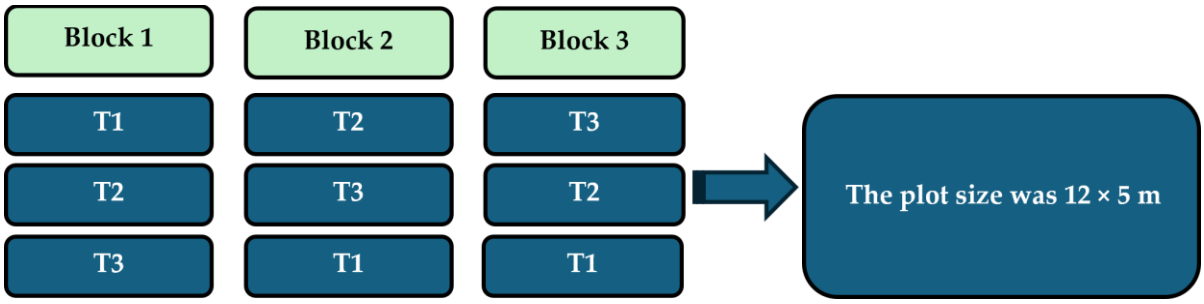


Figure 1. Experimental layouts of the study.

2.2 Preparation, cultivation, and management of cassava

The cassava planting area was prepared using a moldboard plow, followed by disk plow tillage and ridge creation. The stems of Rayong 72 cassava were cut into stakes, soaked in thiamethoxam to prevent mealybugs, and planted along the ridges. Fertilizer application was based on soil analysis results, with N-P2O5-K2O fertilizers at a 20-10-24 formulation at 48 kg/rai for sandy loam soil and a 12-10-8 formulation at 26 kg/rai for clay loam soil, applied at 1 and 3 months after planting (MAP). Weed control included the application of a pre-emergent herbicide (alachlor 48% w/v EC at 500 mL/80 L of water), followed by manual weeding at 3 MAP. Cassava was grown under rainfed conditions throughout the experiment.

2.3 Data collection and analysis

2.3.1 Soil properties: The soil samples collected to measure soil physical properties, including soil bulk density (BD), were determined using the core method by dividing the mass of oven-dried soil by its total volume, typically expressed in g/cm^3. The equation is as follows [17]:

$$BD = Mass\ of\ dry\ soil / The\ total\ soil\ volume \quad (1)$$

Soil particle density (PD) is defined as mass per unit of solid soil components, which were divided into OM and mineral substance, typically expressed in g/cm^3. The equation is as follows [18]:

$$PD = Mass\ of\ solid\ soil\ components / Volume\ of\ solid\ soil\ components \quad (2)$$

Soil porosity (PO) can be calculated from BD and PD values, typically expressed as a percentage. The equation is as follows [19]:

$$PO = [1 - (BD/PD)]\ x\ 100 \quad (3)$$

Soil chemical properties were determined from samples collected at 0-30 cm depth, which were air-dried and passed through a 2-mm sieve before analysis. Soil pH was determined electrometrically in a 1:1 (soil: H_2O) suspension using a pH meter (Model Eutech instrument, PC700). Electrical conductivity (EC) was determined by weighing soil and water at a 1:5 ratio and measuring it with an Electrical Conductivity Meter (Model Eutech instrument, PC700). Soil organic matter was determined in air-dried soil samples, after screening through a 0.5 mm mesh sieve, by the wet combustion method, employing potassium dichromate ($K_2Cr_2O_7$) as the oxidizing agent [20]. Available phosphorus (P) was extracted with Bray-2 solution [21] and determined by the color developing by the molybdenum blue method using a spectrophotometer (Model Thermo Fisher Scientific, Genesys) at an absorbance of 820 nm. Soil exchangeable basic cations (K, Ca, and Mg) were extracted by ammonium saturation with the 1 M NH_4OAc extraction method at pH 7.0 [22]. The levels of K^+, Ca^{2+}, and Mg^{2+} were determined in the soil extract using an atomic absorption spectrophotometer (Model PinAAcle 900H). All measurements were conducted both before and after the experiment at 11 MAP.

The initial physical and chemical properties of the studied soils are summarized in Table 1. In sandy loam soil were characterized by a BD of 1.47 g/cm^3, PD of 2.79 g/cm^3, PO of 46.24% while soil chemical

properties was pH of 6.43, EC of 0.02 dS/m, and OM of 0.48%, with available P, exchangable K, Ca, and Mg content of 6, 23, 23, and 46 ppm, respectively. For clay loam soil, the initial physical properties were BD of 1.52 g/cm^3, PD of 2.69 g/cm^3, and PO of 43.29%. The soil chemical properties of the clay loam soil were pH of 7.27, EC of 0.07 dS/m, an OM content of 1.55%, and available P, exchangeable K, Ca, and Mg contents of 5, 226, 1,613, and 226 ppm, respectively.

Table 1. Initial soil properties in sandy loam and clay loam soils.

Soil properties	Sandy loam	Clay loam
Bulk density (g/cm^3)	1.47	1.52
Particle density (g/cm^3)	2.79	2.69
Soil porosity (%)	46.24	43.29
pH	6.43	6.81
EC (dS/m)	0.02	0.07
OM (%)	0.48	1.55
P (ppm)	6	5
K (ppm)	23	226
Ca (ppm)	23	1,613
Mg (ppm)	46	226

2.3.2 ***Cassava physiology:*** Predawn leaf water potential (LWP) was measured using a pressure bomb from 4:00 to 5:00 a.m., at 3, 4, 5, 6, and 7 MAP [23]. Stomatal conductance (g_s) was measured using the brand LICOR, model LI-6800P, from 8:30 to 11:00 a.m., at 3, 4, 5, and 6 MAP [24]. Five plants per replication were randomly selected, and the fifth fully expanded leaf from the apex was measured. Leaf Greenness (SPAD) was measured using a Chlorophyll Meter SPAD-502 Plus from 8:30 to 12:00 p.m. on the third fully expanded leaf. Three measurement points per leaf were recorded and averaged to obtain a final value per plant. Measurements were conducted at 3, 5, and 7 MAP [25], with five plants randomly sampled per replication.

2.3.3 ***Cassava growth:*** plant height, measured from the base of the stem to the apex using ten randomly selected plants per replication. Stem diameter was measured at the midpoint of the main stem from the same number of sampled plants. Leaf area was determined by randomly selecting ten plants per replication, harvesting all leaves from each plant, and measuring total leaf area using a Li-Cor leaf area meter [26]. All parameters were measured at 3, 5, and 7 MAP.

2.3.4 ***Tuber weight and starch content:*** At 11 MAP, cassava yield was determined by harvesting a random sample of 60 m^2 per treatment. Fresh tuber weight from each area was recorded and averaged, and the mean value was converted to tons per rai. Starch content (%) was measured using a Reimann scale balance [27], with samples collected randomly from 10 plants per replication.

2.3.5 ***Climatic recording*****:** Climate data collected from the meteorological station at Suranaree University of Technology provided monthly patterns of rainfall, temperature, and relative humidity during the experiment period. Daily records of temperature (°C), rainfall (mm), and relative humidity (%RH) were collected throughout the experiment. From June 2024 to May 2025, daily temperatures ranged from 21.10 to 29.9 °C, while relative humidity ranged from 57.6% to 81.6% (Figure 2). The highest rainfall occurred between June and October 2024, followed by a decline from November 2024 to March 2025. This data is crucial for interpreting variations in soil moisture and their potential effects on cassava growth and yield.

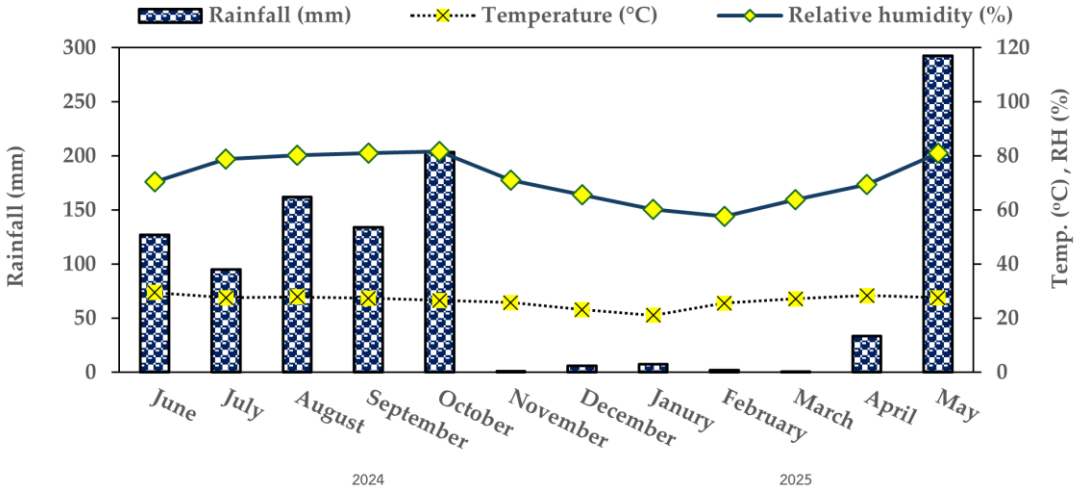


Figure 2. Total monthly rainfall, temperature, and relative humidity in field sites from June 2024 to May 2025

2.3.6 Statistical analysis

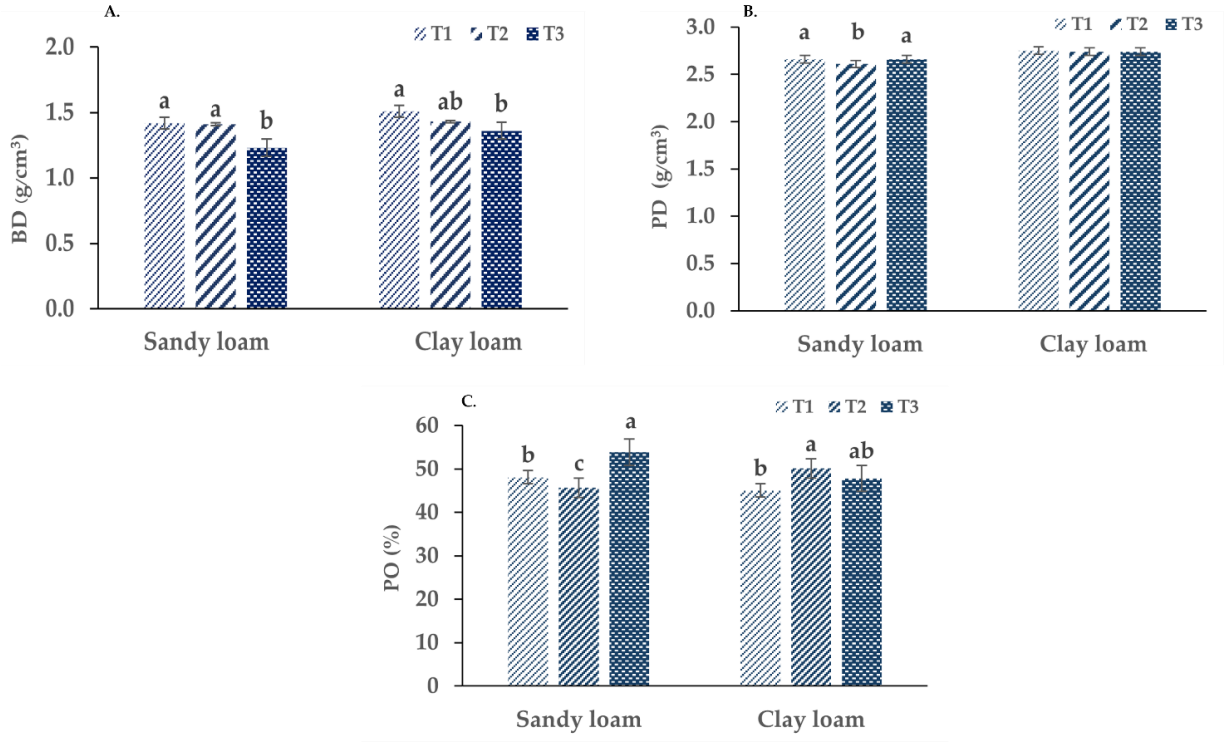
The experimental results were analysed using Analysis of Variance (ANOVA) by SPSS v.16, and mean comparisons among treatments were performed using Duncan's New Multiple Range Test (DMRT) at a 95% confidence level.

3. Results and Discussion

3.1. Soil properties

3.1.1. Soil physical properties

The soil's physical properties were affected by the treatments, as shown in Figure 3. At 11 MAP, in sandy loam soil, the SAP application resulted in the lowest BD and PD values (1.31 g/cm³ and 2.61 g/cm³, respectively) and the highest PO value of 53.85%. In clay loam soil, the SAP application yielded the lowest BD value of 1.43 g/cm³, while the CTS application yielded the highest PO value of 47.86%. The results of the SAP application, with numerous studies showing that it reduced soil BD and improved PO. For example, Cao et al. [25] found that the SAP application (approximately 45 kg/ha) significantly enhanced soil-water retention, increased moisture content by up to 33.5%, and improved soil structure while reducing BD. Similarly, Zheng et al. [26] conducted a meta-analysis of 1,504 paired data points from 310 papers published before July 2022 to evaluate the effects of SAP on crop yield and water productivity, accounting for SAP attributes, initial soil properties, and experimental conditions. They found that the SAP application significantly increased water stable aggregates (WSA) (18.9%) and PO (18.01%). In addition, previous studies reported that SAP could improve soil PO and soil aggregates by affecting the degree of agglutination with soil particles and the process of shrinking and swelling [27-28]. Incorporating CTS into soil as an organic amendment significantly improves physical properties, primarily by forming stable aggregates that enhance soil structure, buffer the soil, improve aggregate stability, increase the population of soil microorganisms, and enhance water retention capacity [29-32]. These organic amendments increase OM, leading to reduced BD and improved water-holding capacity. Similarly, Cassava peels applied at rates up to 25 tons/ha significantly enhance Ultisol fertility by improving soil physical properties, reducing BD (from 0.92 to 0.79 g/cm³), and increasing moisture content to 23.49% [32]. These changes suggest that CTS enhances soil aggregation and pore development, thereby improving soil aeration, water retention, and root proliferation, particularly in structurally constrained sandy loam and clay loam soils. Consistent with these findings, CTS has been reported to increase soil pore space, enhance aeration, and improve moisture storage [9, 28].



T1 = unamended soil (control), T2 = cassava tails and stalk (CTS), and T3 = superabsorbent polymer (SAP)

Figure 3. Effects of soil amendments on soil properties at 11 months after planting (MAP) in sandy loam and clay loam soils: (A) soil bulk density (BD), (B) soil particle density (PD), and (C) soil porosity (PO). The different letters indicate a significant difference at the 95% confidence level using Duncan's New Multiple Range Test (DMRT). Vertical bars represent standard error of the means (n = 4).

3.1.2 Soil chemical properties

The soil's chemical properties were affected by the treatments, as shown in Table 2. At 11 MAP, in sandy loam soil, both treatments increased OM (0.58%) as compared with the control (0.51%). The SAP application showed the highest content of P and K (9 and 69 ppm, respectively), while CTS showed the highest content of Ca (411 ppm). In clay loam soil, both treatments increased OM (~ 1.00%) as compared with the control (0.73%). The SAP application showed the highest Ca content (2,828 ppm), and the CTS application showed the highest Mg content in soil (229 ppm), compared with the control (1,559 ppm and 182 ppm, respectively). The high OM accumulation changed after the application of soil amendments, which may be attributed to increased WSA, improving soil structure and enhancing its stability, thus facilitating the physical protection of OM [28,33-34]. Previous studies reported that SAP has the potential to help superfluous SOM aggregate in the soil layer, thereby preventing it from being immediately decomposed or lost [33, 35]. In addition, SAP can promote the metabolism of soil microorganisms by increasing their populations [36]. It was found that OM, microbial biomass, and soil microorganisms were improved through applying SAP [28]. Both soil amendments in sandy loam increased the availability of P, K, and Ca, supporting better nutrient retention and reduced leaching [34]. Soils with more large macroaggregates have a more stable structure and better nutrient storage under SAP application conditions [28, 37].

Table 2. Soil properties and the effect of soil amendments on soil properties in sandy loam and clay loam soils.

Parameter	pH	EC (dS/m)	OM (%)	P (ppm)	K (ppm)	Ca (ppm)	Mg (ppm)
Sandy loam							
T1	6.51	0.05	0.51	8	53	331	143
T2	6.43	0.06	0.58	7	63	411	122
T3	6.50	0.05	0.58	9	69	268	93
F-test	ns	ns	ns	ns	ns	ns	ns
Clay loam							
T1	6.80	0.10	0.73	117	207	1,559	182
T2	6.73	0.10	1.02	82	97	1,953	229
T3	6.78	0.11	1.00	32	135	2,828	214
F-test	ns	ns	ns	ns	ns	ns	ns

T1 = unamended soil (control), T2 = cassava tails and stalk (CTS), and T3 = superabsorbent polymer (SAP)

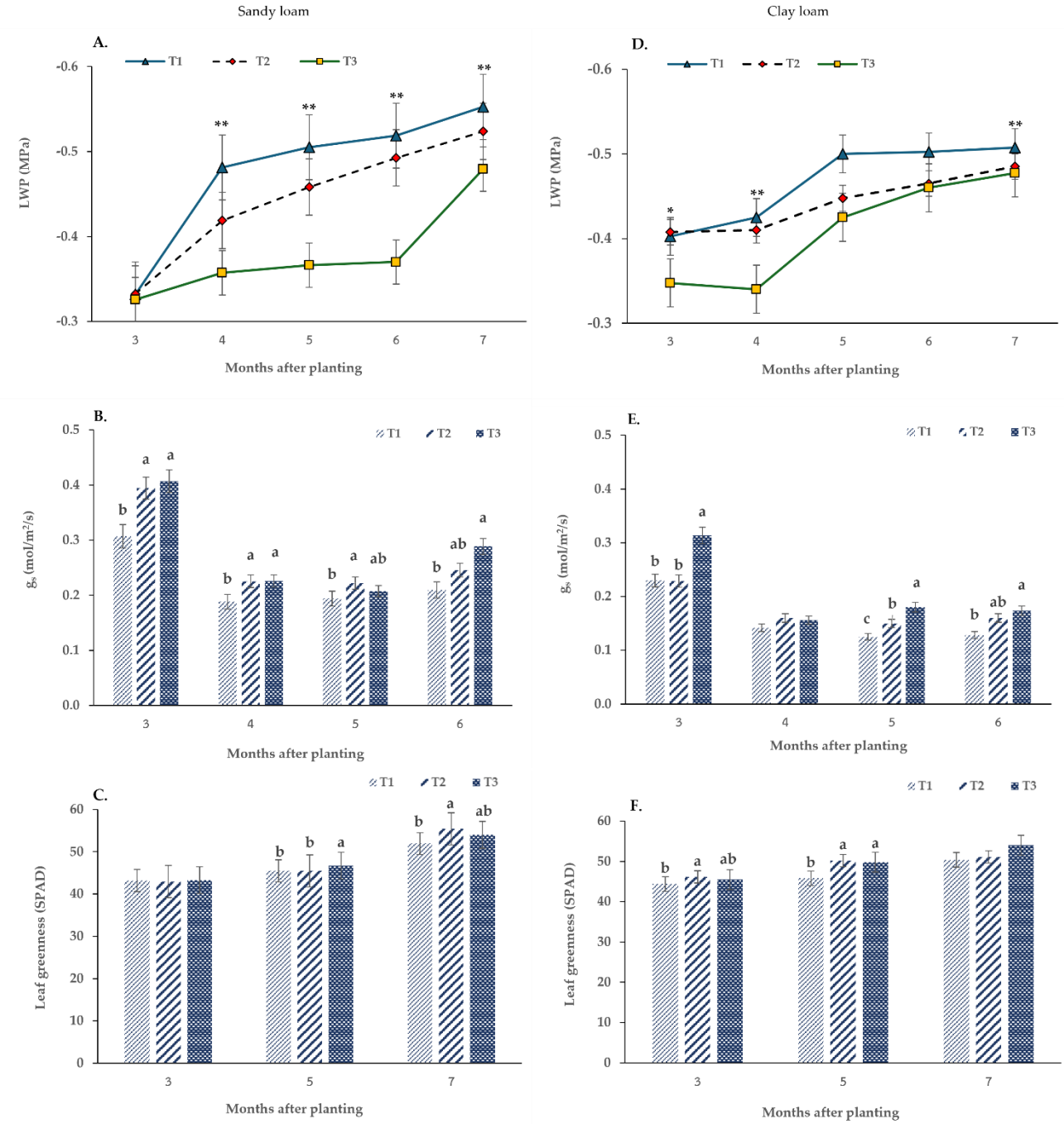
3.2 Cassava physiology

3.2.1 Sandy loam soil

The LWP, g_s, and leaf greenness of cassava in sandy loam soil were significantly affected by both treatments (Figure 4A-C). During 4-7 MAP, all treatments exhibited increased LWP, while SAP resulted in the lowest negative value of LWP followed by CTS, indicating reduced plant water stress compared with the control (Figure. 4A). The main growth stages of cassava (3-6 MAP), both SAP and CTS applications had higher g_s than the control, indicating better stomatal conductance as compared with the control (Figure. 4B). At 5 and 7 MAP, SAP application yielded the highest leaf greenness (Figure. 4C). These results indicated that both soil amendment applications enhanced leaf chlorophyll status as compared with the control.

3.2.2 Clay loam soil

The LWP, g_s, and leaf greenness were affected by the treatments in clay loam soil, as shown in Figure 4D-F. During 3-4 MAP, both SAP and CTS applications showed a slight decrease in LWP. During 4-7 MAP, SAP application showed the lowest negative value of LWP followed by CTS, indicating that lower plant stress as compared with the control (Figure. 4D). At 3, 5, 6 MAP, SAP application showed the highest g_s indicating better stomatal conductance as compared with other treatments (Figure. 4E). During 3-5 MAP, both SAP and CTS applications had higher leaf greenness than the control indicating that both soil amendment applications had higher chlorophyll content as compared with the control (Figure. 4F). The SAP application can enhance soil water retention following irrigation or rainfall and reduce irrigation frequency, thereby lowering overall water use and increasing crop water productivity [28,38-39]. Moreover, SAP has been reported to significantly decrease evapotranspiration by reducing soil evaporation losses [28, 40]. Therefore, our results confirmed that water use during the early growth period after SAP application was significantly lower than that in the control, which was attributed to reduced soil water evaporation. In addition, SAP improves soil water availability and enables plants to sustain physiological activity, including stomatal function and photosynthesis [40]. Sabeliwe and Witbooi [41] reported that SAP increases available moisture in the root zone, reduces water stress, and indirectly supports gas exchange traits such as g_s and photosynthesis. These findings support our results that both soil amendments improved soil moisture status, thereby reducing plant water stress and enhancing stomatal conductance and leaf chlorophyll content.



T1 = unamended soil (control), T2 = cassava tails and stalk (CTS), and T3 = superabsorbent polymer (SAP)

Figure 4. Dynamics of cassava physiology months after planting (MAP) under soil amendments in sandy loam and clay loam soils: sandy loam soil (A) leaf water potential (LWP), (B) stomatal conductance (g_s) and (C) leaf greenness (SPAD); clay loam soil (D) leaf water potential (LWP), (E) stomatal conductance (g_s) and (F) leaf greenness (SPAD). The different letters indicate a significant difference at the 95% confidence level using Duncan's New Multiple Range Test (DMRT). Vertical bars represent the standard error of the means (n = 10).

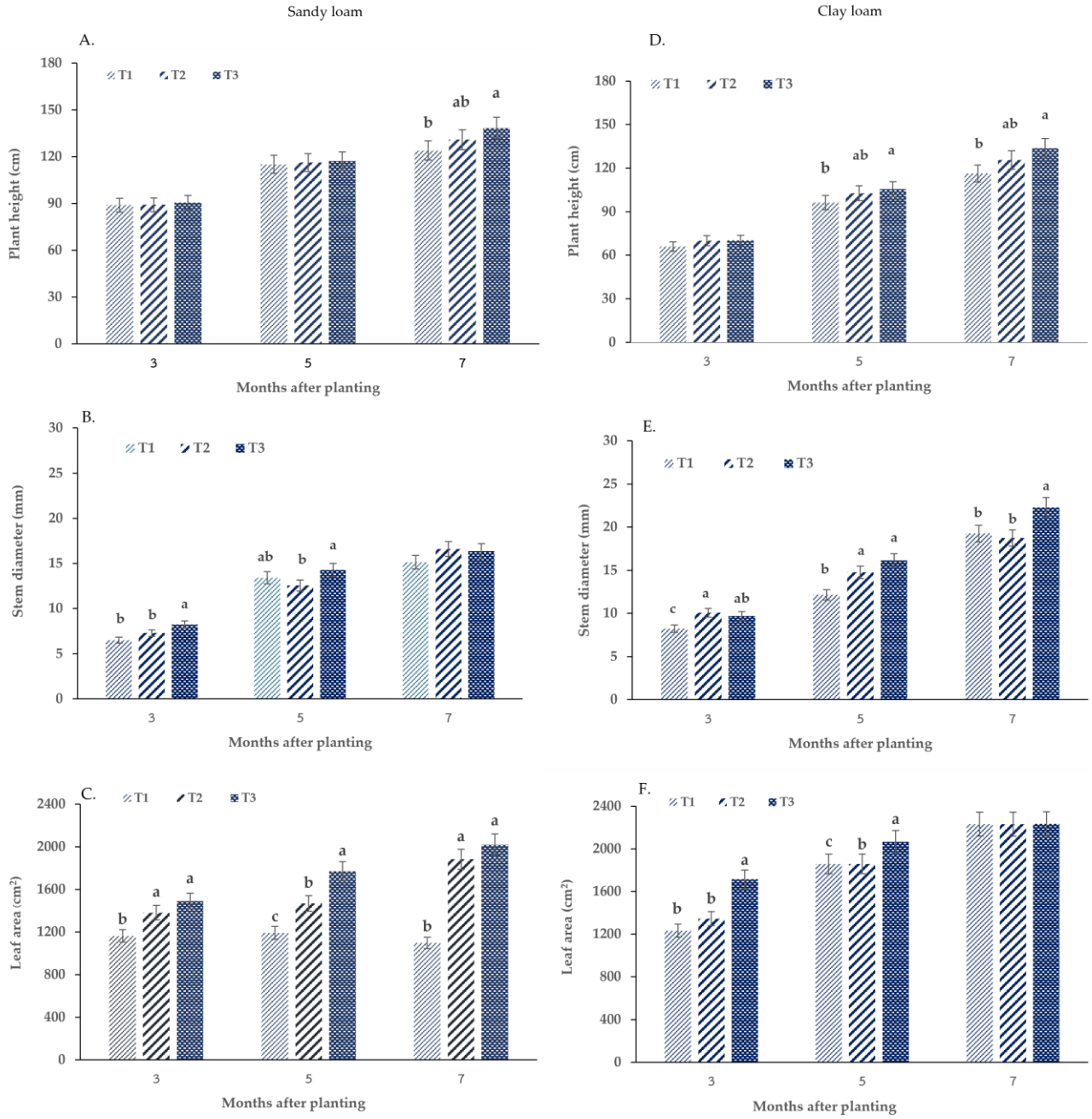
3.3 Cassava growth

3.3.1 Sandy loam soil

Plant height, stem diameter, and leaf area in sandy loam soil were affected by the treatments, as shown in Figure 5A-C. At 7 MAP, SAP produced the tallest plants (Figure 5A). During 3-5 MAP, SAP resulted in the greatest stem diameter (Figure 5B). Throughout the growth stages of cassava (during 3-7 MAP), both SAP and CTS applications exhibited higher leaf area than the control (Figure 5C).

3.3.2 Clay loam soil

The plant height, stem diameter, and leaf area in clay loam soil were affected by the treatments as shown in Figure 5D-F. At later growth stages (5-7 MAP), SAP produced the tallest plants (Figure 5D). At the beginning growth stages of cassava (3 MAP), CTS resulted in the greatest stem diameter, whereas at the intermediate growth stages (5 MAP), both SAP and CTS applications exhibited higher stem diameters than the control. At the late stage (7 MAP), SAP produced the greatest stem diameter (Figure 5E). During 5-7 MAP, SAP also had the largest leaf area (Figure 5F). Both CTS and SAP significantly enhanced cassava growth and played key roles in promoting plant development, particularly by increasing plant height, stem diameter, and leaf area. The CTS contained various plant nutrients and was gradually released during early growth stages [34, 41]. Moreover, the considerable amount of OM in the CTS additionally contributes to the activity of vesicular arbuscular mycorrhizae, which have been reported as important for cassava [34]. These findings align with those of Pereira et al. [42], who reported that OM enrichment improves cassava growth, especially in low-fertility soils. Soil amendments also improve soil structure, nutrient availability, and root-zone aeration, thereby stimulating leaf expansion, stem elongation, and root development [43]. Similarly, Ndunge et al. [44] demonstrated that the SAP application significantly enhanced plant growth and yield compared with the control. Their optimal treatment, 1 g SAP per kg of soil combined with a 5-day irrigation interval, increased plant height by 24.0%, leaf area by 11.7%, the number of mature leaves by 11.1%, and dry weight per plant by 85.9% in cowpea. SAP can also serve as a slow-release carrier for nutrients such as K and N, enabling a sustained nutrient supply over time. However, contrasting results were reported by Alotaibi et al. [45], who found that the SAP application, combined with a 50% reduction in irrigation, significantly reduced several growth and yield parameters, including leaf fresh weight, leaf area, total chlorophyll content, leaf water content, fresh weight per plant, and overall yield. This suggests that while SAP can enhance growth under moderate water deficit conditions, excessive reductions in irrigation may limit its effectiveness.



T1 = unamended soil (control), T2 = cassava tails and stalk (CTS), and T3 = superabsorbent polymer (SAP)

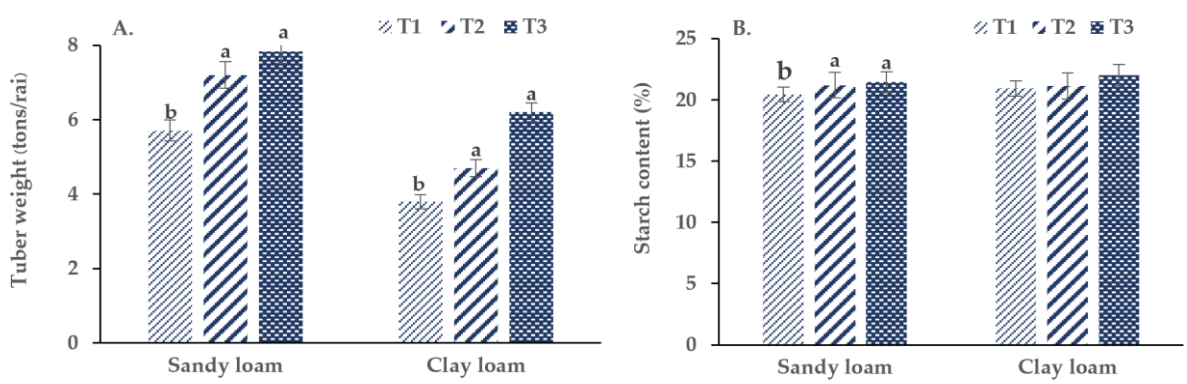
Figure 5. Dynamics of cassava growth under soil amendments in sandy loam and clay loam soils: sandy loam soil (A) plant height, (B) stem diameter, and (C) leaf area; clay loam soil (D) plant height, (E) stem diameter, and (F) leaf area. The different letters indicate a significant difference at the 95% confidence level using Duncan's New Multiple Range Test (DMRT). Vertical bars represent the standard error of the means (n = 10).

3.4 Tuber weight and starch content

Tuber weight was affected by the treatments, as shown in Figure 6A. In both soil textures, SAP and CTS applications produced significantly higher yields than the control. In sandy loam soil, SAP and CTS produced the highest tuber yields (7.83 and 7.20 tons/rai, respectively), corresponding to increases of 26.09-37.13% compared with the control (5.71 tons/rai). Similarly, in clay loam soil, SAP and CTS applications

produced the highest yields (6.20 and 4.71 tons/rai, respectively), meaning improvements of 23.29-62.30% over the control (3.82 tons/rai). Overall, these results indicated that soil amendments significantly enhanced cassava tuber production in both sandy loam and clay loam soils. Starch content was also affected by the treatments, as shown in Figure 6B. In sandy loam soil, both soil amendments increased starch content compared with the control. SAP yielded the highest starch content (21.44%), followed by CTS (21.20%), whereas the control exhibited the lowest (20.43%). These findings indicate that soil amendment application enhanced starch accumulation relative to unamended soil.

Across soil textures, SAP produced the greatest improvements in cassava yield and starch content, likely owing to its superior capacity to retain water and nutrients [46–47]. Previous studies have suggested that yield enhancement following SAP application is associated with increases in water-stable aggregates and soil OM [33, 37, 48]. By maintaining soil moisture in the root zone, SAP reduces plant water stress and supports crop development during dry periods. Moreover, SAP can extend the time required for soil to reach the permanent wilting point (PWP), thereby enabling crops to withstand prolonged drought. For example, the application of natural superabsorbent hydrogel at rates of 0.3–1.0% increased the time needed to reach PWP in loamy sand soils by more than threefold compared with untreated soil [48]. Moreover, SAP acts as a slow-release carrier for fertilizers due to its three-dimensional polymer network, which can absorb water several hundred times its own weight. As soil dries, water and dissolved nutrients are gradually released through diffusion-controlled processes, with release rates governed by polymer concentration and the volume of water stored within the matrix [49]. The CTS application also improved cassava productivity, particularly in coarse-textured soils, by increasing soil organic matter and major nutrient contents. Previous work has shown that CTS applied alone or in combination with bentonite substantially enhanced tuber yield and starch concentration. This finding was reported by Ketkhao et al. [34], who found that amending the soil with CTS at both rates (6.25 and 12.5 tons/ha, respectively) undoubtedly increased cassava yields in both growing seasons. The CTS application played a part in cassava yield improvement by providing secondary and micronutrients, in addition to improving the nutrient retention in soil, which in turn increased nutrient use efficiency, held plant nutrients against leaching, and retained soil moisture [34].



T1 = unamended soil (control), T2 = cassava tails and stalk (CTS), and T3 = superabsorbent polymer (SAP)

Figure 6. Effect of soil amendments on tuber weight at 11 months after planting (MAP) in sandy loam and clay loam soils: (A) tuber weight, (B) starch content. The different letters indicate a significant difference at the 95% confidence level using Duncan's New Multiple Range Test (DMRT). Vertical bars represent standard error of the means (n = 4).

4. Conclusions

The application of CTS and SAP has been proven to be highly effective in enhancing both the physical and chemical properties of soil. These amendments reduce BD and PD, increase PO, and increase nutrient availability in both sandy loam and clay loam soils, which are important requirements for plant growth. They also induce physiological responses and cassava plant growth. Applying SAP can enhance LWP, gs, leaf

greenness, plant height, as well as fresh tuber yield and cassava starch content, particularly in sandy loam soil. The present research also provides evidence that using CTS and SAP is an effective way to improve soil properties and physiological processes of the vegetative community, as well as to enhance cassava growth. Such practices can increase yields and provide a sustainable, appropriate soil management strategy for cassava production systems, especially in areas with soil and water limitations. However, this study was conducted over a single growing season and involved only one cassava cultivar. Future research should therefore investigate the long-term and multi-season effects of CTS and SAP applications across different cultivars and environments to assess soil properties and cassava yield comprehensively.

5. Acknowledgements

This research was financially supported by the Agricultural Research Development Agency (Public Organization), Thailand (ARDA), and was facility-supported by Suranaree University of Technology.

Author Contributions: Conceptualization, S.W., T.M.; carrying out the experiment, data collection, P.K.; T.M., W.P. formal analysis, P.K., T.M., WP; writing, P.K., T.M.; editing, and supervision, S.W., T.M., W.P.

Funding: This research was financially supported by the Agricultural Research Development Agency (Public Organization), Thailand (ARDA), under the fiscal year 2024 budget. Contract No. PRP6707031280.

Conflicts of Interest: The authors declare no conflict of interest.

References

[1] Trade Policy and Strategy Office. The export of cassava has rebounded after 14 months, with exports to China increasing by 25.1%. Available online: https://tpso.go.th/en/home (accessed May 16, 2024).

[2] Arunrat, N.; Kongsurakan, P.; Sereenonchai, S.; Hatano, R. Soil organic carbon in sandy paddy fields of Northeast Thailand: A review. *Agronomy* **2020**, *10*(8), 1061. https://doi.org/10.3390/agronomy10081061

[3] Popradit, A.; Nakhokwik, Y.; Robischon, M.; Saiki, S. T.; Yoshimura, J.; Wanasiri, A.; Ishida, A. Soil degradation and herbicide pollution by repeated cassava monoculture within Thailand's conservation region. *PLoS ONE* **2024**, *19*(8), e0308284. https://doi.org/10.1371/journal.pone.0308284

[4] Kolinguenza, N.; Chabi, F.; Balogun, I.; Daouda, B.; Wayawaya, H. A.; Dockas, O.; Kosh-Komba, E.; Dagbenonbakin, G.; Amadji, G.; Saidou, A. Chemical characteristics of soils in forest and savannah zones and cassava productivity in the Central African Republic. *Niger. J. Soil Sci.* **2024**, *55*(2), 437–444.

[5] Nilnoree, T.; Anusontpornperm, S.; Thanachit, S.; Kheoruenromne, I.; Petprapai, P. Effect of chicken manure and organic wastes from cassava starch manufacturing plant on cassava grown on Dan Khun Thot soil. *Khon Kaen Agric. J.* **2016**, *44*(1), 167–178.

[6] Azarmi, R.; Giglou, M.; Taleshmikail, R. Influence of vermicompost on soil chemical and physical properties in tomato (*Lycopersicum esculentum*) field. *Afr. J. Biotechnol.* **2008**, *7*(14). https://doi.org/10.5897/AJB08.378

[7] Mulugeta, A.; Getahun, B. Effects of organic amendments on soil fertility and environmental quality: A review. *J. Plant Sci.* **2020**, *8* (5), 112–119. https://doi.org/10.11648/j.jps.20200805.12

[8] Cercioglu, M. The role of organic soil amendments on soil physical properties and yield of maize (*Zea mays* L.). *Commun. Soil Sci. Plant Anal.* **2017**, *48*(6), 683–691. https://doi.org/10.1080/00103624.2017.1298787

[9] Bilong, P.; Nguyen, T.; Ramirez, F. Biochar and organic matter additions improve soil structure and water retention in sandy soils. *Agron. J.* **2022**, *114*(2), 1234–1245. https://doi.org/10.1016/j.heliyon.2022.e09570

[10] Eykelbosh, A. J.; Johnson, M. S.; Santos de Queiroz, E.; Dalmagro, H. J.; Guimarães Couto, E. Biochar from sugarcane filtercake reduces soil CO_2 emissions relative to raw residue and improves water retention and nutrient availability in a highly weathered tropical soil. *PLoS ONE* **2014**, *9*(6), e98523. https://doi.org/10.1371/journal.pone.0098523

[11] Liu, Y.; Lan, X.; Hou, H.; Ji, J.; Liu, X.; Lv, Z. Multifaceted ability of organic fertilizers to improve crop productivity and abiotic stress tolerance: Review and perspectives. *Agronomy* **2024**, *14*(6), 1141. https://doi.org/10.3390/agronomy14061141

[12] Jitkhamen, S.; Anusontpornperm, S.; Thanachit, S.; Kheoruenromne, I.; Phun-iam, M. Response of cassava Huay Bong 80 variety to potassium fertilizer in Warin soil series amended with cassava tails and stalk for two consecutive years. *Agric. Sci. J.* **2021**, *52*(2), 164–184.

[13] Thai Tapioca Starch Association. Thai tapioca starch. Available online: https://www.thaitapiocastarch.org/en/ (accessed February 5, 2025).

[14] Leitch, A.; Anusontpornperm, S.; Thanachit, S.; Jindaluang, W.; Phun-iam, M. Cassava response to phosphorus fertilizer in Warin soil series amended with cassava tails and stalk–bentonite mixture. *Trends Sci.* **2023**, *20*(5), 4885. https://doi.org/10.48048/tis.2023.4885

[15] Malik, S.; Chaudhary, K.; Malik, A.; Punia, H.; Sewhag, M.; Berkesia, N.; Nagora, M.; Kalia, S.; Malik, K.; Kumar, D. Superabsorbent polymers as a soil amendment for increasing agricultural production while reducing water losses under water stress conditions. *Polymers* **2022**, *15*(1), 161. https://doi.org/10.3390/polym15010161

[16] Hou, X.; Li, R.; He, W.; Dai, X.; Ma, K.; Liang, Y. Superabsorbent polymers influence soil physical properties and increase potato tuber yield in a dry-farming region. *J. Soils Sediments* **2018**, *18*(3), 816–826.

[17] Blake, G. R. Bulk density. In *Methods of Soil Analysis*; Agronomy Monographs; American Society of Agronomy: Madison, WI, USA, 1965; pp 374–390. https://doi.org/10.2134/agronmonogr9.1.c30

[18] Rühlmann, J.; Körschens, M.; Graefe, J. A new approach to calculate the particle density of soils considering properties of the soil organic matter and the mineral matrix. *Geoderma* **2006**, *130*(3), 272–283. https://doi.org/10.1016/j.geoderma.2005.01.024

[19] Cera, J. S. How to compute soil porosity. **2024**. https://doi.org/10.1515/ssa-2015

[20] Walkley, A.; Black, I. A. An examination of the Degtjareff method for determining soil organic matter and a proposed modification of the chromic acid titration method. *Soil Sci.* **1934**, *37*, 29–37. https://doi.org/10.1097/00010694-193401000-00003

[21] Bray, R. H.; Kurtz, L. T. Determination of total organic, and available forms of phosphorus in soil. *Soil Sci.* **1945**, *59*(1), 39–45. https://doi.org/10.1097/00010694-194501000-00006

[22] Isaac, R. A.; Kerber, J. D. Atomic absorption and flame photometry: Techniques and uses in soil, plant and water analysis. In *Instrumental Methods for Analysis of Soil and Plant Tissue*; Walsh, L. M., Ed.; Soil Science Society of America: Madison, WI, USA, **1971.** https://doi.org/10.2136/1971.instrumentalmethods.c2

[23] Pereira, L. F. M.; Zanetti, S.; Silva, M. D. A. Water relations of cassava cultivated under water deficit levels. *Acta Physiol. Plant.* **2018**, *40*, 1–13. https://doi.org/10.1007/s11738-017-2590-7

[24] Orek, C.; Gruissem, W.; Ferguson, M.; Vanderschuren, H. Morpho-physiological and molecular evaluation of drought tolerance in cassava (*Manihot esculenta* Crantz). *Field Crops Res.* **2020**, *255*, 107861. https://doi.org/10.1016/j.fcr.2020.107861

[25] Cao, Y.; Wang, B.; Guo, H.; Xiao, H.; Wei, T. The effect of superabsorbent polymers on soil and water conservation on the terraces of the Loess Plateau. *Ecol. Eng.* **2017**, *102*, 270–279. https://doi.org/10.1016/j.ecoleng.2017.02.043

[26] Zheng, H.; Mei, P.; Wang, W.; Yin, Y.; Li, H.; Zheng, M.; Cui, Z. Effects of superabsorbent polymer on crop yield, water productivity, and soil properties: A global meta-analysis. *Agric. Water Manage.* **2023**, *282*, 108290. https://doi.org/10.1016/j.agwat.2023.108290

[27] Yang, Y.; Wu, J.; Han, Q.; He, F.; Han, W.; Yang, X. Quantitative analysis of the effect of water-retaining agent on soil pores. *Sci. Soil Water Conserv.* **2011**, *9*, 88–93. https://doi.org/10.3389/fenvs.2022.859434

[28] Yang, Y.; Wu, J.; Zhao, S.; Han, Q.; Pan, X.; He, F.; Chen, C. Assessment of the responses of soil pore properties to combined soil structure amendments using X-ray computed tomography. *Sci. Rep.* **2018**, *8*, 695. https://doi.org/10.1038/s41598-017-18997-1

[29] Spaccini, R.; Piccolo, A.; Mbagwu, J. S. C.; Teshale, A. Z.; Igwe, C. Influence of the addition of organic residues on carbohydrate content and structural stability of some highland soils in Ethiopia. *Soil Use Manage.* **2002**, *18*, 404–411. https://doi.org/10.1111/j.1475-2743.2002.tb00259.x

[30] Ogunlade, M. O.; Adeoye, G. O.; Ipinmoroti, R. R.; Ibiremo, O. S.; Iloyanomon, C. I. Comparative effect of organic and NPK fertilizers on the growth and nutrient uptake of cocoa seedlings. *Niger. J. Soil Sci.* **2006**, *16*, 121–125.

[31] Olatunji, O.; Ayuba, S. A.; Oboh, V. U. Growth and yield of okra and tomato as affected by pig dung and other organic manures: Issues for economic consideration in Benue State. In *Proceedings of the 30th Annual Conference of the Soil Science Society of Nigeria*; University of Agriculture: Makurdi, Nigeria, 2006; pp 91–98.

[32] Amenkhienan, B.; Isitekhale, H. H. E.; Nwobi, N.; Ayemere, E. E.; Oriaifo, S. O. Influences of cassava peels on some soil physical properties, maize growth, and yield in an Ultisol. *Int. J. Innov. Agric. Biol. Res.* **2018**, *6*(3), 31–38.

[33] Yang, Y.; Wu, J.; Zhao, S.; Gao, C.; Pan, X.; Tang, D. W.; Van der Ploeg, M. Effects of long-term superabsorbent polymer and organic manure on soil structure and organic carbon distribution in different soil layers. *Soil Tillage Res.* **2021**, *206*, 104781. https://doi.org/10.1016/j.still.2020.104781

[34] Ketkhao, P.; Anusontpornperm, S.; Thanachit, S.; Kheoruenromne, I.; Phun-iam, M. Effect of bentonite and cassava tails and stalk on cassava planted in an upland Grossarenic Paleustult and soil property changes. *Agric. Nat. Resour.* **2024**, *58*(1), 67–80.

[35] Goebel, M.; Bachmann, J.; Woche, S. K.; Fischer, W. R. Soil wettability, aggregate stability, and the decomposition of soil organic matter. *Geoderma* **2005**, *128*, 80–93. https://doi.org/10.1016/j.geoderma.2004.12.016

[36] Li, X.; He, J. Z.; Liu, Y. R.; Zheng, Y. M. Effects of superabsorbent polymers on soil microbial properties and Chinese cabbage (*Brassica chinensis*) growth. *J. Soils Sediments* **2013**, *13*, 711–719. https://doi.org/10.1007/s11368-013-0657-7

[37] Xu, S.; Zhang, L.; McLaughlin, N. B.; Mi, J.; Chen, Q.; Liu, J. Effect of synthetic and natural water-absorbing soil amendment on soil physical properties under potato production in a semi-arid region. *Soil Tillage Res.* **2015**, *148*, 31–39. https://doi.org/10.1016/j.still.2014.10.002

[38] Singh, A.; Kumar, M. C.; Parmar, R.; Kumar, B. S. Performance of a new superabsorbent polymer on seedling and post-planting growth and water use pattern of chrysanthemum grown under controlled environment. *Acta Hortic.* **2007**, 43–49. https://doi.org/10.17660/ActaHortic.2007.742.5

[39] Verma, A. K.; Sindhu, S. S.; Singh, A.; Kumar, A.; Singh, A.; Chauhan, V. B. S. Conditioning effects of biodegradable superabsorbent polymer and vermi-products on media properties and growth of gerbera. *Ecol. Eng.* **2019**, *132*, 23–30. https://doi.org/10.1016/j.ecoleng.2019.03.012

[40] Islam, M. R.; Hu, Y.; Mao, S.; Mao, J.; Eneji, A. E.; Xue, X. Effectiveness of a water-saving superabsorbent polymer in soil water conservation for corn (*Zea mays* L.) based on eco-physiological parameters. *J. Sci. Food Agric.* **2011**, *91*, 1998–2005. https://doi.org/10.1002/jsfa.4408

[41] Opachat, T.; Anusontpornperm, S.; Thanachit, S.; Kheoruenromne, I. Major plant nutrient release in jasmine rice growing soils amended with biochar and organic wastes: An incubation study. *Int. J. Soil Sci.* **2018**, *13*, 9–17. https://doi.org/10.3923/ijss.2018.9.17

[42] Pereira, L. F. M.; Zanetti, S.; Silva, M. d. A. Water relations of cassava cultivated under water deficit levels. *Acta Physiol. Plant.* **2018**, *40*, 1–13. https://doi.org/10.1007/s11738-017-2590-7

[43] Situ, Y.; Yang, Y.; Huang, C.; Liang, S.; Mao, X.; Chen, X. Effects of several superabsorbent polymers on soil exchangeable cations and crop growth. *Environ. Technol. Innov.* **2023**, *30*, 103126. https://doi.org/10.1016/j.eti.2023.103126

[44] Ndunge, B. D.; Obiero, J. P. O.; Mbuge, D. O. Contribution of superabsorbent polymers to growth and yield of African leafy vegetables. *Adv. Agric.* **2022**, *1*, 8020938. https://doi.org/10.1155/2022/8020938

[45] Alotaibi, M. M.; Alharbi, M. M.; Alsudays, I. M.; Alsubeie, M. S.; Almuziny, M.; Alabdallah, N. M.; Alghanem, S. M. S.; Albalawi, B. F.; Ismail, K. A.; Alzuaibr, F. M.; Moustafa, M. M. I.; Abd-Elwahed, A. H. M.; Hassan, A. H. A.; Khalifa, S. M.; Awad-Allah, M. M. A. Influence of superabsorbent polymer

on growth and productivity of green bean under drought conditions. *Agronomy* **2024**, *14*(6), 1146. https://doi.org/10.3390/w16223186

[46] Shahrajabian, M. H.; Sun, W.; Cheng, Q.; Khoshkharam, M. The impact of soil amendment of superabsorbent polymer on grain yield and yield components of corn in center of Iran. *Commun. Agric. Appl. Biol. Sci.* **2019**, *52*, 151–157.

[47] Negim, O. I. A.; Moharam, M. H. A.; Elsayed, E. F.; Thabit, F. N. The combination between superabsorbent polymers (SAPs) and biofertilizers could be an ecofriendly approach for soil chemical properties improving and sustainable wheat (*Triticum sativum*) production in sandy loam soil. *J. Soil Sci. Plant Nutr.* **2024**, *24*(3), 4349–4365. https://doi.org/10.1007/s42729-024-01839-1

[48] Palma, D.; Lagos, O.; Souto, C.; Pérez, A.; Quezada, L.; Hirzel, J.; Vera, M.; Ulloa, J.; Urbano, B. Evaluation of a natural superabsorbent polymer on water retention capacity in coarse-textured soils. *Water* **2024**, *16*(22), 3186. https://doi.org/10.3390/w16223186

[49] Ghobashy, M. M.; Amin, M. A.; Mustafa, A. E.; El-Diehy, M. A.; El-Damhougy, B. K.; Nady, N. S. Synthesis and application of a multifunctional poly(vinyl pyrrolidone)-based superabsorbent hydrogel for controlled fertilizer release and enhanced water retention in drought-stressed *Pisum sativum* plants. *Sci. Rep.* **2024**, *14*(1), 27734. https://doi.org/10.1038/s41598-024-76255-7

ASEAN
Journal of Scientific and Technological Reports
Online ISSN:2773-8752

Research article

The Influence of Managerial and Operational Characteristics on Food Waste Reduction Practices Among the Restaurants Along the Andaman Coast of Thailand

Mumtas Meraman[1], and Morakot Ditta-Apichai[2*]

[1] College of Innovation and Management, Songkhla Rajabhat University, Songkhla, 90000, Thailand
[2] Faculty of Multidisciplinary Sciences and Entrepreneurship, Thaksin University Phatthalung Campus, Phatthalung, 93210, Thailand
* Correspondence: morakot.d@tsu.ac.th

Citation:
Meraman, M.; Ditta-Apichai, M. The Influence of managerial and operational characteristics on food waste reduction practices among the restaurants along the Andaman Coast of Thailand. *ASEAN J. Sci. Tech. Report.* **2026**, *29*(4), e261801. https://doi.org/10.55164/ajstr.v29i4.261801

Article history:
Received: August 6, 2025
Revised: March 9, 2026
Accepted: March 11, 2026
Available online: March 25, 2026

Publisher's Note:
This article is published and distributed under the terms of the Thaksin University.

Abstract: The food service sector plays a substantial role in the food waste creation. Restaurants in Thailand, driven by tourist demand, substantially contribute to food waste. This study analyzes the managerial and operational attributes influencing restaurants' practices for reducing food waste in Thailand's Andaman coastal region. This quantitative research uses the Waste Hierarchy framework to investigate restaurants' food waste practices. Independent variables are divided into two categories: 1) Manager Characteristics, and 2) Restaurant Characteristics. In total, 353 questionnaires were distributed using proportional allocation. The data were collected via simple random sampling and analyzed using logistic regression. The results indicate that restaurants demonstrated a high level of compliance with prevention practices; however, they showed substantially lower adoption of reuse and recycling practices. The logistic regression models revealed that personal factors (education, age, interest in food waste reduction, and restaurant experience), along with the number of meals served at the restaurant, significantly influence food waste practices. The multiple logistic regression model showed a good fit (model chi-square = 72.78, df = 6, $p < .0001$) and explained 25.2% of the variance. This study offers valuable insights and practical implications by highlighting that manager characteristics, rather than operational attributes, are important in shaping food waste reduction. This insightful information can be used to design and implement policies on human capacity development related to food waste reduction.

Keywords: Food waste management; food waste reduction; hospitality waste; Thai restaurants; the Andaman Coast of Thailand

1. Introduction

Food waste is a global societal issue, and reducing it is one of the Sustainable Development Goals (SDG 12.3) [1]. The 2024 food waste index report from the Food and Agriculture Organization (FAO) of the United Nations and the United Nations Environment Programme (UNEP) [2] revealed that about 19% of all food produced, or approximately 1.05 billion tons, is wasted. Of this total, 60% is household food waste, 28% is from the food service sector, and 12% is from retail. In Thailand, food waste is a significant issue, accounting for about 64% of total municipal solid waste [3]. This substantial amount of organic waste

consists of food waste, with each Thai person producing an average of 86 kilograms annually, or approximately 0.2 kilograms daily [3], exceeding the global average of 79 kilograms per person per year [2]. The excessive edibles discarded cause negative implications for the economic, social, health, and environmental dimensions [4], such as the high cost of waste management [5]; the paradox of food wastage in the presence of starvation and malnutrition [4]; and the increase of global greenhouse gas (GHG) emissions [2]. All challenges highlight the importance of empirical research into the determinants of food waste mitigation, especially in the foodservice industry, which contributes significantly to consumer-generated food waste [6].

Food waste is characterized as the reduction in the quantity or quality of consumable food resulting from the choices and actions of food producers and consumers [7]. Food waste happens throughout the food supply chain process [8], from agricultural production [9] to final household [10-11] or hospitality (out-of-home) consumption [12-13]. The majority of food waste studies have focused on households, while research within the hospitality industry remains limited [4]. Furthermore, most research on food waste management in hospitality has been conducted in developed countries [14]. Consequently, academic research on food waste management and practices requires more diversity. More theory-driven studies are needed, particularly on the factors influencing pro-environmental behavior among hospitality and foodservice stakeholders [15], especially in developing countries such as ASEAN nations [16].

Tourism is a crucial driving force of the Thai economy. The World Bank's Thailand Economic Monitor [17] forecasts that visitor arrivals will rise to 41.1 million in 2025, surpassing pre-COVID-19 levels. Particularly, the Southern Region of Thailand, especially the Andaman Coast, is a significant component of the national economy. It has the highest percentage of international visitors, at about 50.1%, compared to the central (about 18.8%) and northern (around 12.5%) regions [47]. Consequently, there is greater concern about food waste generated by hospitality and foodservice provisions within the tourism industry, particularly in restaurants and catering, due to the growing number of tourists. The complex nature of the hotel and restaurant industry influences various food waste management practices [14]. The food waste hierarchy—a framework to identify and prioritize strategies for minimizing and managing food surplus and waste—is extensively utilized in waste management [18, 48]. However, there are only a few studies on food waste management within the hospitality and foodservice sectors, especially in a developing economy like Thailand. Kattiyapornpong et al. [13] is one of the few recent studies to highlight the food waste hierarchy for five-star hotels and restaurants in Thailand, demonstrating sustainable food waste management and corporate social responsibility. Recent research by Koiwanit and Filimonau [6] reveals that Bangkok restaurant managers view food waste mitigation as the norm, based on frequent personal observations, peer reports, and media coverage. However, there is a need to investigate other relevant factors, such as the personal attitudes of restaurant owners or managers who are responsible for the development and implementation of business strategies and operations [16].

The 20-year strategy (years 2018–2037) of Thai national policies emphasizes zero-waste management, believing that waste has economic value and can be reused and that it is essential to minimize waste and its disposal through effective technology [19]. The Andaman Coast region of Southern Thailand was selected as the pilot study area for its natural ecological beauty and unique culinary offerings. These distinctive features serve as a major attraction for both domestic and international eco- and food-culture tourists. Local restaurants play a significant role in tourism, which, in turn, leads to an increase in food waste. There are 4,064 registered food establishments in the five provinces of the Andaman Coast; specifically, Phuket has the highest number of registered restaurants, totaling 3,308, followed by Krabi with 506 establishments [20]. Consequently, this research aims to address the need for more theory-driven investigations into the factors that influence food waste mitigation. The research objectives are to examine the characteristics of managers and restaurants that influence food waste practices along the Andaman Coast of Thailand. Specifically, this study examines the demographics of restaurant managers or owners and restaurant operational settings in the food waste hierarchy practices of restaurants located in the Andaman coastal area, a major tourist destination in Thailand. The findings will inform practical guidelines and recommendations for restaurants and relevant agencies to develop strategic planning and policies that facilitate food waste reduction. This study provides useful insights

to aid relevant stakeholders, including governments, businesses, and local hospitality entities, in more effective food waste management.

2. Literature Review

The Food and Agriculture Organization of the United Nations (FAO) [21] (p. 2) defines "food waste" (FW) as "the decrease in edible food occurring at the end of the food chain (retail and final consumption), which relates to retailers' and consumers' behavior." Normally, food waste from the hospitality and food services sector (HaFS) is organic waste generated by immediate consumption outside the home, including hotels, restaurants, catering, healthcare, and education [22]. Food waste from the HaFS encompasses any food discarded during processing, including peels from preparation, waste from serving dishes, and leftovers from guests' plates [23].

2.1 Theoretical Framework: The Waste Hierarchy in Food Management

The theory of waste hierarchy, originating in 1979, provides a structured prioritization for sustainable waste management through five key levels: prevention, reuse, recycling, recovery, and disposal [24]. Researchers and practitioners have developed, adopted, and adapted the waste hierarchy principles as general guidelines for waste prevention and sustainable waste management [13, 24]. However, limited research has applied this framework to food waste management in the hospitality sector [13]. The food waste hierarchy can enable hospitality businesses to implement effective food waste management strategies to prevent food waste generation, recycle food waste, and maximize the efficiency of food use [25]. The waste hierarchy, therefore, can serve as a strategic guide that helps hospitality businesses manage their food waste more sustainably. Specifically, the food waste hierarchy (FWH) prioritizes options for waste management based on their environmental, economic, and social sustainability by establishing a clear order of preference: prevention, through minimization of food surplus and avoidable waste, is the most sustainable choice, followed by the redistribution of surplus to food-poor groups and the conversion of food waste into animal feed [48]. In addition to reducing food waste at the sources, lowering food costs, and safeguarding the environment in the hospitality and food services sector (HaFS), the FWH is an important instrument for cost control and corporate social responsibility (CSR) [49].

2.1.1 Prevention: The Role of Managerial Characteristics

The literature has identified various factors influencing the food waste reduction in the HaFS. The human element is the key element in the hospitality industry and strongly dictates the most desirable tier of the waste hierarchy—prevention. Several studies have identified that personal characteristics of restaurant managers impact food waste reduction practices. The literature suggests a strong consensus that educational background and age are primary drivers of waste reduction awareness. For example, higher levels of education consistently correlate with improved waste separation and heightened recycling behaviors across both Thai and Chinese hospitality contexts [11, 26, 27]. Specifically, older individuals prioritize resource efficiency and the reduction of unnecessary food waste [11, 31], which is attributed to their distinct attitudes and understanding of food value [32-34]. However, Lang et al. [35] found that younger restaurant owners exhibited greater awareness of food waste recycling than older restaurant owners in Gansu Province, China. Research also indicates that learning and self-development contribute to reducing waste generation in restaurants and households [10, 28-30]. The literature also identifies that interest in reducing food waste and working experience are essential for the effectiveness of food waste management in the hospitality service industry. Internal factors, particularly the degree of interest and sustainability knowledge among managers and employees, are essential to the implementation of waste reduction methods. Prior studies have shown that strong interest and comprehensive awareness of sustainability significantly improve proactive waste-reduction practices in the restaurant sector [11, 27, 36, 37]. Work experience in the restaurant industry also plays a crucial role. Recent research found that managers or restaurant owners with extensive experience usually have effective communication and motivation skills that help staff understand how to reduce food waste, especially in planning, buying, managing inventory, purchasing, controlling inventory, and adjusting menus to utilize surplus or near-expiry ingredients [38], as well as promoting recycling food-waste behavior [27].

2.1.2 Operational Context and Implementation

In the context of FWH's focus on reuse and recycling, several studies have indicated that the physical and operational characteristics of the restaurant establishment impact waste management practices. For example, the size of a restaurant influences its awareness and behavior related to food waste recycling [27]. Furthermore, restaurants offering multiple meals per day are typically well-planned to reduce food loss and waste [39-41]. However, research in the Thai hospitality industry indicates that although managers may wish to implement recycling initiatives, the absence of local waste management infrastructure in certain areas often leads businesses to rely on less sustainable disposal practices [49]. This issue is especially important for businesses located on the coast or on an island, where logistical challenges make it harder to redistribute food surpluses [14]. While there is no evidence linking award-winning restaurants to food waste reduction, various award schemes, including the Michelin Green Star and Food Made Good awards, incorporate waste reduction into their evaluation criteria [42].

While the waste hierarchy in the HaFS is theoretically robust, its practical application in the tourism environment's geographic context remains underexplored. Most studies focus on stable urban environments, ignoring the unique geographic context of coastal tourism and the influence of personal and operational factors in the food waste hierarchy. Based on the reviewed literature, Figure 1 summarizes and illustrates the variables and hypotheses used to investigate factors influencing restaurants' food waste reduction. Specifically, the selection of the variables was based on established food waste and hospitality literature, ensuring they represent both the human (managerial) variables, including age [11, 31 - 35], education [10, 11, 26, 27, 29, 30], work experience [27, 36, 38], and interests in learning about waste reduction [11, 27, 36 - 38], and operational (restaurant) attributes, including location [14], period of operation [50], number of employees [27], number of meals served [39 - 41], and awards received [42].

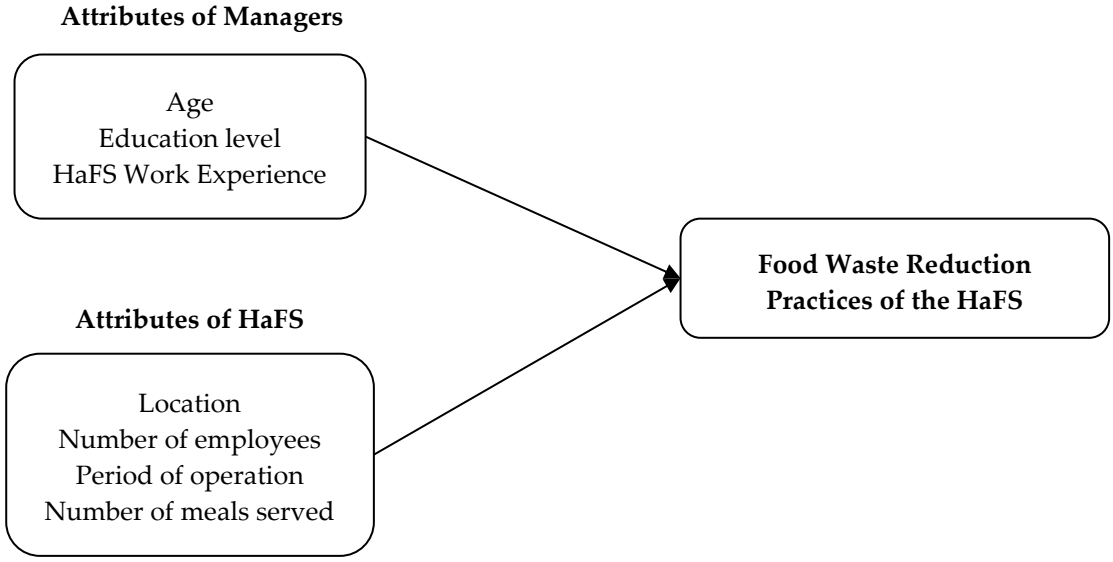


Figure 1. Research Framework of the manager's and restaurant's characteristics influencing the HaFS's food waste reduction practices.

3. Methods

3.1 Research Design

The principles of the waste management hierarchy have been widely applied as a framework for waste reduction strategies [43]. Recently, Kattiyapornpong et al. [13] adopted this framework to investigate food waste management practices among five-star hotels in Bangkok, Thailand. Accordingly, this research adopts these principles as the theoretical framework to investigate the influence of food waste reduction on various

restaurants along the Andaman coast in Southern Thailand. Table 1 illustrates the waste hierarchy concept in waste management and the practices used in HaFS food waste management.

Table 1. The waste hierarchy with the practices of food waste management of the HaFS

The waste hierarchy concept	Practices of the HaFS's food waste management
Reduce: Prevent food waste.	**Policy:** The food waste management policy includes awareness programs, staff training, and clear duty delegation. **Planning:** The process of planning food waste reduction and purchasing to limit food loss through effective procurement management. **Storage and preservation:** The process of storing and preserving food helps minimize food loss due to expiration. **Operation:** Activities related to food preparation, customer services, and earnings that influence food waste control and management efficacy.
Reuse: Redistribution for human consumption.	**Donation for humans:** The restaurant donates the excess food or raw materials suitable for human consumption to local charities or their staff.
Animal feed	**Donation for animal feed:** The restaurant donates the food waste as animal feed.
Recycle: Extraction of compounds of interest; Industrial use; Anaerobic digestion; Composting; Thermal treatment with energy recovery.	**Utilization within the restaurant:** The process of applying controlled processing techniques to food waste to recover residual material, biological value, or energy value
Disposal: Thermal treatment without energy recovery/landfill	**Budgets and expenses for food waste disposal:** The restaurant establishment's budget and actual costs for the collection, transportation, treatment, and ultimate disposal of food waste are referred to as food waste disposal budgets and expenses. **Disposal:** The process of the collection, transportation, and final treatment through landfill or incineration without energy recovery. Thai restaurants do not manage waste on-site; their involvement is limited to budgeting for bins and paying disposal fees to the LAOs [51].

[1] This framework is adapted from Garcia-Garcia et al. [43] and Kattiyapornpong et al. [13].

3.2 Data Collection

This study used a quantitative research design and a Thai-language questionnaire. The questionnaire consisted of three parts. The first two parts reflected the independent variables. The first part consisted of four variables: age, education level, restaurant work experience, and interest in learning about food waste reduction. In the second part, the questions reflected the attributes of HaFS, which consist of five variables: location, period of operation, number of employees, number of meals served, and general awards received. The last part of the questionnaire measured the dependent variables, namely food waste reduction practices. The questionnaires were crafted as checklist questions according to the three-dimensional framework of waste management prioritization: 1) reduction, 2) reuse and recycling, and 3) disposal. Additionally, the survey was developed based on the HaSF's practices for managing food waste, encompassing all three dimensions: Prevention and Reduction (Policy, Planning, Storage and Preservation, and Operation); Reuse and Recycling (Donation and Reuse); and Budgeting and Expenditure for the management and disposal of food waste. The questionnaire survey was submitted to the Songkhla Rajabhat University Human Research Ethics Office and

was approved under Order 045/2023, effective from 8 December 2023 to 7 December 2024. Three environmental specialists carry out content validity testing of the questionnaire. 30 sets of questionnaires were sent to a sample group that did not originate from the target areas to test reliability. The reliability value was then calculated using the alpha coefficient formula according to Cronbach's alpha method, yielding a score of 0.7. The data were collected from representatives of employees and restaurant owners who registered as legal entities, one individual per restaurant in the provinces of Satun, Krabi, Trang, Phang Nga, and Phuket. The total number of restaurants in the area was 4,064, of which the majority are small- and medium-sized businesses (SMEs) [20]. A sample size was therefore estimated using the Krejcie and Morgan [54] table and a quota sample equivalent to the entire population of 360. The samples were chosen using simple random sampling, which was conducted by drawing lots and by recruiting volunteers. The questionnaires were collected both online and on-site; 353 questionnaires (98%) were returned. Data was collected proportionally, with Phuket having the highest number of restaurants at 3,308, or about 81.4% of the total number of the Andaman coastal restaurants [20]. In this study, 293 restaurants were included (83%); followed by Krabi, the second-highest number of restaurants at 506; and 45 restaurants were used as samples (11%). The rest of the sample group is from Phang Nga, Trang, and Satun. 12 samples came from Phang Nga (3%), while Trang and Satun contributed 1% each (4 and 6 samples, respectively). Additionally, the participants were small- and medium-sized restaurants that served dishes on demand rather than buffet style.

3.3 Data Analysis

The independent variable consists of two main parts: the attributes of managers and the attributes of the HaFS (restaurant). The dependent variable is food waste reduction practices. Questions related to food waste reduction practices are multiple-choice. If the answer is "Yes or often/regularly" = 1, and if the respondent marks "No or sometimes" = 0. The score for the food waste reduction practice is calculated from 46 questions related to seven food waste management practices across the three aspects of the waste hierarchy. The criteria for good practice are set at 1, while the non-practice score equals 0. Table 2 shows the scores for each item, determined using criteria set by three experts in environmental management and tourism. The results were analyzed using descriptive statistics and a two-step statistical analysis (simple logistic regression and multiple logistic regression) in R to identify the most influential attributes. Specifically, a simple logistic regression was conducted to examine each managerial and restaurant characteristic (independent variables) in relation to food waste management (dependent variable). Variables that showed statistical significance were then entered into a multiple logistic regression to combine factors and determine predictive models for specific characteristics.

Table 2. Criteria for assessing the practice of food waste management

Waste Hierarchy Concept	Practice of Food Waste Management
Reduce: Prevention of food waste generation (31 Items)	1. Policy: (12 Items): practice score = 1 (if total score = 6) 2. Planning: (4 Items): practice score = 1 (if total score = 2) 3. Storage and preservation: (5 Items): practice score = 1 (if total score = 3) 4. Operation: (10 Items): practice score = 1 (if total score = 5) Total score >= 2
Reuse/Recycle: Redistribution for human consumption/animal feed and Extraction of compounds of interest (12 Items)	5. Donations: (8 Items) practice score = 1 (if total score = 4) 6. Utilization within the restaurant (4 Items): practice score = 1 (if total score = 2) Total score >= 1
Disposal: landfill (3 Items)	7. Budgets and expenses for disposal: (3 Items): practice score = 1 (if total score = 3)

[2] *overall practice score =1 (if total score >= 4)*

Notes: 4 scores or above are needed for overall calculation, with conditions as follows:

A score over 50% is required in either question 1, 2, 5, 6, or 7.

A score over 50% in numbers 3 and 4.

4. Results and Discussion

4.1 The Practice of Waste Reduction Within the Waste Hierarchy

The results, illustrated in Table 3, present the research findings on practices for reducing food waste according to the food waste hierarchy, based on the analysis of managers' and HaFS's attributes. Two factors were utilized to examine the impact on practices for managing food waste based on the analysis of the sample group's independent variables: 1) attributes of managers, which include four factors: age, education level, HaFS work experience, and interest in learning about waste reduction; 2) attributes of HaFS, which include five factors: location, period of operation, number of employees, number of meals served, and general awards received. The dependent variable in this study is the practice of reducing food waste. Table 3 displays the research findings on practices for reducing food waste. The variable in the prevention aspect is in the range of 76.19 to 98.33 percent, moving in the same direction. Regarding the factors of recycling and reuse, the proportion of restaurants that are engaged in these practices varied by variable, ranging from 0 to 33.33 percent. Restaurants with more than 25 employees had the highest number of practices for reducing food waste in this category, accounting for 33.33 percent of the total. However, in the disposal aspect, the study found that none of the restaurants followed any procedures.

These research findings show that most restaurants actively practiced food waste prevention, while reuse and recycling were limited. The most critical factor driving food waste prevention practices in restaurants along the Andaman Coast, perhaps, is the unique local context of abundant and accessible resources. Specifically, food waste is due to poor ingredient purchasing and storage. Food preservation and storage include checking ingredient expiration dates, cleaning food storage areas, arranging food using the 'first-in, first-out' principle, and storing ingredients/food in suitable locations and at appropriate temperatures. The restaurants used the following procedures: trimming ingredients, adjusting menus to use similar ingredients, providing unserved excess cooked food to staff, offering takeout bags to customers, and generating income from food waste, such as shrimp heads. Finally, the average waste per day is about 20-30 kg for 37% of the sample restaurants (131 restaurants), followed by less than 10 kg of food waste in 33% of the samples (118 restaurants), and 10-20 kg for 84 restaurants, which is 23% of the sample group. The remaining restaurants had more than 30 kg of food waste daily. Nonetheless, no disposal practices at the restaurants were reported because the restaurants pay disposal fees to the LAOs. This finding aligns with that of Kattiyapornpong et al. [13], highlighting the critical role of food planning and the procurement of raw materials from local suppliers in reducing food waste. The abundant local supply from both the sea and the land, along with daily access to markets, allows managers to make daily purchases of fresh local ingredients. This daily purchasing eliminates the need to stock or store raw materials, reducing spoilage risk and reducing storage requirements.

Unlike hotel-owned restaurants, which comply with the food waste hierarchy model for food waste reduction as common practice [13], waste disposal practices in typical restaurants in Thailand are fundamentally shaped by the waste management system of local administrative organizations (LAOs), which are responsible for trash collection [51]. The restaurants do not manage waste on-site; their involvement is limited to budgeting for bins and paying disposal fees to the LAOs. Furthermore, the cost of publicly provided waste services is substantially lower than installing on-site disposal systems. Furthermore, over 90% of restaurants prioritize prevention, and thus, the volume of waste to be disposed of is minimal, supporting the prior studies by Ng and Sia [16] in ASEAN and China settings and by Srijuntrapun et al. [49] in Thai restaurants. Therefore, these findings reflect the contextual situation of Thai restaurants regarding the absence of the practices of reusing, recycling, and disposing of food waste.

Table 3. The practice of waste reduction within the waste hierarchy is separated by the restaurant's managerial and operational attributes.

variables	prevention				Reuse/recycle				disposal		overall			
	Non-practice		practice		Non-practice		practice		Non-practice		Non-practice		practice	
	No.	%	No.	%	No.	%	No.	%	No.	%	No.	%	No.	%
Attributes of Managers														
Age														
29-44 Year (Gen Y)	15	6.41	219	93.59	214	91.45	20	8.55	234	100	167	71.37	67	28.63
>45-60 Year (Gen X)	11	9.24	108	90.76	114	95.80	5	4.20	119	100	47	39.50	72	60.50
Education Level														
Below Bachelor degree	11	7.90	142	92.81	144	94.12	9	5.88	153	100	109	71.24	44	28.76
Bachelor's degree & above	15	7.50	185	92.50	184	92.00	16	8.00	299	100	105	52.50	95	47.50
HaFS Work Experience														
< 5 years	6	5.94	95	94.06	98	97.03	3	2.97	101	100	74	73.27	27	26.73
5-10 years	10	6.13	153	93.87	149	91.41	14	8.59	163	100	89	54.60	74	45.40
> 10 years	10	11.24	79	88.76	81	91.01	8	8.99	89	100	51	57.30	38	42.70
Interest in learning about waste reduction														
Not interested	11	6.11	169	93.89	169	93.89	11	6.11	180	100	121	67.22	59	32.78
Interested	15	8.67	158	91.33	159	91.91	14	8.09	173	100	93	53.76	80	46.24
Attributes of HaFS														
Location														
Island and land	2	4.65	41	95.35	33	76.74	10	23.26	43	100	17	39.53	26	60.47
land	24	8.00	276	92.00	285	95.00	15	5.00	300	100	188	62.67	112	37.33
island	0	0	10	100	10	100	0	0	10	100	9	90	1	10
Period of operation														
< 5 years	24	9.45	230	90.55	238	93.70	16	6.30	254	100	151	59.45	103	40.55
5-10 years	1	1.67	59	98.33	54	90.00	6	10.00	60	100	43	71.67	17	28.33
> 10 years	1	2.56	38	97.44	36	92.31	3	7.69	39	100	20	51.28	19	48.72

Table 3. The practice of waste reduction within the waste hierarchy is separated by the restaurant's managerial and operational attributes. (Continue)

variables	prevention				Reuse/recycle				disposal		overall			
	Non-practice		practice		Non-practice		practice		Non-practice		Non-practice		practice	
	No.	%	No.	%	No.	%	No.	%	No.	%	No.	%	No.	%
Attributes of HaFS														
Location														
Number of employees														
Large (> 25 persons)	10	23.81	32	76.19	28	66.67	14	33.33	254	100	24	57.14	18	42.86
Medium (10-25 persons)	16	5.56	272	94.44	281	97.57	7	2.43	60	100	179	62.15	109	37.85
Small (< 10 persons)	0	0	23	100	19	82.61	4	17.39	39	100	11	47.83	12	52.17
Number of meals served														
2 meals per day	24	7.23	308	92.77	312	93.98	20	6.02	332	100	208	62.65	124	37.35
3 meals per day	2	9.52	19	90.48	16	76.19	5	23.81	21	100	6	28.57	15	71.43
General Award Receive														
Non-receive an award	17	7.83	200	92.17	206	94.93	11	5.07	217	100	131	60.37	86	39.63
Receive an award	9	6.62	127	93.38	122	89.71	14	10.29	136	100	83	61.03	53	38.97

[3]1 refers to the age from Strauss and Howe [44].

4.2 Managerial and Operational Factors Influencing the HaFS's Practices of Food Waste Management using Simple Logistic Regression

Using simple logistic regression, the findings regarding factors influencing HaFS's food waste management practices fall into two categories: managers' attributes and restaurants' attributes. Details are shown in Table 4.

Table 4. The managerial and operational variables affecting restaurants' practices to reduce food waste using simple logistic regression.

Variable	b	se. of b	Wald	z	p-value	OR.	95% CI of OR.	
							Lower	Upper
Attributes of Managers								
Age[1]								
29-44 Year (Gen Y)	-	-	-	-	-	1	-	-
>45-60 ปี (Gen X)	1.3398	0.2368	32.011	5.658	0.0001***	3.82	2.41	6.11
Constant	-0.9133	0.1446	-	-6.315	0.0001***	0.40	0.30	0.53
Education								
Below Bachelor degree	-	-	-	-	-	1	-	-
Bachelor degree & above	0.8071	0.2279	12.538	3.541	0.0003***	2.24	1.44	3.52
Constant	-0.9072	0.1786	-	-5.079	0.0001***	0.40	0.28	0.57
Interested in waste reduction								
Not interested	-	-	-	-	-	1	-	-
interested	0.5677	0.2202	6.649	2.579	0.0099 **	1.76	1.15	2.72
Constant	-0.7183	0.1588	-	-4.523	0.0001***	0.49	0.36	0.66
HaFS work experience								
< 5 years	-	-	-	-	-	1	-	-
5-10 years	0.8237	0.2744	9.0109	3.002	0.0026**	2.28	1.34	3.95
> 10 years	0.7140	0.3106	5.2844	2.299	0.0215*	2.04	1.12	3.78
Constant	-1.0082	0.2248	-	-4.484	0.0001***	0.36	0.23	0.56

Table 4. The managerial and operational variables affecting restaurants' practices to reduce food waste using simple logistic regression. (Continue)

Variable	b	se. of b	Wald	z	p-value	OR.	95% CI of. OR	
							Lower	Upper
Location								
Island and land	-	-	-	-	-	1	-	-
Land	-0.9428	0.3340	7.9679	-2.823	0.0048	0.39	0.20	0.74
Island	-2.6221	1.0992	5.6904	-2.385	0.0171	0.07	0.01	0.44
Constant	0.4249	0.3119	-	1.362	0.1731	1.53	0.84	2.87
Period of operation								
< 5 years	-	-	-	-	-	1	-	-
5-10 years	-0.5454	0.3137	3.0227	-1.739	0.0821	0.58	0.31	1.06
> 10 years	0.3313	0.3449	0.9227	0.960	0.3369	1.39	0.70	2.75
Constant	-0.3826	0.1278	-	-2.994	0.0027**	0.68	0.53	0.87
Number of employees								
Large (> 25 persons)	-	-	-	-	-	1	-	-
Medium (10-25 persons)	-0.2084	0.3346	0.3879	-0.623	0.5340	0.81	0.42	1.58
small (< 10 persons)	0.3747	0.5210	0.5172	0.719	0.4720	1.45	0.52	4.09
Constant	-0.2877	0.3118	-	-0.923	0.3560	0.75	0.40	1.37
Number of meals served								
2 meals per day		-	-	-	-	1	-	-
3 meals per day		0.4962	8.347	2.889	0.0039 **	4.19	1.66	12.02
Constant	-0.5173	0.1135	-	-4.559	0.0001***	0.60	0.48	0.74
Receive General Award								
Non-Receive an award	-	-	-	-	-	1	-	-
Receive an award	-0.0277	0.2240	0.0153	-0.124	0.9010	0.97	0.63	1.51
Constant	-0.4209	0.1388	-	-3.032	0.0024**	0.66	0.50	0.86

[4]*p < .05; **p < .01; ***p < .001

4.2.1 Attributes of Managers

There were four independent variables: age, education level, HaFS work experience, and an interest in learning about food waste reduction (Table 4). The results showed that all variables influenced the dependent variable, practices for reducing food waste, as hypothesized. Specifically, the variable of restaurant managers' educational level influenced food waste reduction practices. The group with a bachelor's degree or higher reduced food waste by 2.24 times more than the group with a lower education level, a statistically significant difference (p-value < .05; 95% CI of OR = 1.44-3.52). Specifically, the findings indicated that managers' education level substantially impacted food waste reduction initiatives. The results align with the studies by Bunditsakulchai and Liu [11] and Zhu and Liu [26], which indicate that higher levels of education lead to better food waste separation. In addition, managers' age also influences their practice of food waste reduction. The study found that the group aged 45-60 years (GenX) practiced reducing food waste 3.82 times more than the group under 45 years (GenY), which was statistically significant (p-value < .05; 95% CI of OR = 2.41-6.11) (Table 4). This finding aligns with the literature (e.g., 31, 33-34), which consistently indicates that older people generate less food loss. Bunditsakulchai and Liu [11] emphasized that this older generation values a traditional social norm regarding food, developed through family, educational, and societal institutions, thereby establishing the behavioral basis for reducing food waste among older adults. Therefore, older-generation managers are more likely to achieve reductions in food waste than younger managers.

As for the variable of interest in learning about food waste reduction, Table 4 showed that the interested group had a statistically significant effect on reducing food waste, with an effect size 1.76 times greater (p-value < .05; 95% CI of OR = 1.15-2.72) than those who were not interested. Recent studies conducted by Fatemi et al. [28] and Uzoma et al. [30] also found that self-directed learning and personal growth significantly impact food waste reduction in both domestic and restaurant settings. Willingness to learn [45] and implement sustainable practices (e.g., food preparation and preservation, reusing and repurposing during cooking, designing menus to minimize preparation time, offering appropriate portion sizes, and reducing plate waste) fosters responsible food behaviors [13, 45]. This suggests that managers who are interested in and willing to learn about food waste reduction can be more effective at implementing practices to reduce food waste than those who are less interested or unwilling to learn. When restaurant managers show a strong interest in and dedication to reducing food waste, they are more likely to cultivate an organizational culture that promotes responsible consumption. Importantly, work experience in the restaurant industry significantly influences practices for reducing food waste, according to the research findings. The group with 5-10 years of restaurant work experience and the group with more than 10 years of restaurant work experience influenced practices for reducing food waste 2.28 times and 2.04 times that of the group with less than 5 years of restaurant work experience, respectively, with statistical significance (p-value < 0.05; 95% CI of OR = 1.34-3.95 and 1.12-3.78) (Table 4). This finding corresponds with Lévesque et al. [38], who observed that experienced managers effectively encourage teams, manage inventory, and formulate menus for sustainable food. Research conducted by Hayeebueraheng and Phanthuwongpakdee [36] and Zhao et al. [27] reports similar patterns. In summary, the managerial role is held by either the direct owner or a designated representative with the authority to set the strategic direction for the establishment. Therefore, prioritizing the selection of restaurant managers (i.e., education level, age, interest in learning about waste reduction, and work experience) is a crucial consideration for restaurant owners, as the manager determines the operation, particularly food waste reduction practices.

4.2.2. Attributes of the HaFS

Regarding restaurant attributes, there are five independent variables: period of operation, location, number of employees, number of meals served, and general awards received. The study results presented in Table 4 indicated that only the number of meals served has a significant impact on food waste reduction, as hypothesized. Specifically, selling three meals per day increased food waste reduction practices by 4.19 times

compared with restaurants serving two meals per day, a statistically significant difference (p-value < 0.05; 95% CI of OR = 1.66-12.02). The remaining variables did not influence waste reduction practices (Table 4). This finding aligns with the previous studies (e.g., 39, 40-41), which suggests that restaurants offering a variety of meals are more likely to implement systematic planning strategies to reduce food waste. The lack of significance for location suggests that waste reduction for greater sustainability has become common in the tourism and hospitality industry [14], regardless of where the restaurant is located. The insignificance of the operation period is consistent with the descriptive findings that over 90% of all restaurants excel at prevention (efficiency). This finding also suggests a 'ceiling effect' where the prevention leaves minimal waste available for reuse or recycling. Unexpectedly, contrary to previous studies such as Zhao et al. [27], the size of restaurants did not significantly influence food waste practices in this research finding. Although several award programs incorporate waste reduction in their evaluation criteria [42], achieving award-winning status did not correspond with the implementation of food waste reduction practices. The absence of significant relationships in this study may reflect contextual differences, such as variations in restaurant size or resource availability along Thailand's Andaman coast.

4.3. Managerial and Operational Factors Influencing the HaFS's Practices of Food Waste Management using Multiple Logistic Regression

The findings from the multiple logistic regression analysis presented in Table 5 confirm that attributes of managers, including education level, age, restaurant work experience, and interest in learning about effective waste reduction, still influence food waste reduction.

Table 5. The managerial and operational variables affecting restaurants' practices to reduce food waste using multiple logistic regression

Variable	b	se. of b	Wald	z	p-value	OR.	95% CI. of OR.	
							Lower	Upper
Constant	-2.2596	0.3374	-	-6.697	0.0001***	0.10	0.05	0.20
Age	1.6080	0.2714	35.1054	5.925	0.0001***	4.99	2.96	8.60
Education level	0.7319	0.2498	8.5864	2.930	0.0033**	2.08	1.28	3.41
Interested in learning about waste reduction	0.5742	0.2449	5.4968	2.344	0.0191*	1.78	1.10	2.88
HaFS work Experience (5-10 Years)	0.8174	0.3098	6.9595	2.638	0.0083 **	2.26	1.25	4.21
HaFS workExperience (> 10 Years)	0.0752	0.3528	0.0454	0.213	0.8312	1.08	0.53	2.15
Number of meals served	1.7596	0.5329	10.8995	3.301	0.0009 ***	5.81	2.14	17.78
Model Chi square = 72.78 (df = 6), p = .0001 Nagelkerke R Square = 0.252								

*p < .05; **p < .01; ***p < .001

Details are shown in Table 5, indicating that the group with a bachelor's degree or higher can reduce food waste by 2.08 times compared with the group with a lower education level, which is statistically significant (95% CI of OR = 1.28-3.41). This finding evidently shows that educated managers have the cognitive capacity to understand complex sustainability frameworks [48, 49], such as the food waste hierarchy, and thus, enable them to practice waste reduction. In terms of age, the group aged 45 or older (Gen X) reduced food waste by 4.99 times compared with the group aged 45 or younger (Gen Y), a statistically significant difference (95% CI for OR = 2.96-8.60). This research finding aligns with the literature, especially in Asian settings such as Thailand and China, where younger generations may intend to reduce waste, while older managers often hold practical conservation values that prioritize waste prevention [10, 13, 49]. For the group interested in reducing food waste, the amount of food waste can be reduced by 1.78 times compared to the group that was not interested (95% CI of OR = 1.10-2.88). This research suggests that managers with a self-interest in learning are essential for proactive waste practices in restaurants, supporting Ng and Sia's [16] research. As for

restaurant work experience, the 5-10 years of restaurant work experience still had a statistically significant influence on food waste reduction practices by 2.26 times that of the group that had less than 5 years of restaurant work experience (95% CI of OR = 1.25-4.21), suggesting that managers with years of experience have better demand forecasting [39]. Regarding the attributes of HaFS, the restaurant that served three meals per day still had a significant influence on reducing food waste by 5.81 times compared with restaurants that served two meals per day (95% CI of OR = 2.14-17.78). This finding suggests that full-service operations may implement more structured food inventory and preparation to control costs, whereas limited-service operations may view waste as unavoidable [6]. Based on the appropriateness examination of the model, the multiple logistic regression model was appropriate (Model Chi-square = 72.78, df = 6, $p < .0001$) and able to explain the influence on reducing food waste by 25.2 percent (Nagelkerke R-square = 0.252).

5. Conclusion and Limitations

This study investigated the management characteristics and attributes that influence food waste management in restaurants along the Andaman coast of Thailand. This study employed the waste hierarchy theoretical framework to provide a systematic analysis of how restaurants manage food waste. The results indicated that the manager's attributes, including age, education level, interest in learning about waste reduction, and work experience, have a statistically significant influence on reducing food waste in restaurants located on the Andaman coast of southern Thailand. At the same time, the number of meals served is the only HaFS attribute that shows statistical significance, responding to the call for food waste management in the food service sector [2]. This study contributes to theoretical implications by addressing factors that influence food waste reduction practices within the waste hierarchy framework in hospitality and tourism research highlighting various practices for managing sustainable food waste, along with factors affecting them in restaurants, aiming to facilitate the achievement of the SDG goal (12.3) [1]. The findings of this research also have practical implications, highlighting the important factors that restaurant managers can influence in reducing food waste. The findings of this research suggest that managers' characteristics, rather than physical or operational attributes, play a more critical role in shaping food waste reduction in Thailand's Andaman coastal context. The research findings emphasize that effective reduction of food waste necessitates prioritizing particular attributes of restaurant managers. The managers with educational qualifications (bachelor's degree or higher), age group (Generation X or ≥45 years), at least 5 years of experience in the restaurant industry, and interest in learning are preferable. These characteristics were identified as significantly impacting the effective adoption of food waste reduction initiatives. Effectively reducing food waste lowers operational expenses and promotes responsible food consumption towards sustainability. While restaurants currently rely on local government for food waste management, it is recommended that products such as compost, bio-fertilizer, or paving blocks be produced from collected waste and then returned to the restaurants. This approach will establish a circular feedback loop, enhancing the efficiency and incentivizing sustained food waste reduction by the establishments [38, 46].

For policy recommendations, the results suggested measures across three areas: preventive practices, enhanced reuse and recycling, and measures for entrepreneurs. Restaurants could implement measures such as posting warning signs and increasing disposal fees based on the weight of leftovers, as they currently lack customer participation in promoting waste reduction. For the second aspect, guidelines for reuse or recycling, including food donation and the utilization of food waste, are recommended. Moreover, the restaurant can use innovation and technology to monitor food waste donation and efficient waste disposal in real time. This approach could also lead to the creation of recycled food waste products, such as bio-fertilizers and paving blocks, which would be returned to restaurants to encourage their participation in the BCG economic model [38]. Economic measures are another aspect that could be strengthened; subsidies and tax breaks could be appropriate incentives to encourage the reduction and reuse of food waste [41]. Finally, measures to promote entrepreneurship are recommended [52]. The selection of a suitable manager should be prioritized. A manager should possess qualities of curiosity and a desire to learn and seek new knowledge. They should be open to sustainable development directions, including food preparation and preservation, recycling, menu design to

reduce preparation and cooking time, appropriate portion sizes as options, and reducing waste from customer plates. Sustainable consumption habits occur when employees are confident [53].

Finally, although this study highlights the theoretical contributions and practical implications of applying the waste hierarchy framework to manage food waste in restaurants, it also notes some limitations. This research focuses on food waste practices within the waste hierarchy framework in restaurants, specifically on managerial and restaurant characteristics. The research does not examine the attitudes of the restaurant staff—managers, kitchen staff, and waiters/waitresses—the raw material suppliers, or restaurant customers toward preventing and reducing food waste, which are considered limitations of this research. This research adopts a quantitative methodology, limiting the exploration of the underlying influences on managerial decision-making and practical operations. Future research should incorporate qualitative studies, including in-depth interviews with restaurant managers demonstrating different levels of food waste reduction. Future studies should also examine how restaurants reduce food waste from the perspectives of staff, raw material suppliers, and restaurant customers. It could also include an investigation into the design of a training and awareness-raising program that focuses on capacity building and on fostering positive attitudes towards food waste management. Economic incentives and consumer pressures that may influence the adoption of food-waste-reduction practices in restaurants are other areas worth researching. It is also recommended to investigate how restaurants reduce food waste in various geographical regions for comparative analysis. The sample size is another limitation, as it includes only restaurants along the Andaman coast. The determination of weight is another aspect lacking in this research paper and should be investigated in further research. Finally, conducting research across different settings, including tourism, hospitality, and food service activities in developing countries, could enhance understanding and address existing gaps in the field of study.

6. Acknowledgements

The authors sincerely thank all restaurant operators for their kind provision of data and time for participating in this study. The authors would like to express their gratitude to Associate Professor Dr. Saowalak Roongtawanreongsri and Dr. Nattakit Pipatjaturong for their valuable suggestions.

Author Contributions: Conceptualization, M.M. and M.D.; methodology, M.M. and M.D.; software, M.M.; validation, M.M. and M.D.; formal analysis, M.M.; investigation, M.M.; data curation, M.M.; writing—original draft preparation, M.M and M.D; writing—review and editing, M.D.; funding acquisition, M.M.

Funding: This research was funded by the College of Innovation and Management, Songkhla Rajabhat University (1/2567).

Conflicts of Interest: The authors declare no conflict of interest. The funders had no role in the design of the study, in the collection, analysis, or interpretation of data, in the writing of the manuscript, or in the decision to publish the results.

References

[1] United Nations. *Transforming Our World: The 2030 Agenda for Sustainable Development*; United Nations: New York, 2015. https://sdgs.un.org/2030agenda (accessed October 1, 2025).

[2] United Nations Environment Programme (UNEP). *Food Waste Index Report 2024: Think Eat Save – Tracking Progress to Halve Global Food Waste*; UNEP: Nairobi, 2024. https://www.unep.org/resources/publication/food-waste-index-report-2024 (accessed August 18, 2025).

[3] Pollution Control Department. *Thailand Waste Volume* (in Thai); 2021. https://thaimsw.pcd.go.th/report_country.php?year=2566 (accessed August 18, 2025).

[4] Amicarelli, V.; Bux, C. Food Waste in Italian Households during the COVID-19 Pandemic: A Self-Reporting Approach. *Food Secur.* **2021**, *13*(1), 25–37. https://doi.org/10.1007/s12571-020-01121-z

[5] Awasthi, A. K.; Cheela, V. S.; D'Adamo, I.; Iacovidou, E.; Islam, M. R.; Johnson, M.; Li, J. Zero Waste Approach towards a Sustainable Waste Management. *Resour. Environ. Sustain.* **2021**, *3*, 100014. https://doi.org/10.1016/j.resenv.2021.100014

[6] Koiwanit, J.; Filimonau, V. "Wasting Food Is Normal!": How Food Waste Can Become the (New) Norm in Casual Dining Restaurants. *J. Hosp. Tour. Manag.* **2025**, *62*, 1–13. https://doi.org/10.1016/j.jhtm.2024.12.006

[7] Food and Agriculture Organization of the United Nations (FAO). *The State of Food and Agriculture – Moving Forward on Food Loss and Waste Reduction*; FAO: Rome, 2019. https://openknowledge.fao.org/server/api/core/bitstreams/11f9288f-dc78-4171-8d02-92235b8d7dc7/content (accessed August 30, 2025).

[8] Wang, Y.; Shi, Y.; Zhou, J.; Zhao, J.; Maraseni, T.; Qian, G. Implementation Effect of Municipal Solid Waste Mandatory Sorting Policy in Shanghai. *J. Environ. Manag.* **2021**, *298*, 113512. https://doi.org/10.1016/j.jenvman.2021.113512

[9] Khoshnodifar, Z.; Ataei, P.; Karimi, H. Recycling Date Palm Waste for Compost Production: A Study of Sustainability Behavior of Date Palm Growers. *Environ. Sustain. Indic.* **2023**, *20*, 100300. https://doi.org/10.1016/j.indic.2023.100300

[10] Bravi, L.; Franconi, B.; Murmura, F.; Savelli, E. Factors Affecting Household Food Waste among Young Consumers and Actions to Prevent It: A Comparison among UK, Spain and Italy. *Resour. Conserv. Recycl.* **2020**, *153*, 104586. https://doi.org/10.1016/j.resconrec.2019.104586

[11] Bunditsakulchai, P.; Liu, C. Integrated Strategies for Household Food Waste Reduction in Bangkok. *Sustainability* **2021**, *13*(14), 7651. https://doi.org/10.3390/su13147651

[12] Devaraj, L.; Balasubramanian, P. Optimizing the Redistribution of Surplus Food in the Hospitality Sector: A Paradigm Shift through the Implementation of Food Donation Systems for a Sustainable Future. *Sustainability* **2025**, *17*(8), 3556. https://doi.org/10.3390/su17083556

[13] Kattiyapornpong, U.; Ditta-Apichai, M.; Chuntamara, C. Sustainable Food Waste Management Practices: Perspectives from Five-Star Hotels in Thailand. *Sustainability* **2023**, *15*(13), 10213. https://doi.org/10.3390/su151310213

[14] Filimonau, V.; Delysia, A. Food Waste Management in Hospitality Operations: A Critical Review. *Tourism Manag.* **2019**, *71*, 234–245. https://doi.org/10.1016/j.tourman.2018.10.009.

[15] Dolnicar, S.; Demeter, C. Why Targeting Attitudes Often Fails to Elicit Sustainable Tourist Behaviour. *Int. J. Contemp. Hosp. Manag.* **2024**, *36* (3), 730–742. https://doi.org/10.1108/IJCHM-07-2022-0828

[16] Ng, P. Y.; Sia, J. K. M. Managers' Perspectives on Restaurant Food Waste Separation Intention: The Roles of Institutional Pressures and Internal Forces. *Int. J. Hosp. Manag.* **2023**, *108*, 103362. https://doi.org/10.1016/j.ijhm.2022.103362

[17] World Bank Group. *Thailand Economic Monitor: Unlocking the Growth Potential of Secondary Cities*; World Bank: Bangkok, 2024. https://documents1.worldbank.org/curated/en/099062924133030977/pdf/P50100914f725005f1b9211803e7e17020a.pdf (accessed October 8, 2025).

[18] Giordano, C.; Falasconi, L.; Cicatiello, C.; Pancino, B. The Role of Food Waste Hierarchy in Addressing Policy and Research: A Comparative Analysis. *J. Clean. Prod.* **2020**, *252*, 119617. https://doi.org/10.1016/j.jclepro.2019.119617

[19] Srimachai, T.; Yodkruea, W.; Chuchuang, N.; Chumdaeng, S.; Suankaew, P.; Chobbun, S.; Phuket, K. R. N. Innovative Prototype of Zero-Waste Food Production System to Support Integrated Farming. *ASEAN J. Sci. Technol. Rep.* **2025**, *28*(2), e255925. https://doi.org/10.55164/ajstr.v28i2.255925

[20] Department of Business Development. *List of Restaurants in Phuket, Krabi, Phang Nga, Satun, and Trang* (in Thai); 2023. https://datawarehouse.dbd.go.th/index (accessed August 18, 2025).

[21] Food and Agriculture Organization of the United Nations (FAO). *Global Food Losses and Food Waste – Extent, Causes and Prevention*; FAO: Rome, 2011. https://www.fao.org/3/i2697e/i2697e.pdf (accessed August 30, 2025).

[22] Gover, M.; Swannell, R.; Reynolds, C. Addressing the Food Loss and Waste Challenge—A WRAP Perspective. In *Proceedings of the Workshop Food Loss and Waste Reduction*; von Braun, J., Ed.; Scripta Varia 147; The Pontifical Academy of Sciences: Vatican City, 2020.

[23] Pirani, S.; Arafat, H. Solid Waste Management in the Hospitality Industry: A Review. *J. Environ. Manag.* **2014**, *146*, 320–336. https://doi.org/10.1016/j.jenvman.2014.07.038

[24] Zhang, C.; Hu, M.; Di Maio, F.; Sprecher, B.; Yang, X.; Tukker, A. An Overview of the Waste Hierarchy Framework for Analyzing the Circularity in Construction and Demolition Waste Management in Europe. *Sci. Total Environ.* **2022**, *803*, 149892. https://doi.org/10.1016/j.scitotenv.2021.149892

[25] Srijuntrapun, P.; Ket-um, P.; Attavanich, W. Socio-Demographic Drivers of Household Food Waste Management Practices in Thailand. *PLoS ONE* **2025**, *20*(4), e0321054. https://doi.org/10.1371/journal.pone.0321054

[26] Zhu, Q.; Liu, P. Integrating TRA and SET to Influence Food Waste Reduction in Buffet-Style Restaurants: A Gender-Specific Study. *Sustainability* **2024**, *16*(20), 8999. https://doi.org/10.3390/su16208999

[27] Zhao, J.; Song, Q.; Yuan, X. Awareness of Food Waste Recycling in Restaurants: Evidence from China. *J. Clean. Prod.* **2020**, *244*, 118690. https://doi.org/10.1016/j.jclepro.2019.118690

[28] Fatemi, S. F.; Eini-Zinab, H.; Manafi Anari, F.; Amirolad, M.; Babaei, Z.; Sobhani, S. R. Food Waste Reduction and Its Environmental Consequences: A Quasi-Experimental Study in a Campus Canteen. *Agric. Food Secur.* **2024**, *13*(1), 37–46. https://doi.org/10.1186/s40066-024-00488-y

[29] Schrank, J.; Hanchai, A.; Thongsalab, S.; Sawaddee, N.; Chanrattanagorn, K.; Ketkaew, C. Factors of Food Waste Reduction Underlying the Extended Theory of Planned Behavior: A Study of Consumer Behavior towards the Intention to Reduce Food Waste. *Resources* **2023**, *12*, 93. https://doi.org/10.3390/resources12080093

[30] Uzoma, C. M.; Ugboaja, N. B.; Uwugiaren, N. J. Evaluating Strategies for Reducing Food Waste and Its Influence on Public Health Outcomes. *Int. J. Biol. Pharm. Sci. Arch.* **2024**, *8*(2), 54–62. https://doi.org/10.53771/ijbpsa.2024.8.2.0086

[31] Intarathaworn, S. A Study of Behavior and Measures for Interventions Reducing Food Waste of Households in Bangkok (in Thai). *J. Humanit. Soc. Sci. Sustain. Dev.* **2024**, *7*(1), 106–115.

[32] Secondi, L.; Principato, L.; Laureti, T. Household Food Waste Behaviour in EU-27 Countries: A Multilevel Analysis. *Food Policy* **2015**, *56*, 25–40. https://doi.org/10.1016/j.foodpol.2015.07.007

[33] Stancu, V.; Haugaard, P.; Lähteenmäki, L. Determinants of Consumer Food Waste Behaviour: Two Routes to Food Waste. *Appetite* **2016**, *96*, 7–17. https://doi.org/10.1016/j.appet.2015.08.025

[34] Visschers, V. H. M.; Wickli, N.; Siegrist, M. Sorting Out Food Waste Behaviour: A Survey on the Motivators and Barriers of Self-Reported Amounts of Food Waste in Households. *J. Environ. Psychol.* **2016**, *45*, 66–78. https://doi.org/10.1016/j.jenvp.2015.11.007

[35] Lang, L.; Wang, Y.; Chen, X.; Zhang, Z.; Yang, N.; Xue, B.; Han, W.; Wang, Y. Awareness of Food Waste Recycling in Restaurants: Evidence from China. *Resour. Conserv. Recycl.* **2020**, *161*, 104949. https://doi.org/10.1016/j.resconrec.2020.104949

[36] Hayeebueraheng, S.; Phanthuwongpakdee, N. From Excess to Efficiency: Managing Food Waste at Buffet Restaurant in Thailand. *Creat. Bus. Sustain. J.* **2024**, *46*(2), 83–102. https://doi.org/10.58837/CHULA.CBSJ.46.2.5

[37] Markphan, W.; Nuengmatcha, P.; Markphan, P.; Roongtawanreongsri, S. The Knowledge, Understanding and Waste Management Behavior of Population in the Area of Trang Municipality, Trang Province (in Thai). *ASEAN J. Sci. Technol. Rep.* **2018**, *21*(1), 79–87.

[38] Lévesque, J.; Godin, L.; Perreault, V.; Mikhaylin, S. Identifying the Factors Affecting the Implementation of Food Waste Reduction Strategies in Independent Restaurants: Moving Towards Eco-Efficiency. *J. Clean. Prod.* **2024,** 440, 140765. https://doi.org/10.1016/j.jclepro.2024.140765

[39] Hjorth, P. G.; Boklund, T. I.; Christmas, J.; Henriksen, C.; Mielke, A.; Kubiak, M. A. Preventing Food Waste: Forecasting the Number of Meals for Canteen Kitchens (working paper), 2024. https://doi.org/10.33774/miir-2024-tlrjq (accessed August 30, 2025).

[40] Östergren, K.; Backlund, E. A Model for Cutting Food Waste in Municipal Kitchens: The Gothenburg Case Study. *Adv. Food Secur. Sustain.* **2019**, *4*, 193–218. https://doi.org/10.1016/bs.af2s.2019.07.002

[41] Singh, B.; Jermsittiparsert, K. Reducing Global Food Wastage and Nurturing Sustainable Future. In *Sustainable Development, Humanities, and Social Sciences for Society 5.0*; Wongmahesak, K.; Wekke, I. S.;

Suanpang, P., Eds.; IGI Global Scientific Publishing: Hershey, PA, 2024; pp 455–474. https://doi.org/10.4018/979-8-3693-7989-9.ch022

[42] Huang, Y.; Hall, C. M.; Chen, N. The Sustainability Characteristics of Michelin Green Star Restaurants. *J. Foodserv. Bus. Res.* **2023**, *28*(2), 219–244. https://doi.org/10.1080/15378020.2023.2235258

[43] [43] Garcia-Garcia, G.; Woolley, E.; Rahimifard, S.; Colwill, J.; White, R.; Needham, L. A Methodology for Sustainable Management of Food Waste. *Waste Biomass Valorization* **2017**, *8*(6), 2209–2227. https://doi.org/10.1007/s12649-016-9720-0

[44] Howe, N.; Strauss, W. *Millennials Rising: The Next Great Generation*; Vintage Books: New York, 2009.

[45] Lu, M.-Y.; Ko, W.-H. Sustainable Preparation Behavior for Kitchen Staff in Order to Limit Food Waste. *Foods* **2023**, *12*(16), 3028. https://doi.org/10.3390/foods12163028

[46] Wilts, H.; Schinkel, J.; Koop, C. Effectiveness and Efficiency of Food-Waste Prevention Policies, Circular Economy, and Food Industry. In *Food Waste Reduction and Prevention*; Academic Press, 2020; pp 19–35. https://doi.org/10.1016/B978-0-12-817121-9.00002-4

[47] Ministry of Tourism and Sports. *Domestic and International Tourism Statistics 2024–2025*; Tourism Intelligence Center, 2025. https://www.mots.go.th (accessed February 17, 2026).

[48] Papargyropoulou, E.; Lozano, R.; Steinberger, J. K.; Wright, N.; Bin Ujang, Z. The Food Waste Hierarchy as a Framework for the Management of Food Surplus and Food Waste. *J. Clean. Prod.* **2014**, *76*, 106–115. https://doi.org/10.1016/j.jclepro.2014.04.020

[49] Srijuntrapun, P.; Sukwong, P.; Marshall, A. The Role of Food Waste Hierarchy as Thai Hotels Seek to Fulfill Their Corporate Social Responsibility. *Heliyon* **2022**, *8*(1), e11201. https://doi.org/10.1016/j.heliyon.2022.e11201

[50] Tomaszewska, M.; Bilska, B.; Tul-Krzyszczuk, A.; Kołożyn-Krajewska, D. Sustainable Food Waste Management in Food Service Establishments in Relation to Unserved Dishes. *Sustainability* **2024**, *16*, 6631. https://doi.org/10.3390/su16156631

[51] *Public Health Act, B.E. 2535 (1992)*; Royal Gazette, Vol. 109, Part 38, p 27, 1992. Open Development Thailand. https://opendevelopmentthailand.net (accessed February 19, 2026).

[52] Goossens, Y.; Kuntscher, M.; Lehn, F.; Schmidt, T. *Sustainability Assessment of Food Waste Reduction Measures*; Thünen-Institut, 2021. https://doi.org/10.3220/PB1626851783000

[53] Lu, M.-Y.; Ko, W.-H. Sustainable Preparation Behavior for Kitchen Staff in Order to Limit Food Waste. *Foods* **2023**, *12*(16), 3028. https://doi.org/10.3390/foods12163028

[54] Krejcie, R. V.; Morgan, D. W. Determining Sample Size for Research Activities. *Educ. Psychol. Meas.* **1970**, *30*(3), 607–610. https://doi.org/10.1177/001316447003000308

ASEAN
Journal of Scientific and Technological Reports
Online ISSN:2773-8752

Research article

Comparative Analysis of Rubberwood, Plywood, and Wood-Plastic Composites for Safe Elderly Toy Applications

Pruttipong Pantamanatsopa[1], Chainarong Srivabut[1*], Chatree Homkhiew[1], Worapong Boonchouytan[1], Surasit Rawangwong[1], and Apichon Thongmung Kamnerdwam[1]

[1] Faculty of Engineering, Rajamangala University of Technology Srivijaya, Songkhla, 90000, Thailand

* Correspondence: chainarong.s@rmutsv.ac.th,

Citation:
Pantamanatsopa, P.; Srivabut, C.; Homkhiew, C.; Boonchouytan, W.; Rawangwong, S.; Kamnerdwam, T.A. Comparative analysis of rubberwood, plywood, and wood-plastic composites for safe elderly toy applications. *ASEAN J. Sci. Tech. Report.* **2026**, *29*(4), e260685. https://doi.org/10.55164/ajstr.v29i4.260685

Article history:
Received: August 4, 2025
Revised: February 6, 2026
Accepted: March 8, 2026
Available online: March 25, 2026

Publisher's Note:
This article is published and distributed under the terms of the Thaksin University

Abstract: The objective of this research was to produce toy products for the elderly to develop the potential in various areas of the elderly. Different types of wood materials, namely rubberwood sawn timber, plywood, and wood-plastic composites, were evaluated for their performance based on mechanical, physical, and chemical properties. Samples were compressed using a compression molding machine. The experimental results were analyzed by Analysis of Variance (ANOVA). The findings showed that all mechanical properties of the elderly toy products manufactured from rubberwood (RW) had higher strength values than those of plywood (PW) and wood-plastic composites (WPCs). The lowest water absorption and thickness swelling values of 4.36% and 2.01%, respectively, were observed in elderlytoy products manufactured from WPCs. In contrast, the minimum Ra value of 1.45 μm was observed. Additionally, the results showed that the three types of materials contain heavy metal content that does not exceed the specified standards, indicating that this product is safe for the elderly. Finally, the elderly toy products made from WPCs showed smooth surfaces, greater agglomeration, and fewer pores and voids, due to the strong interfacial adhesion between the plastic matrix and the rubberwood fiber reinforcement.

Keywords: Comparative analysis; mechanical properties; plywood; wood-plastic composites (WPCs); elderly's toys

1. Introduction

Many concepts about the use of toys and games to develop cognitive, psychosocial, motor, emotional, and linguistic skills play a very important role in children's and elderly people's lives [1, 2]. These toys contribute to the development of elderly's performance while nurturing their natural development and growth. It also plays a key role in fostering self-confidence, creativity, and happiness among the elderly [3]. However, playing with toys enhances attention span, memory, and learning, and the elderly willingly participate, while toys are tools they use while performing these actions. The toys offer many ways to play with them, leaving the elderly in charge; imagine, for example, an experiment as they play [4, 5]. The toys have so many functions; in a sense, they are a right for the elderly, and they must be supported. In particular, open-ended toys can encourage imagination and strengthen many areas of natural development, including communication, creativity, motor skills, and problem-solving [6, 7]. Additionally, the provision of areas for elderly people to engage in activities is important, and safety is essential for reducing the risk of accidents related to toys [2, 8]. These are all health-care components; especially, they should take an active role in ensuring that these processes, which are the most excellent parts of elderly care, are healthy and safe.

Toys and activity-based tools designed for elderly users are gaining recognition for their role in rehabilitation, cognitive stimulation, and leisure, particularly within institutional care settings. In contrast to children, elderly individuals commonly experience reduced grip strength, decreased mobility, sensory impairment, and heightened susceptibility to injury, necessitating distinct and carefully considered design approaches. When produced from wood, such products must reconcile the material's natural and sensory advantages with stringent safety and performance requirements [2]. Ergonomic grip design, appropriate weight and balance, and ease of manipulation are critical factors in minimizing physical strain and fatigue. Furthermore, hygiene represents a significant concern in shared care environments, as untreated wooden surfaces may retain moisture and support microbial growth. Consequently, material selection, surface finishing, and construction techniques play a pivotal role in ensuring product safety, durability, and usability. A comprehensive understanding of these requirements is therefore essential for the effective development of wooden toys intended for elderly users [4, 6].

Among the materials used to produce elderly toys, wooden toys have increased in popularity over recent years due to their simple aesthetic, natural materials, good biodegradability, and greater hygienic properties compared to plastic and metal toys [9,10]. One of the most significant advantages of wooden toys is their staying power. Wood is a natural material with an ageless timestamp [11]. These toys have been in circulation for generations and show no signs of stopping. Generally, plastic toys change with trends and see replacement versions that are bigger and brighter [1, 12]. Also, other materials, such as wood-plastic composites (WPCs), are widely used to produce elderly toys [13, 14], as these materials are biocompatible and biodegradable. It can be made from recycled materials or manufactured from renewable resources [15,16]. In contrast, many plastics contain bisphenol A (BPA), as well as polyvinyl chloride (PVC) and phthalates. In addition to plastic toys not necessarily being the most eco-friendly, the chemical exposure from playing with them is something to consider [16]. Therefore, choose toys made from natural materials, such as solid wood, cloth, paper, or wool. Ideas for plastic-free playthings include games and puzzles made from cardboard or wood, which can be among the best potential development and educational toys [17, 18].

Product design for elderly toys is one of the most significant parts of the manufacturing process. The age group will also tell you what play patterns are appropriate. A toy that is fascinating for the elderly may be of no interest to children. The designer or manufacturer must have experience in developing toy products for older people [6, 16]. Additionally, these toys must foster the development of critical thinking and of emotional, physical, and mental abilities [19, 20]. Also, the toy design is an exciting area of product development where industrial design and elderly psychology are blended. The toys are designed to delight, teach, and inspire curiosity among older people [3, 21]. New toy ideas for the elderly are worth considering, researching, and developing. Engineering product development is the step-by-step process that takes an idea from the concept stage through a working prototype stage to mass production and commercialization [22]. The concept is the management of the entire product design process from ideation and planning to the creation of suitable, high-fidelity designs, ensuring a cohesive, user-centric result, but we need to consider which tool can do the work [23, 24]. Product design tools are processes that help build, visualize, and enhance product models. It can create detailed prototype models for concept development, prototyping, and simulation. These tools frequently include features such as drawing, drafting, analysis, modeling, improvement, and rendering [24]. These features enable designers to seamlessly transition from initial concepts to fully realized designs while maintaining consistency and efficiency [23, 25]. The performance evaluation of the toys, namely mechanical, physical, and thermal properties, is an important part in order to more clearly delineate the formal properties of toys. Product standards determine the prototype depending on each type of use. In addition, safety in use and proper application must be taken into account [26]

Surface coating plays a critical role in the production of toys for the elderly because it directly affects safety, durability, hygiene, and user comfort factors that are particularly important for this age group. As aging is often accompanied by reduced tactile sensitivity, diminished motor control, and increased vulnerability to injury, surface coatings help create smoother, more uniform surfaces that minimize the risk of splinters, abrasions, or sharp edges during handling and use [4,9]. In addition, appropriate surface coatings enhance the durability and longevity of toys by protecting the substrate material from wear, moisture, and

chemical degradation. This protection is especially important for toys used in therapeutic or recreational settings, where frequent handling and cleaning are required. Coatings that provide resistance to water, stains, and microbial growth contribute to improved hygiene and help reduce the risk of infection among elderly users [8,11]. Surface coatings also influence the tactile and visual properties of toys, such as texture, warmth, and color stability, thereby enhancing user engagement and sensory stimulation. Non-toxic, low-emission coatings are essential to ensure user safety, as elderly individuals may be more sensitive to volatile organic compounds or other harmful substances [10]. Overall, the selection and application of appropriate surface coatings are integral to ensuring that toys for the elderly are safe, functional, durable, and supportive of both physical and cognitive well-being.

Thus, the purpose of this research was to promote the potential development and create new opportunities for senior citizens to learn together and benefit from playing with elderly toy products. Different types of raw materials, such as rubberwood sawn timber, plywood, and wood-plastic composites, are evaluated based on their mechanical, physical, and chemical properties. The best material was selected to produce elderly toy products through engineering product design and development. The experimental results were compared to product standards for wooden toys. This finding is important for the elderly to be part of society as healthy individuals at every stage of their development.

2. Materials and Methods

2.1 Materials

Different types of wood-based products, namely rubberwood sawn timber (RW), plywood (PW), and wood-plastic composites (WPCs), were selected for the manufacturing of elderly toy prototypes. These materials are produced from natural materials, are environmentally friendly, and are safe for production and use. The surface appearance and physical characteristics of RW, PW, and WPCs are displayed in Figure 1.

In this work, the RW and PW materials were supplied from the Geefin Rubber Tech Co., Ltd. (Songkhla, Thailand). The PW from rubberwood veneer is produced by selecting mature rubberwood logs and conditioning them through steaming or soaking. The logs are rotary-peeled into thin veneers, which are then dried and graded to remove defects. The veneers are arranged in cross-laminated layers to enhance strength and stability. Adhesive is applied between the layers, and the assembly is hot-pressed under controlled conditions. After pressing, the panels are trimmed and sanded to obtain a smooth, uniform PW surface. The density was targeted for RW and PW at 0.68 and 0.80 g/cm3, respectively, with a 20 mm thickness. Before specimen preparation, in accordance with the testing standards, all samples were conditioned at 20±1 ◦C and 65% RH for at least 24 hours. For the WPC panels, the composites were manufactured from recycled polypropylene (rPP) as matrix and rubberwood sawdust (RWS) as reinforcement. The rPP pellets with a density of 0.83 g/cm^3 and a melt flow index of 0.93 g/10 min at 230 ◦C was supplied from Withaya Intertrade Co., Ltd. (Samut Prakan, Thailand) and were used as a matrix in WPC samples. The RWS, with a density of 100 kg/m3, used as a reinforcement material in WPCs, was obtained from Plan Creations Co., Ltd. (Trang, Thailand). Before compounding, the RWS were crushed and sieved through a standard sieve with a mesh size of 80 (less than 180 μm) and dried in an oven at 110±5 ◦C for 8 hours to remove moisture content (1-2%).

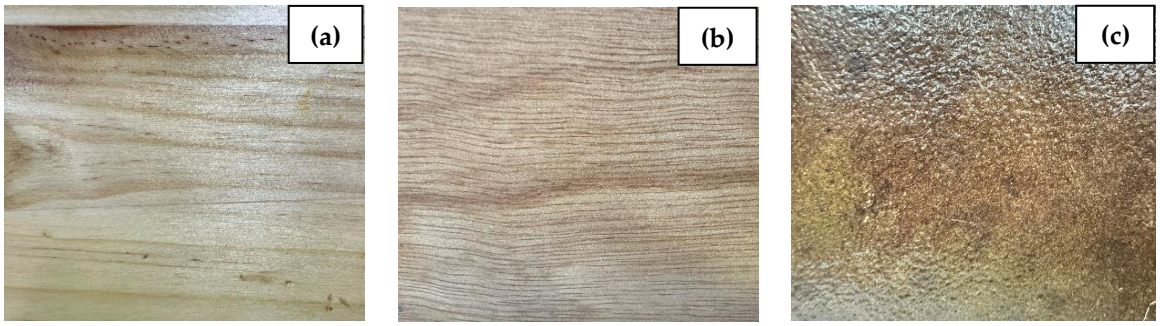


Figure 1. The surface appearances of (a) RW, (b) PW, and (c) WPCs.

2.2 Preparation of the RW, PW, and WPCs samples

The specimens used for all testing were cut in the grain direction from RW and PW, with nominal dimensions of 15 cm (width) × 100 cm (length) × 2 cm (thickness). The WPC samples in this research were produced from two stages. Initially, the WPCs' material was mixed at 60 wt% rPP and 40 wt% RWS. The component ratios, namely rPP and RWS, were compounded uniformly and melt-blended in a twin-screw extruder. The seven temperature zones were set in the range from 175 to 200 ◦C and a screw rotation speed of 50 rpm. The extruded strands were then blown into the air and passed through a cutter, turning them into WPC pellets measuring 3 mm. Subsequently, the WPC pellets were molded in a compression molding machine at 190 ◦C under 870 psi, with 20 min for preheating, compression, and cooling, respectively. The final WPCs panel size was 25 cm (width) × 35 cm (length) × 2 cm (thickness) from a rectangular mold. Finally, all specimens were cut to specific dimensions for mechanical, physical, and thermal tests in accordance with ASTM and JIS standards.

2.3 Surface coating of the RW, PW, and WPCs samples

In this research, the mechanical, physical, and chemical properties were studied under three different conditions. In addition to studying the original wood types, all samples were coated with non-toxic varnish (V) and natural oil (O) by spraying onto the surface of the material. The amount of both Non-toxic varnish and natural oil was standardized across toys. Each coating was applied at approximately 200 g/m², ensuring comparable surface coverage for RW, PW, and WPCs. This uniform application enabled an objective evaluation of the effects of surface treatments on material properties. The coatings were applied using the same method for all specimens. Varnish was applied in two coats by spraying, with light sanding between coats to promote adhesion. Natural oil was applied in two coats by brushing, allowing sufficient absorption into the surface before excess oil was removed. All specimens were coated on all exposed surfaces. After application, coated samples were allowed to cure under controlled ambient conditions (approximately 25 °C). Coated specimens were dried for 1 hr between coats and cured for 3 hrs after the final coat. All samples were fully cured before conducting mechanical, physical, and chemical property tests to ensure stable coating performance. All coating conditions for this study are shown in Table 1.

2.4 Characteristic behavior of the samples

2.4.1 Mechanical properties of samples

The mechanical properties, namely tensile and bending tests, of wood and composite samples were conducted to measure the strength of RW, PW, and WPCs using a Mechanical Universal Testing Machine, Model NRI-TS500-50, from Narin Instrument Co., Ltd. (Samut Prakan, Thailand). The details draw the following conditions of each testing type based on the ASTM standard:

Tensile test

The tensile properties of RW and PW were carried out in accordance with ASTM D143 standards. The tension parallel was applied with a load cell of 5 kN and a crosshead speed of 5 mm/min. The specimen dimensions for the tensile test were 2 cm (width) × 7 cm (length) × 2 cm (thickness). For WPC testing, the tensile test was carried out in accordance with ASTM D638 at a crosshead speed of 5 mm/min. Five replications of each formulation were tested at 25 ◦C for all specimens, and their tensile average values were reported.

Bending test

The three-point bending test of RW and PW was performed according to BS 373 standards, with a crosshead speed of 2 mm/min and a span of 300 mm. The nominal dimension of rubberwood lumber was 2 cm (width) × 7 cm (length) × 2 cm (thickness). For WPC testing, the specimens were tested in accordance with ASTM D790. The composite samples were conditioned with a crosshead speed of 2 mm/min and a span of 80 mm. The specimens were prepared with a nominal size of 100 mm (width) × 13 mm (length) × 6 mm (thickness). All tests were conducted at 25 ◦C, with five replications for each composition.

2.4.2 Physical properties of samples

Water absorption and thickness swelling tests

The water absorption and thickness swelling of the RW, PW, and WPC samples were measured according to ASTM D570. The nominal dimensions of 2 cm (width) × 4 cm (length) × 2 cm (thickness) were cut from the rubberwood sawn timber and conditioned at 20±1 ◦C for 24 h. to remove the moisture content (less than 5%). Five replications of the samples were soaked in distilled water for 2 and 24 hours. with a depth of immersion from the samples to the water surface of about 2.54 cm. Initially, the rubberwood lumber specimens were weighed and measured before soaking in water, and their average values were reported. Subsequently, the specimens were periodically removed from the water, dried with tissue paper on the rubberwood surfaces, reweighed, and remeasured at room temperature (25 ◦C), and immediately returned to the water. For the TS test, the measurements were taken at three locations on each sample: 3 mm from the top and bottom edges, and at the center. The water absorption and thickness swelling of RW, PW, and WPCs samples were calculated according to the following Eqs. (1) and (2):

$$WA_t(\%) = \frac{W_t - W_0}{W_0} \times 100 \quad (1)$$

where WA is the water absorption in percentage, and W_0 and W_t are the sample weights before and after immersion (g).

$$TS_t(\%) = \frac{T_t - T_0}{T_0} \times 100 \quad (2)$$

where TS is the thickness swelling in percentage, and T_o and T_t are the sample thickness before and after immersion (mm).

Density test

The density of different wood types depends on the weight and volume of the materials. The specimens with dimensions of 2 cm (width) × 2 cm (length) × 2 cm (thickness) were cut from the samples and weighed at room temperature (25 ◦C). Five replications were measured in each condition. All samples were conditioned at 50 ± 2 °C and 10% RH before density testing. The density of the RW, PW, and WPCs samples was calculated according to the following Eqs. (3):

$$\rho = \frac{\mathrm{m}}{\mathrm{V}} \quad (3)$$

where ρ is the density of materials, m is the mass of materials, and V is the volume of materials

Surface roughness test

The surface quality of the RW, PW, and WPC samples was determined by surface roughness measurement using a Portable Surface Roughness Measurement Tool (Model SJ-210) from Mitutoyo Co., Ltd. (Bangkok, Thailand). Two roughness parameters, namely average roughness (Ra) and mean peak-to-valley height (Rz), were considered to evaluate the surface characteristics of the samples. Nominal dimensions of 3 cm (width) × 3 cm (length) × 2 cm (thickness) were measured at five replications under a room temperature (25 ◦C). All data for Ra and Rz were obtained from the digital information. The experimental results were

analyzed for the effects of wood type using a one-way ANOVA, specifically for Ra and Rz responses. Before the physical test, all samples manufactured from RW, PW, and WPC were dried in a convection oven at 50±2 ◦C for 24 hours to reduce moisture content.

2.4.3 Chemical properties of samples

The toy materials, namely RW, PW, and WPCs were analyzed the 8 heavy metal content such as Antimony (Sb), Arsenic (As), Barium (Ba), Cadmium (Cd), Chromium (Cr), Lead (Pb), Mercury (Hg), Selenium (Se), respectively, the heavy metal elements were determined by national children's toys standard according to ASTM F 963-23 and EN71-3. Additionally, the results were compared with children's toys after the toy materials were coated with various paints or coatings, which is mainly due to the heavy metal compounds contained in the paint pigments. All of the samples weighed approximately 30 to 50 mg. The experimental condition was produced at a room temperature (25 ◦C).

2.4.4 Morphological observation of samples

A Field Emission Scanning Electron Microscope (FEI Apreo, FEI Company, Oregon, USA) was used to observe voids, cracks, dispersion, and interfacial bonding in the RW, PW, and WPC materials. Before the FE-SEM observation, the sample surface area was coated with gold to prevent electrical charging during imaging. The FE-SEM images were taken at an accelerating voltage of 20 kV with magnifications of 100× and 500×.

Table 1. The mechanical properties analysis of the RW, PW, and WPC samples.

Types of Materials	Tensile test (MPa)	Bending test (MPa)
RW	22.23 (1.23)	73.85 (1.89)
RW (V)	25.56 (1.54)	76.21 (0.96)
RW (O)	24.01 (1.23)	74.22 (1.35)
p-value	*< 0.001**	*< 0.001**
PW	20.89 (2.01)	62.14 (2.52)
PW (V)	23.56 (1.52)	66.20 (1.57)
PW (O)	21.05 (1.52)	64.20 (1.88)
p-value	*< 0.001**	*< 0.001**
WPCs	18.91 (1.14)	42.56 (1.14)
WPCs (V)	20.89 (1.10)	44.90 (0.62)
WPCs (O)	19.44 (0.94)	44.01 (1.10)
p-value	*< 0.001**	*< 0.001**

Note: **Mean within each property is significant (p<0.05)*

3. Results and Discussion

3.1 Mechanical properties analysis

The mechanical properties of the RW, PW, and WPC samples were evaluated through tensile and bending tests before producing the elderly' s toy. The experimental results were statistically analyzed using five samples per mechanical test at the 5% significance level ($\alpha = 0.05$) [15,18]. The ANOVA analysis revealed significant differences in the properties of samples with various wood types.

3.1.1 Tensile strength analysis

Owing to the widespread application of toys produced from RW, PW, and WPCs, the tensile properties are of great importance. The average values of the tensile strengths are displayed in Table 1. The experimental results show clearly that the three wood types (RW, PW, and WPCs) under three conditions, namely untreated (control sample), non-toxic varnishes (V), and natural oil (O), significantly ($p < 0.05$) affected the tensile strength of the samples. It is first necessary to evaluate the uncoated wood surface samples. Specimens made from RW had higher tensile strength than the samples. The ultimate tensile strength of RW was 22.23 MPa, which was also greater than that of PW (20.89 MPa) and WPCs (18.91 MPa). This may be due to the parallel-to-grain test; it was found that the sample had strength and excellent grain adhesion [16,19]. Previous studies have shown that the strength tested in the direction parallel to the grain was substantially

higher than that tested perpendicular to the grain [7,9]. On the other hand, increasing the number of layers for PW increases the number of interfaces. Load is redistributed across more grain directions and more adhesive bondlines; therefore, tensile-strength concentrations in any single veneer are reduced.

For the RW samples, the application of non-toxic varnish coating yielded the highest tensile strength of 25.56 MPa, corresponding to a 15.0% increase relative to the uncoated RW (22.23 MPa). The natural oil coating also enhanced the tensile strength to 24.01 MPa, representing an 8.0% improvement over the control. Similarly, in the case of PW, treatment with non-toxic varnish) increased the tensile strength from 20.89 to 23.56 MPa, reflecting a 12.8% enhancement, while the natural oil coating resulted in a slight improvement to 21.05 MPa. Furthermore, the WPCs coated with non-toxic varnish showed the greatest improvement, with tensile strength increasing from 18.91 to 20.89 MPa, a 10.5% increase. The application of natural oil to WPCs also increased the tensile strength to 19.44 MPa, a 2.8% gain over the uncoated sample. Different types of RW, PW, and WPCs based on tensile strength are compared in Figure 2.

The results demonstrate that coating RW, PW, and WPCs with non-toxic varnish and natural oil led to a measurable improvement in tensile strength compared with uncoated samples. The RW showed the most pronounced increase, likely due to effective oil penetration and enhanced fiber cohesion, which reduced microcrack formation under tensile loading. PW also exhibited improved tensile strength, suggesting that the coating helped stabilize veneer layers and maintain adhesive bond integrity by limiting moisture-induced stresses. In WPCs, the strength enhancement was more moderate but consistent, indicating improved interfacial bonding and stress transfer between the wood filler and polymer matrix. Overall, the coatings reduced surface defects and moisture sensitivity, enabling more uniform load distribution. These findings confirm that environmentally friendly surface treatments can effectively enhance tensile performance across different wood-based materials.

Additionally, these findings confirm the superior performance of non-toxic varnish coatings in enhancing tensile strength across all material types evaluated for elderly toy applications. The observed improvements were statistically significant ($p < 0.05$), supporting the efficacy of both coating methods, with non-toxic varnish demonstrating the most pronounced effect. Additionally, the consistently low standard deviations across measurements indicate high reliability and reproducibility of the results.

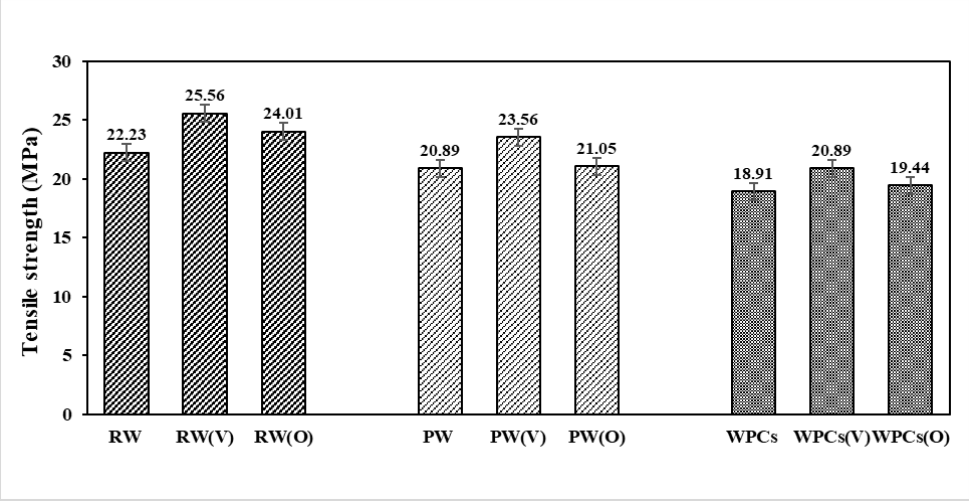


Figure 2. The tensile strength of RW, PW, and WPCs consists of original wood types and wood coated with non-toxic varnishes (V) and natural oil (O)

3.1.2 Bending strength analysis

Three-point bending tests were used to evaluate the strength values of uncoated RW, PW, and WPC samples and of coated surfaces using non-toxic varnishes and natural oil. Average bending strength and statistical analysis (ANOVA) of samples are shown in Table1. It seems that surface coating of the wood panels significantly ($p < 0.05$) improved the bending strength of the specimens. Compared to RW, PW, and WPCs uncoated the surface, the highest bending strength of RW samples was 73.85, followed by the PW and WPCs

values of 62.14 MPa and 42.56 MPa, respectively. This experiment's results agree with Gao et al. (2019), who reported that the product manufactured from wood had the highest average compression strength compared to plywood and wood composites. However, the results show that the bending strength of RW was similar to that of tensile property [27, 28].

As shown in Figure 3, the samples RW, PW, and WPCs coated with non-toxic varnishes and natural oil as a constituent showed higher bending strength. The RW exhibited the highest bending strength among all tested materials, with an average untreated value of 73.85 MPa. Surface treatment with non-toxic varnish (V) significantly increased the bending strength to 76.21 MPa, reflecting a 3.2% improvement, while natural oil treatment (O) produced a more modest enhancement to 74.22 MPa (0.5% increase). The superior performance of the varnish treatment may be attributed to its enhanced surface hardening and moisture-barrier properties, which likely mitigate microcrack propagation under loading conditions. In comparison, the PW demonstrated a lower initial bending strength of 62.14 MPa but exhibited substantial gains following surface treatment. The application of varnish raised the bending strength to 66.20 MPa (+6.5%), whereas oil treatment increased it to 64.20 MPa (+3.3%). These enhancements suggest that surface treatments reinforce the plywood's laminar structure by improving interfacial adhesion and reducing sensitivity to inherent defects. Furthermore, the WPCs exhibited the lowest baseline bending strength at 42.56 MPa. Nevertheless, similar improvement trends were observed: varnish coating increased the bending strength to 44.90 MPa (+5.5%), while oil coating elevated it to 44.01 MPa (+3.4%). Although WPCs demonstrated lower absolute strength values, the relative improvements following surface treatment indicate that such coatings can effectively compensate for the material's limited internal bonding and matrix cohesion.

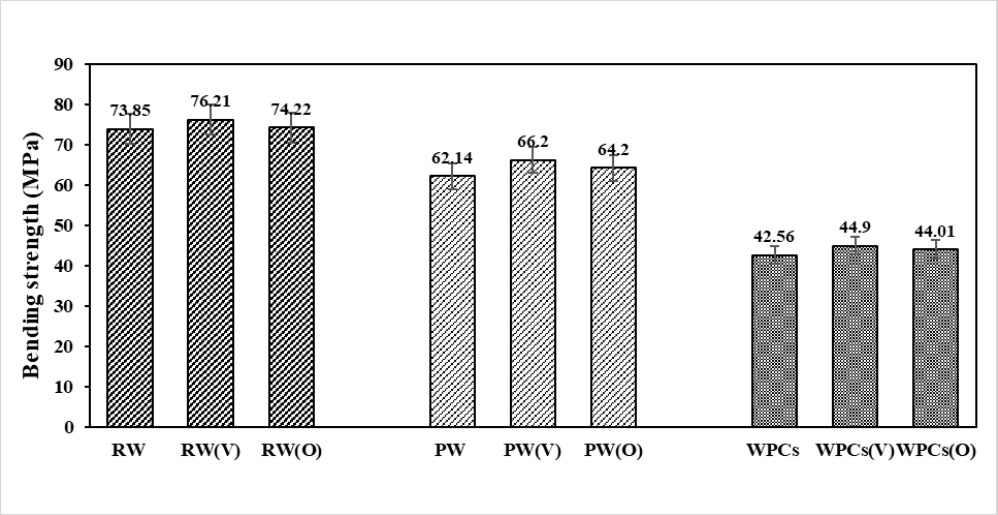


Figure 3. The bending strength of RW, PW, and WPCs consists of original wood types and wood coated with non-toxic varnishes (V) and natural oil (O)

The experimental results showing enhanced bending strength of RW, PW, and WPCs after surface coating with non-toxic varnish and natural oil can be explained by several complementary strengthening mechanisms. Bending performance is highly sensitive to surface integrity because maximum tensile and compressive stresses develop at the outer layers; the applied coatings form a continuous protective film that reduces surface flaws and delays crack initiation under flexural loading. For RW, natural oils penetrate surface pores and cell walls, improving fiber cohesion and reducing moisture-induced swelling and shrinkage, which helps preserve structural continuity during bending. For PW, the coating further stabilizes veneer interfaces and minimizes stress concentration at glue lines. In WPCs, the surface treatment improves interfacial compatibility between wood particles and the polymer matrix near the surface, promoting more effective stress transfer. Additionally, moisture regulation by the coatings reduces long-term degradation and stiffness loss, allowing the materials to sustain higher bending loads before failure [11].

Table 2. The physical properties analysis of the RW, PW, and WPCs samples

Types of Materials	Water Absorption (%)	Thickness Swelling (%)	Density test (g/cm^3)	Surface roughness	
				Ra (μm)	Rz (μm)
RW	7.20 (0.22)	6.56 (0.41)	0.57 (0.01)	4.12 (0.57)	9.77 (0.25)
RW (V)	5.56 (0.39)	3.11 (0.47)	0.61 (0.03)	2.85 (0.91)	7.20 (0.41)
RW (O)	6.98 (0.52)	4.22 (0.55)	0.64 (0.02)	3.45 (0.41)	8.69 (0.66)
p-value	*< 0.001**	*< 0.001**	*0.001**	*< 0.001**	*< 0.001**
PW	8.85 (0.42)	7.25 (0.12)	0.62 (0.02)	5.69 (0.52)	12.89 (0.20)
PW (V)	5.84 (0.75)	4.35 (0.56)	0.65 (0.02)	3.16 (1.22)	10.56 (0.50)
PW (O)	6.44 (0.19)	5.69 (0.51)	0.70 (0.03)	4.12 (0.57)	11.69 (0.41)
p-value	*< 0.001**	*< 0.001**	*0.001**	*< 0.001**	*< 0.001**
WPCs	6.25 (0.19)	5.89 (0.22)	0.80 (0.01)	1.98 (0.21)	4.56 (0.61)
WPCs (V)	4.36 (0.27)	2.01 (0.41)	0.83 (0.02)	1.45 (0.85)	3.96 (0.10)
WPCs (O)	5.85 (0.42)	3.89 (0.74)	0.86 (0.01)	2.01 (0.11)	6.58 (0.27)
p-value	*< 0.001**	*< 0.001**	*0.001**	*0.001**	*< 0.001**

Note: **Mean within each property is significant ($p<0.05$)*

The results underscore the effectiveness of surface treatments, particularly non-toxic varnish, in enhancing the bending strength of wood-based materials. The RW exhibited the highest absolute bending strength, affirming its suitability for elderly toy applications. Although the PW and WPCs demonstrated comparatively lower baseline strengths, both materials showed notable improvements following surface treatment [5, 16]. These enhancements suggest that such treatments may broaden their applicability in contexts that require greater mechanical resilience, including the development of elderly-friendly toys and sustainable furniture designs.

3.2 Physical properties analysis

The physical properties are an important part of evaluating the performance of an elderly person's toy. The responses, namely water absorption, thickness swelling, and surface roughness, are investigated. All experimental results were analyzed using analysis of variance (ANOVA) [18,27]. These physical results make them suitable for product design involving products with toys, especially elderly toys. Thus, it is important to consider this factor when using it in specific applications [28].

3.2.1 Water absorption (WA) and thickness swelling (TS) analysis

Water absorption and thickness swelling are critical indicators of dimensional stability and durability in hygroscopic environments, especially for materials intended for elderly toy applications. Table 2 summarizes the WA and TS values of untreated and treated wood-based composites, including sawn timber (RW), plywood (PW), and wood-plastic composites (WPCs). All treatments significantly affected both parameters ($p < 0.05$), indicating the efficacy of surface protection methods. The WA and TS with different wood and surface coatings are displayed in Figure 4 (a) and (b). Untreated RW exhibited water absorption of 7.20% and thickness swelling of 6.56%, reflecting its porous structure and high moisture uptake. Varnish treatment (RW(V)) significantly reduced WA to 5.56% and TS to 3.11%, representing a 22.8% and 52.6% decrease, respectively, compared to the control. Similarly, oil-treated samples (RW(O)) showed moderate improvements, with WA reduced to 6.98% and TS to 4.22%. The pronounced reduction in TS under varnish treatment highlights the sealing effect of polymeric coatings, which inhibit water ingress into cellular voids and limit dimensional changes. PW displayed the highest baseline water absorption (8.85%) and TS (7.25%) among all material types, likely due to adhesive interfaces and layered grain orientation that promote capillary pathways. Upon varnish treatment (PW(V)), WA dropped significantly to 5.84% and TS to 4.35%, yielding reductions of 34.0% and 40.0%, respectively. Oil treatment (PW(O)) also improved WA and TS, reducing them to 6.44% and 5.69%, respectively. These results suggest that although both surface modifications enhance water resistance, varnish remains more effective in limiting both water uptake and dimensional instability due to its continuous film formation across the surface. WPCs exhibited inherently lower water affinity due to the

hydrophobic nature of thermoplastic matrices, with baseline WA and TS values of 6.25% and 5.89%, respectively. After varnish treatment (WPCs(V)), WA further decreased to 4.36%, and TS decreased to 2.01%, corresponding to reductions of 30.2% and 65.9%, respectively. Oil-treated WPCs (WPCs(O)) recorded WA of 5.85% and TS of 3.89%, showing modest yet notable improvements. The relatively low untreated TS value indicates inherent dimensional stability, which is significantly bolstered by surface sealing, especially with varnish. The data support the conclusion that polymer-based coatings synergize well with composite matrices to suppress moisture-induced expansion further. All sample groups demonstrated statistically significant improvements in both WA and TS upon treatment ($p = < 0.001$), affirming the efficacy of protective coatings. Varnish consistently outperformed oil in minimizing water-related degradation across all material types. The highest performance was observed in WPCs(V), which achieved the lowest TS of 2.01%, indicating exceptional dimensional resilience. Conversely, untreated PW exhibited the poorest moisture resistance, underscoring the need for protective strategies in layered wood products.

Moisture-induced dimensional instability can pose significant safety concerns for wooden toys for the elderly, including surface splintering, warping, and microbial growth in moist conditions. The findings of this study indicate that WPCs treated with varnish (WPCs(V)) offer the most stable, moisture-resistant option, making them ideally suited for environments with variable humidity. Varnished sawn timber (RW(V)) and plywood (PW(V)) also performed well, though the inherently hygroscopic nature of natural wood requires careful material selection and treatment optimization. Additionally, the choice between natural and composite materials should consider not only mechanical and acoustic performance (as discussed elsewhere in the paper) but also hygrothermal performance, particularly in elderly care facilities, where product durability and hygiene are paramount [14, 18].

3.2.2 Density analysis

Density is a fundamental physical property that influences a material's mechanical performance, moisture resistance, dimensional stability, and acoustic response, factors critical for elderly toy applications. Table 2 presents the density values of untreated and treated specimens of sawn timber (RW), plywood (PW), and wood-plastic composites (WPCs). Surface treatments with varnish and oil consistently increased density across all material types, with statistically significant differences ($p = 0.001$).

The untreated RW exhibited a baseline density of 0.57 g/cm³, consistent with typical values for lightweight tropical hardwoods. Upon application of varnish (RW(V)), density increased to 0.61 g/cm³, while oil treatment (RW(O)) yielded an even higher density of 0.64 g/cm³, a 12.3% increase over the untreated sample. The density increment is attributable to surface impregnation and pore-filling by finishing agents, which partially saturate the wood's cellular voids. Oil, being more penetrative, likely infiltrated deeper into the lumens and middle lamella, resulting in higher overall mass per volume. These enhancements indicate improved structural compactness, which correlates with greater dimensional stability and resistance to mechanical fatigue, both of which are essential for safe, long-lasting toy use. Plywood samples demonstrated a higher baseline density (0.62 g/cm³) than RW, reflecting their layered veneer configuration and adhesive content. Varnish-treated PW (PW(V)) reached 0.65 g/cm³, while oil-treated PW (PW(O)) showed a substantial increase to 0.70 g/cm³, representing a 12.9% improvement over the untreated variant. The significant density increase in PW(O) may be due to oil penetrating through glue lines and inter-veneer gaps, where it adds mass without significant volumetric expansion. This is due to PW being a laminated composite in which adjacent veneers are bonded by adhesive layers that are not completely impermeable. Micro-voids, capillaries, and discontinuities naturally exist within glue lines due to adhesive shrinkage, incomplete wetting, or pressing conditions. These features act as preferential pathways for oil ingress []. This densification is advantageous for toy durability, as it enhances impact resistance and load-bearing capacity while also improving surface smoothness and splinter resistance, thereby enhancing user safety for elderly individuals. WPCs had the highest intrinsic density (0.80 g/cm³) among all tested materials due to the presence of polymer matrices (e.g., polyethylene or polypropylene) and uniformly distributed wood particles. Surface treatments further improved this value to 0.83 g/cm³ (WPCs(V)) and 0.86 g/cm³ (WPCs(O)). The 7.5% increase in density post-oil treatment suggests not only surface adherence but also limited penetration into voids between wood fibers and polymer domains, despite the composite's generally low porosity. The resulting densified surface layer

enhances the moisture barrier properties and abrasion resistance, making WPCs highly favorable for hygienic, durable toy products where surface integrity and long-term cleanliness are crucial.

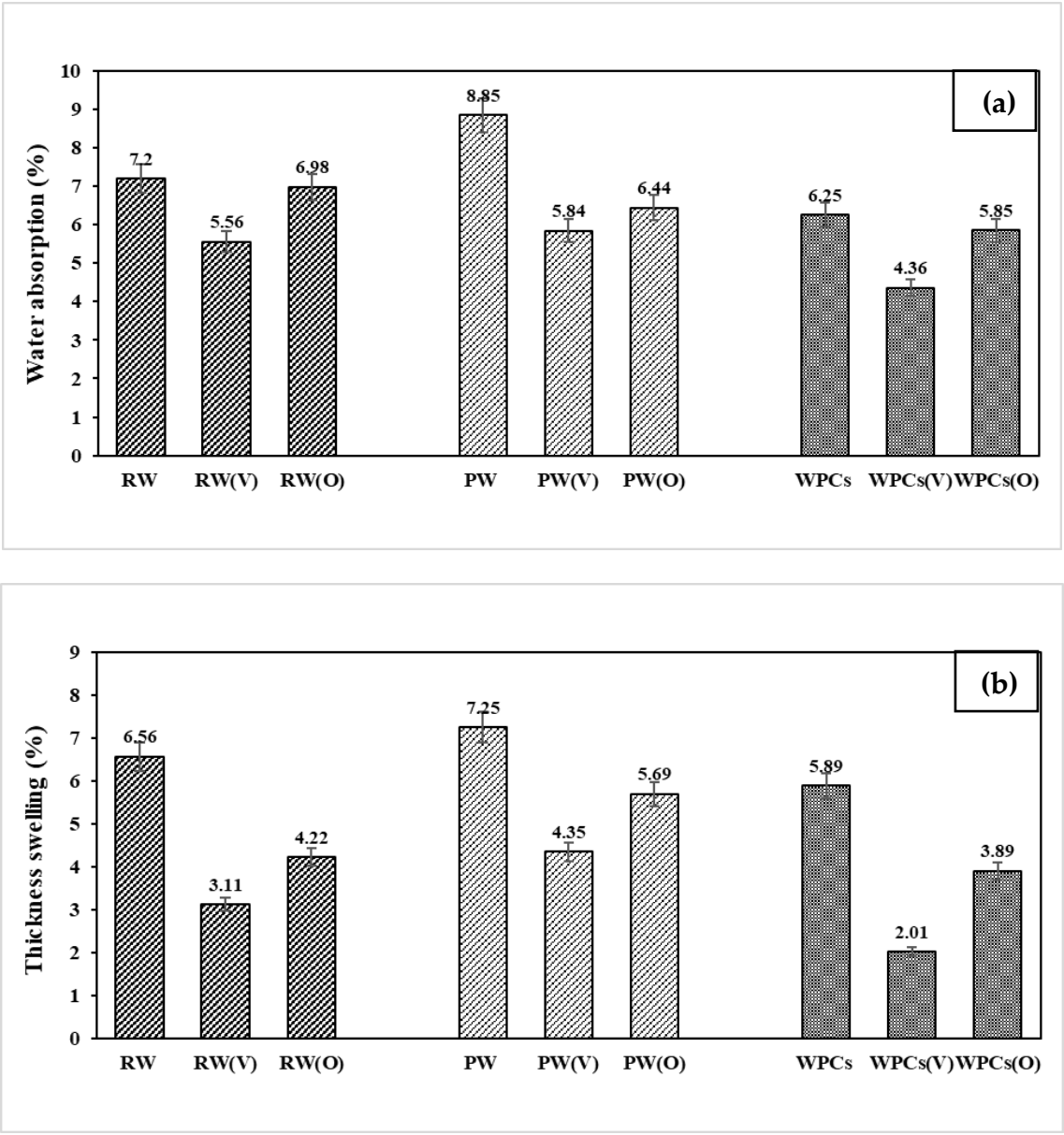


Figure 4. Effect of wood types with uncoated and coated surfaces of RW, PW, and WPCs samples: (a) water absorption and (b) thickness swelling properties.

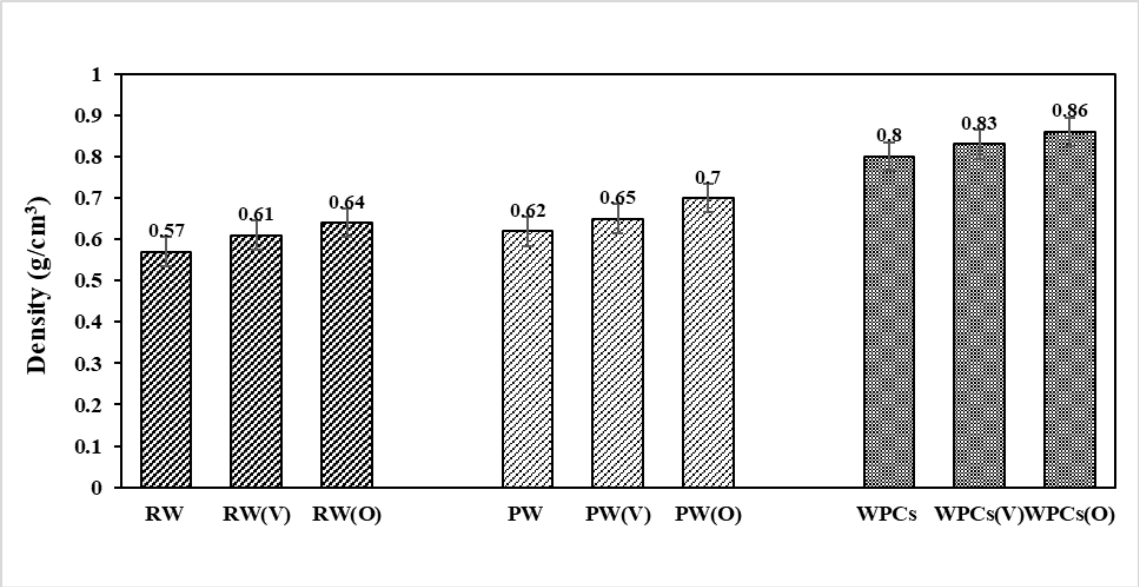


Figure 5. Effect of wood types with uncoated and coated surfaces of RW, PW, and WPCs samples on density analysis

Across all material types, density increases from both varnish and oil treatments were statistically significant (p = 0.001), confirming the physical impact of surface modification. Oil consistently produced greater density increases than varnish, likely due to its higher absorption and mass retention within the porous matrix [3,19]. These findings are especially relevant for elderly toy applications, where mechanical durability, dimensional consistency, and weight optimization must be balanced for both usability and safety. Moreover, the higher densities observed in treated WPCs and PW suggest enhanced structural performance, while treated RW remains a viable low-density alternative where lightweight handling is prioritized [11,22].

3.2.3 Surface roughness analysis

Surface roughness plays a pivotal role in determining tactile comfort, safety, hygiene, coating adhesion, and aesthetic appeal, all of which are crucial for elderly-oriented products. The roughness parameters Ra (arithmetical mean deviation) and Rz (mean peak-to-valley height) are presented in Table 2 for all untreated and treated material types. Results demonstrate that both varnish and oil surface treatments significantly improved surface smoothness, with varnish performing better in most cases.

As shown in Figure 5, the untreated sawn timber exhibited moderate surface roughness, with Ra = 4.12 μm and Rz = 9.77 μm, indicative of the naturally open grain structure and cellular porosity of raw wood. In the absence of coating, the results indicate that surface roughness is strongly influenced by specimen preparation. Differences in machining method and cutting direction resulted in noticeable variations in surface texture, including fiber tearing and tool marks. Sanding procedures further modified roughness by reducing machining defects, with finer grit sizes producing smoother surfaces. In PW, the alternating veneer orientations amplified these effects, resulting in non-uniform roughness across specimens. Surface finishing before measurement reduced roughness by filling surface irregularities and limiting fiber protrusion. Overall, the findings highlight the need for consistent and controlled specimen preparation to ensure reliable surface roughness measurements.

After varnish application (RW(V)), roughness was reduced to Ra = 2.85 μm and Rz = 7.20 μm, corresponding to 30.8% and 26.3% reductions, respectively. This is attributed to the film-forming nature of varnish, which fills in surface voids and levels micro-irregularities. Oil treatment (RW(O)) also improved surface characteristics, yielding Ra = 3.45 μm and Rz = 8.69 μm, though its effect was less pronounced than that of varnish. Oils primarily penetrate surface fibers, enhancing grain definition rather than forming a uniform surface layer. These improvements are critical for reducing splinter risk and enhancing tactile safety, especially in hand-held toys for the elderly. Plywood exhibited the highest initial roughness of all materials, with Ra = 5.69 μm and Rz = 12.89 μm, due to interfacial undulations between veneers and inconsistent grain

directions. Varnish treatment (PW(V)) significantly reduced surface irregularity to Ra = 3.16 μm and Rz = 10.56 μm, resulting in 44.5% and 18.1% reductions, respectively. Oil treatment (PW(O)) achieved moderate reductions to Ra = 4.12 μm and Rz = 11.69 μm, still offering improved smoothness but with limited peak-to-valley correction. These changes suggest that while oil improves the surface at a microstructural level, varnish is more effective in sealing and leveling layered wood products. For elderly toy applications, smoother plywood surfaces enhance cleanability and reduce the potential for microbial harborage in micro-crevices. Untreated WPCs had the lowest baseline roughness among all materials, with Ra = 1.98 μm and Rz = 4.56 μm, owing to the homogeneous dispersion of wood particles in the polymer matrix and minimal grain irregularities. Varnish-treated WPCs (WPCs(V)) further improved smoothness, with Ra = 1.45 μm and Rz = 3.96 μm, which represents reductions of 26.8% and 13.2%, respectively. Interestingly, oil-treated WPCs (WPCs(O)) had a slight increase in Rz to 6.58 μm, despite a nearly unchanged Ra (2.01 μm). This suggests that non-uniform oil absorption or partial surface aggregation might have introduced localized peaks or valleys, increasing peak-to-valley variation. Despite this, the overall surface profile remained smoother than untreated wood-based materials. The excellent surface quality of WPCs, especially when varnish-treated, reinforces their suitability for products that require high tactile comfort, low microbial retention, and aesthetically pleasing finishes. All of the experimental results are shown in Figure 6 (a) and (b)

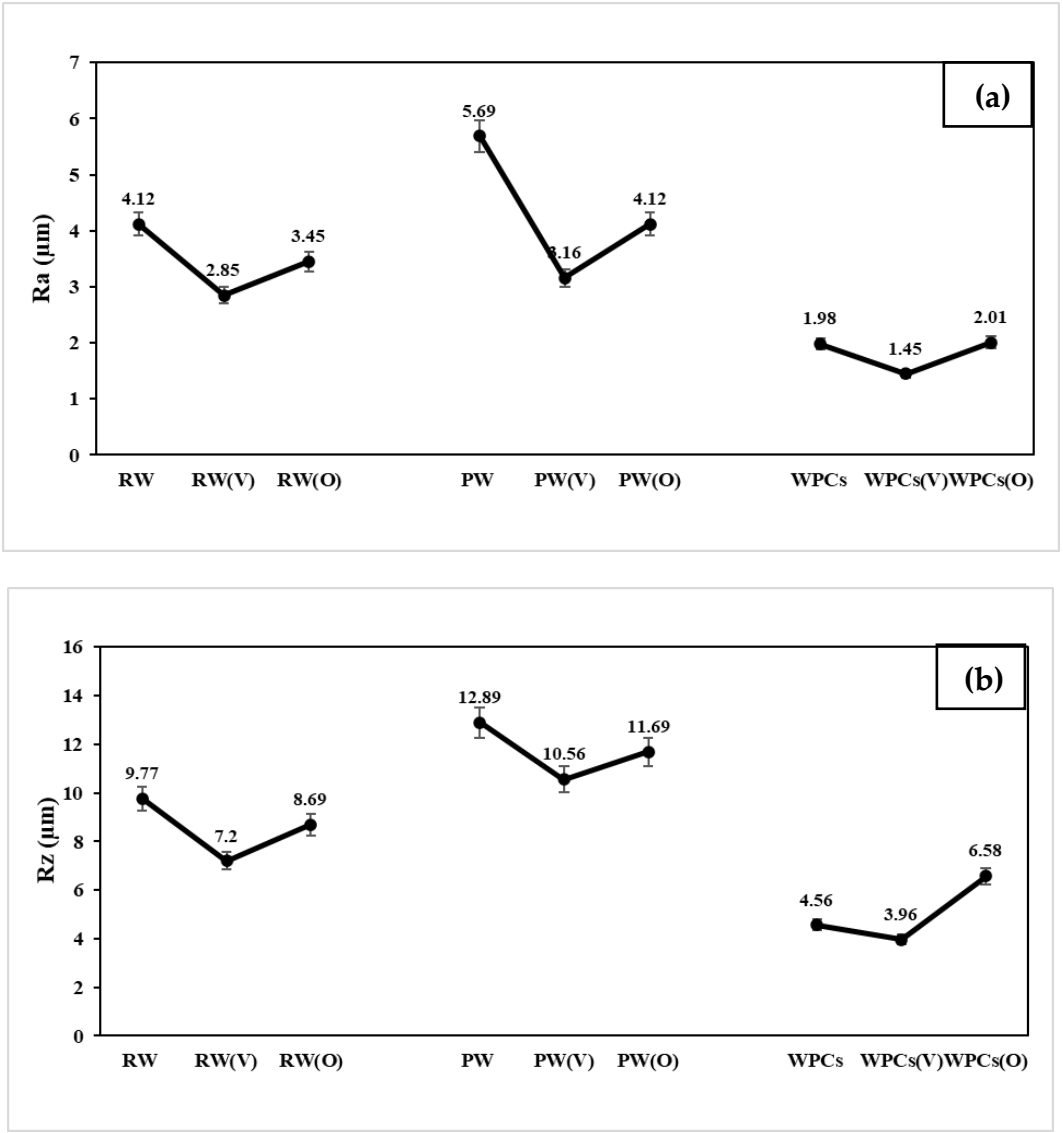


Figure 6. Effect of wood types with uncoated and coated surface of RW, PW, and WPCs samples on surface roughness properties: (a) Ra and (b) Rz.

Statistical analysis confirmed that all surface treatments produced significant improvements in Ra and Rz values across material types ($p < 0.05$). The largest improvements were observed in sawn timber and plywood, both of which have naturally uneven or fibrous textures. Varnish outperformed oil in all cases due to its ability to create a uniform sealing layer that masks surface irregularities. In elderly applications, surface roughness is more than an aesthetic concern—it directly impacts usability, hygiene, and injury prevention. Materials with smoother surfaces are less likely to harbor pathogens, cause skin irritation, or lead to splinters. Thus, varnish-treated WPCs, followed by varnish-treated RW and PW, emerge as optimal candidates for safe and ergonomic toy surfaces.

Table 3. Heavy metal content based on chemical analysis from different RW, PW, and WPC materials

Elements	Initials	RW (mg/kg)	PW (mg/kg)	WPCs (mg/kg)
Antimony	Sb	12.44	13.45	20.62
Arsenic	As	3.56	4.78	5.01
Barium	Ba	256.21	285.69	331.02
Cadmium	Cd	20.54	22.01	28.56
Chromium	Cr	15.89	17.20	19.52
Lead	Pb	8.14	10.14	14.19
Mercury	Hg	21.09	22.02	26.10
Selenium	Se	156.23	159.85	193.82

3.3 Chemical properties analysis

The evaluation of toxic and recalcitrant heavy metal content in elderly toys is critical to ensure environmental health and safety [1,3,4]. Although several techniques have been developed to address the heavy metal content of children's and the elderly's toys, they still face many challenges. In addition, there is still a lack of a comprehensive and insightful understanding of the relevant mechanisms. Generally, the prevalent methods for heavy metal content elimination, such as physical separation and chemical decomplexation, are briefly presented and evaluated. In particular, the characterization methods for heavy metal content, which provide valuable information on the speciation distribution of heavy metals, are underlined and discussed. In this work, the heavy metal content elimination of elderly's toy was measured using chemical decomplexation with eight elements, namely Antimony (Sb), Arsenic (As), Barium (Ba), Cadmium (Cd), Chromium (Cr), Lead (Pb), Mercury (Hg), and Selenium (Se), as shown in Table 3. Compared to toy products according to the ASTM F 963 standards (ASTM 2008), which are watercolor products that can be touched directly with their hands. It is found that the amounts of Sb, As, Ba, Cd, Cr, Pb, Hg, and Se must not exceed 60, 25, 1,000, 75, 60, 90, 60, and 500 mg/kg, respectively [5]. As expected, the RW, PW, and WPC materials can be used to produce the elderly's toy. The toy made from RW had lower heavy metal content than that of PW and WPCs. The results show the minimum heavy metal content values of 12.44, 3.56, 256.21, 20.54, 15.89, 8.14, 21.09, and 156.23 mg/kg, respectively. The outcome of this study agreed with toy safety directive migration limits that define ranges for heavy metals like Cd, Pb, As, and Sb in scraped toy material, for example, the Cd (20.54 mg/kg) lies close to some total content limits for wood (50 mg/kg) and below many toy migration thresholds [29]. Pb (8.14 mg/kg) and As (3.56 mg/kg) are well below many regulatory benchmarks (Pb is often allowed 90 to 160 mg/kg in toy material analyses), indicating low total content relative to industry limits. Sb (12.44 mg/kg) is also below many established migration-based values (45-560 mg/kg in toy materials) [30].

In general, the higher the heavy metal content, the more colorful and bright the toys are. Previous industrial studies have shown that the brighter the color of toys, the higher their heavy metal content, such as Pb. Pb compounds mainly cause this in paint pigments such as yellow, red, and white, which can maintain bright colors for a long time. This may suggest that the brighter the color, the more likely it is that there will be a large amount of Pb [2,7]. Additionally, the heavy metal content causes damage to elderly's health. The surface coating may introduce heavy metals into the body through contact friction with the human body or through the action of a suitable solvent. It can be stated that the heavy metal content can migrate into the

human body through a suitable medium. FE-SEM micrographs of elderly toys made from different materials are shown in Figure 7. Micrographs of the toy with RW, PW, and WPCs are shown in Figures 7(a), 7 (b), and 7 (c), respectively. The outcome of this study found that the elderly's toy manufactured from WPC material had a higher density than those manufactured from RW and PW materials. This might explain the high density of the elderly's toy made from WPCs, due to the rubberwood flour containing high amounts of lignin and natural waxes, which produce better dispersion and adhesion to non-polar hydrocarbon plastics. Additionally, the use of additives, such as filler-added composite materials, and the compounding of non-cellulosic products, such as lignin, hemicellulose, and waxes, makes it easier for the rubberwood particles to adhere to the recycled polypropylene matrix. High-density toy products resulted in higher toy weight [14,28]. For the elderly's toy, this suggests that this factor is a part of variety for learning, it stimulates the muscle response of the elderly, especially small muscles (fine motor skill) in muscle parts from the wrists, palms, and every finger, because most wooden or wood composite toys are quite heavy and not light [18,20]. Therefore, the elderly were able to get some exercise by touching weighty toys. This is a way to train the elderly to notice, feel, and differentiate volume and weight.

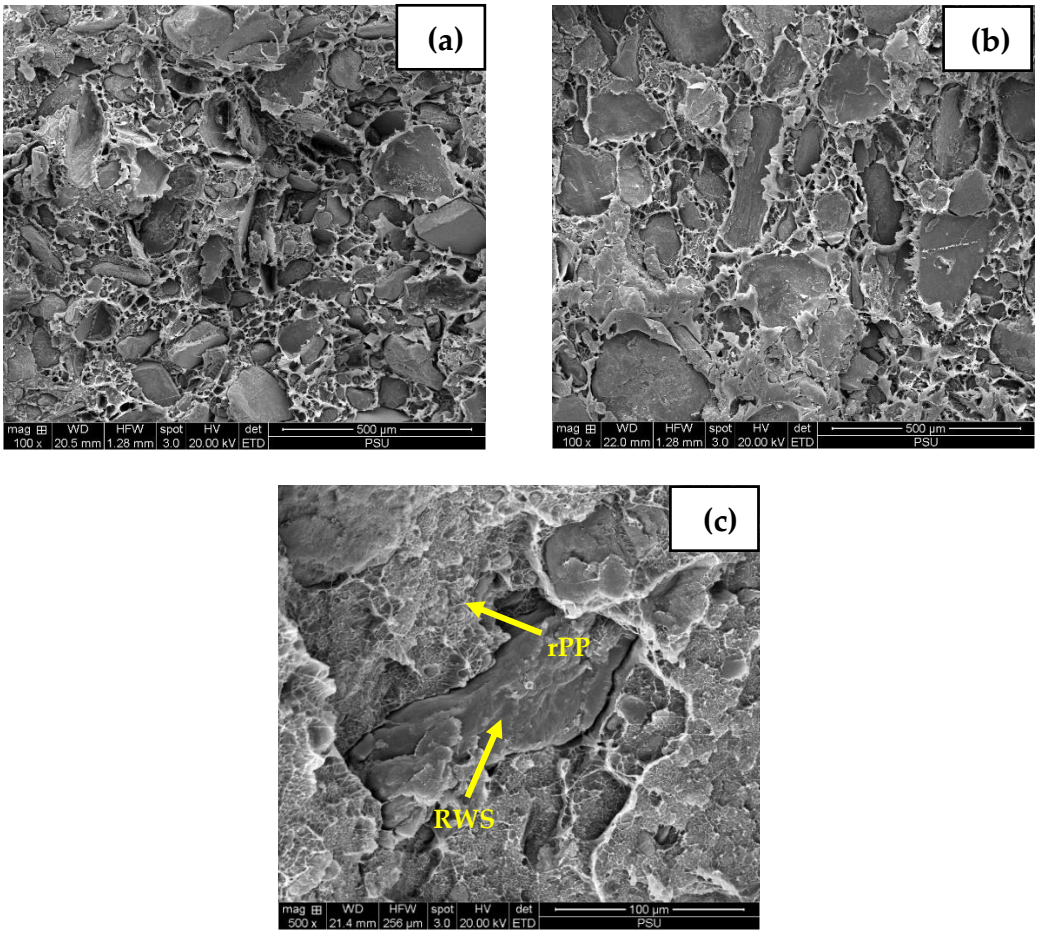


Figure 7. FE-SEM images of the different types of materials at magnifications of 100×: (a) RW, (b) PW, and (c) WPCs.

4. Conclusions

The goal of this research is to develop toys that enhance the potential of older people in various areas. The elderly's toy products were evaluated for their performance based on mechanical, physical, and chemical properties to ensure appropriate use for the elderly. The following conclusions could explain these results:

• All mechanical properties, namely tension and bending tests, showed that the elderly's toy products manufactured from RW had enhanced strength values compared to those of the PW and WPC samples.

• The lowest WA and TS properties, 4.36% and 2.01%, were observed in elderly toy products manufactured from WPC samples, whereas the minimum Ra value of 1.45 μm was observed in WPC samples.

• The density of the samples increases with both varnish and oil treatments. Oil consistently produced greater density increases than varnish. The highest surface treatments were improved for WPCs, with values of 0.83 g/cm³ (V) and 0.86 g/cm³ (O).

• Both the varnish and oil surface treatments significantly improved the smoothness of the samples' surfaces. The minimum Ra value of 1.45 μm was observed in WPCs.

• Heavy metal content, based on chemical analysis, of elderly toy products manufactured from different RW, PW, and WPCs was found to be within specified standards, indicating that these products are safe for the elderly.

• The surface observation of the samples and the product is clearly explained by the presence of fractures and cracks. The elderly' s toy products made from WPCs showed smooth surfaces, greater agglomeration, and fewer pores and voids, due to the strong interfacial adhesion between the plastic matrix and the rubberwood fiber reinforcement.

Based on the study's experimental results, several limitations can be identified. The study focused on a limited number of wood types and did not account for long-term durability and aging effects typical of care facilities. In addition, user-based evaluations involving elderly participants were not included. Future research should expand the range of materials and coatings, examine long-term safety and hygiene performance, and incorporate usability testing with elderly users to better inform design and material selection.

5. Acknowledgements

The authors gratefully acknowledge the financial support from the Thailand Science Research and Innovation (Research Grant Code: 66A171000010) and the Rajamangala University of Technology Srivijaya (RMUTSV), Thailand. We would also like to thank Mr. Surasit Insaeng and Mr. Poramin Chidchai for their support of this work.

Author Contributions: Pantamanatsopa, P. and Srivabut, C.; performed the experiments, Homkhiew, C. and Srivabut, C.; writing-original draft preparation, Boonchouytan, W. and Kamnerdwam, A.T.; writing-review and editing, Rawangwong, S.; supervision. All authors have read and agreed to the published version of the manuscript.

Funding: This research was funded by the Thailand Science Research and Innovation, grant number 66A171000010, 2023.

Conflicts of Interest: The authors declare no conflict of interest.

References

[1] Mustafa, O. Contribution of plays and toys to children's value education. *Asia J. Res. Educ. Soc. Sci.* **2018**, *4*, 146-149. https://doi.org/10.20448/journal.522.2018.42.146.149

[2] Dag, N.C.; Turkkan, E.; Kacar, A; Day, H. Children's only profession: Playing with toys. *North. Clin. Istanb.* **2021**, *8*, 414-420. https://doi.org/10.14744/nci.2020.48243

[3] Dauch, C.; Imwalle, M.; Ocasio ,B.; Metz, A.E. The influence of the number of toys in the environment on toddlers' play. *Infant. Behav. Dev.* **2017**, *50*, 78-87. https://doi.org/10.1016/j.infbeh.2017.11.005

[4] Komis, V.; Karachristos, C.; Mourta, D.; Sgoura, K.; Misirli, A.; Jaillet, A. Smart toys in early childhood and primary education: A systematic review of technological and educational affordances. *Appl. Sci.* **2021**, *11*, 8653. https://doi.org/10.3390/app11188653

[5] Guha, S.; Murthy, K. Understanding the role toys in child development: Special focus on traditional channapatna toys. *Indian J. Appl. Res.* **2017**, *7*, 406-410. https://doi.org/10.36106/IJAR

[6] Gao, H.; Fu, J.; Xing, X. Research on the design of children's toys and teaching AIDS based on sound science. *E3S Web of Conferences.* **2021,** *179*, 02025. https://doi.org/10.1051/e3sconf/202017902025

[7] Bai, O. Research on the design of interactive children's vocal enlightenment toys based on audiovisual association experience. *Occup. The. Int.* **2023**, 35495176. https://doi.org/ 10.1155/2023/9824371

[8] Lang, L. Research on design method of children's teaching assisted toys based on STEAM education. *Open J. Soc. Sci.* **2021**, *9*, 628-635. https://doi.org/10.4236/jss.2021.99046

[9] Gavrilova, M.; Sukhikh, V.; Veresov, N. Do executive function and family factors predict children's preference for trendy over classic toys? An experimental investigation. *Front. Psychol.* **2023**, *14*, 1-6. https://doi.org/10.3389/fpsyg.2023.1190876

[10] Ma, M.Y.; Lee, Y.H. Children with autism and composite tactile-visual toys during parent-child interaction. *Interact. Stud.* **2014**, *15*, 120-124. https://doi.org/10.1075/is.15.2.13ma.

[11] Salim, R.; Johansson, J. The influence of raw material on the wood product manufacturing. *Procedia CIRP.* **2016**, *57*, 764-768. https://doi.org/10.1016/j.procir.2016.11.132

[12] Rodrigues, M.O.; Abrantes, N.; Gonçalves, F.J.M.; Nogueira, H.; Marques, C.J.; Gonçalves, A.M.M. Impacts of plastic products used in daily life on the environment and human health: What is known? *Environ. Toxicol. Pharmacol.* **2019**, *72*, 103239. https://doi.org/10.1016/j.etap.2019.103239

[13] Elsheikh, A.H.; Panchal, H.; Shanmugan, S.; Muthuramalingam, T.; El-Kassas, A.M.; Ramesh, B. Recent progresses in wood-plastic composites: Pre-processing treatments, manufacturing techniques, recyclability and eco-friendly assessment. *Clean. Eng. Technol.* **2022**, *8*, 100450. https://doi.org/10.1016/j.clet.2022.100450

[14] Khamtree, S.; Homkhiew, C.; Srivabut, C.; Ratanawilai, T.; Rawangwong, S.; Hiziroglu, S. Evaluation of mechanical properties of composites made from recycled plastic and waste rubberwood using multiply-response surface optimization as green building materials. *Fiber. Polym.* **2023**, *24*, 2819-2834. https://doi.org/10.1007/s12221-023-00266-w

[15] Homkhiew, C.; Srivabut, C.; Boonchouytan, W.; Ratanawilai, T.; Rawangwong, S. Optimization of the physical properties of recycled plastic hybrid composites reinforced with Rubberwood flour and crab shell flour for underwater use. *Compos. C: Open Access* **2023**, *12*, 100411. https://doi.org/10.1016/j.jcomc.2023.100411

[16] Hala, B.; Kamal, G.; Hamid, E.; Denis, R.; Rachid, B.; Qaiss, A.E.K. Mechanical, thermal, and rheological properties of polypropylene hybrid composites based clay and graphite. *J. Compos. Mater.* **2016**, *51*, 36-43. https://doi.org/10.1177/0021998317690597

[17] Laraba, S.R.; Rezzoug, A.; Halimi, R.; Wei, L.; Yang, Y.; Abdi, S.; Li, Y.; Jie, W. Development of sandwich using low-cost natural fibers: Alfa-Epoxy composite core and jute/metallic mesh-Epoxy hybrid skin composite. *Ind. Crops. Prod.* **2022**, *184*, 115093. https://doi.org/10.1016/j.indcrop.2022.115093

[18] Homkhiew, C.; Cheewawuttipong, W.; Srivabut, C.; Boonchouytan, W.; Rawangwong, S. Machinability of wood-plastic composites from the CNC milling process using the Box-Behnken design and response surface methodology for building applications. *J. Thermoplas. Compos. Mater.* **2024**, 1-20. https://doi.org/10.1177/08927057241248036

[19] Guo, G.; Finkenstad, V.L.; Nimmagadda, Y. Mechanical properties and water absorption behavior of injection-molded wood fiber/carbon fiber high-density polyethylene hybrid composites. *Adv. Compos. Hybrid Mater.* **2019**, *2*, 690-700. https://doi.org/10.1007/s42114-019-00116-5

[20] Liu, H.; Wang, J.; Gong, C.; Cheng, F. Morphology and mechanical properties of PVC/straw-fiber coated with liquid nitrile-butadiene rubber composites. *J. Appl. Polym. Sci.* **2016**, *133*, 44119. https://doi.org/10.1002/app.44119

[21] Kara, N.; Cagiltay, K. Smart toys for preschool children: A design and development research. Electron Commer. *Res. Appl.* **2020**, *39*, 100909. https://doi.org/10.1016/j.elerap.2019.100909

[22] Xian, Y.; Wang, C.; Wang, G.; Ren, W.; Cheng, H. Understanding the mechanical and interfacial properties of core–shell structured bamboo-plastic composites. *J. Appl. Polym. Sci.* **2015**, *133*, 43053. https://doi.org/10.1002/app.43053

[23] Prabhu, R.; Mendonca, S.; Souza, R.; Bhat, T. Effect of water absorption on the mechanical properties of alkaline treated bamboo and flax fiber reinforced epoxy composites. *Trends. Sci.* **2022**, *19*, 5779. https://doi.org/10.48048/tis.2022.5779

[24] Xue, L.; Yi, X.; Zhang, Y. Research on optimized product image design integrated decision system based on Kansei Engineering. *Appl. Sci.* **2022**, *10*, 1198. https://doi.org/10.3390/app10041198

[25] Lu, R.J.; Feng, Y.X.; Zheng, H.; Tan, J.R. A product design based on interaction design and axiomatic design theory. *Procedia CIRP.* **2016**, *53*, 125-129. https://doi.org/10.1016/j.procir.2016.07.061.

[26] Essabir, H.; Boujmal, R.; Bensalah, M.O.; Rodrigue, D.; Bouhfid, R.; Qaiss, A.E.K. Mechanical and thermal properties of hybrid composites: oil-palm fiber/clay reinforced high density polyethylene. *Mech. Mater.* **2016**, *98*, 36-43. https://doi.org/10.1016/j.mechmat.2016.04.008

[27] Srivabut, C.; Homkhiew, C.; Rawangwong, S.; Boonchouytan, W. Possibility of using municipal solid waste for manufacturing wood-plastic composites: effects of natural weathering, wood waste types, and contents. *J. Mater. Cycles. Waste Manag.* **2022**, *24*, 1407-1422. https://doi.org/10.1007/s10163-022-01443-4

[28] Saeb, M.R.; Moghri, M. Application of response surface methodology in describing fusion characteristics of rigid poly(vinyl chloride) / nanoclay/ wood flour/ calcium carbonate hybrid nanocomposites. *J. Vinyl. Technol.* **2014**, *34*, 183-190. https://doi.org/10.1002/vnl.21387

[29] Guney, M; Zagury, G.J. Bioaccessibility of As, Cd, Cu, Ni, Pb, and Sb in toys and low-cost jewelry. *Environ. Sci. Technol*. **2013**, *48*, 1238-1246. https://doi.org/10.1021/es4036122

[30] Fadaei, A. An investigation into the present levels of contamination in children's toys and jewelry in different countries: a systematic review. *Rev. Environ. Health*. **2023**, *38*, 601-611. https://doi.org/10.1515/reveh-2022-0064

ASEAN
Journal of Scientific and Technological Reports
Online ISSN:2773-8752

Research article

The Preparation and Characterisation of a Bioplastic Film from Acrylated Epoxidized Soybean Oil (AESBO)

Apatsara Uchupap[1], Suppachai Sattayanurak[2], Ismail Ibrahim[3], Mohd Hafiz Zainol[3], Tulyapong Tulyapitak[1], Anuwat Saetung[1], and Weerawut Naebpetch[2, 4*]

[1] Faculty of Science and Technology, Prince of Songkla University, Pattani Campus, Pattani, 94000, Thailand
[2] Faculty of Engineering, Thaksin University, Phatthalung, 93210, Thailand
[3] Faculty of Chemical Engineering & Technology, Universiti Malaysia Perlis (UniMAP), Kompleks Pusat Pengajian Jejawi 2, 02600 Arau Perlis, Malaysia
[4] Center of Rubber Technology for Community, Faculty of Engineering, Thaksin University; Phatthalung, 93210, Thailand
* Correspondence: weerawut.n@tsu.ac.th

Citation:
Uchupap, A.; Sattayanurak, S., Ibrahim, I.; Zainol M.H.; Tulyapitak, T.; Saetung A., and Naebpetch, W. The preparation and characterisation of a bioplastic film from acrylated epoxidized soybean oil (AESO). *ASEAN J. Sci. Tech. Report.* **2026**, *29*(4), e261617. https://doi.org/10.55164/ajstr.v29i4.261617.

Article history:
Received: September 29, 2025
Revised: March 1, 2026
Accepted: March 8, 2026
Available online: March 25, 2026

Publisher's Note:
This article is published and distributed under the terms of the Thaksin University.

Abstract: This study successfully demonstrates the synthesis of epoxidized soybean oil (ESBO) via reaction with formic acid and hydrogen peroxide, followed by acrylation with varying ratios of acrylic acid. The characterization techniques, including FT-IR and ^{1}H-NMR, confirmed the formation of key functional groups such as oxirane and hydroxyl, as well as the reduction of carbon–carbon double bonds, indicating successful epoxidation and acrylation. The appearance of new peaks in the 1H-NMR spectra further supports the formation of the epoxide and acrylate functionalities. FT-IR analysis revealed clear spectral changes correlating with these transformations. The kinetics study using 5 wt% photoinitiator demonstrated that the acrylated epoxidized soybean oil (AESBO) film could be rapidly stabilized within 60 seconds under UV curing. These findings highlight the potential of AESBO as a sustainable precursor for bioplastic films, offering promising chemical stability. Further optimization may enhance its suitability for various biodegradable polymer applications.

Keywords: soybean oil; epoxidation; acrylation; UV cured; biopolymer

1. Introduction

Currently, vegetable oils are attracting increasing attention in various areas of research due to their biodegradability, environmental friendliness, and favorable performance characteristics [1]. There is a growing interest in replacing petroleum-based oils with vegetable oils, prompting the development of various chemical modification methods to produce fully biodegradable alternatives [2]. In terms of global production, soybean oil ranks among the highest, second only to palm oil. Between 2012 and 2016, soybean oil was widely utilized in numerous applications, both for consumption and industrial purposes. These include its use in lubricants, coatings, and printing inks, such as oil-based paints and ink formulations [3]. Soybean oil is a triglyceride rich in unsaturated fatty acids. It contains both saturated and unsaturated fatty acids, including stearic acid (a saturated fatty acid), oleic acid (with one double bond), linoleic acid (with two double bonds), and linolenic acid (with three double bonds), all of which are located along the fatty acid chains. A key characteristic of soybean oil is the presence of reactive double bonds within its chemical structure [4]. These double bonds enable the oil to undergo crosslinking reactions through processes such as

polymerization, epoxidation, and UV curing. In particular, the modification of soybean oil via acrylation using acrylic acid, followed by UV curing, has gained increasing interest. This approach not only enhances the commercial value of soybean oil but also offers insights into the potential for similar modifications in other vegetable oils, supporting the development of sustainable, bio-based materials [5].

UV curing is an emerging technology that has gained significant attention in recent years for its precision, high processing speed, and alignment with sustainability objectives. It is regarded as an environmentally friendly method that aligns with the demands of modern industrial applications. Numerous studies have demonstrated the successful utilization of various vegetable oils, including sunflower oil, soybean oil, sesame oil, olive oil, and canola oil, in UV-curable systems. These oils are typically modified via acrylation reactions, in which acrylic acid serves as the primary reactant, producing materials that can be efficiently cured under UV irradiation [6]. In addition, other research has investigated the epoxidation of vegetable oils to facilitate UV curing [7, 8]. Because vegetable oils do not naturally contain epoxide groups, epoxidation is a necessary preliminary step. This process introduces epoxide groups onto the double bonds of fatty acid chains, typically using reagents such as hydrogen peroxide and formic acid. The resulting epoxidized oils can then undergo acrylation, forming acrylate groups capable of polymerizing under UV light.

One key factor enabling the UV-curable polymerization of vegetable oils is the acrylation process. Acrylation involves the introduction of acrylate (–CH=CH–COOR) or methacrylate groups into oil molecules, thereby incorporating vinyl functionalities (C=C) that can undergo radical polymerization. During UV curing, the addition of a photoinitiator generates free radicals that initiate polymerization of the vinyl groups, resulting in crosslinking and the formation of a polymer network. This modification renders the oils UV-curable and suitable for advanced material applications. Numerous studies have demonstrated the feasibility and efficiency of acrylating various vegetable oils. Acrylation increases the crosslinking density of cured films, thereby enhancing their mechanical properties, such as tensile strength and Young's modulus, due to the greater structural functionality of the prepolymers [9]. Additionally, the use of photoinitiators and suitable comonomers can optimize the UV curing process by reducing irradiation time and increasing double bond conversion efficiency [10]. For example, acrylated rapeseed oil (ARO) has shown improved UV-curing properties, especially when modified with a furan-based ester reactive diluent (UES), which significantly reduces viscosity. and enhances crosslinking density, leading to improved tensile strength and storage modulus [11]. The development of bioplastic films from the UV-curable polymerization of vegetable oils following acrylation offers several significant advantages. Primarily, by using sustainable and biodegradable alternatives to petroleum-based precursors, the technology addresses environmental concerns and resource depletion [1, 3]. Secondarily, UV curing is a high-speed, energy-efficient, and solvent-free processing method that enables film stabilization within seconds and is highly compatible with modern industrial sustainability objectives [6, 11]. This research, therefore, aims to investigate and analyze the structural and property changes in soybean oil after epoxidation with formic acid, followed by acrylation at varying ratios. Furthermore, it examines the film-forming ability of the acrylated product in the presence of a photoinitiator, focusing on the kinetics and optimal curing time for stable film formation.

2. Materials and Methods

2.1 Materials

Soybean oil (SBO) was sourced from Thai Vegetable Oil Public Company Limited, Thailand. Formic acid (90%) was obtained from Elago Enterprises Pty Ltd., Australia. Hydrogen peroxide (H_2O_2, 35%) was purchased from Chem-Supply Pty Ltd., Australia. Acrylic acid (AA, 99%) was supplied by Sigma-Aldrich Chemie GmbH, Germany. Ethyl acetate was purchased from Modern Chemical Co., Ltd., Thailand. The photoinitiator 2-hydroxy-2-methylpropiophenone (Darocur 1173; PI-1173) was purchased from Sigma-Aldrich, Germany. Sodium bicarbonate ($NaHCO_3$) and sodium chloride (NaCl) were obtained from Elago Enterprises Pty Ltd., Australia. Magnesium sulfate ($MgSO_4$) was sourced from Panreac Química S.L.U., Spain.

2.2 Preparation of ESBO

For the preparation of ESBO, a molar ratio of 1:4:4 (SBO: formic acid: hydrogen peroxide) was used.

Specifically, SBO (100 g), formic acid (23 g), and hydrogen peroxide (44 g) were mixed in a four-neck glass reaction vessel and maintained at 60°C for 2 hours. Laboratory installation of the epoxidation reaction apparatus used for soybean oil modification as shown in Figure 1. After completion of the reaction, the resulting oil was removed and cooled to room temperature. The product was then transferred to a separating funnel and washed with ethyl acetate, followed by repeated washes with distilled water, sodium bicarbonate ($NaHCO_3$), and sodium chloride (NaCl) until the aqueous phase reached pH 7. The cleaned oil layer was then separated, dried using magnesium sulfate ($MgSO_4$), and filtered through filter paper. The remaining solvent was removed by vacuum evaporation to obtain the purified ESBO—Schematic of ESBO reaction as shown in Figure 2.

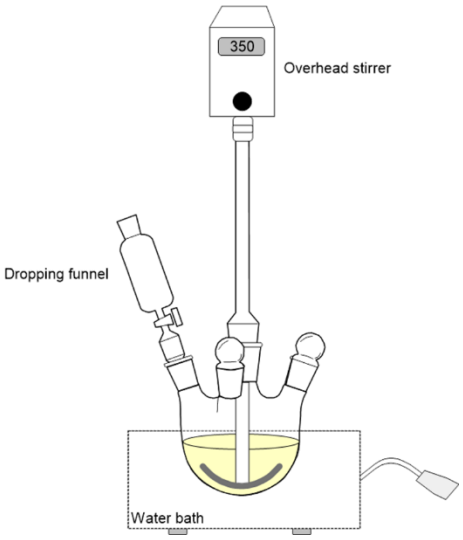


Figure 1. Example of installation of reaction equipment

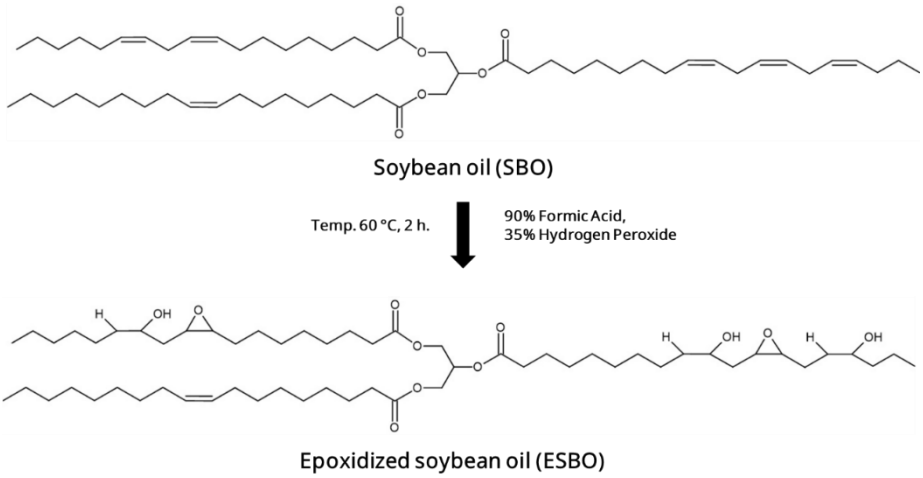


Figure 2. Schematic of ESBO reaction.

2.3 Preparation of AESBO

AESBO was prepared using ESBO-2–acrylic acid ratios of 1:1, 1:1.5, and 1:2 at 110°C for 8 h. Installation of acrylation reaction equipment is shown in Figure 3. After completion of the reaction, the AESBO was removed and allowed to cool to room temperature. It was then transferred to a separating funnel and washed with ethyl acetate, followed by repeated washings with distilled water, sodium bicarbonate ($NaHCO_3$), and sodium chloride (NaCl) until the aqueous layer reached neutral pH (7). The cleaned oil layer was then separated and dried using magnesium sulfate ($MgSO_4$), followed by filtration through filter paper. The solvent was subsequently removed by vacuum evaporation to obtain the purified AESBO—Schematic of

AESBO reaction as shown in Figure 4.

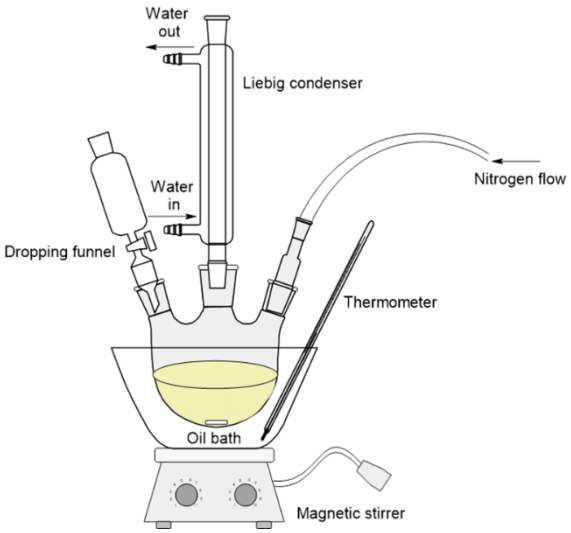


Figure 3. Installation of acrylic reaction equipment.

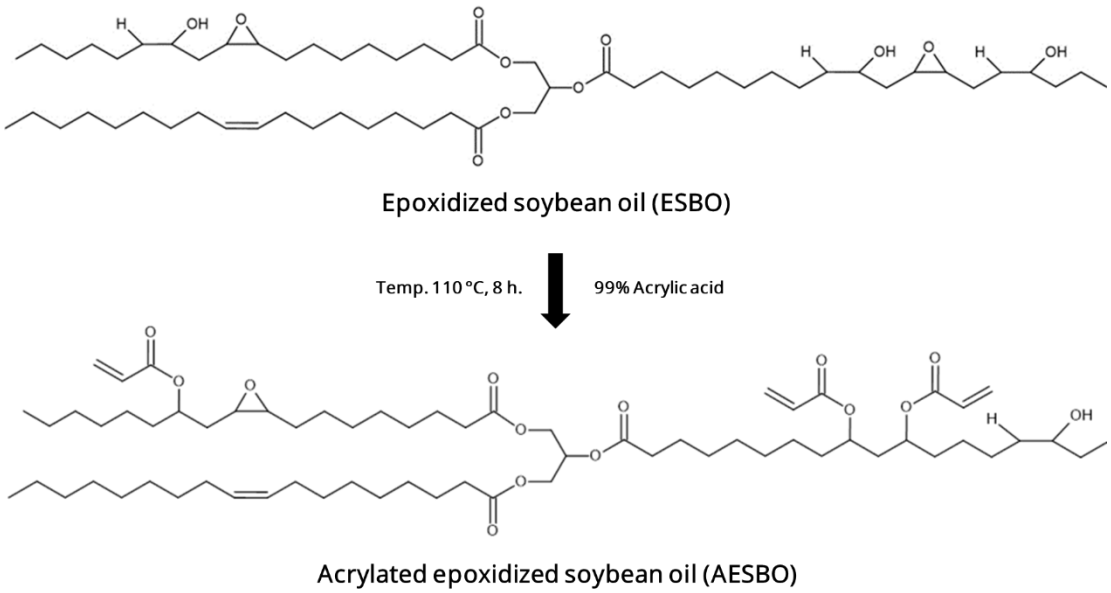


Figure 4. Schematic of AESBO reaction.

2.4 Preparation of the UV-curable bioplastic films

Photoinitiator (Darocur 1173) was incorporated at concentrations of 5 wt%. Darocur 1173 was added to AESBO-1, AESBO-1.5, and AESBO-2 formulations. Following this, the AESBO film samples were formed by casting into silicone molds with a cavity size of 4 cm x 10 cm x 0.3 cm and cured using a UV source with a power output of 400 W. The distance between the film samples and the center of the UV lamp was maintained at 15 cm. The UV curing kinetics were studied over 0-420 seconds. The preparation process for the UV-cured AESBO film is shown in Figure 5.



Figure 5. Preparation process of UV-cured AESBO film.

2.5 Chemical analysis of SBO

The chemical properties of the modified SBO were analyzed. The acid value was determined by titration to assess the free fatty acid content of the oil, following ISO 660:2009. The hydroxyl (OH) value was measured by titration to determine the number of hydroxyl groups in the oil structure, in accordance with ISO 14900:2001. The iodine value, used to evaluate the degree of unsaturation (double bonds), was determined via titration according to ISO 3961:2009.

2.5.1 Determination of Acid Value

The acid value is determined to assess the acidity of SBO before and after chemical modification. A 5 g sample of oil is accurately weighed and transferred into a clean Erlenmeyer flask. Then, 50 mL of the titration solvent, prepared by mixing benzene and ethanol in a 1:1 volume ratio, is added. The mixture is shaken thoroughly to ensure uniform dissolution. Titration is then performed with 0.1 N potassium hydroxide (KOH) solution, using phenolphthalein as the indicator. The endpoint of the titration is indicated by a color change from colorless to pale pink, which persists for at least 30 seconds. The volume of KOH used is recorded and used to calculate the acid value using the following formula:

$$\text{Acid no.} = 56.1 \times \frac{\text{A}-\text{B}}{\text{W}} \times \text{N} \quad (1)$$

Where A is the volume of KOH used to titrate the sample, (mL)
B is the volume of KOH used to titrate the blank (mL)
W is the weight of the sample (g)
N is the KOH concentration, (N)

2.5.2 Determination of Hydroxyl (OH) Value

The hydroxyl value is determined to quantify the number of hydroxyl groups in SBO before and after modification. A 3 g sample of the oil is accurately weighed and placed in a round-bottom flask. To this, 20 mL of the phthalic mixture (prepared by mixing 1 part phthalic anhydride with 6 parts pyridine by volume) is added. The mixture is then refluxed at 100 ± 5°C for 1 hour. After refluxing, the mixture is cooled to room temperature, and 50 mL of distilled water is carefully added through the mouth of the condenser. The mixture is then titrated with 1 N potassium hydroxide (KOH) using phenolphthalein as the indicator. The endpoint is reached when the color changes from colorless to pink. The volume of KOH used is recorded, and the hydroxyl value is calculated using the following formula:

$$\text{OH-Value} = 56.1 \times \left[\frac{(v_2 - v_1)}{W}\right] + Acid\ no. \quad (2)$$

Where V_1 is the volume of KOH used to titrate the sample, (mL)
V_2 is the volume of KOH used to titrate the blank (mL)
W is the weight of the sample (g)

2.5.3 Determination of Iodine Value

The iodine value is used to assess the degree of unsaturation, i.e., the number of double bonds in the SBO structure before and after modification. A 0.05 g sample of oil is accurately weighed and transferred into a clean Erlenmeyer flask. Then, 20 mL of Wijs solution (iodine dissolved in glacial acetic acid with iodine monochloride as the active reagent) is added to the flask. The mixture is kept in the dark at room temperature for 30 minutes to allow the reaction to proceed. After the reaction period, the mixture is titrated with 0.1 N sodium thiosulfate solution, using starch solution as an indicator. The endpoint of the titration is identified by a color change from brown to colorless. The volume of sodium thiosulfate used is then recorded and used to calculate the iodine value using the following formula:

$$\text{Iodine no.} = \frac{[(V_1 - V_2) \times N \times 126.9 \times 100]}{W \times 1000} \quad (3)$$

Where V_1 is the volume of Sodium thiosulfate used to titrate the blank (mL)
V_2 is the volume of Sodium thiosulfate used to titrate the sample, (mL)
W is the weight of the sample (g)
N is Sodium thiosulfate concentration, (N)

2.6 Characterizations

The ^{1}H-NMR spectra were recorded using a Bruker 400 Fourier Transform spectrometer operating at 400 MHz to investigate the chemical structure of the modified SBO. Samples were dissolved in $CDCl_3$, with tetramethylsilane (TMS) used as the internal standard. The FTIR-ATR technique was employed to examine the chemical bonds and interactions among SBO, ESBO, and AESBO. The kinetics of AESBO photo-crosslinking reactions were monitored by real-time infrared spectroscopy in ATR transmission mode using a Tensor 27 Fourier Transform Infrared Spectrometer (Bruker, Germany) over a wavenumber range of 4000 cm^{-1} to 500 cm^{-1}.

3. Results and Discussion

3.1 Modification of SBO

In Table 1, SBO initially exhibited an iodine value within the standard range of 127–138 I_2/100 g. The oil was then structurally modified via epoxidation with formic acid and hydrogen peroxide at a molar ratio of 1:4:4. Following the reaction, the iodine value decreased to 12.06 I_2/100 g, indicating that epoxide rings had replaced the double bonds in the main structure. This is because the iodine value reflects the number of double bonds present in the structure. At the same time, the acid number and hydroxyl (OH) value increased to 10.90 mg KOH/g and 242.22 mg KOH/g, respectively. Subsequently, ESBO-2 was acrylated with acrylic acid at ratios of 1:1, 1:1.5, and 1:2. The acid number increased, indicating an excess of unreacted acrylic acid, which corresponded to the increasing ratio. A similar trend was seen with the OH value. However, at a 1:2 ratio, the oil became denatured, forming a gel rather than remaining a liquid, and therefore could not be tested, as shown in Figure 6.

Following 2 hours of epoxidation, the resulting ESBO-2 exhibited a cloudy white appearance, in contrast to the clear yellow color of the unmodified SBO, as shown in Figure 6. Upon acrylation, the AESBO-1 sample showed increased viscosity and a darker yellow hue than ESBO-2. When compared further with AESBO-1.5, it was observed that AESBO-1.5 had even higher viscosity and a slightly deeper color than AESBO-1. However, in the case of AESBO-2, the material underwent a phase transformation from a viscous liquid to a non-flowing gel, indicating over-crosslinking or excessive reaction extent. This transformation is attributed to two simultaneous reaction mechanisms. Firstly, the high molar ratio of acrylic acid facilitated extensive ring-opening of the epoxide groups, leading to a high density of acrylate functionalities on each triglyceride molecule, which promoted premature intermolecular crosslinking. Secondly, under the reaction conditions of 110 °C for 8 h, the excess acrylic acid likely underwent self-polymerization, leading to the formation of an interconnected poly(acrylic acid) network entangled with the modified oil matrix, resulting in a rigid three-dimensional structure and gelation even before UV curing was initiated [21]. Based on these observations, AESBO-1.5 was selected as the optimal formulation for studying UV curing kinetics due to its suitable viscosity and stability.

Table 1. Chemical characteristics of SBO before and after modification.

Oil type	Ingredients (mol)		Acid no. (mg KOH/g)	OH-Value (mg KOH/g)	Iodine no. (I_2/100g)
	ESBO-2	Acrylic acid			
SBO [6]	-	-	0.3-3.0	4-8	127-138
ESBO-2	-	-	10.90	242.22	12.06
AESBO-1	1	1	9.87	265.21	-
AESBO-1.5	1	1.5	13.52	223.67	-
AESBO-2	1	2	-	-	-

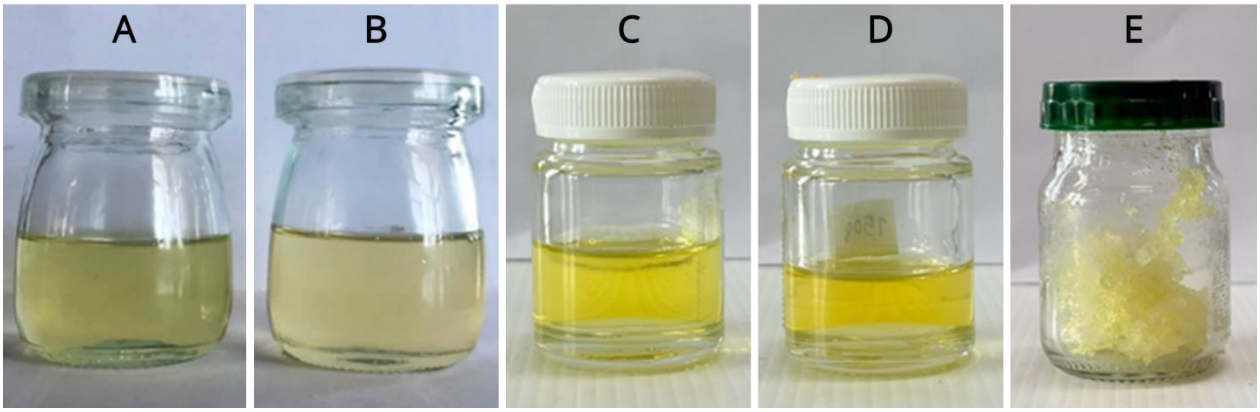


Figure 6. Visual appearance of (a) SBO, (b) ESBO-2, (c) AESBO-1, (d) AESBO-1.5, and (e) AESBO-2.

The ^{1}H-NMR spectra of SBO and modified SBO are shown in Figure 7. After 2 hours of reaction, significant structural changes were revealed. In the unmodified SBO, a prominent signal was observed at 5.3–5.6 ppm, corresponding to the carbon–carbon double bonds (C=C) present in the fatty acid chains. Following epoxidation with formic acid and hydrogen peroxide, the signal intensity decreased markedly, indicating successful conversion of the double bonds. Concurrently, a new signal emerged at 3.0–3.15 ppm, which is characteristic of the methine protons in the oxirane (epoxide) ring, confirming the formation of ESBO-2 [12].

The structure of AESBO was confirmed by ^{1}H-NMR spectroscopy. Signals observed at 4.0–4.4 ppm correspond to the glyceride backbone, while those in the range of 2.8–3.3 ppm are attributed to the methine protons of the epoxide ring. Following the acrylation reaction, a noticeable reduction in the intensity of the epoxide-associated peaks was observed, indicating ring-opening. Simultaneously, new peaks emerged in the range of 5.6–6.4 ppm, which are characteristic of the vinyl protons of the acrylate ester. These signals confirm the successful introduction of acrylate groups, as they represent the three distinct protons attached to the carbon–carbon double bond (C=C) of the acrylate moiety [13–16].

The FT-IR spectra of SBO and modified SBO are shown in Figure 8. After 2 hours of reaction with formic acid and hydrogen peroxide, significant structural changes were revealed. The absorption band at 3010 cm^{-1}, attributed to the =C–H stretching vibrations in SBO, decreased in intensity during the reaction, indicating consumption of double bonds. In contrast, the broad peak at 3400 cm^{-1}, corresponding to hydroxyl (–OH) groups, was observed to increase in the spectrum of ESBO-2, suggesting the formation of hydroxyl groups via side reactions or ring-opening. Additionally, a distinct absorption at 820 cm^{-1} appeared, confirming the presence of oxirane (epoxide) rings in the modified oil.

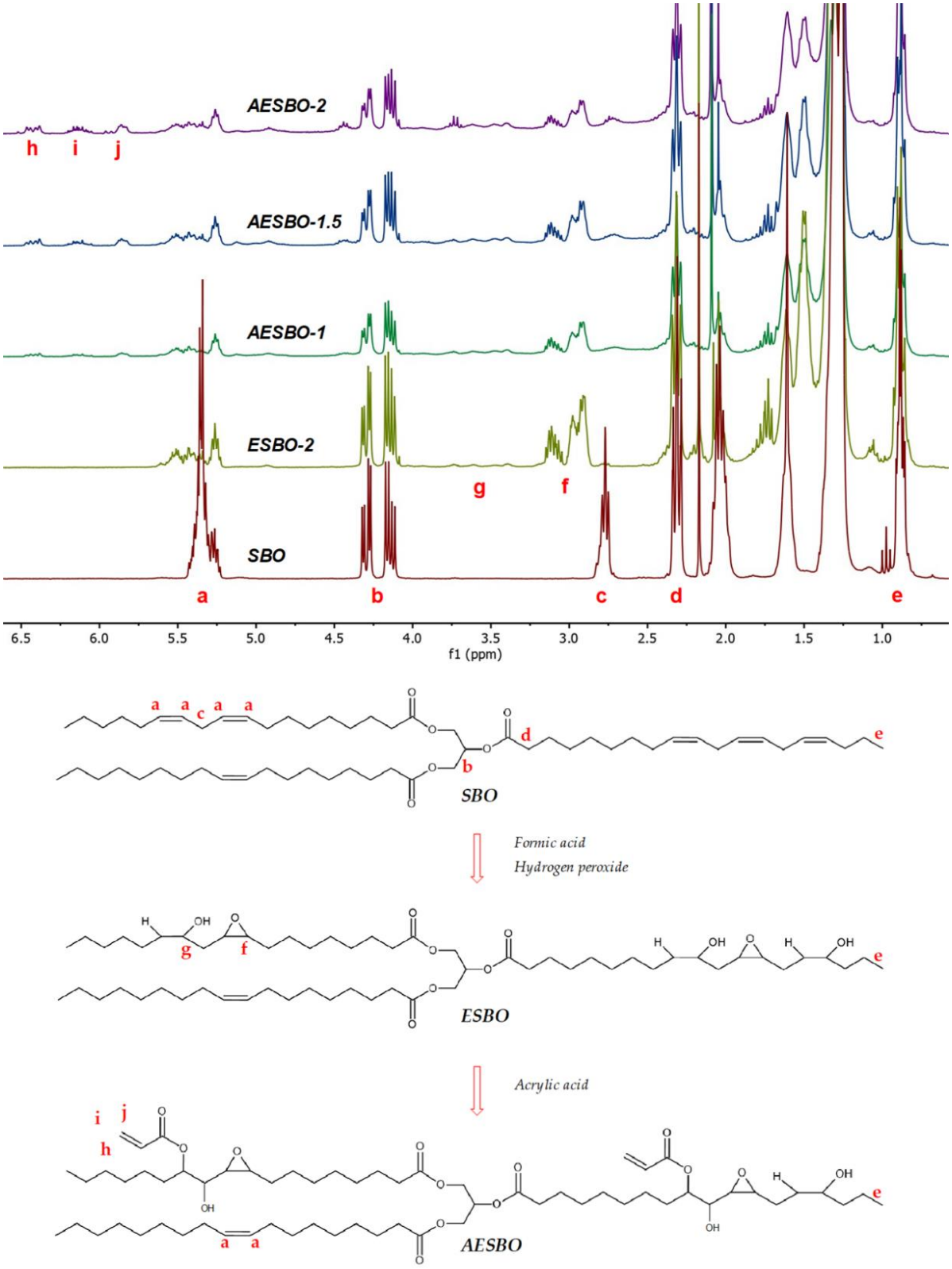


Figure 7. ^{1}H-NMR spectra of a series of SBO, ESBO-2, and AESBO with a difference ratio of acrylic acid.

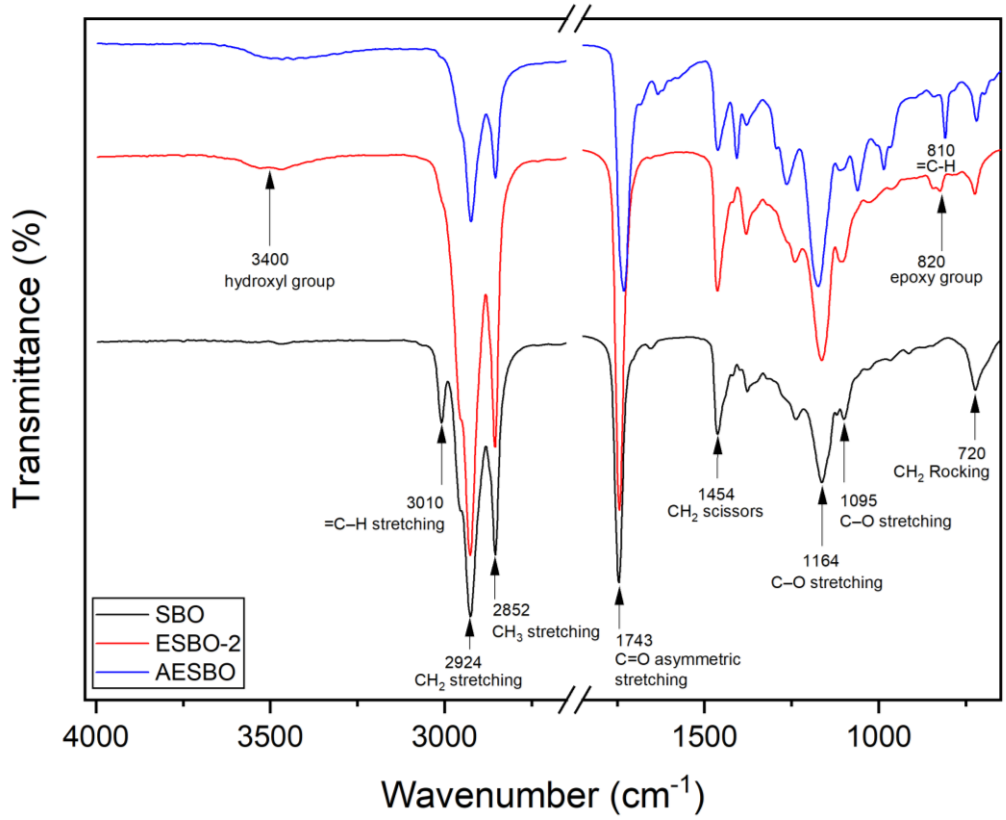


Figure 8. The FT-IR spectra of SBO, ESBO-2, and AESBO.

The results of the AESBO reaction, confirmed by FT-IR analysis, demonstrated the appearance of new absorption bands at 1630 cm^{-1} and 810 cm^{-1}, both corresponding to the stretching vibrations of carbon–carbon double bonds (C=C). These peaks provide clear evidence that acrylation occurred through ring-opening of the epoxide rings, leading to the formation of acrylate functional groups. The distinct peak at 810 cm^{-1}, in particular, is indicative of C=C stretching in the acrylate moiety. Similar absorption patterns have been reported in the FT-IR spectra of acrylated epoxidized flaxseed oil polymers [17, 18].

3.2 Photo-crosslinking of AESBO

The kinetics of the UV curing of AESBO-1.5 containing 5 wt% Darocur 1173 (AESBO-1.5-PI5%) were analyzed using FT-IR spectroscopy, as shown in Figure 9. Key absorption peaks associated with the acrylate (C=C) groups were observed at 810 cm^{-1} and 1640 cm^{-1}. These peaks decreased in intensity with increasing UV irradiation time, reflecting the consumption of C=C bonds through photopolymerization [19]. The decrease in the 810 cm^{-1} band, in particular, was used to monitor the crosslinking kinetics of the AESBO film, as it corresponds to the out-of-plane deformation of the C=C bond in acrylate groups [6]. Upon UV exposure from 0 to 420 seconds, the conversion of double bonds increased steadily. After 60 seconds of irradiation, the 810 cm^{-1} peak showed no further change, indicating that the UV-curing process had reached completion. This confirms that AESBO-1.5, when combined with 5 wt% Darocur 1173, can be fully cured within 60 seconds under 400 W UV light [20].

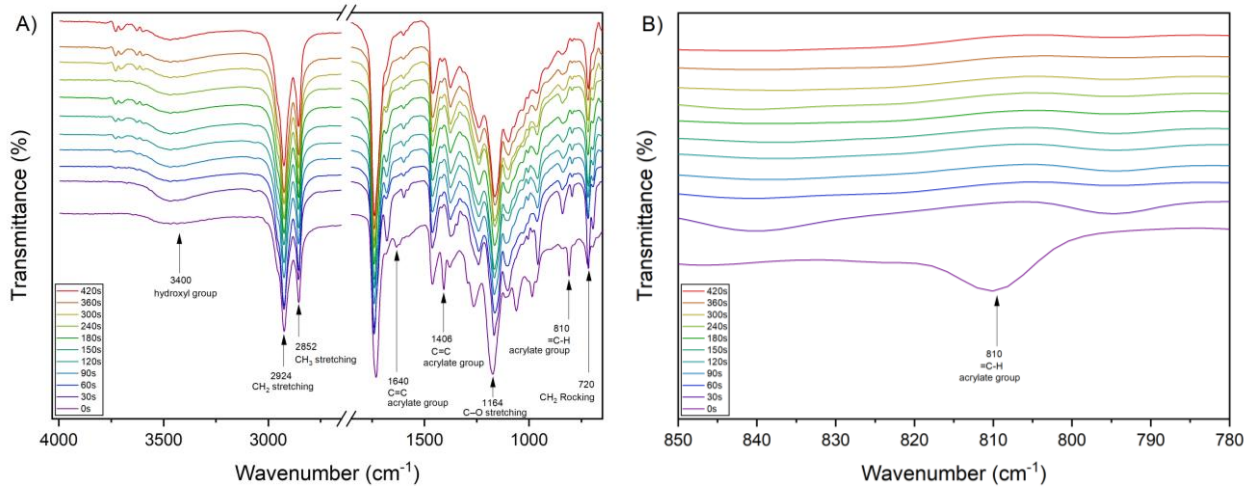


Figure 9. FT-IR spectra of UV-cured reaction kinetics of AESBO-1.5-PI5%.

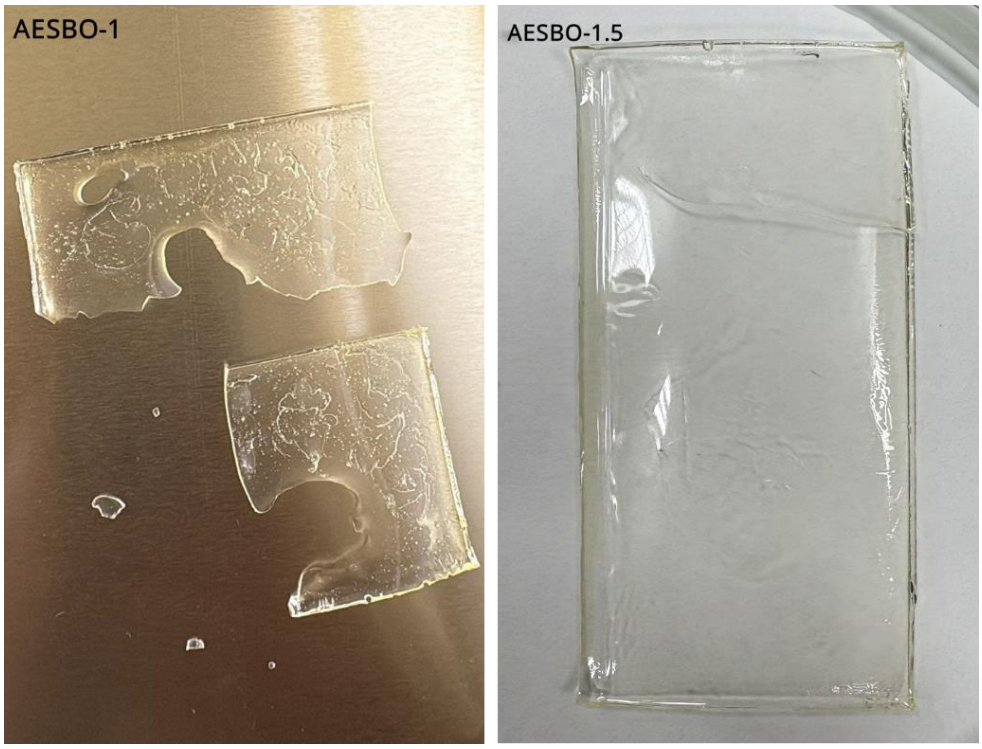


Figure 10. The AESBO-1 and AESBO-1.5 films.

In Figure 10, the AESBO-1 and AESBO-1.5 film sheets can be clearly distinguished. The AESBO-1 film appeared brittle and lacked sufficient strength to maintain its shape fully. In contrast, the AESBO-1.5 film exhibited improved strength and better shape retention, although brittleness remained. This indicates that increasing the acrylic acid ratio in the reaction enhances the film's ability to maintain its form more completely. A schematic diagram of the crosslinking reaction of AESBO is shown in Figure 11. Several strategies can be employed to enhance the toughness of bioplastic films derived from acrylated epoxidized soybean oil (AESO). To avoid excessive brittleness, the crosslink density can be optimized by incorporating flexible bio-based plasticizers, such as citrate esters or oligomeric polyols, which improve chain mobility. A tougher polymer matrix can be produced by blending ductile biodegradable polymers. Energy absorption during deformation can be improved by adding bio-based elastomeric modifiers, rubber nanoparticles, or core–shell impact modifiers. Toughness may be increased by reinforcement with well-dispersed nanofillers, such as cellulose

nanocrystals or graphene oxide, at low loadings, thereby improving crack deflection and stress transfer mechanisms. Additionally, tailoring the photoinitiator content, UV intensity, and UV curing time can help achieve a balanced network structure, and incorporating chain extenders or reactive diluents to increase molecular entanglement can significantly improve elongation at break and impact resistance without compromising mechanical strength.

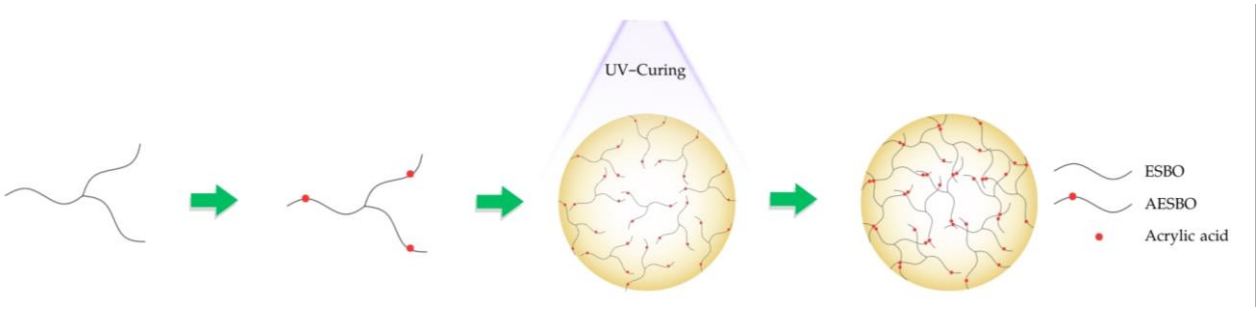


Figure 11. A schematic diagram of the crosslinking reaction of AESBO.

4. Conclusions

This study focuses on the development of a sustainable and environmentally friendly UV-cured material derived from AESBO. The process began with the epoxidation of SBO using formic acid and hydrogen peroxide at 60°C for 2 hours, followed by a ring-opening reaction. Acrylation was then performed using acrylic acid at molar ratios of 1:1, 1:1.5, and 1:2 for 8 hours. The structural modifications were confirmed through FT-IR and ^{1}H-NMR spectroscopy. The UV-curing behavior of the AESBO was investigated using 5 wt% Darocur 1173 as a photoinitiator under 400 W UV irradiation. Kinetic analysis revealed that film stability increased over time, reaching complete stability at 60 seconds, beyond which no significant changes were observed. These results highlight the potential of AESBO as a renewable and UV-curable material suitable for environmentally conscious applications. However, plastic films can be successfully fabricated from soybean oil–based materials; their physicochemical and functional properties must be fully evaluated before practical application. In particular, the systematic investigation of potential residual chemicals remaining from the synthesis and curing reactions is essential to ensure material safety, stability, and regulatory compliance. Detailed characterization of residual monomers, initiators, and other reactive species will provide critical insight into the suitability of the film for end-use applications, especially in contexts where human or environmental exposure may occur. The production of bioplastic film from soybean oil with UV curing offers several distinct advantages over the production of conventional petroleum-based plastics and thermally cured biopolymers. The use of renewable, plant-based resources reduces dependence on fossil fuels and lowers the carbon footprint, while UV curing enables rapid polymerization at ambient temperatures, minimizing energy consumption, processing time, and thermal degradation. Compared with traditional plastics such as polyethylene and polypropylene, soybean oil-based films can provide improved sustainability, inherent flexibility due to their long aliphatic chains, and tunable mechanical and barrier properties through formulation control. Compared with other bioplastics, such as polylactic acid, UV-cured soybean oil films often exhibit greater toughness and less brittleness, along with solvent-free and low-VOC processing. Overall, the combination of renewable feedstock and energy-efficient UV curing makes soybean oil-based bioplastic films an environmentally friendly, versatile, and industrially attractive alternative to conventional polymer films.

5. Acknowledgements

The author gratefully acknowledges the Faculty of Science and Technology, Prince of Songkhla University, Pattani Campus, for providing a personal scholarship under Grant No. 14/2566. The Center of Rubber Technology for Community (CRTC), Faculty of Engineering, Thaksin University, is also acknowledged for providing space and machinery for research.

Author Contributions: Conceptualization, A.S. and W.N.; methodology, A.S., W.N., T.T., and S.S.; validation,

all authors; formal analysis, A.U.; investigation, all authors; resources, A.S. and W.N.; data curation, all authors; writing—original draft preparation, A.U. and W.N.; writing—review and editing, all authors; visualization, A.S. and W.N.; supervision, A.S. and W.N.; project administration, W.N.; funding acquisition, A.S. and W.N.

Funding: This research was funded by Prince of Songkhla University, Pattani Campus, through a personal scholarship under Grant No. 14/2566.

Conflicts of Interest: The authors declare that they have no known competing financial interests or personal relationships that could have influenced the work reported in this paper.

References

[1] Shijie, D.; Zongqiang, M. Chemical Modification of Soybean Oil for Lubricant. In *Proceedings of ISES World Congress 2007*; Springer: Berlin, Heidelberg, 2008; pp 2430–2433. https://doi.org/10.1007/978-3-540-75997-3_492

[2] Siriwong, C.; Khansawai, P.; Boonchiangma, S.; Sirisinha, C.; Sae-Oui, P. The Influence of Modified Soybean Oil as Processing Aids in Tire Application. *Polym. Bull.* **2021**, *78*, 3589–3606. https://doi.org/10.1007/s00289-020-03296-z

[3] Song, H.; Taylor, D. C.; Zhang, M. Bioengineering of Soybean Oil and Its Impact on Agronomic Traits. *Int. J. Mol. Sci.* **2023**, *24*, 2256. https://doi.org/10.3390/ijms24032256

[4] Parreira, T. F.; Ferreira, M. M.; Sales, H. J.; De Almeida, W. B. Quantitative Determination of Epoxidized Soybean Oil Using Near-Infrared Spectroscopy and Multivariate Calibration. *Appl. Spectrosc.* **2002**, *56*, 1607–1614. https://doi.org/10.1366/000370202321115887

[5] Saithai, P.; Jonjanekieat, S.; Chinpa, W.; Tanrattanakul, V. Preparation of Epoxidized Soybean Oil. *KMUTT Res. Dev. J.* **2007**, *30*, 583–590.

[6] Vazquez-Martel, C.; Becker, L.; Liebig, W. V.; Elsner, P.; Blasco, E. Vegetable Oils as Sustainable Inks for Additive Manufacturing: A Comparative Study. *ACS Sustainable Chem. Eng.* **2021**, *9*, 16840–16848. https://doi.org/10.1021/acssuschemeng.1c06784

[7] Saithai, P.; Lecomte, J.; Dubreucq, E.; Tanrattanakul, V. Effects of Different Epoxidation Methods of Soybean Oil on the Characteristics of Acrylated Epoxidized Soybean Oil-co-Poly(methyl methacrylate) Copolymer. *Express Polym. Lett.* **2013**, *7*, 910–924. https://doi.org/10.3144/expresspolymlett.2013.89

[8] Branciforti, D. S.; Lazzaroni, S.; Milanese, C.; Castiglioni, M.; Auricchio, F.; Pasini, D.; Dondi, D. Visible Light 3D Printing with Epoxidized Vegetable Oils. *Addit. Manuf.* **2019**, *25*, 317–324. https://doi.org/10.1016/j.addma.2018.11.020

[9] Su, Y.; Lin, H.; Zhang, S.; Yang, Z.; Yuan, T. One-Step Synthesis of Novel Renewable Vegetable Oil-Based Acrylate Prepolymers and Their Application in UV-Curable Coatings. *Polymers* **2020**, *12*, 1165. https://doi.org/10.3390/polym12051165

[10] Barkane, A.; Platnieks, O.; Jurinovs, M.; Kasetaite, S.; Ostrauskaite, J.; Gaidukovs, S.; Habibi, Y. UV-Light Curing of 3D Printing Inks from Vegetable Oils for Stereolithography. *Polymers* **2021**, *13*, 1195. https://doi.org/10.3390/polym13081195

[11] Briede, S.; Platnieks, O.; Darzina, M.; Jirgensons, A.; Gaidukovs, S. Effect of Novel Furan-Based Ester Reactive Diluent on Structure and Properties of UV-Crosslinked Acrylated Rapeseed Oil. *J. Polym. Sci.* **2023**, *61*, 3318–3328. https://doi.org/10.1002/pol.20230451

[12] Clark, A. J.; Ross, A. H.; Bon, S. A. F. Synthesis and Properties of Polyesters from Waste Grapeseed Oil: Comparison with Soybean and Rapeseed Oils. *J. Polym. Environ.* **2017**, *25*, 1–10. https://doi.org/10.1007/s10924-016-0883-3

[13] Tang, Q.; Li, Q.; Luo, Y.; Pan, X.; Xi, Z.; Zhao, L. Development of an Innovative Biobased UV Coating Synthesized from Acrylated Epoxidized Soybean Oil and Poly(octamethylene maleate (anhydride) citrate). *Ind. Eng. Chem. Res.* **2021**, *60*, 9797–9806. https://doi.org/10.1021/acs.iecr.1c01258

[14] Mendes-Felipe, C.; Isusi, I.; Gómez-Jiménez-Aberasturi, O.; Prieto-Fernandez, S.; Ruiz-Rubio, L.; Sangermano, M.; Vilas-Vilela, J. L. One-Step Method for Direct Acrylation of Vegetable Oils: A Biobased Material for 3D Printing. *Polymers* **2023**, *15*, 3136. https://doi.org/10.3390/polym15143136

[15] Mekarat, S.; Suwan, A.; Chaisit, T.; Thongseenuch, S.; Saetung, A.; Saetung, N. Synthesis of Palm Oil-Based Bio-Polyol by Thiol-Ene Reaction: Preliminary Study of Its Potential as Cationic Waterborne Polyurethane for Coating Application. *Prog. Org. Coat.* **2024**, *194*, 108586. https://doi.org/10.1016/j.porgcoat.2024.108586

[16] Yıldız, Z. Usage of UV-Curable Soybean Oil Based Coating Formulations for Pretreated Cotton Fabrics. *Text. Apparel* **2022**, *32*, 232–242. https://doi.org/10.32710/tekstilvekonfeksiyon.940434

[17] Wuzella, G.; Mahendran, A. R.; Müller, U.; Kandelbauer, A.; Teischinger, A. Photocrosslinking of an Acrylated Epoxidized Linseed Oil: Kinetics and Its Application for Optimized Wood Coatings. *J. Polym. Environ.* **2012**, *20*, 1063–1074. https://doi.org/10.1007/s10924-012-0511-9

[18] Rana, A.; Evitts, R. W. Synthesis and Characterization of Acrylated Epoxidized Flaxseed Oil for Biopolymeric Applications. *Int. Polym. Process.* **2015**, *30*, 331–336. https://doi.org/10.3139/217.2961

[19] Barkane, A.; Platnieks, O.; Jurinovs, M.; Gaidukovs, S. Thermal Stability of UV-Cured Vegetable Oil Epoxidized Acrylate-Based Polymer System for 3D Printing Application. *Polym. Degrad. Stab.* **2020**, *181*, 109347. https://doi.org/10.1016/j.polymdegradstab.2020.109347

[20] Tsupphayakorn-aek, P.; Suwan, A.; Tulyapitak, T.; Saetung, N.; Saetung, A. A Novel UV-Curable Waterborne Polyurethane-Acrylate Coating Based on Green Polyol from Hydroxyl Telechelic Natural Rubber. *Prog. Org. Coat.* **2022**, *163*, 106585. https://doi.org/10.1016/j.porgcoat.2021.106585

[21] Xu, Q.; Lin, J.; Jiang, G. Synthesis, Characterization and Properties of Soybean Oil-Based Polyurethane. *Polymers* **2022**, *14*, 2201. https://doi.org/10.3390/polym14112201

ASEAN
Journal of Scientific and Technological Reports
Online ISSN:2773-8752

Research article

Evaluation of the Nutritional, Mineral, and Estimated Metabolizable Energy Values of Agricultural Biomass Raw Materials Used for the Development of Concentrated Fermented Feed for Beef Cattle in Mukdahan Province, Northeast Thailand

Nathaporn Jirawattanasomkul[1, 2], Wuttichai Roschat[1, 2*], Tappagorn Leelatam[1, 2], Sasithon Phanphli[1], Watanya Chaipikun[1], Aekkaphon Thammayod[1, 2], Noppharat Khotsuno[1, 2], Permsak Yeemin[1], Nattapong Wongma[1], and Sunti Phewphong[2]

[1] Faculty of Science and Technology, Sakon Nakhon Rajabhat University, Sakon Nakhon, 47000, Thailand
[2] Biomass Energy Research Laboratory, Center of Excellence on Alternative Energy, Research and Development Institution, Sakon Nakhon Rajabhat University, Sakon Nakhon, 47000, Thailand
* Correspondence: roschat1@gmail.com

Citation:
Jirawattanasomkul, N.; Roschat, W.; Leelatam, T.; Phanphli, S.; Chaipikun, W.; Thammayod, A.; Khotsuno, N.; Yeemin, P.; Wongma, N.; Phewphong, S. Evaluation of the nutritional, mineral, and Estimated Metabolizable Energy values of agricultural biomass raw materials used for the development of concentrated fermented feed for beef cattle in Mukdahan Province, Northeast Thailand. *ASEAN J. Sci. Tech. Report.* **2026**, *29*(4), e262452. https://doi.org/10.55164/ajstr.v29i4.262452.

Article history:
Received: August 6, 2025
Revised: March 9, 2026
Accepted: March 11, 2026
Available online: March 25, 2026

Publisher's Note:
This article is published and distributed under the terms of the Thaksin University.

Abstract: This study evaluated the nutritional, mineral, and estimated metabolizable energy (EME) profiles of eight locally available agricultural biomass raw materials to support the development of a cost-effective concentrated fermented feed (CFF) for beef cattle in Mukdahan Province, Northeast Thailand. Finely ground maize kernels, soybean meal, palm kernel meal, rice bran, dried cassava chips, cassava pulp, washed cassava peels, and fresh cassava starch residue were analyzed for proximate composition, EME, and essential minerals (Ca, Mg, P, Fe, Zn, Na, and K), with all values reported on an as-fed basis. A CFF formulation (1,000 kg batch) was developed from these raw materials and compared with five commercial beef cattle feeds. Soybean meal, palm kernel meal, and rice bran exhibited the highest protein contents, while rice bran showed the greatest calculated EME value (4097 kcal/kg of sample). Cassava-based by-products were rich in carbohydrates but relatively low in protein and fat. Mineral analysis revealed substantial variation among raw materials, with high concentrations of P, Mg, Ca, and K in several biomass sources. The formulated CFF contained 12.16 ± 0.21% crude protein, 3.29 ± 0.05% fat, and 47.56 ± 0.90% carbohydrates. The calculated EME content was 2685 kcal/kg of sample, which is highly comparable to the nutrient profiles of commercial feeds available in the market. Importantly, CFF production costs were markedly lower (4.50 THB/kg) than those of commercial products (10.67–15.33 THB/kg), demonstrating significant economic advantages. Overall, the results confirm that locally sourced biomass can be effectively used to formulate nutritionally adequate, mineral-rich, and low-cost fermented feed, thereby contributing to sustainable beef cattle production and reducing farmers' feed expenses.

Keywords: Agricultural biomass; fermented feed; beef cattle nutrition; nutritional composition; estimated metabolizable energy (EME) evaluation

1. Introduction

Thailand is an agriculture-driven nation with approximately 20 million people (28% of the population) engaged in the sector. Agriculture is vital to national economic development, with crop cultivation—including rice, rubber, cassava, oil palm, maize, and soybean—serving as both key export commodities and essential raw materials for livestock feed and various agro-industries [1–5]. According to the Land Development Department (2019), agricultural land covers approximately 153 million rai (47.77% of the total area) and supports 5.8 million farming households. This extensive base ensures national food security and provides a steady supply of raw materials for domestic and export markets, thereby strengthening economic stability and long-term competitiveness [5–7]. The livestock sector is also an important component of Thailand's agricultural economy. Data from the Department of Livestock Development (DLD, 2021) indicate that the country had 3,302,406 livestock farmers, accounting for approximately 16.5% of total agricultural households. Most farmers raise beef, dairy, and buffalo cattle, swine, and native chickens. Notably, the beef cattle population reached 7,364,967 head in 2021. In Livestock Zone 4 (Central Northeast and Upper Northeast regions), Mukdahan Province alone recorded about 17,477 beef cattle farmers managing 79,071 head, generating an estimated total income of 2.4 billion Thai Baht (based on an average sale price of 30,000 Baht per head). These statistics highlight beef cattle production as a viable pathway to enhance rural income and economic resilience [8–10].

Feed cost is recognized as the most significant expense in cattle production systems, accounting for more than 60% of the total production cost. The continuous rise in raw material prices—particularly for imported soybean meal—has intensified this financial burden. Consequently, developing cost-effective feed formulations using locally available agricultural by-products has become a practical strategy to reduce production costs while simultaneously creating market opportunities for local crop producers [11–13]. Several studies have addressed this issue. Sooksoi [14] reported that rice straw used as roughage by dairy farmers in Sa Kaeo Province had low nutritional quality, characterized by a low protein content (2.78%) and high levels of cell wall and lignocellulosic fiber (78.05% and 56.89%, respectively). Munier et al. [15] demonstrated that corn cob silage significantly improved average daily gain and body condition score in Donggala cattle, with inclusion levels of 30.5–31% yielding the best results ($p < 0.05$). Dagaew et al. [16] further showed that cassava solid yeast waste (CSYW) could completely replace soybean meal in concentrate diets for Thai native beef cattle without adverse effects on feed intake, digestibility, or rumen fermentation, while increasing rumen ammonia–nitrogen and total bacterial populations ($p < 0.05$).

Despite the potential of agricultural by-products, a research gap exists regarding the mineral and EME profiling of biomass unique to the Mukdahan border trade zone. While previous studies focused on single-ingredient replacements or silage quality, Mukdahan offers a unique industrial landscape with high volumes of residues from sugar, cassava, and oil palm plants. Lack of integrated data on these local materials hinders the development of a CFF tailored to regional production. Without precise EME and mineral evaluations on an as-fed basis, farmers rely on expensive commercial feeds or unbalanced residues, which limits efficiency. This study addresses this gap by mapping local biomass to develop a scientifically formulated, cost-effective CFF. Additionally, fermentation technology enhances feed quality through pre-digestion, where microbial enzymes degrade complex carbohydrates and anti-nutritional factors, improving bioavailability and palatability. Fermented feeds also provide beneficial microorganisms and organic acids that stabilize ruminal pH and improve fermentation efficiency. These biological improvements enhance feed intake and metabolic health, offering a superior alternative to non-fermented local diets.

In Nong Sung District, Mukdahan Province, the Nong Sung Agricultural Cooperative Limited has established an integrated beef cattle production model encompassing upstream (breeding management), midstream (feed development), and downstream (processing and marketing) operations. This holistic system strengthens the economic sustainability of both livestock and crop farmers. However, the recent escalation in feed prices, driven by the high cost of imported protein sources, has negatively affected production profitability and farmer income. Therefore, this study was designed with the primary objective to conduct a comprehensive laboratory-based evaluation of eight locally available agricultural biomass raw materials in Mukdahan Province. Specifically, the research aims to: (1) determine the proximate composition and essential

mineral profiles (Ca, Mg, P, Fe, Zn, Na, and K) of regional biomass; (2) EME values based on chemical analysis; and (3) develop a cost-effective CFF formulation by comparing its laboratory-derived nutritional profile and production cost with commercial alternatives. It should be noted that this study focuses exclusively on the nutritional and economic characterization of the feed, and does not include in vivo animal performance trials.

2. Materials and Methods

2.1 Materials and sampling procedure

Agricultural biomass raw materials were collected from various locations in Mukdahan Province, Thailand, during the period from October to December, 2023. To ensure data representativeness, each biomass material was collected in three independent batches (n = 3) from different local sources, including sugar mills, cassava starch factories, palm oil extraction plants, and community rice mills. The collected materials included finely ground maize kernels (FMK), soybean meal (SBM), palm kernel meal (PKM), rice bran (RB), dried cassava chips (DCC), cassava pulp after starch extraction (CSP), washed cassava peels (WCP), and fresh cassava starch residue (CSR) as displayed in Figure 1. For the formulated feeds, the CFF was developed in collaboration between the Nong Sung Agricultural Cooperative Limited and the Appropriate Technology Center at Sakon Nakhon Rajabhat University. A total of 3 independent 1,000-kg CFF batches were produced and sampled for analysis. Furthermore, five commercial beef cattle feeds were procured from different local distributors: one pelleted feed (12% protein, C1), three pelleted feeds from different manufacturers (14% protein, C2, C3, and C4), and one powdered feed (14% protein, C5), as shown in Figure 2. From each commercial product, three separate bags were randomly sampled as replicates. All biomass, CFF, and commercial feed samples were oven-dried at 60°C until constant weight was reached, then finely ground to pass through a 1-mm screen to ensure uniformity for subsequent analytical procedures. To ensure consistent comparison across all analyses, including proximate composition, minerals, and EME values, all nutritional data in this study are reported on an as-fed basis. This approach was selected to provide practical information that aligns with local farmers' actual feeding practices.



Figure 1. Agricultural biomass raw materials collected from Mukdahan Province, Thailand, including finely ground maize kernels, cassava pulp (after starch extraction), dried cassava chips, rice bran, washed cassava peels, soybean meal, palm kernel meal, and fresh cassava starch residue used for CFF formulation.

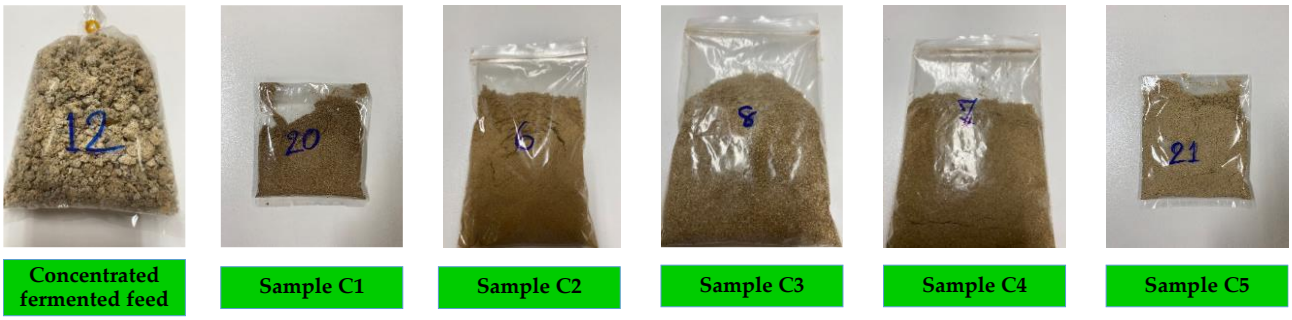


Figure 2. Concentrated fermented feed (CFF) was developed in collaboration between the Nong Sung Agricultural Cooperative Limited and the Appropriate Technology Center, SNRU, along with commercial beef cattle feeds (C1–C5) collected from the Mukdahan market for comparative analysis.

The key reagents used in this study included analytical reagent (AR) grade chemicals as follows: sodium hydroxide (NaOH), boric acid (H_3BO_3), hydrochloric acid (HCl), sulfuric acid (H_2SO_4), copper (II) sulfate ($CuSO_2$), acetone (C_3H_6O), hydrogen peroxide (H_2O_2), nitric acid (HNO_3), strontium chloride hexahydrate ($SrCl_2{\cdot}6H_2O$), and perchloric acid ($HClO_4$), all supplied by Ajax Finechem (Australia). Hexane (C_6H_{14}) of AR grade was obtained from KEMAUS (Australia). Standard solutions of calcium (Ca), magnesium (Mg), zinc (Zn), iron (Fe), sodium (Na), potassium (K), and phosphorus (P) were also AR grade and supplied by Ajax Finechem. In addition, methylene blue and methyl red were used as analytical indicators.

2.2 Preparation of the biomass raw materials and beef cattle feed samples

The collected biomass was oven-dried and ground into a fine powder before being sealed in zip-lock bags for subsequent analysis. The moisture content of the samples was determined following the method described by Phewphong et al. [17], Suwannatrai et al. [18], and Preecharram et al. [19, 21]. Initially, empty beakers were dried in a hot-air oven at 105 °C until a constant weight was obtained and then cooled in a desiccator. The weight of the dried beaker (W_B) was recorded. Approximately 5 g of the sample was weighed into the beaker, and its total weight (W_S) was recorded. The beakers containing the samples were then dried in the oven at 105 °C for 3 h, cooled in a desiccator for 30 min at room temperature, and reweighed. The drying and weighing process was repeated at 30 min intervals until a constant weight (W_T) was achieved. Each determination was performed in triplicate. The percentage of moisture content was calculated using Eq. (1):

$$\text{Moisture content (\%)} = [W_S - (W_T - W_B) / W_S] \times 100 \quad (1)$$

where W_S is the weight of the sample before drying (g), W_T is the weight of the beaker with the dried sample (g), and W_B is the weight of the empty beaker (g).

2.3 The proximate analysis of the biomass raw materials and beef cattle feed samples

2.3.1 Determination of crude protein content

The total crude protein content of the biomass raw materials and beef cattle feed samples was determined following the AOAC method [20] and previous studies by Phewphong et al. [17] and Preecharram et al. [19, 21]. Briefly, 1.0 g of the finely ground sample was weighed into a digestion tube. Two catalyst tablets containing 10 g of potassium sulfate (K2SO4) and 1 g of copper (II) sulfate (CuSO4) were added to accelerate digestion. Subsequently, 15 mL of concentrated sulfuric acid was carefully added, and the mixture was gently shaken to homogenize. The digestion tube was then placed in a digestion apparatus equipped with an acid fume trap and heated at 420 °C for approximately 1 h or until the solution became clear green, indicating complete digestion. The tube was removed and allowed to cool to room temperature while the fume trap remained active to absorb any residual acid vapors. For steam distillation, the distillation apparatus was first rinsed with distilled water and then prepared by adding 80 mL of distilled water, 50 mL of 32% (w/v) sodium hydroxide, and 30 mL of 4% boric acid containing mixed indicators (methylene blue and methyl red) into a 250 mL conical flask. The digestion tube was attached to the distillation unit, ensuring that the glass tip was

immersed in the solution. The system was closed and distillation was performed for approximately 5 min. After distillation, the contents of the conical flask were titrated with 0.1 N hydrochloric acid (HCl) until the color changed from green to purple. All analyses were performed in triplicate. The total nitrogen content was calculated and converted to crude protein using the following equations (2) and (3):

$$\text{Nitrogen (\%)} = [(0.014007) \times (V_1 - V_2) \times N_{HCl} / \text{Sample weight (g)}] \times 100 \quad (2)$$

$$\text{Protein (\%)} = \text{Nitrogen (\%)} \times 6.25 \quad (3)$$

where V_1 is the volume of 0.1 N HCl required to titrate the sample (mL), V_2 is the volume used for the blank titration (mL), N_{HCl} is the exact normality of the HCl used (0.1 N), and 0.014007 is the milliequivalent weight of nitrogen. The conversion factor of 6.25 was used to convert nitrogen content to protein content.

2.3.2 Determination of fat content

The fat content of the samples was determined using the Soxhlet extraction technique, following the procedures described by Phewphong et al. [17], Preecharram et al. [19, 21], and Suwannatrai et al. [18, 22]. First, an aluminum dish was dried in a hot air oven at 105 °C for 1 h, cooled in a desiccator for 30 min, and reheated at 30 min intervals until a constant weight was obtained (M_1). Approximately 1 g of the dried sample was accurately weighed using a four-decimal analytical balance and transferred into a thimble (M_0). The thimble containing the sample was placed in the Soxhlet extractor, and 120 mL of analytical-grade hexane was added as the solvent. The extraction was carried out under reflux for 3 h. After extraction, the solvent was removed using a rotary evaporator, and the remaining oil residue was oven-dried at 105 °C for 30 min, cooled in a desiccator, and reweighed. The drying process was repeated every 30 min until a constant weight was achieved (M_2). All experiments were conducted in triplicate.

The percentage yield of the extracted oil was calculated based on the dry weight of the sample using Eq. (4):

$$\text{\%Yield of oil} = [(M_2 - M_1) / M_0] \times 100 \quad (4)$$

where M_0 is the initial sample weight (g), M_1 is the weight of the empty aluminum dish (g), and M_2 is the weight of the aluminum dish containing the extracted oil (g).

2.3.3 Determination of crude fiber content

The crude fiber content of the samples was determined from the defatted residues obtained after Soxhlet extraction, following the procedures described by Phewphong et al. [17], Preecharram et al. [19,21], Suwannatrai et al. [18, 22], and Salami and Afolayan [23]. Approximately 1 g of the defatted sample was placed in a sintered glass crucible. A total of 200 mL of 0.128 M sulfuric acid solution was added, and the mixture was heated to boiling for 30 min. During boiling, the volume was maintained constant by adding distilled water as needed. The mixture was then filtered through the sintered glass crucible under suction and washed with hot distilled water three times (50 mL each). Subsequently, 200 mL of 0.313 M sodium hydroxide solution was added, and the mixture was again boiled for 30 min while maintaining a constant volume by adding distilled water. The residue was filtered under suction and washed with hot distilled water three times (50 mL each).

The remaining residue was further washed with 25 mL of 0.128 M sulfuric acid, then with 25 mL of hot distilled water until the acid was completely removed, and finally washed three times with 50 mL of acetone. The crucible containing the residue was dried in a hot air oven at 105 °C for 1 h, then ignited in a muffle furnace at 550 °C until a white ash was obtained. The crucible was cooled in a desiccator and weighed. All analyses were performed in triplicate. The crude fiber content (%) was calculated using Eq. (5):

$$\text{Crude fiber content (\%)} = [(M_1 - M_2) / M_0] \times 100 \quad (5)$$

where M_1 is the weight of the crucible with the dried residue (g), M_2 is the weight of the crucible with ash after ignition (g), and M_0 is the sample weight (g).

2.3.4 Determination of ash content

The ash content of the samples was determined according to the standard procedures reported by Phewphong et al. [17], Preecharram et al. [19,21], and Suwannatrai et al. [18, 22]. Briefly, a clean crucible was dried in an oven at 105 °C until a constant weight was achieved, cooled in a desiccator, and weighed to obtain the empty crucible weight (W_B). Approximately 1 g of the sample (W_0) was placed into the crucible and incinerated in a muffle furnace at 550 °C until white ash was obtained. After cooling in a desiccator, the crucible containing the ash was weighed (W_T). The ash content was calculated using the following Eq. (6):

$$\text{Ash content (\%)} = [(W_T - W_B) / W_0] \times 100 \quad (6)$$

where W_T is the weight of the crucible with the ash (g), W_B is the weight of the empty crucible (g), and W_0 is the weight of the sample (g). All measurements were performed in triplicate to ensure accuracy.

2.3.5 Determination of carbohydrate content

The carbohydrate content of the samples was estimated by difference, based on the proximate composition including moisture, crude protein, crude fat, ash, and crude fiber, following the method described by Phewphong et al. [17], Preecharram et al. [19, 21], and Suwannatrai et al. [18, 22]. The carbohydrate content was calculated using the following Eq. (7):

$$\text{Carbohydrate (\%)} = 100 - (\%\text{Moisture} + \%\text{Protein} + \%\text{Fat} + \%\text{Ash} + \%\text{Crude Fiber}) \quad (7)$$

For samples with high moisture content, carbohydrate content was calculated on a dry-weight basis to ensure accuracy.

2.3.6 Determination of EME content

The EME content of the samples was estimated based on their proximate composition, following the approach described by Phewphong et al. [17], Preecharram et al. [19, 21], Suwannatrai et al. [18, 22], and Salami and Afolayan [23]. The energy values reported in this study are referred to as EME and are calculated from modified Atwater factors derived from proximate analysis data. It is important to acknowledge that these values represent theoretical energy yields rather than direct physiological measurements from in vivo ruminant digestion trials (in vivo ME). This estimation approach is commonly used in laboratory-scale nutritional screenings to provide a rapid and cost-effective energy profile of various feed ingredients. The calculation accounted for each macronutrient using the following energy values: 4 kcal/g for total carbohydrates, 4 kcal/g for crude protein, and 9 kcal/g for crude fat. The total energy content was then calculated as the sum of these contributions using Eq. (8):

$$\text{EME (kcal/100 g of sample)} = (4 \times \text{Carbohydrates}) + (4 \times \text{Protein}) + (9 \times \text{Fat}) \quad (8)$$

This approach provides estimates of the caloric value of biomass raw materials and beef cattle feed samples, allowing comparison of energy density across different formulations. Furthermore, the experimental results were processed and reported as kcal/kg of sample, as this unit is widely recognized, easy to understand, and commonly used in practical feed formulation.

2.4 Determination of mineral content in biomass raw materials and beef cattle feed samples

The mineral composition of the biomass raw materials and beef cattle feed samples was determined following standard procedures, based on the AOAC method [24] and the approaches described by Phewphong et al. [17], Preecharram et al. [19], and Bvenura and Afolayan [25]. Approximately 1 g of each sample was accurately weighed into a 100 mL beaker, after which 20 mL each of concentrated nitric acid (HNO_3) and hydrogen peroxide (H_2O_2) was added. The mixture was digested on a hot plate until a clear solution was obtained, ensuring that the solution did not completely dry. The digested solution was allowed to cool to room temperature, filtered, and the filtrate was collected in a 100 mL volumetric flask, adjusted to

volume with distilled water, and thoroughly mixed prior to analysis using an Atomic Absorption Spectrometer (AAS, iCE3000 series, Thermo, USA).

2.4.1 Determination of Magnesium (Mg) and Calcium (Ca)

The concentrations of Mg and Ca in the biomass raw materials and beef cattle feed samples were determined using an AAS. The digested sample solutions prepared as described in Section 2.4 were used for this analysis. For the preparation of reagents, a mixed acid solution of nitric acid (HNO_3, 69–70%) and perchloric acid ($HClO_4$, 69–72%) in a 1:1 v/v ratio was prepared and thoroughly mixed. Additionally, a strontium chloride solution was prepared by dissolving 61 g of $SrCl_2 \cdot 6H_2O$ in 420 mL of 36–38% HCl, then diluting to 1000 mL with distilled water. Working standard solutions of Mg and Ca at concentrations of 0, 2, 4, 6, 8, and 10 ppm were prepared by adding 5 mL of the strontium chloride solution to each flask, followed by pipetting appropriate volumes (0, 1, 2, 3, 4, and 5 mL) of 10 ppm stock solutions into 50 mL volumetric flasks, and adjusting the volume to the mark with distilled water. The digested sample solutions were then analyzed using AAS, and the absorbance values were compared with those of the working standards to determine the concentrations of Mg and Ca in the samples. The mineral content in the samples was calculated using the following eq. (9):

$$\text{Mg or Ca (\%)} = [(\text{ppm} \times \text{dilution factor}) / (\text{Wt. of sample (g)} \times 10^6)] \times 100 \quad (9)$$

where ppm is the concentration obtained from the AAS measurement, the dilution factor accounts for any dilution of the digested sample solution, and Wt. of sample is the weight of the original sample used for digestion. This approach ensures that the concentrations of Mg and Ca are accurately determined from the solutions prepared in Section 2.4, providing a direct link between sample digestion and mineral analysis.

2.4.2 Determination of Na, K, Zn, and Fe

The concentrations of Na, K, Zn, and Fe in the biomass raw materials and beef cattle feed samples were determined using the digested sample solutions prepared in Section 2.4. For reagent preparation, a mixed acid solution of nitric acid (HNO_3, 69–70%) and perchloric acid ($HClO_4$, 69–72%) in a 1:1 v/v ratio was used. Working standard solutions for each mineral were prepared at appropriate concentrations: 0, 2, 3, 4, and 5 ppm for Na, K, and Zn, and 0, 1, 2, 3, 4, and 5 ppm for Fe. The standards were prepared by pipetting suitable volumes of 100 ppm stock solutions into 50 mL volumetric flasks and adjusting the volume with distilled water. The digested sample solutions were analyzed using an AAS. The absorbance values of the samples were compared to those of the working standards, and the concentrations of each mineral were calculated using the following eq. (10):

$$\text{Mineral (\%)} = [(\text{ppm} \times \text{dilution factor}) / (\text{Wt. of sample (g)} \times 10^6)] \times 100 \quad (10)$$

where ppm is the concentration obtained from the AAS measurement, the dilution factor accounts for any dilution of the digested sample solution, and Wt. of sample is the weight of the original sample used for digestion. This procedure ensures accurate determination of Na, K, Zn, and Fe from the digested solutions prepared as described in Section 2.4.

2.4.3 Determination of P

The P content in the biomass raw materials and beef cattle feed samples was determined using the digested sample solutions from Section 2.4. A molybdovanadate reagent was prepared by dissolving 40 g of ammonium molybdate in 400 mL of hot distilled water and 2 g of ammonium metavanadate in 300 mL of hot distilled water, followed by the addition of 450 mL of HClO4 (69–72%) and thorough mixing. The final solution was diluted to 2000 mL with distilled water. Working standard solutions of P at concentrations of 1, 2, 4, 6, 8, 10, and 12 ppm were prepared by pipetting suitable volumes of a 100 ppm stock solution into 50 mL volumetric flasks and adjusting the volume to the mark with distilled water. The digested sample solutions were analyzed using a UV-Vis spectrophotometer. The absorbance of each sample was compared to the standard calibration curve, and the phosphorus content was calculated using the eq. (11):

$$P\ (\%) = [(ppm \times dilution\ factor) / (Wt.\ of\ sample\ (g) \times 10^6)] \times 100 \quad (11)$$

Where ppm is the phosphorus concentration obtained from the spectrophotometer, the dilution factor accounts for any sample dilution, and Wt. of sample is the weight of the original sample. This method ensures that phosphorus content is accurately determined from the digested solutions prepared in Section 2.4.

2.5 Analysis of Feed Cost for Beef Cattle

The feed cost analysis in this study was conducted by collecting and comparing data on commercially available cattle feed and feed formulated by Nong Sung Agricultural Cooperative Limited. Detailed information was gathered for each feed type, including the feed name, composition of raw materials, and the cost of each ingredient and the final feed product. The data collection process involved direct surveys and interviews with local farmers to ensure accuracy and representativeness of the feed types commonly used in the region. The analysis aimed to evaluate the economic efficiency of different feed formulations by calculating the total feed costs required to raise beef cattle under local farming practices in Nong Sung District, Mukdahan Province. This comparative approach provides insights into potential cost savings and the financial feasibility of using cooperative-formulated feed versus commercially available feed. The resulting data serve as a practical database that can support farmers and cooperative members in strategic planning, budgeting, and optimization of feeding strategies for sustainable beef cattle production.

3. Results and Discussion

3.1 Analysis of the nutritional composition of biomass raw materials for CFF

This study investigated the nutritional composition of various biomass raw materials intended for the development of CFF formulations. The objective was to establish a scientific basis for selecting suitable and locally available ingredients for cost-effective feed production. Eight biomass feed ingredients—FMK, SBM, PKM, RB, DCC, CSP, WCP, and CSR—were analyzed for their proximate composition. The proximate composition of these materials—focusing on protein, carbohydrate, and fat—was determined, as these nutrients are essential for muscle development, energy supply, and growth performance in beef cattle. Among them, protein content plays a particularly critical role in formulating feeds tailored to different growth stages, including the starter (under 1 year), grower (around 2 years), and fattening (2–3 years) phases [26, 27].

As shown in Table 1 and Figure 3, SBM, PKM, and RB contained the highest protein levels (43.81%, 14.21%, and 11.75%, respectively), while fat was highest in RB (12.69%), PKM (9.70%), and FMK (2.22%), significantly exceeding cassava-based by-products (0.31–1.03%). These variations result from the biochemical characteristics of plant tissues, genetics, and processing methods. Cassava by-products are carbohydrate-rich, whereas soybeans and palm kernels accumulate higher levels of lipids and proteins, consistent with prior studies on starch and oilseed processing [28]. Industrial operations—such as starch extraction and oil pressing—substantially alter nutrient profiles by concentrating or removing macronutrients, such as residual oil retention in PKM [29]. Furthermore, environmental factors such as soil fertility and harvest maturity, along with the physiological roles of different plant parts (e.g., bran vs. root), contribute to the observed nutrient variability [30]. Consequently, rice bran and oilseed meals naturally exhibit higher protein and lipid contents than root-based biomass.

The proximate composition aligns with previous reports, with minor variations due to sources and processing. Suksroi [14] and Promthep and Siriamornpun [31] reported protein levels in cassava residues and maize consistent with our findings. Notably, the fat content observed in rice bran (12.69%) and palm kernel meal (9.70%) in this study is higher than some reported averages. This elevation is likely due to mechanical extraction methods, such as expeller pressing, which typically yield higher residual oil content than solvent extraction. Furthermore, the high carbohydrate content in cassava-based materials (55.54%–83.49%) reflects the efficiency of the local processing stage in preserving starch fractions. Variation within species was also noted by Kraiprom et al. [32] regarding oil-palm fractions. Recent studies by Budianto [33] and Bamikole [34] further indicate that such nutrient fluctuations in maize and cassava-based diets directly affect ruminal fermentation, digestibility, and growth performance. These findings emphasize that plant genotype and processing methods determine nutrient profiles, underscoring the need for precise synchronization in CFF

formulation to enhance productivity. Generally, Proximate composition is driven by genotype, soil fertility, and processing. Feed selection should align with the specific nutritional needs of beef cattle growth stages. High-protein SBM, PKM, and RB support muscle development in pre-weaning calves, while the high fat content in PKM and RB provides energy for the growing stage. For fattening, SBM, FMK, and WCP offer an ideal protein-fat balance for weight gain. Utilizing local biomass reduces costs while ensuring nutrient adequacy. However, raw material selection must also account for regional availability, affordability, and storage stability within farming communities.

Table 1. Proximate composition (%) of biomass raw materials used for CFF formulation for beef cattle.

Biomass raw material	Moisture (%)	Ash (%)	Fat (%)	Protein (%)	Fiber (%)	Carbohydrate (%)
Finely ground maize kernels (FMK)	8.00±0.25	1.84±0.08	2.22±0.12	6.83±0.15	3.55±0.10	77.56±0.28
Soybean meal (SBM)	8.40±0.20	6.86±0.04	1.86±0.09	43.81±0.42	6.24±0.25	32.83±0.54
Palm kernel meal (PKM)	3.29±0.18	3.86±0.07	9.70±0.21	14.21±0.30	18.52±0.31	50.42±0.52
Rice bran (RB)	4.53±0.15	5.82±0.06	12.69±0.26	11.75±0.22	3.08±0.08	62.12±0.35
Dried cassava chips (DCC)	6.38±0.18	4.41±0.05	0.49±0.02	2.22±0.10	3.01±0.10	83.49±0.27
Cassava pulp–after starch extraction (CSP)	9.79±0.22	3.99±0.08	0.46±0.03	2.52±0.09	13.62±0.20	69.62±0.32
Washed cassava peels (WCP)	10.42±0.24	9.13±0.07	1.03±0.04	6.62±0.14	17.26±0.22	55.54±0.30
Fresh cassava starch residue (CSR)	16.09±0.30	5.80±0.09	0.31±0.03	1.99±0.08	16.64±0.20	59.17±0.25

Note: Values are expressed as mean ± standard deviation (SD, n = 3), and all nutritional, mineral, and EME values are expressed on an as-fed basis.

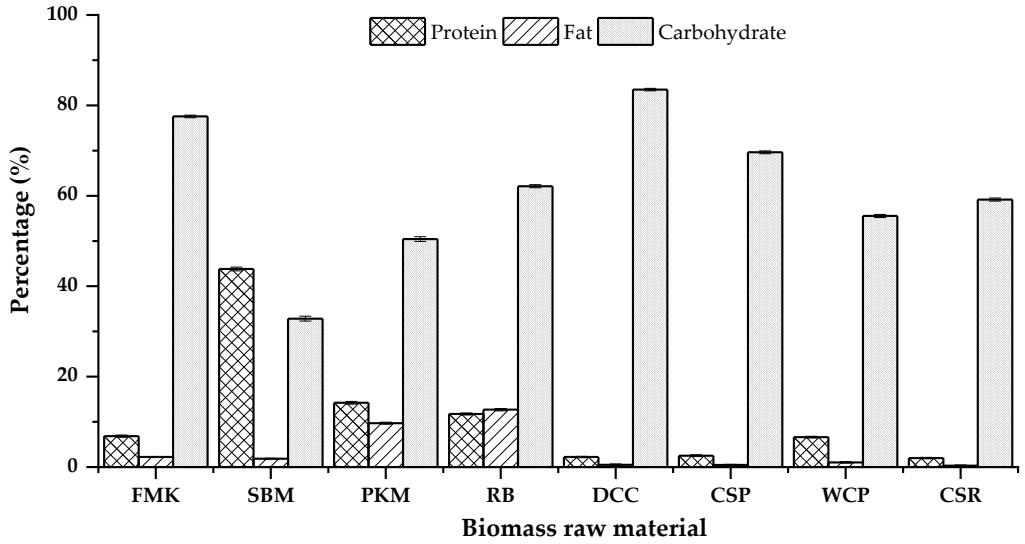


Figure 3. Proximate composition (carbohydrate, protein, and fat contents) of biomass raw materials used for CFF formulation.

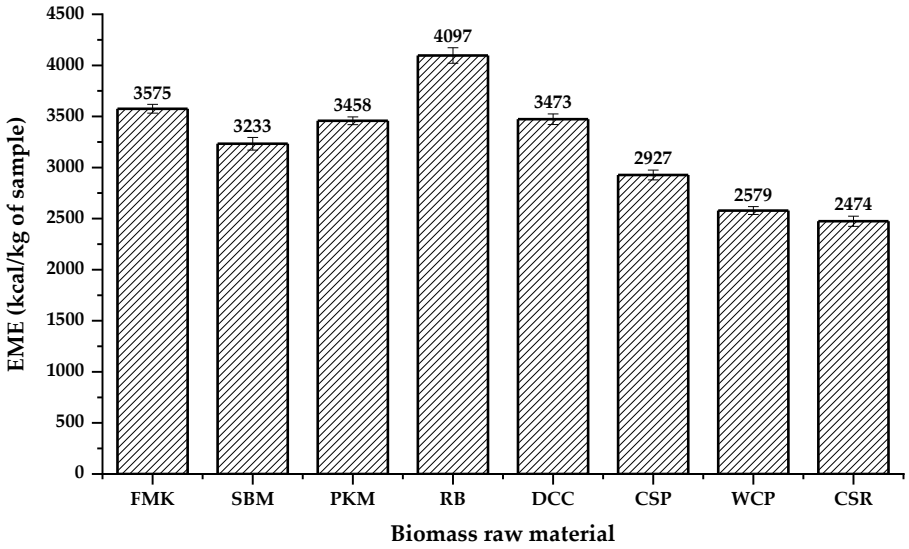


Figure 4. EME values of biomass raw materials used for CFF formulation.

3.2 Nutritional EME analysis of biomass raw materials for CFF formulation

In this study, the nutritional EME content of eight biomass raw materials intended for beef cattle feed was analyzed as illustrated in Figure 4. The experimental results were processed and reported on a kcal/kg sample (as-fed basis) to facilitate practical application and standardized comparison, as this unit is widely recognized in livestock feed formulation. The calculated EME content of the samples ranged from 2474 to 4,097 kcal/kg. Among the materials analyzed, RB exhibited the highest EME density at 4097 kcal/kg, primarily due to its superior fat (12.69%) and protein (11.75%) levels, which aligns with recent studies highlighting RB as a nutrient-rich feedstuff. In contrast, CSR provided the lowest EME value (2474 kcal/kg), while other materials such as FMK, PKM, and SBM showed intermediate to high values of 3575, 3458, and 3233 kcal/kg, respectively. These findings are consistent with prior research indicating that cassava by-products are effective EME sources for ruminants; for instance, cassava chips have been estimated via indirect calorimetry to provide an EME of approximately 10.63 MJ/kg DM (equivalent to 2327 kcal/kg as-fed) for lactating cattle. The observed variations in EME content are attributed to differences in chemical composition, which are further influenced by plant variety, cultivation conditions, and harvest stages. Therefore, selecting biomass for beef cattle should involve a balanced consideration of EME density, protein-mineral profiles, and the economic efficiency of replacing conventional feed sources with agro-industrial by-products to enhance overall returns.

3.3 Analysis of essential minerals (Ca, Mg, P, Fe, Na, Zn, and K) of biomass raw materials for CFF formulation

The analysis of essential minerals—Ca, Mg, P, Fe, Na, Zn, and K—in the biomass raw materials used for developing the CFF formulation showed that these minerals were present in all eight feed ingredients, including FMK, SBM, PKM, RB, DCC, CSP, WCP, and CSR, as presented in Table 2. In this study, the minerals were classified into three groups based on their physiological functions and importance: bone-supporting minerals (Ca, Mg, and P), blood- and nervous system-supporting minerals (Fe and Zn), and minerals that support the nervous and muscular systems (Na and K) [39]. Among the bone-supporting minerals, P was the most abundant, with RB containing the highest concentration and DCC the lowest. Mg was also highest in RB, whereas the other samples contained Mg at relatively similar levels (0.0732–0.2961%). Ca was found at the highest level in CSR and at the lowest level in FMK. Regarding blood and nervous system-supporting minerals, CSR had the highest Zn content, while DCC exhibited the lowest. For Fe, WCP contained the highest concentration, whereas RB had the lowest among the biomass samples. The relatively higher Fe content observed in WCP compared to other ingredients may be attributed to residual soil particles adhering to the outer peel surface, a common occurrence in agro-industrial root processing. These results indicate substantial variation in mineral composition across biomass types, highlighting the importance of selecting appropriate

raw materials to ensure that cattle diets meet both energy and essential mineral requirements for growth, skeletal development, and physiological functions.

Table 2. Mineral composition of biomass raw materials used for CFF formulation.

Biomass raw material	Na (%)	Zn (%)	Fe (%)	K (%)	Mg (%)	Ca (%)	P (%)
Finely ground maize kernels (FMK)	0.0122	0.0034	0.0138	0.4051	0.1044	0.0475	0.1813
Soybean meal (SBM)	0.0222	0.0057	0.0164	0.4099	0.2961	0.2997	0.4969
Palm kernel meal (PKM)	0.0126	0.0037	0.0178	0.4679	0.1942	0.2826	0.3105
Rice bran (RB)	0.0163	0.0076	0.0109	1.6250	0.7665	0.0801	1.3203
Dried cassava chips (DCC)	0.0147	0.0013	0.1714	0.0529	0.0732	0.1358	0.0036
Cassava pulp after starch extraction (CSP)	0.0471	0.0020	0.0335	0.2701	0.1398	0.5576	0.0195
Washed cassava peels (WCP)	0.3019	0.0036	0.4635	0.4628	0.1198	0.4877	0.0278
Fresh cassava starch residue (CSR)	0.0268	0.0901	0.3185	0.6378	0.1993	0.5584	0.2957

Note: All experimental values presented in Table 2 are the mean of three independent replicates with relative standard deviations (%RSD) less than 5%, and all nutritional, mineral, and EME values are expressed on an as-fed basis.

Regarding nervous and muscular system minerals, K concentrations exceeded Na in all samples, with RB, CSR, and PKM containing the highest K levels. Na was generally low, with WCP showing the highest and FMK the lowest concentrations (Table 2). These findings align with those of Burhan et al. [40] and Bayero et al. [41], who reported similar mineral hierarchies across various biomass sources, confirming that concentrations vary widely by species and source. The variation in essential minerals across the eight biomass types is likely driven by regional soil characteristics, fertilization regimes, and harvesting methods [17, 42, 43]. In Mukdahan's Nong Sung District, samples exhibited high levels of major minerals (Ca, Mg, P, and K) derived from soil fertilization, while minor minerals (Na and Zn) remained low, consistent with previous reports. Notably, specific trace elements, such as Fe in WCP, were exceptionally high (0.4635%). While these materials provide a foundation for bone, nervous, and muscular health, farmers should follow Department of Livestock Development recommendations for mineral supplementation to ensure a precise nutritional balance for optimal growth and physiological function.

3.4 Nutritional analysis of the CFF formulated from biomass raw materials compared with commercial beef cattle feed

This study evaluated a CFF formulated from eight local biomass materials, produced at a 1,000 kg scale. The mixture comprised CSR (600 kg), a DCC/CSP/WCP blend (200 kg), FMK (60 kg), PKM (20 kg), SBM (54 kg), and RB (54 kg). Supplements including urea (4 kg), dicalcium phosphate (3 kg), mineral premix (3 kg), and molasses (2 kg) were added to optimize nitrogen and phosphorus levels and fermentation efficiency. Following 10 days of anaerobic fermentation (28–30 °C), the CFF contained 12.16% crude protein, 3.29% crude fat, and 47.56% carbohydrates (Table 3, Figure 5), meeting the requirements for growth and EME supply in beef cattle. These results align with Anorach [44], who reported ~12% protein in fermented pumpkin-cassava substrates. Similarly, Puttha and Tangtaweewipat [45] observed protein levels of 8.40% in fermented maize and 10.6% in Napier grass silage. These findings confirm that local biomass is a viable substrate for nutritionally balanced, cost-effective fermented feed.

Table 3. Proximate composition of the CFF formulated from biomass raw materials compared with commercial beef cattle feeds.

Formulated and commercial feeds	Moisture (%)	Ash (%)	Fat (%)	Protein (%)	Fiber (%)	Carbohydrate (%)
Concentrated fermented feed (CFF)	11.74±0.20	4.60±0.08	3.29±0.05	12.16±0.21	32.39±0.80	47.56±0.90
The commercial beef cattle feeds C1	8.88±0.15	8.92±0.14	2.71±0.05	12.13±0.20	19.50±0.40	47.86±0.85
The commercial beef cattle feeds C2	7.76±0.14	8.22±0.12	1.60±0.03	10.90±0.18	13.22±0.30	58.30±1.00
The commercial beef cattle feeds C3	7.71±0.15	13.45±0.25	3.62±0.06	12.85±0.22	35.91±0.85	26.46±0.60
The commercial beef cattle feeds C4	5.93±0.12	16.87±0.30	0.48±0.01	17.34±0.30	20.85±0.50	38.53±0.75
The commercial beef cattle feeds C5	9.99±0.18	14.10±0.25	2.33±0.04	16.74±0.28	23.29±0.60	33.55± 0.70

Note: Values are expressed as mean ± standard deviation (SD, n = 3), and all nutritional, mineral, and EME values are expressed on an as-fed basis.

Comparison with Thaowarn [46] showed that TMR formulations (13.18–13.47% CP) were slightly lower than the theoretical 14% value. Such deviations often stem from natural variations in raw material quality, leading to discrepancies between calculated and analytical values. A similar trend was observed in commercial samples (C1–C5), where analyzed protein levels did not precisely match label declarations. These inconsistencies are supported by Kilama et al. [47] and Chen et al. [48], who identified significant batch-to-batch variability in commercial feeds and TMRs due to fluctuations in byproduct quality, mixing accuracy, and changes in dry matter content during storage. Consequently, these factors collectively influence the final nutrient profile delivered to livestock.

The higher fiber content in CFF compared to commercial pellets has key practical implications. While reducing energy density (EME), high fiber levels support rumen health by stimulating chewing and stabilizing ruminal pH via acetate production, preventing metabolic disorders such as acidosis. This makes CFF ideal for maintenance or grower rations, particularly for local or crossbred cattle. For finishing stages, CFF can be supplemented with high-energy ingredients or serve as a fermented roughage replacer. In contrast, commercial feeds are formulated for specific energy and protein targets. However, when CFF is used within a TMR strategy—blending roughage, concentrates, and minerals—it enhances ration consistency, reduces labor, and ensures a steady nutrient supply.

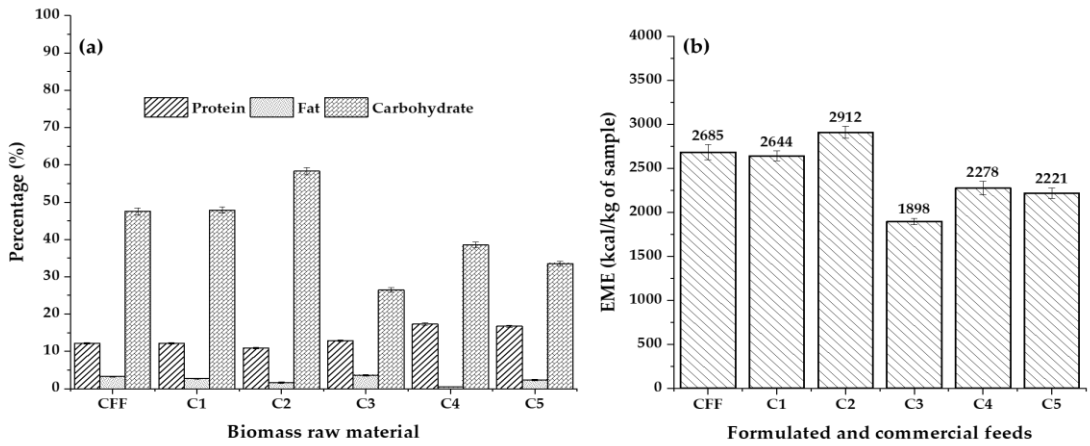


Figure 5. (a) proximate composition (carbohydrate, protein, and fat contents) and (b) EME values of the CFF formulated from biomass raw materials compared with commercial beef cattle feeds.

3.5 Nutritional EME analysis of the CFF formulated from biomass raw materials compared with commercial beef cattle feed

The EME evaluation revealed that the CFF, formulated from locally available biomass, possessed an EME value of 2685 kcal/kg of sample. This EME density places the CFF within the competitive mid-range compared to the examined commercial beef cattle feeds (Figure 5b). Among the commercial formulations, C2 exhibited the highest EME content (2912 kcal/kg), while the CFF outperformed several other commercial options, including C1 (2644 kcal/kg), C4 (2278 kcal/kg), and C5 (2221 kcal/kg). These results demonstrate that the CFF formulation provides a robust EME profile, making it a viable and high-quality alternative to standard commercial feeds. EME differences reflect variations in crude fat, non-structural carbohydrates, and fermentable fiber—key determinants in ruminant diets [17, 19]. The moderate EME in CFF aligns with the biochemical traits of cassava residues, RB, and PKM. While fermentation enhances digestibility and nutrient accessibility, it does not substantially increase caloric density [28, 36]. Despite lower EME, CFF is nutritionally adequate for smallholder or semi-intensive systems where cost-effective resources are vital. Improved ruminal degradability in fermented biomass can enhance microbial protein synthesis, partially compensating for lower gross EME [31, 38]. Furthermore, relying on local biomass offers economic and sustainability benefits, reducing dependence on high-cost commercial feeds [1, 5]. These findings corroborate evidence that fermented agro-industrial residues are viable, nutritionally acceptable, and environmentally aligned alternatives for ruminant production [35, 47, 48].

3.6 Analysis of essential minerals (Ca, Mg, P, Fe, Na, Zn, and K) of the CFF formulated from biomass raw materials compared with commercial beef cattle feed

The mineral composition of the CFF formulated from biomass raw materials demonstrated distinct variations when compared with commercial beef cattle feeds (C1–C5) (Table 4). Among the macrominerals, Ca was the predominant element in both CFF and commercial feeds, with Ca concentrations in CFF (0.4825%) comparable to those reported for commercial feeds (0.5323–0.5843% in most samples). Mg and P levels in CFF (0.1750% and 0.160%, respectively) were within the range typically observed in fermented feed ingredients and commercial formulations, reflecting their roles as essential structural and metabolic minerals [39–41]. For the trace minerals, Zn and Fe exhibited greater variability between feed types. CFF contained a higher Zn concentration (0.0308%) than all commercial feeds (0.0034–0.0064%), indicating that the biomass ingredients contributed a relatively higher Zn supply. Conversely, Fe content in commercial feeds varied widely (0.0546–0.1324%), whereas CFF showed moderate Fe levels (0.0878%), suggesting that mineral supplementation practices among manufacturers influence Fe concentration more strongly than fermentation-derived feed production. Regarding sodium and potassium, K was consistently more abundant than Na across all feed samples. CFF exhibited a K concentration of 0.1927%, similar to certain commercial formulations, while Na content was considerably lower (0.0268%), which is characteristic of biomass-based fermented feeds. The relatively low Na levels across feeds indicate the need for external salt supplementation in practical feeding systems, as recommended by livestock authorities.

Overall, differences in mineral profiles between CFF and commercial feeds can be attributed to variations in raw material composition, soil mineral status in cultivation areas, fertilization practices, and the specific formulation ratios used during feed production. These findings are consistent with previous reports indicating that the mineral content of forage and feed ingredients varies widely depending on agricultural conditions and processing methods. The results confirm that CFF provides essential macro- and micro-minerals beneficial for bone development, blood and nerve function, and muscular activity, although certain minerals may still require targeted supplementation to meet the full nutritional requirements of beef cattle [38–42].

3.7 Comparative analysis of feed cost for beef cattle

Feed ingredient cost is a major determinant in beef cattle diet formulation, particularly for smallholder and commercial operations. High-protein ingredients such as SBM and energy-rich corn kernels are relatively expensive due to high market demand and their nutritional value. RB, while locally abundant, commands moderate prices because of its potential for value-added products. In contrast, PKM and cassava by-products, including DCC, CSP, and WCP, provide substantial protein and energy at lower costs, making them attractive

alternatives for cost-sensitive feed formulations. The nutrient–cost analysis indicates that low-cost biomass materials, such as PKM and RB, can effectively substitute expensive ingredients without compromising protein and energy content. For example, PKM offers protein levels comparable to SBM at approximately one-third the cost. By optimizing the proportion of low-cost, nutrient-dense ingredients and reducing the use of high-cost feedstuffs, farmers can formulate economically efficient fermented concentrate feeds that meet the nutritional requirements of beef cattle.

Commercial feed prices (C1–C5) ranged from 10.67 to 15.33 THB/kg, whereas a 1,000 kg batch of fermented feed formulated with local biomass cost 4,500 THB, or 4.50 THB/kg (Table 5). This demonstrates that integrating locally available biomass by-products into fermented feed significantly reduces production costs while maintaining adequate nutritional quality. Ingredients such as DCC, WCP, and PKM contributed most to cost savings without compromising protein and energy levels. Furthermore, the economic advantage of low-cost biomass is amplified in large-scale production, where ingredient costs account for a major portion of total feed costs. Strategic blending of high- and low-cost ingredients allows flexibility to meet target protein and energy levels, supporting growth across different production stages. This approach also promotes sustainable livestock practices by utilizing agro-industrial residues, reducing waste, and improving feed cost-efficiency, particularly benefiting smallholder farmers with limited resources. Future studies should evaluate nutrient digestibility and growth performance of cattle fed these cost-effective fermented feeds under field conditions.

Table 4. Mineral composition of the CFF formulated from biomass raw materials compared with commercial beef cattle feed.

Formulated and commercial feeds	Na (%)	Zn (%)	Fe (%)	K (%)	Mg (%)	Ca (%)	P (%)
Concentrated fermented feed (CFF)	0.0268	0.0308	0.0878	0.1927	0.1750	0.4825	0.160
The commercial beef cattle feeds C1	0.4056	0.0064	0.0690	0.0751	0.1988	0.5843	0.2391
The commercial beef cattle feeds C2	0.3661	0.0062	0.0546	0.7129	0.1783	0.5323	0.1911
The commercial beef cattle feeds C3	0.5310	0.0058	0.1284	0.6247	0.1953	0.1185	0.1734
The commercial beef cattle feeds C4	0.3490	0.0034	0.1228	0.4667	0.1310	0.6500	0.1232
The commercial beef cattle feeds C5	0.2776	0.0057	0.1324	0.7956	0.2132	0.5774	0.2179

Note: All experimental values presented in Table 4 are the mean of three independent replicates, with relative standard deviations (%RSD) less than 5%.

Table 5. Example of cost calculation for the fresh fermented feed formulation.

Raw material	Fresh weight (kg)	Price per kg (THB)	Total cost (THB)
Cassava starch residue (CSR)	660	1.20	792
Dried cassava chips (DCC) + Cassava pulp after starch extraction (CSP) + Washed cassava peels (WCP)	200	7.00	1,400
Palm kernel meal (PKM)	20	7.30	146
Soybean meal (SBM)	54	24.00	1,296
Rice bran (RB)	54	10.00	540
Urea	4	25.00	100
Dicalcium phosphate	3	35.00	105
Mineral premix	3	35.00	105
Molasses	2	8.00	16
Total formulation weight	1,000 kg	-	4,500 THB
Cost per kilogram	4.50 THB/kg		

Note: Production costs were calculated based on local market prices in Mukdahan Province at the time of the study. In the original dataset, dried cassava chips (DCC) were priced at 7 THB/kg; since the combined 200 kg mixture includes DCC, CSP, and WCP without separate pricing, 7 THB/kg was applied as the representative value for this portion. It should be noted that ingredient prices may fluctuate depending on seasonal availability and regional market conditions.

4. Conclusions

This study demonstrated that agricultural biomass raw materials available in Mukdahan Province possess diverse nutritional and mineral compositions suitable for the development of CFF for beef cattle. Key protein-rich ingredients such as soybean meal, palm kernel meal, and rice bran, combined with carbohydrate-rich cassava by-products, provided a balanced nutrient foundation for feed formulation. Mineral analyses confirmed that the biomass sources supplied essential macro- and micro-elements required for skeletal development, metabolism, and physiological function. The formulated CFF exhibited nutritional values comparable to commercial beef cattle feeds, with adequate crude protein, fermentable carbohydrates, and essential minerals. Although its EME was moderately lower, the fermentation process is expected to potentially improve nutrient availability and palatability, though this requires further validation through digestibility trials. A major contribution of this work is the demonstration of substantial cost reduction—CFF production cost (4.50 THB/kg) was less than half of commercial feeds—highlighting its economic feasibility for smallholder farmers. The findings advance current knowledge on feed development using local biomass and reinforce the potential of agro-industrial residues for sustainable livestock production. Limitations include the lack of in vivo feeding trials and digestibility assessments. Future research should evaluate growth performance, actual nutrient digestibility, rumen fermentation characteristics, and long-term economic returns from incorporating CFF into actual farm management systems.

5. Acknowledgements

This research was supported by the Programs of Environmental Science, Biology, and Chemistry, as well as the Innovation in Chemistry for Community Research Unit and the Appropriated Technology Center at the Faculty of Science and Technology. Additional support, including equipment and research resources, was provided by the Biomass Energy Research Laboratory within the Center of Excellence on Alternative Energy, Research and Development Institute, Sakon Nakhon Rajabhat University, Thailand.

Author Contributions: Conceptualization, N.J., W.R., T.L., P.Y., N.W., and S.P.; methodology, N.J., W.R., T.L., S.P., W.C., A.T., N.K., and S.P.; validation, N.J., W.R., T.L., A.T., N.K., P.Y., and N.W.; formal analysis, N.J., W.R., and T.L.; investigation, N.J., W.R., T.L., S.P., W.C., A.T., and S.P.; resources, W.R., T.L., N.K., P.Y., N.W., and S.P.; data curation, N.J., W.R., T.L., S.P., W.C., A.T., N.K., and S.P.; writing—original draft preparation, N.J., W.R., T.L., S.P., W.C., and N.K.; writing—review and editing, N.J. and W.R.; visualization, W.R., T.L., A.T., and N.K.; supervision, P.Y., and N.W.; project administration, W.R., T.L., and N.K.; funding acquisition, W.R., T.L., and N.K. All authors have read and agreed to the published version of the manuscript.

Funding: This project was supported by the Thailand Science Research and Innovation (TSRI) through the National Science, Research, and Innovation Fund (NSRF) at Sakon Nakhon Rajabhat University [Contact No. FF-SNRU_50/2026].

Conflicts of Interest: The authors declare no known competing financial interests or personal relationships that could have appeared to influence the work reported in this paper.

Declaration of generative AI and AI-assisted technologies in the writing process: The authors acknowledge that generative AI tools were used to improve language clarity, grammar, and formatting in this manuscript. No content, data interpretation, or results were generated or altered by AI.

References

[1] Thammayod, A.; Roschat, W.; Leelatam, T.; Phewphong, S.; Maneerat, B.; Leelatam, N.; Thangthong, A.; Moonsin, P.; Promarak, V. Development of High-Quality Organic Fertilizer from Biomass Waste and the Application of Biochar in Local Areas of Sakon Nakhon Province, Northeastern Thailand. *Trends Sci.* **2025**, *22*, 9105. https://doi.org/10.48048/tis.2025.9105

[2] Ruamchimplee, T.; Kumdee, O.; Donsri, W.; Noiprasan, N.; Rengkounkway, M. The Desire to Improve Quality of Life through Integrated Farming Practices among Farmers in Ban Na Sao Ung Village, Lom Kao District, Phetchabun Province. *J. Soc. Sci. Cult.* **2025**, *9*, 236–249.

[3] Romyen, A.; Nunti, C.; Neranon, P. Trade Efficiency under FTA for Thailand's Agricultural Exports: Copula-Based Gravity Stochastic Frontier Model. *Econ. Struct.* **2023**, *12*, 9. https://doi.org/10.1186/s40008-023-00303-0

[4] Tansuchat, R.; Suriyankietkaew, S.; Petison, P.; Punjaisri, K.; Nimsai, S. Impacts of COVID-19 on Sustainable Agriculture Value Chain Development in Thailand and ASEAN. *Sustainability* **2022**, *14*, 12985. https://doi.org/10.3390/su142012985

[5] Kumsueb, B.; Kitchaicharoen, J.; Jintrawet, A.; Limnirunkul, B.; Kono, Y. Transformation towards Organic Cassava Production in Yasothon Province, Thailand. *Curr. Appl. Sci. Technol.* **2024**, *25*, e0260947. https://doi.org/10.55003/cast.2024.260947

[6] World Bank. *Thailand Rural Income Diagnostic*; 2022. https://documents1.worldbank.org/curated/en/099005010202299399/pdf/P1775991e5f180ee130cf14572184e61f60735628d80.pdf (accessed Nov 5, 2025).

[7] Bank of Thailand. *Agriculture Landscape in Thailand*; 2022. https://www.bot.or.th/content/dam/bot/financial-innovation/sustainable-finance/green/taxonomy/03_EN_Thailand_Taxonomy-Agriculture_Sector.pdf (accessed Nov 5, 2025).

[8] Boonthongniam, N. Data on the Number of Livestock Farmers and Animal Population in 2021; Department of Livestock Development: Thailand, 2021. https://ict.dld.go.th/webnew/images/stories/stat_web/yearly/2564/province/T2-1-Cattle.pdf (accessed Nov 5, 2025).

[9] Lambertz, C.; Chaikong, C.; Maxa, J.; Schlecht, E.; Gauly, M. Characteristics, Socioeconomic Benefits and Household Livelihoods of Beef Buffalo and Beef Cattle Farming in Northeast Thailand. *J. Agric. Rural Dev. Trop. Subtrop.* **2012**, *113*, 155–164.

[10] Bunmee, T.; Chaiwang, N.; Kaewkot, C.; Jaturasitha, S. Current Situation and Future Prospects for Beef Production in Thailand—A Review. *Asian-Australas. J. Anim. Sci.* **2018**, *31*, 968–975. https://doi.org/10.5713/ajas.18.0201

[11] Khunchaikarn, S.; Mankeb, P.; Suwanmaneepong, S. Economic Efficiency of Beef Cattle Production in Thailand. *J. Manag. Inf. Decis. Sci.* **2022**, *25*, 1–9.

[12] Thannithi, W.; Intawicha, P.; Kongmuang, N.; Inyawilert, W.; Tiantong, A.; Saengwong, S. Understanding Smallholder Beef Production: Cost Structures, Market Channels and Pathways to Enhanced Profitability. *Adv. Anim. Vet. Sci.* **2025**, *13*, 16–25. https://doi.org/10.17582/journal.aavs/2025/13.1.16.25

[13] Polyorach, S.; Sitthigripong, R.; Mitchaothai, J.; Lukkananukool, A.; Chaosap, C.; Srikitkasemwat, K.; Thammakarn, C.; Nampukdee, R. Evaluation of Production Performance, Feed Cost and Nutritional Digestibility of Charolais- and Wagyu-Cross Beef Cattle Raised by Pineapple Co-Products Diet. *J. Mahanakorn Vet. Med.* **2022**, *16*, 263–271.

[14] Sooksoi, P. Evaluation of Roughage and Agricultural Residue Quality for Dairy Farmers in Sakaeo Province. *King Mongkut's Agric. J.* **2020**, *38*, 376–381.

[15] Munier, F. F.; Wardi, W.; Takdir, M. The Effect of Fermented Corncob Feed on Daily Weight Gains and Body Condition Score of Donggala Cattle in Central Sulawesi. In *Proc. 9th Int. Semin. Trop. Anim. Prod.*; Atlantis Press, 2022; pp 328–331. https://doi.org/10.2991/absr.k.220207.069

[16] Dagaew, G.; Wongtangtintharn, S.; Suntara, C.; Prachumchai, R.; Wanapat, M.; Cherdthong, A. Feed Utilization Efficiency and Ruminal Metabolites in Beef Cattle Fed Cassava Pulp Fermented with Yeast Waste as a Replacement for Soybean Meal. *Sci. Rep.* **2022**, *12*, 16090. https://doi.org/10.1038/s41598-022-20471-6

[17] Phewphong, S.; Roschat, W.; Namwongsa, K.; Wonam, A.; Kaisri, T.; Duangpakdee, P.; Leelatam, T.; Moonsin, P.; Promarak, V. Evaluation of the Nutritional, Mineral, and Antioxidant Potential of Roselle (Hibiscus sabdariffa Linn.) Seeds from Roi Et Province in Thailand. *Trends Sci.* **2023**, *20*, 6664. https://doi.org/10.48048/tis.2023.6664

[18] Suwannatrai, K.; Namwongsa, K.; Phanomkhet, N.; Tawil, S.; Roschat, W. Analysis of the Nile Tilapia (*Oreochromis niloticus* L.) Proximate Composition in Sakon Nakhon Province, Thailand. *Creative Sci.* **2023**, *15*, 251073. https://doi.org/10.55674/cs.v15i1.251073

[19] Preecharram, S.; Phosri, S.; Theansungnoen, T.; Roschat, W.; Arthan, S.; Lasopha, S.; Jandaruang, J. Nutritional Values and Their Potential Applications in Food Products of Krabok Seed (Irvingia malayana). *Trends Sci.* **2024**, *21*, 7316. https://doi.org/10.48048/tis.2024.7316

[20] AOAC. *Official Methods of Analysis*, 17th ed.; Assoc. Off. Anal. Chem.: MD, USA, 2000.

[21] Preecharram, S.; Posoongnoen, S.; Thummavongsa, T.; Pasom, W.; Panyakom, S.; Sripakdee, T.; Jandaruang, J. Values, Bioactive Compounds, and Antioxidant Activities of Brown Rice and Germinated Brown Rice, and Their Pellet Products. *Creative Sci.* **2025**, *17*, 257996. https://doi.org/10.55674/cs.v17i1.257996

[22] Suwannatrai, K.; Namwongsa, K.; Phanomkhet, N.; Nuntapanich, H.; Roschat, W. Analysis of nutritional value, total phenolic and flavonoid contents, and antioxidant activities from ethanolic extracts of roasted broken brown rice powder. *SNRU Journal of Science and Technology* **2022**, 14(2), 246426. https://doi.org/10.55674/snrujst.v14i2.246426

[23] Salami, S. O.; Afolayan, A. J. Evaluation of Nutritional and Elemental Compositions of Green and Red Cultivars of Roselle. *Sci. Rep.* **2021**, *11*, 1–13. https://doi.org/10.1038/s41598-020-80433-8

[24] AOAC. *Official Methods of Analysis*, 18th ed.; Sci. Res. Publ.: Washington, DC, 2010.

[25] Bvenura, C.; Afolayan, A. J. The Role of Wild Vegetables in Household Food Security in South Africa: A Review. *Food Res. Int.* **2015**, *76*, 1001–1011. https://doi.org/10.1016/j.foodres.2015.06.013

[26] Oh, J.; Cho, H.; Jeong, S.; Kang, K.; Lee, M.; Jeon, S.; Kang, H.; Seo, S. Effects of Dietary Crude Protein Level of Concentrate Mix on Growth Performance, Rumen Characteristics, Blood Metabolites, and Methane Emissions in Fattening Hanwoo Steers. *Animals* **2024**, *14*, 469. https://doi.org/10.3390/ani14030469

[27] Kim, W. S.; Ghassemi Nejad, J.; Peng, D. Q.; et al. Effects of Different Protein Levels on Growth Performance and Stress Parameters in Beef Calves under Heat Stress. *Sci. Rep.* **2022**, *12*, 8113. https://doi.org/10.1038/s41598-022-09982-4

[28] Weligama Thuppahige, V. T.; Moghaddam, L.; Welsh, Z. G.; Wang, T.; Xiao, H.-W.; Karim, A. Extraction and Characterisation of Starch from Cassava Agro-Industrial Wastes. *LWT-Food Sci. Technol.* **2023**, *182*, 114787. https://doi.org/10.1016/j.lwt.2023.114787

[29] Banditvong, C.; Laosiripojana, N.; Varongchayakul, S.; Songkasiri, W. Utilization of Cassava Pulp to Produce Micro- and Nano-Cellulose. *Sci. Eng. Connect.* **2024**, *47*, 322–347.

[30] Imran, M.; Lee, S.-G.; Park, S.-Y.; et al. Influence of Environmental Factors and Genotype on Natural Variation in Maize Seeds. *Sustainability* **2024**, *16*, 10451. https://doi.org/10.3390/su162310451

[31] Srisikam, S.; Lueanglawan, P. *The Use of Yeast-Fermented Cassava Pulp in Beef Cattle Diets on Rumen Fermentation and Production Performance*; Master's Thesis, Burapha University, Thailand.

[32] Kraiprom, T.; Jantarat, S.; Madting, P.; Dueraso, H. Study of Nutritive Value of Oil Palm Frond Silage with Molasses. *J. Sci. Technol. Yala Rajabhat Univ.* **2018**, *3*, 94–100.

[33] Budianto, M. The Effects of Energy and Protein Content in Maize Forage-Based Complete Diet on In Vitro Ruminal Fermentation, Gas Production, and Feed Degradability. *J. Sci. Agric. Technol.* **2023**, *4*, 27–33. https://doi.org/10.14456/jsat.2023.5

[34] Bamikole, A. A. Evaluation of Proximate and Fibre Composition, Metabolizable Energy, and Organic Matter Digestibility of Maize (Zea mays) and Wheat (Triticum aestivum) Hydroponic Fodder. *Pak. J. Nutr.* **2024**, *23*, 39–45. https://doi.org/10.3923/pjn.2024.39.45

[35] Gunha, T.; Kongphitee, K.; Binsulong, B.; Sommart, K. Net Energy Value of a Cassava Chip Ration for Lactation in Holstein–Friesian Crossbred Dairy Cattle Estimated by Indirect Calorimetry. *Animals* **2023**, *13*, 2296. https://doi.org/10.3390/ani13142296

[36] Manzoor, A.; Pandey, V. K.; Dar, A. H.; Fayaz, U.; Das, K. K.; Shams, R.; Ahmad, S.; Bashir, I.; Fayaz, J.; Singh, P.; Khan, S. A.; Ganaie, T. A. Rice Bran: Nutritional, Phytochemical, and Pharmacological Profile and Its Contribution to Human Health Promotion. *Food Chem. Adv.* **2023**, *2*, 100296. https://doi.org/10.1016/j.focha.2023.100296

[37] Zhao, J.; Zhu, Q.; Song, X.; Yang, M.; Liu, L. Development of Prediction Equations for Digestible and Metabolizable Energy in Cereal Processing By-Products Fed to Growing Pigs. *Animals* **2024**, *14*, 3101. https://doi.org/10.3390/ani14213101

[38] Suriyapha, C.; Suntara, C.; Wanapat, M.; Cherdthong, A.; Kang, S.; Polyorach, S. Effects of Substituting Agro-Industrial By-Products for Soybean Meal on Beef Cattle Feed Utilization and Rumen Fermentation. *Sci. Rep.* **2022**, *12*, 21630. https://doi.org/10.1038/s41598-022-26191-1

[39] Department of Livestock Development. *Mineral Contents in Forage Plants*; n.d. https://nutrition.dld.go.th/nutrition/images/knowledge/old_knowledge/pro27.html (accessed Nov 10, 2025).

[40] Burhan, K. A. R. A.; Ertek, A.; Bekir, A. T. A. R. Mineral Nutrient Content of Sweet Corn under Deficit Irrigation. *J. Agric. Sci.* **2016**, *22*, 54–61. https://doi.org/10.1501/Tarimbil_0000001367

[41] Bayero, A. S.; Datti, Y.; Abdulhadi, M.; Yahya, A. T.; Salihu, I.; Lado, U. A.; Imrana, B. Proximate Composition and Mineral Contents of *Glycine max* (Soybeans) Available in Kano State, Nigeria. *Chemsearch J.* **2019**, *10*, 62–65.

[42] Grzyb, A.; Wolna-Maruwka, A.; Niewiadomska, A. Environmental Factors Affecting the Mineralization of Crop Residues. *Agronomy* **2020**, *10*, 1951. https://doi.org/10.3390/agronomy10121951

[43] Ahmed, W.; Liu, K.; Qaswar, M.; Huang, J.; Huang, Q.; Xu, Y.; Ali, S.; Mehmood, S.; Ammar Asghar, R. M.; Mahmood, M.; Zhang, H. Long-Term Mineral Fertilization Improved Grain Yield and Phosphorus Use Efficiency by Changing Soil P Fractions. *Agronomy* **2019**, *9*, 784. https://doi.org/10.3390/agronomy9120784

[44] Atsawat, A. *Development of Animal Feed from Pumpkin and Fermented Cassava for Beef Cattle Feeding*; Doctoral Dissertation, University of Phayao, Thailand, 2019. http://www.updc.clm.up.ac.th//handle/123456789/1001 (accessed Nov 10, 2025).

[45] Puttha, W.; Tangtaweewipat, S. Nutrient Chemical Composition and Effect of Replacing Either Fermented Corn Grain or Fermented Napier Grass in Commercial Diet for Royal Project Black Pig. *King Mongkut's Agric. J.* **2022**, *40*, 302–314.

[46] Thaowarn, M. Effect of Using Pakchong 1 Napier Grass Silage in Total Mixed Ration on Productive Performance of Goats and Acceptance among Smallholder Farmers. *PSU Libr. J.* **2016**, *27*, 116–122.

[47] Kilama, J.; Yakir, Y.; Shaani, Y.; Adin, G.; Kaadan, S.; Wagali, P.; Sabastian, C.; Ngomuo, G.; S. J., M. Chemical Composition, In Vitro Digestibility, and Storability of Selected Agro-Industrial By-Products. *Heliyon* **2023**, *9*, e14581. https://doi.org/10.1016/j.heliyon.2023.e14581

[48] Chen, Y. H.; Chen, Y. M.; Tu, P. A.; Chen, C. Y.; Wang, H. T. Stabilizing Total Mixed Ration Dry Matter to Mitigate Environmental Relative Humidity Effects on Lactating Cow Performance. *Animals* **2025**, *15*, 1137. https://doi.org/10.3390/ani15081137

ASEAN
Journal of Scientific and Technological Reports
Online ISSN:2773-8752

Research article

Effects of Hydroponic Cultivation Systems on Growth Performance and Yield of Pakchoi (*Brassica rapa* var. *chinensis*)

Pakamas Thaenkaew[1], Ronnarit Khuengphukhiao[1*], Sirawat Surachotivet[1], and Khitaphat Khongthaen[1]

[1] Faculty of Engineering, Pathumwan Institute of Technology, Bangkok, 10330, Thailand
* Correspondence: ronna_rit@hotmail.com

Citation:
Thaenkaew, P.; Khuengphukhiao, R.; Surachotivet, S.; Khongthaen K. Effects of hydroponic cultivation systems on growth performance and yield of pakchoi (*Brassica rapa* var. *chinensis*). *ASEAN J. Sci. Tech. Report.* **2026**, *29*(4), e261311. https://doi.org/10.55164/ajstr.v29i4.261311.

Article history:
Received: September 16, 2025
Revised: February 19, 2026
Accepted: March 10, 2026
Available online: March 25, 2026

Publisher's Note:
This article is published and distributed under the terms of the Thaksin University.

Abstract: The purpose of this study was to investigate the effects of different hydroponic systems on the growth and yield of Pakchoi (*Brassica rapa* var. *chinensis*). The experiment was conducted using a Randomized Complete Block Design (RCBD) to compare three hydroponic cultivation systems: (1) Deep Flow Technique (DFT), (2) Nutrient Film Technique (NFT), and (3) Drip Hydroponics System (DHS). Each treatment consisted of 10 individual plants, yielding a total of 30 experimental units. Plants were cultivated for 35 days after transplanting under controlled laboratory conditions. The nutrient solution was maintained at a pH range of 5.5–6.5 and an electrical conductivity (EC) of 1.5–2.5 mS cm^{-1}. Environmental parameters were carefully regulated, including temperature (20–25 °C), relative humidity (60–70%), and light intensity (200–250 μmol m^{-2} s^{-1}), under a 16 h light/8 h dark photoperiod. The results indicated that the cultivation system had a statistically significant effect ($p < 0.05$) on plant height, leaf width, and fresh weight yield. Pakchoi grown under the DHS treatment exhibited superior growth performance, with an average plant height of 41.71 cm, leaf width of 14.67 cm, and fresh weight yield of 64.8 g, all of which were higher than those observed in the NFT and DFT systems. In addition, qualitative observations revealed improved leaf expansion and greater canopy development under the DHS treatment. These findings demonstrate that the Drip Hydroponics System is an effective cultivation approach for enhancing Pakchoi growth and yield under controlled-environment conditions.

Keywords: Hydroponics; pakchoi; growth performance; yield; drip hydroponics

1. Introduction

Hydroponic cultivation is an agricultural technology that replaces soil with nutrient solutions for crop production [1]. This approach minimizes soil-borne diseases, reduces land requirements, and has been widely adopted in both commercial and research contexts [2]. Nevertheless, hydroponic systems require precise management of fertilizer application and close monitoring of environmental parameters, particularly pH and electrical conductivity (EC), which directly influence nutrient uptake and plant growth. Proper regulation of these factors can significantly enhance crop performance and yield. Recent advances in hydroponic technology have focused on improving production efficiency through automation and sustainable practices. For instance, automated irrigation and fertigation systems have been widely implemented in vertical farming operations [3]. In addition, the integration of organic fertilizers

and beneficial microorganisms has been explored to reduce reliance on chemical inputs and enhance system sustainability [4–5]. Complementary technologies, such as LED lighting, have been adopted to stabilize light conditions, improve photosynthetic efficiency, and enhance crop quality, thereby reducing dependence on fluctuating natural sunlight [6]. Furthermore, non-thermal plasma treatments have been introduced to mitigate salinity stress [7], while biological agents, including chitosan nanoparticles, have been investigated to improve sustainability and plant resilience in hydroponic systems [8].

Several hydroponic systems are commonly employed in commercial production. The drip irrigation system (DIS) is recognized for its ability to conserve water and improve yield quality [9]. The nutrient film technique (NFT), also known as the thin-film system, is particularly suitable for small, fast-growing plants due to its efficient nutrient delivery [10]. In contrast, the deep flow technique (DFT) provides greater root-zone volume and stability, making it more suitable for supporting larger plants and achieving higher yields [11]. Each of these systems offers distinct advantages and limitations in terms of resource efficiency, crop compatibility, and commercial applicability. Commercial growers widely favor Pakchoi because it reaches maturity in 30–35 days, requires relatively low nutrient levels, and yields high per-unit-area. These characteristics make Pakchoi an ideal crop for hydroponic cultivation, particularly in urban farming, greenhouse production, and vertical farming systems where land and water use efficiency are critical. Selecting an appropriate hydroponic system is therefore essential for maximizing yield and product quality while ensuring economically and environmentally sustainable production. Although several studies have investigated the hydroponic cultivation of Brassica crops, few have specifically focused on Pakchoi. Therefore, the objective of this study was to compare the growth and yield performance of Pakchoi cultivated under three hydroponic systems: DFT, NFT, and DIS. Growth parameters, including plant height and leaf width, as well as fresh weight yield, were evaluated and subjected to statistical analysis to determine the most suitable system for commercial Pakchoi production.

2. Materials and Methods

The experiment was conducted in a hydroponic cultivation unit measuring 0.85 × 1.20 × 1.20 meters. Environmental parameters were controlled using artificial lighting, including LED white light and a night light, while maintaining the room temperature between 20 and 25 °C. The nutrient solution applied for cultivating Pakchoi was adjusted to a pH range of 5.5–6.5 and an electrical conductivity (EC) range of 1.5–2.5 mS/cm. The experiment was arranged in a Randomized Complete Block Design (RCBD) with three hydroponic cultivation systems: Deep Flow Technique (DFT), Nutrient Film Technique (NFT), and Drip Hydroponics System (DHS). Each treatment comprised 10 individual Pakchoi plants, yielding a total of 30 experimental units. Each plant was considered as one replicate for statistical analysis. Three hydroponic systems were evaluated:

1. Static Hydroponics (Deep Flow Technique, DFT) This system consisted of a tank filled with nutrient solution in which the plant roots were immersed. The solution was not continuously circulated; however, aeration was provided through an air stone to increase dissolved oxygen levels.

2. Nutrient Film Technique (NFT): Plant roots were continuously supplied with a thin film of nutrient solution combined with oxygen from the surrounding air.

3. Drip Hydroponics System: Nutrient solution was delivered directly to the root zone in pulses or at predetermined intervals. This method enabled precise regulation of nutrient supply and timing, thereby reducing water consumption.

Pakchoi seedlings were germinated for 14 days before transplantation. After transplanting, plants were grown under hydroponic conditions for 35 days, corresponding to the typical commercial harvest period for Pakchoi. Final harvest and yield measurements were conducted at the end of the cultivation period (Day 35 after transplanting). During the early stage of transplantation, plain water was used in the troughs without nutrient supplementation, and water pH was monitored. From the first day after transplantation, the solution was replaced with a nutrient medium maintained at pH 5.5–6.5 and EC 1.5–2.5 mS/cm throughout the growing cycle. Environmental conditions were maintained under controlled indoor conditions throughout the experiment. The cultivation room temperature was maintained at 20–25 °C, relative humidity

ranged between 60–70%, and light was supplied using white LED lamps with an average light intensity of approximately 200–250 μmol m^{-2} s^{-1} at canopy level under a 16 h light / 8 h dark photoperiod. These environmental conditions were kept constant across all treatments to minimize external factors that could affect plant growth. Growth performance was assessed by measuring plant height, defined as the distance from the base of the stem to the tip of the tallest leaf. Measurements were taken at 7-day intervals from the time of transplantation until harvest. Leaf width was determined by measuring the broadest point of the most fully developed leaf on each plant, conducted concurrently with height measurements. Growth rate for both height and leaf width was calculated according to Equation (1), where X_0 = initial value and X_t = Value at time t. Fresh biomass was recorded in grams (g) using a digital scale. The collected data were subjected to analysis of variance (ANOVA) to identify significant differences in growth and yield across the hydroponic systems, using Design-Expert 7.0 statistical software.

$$\text{Growth Rate (\%)} = (X_t - X_0) / X_0 \times 100 \quad (1)$$



Figure 1. Operational Procedure Diagram

3. Results and Discussion

In the experiment, Pakchoi was cultivated using three hydroponic systems: a stagnant-water system (Deep Flow Technique, DFT), a whirlpool system (Nutrient Film Technique, NFT), and a drip irrigation system (Drip Hydroponics System, DHS). Data were collected for plant height, leaf width, plant height growth rate, leaf width growth rate, and yield, as presented in Figures 2(a)–4(a). These figures illustrate the normality tests for plant height growth rate, leaf width growth rate, and yield. Figures 2(b)–4(b) present the constant variance tests, showing the relationship between stochastic tolerance and predicted values, which indicate no correlation between stochastic deviation and predicted values. Figures 2(c)–4(c) illustrate the relationship between stochastic tolerance and the data sequence, while Figure 4(d) shows the relationship between observed experimental values and predicted values. The close agreement between observed and predicted results confirms that the statistical models applied were appropriate for predicting experimental outcomes. Furthermore, the absence of heteroscedasticity indicates that plant height growth rate, leaf width growth rate, and yield data were suitable for analysis of variance without the need for data transformation. In addition to quantitative measurements of plant height, leaf width, and fresh weight, visual observations revealed that plants grown under the DHS treatment had more fully expanded leaves and greater canopy coverage than those grown under DFT and NFT systems. The enhanced growth performance observed under DHS can be attributed to precise nutrient delivery, reduced root-zone waterlogging, and improved oxygen availability. Although production costs were not quantitatively evaluated in this study, DHS is expected to require a higher initial investment; however, it may provide long-term benefits through improved yield efficiency and reduced water and nutrient losses.

The adequacy analysis of the statistical models (Figures 2–4) confirms that the experimental data were sufficiently robust for evaluating the effects of the hydroponic systems. Consequently, the data were analyzed using analysis of variance (ANOVA). The model for plant height yielded an F-value of 121.86 and a p-value < 0.0001, indicating that the hydroponic systems (DFT, NFT, and DHS) had a statistically significant effect on plant height ($p < 0.05$). The goodness-of-fit statistics yielded $R^2 = 0.90$, Adjusted $R^2 = 0.89$, and Predicted $R^2 = 0.87$, consistent with Figure 5(a). The results demonstrate that the drip irrigation system achieved the highest average plant height, with mean values of 30.49 cm (DFT), 37.11 cm (NFT), and 41.71 cm (DHS). Compared with DFT and NFT, the DHS system increased plant height by 26.90% and 11.03%, respectively. For leaf width growth rate, the statistical model yielded an F-value of 67.61 and a p-value < 0.0001, confirming significant differences among the hydroponic systems ($p < 0.05$). The model fit parameters were $R^2 = 0.83$, Adjusted $R^2 = 0.82$, and Predicted $R^2 = 0.79$, as shown in Figure 5(b). At weeks 1 and 5, the drip irrigation system produced the highest average leaf width (14.67 cm), followed by NFT (11.87 cm) and DFT (9.42 cm). The DHS system outperformed DFT and NFT by 35.76% and 19.09%, respectively. These findings are consistent with those reported by [12], who indicated that commonly used hydroponic systems exhibit distinct characteristics that differentially influence plant growth. Regarding yield, the model yielded an F-value of 242.2 ($p < 0.0001$), indicating that hydroponic systems had a statistically significant effect on yield ($p < 0.05$). The model fit values were $R^2 = 0.94$, Adjusted $R^2 = 0.94$, and Predicted $R^2 = 0.93$, corresponding to Figure 5(c). The highest average yield was obtained under the drip irrigation system (64.8 g), followed by NFT (44.5 g) and DFT (26.9 g). Overall, DHS outperformed DFT and NFT by 58.49% and 31.33%, respectively. These results are consistent with previous studies reporting that effective water circulation enhances plant growth [13] and that irrigation regimes significantly influence crop growth and yield [14]. Although quantitative assessments in this study focused on plant height, leaf width, and fresh weight, qualitative observations throughout the cultivation period revealed clear differences in plant architecture among the hydroponic systems. Plants grown under the DHS treatment consistently exhibited a greater number of fully expanded leaves and a more extensive canopy than those grown under DFT and NFT systems. This enhanced leaf development suggests an increased photosynthetic surface area, which likely contributed to the significantly greater biomass accumulation observed at harvest. Furthermore, weekly growth monitoring revealed more stable, uniform growth patterns in DHS-grown plants, whereas plants cultivated under DFT and NFT systems exhibited slower, less consistent development during the early growth stages. These qualitative and temporal growth patterns support the quantitative findings and suggest that incorporating additional growth indicators—such as leaf number, leaf area index, and daily growth rate—could provide more comprehensive insights into system performance in future studies.

Leafy vegetables are generally reported to grow rapidly in liquid-based hydroponic systems, including NFT, deep-water culture (DWC), ebb-and-flow, and aeroponics, as plant roots receive a continuous supply of nutrients in oxygenated aqueous environments [15]. In NFT systems, oxygen availability is partially maintained by exposing root tips to air; however, this configuration may result in uneven nutrient distribution and increased sensitivity to flow interruptions. In DWC systems, adequate root oxygenation relies heavily on supplemental aeration, and insufficient dissolved oxygen levels may induce hypoxic stress unless additional aeration is provided [16,17]. The superior growth performance and yield observed in the Drip Hydroponics System (DHS) are attributable to a combination of physiological and system-level advantages. DHS enables precise and uniform delivery of nutrient solution directly to the root zone, ensuring consistent nutrient availability throughout the cultivation cycle. In addition, intermittent nutrient solution application minimizes prolonged root submergence, thereby improving root-zone aeration and oxygen diffusion compared with DFT systems. This optimized balance of water, nutrients, and oxygen promotes efficient nutrient uptake, enhanced root development, and increased photosynthetic efficiency, ultimately resulting in greater biomass accumulation and yield. The statistically significant differences observed among hydroponic systems further support these conclusions. Overall, the findings align with previous studies demonstrating that drip-based hydroponic systems improve water-use efficiency, stabilize growth rates, and enhance crop productivity relative to static or continuous-flow hydroponic systems.

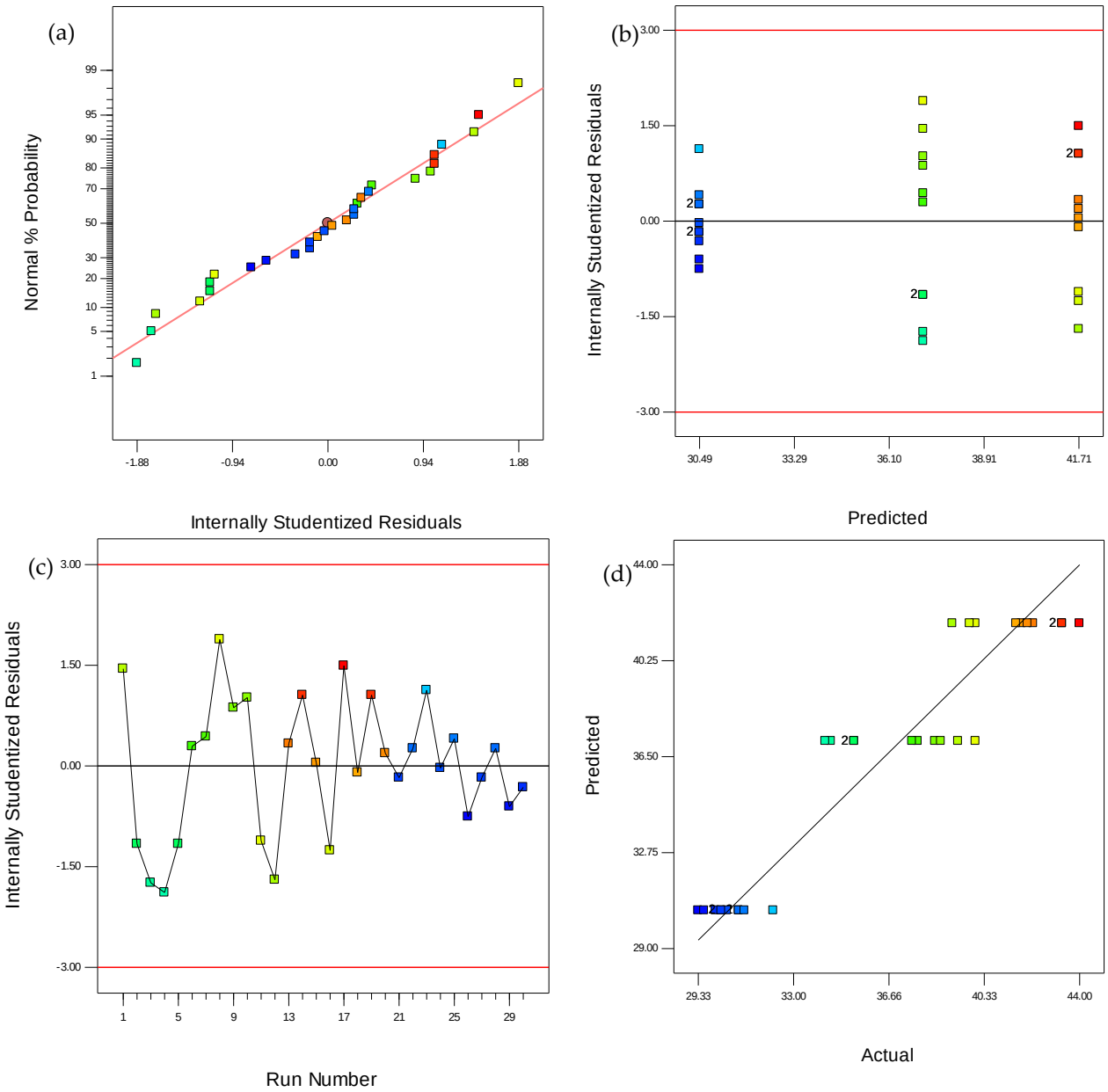


Figure 2. Diagram of the random tolerance of the growth rate of the early height (a) Normal distribution test of the data, (b) Constant variance test, (c) Graph of the relationship between random and ordinal tolerances, and (d) Graph of the relationship between the actual experimental results and the predicted values.

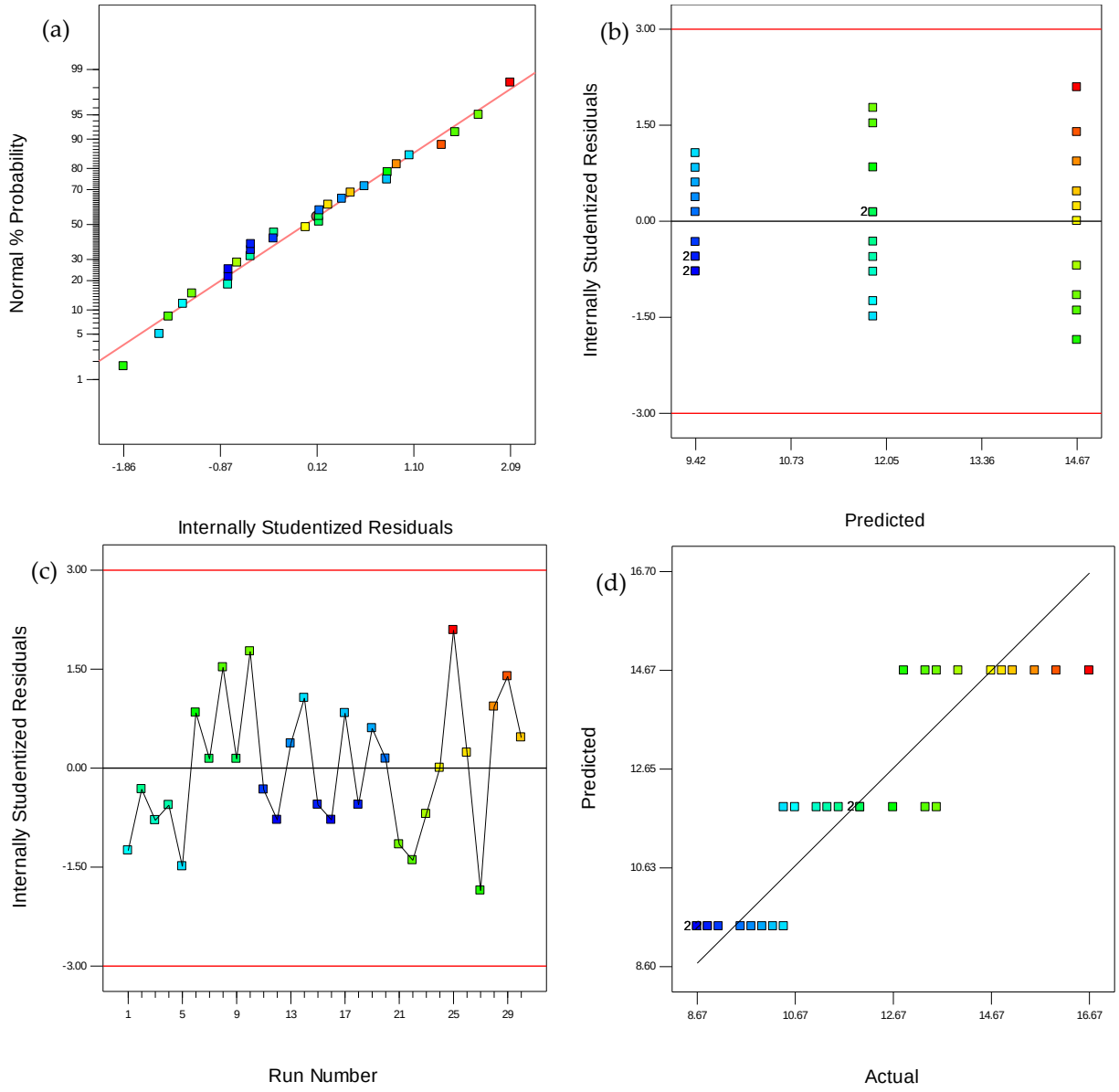


Figure 3. Random tolerance diagram of leaf width growth rate (a) Normal distribution test of data, (b) constant variance test, (c) Graph of the relationship between random and ordinal tolerances, and (d) graph of the relationship between actual experimental results and predicted values.

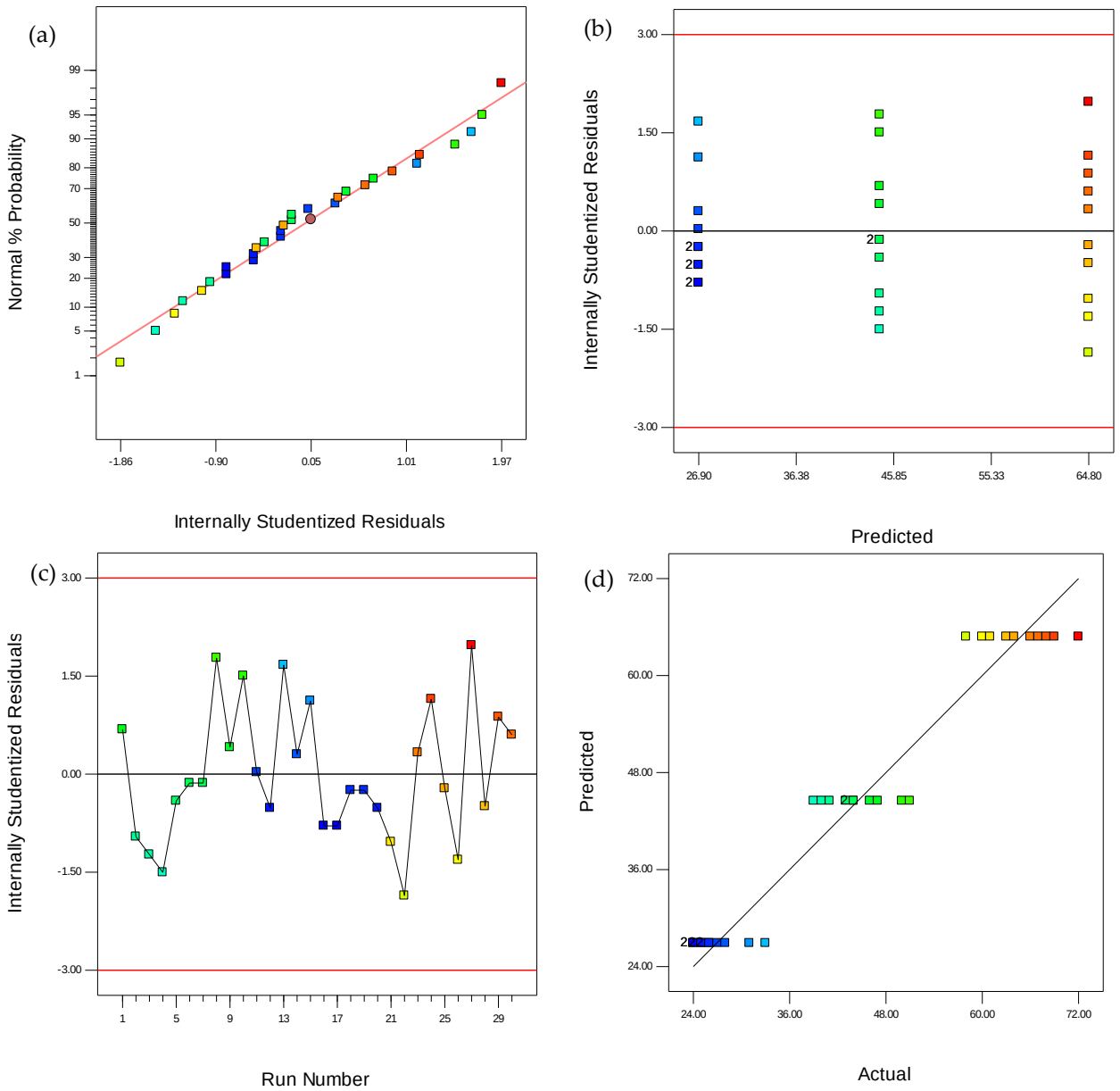


Figure 4. Output random tolerance diagram (a) Normal distribution test of data, (b) Constant variance test, (c) Graph of the relationship between random and ordinal tolerances, and (d) Graph of the relationship between actual experimental results and predicted values.

4. Conclusions

This study compared three hydroponic cultivation systems—Deep Flow Technique (DFT), Nutrient Film Technique (NFT), and Drip Hydroponics System (DHS)—to evaluate their effects on Pakchoi (Brassica rapa var. chinensis) growth and yield. Growth performance was assessed based on plant height, leaf width, and the growth rates of these traits, while yield was evaluated as fresh weight. The results demonstrated that the Drip Hydroponics System (DHS) consistently outperformed the other two systems in promoting plant height and leaf expansion. Although all three hydroponic systems influenced Pakchoi growth and productivity, DHS was particularly effective in enhancing early vegetative growth and overall yield compared with DFT and NFT. Regarding leaf width, average values of 9.42 cm, 11.87 cm, and 14.67 cm were recorded under DFT, NFT, and DHS, respectively, indicating superior leaf development under drip irrigation. Yield analysis further confirmed the advantages of DHS. The mean fresh weights were 26.9 g for DFT, 44.5 g for NFT, and 64.8 g for DHS. Accordingly, the drip irrigation system produced yields that were

58.49% higher than those obtained with DFT and 31.33% higher than those achieved with NFT. Overall, these findings indicate that the Drip Hydroponics System is the most suitable method for the commercial cultivation of Pakchoi, as it delivers higher yields, promotes stronger vegetative growth, and allows more effective control of crop quality compared with stagnant water and whirlpool hydroponic systems.

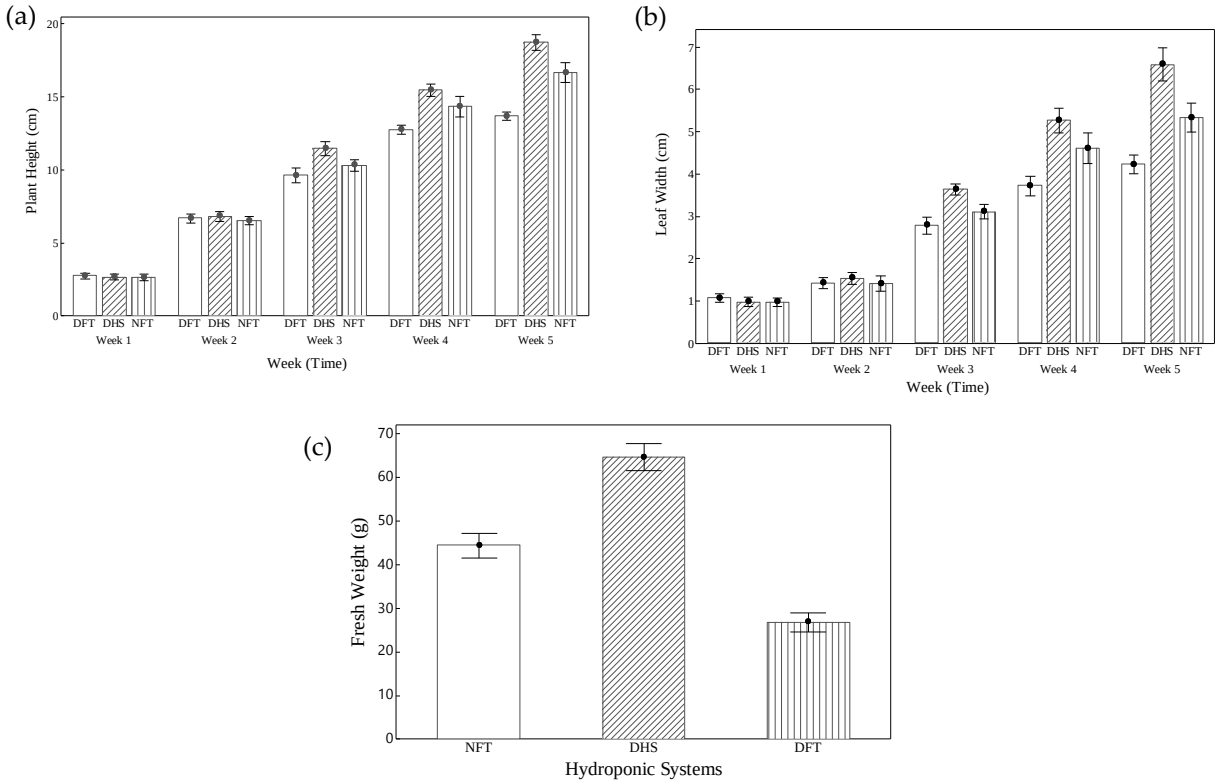


Figure 5. Cantonese planting system diagram with hydroponics (a) Plant height, (b) leaf width, and (c) Cantonese vegetable yield.

5. Acknowledgements

The authors wish to acknowledge all the support provided by Pathumwan Institute of Technology for the realization of this research

Author Contributions: For research articles with several authors, a short paragraph specifying their individual contributions must be provided. The following statements should be used "Conceptualization, ronnarit, Pakamas, Sirawat. and khitaphat; methodology, Pakamas.; software, ronnarit.; validation, ronnarit., Pakamas. and Sirawat.; formal analysis, ronnarit.; investigation, Sirawat; resources, ronnarit., Pakamas., Sirawat.; data curation, khitaphat.; writing—original draft preparation, Pakamas.; writing—review and editing, ronnarit.; visualization, ronnarit;

Funding: This research received no external funding, and no funding was received for the APC.

Conflicts of Interest: The authors declare no conflict of interest. This research received no external funding.

References

[1] Nugraha, R. U.; Susila, A. D. Source as a Substitute for AB Mix in Hydroponic Leafy Vegetable Cultivation. *Indones. J. Hortic.* **2015**, *6*, 11–19. https://doi.org/10.29244/jhi.6.1.11-19

[2] Sapkota, S.; Sapkota, S.; Liu, Z. Effects of Nutrient Composition and Lettuce Cultivar on Crop Production in Hydroponic Culture. *Horticulturae* **2019**, *5*, 72. https://doi.org/10.3390/horticulturae5040072

[3] Chuah, Y. D.; Khor, J. S.; Lim, I. Y.; Ng, C. K. Assessment of Automated Fertigation and Irrigation on the Growth of Bok Choy in a Hydroponic Vertical Farming System. *AIP Conf. Proc.* **2024**, *3161*, 020168. https://doi.org/10.1063/5.0230068

[4] Kano, K.; Kitazawa, H.; Suzuki, K.; Widiastuti, A.; Odani, H. Effects of Organic Fertilizer on Bok Choy Growth and Quality in Hydroponic Cultures. *Agronomy* **2021**, *11*, 491. https://doi.org/10.3390/agronomy11030491

[5] Pearson, C.; Gawel, R.; Maki, D. Effects of Vermicompost and Beneficial Microbes on Biomass and Nutrient Density in Purple Lady Bok Choy in a Vertical Hydroponic System. *Fine Focus* **2023**, *9*, 45–60. https://doi.org/10.33043/FF.9.1.46-64

[6] Gobilik, J.; Rechard, C. T.; Maludin, A. J.; Alam, M. A. Efficacy of Column Hydroponic System for Increasing Growth and Yield of Pak-Choy per Unit Area. *Trans. Sci. Technol.* **2021**, *8*, 60–68.

[7] Veerana, M.; Ketya, W.; Choi, E. H.; Park, G. Non-Thermal Plasma Enhances Growth and Salinity Tolerance of Bok Choy in Hydroponic Culture. *Front. Plant Sci.* **2024**, *15*, 1445791. https://doi.org/10.3389/fpls.2024.1445791

[8] Maluin, F. N.; Hussein, M. Z.; Wayayok, A.; Nik Ibrahim, N. L.; Hashim, N. Chitosan Nanoparticles as a Sustainable Alternative Nutrient Formulation in Hydroponically Grown *Brassica rapa* Microgreen. *Arch. Agron. Soil Sci.* **2023**. https://doi.org/10.1080/03650340.2022.2155952

[9] Ali, A.; Xia, C.; Jia, C.; Faisal, M. Investment Profitability and Economic Efficiency of the Drip Irrigation System: Evidence from Egypt. *Irrig. Drain.* **2020**, *69*, 1033–1050. https://doi.org/10.1002/ird.2511

[10] Jan, S.; Rashid, Z.; Ahngar, T. A.; Iqbal, S.; Naikoo, M. A.; Majeed, S.; Bhat, T. A.; Gul, R.; Nazir, I. Hydroponics—A Review. *Int. J. Curr. Microbiol. Appl. Sci.* **2020**, *9*, 1779–1787. https://doi.org/10.20546/ijcmas.2020.908.206

[11] Wiangsamut, B.; Koolpluksee, M. Yield and Growth of Pak Choi and Green Oak Vegetables Grown in Substrate Plots and Hydroponic Systems with Different Plant Spacing. *Int. J. Agric. Technol.* **2020**, *16*, 491–502.

[12] Manggala, B.; Debra, M.; Chaichana, C.; Syahputra, W. N. H.; Lutfi, M. Effects of Various Hydroponic Systems in Increasing Caisim Productivity under LED Grow Light. *Int. J. Food Agric. Nat. Resour.* **2023**, *4*, 53–58. https://doi.org/10.46676/ij-fanres.v4i2.143

[13] Wiangsamut, B.; Wiangsamut, M. E. L. Assessment of Four Species of Vegetables Grown in Deep Flow Technique and Nutrient Film Technique Hydroponic Systems. *Int. J. Agric. Technol.* **2021**, *17*, 1183–1198.

[14] Salman, A. D.; Abdulrasool, I. J. Effect of Ozone Enrichment and Spraying with Coconut Water and Moringa Extract on Broccoli under Hydroponic System. *Iraqi J. Agric. Sci.* **2022**, *53*, 406–414. https://doi.org/10.36103/ijas.v53i2.1549

[15] Majid, M.; Khan, J. N.; Ahmad Shah, Q. M.; Masoodi, K. Z.; Afroza, B.; Parvaze, S. Evaluation of Hydroponic Systems for the Cultivation of Lettuce and Comparison with Soil-Based Cultivation. *Agric. Water Manage.* **2021**, *245*, 106572. https://doi.org/10.1016/j.agwat.2020.106572

[16] Riggio, G. M.; Jones, S. L.; Gibson, K. E. Risk of Human Pathogen Internalization in Leafy Vegetables during Hydroponic Cultivation. *Horticulturae* **2019**, *5*, 25. https://doi.org/10.3390/horticulturae5010025

[17] Yang, T.; Samarakoon, U.; Altland, J. Growth, Phytochemical Concentration, Nutrient Uptake, and Water Consumption of Butterhead Lettuce in Response to Hydroponic System Design and Growing Season. *Sci. Hortic.* **2024**, *332*, 113201.

ASEAN
Journal of Scientific and Technological Reports
Online ISSN:2773-8752

Research article

A Framework for a Geospatial Predictive Decision Support System for Hazard Risk Profiling

Anna Monica Paculaba[1*], and Thelma Palaoag[2]

[1] Samar State University, Catbalogan City, Samar, 6700, Philippines
[2] University of the Cordilleras, Baguio City, Benguet, 2600, Philippines
* Correspondence: monica.paculaba@ssu.edu.ph

Citation:
Paculaba, M.A.; Palaoag, T. A framework for a geospatial predictive decision support system for hazard risk profiling. *ASEAN J. Sci. Tech. Report.* **2026**, *29*(4), e261475. https://doi.org/10.55164/ajstr.v29i4.261475.

Article history:
Received: September 23, 2025
Revised: January 21, 2026
Accepted: January 25, 2026
Available online: March 25, 2026

Publisher's Note:
This article is published and distributed under the terms of the Thaksin University.

Abstract: Natural hazards consistently pose significant challenges to urban communities, particularly in regions vulnerable to these threats, such as Catbalogan City, Samar, Philippines. Effective hazard risk profiling is essential for proactive disaster preparedness, resource allocation, and policy development. However, current approaches utilized by Catbalogan City and many Local Government Units (LGUs) in the Philippines continue to rely on static hazard maps and descriptive assessments, which limit predictive capability and decision-support effectiveness. This paper presents a conceptual, expert-validated framework for a Geospatial Predictive Decision Support System (GPDSS) to enhance hazard risk profiling and disaster preparedness. The study synthesizes findings from existing hazard-mapping, predictive modeling, and decision-support literature using a systematic review, a design science research approach, and a structured framework development process. The findings reveal persistent reliance on static data, regression-based analyses, and limited integration of decision-support mechanisms. These findings serve as the foundation for the proposed GPDSS framework, which integrates spatiotemporal geospatial datasets, GIS-based analysis, predictive modeling using machine learning techniques, and AI-assisted policy interpretation. Domain experts evaluated the framework, confirming its conceptual relevance, usability, scalability, and innovation for local disaster-risk governance. Rather than a deployed system, the proposed GPDSS is positioned as a governance-oriented framework that offers conceptual advantages over traditional hazard-mapping approaches by enabling predictive risk assessment, interactive visualization, and policy-oriented decision support. The study introduces a scalable, adaptive, and innovative framework intended to guide future system development and implementation for disaster-risk governance in hazard-prone localities in the Philippines.

Keywords: Disaster risk management; predictive analytics; information system framework; artificial intelligence; machine learning

1. Introduction

Natural hazards, including floods, typhoons, landslides, and earthquakes, continue to pose escalating risks to urban communities worldwide due to climate change, rapid urbanization, and environmental degradation [1–2]. These hazards exert increasing pressure on governments to strengthen disaster preparedness, mitigation, and recovery mechanisms, particularly in highly

vulnerable regions [3]. Consequently, there is a growing need to understand localized hazard dynamics and translate risk information into actionable, evidence-based governance strategies [4].

The Philippines is among the most hazard-prone countries globally, experiencing an average of 20 tropical cyclones annually, with 8 to 9 making landfall [5]. Situated along the Pacific Ring of Fire and within the Western Pacific typhoon belt, the country is exposed to multiple hazards, including earthquakes, volcanic eruptions, flooding, and storm surges [6–7]. Although the Philippine Disaster Risk Reduction and Management Act (RA 10121) institutionalized disaster risk governance frameworks [8], implementation at the local government level often remains reactive, constrained by fragmented datasets, static hazard assessments, and limited predictive risk-analysis capabilities. The Eastern Visayas region, particularly Samar Province, consistently ranks among the most disaster-affected areas in the Philippines [9]. As the provincial capital, Catbalogan City faces persistent exposure to typhoons, flooding, and landslides due to its coastal geography, complex terrain, and socio-economic vulnerabilities [10]. Despite these conditions, disaster preparedness efforts in Catbalogan City continue to rely heavily on static hazard maps and manual assessments, which provide limited foresight for anticipatory planning, scenario analysis, and timely resource allocation.

Geographic Information Systems (GIS) have been widely adopted to support hazard profiling and disaster management by integrating spatial datasets such as topography, land use, infrastructure, and hazard zones [11–13]. While GIS-based approaches are effective for spatial visualization and descriptive risk assessment, many existing applications remain focused on historical conditions and are largely map-centric, offering limited predictive and decision-support capabilities. [14–16]. Recent studies emphasize that integrating GIS with predictive analytics and machine-learning techniques substantially enhances hazard-risk forecasting capabilities. Machine-learning models, such as Random Forest, Support Vector Machines, and Neural Networks, have demonstrated significantly higher predictive accuracy than conventional interpolation and regression-based approaches, with reported accuracies reaching up to 96% in selected hazard-mapping applications [17–19]. These approaches enable spatio-temporal modeling and forward-looking risk estimation, shifting disaster management from reactive response toward proactive preparedness [20–25]. However, predictive accuracy alone is insufficient to support effective disaster governance. Decision Support Systems (DSS) are required to transform analytical outputs into actionable insights for planners and policymakers [26–29]. In disaster-risk contexts, Spatial Decision Support Systems (SDSS) integrate geospatial data, analytical models, and user interfaces to facilitate time-sensitive decision-making through dashboards, scenario simulations, and policy-support tools [27–28].

Recent advancements further highlight the role of Artificial Intelligence (AI), particularly Natural Language Interfaces and Conversational AI, in supporting evidence-based policymaking and governance. These AI-assisted tools can interpret analytical outputs, generate policy-relevant summaries, and provide context-aware recommendations to decision makers [30–33]. Embedding such AI-assisted policy modules into decision-support systems enhances transparency, adaptability, and responsiveness in local disaster risk governance. Despite these technological developments, many local government units (LGUs) in the Philippines, including Catbalogan City, continue to depend on fragmented systems and static hazard maps. National initiatives such as Project NOAH (Nationwide Operational Assessment of Hazards) and Project TANAW (Topographical Analysis and Angular Assessment of City Works) demonstrate the value of geospatial hazard mapping and visualization for disaster management [34–35]. However, these initiatives remain largely descriptive and centralized, offering limited integration of predictive machine-learning analytics, barangay-level socio-economic data, and interactive decision-support functionalities aligned with LGU decision-making workflows. These limitations underscore the need for a localized, governance-oriented Geospatial Predictive Decision Support System (GPDSS) that integrates dynamic geospatial datasets, predictive analytics, and AI-assisted policy support within a unified framework. Such a system is particularly relevant for Catbalogan City, where multi-hazard exposure requires anticipatory planning and data-driven decision-making at the barangay level.

Accordingly, this study aims to develop a conceptual framework for a Geospatial Predictive Decision Support System (GPDSS) for hazard risk profiling. The proposed framework integrates geospatial data, predictive modeling, and an AI-assisted decision interface to support barangay-level hazard-risk classification

and policy-relevant recommendations. Positioned explicitly as a framework proposal and expert-validated design, rather than a deployed system, the study contributes a scalable, governance-focused model intended to guide proactive disaster risk management in Catbalogan City and other hazard-prone localities in the Philippines.

2. Materials and Methods

2.1 Materials

2.1.1 Research Design

This study employed a Design Science Research (DSR) approach, well-suited to the development and evaluation of innovative artifacts such as frameworks and decision support systems. The DSR cycle consisted of three iterative phases: (a) problem identification and requirements analysis, (b) framework design and development, and (c) evaluation and refinement [36-37]. This ensured that the proposed Geospatial Predictive Decision Support System (GPDSS) framework was both scientifically rigorous and contextually relevant to Catbalogan City's disaster preparedness needs.

2.1.2 Data Sources

For the proposed GPDSS framework, relevant hazard, geospatial, and socio-economic datasets are identified from national and local data repositories commonly used for disaster risk assessment and governance in the Philippines. These datasets are intended to be requested and integrated during the system implementation phase, consistent with the conceptual scope of the present study. The primary data categories include meteorological, geological, topographic, and socio-economic information sourced from government agencies such as the Philippine Atmospheric, Geophysical and Astronomical Services Administration (PAGASA), the Philippine Institute of Volcanology and Seismology (PHIVOLCS), the National Mapping and Resource Information Authority (NAMRIA), the Philippine Statistics Authority (PSA), and the Catbalogan City Disaster Risk Reduction and Management Council (CDRRMC). Table 1 summarizes the proposed data sources, including data type, temporal coverage, spatial resolution, and responsible agencies, to clarify data derivation and intended system integration.

Table 1. Proposed Data Sources for the GPDSS Framework

Data Type	Source Agency	Temporal Coverage	Spatial Resolution
Meteorological (rainfall, typhoon tracks)	PAGASA	Hourly / Daily	Station-based / Grid
Geological (fault lines, landslide records)	PHIVOLCS	Event-based	Municipal / Site-specific
Topographic (DEM, land use)	NAMRIA	Periodic updates	10–30 meters
Socio-economic (population, housing, vulnerability indicators)	PSA	Census-based	Barangay level
Disaster incident records	CDRRMC	Event-based	Barangay level

Although actual data acquisition and integration were beyond the scope of this framework proposal, data availability, interoperability, and quality considerations were incorporated into the framework design. The GPDSS conceptual architecture assumes standardized data formats, metadata documentation, and validation procedures to support reliable spatio-temporal analysis.

Data privacy and security are recognized as critical governance considerations, particularly for community-level socio-economic information. Any future implementation of the proposed framework shall comply with national data privacy regulations and local government data-sharing protocols to ensure ethical and responsible data use.

2.2 Methods

2.2.1 Systematic Review of Literature

A systematic review [38] was conducted to examine existing approaches to hazard risk profiling, predictive modeling, geospatial decision support, and AI-assisted policymaking. The review adhered to a

structured process. Literature searches were conducted using Scopus, Web of Science, and Google Scholar. Search terms focused on hazard risk profiling, geospatial analysis, predictive modeling, machine learning, and decision-support systems. Broader concepts, including spatial decision support, early warning systems, and risk assessment frameworks, were also considered during the screening stage to capture relevant interdisciplinary studies. The initial search yielded approximately 100 records. Following title, abstract, and full-text screening, studies were excluded due to duplication, limited relevance to predictive hazard-risk profiling, absence of geospatial or analytical methods, insufficient methodological detail, or non–peer-reviewed status. A total of 20 studies were retained for synthesis, representing those most directly aligned with the objectives of framework design and gap identification. The relatively high exclusion rate reflects the review's focused emphasis on predictive and decision-support–oriented research rather than descriptive hazard mapping. The study selection process followed the core principles of the PRISMA guidelines. A PRISMA flow diagram illustrates the identification, screening, eligibility, and inclusion stages, with exclusion reasons described in the accompanying text. A formal PRISMA checklist was not included, as the review was intended to support conceptual framework development rather than comprehensive evidence synthesis. A formal quality appraisal using tools such as CASP or the Newcastle–Ottawa Scale was not conducted. This decision was intentional, as the review focused on identifying methodological trends and functional gaps rather than comparing study quality or empirical performance. This limitation is acknowledged in the discussion. Figure 1 presents the PRISMA flow diagram summarizing the identification, screening, eligibility, and inclusion process.

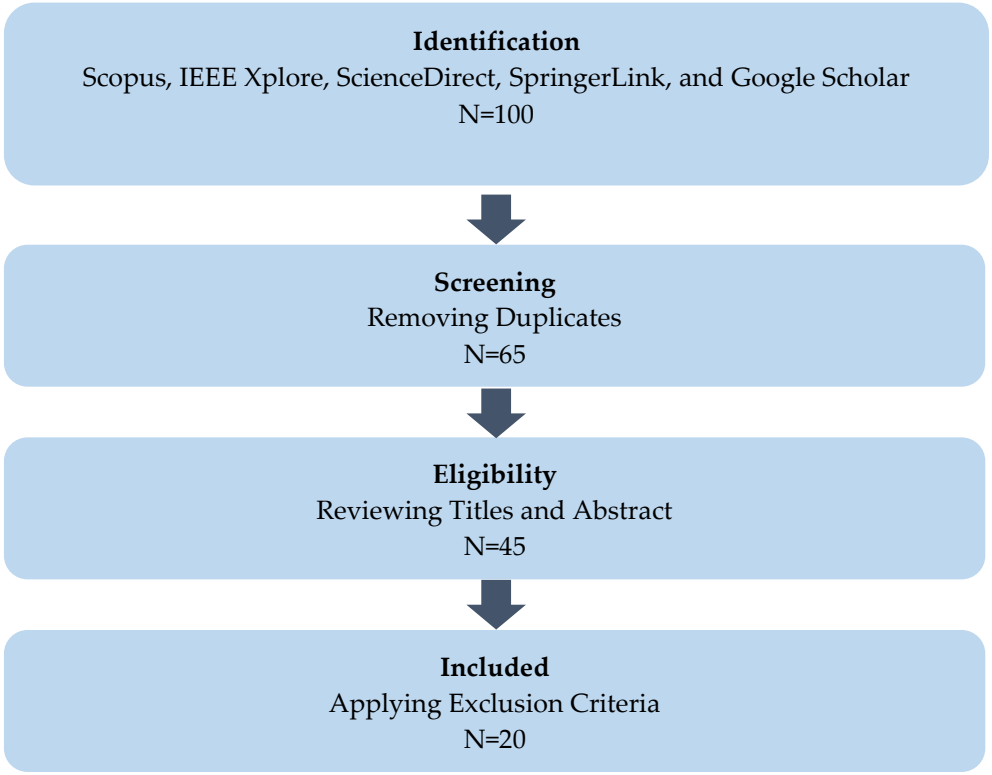


Figure 1. PRISMA Flow Diagram for the Systematic Review

Table 2. Summary of Included Studies

Author(s) & Year	Focus of Study	Methodology	Relevance to Hazard Risk Profiling
Farhadi & Najafzadeh, 2021 [39]	Flood risk mapping using remote sensing and Random Forest	Random Forest combined with remote-sensing inputs	Demonstrates the application of Random Forest for flood-risk mapping using satellite imagery
Mobley et al., 2021 [40]	Continuous flood-hazard quantification	Random Forest spatial classification	Example of a large-scale Random-Forest application for flood-probability mapping
De Vries et al., 2020 [41]	Rapid monitoring of flood events	Sentinel-1 synthetic-aperture-radar (SAR) time-series anomaly detection	Presents an algorithm for rapid flood detection using Sentinel-1 data
Yang et al., 2021 [42]	High-resolution flood-inundation archive	SAR-based inundation mapping (10 m resolution)	Provides a high-resolution inundation dataset for model validation
Islam et al., 2022 [43]	Urban flood mapping using Sentinel-1	Polarization analysis of vertical–horizontal and vertical–vertical bands	Evaluates Sentinel-1 polarizations for urban flood detection
Deng et al., 2022 [44]	Landslide susceptibility at the slope-unit scale	Information-Value analysis with Random Forest	Demonstrates slope-unit landslide susceptibility mapping using Information-Value–Random-Forest hybrid
Zhou et al., 2021 [45]	Hybrid models for landslide susceptibility	Hybrid machine-learning models combining Random Forest with other algorithms	Shows improved landslide-susceptibility prediction through hybrid modeling
Taalab, 2018 [46]	Landslide susceptibility mapping	Random Forest integrated with geographic information systems (GIS)	Demonstrates Random Forest application across heterogeneous regions for landslide susceptibility
Tehrany et al., 2019 [47]	Flood-susceptibility assessment	Evidential-belief approach combined with a machine-learning ensemble	Presents a robust ensemble approach for flood-susceptibility mapping
Althuwaynee et al., 2014 [48]	Landslide susceptibility mapping	Bivariate statistical analysis and Dempster–Shafer evidential-belief function	Provides a classic baseline method for landslide-susceptibility mapping
Luu et al., 2021 [49]	Flood susceptibility in Quang Binh, Vietnam	GIS combined with ensemble machine-learning models	Demonstrates a regional ensemble machine-learning plus GIS pipeline for flood mapping

Table 2. Summary of Included Studies (Continue)

Author(s) & Year	Focus of Study	Methodology	Relevance to Hazard Risk Profiling
Li et al., 2024 [50]	Landslide susceptibility with space–ground data integration	Space–ground data integration with Random Forest	Demonstrates replicable methods for landslide assessment
Zhang et al., 2023 [51]	Landslide susceptibility comparison	Random Forest versus Extreme Gradient Boosting	Benchmark tree-based models for landslide susceptibility
Toma et al., 2024 [52]	Sentinel-1 flood mapping on Google Earth Engine	Sentinel-1 SAR processing with Google Earth Engine	Demonstrates scalable and rapid urban-flood mapping workflows
Albertini et al., 2024 [53]	Multi-source flooded-area mapping	Multi-source Random-Forest classification	Integrates varied geospatial inputs for flooded-area mapping
Saber, 2023 [54]	Ensemble gradient models for flood risk	Light Gradient Boosting Machine, CatBoost, and Random Forest	Supports gradient-boosting model selection for predictive flood mapping
Schoppa et al., 2020 [55]	Flood-prediction model comparison	Random Forest compared with physics-based hydrodynamic models	Validates Random Forest as a surrogate for computationally intensive hydrodynamic models
Lagmay et al., 2017 [34]	National hazard mapping and near-real-time dissemination (Philippines)	Multi-hazard GIS mapping, remote sensing, and web dissemination	Operational Philippine program for hazard mapping and public dissemination
Papadakis et al., 2024 [32]	Explainable and transparent artificial intelligence for public policymaking	Frameworks and real-world case studies applying explainable artificial intelligence methods	Guides the design of explainability and governance features for AI policy modules
Amarasinghe, 2023 [56]	Explainable machine-learning methods for public policy	Review of interpretability techniques such as SHAP and LIME	Provides approaches for integrating transparent AI tools into decision-support systems

Table 2 presents the 20 studies included in the systematic review, detailing the authors, research focus, methodologies employed, and relevance to hazard risk profiling. The review shows that flood-related research predominates, with roughly 60% of the studies [39-53] [49][52-55] focusing on flood risk mapping, rapid inundation detection, or continuous flood hazard quantification. Landslide susceptibility represents the next most common hazard, accounting for about 30% of the studies [44-46][48][50-51]. Only one paper, or 20%, offered a broad, multi-hazard perspective at the national scale [34]. Methodologically, machine learning dominates hazard prediction and mapping. Random Forest is the most frequently implemented algorithm, either as a stand-alone classifier [39-40] or in hybrid and ensemble forms with techniques such as Extreme Gradient Boosting and Light Gradient Boosting Machine [51][54]. These models are commonly paired with remote sensing and Geographic Information Systems (GIS) for spatial analysis, as demonstrated by Sentinel-1 synthetic-aperture radar applications [41-42][52]. Classic statistical approaches, such as bivariate analysis and evidential-belief functions [51-52], appear less frequently but provide important baselines for model validation. The review also highlights the emerging integration of artificial intelligence for policy support. It presents frameworks for explainable and transparent AI in public policymaking, illustrating how machine-learning outputs can be translated into interpretable insights for governance [32][56]. These studies underscore the value of embedding explainable artificial intelligence and interactive decision-support features within hazard-risk systems. However, despite these advances, the review highlighted persistent gaps:

a) continued reliance on static hazard maps rather than dynamic spatio-temporal models,
b) limited integration of predictive analytics with GIS visualization, and
c) inadequate incorporation of artificial-intelligence–driven policy tools and interactive decision-support features to translate analytical outputs into practical governance actions.

These findings directly inform the design of the proposed Geospatial Predictive Decision Support System (GPDSS) for hazard risk profiling in Catbalogan City, Samar. By integrating remote sensing, GIS, advanced machine-learning models, and AI-assisted policy guidance into a single platform, the GPDSS seeks to address documented gaps and enable anticipatory, evidence-based disaster risk governance at the local level.

2.2.2 Framework Development Process

The development of the proposed Geospatial Predictive Decision Support System (GPDSS) follows key principles of information systems development, emphasizing structured lifecycles, process models, and formal methodologies to guide system development [57]. This approach provides a systematic method for designing and evaluating public-sector information systems by combining rigorous data collection with iterative framework development, ensuring that the resulting platform is both robust and fit for local government use [58-59]. In particular, the development strategy highlights the importance of functional design and modular architecture to deliver a maintainable, web-based decision-support application that integrates geospatial analytics and AI-assisted policy reporting.



Figure 2. Framework Development Process

Figure 2 presents the framework development process, which served as the primary guide for creating the GPDSS. The process comprises three major phases [60]. Application Modeling Phase – requirements are gathered regarding the system's objectives, core functions, data flows, and expected outputs for hazard risk profiling and policy support. From these requirements, the main components and data modules are identified. Building-Block Tailoring Phase – the essential building blocks of the system are customized to meet the specific needs of the GPDSS, including geospatial data integration, temporal predictive modeling, and AI-assisted report generation for policymaking. Component Composition Phase – all customized components are integrated

to form the complete decision-support platform, ensuring seamless interaction between the geospatial predictive analytics engine and the AI-based policy-reporting module. This structured development process ensures that the GPDSS is both technically sound and aligned with the decision-making requirements of the Catbalogan City local government.

3. Results and Discussion

This section presents the study's results in terms of the designed framework components, the synthesis of systematic review findings, and expert evaluation outcomes, focusing on the conceptual development and assessed feasibility of the proposed GPDSS framework. The systematic review of 20 selected studies identified three recurring patterns in hazard risk profiling research: (a) reliance on static datasets, (b) predominant use of conventional statistical or regression-based models, and (c) limited integration of decision-support functionality.

3.1 Gap from Findings from the Systematic Review

The systematic review examined existing research on hazard-risk profiling and decision-support systems to identify limitations in current practices. The review highlighted key gaps, including reliance on static hazard maps, limited application of predictive analytics, and inadequate integration of multi-agency datasets, which guided the design of the proposed GPDSS framework.

Table 3. Summary of Findings from the Systematic Review

Theme	Key Observations from Literature	Implication for the Proposed Framework
Data Dependence	Hazard maps and census records dominate, with limited use of temporal satellite observations and other time-varying geospatial datasets.	Incorporate multi-source temporal data, such as satellite imagery and historical hazard records, to enable dynamic spatio-temporal analysis.
Analytical Approaches	Regression and other classical statistical methods remain common; machine-learning techniques are used mainly for hazard prediction but are not the focus of AI in this study.	Apply appropriate predictive models for temporal hazard forecasting.
Decision-Support Limitations	Most existing systems provide static visualization and lack mechanisms to translate analytical outputs into actionable governance.	Develop an AI-assisted Geospatial Predictive Decision Support System (GPDSS) that uses predictive results to automatically generate interpretive reports and policy options for local government decision makers.

Themes are derived from the systematic review of 20 studies on hazard risk profiling.

Table 3 presents the gaps derived from the systematic literature review. It revealed three critical gaps that inform the conceptualization and design of the proposed GPDSS. First, the extant literature demonstrates a pronounced dependence on static data sources, with hazard maps and census records serving as the primary inputs for risk assessment. The limited adoption of temporal satellite observations and other time-varying geospatial datasets constrains the capacity to capture evolving hazard dynamics. Addressing this shortcoming requires incorporating multi-source temporal data, such as satellite imagery and historical hazard records, to enable dynamic spatio-temporal analysis within the GPDSS framework. Second, the review indicates that analytical approaches remain dominated by regression and other classical statistical techniques, while the application of machine-learning methods is largely confined to hazard prediction and does not extend to

policy formulation. For the proposed system, this finding underscores the need to employ appropriate predictive models for temporal hazard forecasting, while clearly delimiting the role of artificial intelligence to post-analysis functions rather than predictive accuracy. Third, most existing platforms exhibit marked decision-support limitations. Current systems primarily provide static visualizations and lack mechanisms to translate analytical outputs into actionable governance strategies. To overcome this deficit, the GPDSS will incorporate an AI-assisted decision-support module that interprets predictive results and automatically generates policy-relevant reports and recommendations tailored to the needs of local government decision-makers. Collectively, these findings highlight the necessity for a comprehensive, responsive, and policy-oriented geospatial framework. By integrating diverse temporal datasets, employing robust predictive modeling, and embedding AI-driven policy guidance, the GPDSS aims to bridge the identified gaps and advance proactive, evidence-based disaster-risk governance at the local level.

3.2 Novel Contributions of the Proposed GPDSS Framework

While the proposed GPDSS adopts a three-layer architecture commonly found in decision support system (DSS) literature, comprising Data, Analytics, and Decision-Support layers, the novelty of the framework lies not in the architecture itself but in its governance-oriented integration and localized application. Existing Philippine disaster-management initiatives, such as Project NOAH and Project TANAW, primarily focus on hazard visualization, monitoring, and descriptive spatial analysis. Although these systems provide valuable geospatial insights, they remain largely centralized, map-centric, and focused on historical conditions, with limited integration into local government decision-making workflows. In contrast, the proposed GPDSS framework introduces several distinct contributions. First, it emphasizes barangay-level predictive hazard-risk profiling by integrating spatio-temporal environmental, geospatial, and socio-economic datasets. This shifts hazard assessment from static mapping toward anticipatory, data-driven risk estimation tailored to local governance needs. Second, the framework conceptually integrates predictive analytics with decision-support functionality. Rather than treating predictive models as standalone analytical tools, the GPDSS is designed to translate predictive outputs into policy-relevant insights through dashboards, scenario analysis, and structured decision-support mechanisms aligned with LGU planning and resource-allocation processes. Third, the framework incorporates an AI-assisted policy interpretation component using Natural Language Interfaces and Conversational AI. This feature is intended to support local officials by summarizing analytical results, generating context-aware recommendations, and enhancing the interpretability of complex predictive outputs, capabilities that are not explicitly addressed in existing Philippine hazard-management systems. Finally, the proposed GPDSS adopts a modular and scalable design philosophy. Although conceptual in nature, the framework is structured to facilitate future implementation across multiple local government units by allowing the integration of locality-specific datasets and retraining of predictive models. This scalability positions the framework as a transferable governance tool rather than a site-specific technical solution. Collectively, these contributions distinguish the proposed GPDSS framework from existing disaster-risk tools by foregrounding predictive capability, decision-support integration, and governance applicability at the local level, thereby addressing critical gaps identified in the systematic review and expert evaluation.

3.3 Proposed Framework for GPDSS

Based on the hazard and disaster challenges identified in Catbalogan City, Samar, insights synthesized from the systematic review of relevant literature, and framework development process, this section presents the proposed Geospatial Predictive Decision Support System (GPDSS) for the hazard risk profiling framework. The framework integrates multi-source geospatial data, predictive analytics, and interactive decision-support components to guide evidence-based hazard risk profiling and disaster-management planning.

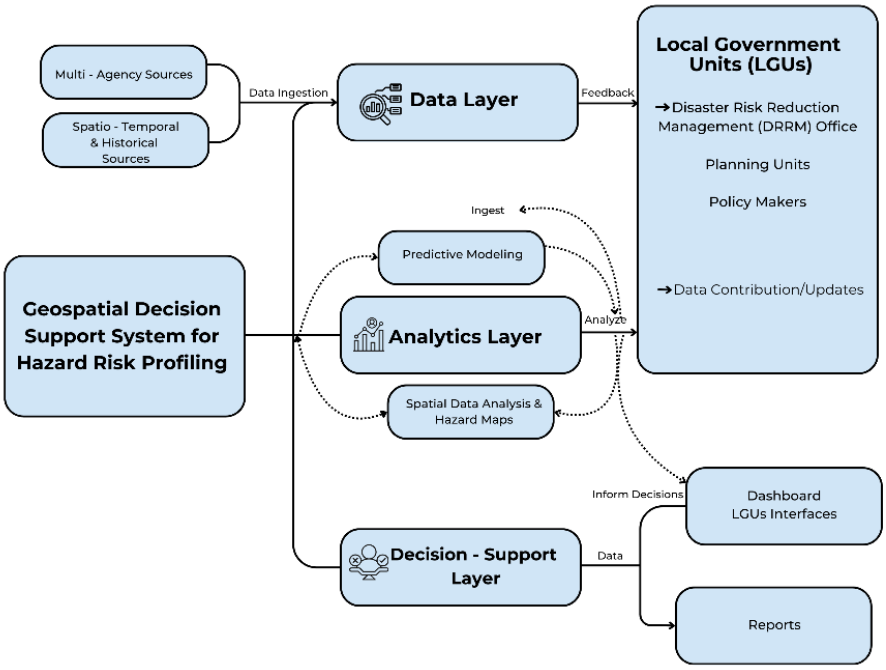


Figure 3. Conceptual framework of the proposed Geospatial Predictive Decision Support System (GPDSS) for hazard risk profiling and local disaster-risk governance.

The proposed GPDSS framework addresses the limitations of static hazard mapping by integrating dynamic spatio-temporal datasets, advanced predictive analytics, and interactive decision-support tools, in contrast to conventional hazard maps, which are typically dependent on historical data and infrequent updates. The GPDSS framework illustrates a cyclical process of data integration, analytical processing, and stakeholder engagement. The workflow begins with the Data Ingestion phase, where information is aggregated from diverse streams, specifically Multi-Agency Sources and Spatio-Temporal & Historical Sources such as PAGASA, PHIVOLCS, NAMRIA, and PSA, as well as local records from the Catbalogan City CDRRMC. This raw data is funneled into the Data Layer, which serves as the primary repository and foundational structure for the system. By centralizing disparate datasets, the framework ensures that subsequent analyses are based on a comprehensive, unified information base. From the Data Layer, the framework transitions to the Analytics Layer, a sophisticated processing core that converts raw data into actionable intelligence. This layer utilizes two primary methodologies: Predictive Modeling, which forecasts future risks, and Spatial Data Analysis, which produces visualized Hazard Maps. These analytical outputs are then utilized by the Decision-Support Layer, which synthesizes the findings to provide clear, evidence-based guidance. The final delivery of this intelligence is facilitated through specialized LGU Dashboard Interfaces and comprehensive Reports, designed to "Inform Decisions" for end-users. The framework culminates in a dynamic interaction with Local Government Units (LGUs), specifically targeting Disaster Risk Reduction Management (DRRM) offices, Planning Units, and Policy Makers. This stage represents the practical application of the system's outputs in real-world governance and risk mitigation. Crucially, the model establishes a continuous feedback loop: LGUs provide feedback back to the Data Layer and offer Data Contributions or Updates based on localized observations. This iterative relationship ensures that the GDSS remains up to date, relevant, and highly responsive to the evolving needs of the communities it serves.

Applying the framework within the context of Catbalogan City underscores its practical applicability. The city's repeated exposure to typhoons, coastal flooding, and landslides, combined with notable socio-economic vulnerabilities, underscores the need for a data-driven decision-support mechanism. Although the framework emerges from a broad synthesis of international and local scholarship, the hazard profile and governance conditions of Catbalogan provide a realistic testbed and illustrate how the system can strengthen local disaster risk reduction and management (DRRM) strategies. Finally, the framework's modular

architecture promotes scalability and transferability. Its core design can be readily adapted to other Philippine cities or similarly hazard-prone localities by integrating site-specific datasets and refining predictive models. Such adaptability extends the framework's relevance beyond Catbalogan and aligns with global imperatives for climate-resilient urban planning and evidence-based DRRM policy making.

3.4 Comparison of Traditional Approaches and the Proposed Framework

A comparative analysis between traditional hazard mapping practices in the Philippines, particularly in Catbalogan City, Samar, and the proposed Geospatial Predictive Decision Support System (GPDSS) framework was conducted.

Table 4. Comparison of Traditional Approaches and the Proposed Framework

Feature	Traditional Hazard Mapping	Proposed GPDSS Framework
Data Source	Static hazard maps, census data	Dynamic hazard maps, spatio-temporal datasets
Analytical Techniques	Descriptive statistics, regression	Predictive modeling, machine learning, scenario simulation
Decision-Support Features	Limited to static maps	Interactive dashboards, risk maps, and policy recommendation tools
Adaptability	Location-specific, non-scalable	Scalable and adaptable to multiple localities
End-Users	Planners, technical experts	LGUs, policymakers, and communities

The comparison highlights the advantages of the proposed GPDSS over traditional hazard-mapping practices.

Table 4 illustrates the comparative analysis of the traditional approaches and the proposed framework of the study. It highlights the substantive advantages of the proposed Geospatial Predictive Decision Support System (GPDSS) over conventional hazard-mapping practices currently used in the Philippines, particularly in Catbalogan City, Samar. Traditional approaches rely primarily on static hazard maps and census data, which provide only a static snapshot of risk conditions and are infrequently updated. In contrast, the GPDSS integrates dynamic hazard maps and spatiotemporal datasets, enabling continuous monitoring and incorporating evolving environmental and socio-demographic variables. Analytically, existing methods emphasize descriptive statistics and regression-based analyses, which are limited to retrospective or static evaluations. The proposed framework advances beyond these techniques by integrating predictive modeling, machine learning, and scenario simulation, thereby enabling forward-looking hazard forecasts and risk assessments. From a decision-support perspective, traditional systems offer limited functionality, typically confined to static map dissemination. The GPDSS introduces interactive dashboards, dynamic risk maps, and policy recommendation tools, providing local government units and policymakers with actionable insights for proactive planning and resource allocation.

In terms of adaptability, traditional hazard mapping tends to be location-specific and non-scalable, restricting its broader application. By contrast, the GPDSS is modular, scalable, and adaptable across multiple localities, ensuring relevance for diverse geographic and administrative contexts. Finally, while conventional methods are primarily designed for technical experts and planners, the GPDSS explicitly targets a broader user base, including local government units, policymakers, and community stakeholders, thereby fostering participatory and inclusive disaster risk governance. Overall, the proposed GPDSS framework addresses the limitations of traditional hazard mapping by combining dynamic data integration, advanced predictive analytics, and AI-assisted decision support, thereby enhancing the capacity for anticipatory, evidence-based disaster risk management.

3.5 Expert Validation Result

To ensure methodological robustness and contextual applicability, the proposed Geospatial Predictive Decision Support System (GPDSS) conceptual framework was subjected to expert validation using a structured evaluation matrix. Expert-based assessment is a recognized and widely employed method for

establishing the quality, feasibility, and potential utility of decision-support frameworks [61-62]. Using the adapted evaluation matrix, 12 domain experts, including disaster-risk management officials, geographic information systems (GIS) analysts, and information-technology practitioners, independently evaluated the framework across four key dimensions: relevance, usability, scalability, and innovation.

Table 5. Expert Validation Results of the GPDSS Framework

Validation Dimension	Indicators for a Conceptual Framework	Mean	Representative Expert Feedback	Interpretation
Relevance	Alignment with local DRRM priorities; potential to inform LGU policy and planning once implemented	4.6	"Directly addresses Catbalogan's hazard risks; highly relevant for future DRRM initiatives."	Extremely Acceptable
Conceptual Usability	Clarity and logical coherence of the proposed structure; feasibility of eventual interface design	4.5	"The framework is clearly organized and would be intuitive to translate into an operational system."	Highly Acceptable
Scalability	Transferability of the framework to other municipalities or hazard-prone areas	4.5	"Design can be readily adapted to other municipalities with appropriate local data inputs."	Highly Acceptable
Innovation	Novel integration of predictive analytics and geospatial modeling at the conceptual level	4.7	"Combines machine-learning forecasting with GIS-based risk profiling in an original way for local governance."	Extremely Acceptable

Experts rated each criterion using a five-point Likert scale with the following interpretation: 4.51–5.00 = Extremely Acceptable, 3.31–4.50 = Highly Acceptable, 2.51–3.30 = Acceptable, 1.51–2.50 = Needs Improvement, and 1.00–1.50 = Not Acceptable. Mean scores represent the average of twelve independent expert evaluations of the proposed GPDSS framework.

Table 5 presents the results of the expert evaluation of the GPDSS framework. The findings show that the expert panel assigned ratings of 4.5-4.7 across all evaluation criteria, indicating strong support for the framework's theoretical robustness and future implementation potential. Reviewers emphasized its relevance to Catbalogan City's disaster-risk reduction requirements and noted the framework's logical coherence and conceptual feasibility. Experts further affirmed its scalability, highlighting its capacity to be adapted to other hazard-prone municipalities through the integration of local datasets and retraining of predictive models. The strong rating for innovation reflects how original this framework is in combining machine-learning predictive analytics with GIS-based spatio-temporal analysis for municipal disaster management. This finding aligns with the study by [63], which stresses the importance of user-centred design approaches in disaster risk visualisation. The acknowledgment of scalability in the expert feedback is also supported by recent systematic reviews of disaster management systems, which highlight the need for adaptable, technology-enabled frameworks across diverse localities [64]. It should be noted that the results presented in this section pertain to framework design and expert-based assessment, and do not represent operational system performance or predictive accuracy metrics. These aspects are identified as directions for future work, including prototype development, empirical testing, and pilot implementation in Catbalogan City, Samar, Philippines.

4. Conclusions

The increasing frequency and complexity of natural hazards in the Philippines underscore the need for more proactive, data-driven approaches to local disaster risk governance. This study presented a Geospatial Predictive Decision Support System (GPDSS) framework designed to address identified gaps in existing hazard risk profiling practices, particularly the reliance on static datasets, conventional analytical methods, and limited decision-support integration. By synthesizing findings from a systematic review and expert evaluation, the study contributes a governance-oriented framework that integrates geospatial analysis, predictive modeling, and AI-assisted decision support for barangay-level hazard risk profiling. The primary contribution of this study lies in the conceptual design and expert validation of a localized, predictive, and decision-support–oriented framework rather than in the development of an operational system. The proposed GPDSS framework emphasizes anticipatory planning, policy relevance, and alignment with local government unit (LGU) workflows, distinguishing it from existing hazard mapping initiatives that remain largely descriptive and centralized. This study is subject to several limitations. First, the framework was evaluated through expert-based assessment rather than empirical system implementation or performance testing. Second, actual data acquisition, model training, and system deployment were beyond the scope of the present work. As such, predictive accuracy metrics, system responsiveness, and operational effectiveness were not assessed. Future research will focus on translating the proposed framework into a functional prototype by integrating real-time and historical hazard data from relevant national and local agencies. Subsequent phases include model training and validation, pilot testing in Catbalogan City, Samar, and evaluation of system performance under multi-hazard scenarios involving floods, landslides, and typhoons. Further work will also examine system sustainability, maintenance requirements, capacity-building for LGU personnel, and ethical considerations related to data privacy and algorithmic transparency. Generally, the proposed GPDSS framework provides a structured foundation for advancing predictive, data-driven disaster risk governance at the local level. It offers a scalable reference model for future geospatial decision-support system development in hazard-prone communities in the Philippines.

5. Acknowledgements

The authors acknowledged Samar State University, the University of the Cordilleras, and the Department of Science and Technology of the Philippines for their support in conducting this study.

Author Contributions: Conceptualization, methodology, validation, formal analysis, resources, data curation, writing—original draft preparation, writing—review and editing, and funding acquisition are contributed by A.M.P.; T.P contributes Project administration, and supervision.

Funding: This research was funded by the Department of Science and Technology of the Philippines.

Conflicts of Interest: The authors declare no conflict of interest.

References

[1] Peduzzi, P.; Pascal, P. Revealing the Underlying Drivers of Disaster Risk: A Global Analysis. *EGU Gen. Assem. Conf. Abstr.* **2017**, *19*, 5306.

[2] Chai, J.; Wu, H.-Z. Prevention/Mitigation of Natural Disasters in Urban Areas. *Smart Constr. Sustain. Cities* **2023**, *1*, 4. https://doi.org/10.1007/s44268-023-00002-6

[3] Franzke, C. L. E.; Lee, J.-Y.; O'Kane, T.; Merryfield, W.; Zhang, X. Extreme Weather and Climate Events: Dynamics, Predictability and Ensemble Simulations. *Asia-Pac. J. Atmos. Sci.* **2023**, *59*, 1–2. https://doi.org/10.1007/s13143-023-00317-5

[4] Marcus, H.; Hanna, L. Barriers to Climate Disaster Risk Management for Public Health. *Disaster Med. Public Health Prep.* **2022**, *16*, 1351–1354. https://doi.org/10.1017/dmp.2021.162

[5] Santos, G. D. C. Tropical Cyclones in the Philippines: A Review. *Trop. Cyclone Res. Rev.* **2021**, *10*, 191–199. https://doi.org/10.1016/j.tcrr.2021.09.003

[6] Holden, W.; Nadeau, K.; Porio, E. An Archipelago of Hazards; Springer, 2017; pp 17–23. https://doi.org/10.1007/978-3-319-50782-8_4

[7] Iuchi, K.; Jibiki, Y.; Solidum, R.; Santiago, R. Natural Hazards Governance in the Philippines. In *Oxford Research Encyclopedia of Natural Hazard Science*; Oxford University Press, 2019. https://doi.org/10.1093/acrefore/9780199389407.013.233

[8] Republic of the Philippines. *Republic Act No. 10121*; 2010. https://www.officialgazette.gov.ph/2010/05/27/republic-act-no-10121/ (accessed Sept 23, 2025).

[9] Pantolla, H.; Atibagos-Nacion, N. Spatial Analysis of Poverty Incidence and Road Networks in Eastern Visayas Region, Philippines. *Philipp. J. Sci.* **2023**, *152*. https://doi.org/10.56899/152.04.01

[10] Orale, R. L.; Montecastro, D. Catbalogan, Philippines Sky City Mega Project: Environmental and Operational Challenges. In *Proc. Int. Conf. Utility Exhib. Energy Environ. Clim. Change*; IEEE, 2022; pp 1–12. https://doi.org/10.1109/ICUE55325.2022.10113494

[11] Adu, S. A.; Gyang, P. A.-E.-M.; Yakin, Z. The Role of GIS and Spatial Analysis in Enhancing Urban Resilience. *World J. Adv. Res. Rev.* **2025**, *27*, 746–754. https://doi.org/10.30574/wjarr.2025.27.1.2567

[12] Sharma, S. Geographical Information System (GIS). *Int. J. Adv. Res. Sci. Commun. Technol.* **2025**, 612–614. https://doi.org/10.48175/IJARSCT-26278

[13] Chen, Y. Flood Hazard Zone Mapping Using GIS and Multi-Criteria Analysis. *J. Hydrol.* **2022**, *612*, 128268. https://doi.org/10.1016/j.jhydrol.2022.128268

[14] Daud, M.; Ugliotti, F. M.; Osello, A. Use of Web-GIS for Natural Hazard Management: A Review. *Sustainability* **2024**, *16*, 4238. https://doi.org/10.3390/su16104238

[15] Page-Tan, C.; Fraser, T.; Aldrich, D. P. Mapping Resilience. In *Disaster and Emergency Management Methods*; Routledge: New York, 2021; pp 339–354. https://doi.org/10.4324/9780367823948-22

[16] Bhunia, G. S.; Shit, P. K. Geospatial Technology for Multi-Hazard Risk Assessment; Springer, 2022; pp 1–18. https://doi.org/10.1007/978-3-030-75197-5_1

[17] Roy, P. P.; Abdullah, M. S.; Siddique, I. M. Machine Learning Empowered GIS for Spatial Analysis. *World J. Adv. Res. Rev.* **2024**, *22*, 1387–1397. https://doi.org/10.30574/wjarr.2024.22.1.1200

[18] Ekeanyanwu, C. V.; Obisakin, I. F.; Aduwenye, P.; Dede-Bamfo, N. Merging GIS and Machine Learning Techniques: A Review. *J. Geosci. Environ. Prot.* **2022**, *10*, 61–83. https://doi.org/10.4236/gep.2022.109004

[19] Hamdy, O.; Gaber, H.; Abdalzaher, M. S.; Elhadidy, M. Seismic Hazard Exposure Using Machine Learning and GIS. *Sustainability* **2022**, *14*, 10722. https://doi.org/10.3390/su141710722

[20] Sachdeva, S.; Kumar, B. GIS, Spatial Analysis and Remote Sensing in India: A Machine Learning Perspective; Springer, 2022; pp 29–41. https://doi.org/10.1007/978-981-16-2594-7_3

[21] Aljohani, A. Predictive Analytics and Machine Learning for Supply Chain Risk Mitigation. *Sustainability* **2023**, *15*, 15088. https://doi.org/10.3390/su152015088

[22] Attah, R. U.; Garba, B. M. P.; Gil-Ozoudeh, I.; Iwuanyanwu, O. GIS and Data Analytics for Public Sector Decision-Making. *Magna Sci. Adv. Res. Rev.* **2024**, *12*, 152–163. https://doi.org/10.30574/msarr.2024.12.2.0191

[23] Akindote, O. J.; Adegbite, A. O.; Dawodu, S. O.; Omotosho, A.; Anyanwu, A.; Maduka, C. P. Big Data Analytics and GIS in Healthcare Decision-Making. *World J. Adv. Res. Rev.* **2023**, *20*, 1293–1302. https://doi.org/10.30574/wjarr.2023.20.3.2589

[24] Wikner, A.; Pathak, J.; Hunt, B.; Girvan, M.; Arcomano, T.; Szunyogh, I.; Pomerance, A.; Ott, E. Combining Machine Learning with Knowledge-Based Modeling. *Chaos* **2020**, *30*. https://doi.org/10.1063/5.0005541

[25] Waghmare, R.; S., B. A. Geo-Spatial Data Analysis for Disaster Impact Forecasting. *Int. J. Multidiscip. Res.* **2025**, *7*. https://doi.org/10.36948/ijfmr.2025.v07i03.44274

[26] Eom, S. B. Decision Support Systems. In *Oxford Research Encyclopedia of Politics*; Oxford University Press, 2020. https://doi.org/10.1093/acrefore/9780190228637.013.1008

[27] Fang, Z.; Yue, P.; Zhang, M.; Xie, J.; Wu, D.; Jiang, L. Disaster Decision Support Using Geospatial Resources. *Int. J. Appl. Earth Obs. Geoinf.* **2023**, *117*, 103217. https://doi.org/10.1016/j.jag.2023.103217

[28] Poli, G.; Cuntò, S.; Muccio, E.; Cerreta, M. Spatial Decision Support System for Sustainability Assessment. *Land Use Policy* **2024**, *141*, 107123. https://doi.org/10.1016/j.landusepol.2024.107123

[29] Elkady, S.; Hernantes, J.; Labaka, L. Decision Support Systems for Community Resilience. *Heliyon* **2024**, *10*, e33116. https://doi.org/10.1016/j.heliyon.2024.e33116

[30] Hisham, A. B.; Yusof, N. A.; Salleh, S. H.; Abas, H. AI Applications in Policymaking. *J. Sci. Technol. Innov. Policy* **2024**, *10*, 7–15. https://doi.org/10.11113/jostip.v10n1.148

[31] Papadakis, T.; Christou, I. T.; Ipektsidis, C.; Soldatos, J.; Amicone, A. Explainable and Transparent Artificial Intelligence for Public Policymaking. *Data Policy* **2024**, *6*, e10. https://doi.org/10.1017/dap.2024.3

[32] Ramezani, M.; Takian, A.; Bakhtiari, A.; Rabiee, H. R.; Ghazanfari, S.; Mostafavi, H. The Application of Artificial Intelligence in Health Policy: A Scoping Review. *BMC Health Serv. Res.* **2023**, *23*, 1416. https://doi.org/10.1186/s12913-023-10462-2

[33] Sánchez, J. M.; Rodríguez, J. P.; Espitia, H. E. Artificial Intelligence in Agricultural Public Policy Decision-Making. *Processes* **2020**, *8*, 1374. https://doi.org/10.3390/pr8111374

[34] Lagmay, A. M. F.; Racoma, B. A.; Aracan, K. A.; Alconis-Ayco, J.; Saddi, I. L. Disseminating Near-Real-Time Hazards Information and Flood Maps in the Philippines through Web-GIS. *J. Environ. Sci.* **2017**, *59*, 13–23. https://doi.org/10.1016/j.jes.2017.03.014

[35] Tabiongan, R. C.; Tanseco, L. A.; Carcellar, C. J. B.; Chui, M. Y. S.; Cortel, J. R.; Llema, S. B. R. Project TANAW: 3D-Printed Urban Model with Geohazard Simulations. *Mindanao J. Sci. Technol.* **2025**, *22*. https://doi.org/10.61310/mjst.v22iS1.2218

[36] Scales, J. A Design Science Research Approach to Project Scheduling. *Syst. Res. Behav. Sci.* **2020**, *37*, 804–812. https://doi.org/10.1002/sres.2743

[37] Gregor, S.; Zwikael, O. Design Science Research and the Co-Creation of Project Management Knowledge. *Int. J. Proj. Manag.* **2024**, *42*, 102584. https://doi.org/10.1016/j.ijproman.2024.102584

[38] Online Learning and the IT Sector: A Systematic Literature Review Using PRISMA. *Cent. Eur. Manag. J.* **2023**. https://doi.org/10.57030/23364890.cemj.31.2.62

[39] Farhadi, H.; Najafzadeh, M. Flood Risk Mapping Using Remote Sensing and Random Forest. *Water* **2021**, *13*, 3115. https://doi.org/10.3390/w13213115

[40] Mobley, W.; Sebastian, A.; Blessing, R.; Highfield, W. E.; Stearns, L.; Brody, S. D. Continuous Flood Hazard Mapping Using Random Forest. *Nat. Hazards Earth Syst. Sci.* **2021**, *21*, 807–822. https://doi.org/10.5194/nhess-21-807-2021

[41] DeVries, B.; Huang, C.; Armston, J.; Huang, W.; Jones, J. W.; Lang, M. W. Monitoring Flood Events Using Sentinel-1 and Landsat Data. *Remote Sens. Environ.* **2020**, *240*, 111664. https://doi.org/10.1016/j.rse.2020.111664

[42] Yang, Q.; Shen, X.; Anagnostou, E. N.; Mo, C.; Eggleston, J. R.; Kettner, A. J. High-Resolution Flood Inundation Archive from Sentinel-1 SAR. *Bull. Am. Meteorol. Soc.* **2021**, *102*, E1064–E1079. https://doi.org/10.1175/BAMS-D-19-0319.1

[43] Islam, M. T.; Meng, Q. Sentinel-1 SAR for Rapid Urban Flood Mapping. *Int. J. Appl. Earth Obs. Geoinf.* **2022**, *113*, 103002. https://doi.org/10.1016/j.jag.2022.103002

[44] Deng, H.; Wu, X.; Zhang, W.; Liu, Y.; Li, W.; Li, X.; Zhou, P.; Zhuo, W. Landslide Susceptibility Mapping Using Random Forest. *Remote Sens.* **2022**, *14*, 4245. https://doi.org/10.3390/rs14174245

[45] Zhou, X.; Wen, H.; Zhang, Y.; Xu, J.; Zhang, W. Landslide Susceptibility Mapping Using Hybrid Random Forest. *Geosci. Front.* **2021**, *12*, 101211. https://doi.org/10.1016/j.gsf.2021.101211

[46] Taalab, K.; Cheng, T.; Zhang, Y. Landslide Susceptibility Mapping Using Random Forest. *Big Earth Data* **2018**, *2*, 159–178. https://doi.org/10.1080/20964471.2018.1472392

[47] Shafapour Tehrany, M.; Kumar, L.; Shabani, F. GIS-Based Ensemble Technique for Flood Susceptibility Mapping. *PeerJ* **2019**, *7*, e7653. https://doi.org/10.7717/peerj.7653

[48] Althuwaynee, O. F.; Pradhan, B.; Park, H.-J.; Lee, J. H. Landslide Susceptibility Mapping Using Statistical Models. *Catena* **2014**, *114*, 21–36. https://doi.org/10.1016/j.catena.2013.10.011

[49] Luu, C.; Pham, B. T.; Phong, T. V.; Costache, R.; Nguyen, H. D.; Amiri, M.; Bui, Q. D.; Nguyen, L. T.; Le, H. V.; Prakash, I.; Trinh, P. T. GIS-Based Models for Flood Susceptibility Prediction. *J. Hydrol.* **2021**, *599*, 126500. https://doi.org/10.1016/j.jhydrol.2021.126500

[50] Li, M.; Wang, H.; Chen, J.; Zheng, K. Landslide Susceptibility Using Random Forest and Multi-Source Data. *Ecol. Indic.* **2024**, *158*, 111600. https://doi.org/10.1016/j.ecolind.2024.111600

[51] Zhang, W.; He, Y.; Wang, L.; Liu, S.; Meng, X. Landslide Susceptibility Mapping Using Machine Learning. *Geol. J.* **2023**, *58*, 2372–2387. https://doi.org/10.1002/gj.4683

[52] Toma, A.; Șandric, I.; Mihai, B.-A. Flood Mapping from Sentinel-1 Imagery. *Eur. J. Remote Sens.* **2024**, *57*. https://doi.org/10.1080/22797254.2024.2414004

[53] Albertini, C.; Gioia, A.; Iacobellis, V.; Petropoulos, G. P.; Manfreda, S. Random Forest Classification in Flood Mapping. *Remote Sens. Appl.* **2024**, *35*, 101239. https://doi.org/10.1016/j.rsase.2024.101239

[54] Saber, M.; Boulmaiz, T.; Guermoui, M.; Abdrabo, K. I.; Kantoush, S. A.; Sumi, T.; Boutaghane, H.; Hori, T.; Binh, D. V.; Nguyen, B. Q.; Bui, T. T. P.; Vo, N. D.; Habib, E.; Mabrouk, E. Flood Risk Assessment Using Ensemble Learning. *Geomatics Nat. Hazards Risk* **2023**, *14*. https://doi.org/10.1080/19475705.2023.2203798

[55] Schoppa, L.; Disse, M.; Bachmair, S. Evaluating Random Forest for Flood Discharge Simulation. *J. Hydrol.* **2020**, *590*, 125531. https://doi.org/10.1016/j.jhydrol.2020.125531

[56] Amarasinghe, K.; Rodolfa, K. T.; Lamba, H.; Ghani, R. Explainable Machine Learning for Public Policy. *Data Policy* **2023**, *5*, e5. https://doi.org/10.1017/dap.2023.2

[57] Meneses, B.; Varajão, J. Framework of Information Systems Development Concepts. *Bus. Syst. Res. J.* **2022**, *13*, 84–103. https://doi.org/10.2478/bsrj-2022-0006

[58] Bahar, I. A. A.; Nasirin, S.; Ismail, H.; Nistah, N. M.; Amboala, T.; Seman, E. A. A.; Lada, S. Validating Public Information Systems Framework. In *Advances in Information Systems*; Springer, 2021; pp 319–328. https://doi.org/10.1007/978-3-030-72660-7_31

[59] Gao, Z. Development of Web Information Systems in Enterprise Management. *J. Inf. Syst. Eng. Manag.* **2023**, *8*, 22733. https://doi.org/10.55267/iadt.07.13841

[60] P&P Software. *Development Process*; OBS Framework. https://www.pnp-software.com/Obs Framework/doc/indexDevelopmentProcess.html (accessed Sept 21, 2025).

[61] Ji, M.; Genchev, G. Z.; Huang, H.; Xu, T.; Lu, H.; Yu, G. Evaluation Framework for Successful Artificial Intelligence–Enabled Clinical Decision Support Systems: Mixed Methods Study. *J. Med. Internet Res.* **2021**, *23*(6), e25929. https://doi.org/10.2196/25929

[62] Neville, K.; O'Riordan, S.; Pope, A.; O'Lionaird, M. Evaluating an Emergency Management Decision Support System with Practitioner-Driven Scenarios: Action Design Research. *ICIS Proc.* **2018**.

[63] Twomlow, A.; Grainger, S.; Cieslik, K.; Paul, J. D.; Buytaert, W. A User-Centred Design Framework for Disaster Risk Visualisation. *Int. J. Disaster Risk Reduct.* **2022**, *77*, 103067. https://doi.org/10.1016/j.ijdrr.2022.103067

[64] Khan, S. M.; Shafi, I.; Butt, W. H.; Diez, I. de la T.; Flores, M. A. L.; Galán, J. C.; Ashraf, I. A. A Systematic Review of Disaster Management Systems: Approaches, Challenges, and Future Directions. *Land* **2023**, *12*(8), 1514. https://doi.org/10.3390/land12081514

ASEAN
Journal of Scientific and Technological Reports
Online ISSN:2773-8752

Research article

Design and Development of a Smart Automated System for Poultry Farm Management Using Internet of Things (IOT)

Jaiinder Preet Singh [1], Piyush Gulati[1*], Vikas Sharma[2], Hemant Kumar[1], Prakash Mahto[1], and Ashish Choudhary[1]

[1] School of Mechanical Engineering, Lovely Professional University, Phagwara, Punjab, India
[2] University Center of Research and Development (UCRD), Chandigarh University, Punjab, India
* Correspondence: piyush.14775@lpu.co.in

Citation:
Singh, P.J.; Gulati, P.; Sharma, V.; Kumar, H.; Mahto, P.; Choudhary, A. Design and development of a smart automated system for poultry farm management using internet on things (IOT). *ASEAN J. Sci. Tech. Report.* **2026**, *29*(4), e261801. https://doi.org/10.55164/ajstr.v29i4.261801.

Article history:
Received: July 30, 2025
Revised: December, 2025
Accepted: February 7, 2026
Available online: March 25, 2026

Publisher's Note:
This article is published and distributed under the terms of the Thaksin University.

Abstract: Worldwide, poultry farming is one of the fastest-growing sectors and is a key source of livelihood for thousands of small and medium-sized farmers in India, but maintaining optimal environmental conditions - temperature, humidity, and air quality - is critical and also difficult for the health and mortality of chicks. This research work leads to the design and development of a smart, automated poultry farm management system using the Internet of Things (IoT). The system consists of two major components: a hardware module built around a Raspberry Pi and a user-friendly mobile application. The hardware module includes environmental sensors: DHT22 for temperature and humidity, MQ137 for ammonia, and MQ135 for CO_2. The solution tracks environmental conditions and transmits all information in real time to the mobile app via Firebase Cloud. The mobile app allows farmers to remotely control all environmental parameters. It includes features that recommend rationing feed for future chicks based on age, record mortality rates, batch dates, breed, feed log, and sales records, and that provide access to all information via graphical apps for better visualization. It was observed to reduce chick mortality from 5% to 1.66%, which was a savings of approximately USD 34 (for every batch of 5000 chicks) and or a projected annual benefit of around USD 210. This solution has allowed farmers to be more productive and profitable while also reducing labour and stress during adverse weather conditions. It is worth noting that this success demonstrates the potential to transform traditional poultry farming into a smarter, more sustainable approach through the use of IoT.

Keywords: IoT; poultry farm; smart farming; automation; livestock monitoring

1. Introduction

Poultry farming is an important aspect of global agriculture. The wide variety of chicken products (eggs and meat) provides a good source of protein for the population. According to the Food and Agriculture Organization (FAO), the world produced 137 million tonnes of poultry meat in 2021, and it continues to increase due to population growth and changing diets [1]. India's meat production in FY 2023-24 was 10.25 million tonnes, which was up 4.95 percent from the previous year. Egg production was 142.77 billion, up 3.18 percent from the previous year. The meat-producing states were West Bengal (12.62%), Uttar Pradesh (12.29%), and Maharashtra (11.28%), and the egg-producing states were Andhra Pradesh (17.85%), Tamil

Nadu (15.64%), and Telangana (12.88%) [2]. In India, poultry farming contributes about 3% of the total agricultural GDP and supports millions of small- and medium-scale farmers [3].

Traditional poultry farming relies heavily on manual monitoring of farm conditions. Much monitoring is very rudimentary, produces insufficient data, and is inefficient and error-prone. Farmers find it hard to cope with changes in potential temperature and humidity caused by weather fluctuations. The farmers find it difficult to control harmful gases, ammonia (NH_3) and carbon dioxide (CO_2), when they accumulate in farms where airflow is restricted, leading to respiratory problems for the birds [4]. Another issue for farmers is feed management, which generally involves an inappropriate or unviable feed schedule or insufficient feed provision, which may affect poultry weight gains and feed conversion ratios, negatively impacting optimal growth rates and, ultimately, feed conversion ratios [5], resulting in economic losses. Countries with advanced poultry industries have been able to mechanize systems to manage these problems much more easily. However, the price implications and the scope of operations have prevented smaller and medium-scale farmers in India from benefiting from the technology. To address these hurdles, IoT-based smart farming offers a practical, economical, and easy-to-use alternative. These automated systems use sensor and actuator technology to monitor and control key environmental parameters continuously. Using smart control and Machine Learning, the systems can manually or automatically ventilate, cool, and heat to maintain optimal conditions for poultry health, growth, etc. Additionally, the automated system can use analytical processes to manage feeds, producing highly specific recommendations based on chick age and number.

Three theme groupings can be used to broadly categorize current research on smart poultry farming, viz., environmental monitoring systems, feeding and farm operations management, and AI-based analytics systems. To enhance chicken welfare, environmental monitoring and control systems focus on detecting temperature, humidity, and hazardous gases, as well as automating ventilation and climate management. Research by Kristensen and Wathes [1], Lashari et al. [5], Phiri et al. [4], Liu et al. [7], Esnaola-Gonzalez et al. [13], Kale et al. [19], and Sasirekha et al. [21] shows how IoT-enabled sensing and cloud-based platforms can effectively maintain ideal environmental conditions inside poultry houses. Feed optimization, bird tracking, mortality monitoring, and behavioral evaluation are the main focuses of research on feed, behavior monitoring, and farm operations management. Research by Broderick et al. [2], Dorninger et al. [3], Cruz et al. [8], Sharma and Aggarwal [23], Neethirajan [24], and Li [22] emphasizes how computer vision, tracking systems, and automated feeding procedures may increase productivity and decrease manual intervention. Predictive modeling, anomaly detection, and intelligent decision support for poultry management are the main focuses of AI and machine learning-based analytics. The use of deep learning, AIoT, and ML approaches for disease detection, behavior analysis, and predictive health diagnostics is demonstrated in studies such as Ahmed and Salih [9], Ehsan and Mohtavipour [10], Singh [11], Gandhi [16], and Rajendran et al. [24].

Despite these developments, most current systems focus only on feeding management, environmental control, or intelligent analytics. For small- and medium-sized poultry farms in developing nations like India, there remains a glaring research gap for an integrated, affordable, and field-validated smart poultry management system that combines real-time environmental monitoring, feed recommendations, mortality tracking, and farm record management. To overcome these restrictions, the current study aims to use IoT and cloud-connected mobile applications to design and build a smart, automated poultry farm management system that offers Indian poultry farmers a comprehensive, practical, and reasonably priced solution. The proposed Intelligent Automated Poultry Management System (IAPMS) stands out for accessibility, integration, cost-effectiveness, and field validation, especially for small and medium-sized farms in developing nations, despite several recent studies investigating IoT-based poultry monitoring. Through a mobile application, sensor data, ML-based recommendations, and actuator reactions work together in a closed-loop control architecture. It also goes beyond disease detection by providing a comprehensive farm management platform that combines cloud-based data persistence, productivity analytics, and environmental control. Together, these characteristics improve the system's usability, efficacy, and suitability for practical implementation in chicken farming settings with limited resources.

2. Materials and Methods

2.1 Overall System Architecture

2.1.1. Block diagram of the system

The proposed remote poultry management system is a low-cost, intelligent solution that automates and simplifies key farm operations. It uses a modular architecture, is based on input sensors, Raspberry Pi, relay boards, actuators, cloud connection, and a mobile application to provide easy control of poultry operations. The scalable Automation approach uses input sensors to monitor environmental conditions, including temperature, humidity, and ammonia/gases. The software enables real-time, automated responses using a built-in machine learning model to determine when action is needed and what action to take- if any. The system features dual-mode operation, allowing actuator control (fans, lights, heaters, etc) to be either manually or automatically controlled. The mobile app is intuitive and allows farmers to access real-time control of their operations even when they are away from the farm. Mobile app features also provide real-time camera access to the farm, enabling farmers to visually check on the flock without physically being there. Figure 1 shows the system block diagram. The app includes a sophisticated feed advisory feature that calculates the optimal feed requirements based on the number and age of chicks, helping promote healthy chick movement. The Mobile app enables disease prevention by including vaccination reminders tailored to target species/breeds and proper poultry management to ensure they remain productive. All data from the farm, including environmental statistics, sales, mortality, etc., is stored in the cloud and can be easily organized into graphical data in the mobile app for user functionality.

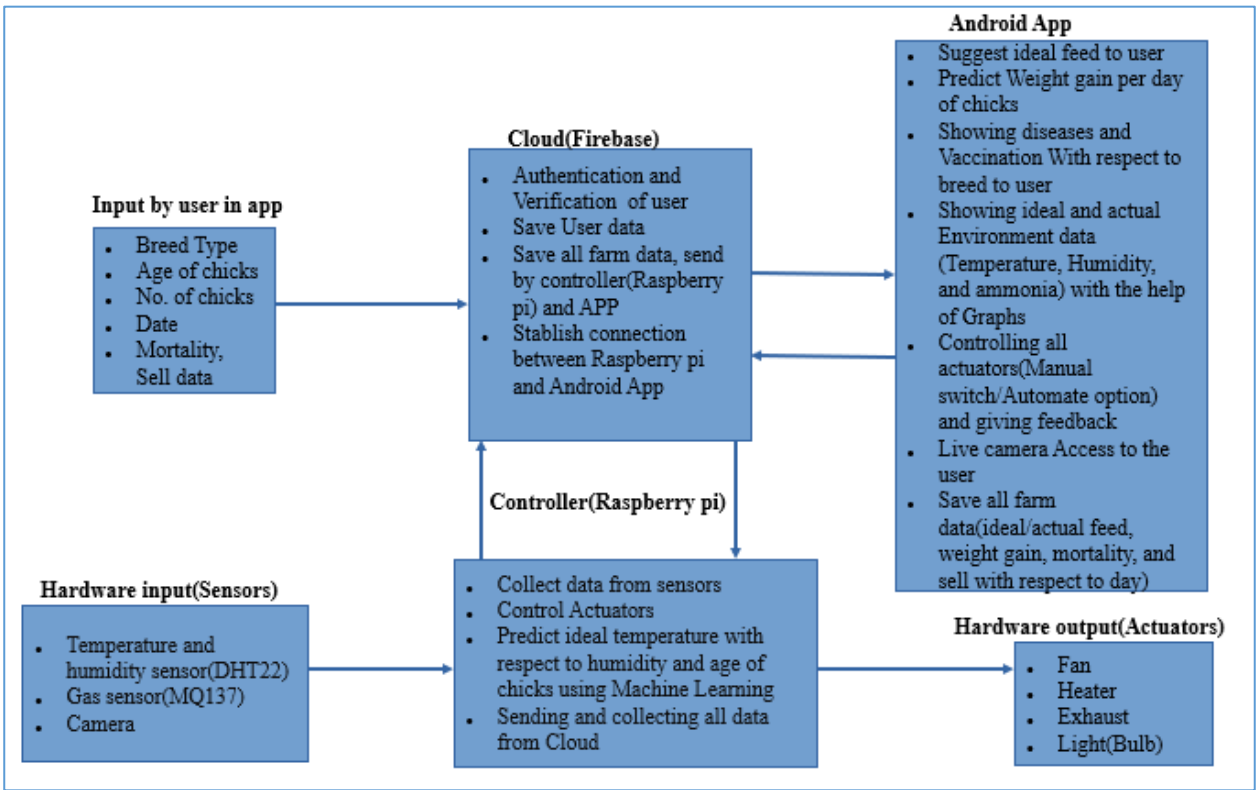


Figure 1. Block Diagram of the System

2.1.2 Brief explanation of the working mechanism

An experimental setup was created at a Jassal poultry farm to test and evaluate the performance and reliability of the IoT-based poultry management system. The system hardware consisted of a Raspberry Pi 4 Model B as the primary processing unit, with integrated DHT22 and MQ137 sensors to measure environmental temperature, humidity, and ammonia gas levels, respectively. An ADS1115 analog-to-digital converter was

used to read and convert the MQ137 sensor's analog output to a digital value. To control the farm's actuators (fans, heaters, exhaust systems, and lights), a 4-channel relay module was used to actuate the farm in accordance with sensor data or user input. A 5MP Raspberry Pi camera module was mounted inside the farm to provide video streaming for surveillance and remote monitoring. Every data and control function was also connected to a custom mobile app developed in Android Studio to run on an Android mobile device. The mobile app communicates with the Raspberry Pi through Firebase Cloud. The Firebase platform was used to provide authentication, sync the real-time database, and provide long-term data storage. Figure 2 represents the circuit diagram for the hardware used in the present research work.

2.2 Hardware Components

The optimal temperature for a chicken house is predicted using a supervised regression-based machine learning algorithm. Poultry management recommendations and past farm data are used to train the model offline. Relative humidity, current temperature, and chick age (days) are examples of input features. The appropriate temperature for optimal chick growth and comfort is the aim variable. The trained model provides real-time inference and decision support. Figure 2 and Figure 3 represent the circuit diagram for the poultry farm control and the various hardware components used, respectively.

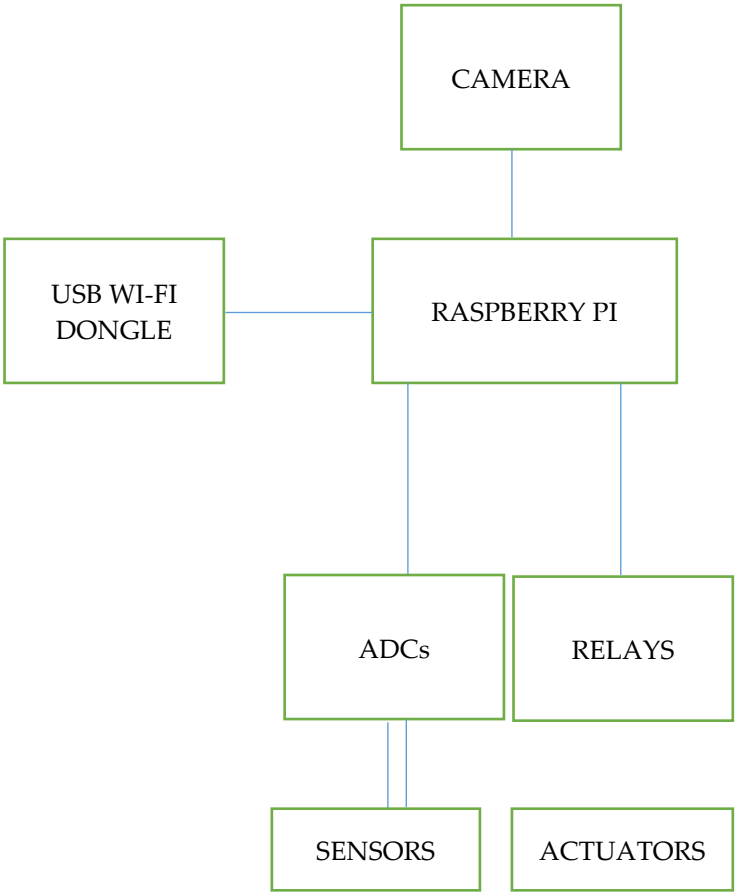


Figure 2. Circuit Diagram for poultry farm control

The list below contains the hardware components and modules used in the proposed solution.

a) *Raspberry Pi:*

At the heart of the system is a Raspberry Pi 4 Model B (2GB), selected for its high performance, 1.5 GHz quad-core ARM Cortex-A72 processor, and 2 GB LPDDR4 RAM. The single-board computer is affordable while capable of processing and streaming real-time data and video, and managing data. The Pi features dual-band Wi-Fi, Bluetooth 5.0, and Gigabit Ethernet connections for reliability. USB 3.0 ports, a 40-pin GPIO

header, a dedicated camera port 27, and a dedicated display port place the model in a range, making it a strong candidate for smart/bind farming solutions. Cloud platforms such as Firebase and Google Cloud extend the ability to achieve higher-level, scalable automation via an infinitely connected computer system, creating an effective, practical solution for small- to medium-sized poultry farms.

b) *DHT22 Sensor:*

The DHT22 sensor was chosen for temperature and humidity monitoring due to its accuracy and reliability. It has a temperature accuracy of ±0.5°C and humidity accuracy of ±2–5% RH. It operates at temperatures between -40°C and +80°C and humidity levels of 0 to 100% RH. Its sampling rate is 0.5 Hz (1 every 2 seconds) and is low power (< 2.5 mA), making it very useful for continuous monitoring of poultry environment factors. Figure 2a and 2 b show the complete hardware system.

c) *MQ-137 Sensor and ADS1115 ADC:*

The MQ-137 sensor was used for ammonia (NH_3) gas detection, a crucial factor in poultry health. This sensor operates at temperatures from -10°C to 50°C and a humidity range of 20% to 90% RH. It outputs an analog (sensor) signal. Because the Raspberry Pi does not have an analog input, an ADS1115 16-bit ADC was used to convert the sensor's output to a digital signal with minimal error.

d) *Relay Module:*

The relay module allows the control of electrical items, such as fans, lights, heaters, and exhaust systems, among others. All of these items can be automatically controlled to switch on or off based on sensors, or manually via the mobile application, to support improved climate control.

e) *Camera Module:*

The Raspberry Pi Camera Module V1 has a 5MP sensor for real-time video monitoring. This camera connects directly to the Raspberry Pi and provides remote visual monitoring of the user's poultry and farming practices.

f) *Wi-Fi Dongle:*

A USB SIM-based 4G LTE dongle was used to provide data connectivity for real-time data transmission, remote monitoring, and cloud capture and transmission.

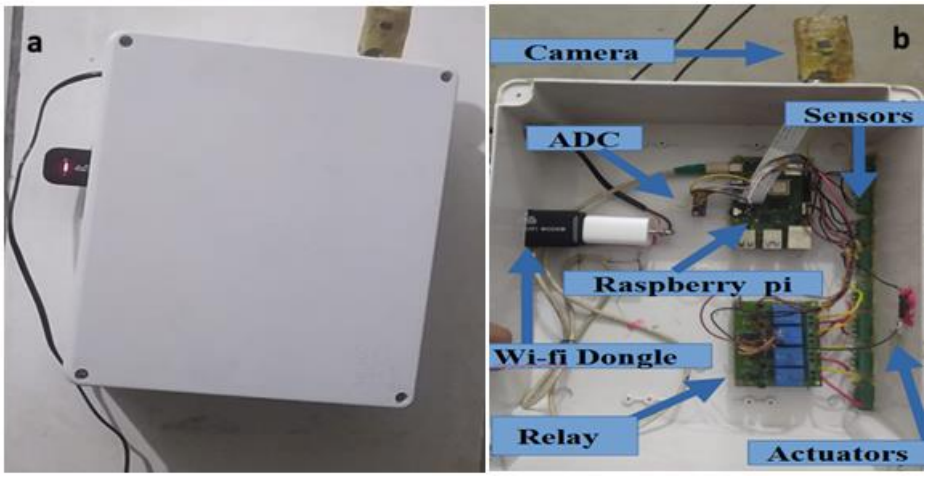


Figure 3. a) Hardware device (outer box) used in the present research, b) Various hardware components used

2.3 Software Design

2.3.1 Android Application and Cloud-Based Integration:

A customized Android application was developed using Android Studio, allowing users to register, link their farms via a unique hardware identifier, enter batch details (Breed, Number of chicks, Start date, and feed type), use the application to display and monitor data, control actual equipment, including regulated alerts; and then maintain all crucial farm records in the cloud. The poultry farm is monitored and controlled using a custom Android mobile application developed in Android Studio.

2.3.2 App User Interface (UI):

The application interface is divided into five sections:

a) The application will indicate ideal feed intake, expected daily gain, and total weight, and allow the user to report actual feed intake, mortality, and sales (number, weight, and date).
b) Alerts the user to disease risk and vaccinations based on breed and age.
c) Will report environmental conditions (temperature, humidity, ammonia, etc.) in actual and ideal values with machine learning predictions.
d) Will allow the user to control actuators (manual or automatic), i.e., fans, lights, exhausts, and heaters
e) Will allow the user to view live farm video through the camera module, and all farm data is stored in the cloud.

2.3.3 Cloud Integration:

The system uses Firebase Cloud Messaging as a middleman between the mobile application and hardware.

The Firebase service used is:

- Authentication for secure user login and account management.
- Firestore Database to store all farm data, including poultry farm data.
- Firebase Realtime Database- to manage live update data from the mobile application and device.

Figure 4 shows the flow of data through the hardware interface and the output on the Android mobile app. Figure 5a, b shows the user interface of the Android application, along with the camera-enabled system, which has a provision to enter data and obtain outputs in the form of temperature, humidity, and ammonia level.

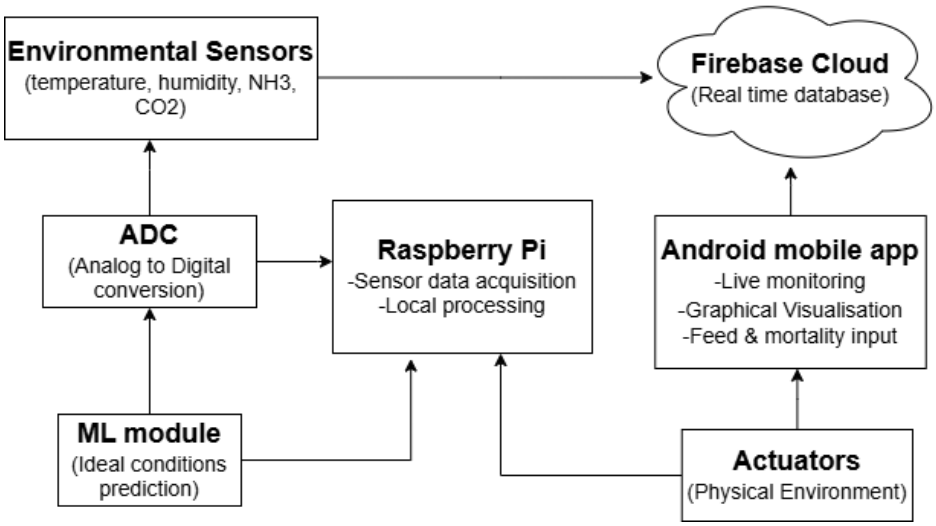


Figure 4. Flowchart representing the data flow decision process of the installed hardware and software

The application's primary operational dashboard, shown in Figure 5(a), allows users to view and enter crucial farm parameters for batch management and production performance. Batch details, including batch number, bird age (in days), total number of chicks, cumulative feed consumption, daily and total weight gain, mortality count, and sales data, are displayed on the interface. Daily feed intake, mortality records, and sales data can be manually entered and stored in a cloud database for time-stamped recordkeeping and performance assessment. Along with ideal reference values generated by the Machine Learning (ML) model, the dashboard also displays current environmental characteristics, including temperature, humidity, and ammonia concentration. The camera-enabled monitoring mode of the application, which displays live video streaming from the Raspberry Pi camera module, is shown in Figure 5(b). Without being physically present at the farm, this function enables remote visual observation of bird behavior, stocking density, feeding activity,

and overall farm hygiene. To ensure contextual awareness of agricultural circumstances, environmental elements are updated in tandem with the live video feed.

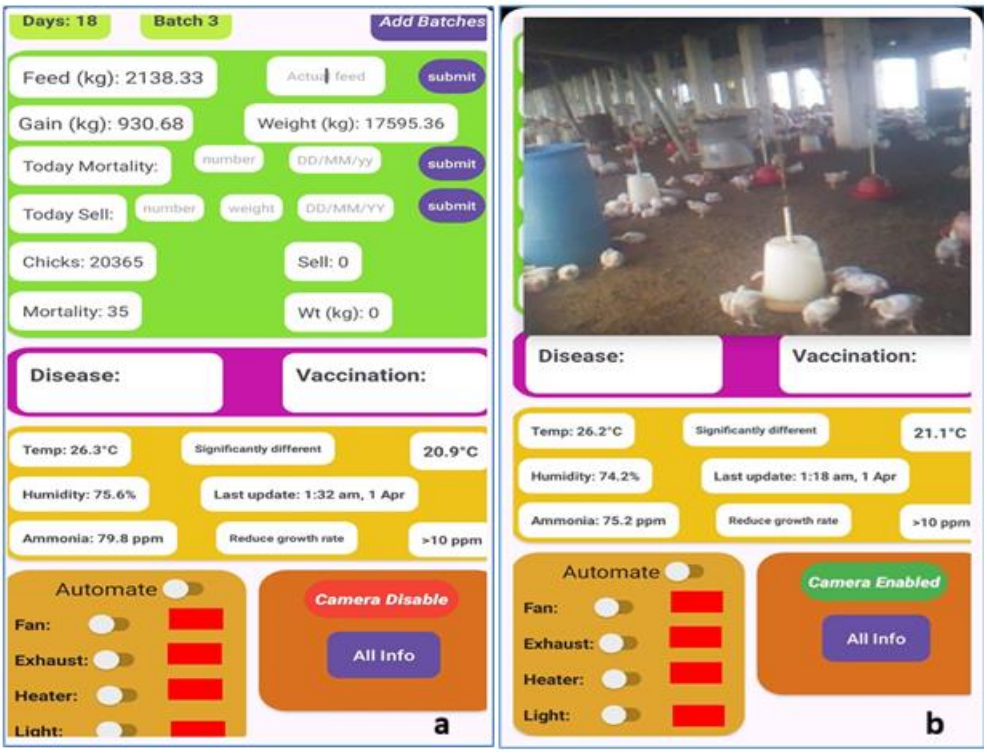


Figure 5. a) User interface of the Android App b) User interface when the camera is enabled

2.3.4 Data Collection and Processing Method:

The environmental data, temperature, humidity, ammonia levels, and ideal temperature (according to humidity and age of chicks) are collected by the Raspberry Pi and sent to Firebase Firestore. The data is stored in an array, with each data record time-stamped for accurate data tracking and time-lapse analysis. When collecting environmental data, the IoT system also collects user-input data on actual feed intake, mortality counts, mortality dates, number of birds sold, selling weights, and selling dates. This user-input data is also stored in Firebase for future analysis and evaluation of farm performance.

2.3.5 Processing Method:

When the user opens the mobile application, it retrieves all relevant environmental and user-input data from Firebase and displays it in a user-friendly format. It will also retrieve configuration and control data from Firebase and operate appropriately when the hardware is powered up.

2.4 Power Management

Power management must be considered for any automated IoT system, especially on poor and semi-urban poultry farms, where achieving stable power is potentially difficult. Accordingly, the proposed smart poultry management system was devised with energy-efficient and power-management designs to facilitate continuous monitoring and control.

The system power supply was powered from 7-24V using a regulated AC-to-DC adapter that provided 5V to the Raspberry Pi, which was also the power control controller for the overall system. The main controller (Raspberry Pi) controls all sensors and actuators via GPIO pins. However, to protect against failure points and prevent potential overload of the GPIO pins and component failure during use, there are also voltage-regulated designs (which automatically drop as the supply voltage increases) as well as protection designs (diodes) on various sensor/actuator circuits. For the actuators/devices that require higher-voltage (high-side) operation (heating elements and ventilation fans, etc.), the operations are relatively controlled with

the established relay schematic on a power supply of their own, with regulated power that continuously provides medium power. Table 1 summarizes the equipment used and the respective component costs.

Table 1. Equipment used for the poultry monitoring system with cost

Category	Component/Module	Purpose	Approx Unit cost (USD)
Hardware	Raspberry Pi 4 Model B (2GB RAM)	CPU for the sensor data acquisition, cloud communication, and actuator control	42
	DHT22 Sensor	Temperature and humidity monitoring	4
	MQ-137 Gas sensor	Ammonia gas detection	14
	ADS1115 (16-bit ADC)	Analog-to-digital conversion for gas sensor output	7
	Relay Module (4–8 Channel)	Switching control	5
	Raspberry Pi Camera Module V1 (5 MP)	Live video monitoring	14
	4G LTE USB Wi-Fi Dongle	Internet connection	12
	Enclosure, wiring, connectors	Connecting wires	7
Power supply	AC–DC Regulated Adapter	Power supply for system operations	6

With a total deployment cost of about USD 110–120, the suggested system is intended to be an affordable yet scalable smart chicken farm management solution. The suggested approach offers a far more economical option without sacrificing crucial monitoring and control features compared to commercial smart poultry automation systems in industrialized nations, which frequently cost between $500 and $1000.

3. Results and Discussion

The intelligent automated poultry management system underwent extensive field tests to assess its performance, accuracy, reliability, and overall impact on poultry production management. The evaluation was comprehensive and included sections on sensor accuracy, system response, program usability, financial benefits, and limitations encountered during the deployment of the intelligent automated poultry management system (IAPMS).

3.1 Sensor accuracy and system response

The hardware system, constructed by interfacing a Raspberry Pi with a DHT22 (temperature and humidity), MQ137 (ammonia), MQ135 (CO_2), and 1 feed level sensor, operated mostly as expected in our test scenarios. The DHT22 displayed consistent temperatures within ±0.5°C and humidity within ±2% RH, as measured by reference digital instruments. The MQ137 and MQ135 were capable of detecting the changes in ammonia and carbon dioxide, but had to be calibrated fairly often, especially in high-dust environments encountered in poultry houses.

The data intercepted from the sensor was sent to the Raspberry Pi and uploaded to Firebase Cloud. The system had low latency, with approximately 1.7 seconds elapsed from the time the data was captured to the time it was relayed. The actuators responded quickly when environmental conditions changed, in most

cases initiating responses (fan, heater, feeder) with a nominal time of 2-3 seconds from the input command from the mobile application or from environmental thresholds.

3.2 Real-time monitoring and user interface

The mobile application was developed, integrating Firebase backend capabilities, and was important for the implementation of real-time monitoring and management of poultry production. The app dashboard, accessed by an Administrator or Manager, displayed real-time environmental conditions, fed recommendations based on chick age, and presented historical data in a time-series charting and tabular format. Screenshots taken during deployment showed a clean, user-friendly interface with color-coded alerts, mortality records by batch, and graphs of ammonia and CO_2 levels over time. The user could turn controls on and off manually or let the system run solely on sensor inputs.

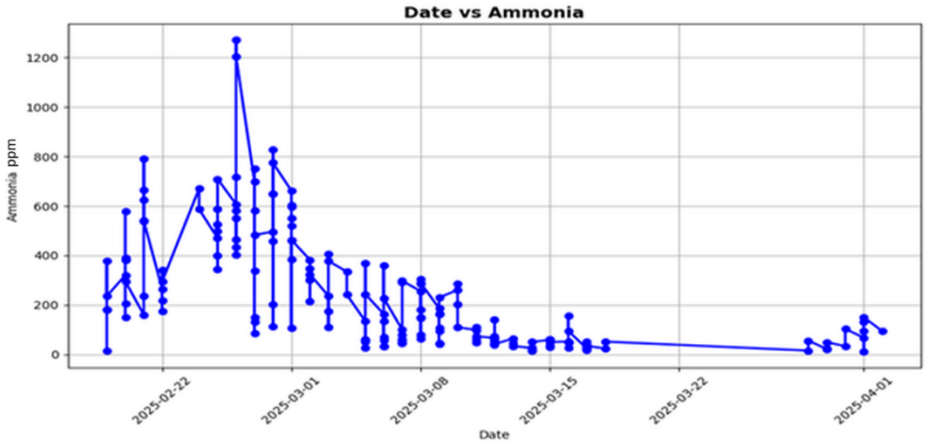


Figure 6. Graphical Analysis of Ammonia Vs Time

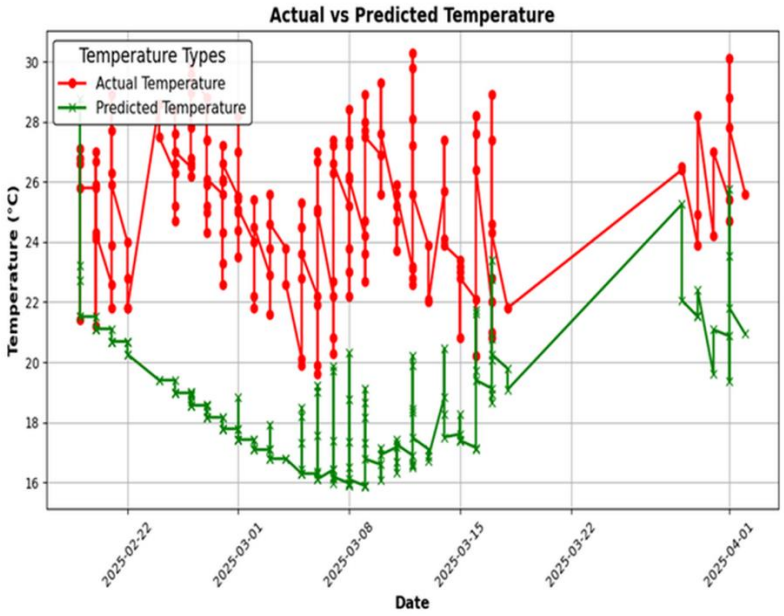


Figure 7. Graphical Analysis of Actual and Predicted Temperature

The graph in Figure 6 above depicts fluctuations in ammonia concentration over time while the system was installed at Jassal Poultry Farm. At first, ammonia concentrations were highly variable, peaking at 1200 ppm, which is detrimental to poultry health and often results in higher mortality and slower growth. Implementing the smart automated monitoring system, however, clearly demonstrates a reduction in ammonia levels throughout the period of activity, particularly after the early part of March. By the end of the period of reference (April 1st, 2025), ammonia levels would remain stable at less than 50 ppm, which is an ideal concentration for a poultry environment. This strongly illustrates how our systems and processes would optimize the birds' health in the study, as the farmers were able to take action quickly based on real-time alerts and remote controls via the mobile application. Not only were mortality rates significantly reduced, but flock performance also improved. A combination of poor ventilation techniques, poultry litter buildup, and a lack of ongoing environmental feedback before system installation can be blamed for the initially high and erratic ammonia concentrations seen during the early stages of deployment (Figure 6). After installing the intelligent automated poultry management system (IAPMS), prompt activation of ventilation systems and exhaust fans was enabled by continuous monitoring and real-time notifications. Ammonia levels consequently steadily dropped and stabilized.

Figure 7 further demonstrates that the actual temperature readings showed variability. At the same time, the system's machine learning algorithm provided accurate ideal temperatures from chick age and humidity levels, and while we could notice that the values were not at ideal levels initially, through time, the predicted values aligned more steadily with the real conditions provided to establish the conditions for the farmers to maintain the environment. This intelligent process predicted conditions to make adjustments, allowing birds to adapt and reducing discomfort to optimize overall performance. As members of the poultry technologies roast of an ML system, farmers could get real-time, permanent data to make informed decisions while using the mobile application, in support of environmental issues and farm efficiency. A supervised regression-based machine learning model trained offline using standard poultry management guidelines and historical farm data produced the projected temperature values shown in Figure 7. The model's target output is the optimal temperature, and its input features include chick age and relative humidity. The Raspberry Pi was used to implement the model for real-time inference and decision assistance. Due to pre-existing environmental conditions and delayed correction activities, such as inadequate insulation, delayed ventilation response, and legacy agricultural practices, the measured (actual) temperatures during the initial deployment period differed from the projected optimum temperatures. The actual temperature values steadily aligned with the anticipated optimal range as the system gradually adjusted actuator responses based on ML guidance and real-time input.

3.3 Effectiveness and Economic Value

On the performance side, the system maintained over 97% uptime during a 30-day continuous test period at Jassal Poultry Farm in Punjab. The system had negligible latency, and the end-user was always aware of and in control of it in real time. As illustrated by the data in Figure 8, the application of the smart poultry farm device led to a substantial decrease in chick mortality. In fact, during the first use of the device, 250 chicks were lost (5.0%). Following the use of the smart poultry farm device, mortality would not exceed 83 chicks (1.66%). This reduction in mortality demonstrates the application of the device in supporting better living conditions for the chick growth stage of the overall poultry system, particularly through better management of ammonia and temperature. Because poultry is a more delicate animal, it has better living conditions, so it will survive and thrive. Figure 9 shows the actual daily feed given to the chicks compared to the ideal quantities suggested by the system. The actual feed closely mirrored or surpassed the ideal feed early on; now, starting on day 20, the actual quantity of feed is less than the ideal level. The system uses machine learning to suggest how much feed to provide per day for the chicks, based on their age and environmental conditions. This helps ensure that chicks do not get under- or overfed, so they do not achieve optimal growth or flock health.

3.4 Aspects of Improving Poultry Farm Efficiency

The implementation of the smart poultry farm management device improved efficiency and reduced lost opportunities for poultry farmers. Farmers using conventional methods were often limited by a chick

mortality rate of about 4-6%, primarily due to inadequate control of temperature and humidity and environmental factors. The introduction of the smart system reduced the mortality rate to 1.66%. Out of 5000 chicks, there were 83 deaths, compared with 250 in the prior fallow period.

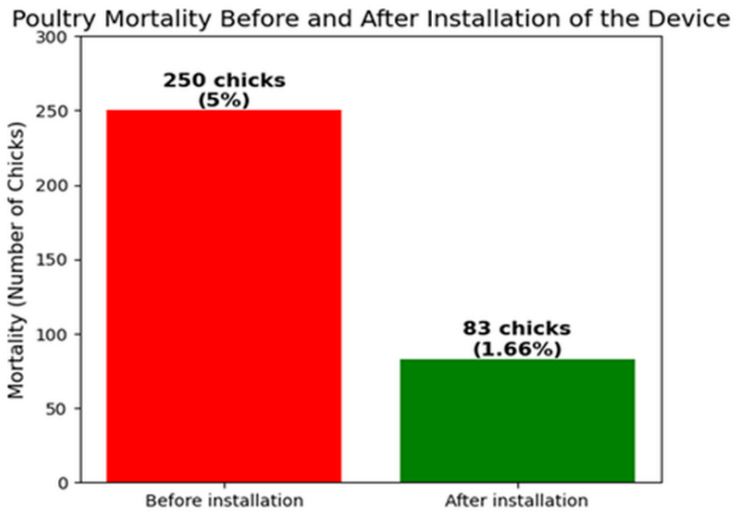


Figure 8. Mortality before and after the installation of the device on the farm

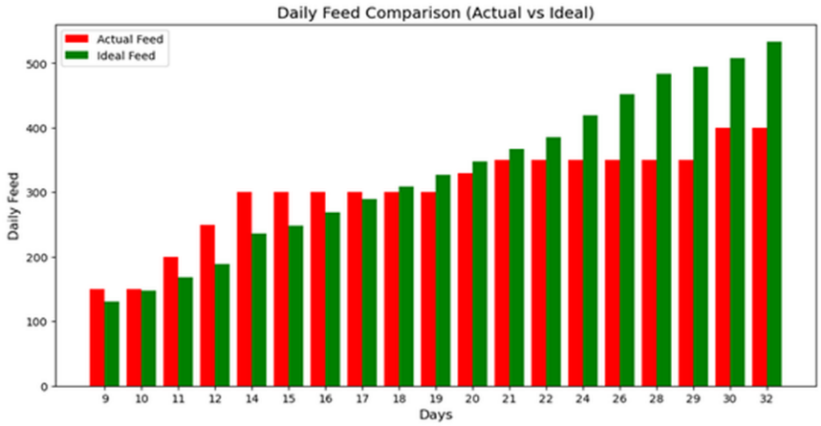


Figure 9. Ideal and Actual feed

The technique greatly enhanced growth performance and feed consumption efficiency, while reducing mortality. Growth performance was uneven before installation due to erratic feeding schedules and shifting environmental conditions. Following implementation, Figure 6 shows that both underfeeding and feed waste were reduced, with actual feed intake nearly matching the ML-recommended ideal feed curve.

Farmers who use conventional agricultural methods must pay USD 55.8 per week for the lodging of 250 chicks. He is saving USD 37.2 per batch after purchasing the equipment, but he is losing USD 18.5 per batch (83 chicks at USD 0.22 each). Farming six batches for USD 600 a year results in a yearly savings of USD 223.7. Additionally, the device eliminates labor by automating manual monitoring, reducing costs without compromising efficiency. The system's economic advantages, which immediately produced an outstanding return on investment (ROI) in year one, far exceed those of the system.

4. Conclusions

According to the graphical analysis and observed findings, temperature stability, in conjunction with ammonia control, had a major impact on lowering the mortality rate. As seen in Figure 6, ammonia

concentrations initially reached dangerously high levels (>1000 ppm), known to cause immunosuppression, respiratory stress, and increased chick mortality. After the intelligent automated poultry management system was installed, ammonia levels were lowered to less than 50 parts per million, thanks to real-time detection and closed-loop control that enabled prompt ventilation and exhaust activation. The following are the conclusions drawn from the research work:

- An automated IoT-based poultry farm management system has been successfully developed using low-cost components, including a Raspberry Pi and multiple environmental sensors (DHT22, MQ137, and MQ135).
- The system provided real-time monitoring of fundamental environmental parameters: temperature, humidity, ammonia, and CO_2 concentration, providing better overall environmental control within the poultry houses.
- The mobile application supported farmers with an easy-to-access live data stream, graphical displays, and reporting of environmental parameters, feed recommendations, mortality listings/historical mortality, and batch data.
- Implementing the system in the field greatly improved operational efficiency and reduced base mortality from 5% to 1.66%, leading to an annual total cost benefit of over USD 210 for small-scale poultry farms.
- It also provided very reliable data, with greater than 97% uptime, and reduced latency between the sensors and applications (including 2 seconds).
- The smart system reduced labour requirements compared to manual methods, which typically required the farmer to visit the poultry multiple times a day to monitor the birds, and enabled the farmer to start deriving conclusions from the data and data-derived insights.
- The hardware and software were designed to be useful, scalable, and flexible to a range of farm sizes and local conditions.
- The design of this system will support redevelopment with enhancements (e.g., solar power integration, offline caching, and the introduction of AI tools for predictive analytics) and address poultry health before issues arise.

5. Acknowledgement

The authors would like to thank Jassal Poultry Farm, Phagwara, Punjab, India, for providing the farm premises for all experimentation.

Author Contributions:

a. Conceptualization: Jaiinder Preet Singh, Piyush Gulati
b. Methodology: Jaiinder Preet Singh, Piyush Gulati, Vikas Sharma
c. Hardware: Hemant Kumar, Prakash Mahto, Ashish Choudhary
d. Software: Hemant Kumar, Prakash Mahto, Ashish Choudhary
e. Investigation: Jaiinder Preet Singh, Hemant Kumar, Prakash Mahto, Ashish Choudhary
f. Data Curation: Hemant Kumar, Prakash Mahto, Ashish Choudhary
g. Writing-Original draft preparation: Hemant Kumar, Prakash Mahto, Ashish Choudhary
h. Writing-review and editing: Jaiinder Preet Singh, Piyush Gulati, Vikas Sharma
i. Supervision: Jaiinder Preet Singh, Piyush Gulati

Future Work:

While the progress made so far with the current system for automating poultry farm management using IoT has been good, there are many opportunities for future enhancement. One of the main areas will be to incorporate solar power so the system can run in circumstances where the power supply is unreliable, promoting sustainability and reducing long-term energy costs. Another opportunity for enhancement will involve the application of artificial intelligence (AI) algorithms, which will enable predictive analytics for disease detection, feed optimization, and early warning alerts based on historical and real-time data. The mobile app will be improved by adding offline functionality with local data caching and processing, so that

farmers can continue operating even in poor internet conditions and not lose surveillance or control of their poultry. To increase accessibility, particularly for farmers without a technological background, adding voice commands in regional languages will help. The current sensor array could be extended to include hydrogen sulfide (H_2S) sensors and cameras for behaviour monitoring, which would provide a better overview of overall poultry health and the environment. There will be improvements to the alerts and notifications system, via SMS and app notifications, to inform and guide users in serious situations. Another area of development will be a centralised cloud-based dashboard that supports multiple farms. With a general overview of many farms, the development of a module for inventory tracking, and possibly a market-monitoring module as well, a smart poultry business can be managed end-to-end.

Funding: This research received no external funding.

Conflict of interest: The authors declare no conflict of interest.

References

[1] Kristensen, H. H.; Wathes, C. M. Ammonia and poultry welfare: A review. *Worlds Poult. Sci. J.* **2000**, *56*(3), 235–245. https://doi.org/10.1079/WPS20000018

[2] Broderick, T. J.; Gutierrez, O.; Lee, J. T.; Duong, T. Evaluation of functional feed additive administration in broiler chickens to 21 d. *J. Appl. Poult. Res.* **2021**, *30*(2), 100121. https://doi.org/10.1016/j.japr.2020.100121

[3] Dorninger, C. G.; Aleschko, M.; Gußl, A. H.; Fruhauf, S.; Thamhesl, M.; Doupovec, B.; Schatzmayr, D.; Moll, W. D.; Pender, C. Recent advances in enzyme technologies for mitigating mycotoxin contamination in poultry feed. *J. Appl. Poult. Res.* **2025**, *34*(3), 100544. https://doi.org/10.1016/j.japr.2025.100544

[4] Phiri, H.; Kunda, D.; Phiri, J. An IoT smart broiler farming model for low income farmers. *Int. J. Eng. Sci.* **2018**, *6*(3), 95–110. https://doi.org/10.3991/ijes.v6i3.9287

[5] Lashari, M. H.; Memon, A. A.; Shah, S. A. A.; Nenwani, K.; Shafqat, F. IoT based poultry environment monitoring system. In *Proc. IEEE Int. Conf. Internet of Things and Intelligence System (IOTAIS)*; IEEE, 2018; pp 1–5. https://doi.org/10.1109/IOTAIS.2018.8600837

[6] Gondchawar, N.; Kawitkar, R. S. IoT-based smart agriculture. *Int. J. Adv. Res. Comput. Commun. Eng.* **2016**, *5*(6), 838–842.

[7] Liu, M.; Chen, H.; Zhou, Z.; Du, X.; Zhao, Y.; Ji, H.; Teng, G. Development of an intelligent service platform for a poultry house facility environment based on the internet of things. *Agriculture* **2024**, *14*(8), 1277. https://doi.org/10.3390/agriculture14081277

[8] Cruz, E.; Hidalgo-Rodriguez, M.; Acosta-Reyes, A. M.; Rangel, J. C.; Boniche, K.; Gonzalez-Olivardia, F. ACMSPT: Automated counting and monitoring system for poultry tracking. *AgriEngineering* **2025**, *7*(3), 86. https://doi.org/10.3390/agriengineering7030086

[9] Ahmed, B. A.; Salih, A. M. Design of poultry farm monitoring and disease detection system using IoT and image processing. *Sudan Univ. Sci. Technol. Repository* **2020**.

[10] Ehsan, T. Z.; Mohtavipour, S. M. Broiler-Net: A deep convolutional framework for broiler behavior analysis in poultry houses. *arXiv* **2024**, arXiv:2401.12176.

[11] Singh, D. The role of Internet of Things, computer vision, and sound analysis in a smart poultry farm. *ACS Agric. Sci. Technol.* **2023**, *3*(4), 567–578.

[12] Shaikh, N.; Chakraborty, C. Systematic review on IoT in smart livestock management systems. *Sustainability* **2024**, *16*(10), 4073. https://doi.org/10.3390/su16104073

[13] Esnaola-Gonzalez, I.; Gómez-Omella, M.; Ferreiro, S.; Fernandez, I.; Lázaro, I.; García, E. An IoT platform towards the enhancement of poultry production chains. *Sensors* **2020**, *20*(6), 1549. https://doi.org/10.3390/s20061549

[14] Padua, J. N.; Malubay, J. C.; Dionisio, R.; Tandingan, Jr. IoT-based smart poultry farming: Enhancing security and monitoring for high-quality production. *Int. J. Res. Innov. Technol. Comput. Commun.* **2023**, *11*(4), 112–116.

[15] Ahamed, A. K.; Raj, R. Robotics for poultry farming: Challenges and opportunities. *arXiv* **2023**, arXiv:2311.05069.
[16] Gandhi, K. I. AIoT-driven edge computing for rural small-scale poultry farming: Smart environmental monitoring and anomaly detection for enhanced productivity. *Int. J. Recent Innov. Trends Comput. Commun.* **2023**, *11*(8), 44–52. https://doi.org/10.17762/ijritcc.v11i8.7923
[17] Gowda, S. B.; Rashmitha, K.; Rakshitha, K.; Vijaylaxmi. A witted management of poultry farm using IoT. *Int. J. Eng. Res. Technol.* **2020**, *8*(15).
[18] Lu, J.; Hu, D.; Ye, Y.; Liu, A.; Zhang, Z.; Peng, X. The composite visual-laser navigation method applied in indoor poultry farming environments. *arXiv* **2025**, arXiv:2504.08431.
[19] Kale, M.; Charkha, S.; Dehankar, P.; Sharma, P.; Choudhary, A.; Jakhete, M.; Javanjal, V. IoT-based smart poultry farm monitoring and controlling using Raspberry Pi. *Int. J. Intell. Syst. Appl. Eng.* **2024**, *12*, 373–379.
[20] Barrios, J.; Carrillo, J. Wireless technologies for agricultural monitoring using IoT with energy harvesting capabilities. *arXiv* **2020**, arXiv:2005.02477.
[21] Sasirekha, R.; Kaviya, R.; Saranya, G.; Mohamed, A.; Iroda, U. Smart poultry farm monitoring using IoT and cloud computing. *E3S Web Conf.* **2023**, *399*, 04055. https://doi.org/10.1051/e3sconf/202339904055
[22] Li, Z. Application of computer vision in poultry behavior analysis. *ACS Agric. Sci. Technol.* **2023**, *3*(6), 634–642.
[23] Sharma, S.; Aggarwal, A. IoT-based automated poultry farm management system. *Sustainability* **2021**, *13*(12), 6734.
[24] Neethirajan, S. Automated tracking systems for the assessment of farmed poultry. *Animals* **2022**, *12*(3), 232. https://doi.org/10.3390/ani12030232
[25] Gupta, R.; Rao, S. Energy-efficient IoT solutions for poultry farming. *arXiv* **2021**, arXiv:2005.02477.
[26] Orakwue, S. I. IoT-based smart monitoring system for efficient poultry farming. *Webology* **2022**. https://doi.org/10.14704/WEB/V19I1/WEB19270

ASEAN
Journal of Scientific and Technological Reports
Online ISSN:2773-8752

Research article

Histology and Histochemistry of the Digestive Tract of Transverse-bar Barb, *Hampala macrolepidota* Kuhl & Van Hasselt, 1823

Akapon Vaniksampanna[1], Sonchai Intachai[2], Wankuson Chanasit[2], Sakorn Khongsud[2], and Akkanee Pewhom[2*]

[1] Innovative Learning Center, Srinakharinwirot University, Bangkok, 10110, Thailand
[2] Faculty of Science and Digital Innovation, Thaksin University, Phatthalung, 93210, Thailand
* Correspondence: akkanee.p@tsu.ac.th

Citation:
Vaniksampanna, A.; Intachai, S.; Chanasit, W.; Khongsud, S.; Pewhom, A. Histology and histochemistry of the digestive tract of transverse-bar barb, *Hampala macrolepidota* Kuhl & Van Hasselt, 1823. *ASEAN J. Sci. Tech. Report.* **2026**, *29*(4), e263072. https://doi.org/10.55164/ajstr.v29i4.260372

Article history:
Received: December 31, 2025
Revised: February 20, 2026
Accepted: February 22, 2026
Available online: March 25, 2026

Publisher's Note:
This article is published and distributed under the terms of the Thaksin University.

Abstract: *Hampala macrolepidota* is an important local fishery species; the information on its anatomy and microanatomy is scarce. Therefore, the histology and histochemistry of its digestive tract were systematically investigated. The digestive tracts of adult fish were removed and processed using the paraffin technique. Sections of 5 μm thickness were stained with hematoxylin and eosin (H&E), periodic acid-Schiff's (PAS), and alcian blue (AB), pH 2.5 and pH 1.0. Its digestive tract consisted of the oropharynx, esophagus, and intestine, with no stomach observed. The stratified epithelium of the oropharynx was weakly positive-stained with PAS and AB at pH 2.5 and pH 1.0. In contrast, in the esophagus, mucous and goblet cells were strongly positively stained with all stains, indicating the secretion of neutral mucin and carboxylated and sulfated acid mucins. The intestine can be divided into three regions: anterior, middle, and posterior. Meanwhile, the enterocytes were positively stained with PAS; however, the goblet cells were positively stained with PAS at pH 2.5 and pH 1.0. The goblet cells secreted neutral mucins, as well as carboxylated and sulfated acidic mucins. The middle intestine showed crypt-like glands and the highest histometric values, indicating that it served as the main site of digestion and nutrient absorption, despite the absence of a stomach. The muscular layer varied regionally, with skeletal muscle in the oropharynx and esophagus and smooth muscle in the intestine. The intestinal coefficient was 0.69, indicating that it was a carnivorous fish. These findings provided fundamental data relevant to aquaculture, ecology, and comparative vertebrate anatomy.

Keywords: Digestive tract; *Hampala macrolepidota*; histochemistry; microanatomy; mucopolysaccharides

1. Introduction

The digestive system is a vital organ system responsible for converting nutrients into energy to sustain animal activity. Among vertebrate digestive systems, there are many differences in anatomy, microanatomy, physiology, and function, especially in teleosts [1], depending on evolutionary processes, feeding habits [2], and taxonomy [3]. Overall, the general structure of the gastrointestinal tract is mostly similar, although variations among species can be observed [4], resulting in different functional physiology in each species [5]. Generally, the fish digestive tract comprises the pharynx, esophagus, stomach, and intestine [6]. In some teleost species, the stomach is absent, including members of the

families Cyprinidae, Labridae, Gobiidae, Scaridae, some Poeciliidae [7], and such species as *Puntius stoliczkanus* [8], *Sphoeroides testudineus* [2], *Barbus altianalis* [9], *Schizothorax esocinus* [10], *Xiphophorus maculatus*, and *X. hellerii* [11].

The pharynx is the first portion of the digestive tract, connecting the oral cavity and gills to the muscular esophagus [12]. The caudal end of the esophagus connects to the stomach, which may be straight, U-shaped, or J-shaped based on the species and feeding habits [13, 14]. The intestine forms the final portion of the tract and opens to the exterior. In stomachless fish, the esophagus connects directly to the intestine, a unique characteristic [7]. Moreover, intestinal length depends on feeding habits [12], with herbivorous, carnivorous, and omnivorous fish having the longest, shortest, and intermediate lengths, respectively [15]. The intestinal coefficient (IC; the ratio of intestinal length to standard length) is widely used as a criterion for identifying feeding habits [12] or food preferences [16]. Herbivorous fish typically have IC values ranging from 0.8 – 15.0 [17], while carnivorous and omnivorous fish have values of 0.2 – 2.5 and 0.6 – 8.0, respectively [12]. In teleosts, the alimentary system has multiple functions, including food digestion and nutrient absorption [18], osmoregulation [19], hormone secretion [20], and immune defense [21]. Studies of the fish digestive tract are therefore crucial, as they contribute to many related fields. Numerous studies have examined digestive morphology and histology, including the pharynx to intestine in *B. altianalis* [9]; the esophagus and stomach in *Parupeneus forsskali*, *Papilloculiceps longiceps*, and *Acanthurus sohal* [14]; and the esophagus to intestine in *Oligosarcus hepsetus* [22], *Lates calcarifer* [23], *Sparus aurata* [6], *Larimichthys crocea* [12], *Pisodonophis boro* [24], *Hydrocynus forskahlii* [25], and *Trichomycterus bogotensis* [16]. Some studies have focused only on the stomach [26] or the intestine [11], such as in *P. stoliczkanus* [8]. Histochemical analyses have also been performed, primarily focusing on the types of mucopolysaccharides and glycoproteins secreted by cells in different regions of the tract and their functional significance [12]. Thus, histological studies of the digestive tract provide important tools for assessing gut health, digestive adaptation, environmental conditions [11], taxonomy, and feeding habits [27], with applications in feed management [12].

The transverse-bar barb, *Hampala macrolepidota*, is a member of the family Cyprinidae and is distributed across Southeast Asia, including Laos, Indonesia, and Thailand [28]. Adult *H. macrolepidota* have an elongated, laterally compressed body with dark transverse bars across the longitudinal axis. A previous study reported that *H. macrolepidota* is a carnivorous (piscivorous) species with a predatory ecological role, feeding on fish, shrimp, crabs, mollusks, and aquatic insects [29]. *H. macrolepidota* is regarded as a highly desirable species among fishermen, highly valued for consumption and economically important, which makes it one of the principal target fishes in many regions [28]. However, *H. macrolepidota* is classified as "Least Concern" [30], its populations are declining [31], and life-history traits and biological data remain scarce [32], particularly regarding anatomy, microanatomy, histochemistry, and physiology. Therefore, in this study, the histology and histochemistry of the digestive tract of *H. macrolepidota* were systematically investigated. The findings will help fill critical knowledge gaps and provide fundamental data for applications in physiology, fish health assessment, and aquaculture.

2. Materials and Methods

2.1 Fish and tissue collection

Ten healthy adult *H. macrolepidota* (five females and five males; mean standard length = 39.01 ± 0.45 cm) were wild-caught from natural freshwater habitats in Phatthalung Province, Thailand (7°46′43.9″N, 100°11′42.8″E) between July 2024 and March 2025. Fish were considered healthy based on normal external appearance and the absence of lesions and signs of disease. Standard length was measured using a measuring tape to the nearest 1 mm (0.1 cm), and each measurement was taken twice to ensure accuracy. *H. macrolepidota* were anesthetized with 100 mg·L^{-1} of tricaine methanesulfonate (MS-222) solution. The body was opened longitudinally from the anus to the mouth. The digestive tract was then removed, photographed, and measured with the measuring tape. Subsequently, the digestive tract was fixed in Bouin's fixative for 72 hours and then preserved in 70% ethanol. The intestinal length was used to calculate the intestinal coefficient (IC) according to the following equation [8, 12, 16, 23].

$$\text{IC} = \frac{\text{Intestinal length (IL)}}{\text{Standard length (SL)}}$$

This research was approved by the Animal Ethics Screening Committee, Thaksin University (Permit number: COA TSU 2024-009; IACUC No. 0009).

2.2 Histology and histochemistry study

The digestive tract was cut into small pieces and processed using the paraffin method. The organs were dehydrated through a graded ethanol series (70%, 80%, 95%, and absolute alcohol, two changes at each concentration). The resulting samples were then cleared in xylene (two changes) and infiltrated with Paraplast (two changes). The organs were embedded in Paraplast Plus® (Sigma-Aldrich, USA) using an embedding center to produce tissue blocks. Serial sections of 5 μm thickness were cut with a rotary microtome and mounted on glass slides. The sections were stained with hematoxylin and eosin (H&E) for general tissue components, periodic acid Schiff's (PAS) for neutral mucopolysaccharides, alcian blue pH 2.5 (AB pH 2.5), and alcian blue pH 1.0 (AB pH 1.0) for carboxylated and sulfated acid mucopolysaccharides, respectively [33]. Permanent slides were examined under a compound light microscope (Olympus CX31) and photographed with a digital camera (Canon EOS 700D).

2.3 Histometric and statistical analysis

The photographs were examined, and the epithelium layer thickness, mucosal fold (villi) width, mucosal fold (villi) height, and muscular layer thickness were measured using ImageJ software. Measurements were obtained from randomly selected regions across multiple fields per section of each structure from all ten fish examined. SPSS was used to analyze the data, and Duncan's multiple-range test was employed to differentiate the parameters of the anterior, middle, and posterior intestines. The data are presented as mean ± standard deviation, and $p < 0.05$ was considered statistically significant.

3. Results and Discussion

3.1 Gross anatomy of the digestive tract

The digestive tract of *H. macrolepidota*, with a mean length of 32.49 ± 0.91 cm (Table 1), was located within the abdominal cavity, with the intestine covered by the swim bladder. Its tract consisted of the oropharyngeal cavity, esophagus, and intestine (Figures 1A – 1I), similar to those of *Belone belone* [34], *B. altianalis* [9], *X. maculatus*, and *X. hellerii* [11]. No difference in gross anatomy or histology was observed between individuals and sexes. The oropharyngeal cavity formed the oral cavity with dilated folds, whereas the esophagus was a short muscular tube (Figures 1A - 1B, 1F). The intestine was the longest portion; however, no stomach was found in this species (Figures 1A-1B). The absence of stomach was similar to that reported in *S. testudineus* [2] and *B. belone* [34]. Furthermore, the observation was a unique characteristic found in families such as Cyprinidae, Labridae, Cyprinodontidae, Gobiidae, Scaridae, and some members of Poeciliidae [7].

The oropharyngeal cavity and esophagus were short regions with a mean length of 3.78 ± 0.23 cm (Table 1). The oropharyngeal cavity possessed thick longitudinal folds and a wide dilated area (Figure 1F). Its terminal end is connected to the short tubular esophagus. The junction between two regions was marked by the narrow tubular opening of the esophagus (Figures 1A, 1C, 1F). The main difference between the oropharynx and esophagus was that the oropharynx had taller folds than the esophagus (Figure 1F). In *H. macrolepidota*, the esophagus is connected directly to the intestine, as in other stomachless fish such as *B. altianalis* [9], *S. esocinus* [10], *X. maculatus*, and *X. hellerii* [11]. At the junction between the esophagus and intestine, a constriction was observed (Figures 1A - 1C). The intestine of *H. macrolepidota* (mean length 27.01 ± 1.54 cm; Table 1) was divided into three regions: anterior, middle, and posterior (Figures 1A - 1E). The anterior intestine extended caudally before ascending to form the middle intestine, while the posterior intestine descended toward the anus (Figure 1A). These results were similar to those reported in *S. testudineus* [2]. The external wall of the intestine was attached to the abdominal wall by a thin membrane, while the internal wall contained longitudinal folds (Figures 1G - 1I).

The wall of all portions of the gastrointestinal tract contained longitudinal folds, similar to other stomachless fish such as *B. altianalis* [9], *S. esocinus* [10], *H. forskahlii* [25], and other carnivorous fish such as *Trichomycterus brasiliensis* [35]. In addition, *H. macrolepidota* lacked pyloric caeca, a condition commonly reported in carnivorous fishes. In contrast, pyloric caeca are well developed in herbivorous and omnivorous fishes, where they play an important role in prolonging food retention time, enhancing enzymatic digestion, and facilitating nutrient absorption, particularly of plant-derived materials that are structurally complex and difficult to digest [13]. Therefore, the absence of pyloric caeca in the carnivorous *H. macrolepidota* is consistent with its feeding habit and functional digestive strategy, which relies primarily on intestinal digestion of animal prey rather than extended processing of plant material [13], a condition similarly reported in other carnivorous fishes such as *T. bogotensis* [16], *P. boro* [24], *Ariopsis seemanni* [36], and *Pimelodus blochii* [37].

Table 1. Mean ± standard deviation (SD) of standard length, digestive tract length, oropharyngeal–esophageal length, intestinal length (cm), and intestinal coefficient (IC) in *H. macrolepidota* (n = 10).

	Standard length (cm)	**Digestive tract length** (cm)	**Oropharynx-esophagus length** (cm)	**Intestinal length** (cm)	**IC**
$\bar{x}$ ±SD	39.01 ± 0.45	32.49 ± 0.91	3.78 ± 0.23	27.01 ± 1.54	0.69

3.2 Histology and histochemistry

3.2.1 oropharynx

The histological characteristics of the oropharyngeal wall comprised three layers, including the mucosa (epithelium, lamina propria, and absence of muscularis mucosae), submucosa, and muscular layer (Figure 2A). The mean mucosal fold width and height were 2,613.22 ± 93.04 μm and 2,899.77 ± 29.69 μm, respectively (Table 2). The epithelium was lined by non-keratinized stratified squamous epithelium that was composed of multiple cell layers (Figures 2A – 2F), similar to those observed in *B. altianalis* [9], *X. maculatus*, and *X. hellerii* [11]. The apical cells were flat with flattened nuclei, whereas the cells in the basal and intermediate regions were cuboidal or polygonal with oval nuclei (Figures 2A – 2F). The epithelium comprised approximately 35.09 ± 1.89 cell layers and showed a mean epithelial thickness of 679.06 ± 137.79 μm (Table 2). The apical epithelial cells of the oropharynx were weakly positive for PAS (Figure 2D), AB pH 2.5 (Figure 2E), and AB pH 1.0 (Figure 2F). However, at the short junction between the oropharynx and esophagus, the sparse globular mucous cell exhibited strong positive staining with PAS (Figure 3D), AB pH 2.5 (Figure 3E), and AB pH 1.0 (Figure 3F). Beneath the epithelium, the lamina propria was observed, consisting of dense connective tissue. Blood vessels containing red blood cells and numerous fibroblasts were prominent in this layer (Figures 2A - 2B). The stratified squamous epithelium facilitated the food transport and protected the underlying connective tissue from mechanical and chemical injuries, as well as bacterial invasion [22]. Its non-keratinized characteristic additionally supported the food transport [11]. In contrast, the muscularis externa contained a longitudinal layer of skeletal muscle (Figures 2A, 3A), consistent with stomachless fish such as *B. altianalis* [9]. This skeletal muscle allowed the pharynx to reject unwanted food, and provided voluntary control of swallowing, with the mean muscular layer thickness of 1,300.34 ± 197.86 μm (Table 2).

Furthermore, at the transitional junction between the oropharynx and cranial esophagus, the epithelium gradually changed from stratified squamous to stratified squamous/cuboidal epithelium with a mean cell layer of 10.33 ± 2.00 cell layers (Figures 3A - 3B). This short transitional segment is composed of apical squamous/cuboidal cells, intermediate polygonal cells, and sparse globular mucous cells (Figures 3B - 3F). In addition, near the base of the epithelium, club cells (alarm cells) were observed, which were large, oval to round with a prominent nucleus (Figures 3B – 3F). The cytoplasm was stained with eosin (Figures 3B - 3C), meanwhile displayed weak staining with PAS (Figure 3D), similarly to *B. altianalis* [9], *T. bogotensis* [16], *T. brasiliensis* [35], *A. seemanni* [36] and *Pimelodus pictus* [38]. Whereas these cells were consistently negative with staining AB pH 2.5 (Figure 3E) and AB pH 1.0 (Figure 3F). In contrast, the club cells had rarely been reported in fishes, possibly because most digestive tract studies began at the esophagus rather than the oropharynx [12, 22, 24]. These findings suggested that club cells functioned in producing and secreting substances, including alarm pheromones released on the approach of predators [39]. However, the presence of club cells in the

epidermis of fish suggests that club cells in the esophagus might be associated with the secretion of substances that defend against parasites and pathogens, as well as play roles in immune responses and healing [40, 41]. Future studies are seriously explored to clarify the precise function of these cells. In the present work, however, the oropharynx of *H. macrolepidota* lacked taste buds (Figures 3A - 3F).

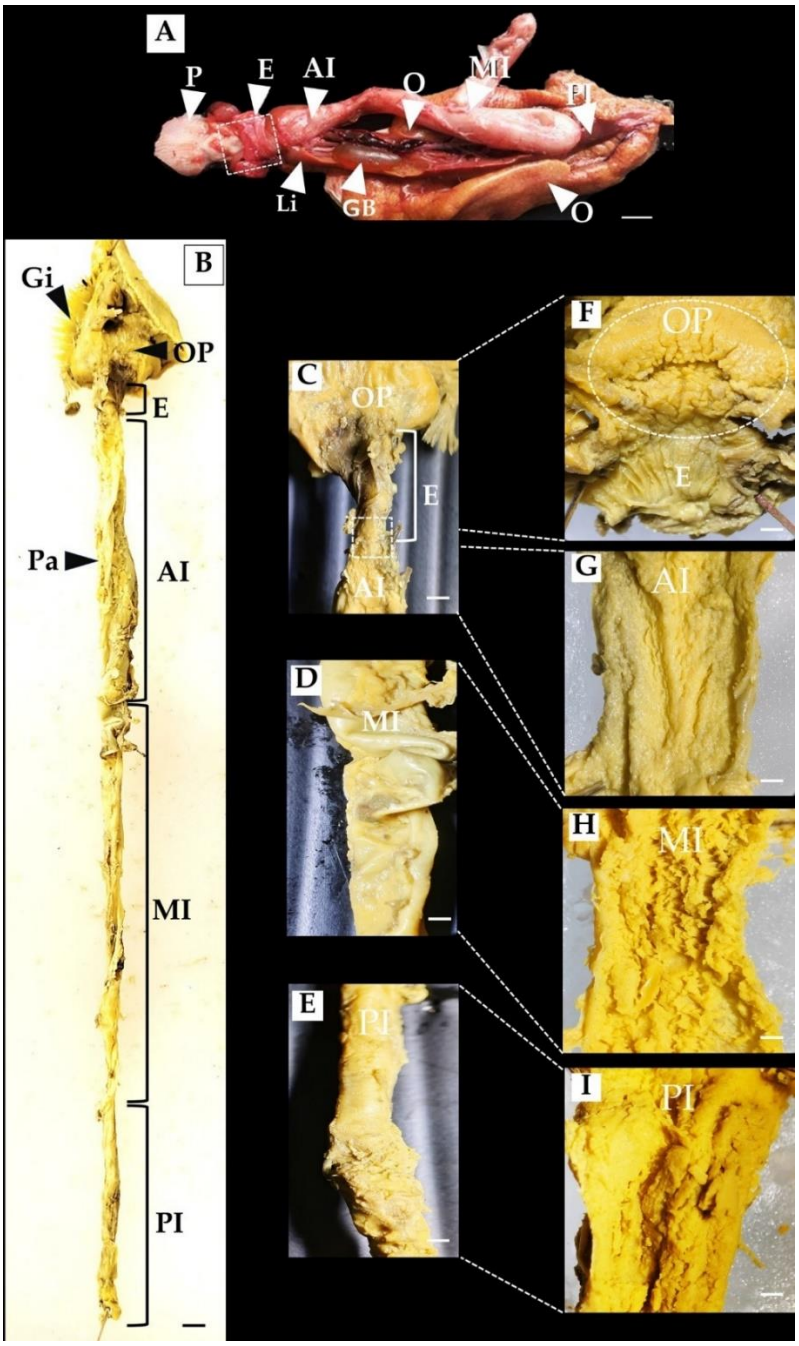


Figure 1. (1A) The fresh digestive tract in its true position among the reproductive system of *H. macrolepidota*. (1B) The fixed and extended digestive tract, consisting of oropharynx (OP), pharynx (P), esophagus (E), anterior intestine (AI), middle intestine (MI), and posterior intestine (PI). (1C) The enlarged view of the oropharynx, esophagus, and anterior intestine, where the square dotted line frame represents the constricting junction between the esophagus and anterior intestine. (1D - 1E) The enlarged view of the middle and posterior intestines, respectively. (1F) The interior wall of the oropharynx (the oval dotted line frame) and esophagus. (1G, 1H and 1I) The interior wall of the anterior, middle, and posterior intestines, respectively. Gall bladder (GB), gill (Gi), liver (Li), ovary (O), and pancreas (Pa).

3.2.2 Esophagus

The esophageal wall consisted of four layers: mucosa, submucosa, muscularis, and serosa. The mucosa formed thick longitudinal folds projecting into the lumen (Figures 3A, 4A), with mean fold width and height of 409.39 ± 59.99 μm and 609.09 ± 96.41 μm, respectively (Table 2). The mucosal layer of the esophagus was lined with the non-keratinized stratified squamous epithelium, containing 5 - 7 layers of epithelial cells (Figures 4C - 4F), which were fewer than those observed in the oropharynx. The mean epithelial thickness was 71.47 ± 6.36 μm (Table 2). The stratified squamous epithelium was consistent with that reported in *S. testudineus* [2], *B. altianalis* [9], *X. maculatus*, X. *hellerii* [11], *L. crocea* [12], *Serrasalmus nattereri* [13], *P. forsskali*, *P. longiceps* [14], *O. hepsetus* [22], *B. belone* [34], and *Scorpaena porcus* [42]. However, in *S. testudineus* [2], the esophagus was divided into two regions: a straight tube and an abdominal pouch, owing to its pouch-like appearance, whereas in *H. macrolepidota*, the esophagus showed the same structure throughout the tube. The epithelium displayed five cell types: apical squamous cells, mucous cells, non-mucous cells, goblet cells, and basal cells (Figures 4C - 4F). The apical squamous cells were flattened and located near the lumen, whereas the mucous cells were oval or globular, with flattened or ovoid nuclei at the cell base. The goblet cells exhibited a characteristic goblet shape, with nuclei similar to those observed in mucous cells. The basal cells were flat or cuboidal, whereas non-mucous cells were cuboidal or polygonal, with round or oval nuclei (Figures 4C - 4F). With H&E staining, the cytoplasm of mucous and goblet cells appeared clear (Figure 4C). PAS staining revealed magenta (Figure 4D), while staining with AB at pH 2.5 (Figure 4E) and pH 1.0 (Figure 4F) resulted in intense blue. These results indicated that the mucous and goblet cells secreted neutral and acidic mucins, consistent with the previous reports in *S. aurata* [6], *L. crocea* [12], *S. nattereri* [13], *O. hepsetus* [22], *L. calcarifer* [23], *P. boro* [24], *B. belone* [34], and *T. brasiliensis* [35]. In contrast, the cytoplasm of apical squamous, basal, and non-mucous cells was negatively stained with PAS (Figure 4D), AB pH 2.5 (Figure 4E), and AB pH 1.0 (Figure 4F). Moreover, the esophagus exhibited a greater number of goblet and mucous cells than the oropharynx, consistent with the observations in other stomachless fishes, including *B. altianalis* [9], *X. maculatus*, and *X. hellerii* [11]. These phenomena indicated that these mucous and goblet cells were equivalent to the esophageal glands of higher vertebrates [12].

The esophagus and oropharynx of *H. macrolepidota* were lined with the stratified squamous epithelium, which protected the luminal epithelium from mechanical injury and abrasion [43]. In addition, the multilayered cells served as a defensive barrier against pathogens and parasites. Besides, taste buds were globular in the esophageal epithelium, consisting of columnar taste cells with oval nuclei, while the basal cells were located near the base of each bud (Figures 4C – 4D). The observations were comparable to those described in *B. altianalis* [9], *G. maculatum* [17], *T. brasiliensis* [35], and *Pristolepis fasciata* [44]. The results indicated that the esophagus of *H. macrolepidota* played a primary role in the food conduction and a secondary role in the taste reception. The taste buds functioned as chemoreceptors, enabling fish to select food and reject unsuitable items [45], reflecting the predatory behavior of *H. macrolepidota*. However, in some fish, such as *L. crocea* [12], their taste buds were absent. Furthermore, esophageal glands were absent in *H. macrolepidota*, unlike in *S. testudineus* [2] and *O. hepsetus* [22]. However, the esophageal glands of *S. testudineus* were globular unicellular mucous glands rather than multicellular ones. Thus, the unicellular glands of *S. testudineus* might be functionally similar to the mucous cells of *H. macrolepidota*. The absence of esophageal glands was a common characteristic observed in teleosts. The glycoconjugates secreted by mucous and goblet cells might compensate for the absence of salivary and esophageal glands and perform functions equivalent to those of mammalian salivary glands [46, 47]. Other studies have suggested that neutral mucins produced by these cells might aid in food digestion within the esophagus [22]. Although the digestive role of the esophagus remained unclear, the present study observed the secretion of acidic mucins, which could create a favorable environment for digestion, consistent with the studies of Ghosh and Chakrabarti [27] and de Oliveira Ribeiro and Fanta [35]. Furthermore, the mucins might play an important role in lubricating the esophageal mucosa during the passage of food from the oropharynx to the anterior intestine [35, 48] and in protecting the epithelium [11]. In addition, the mucins protected the mucosa from mechanical injury (solid food) and harmful microorganisms [2, 49]. Beneath the epithelium, the lamina propria consisted of dense connective tissue without a muscularis mucosae; consequently, the boundary between the lamina propria and submucosa was indistinct (Figure 4A).

This feature was reported in several fish species, including *L. crocea* [12], *O. hepsetus* [22], *T. brasiliensis* [35], and *S. porcus* [42], indicating that it represented a common histological characteristic among fish [50]. The dense connective tissue likely strengthened, expanded, and supported the esophagus, reflecting *H. macrolepidota*'s carnivorous habit, and similar findings were reported in *S. testudineus* [2] and *S. porcus* [42]. Deeper within the esophageal wall, beneath the submucosa, two sublayers of muscle were observed in the esophagus of *H. macrolepidota*: an inner longitudinal and an outer circular layer (Figures 4A - 4B). The mean muscular thickness was 809.36 ± 29.42 μm (Table 2). These two arrangements of skeletal muscle are similar to those described in *S. aurata* [6], *L. crocea* [12], *O. hepsetus* [22], and *P. boro* [24]. However, this appearance differed from *B. belone* [34], which exhibited two longitudinal skeletal muscle layers separated by thin connective tissue, as well as from *L. calcarifer* [23] and *H. forskahlii* [25], which showed an inner circular and outer longitudinal arrangement. In contrast, species such as *P. forsskali* [14] and *Lepidorhombus whiffiagonis* [51] possessed only a single longitudinal muscle layer. The presence of skeletal muscle in the esophagus indicated that *H. macrolepidota* could reject unwanted food or prey and assist in swallowing. Although the oropharynx and esophagus were relatively short, the longitudinal folds and skeletal muscle in these regions suggested that the lumen could expand and distend during swallowing [52]. Externally, the serosa was composed of connective tissue, nerve fibers, blood vessels, and a mesothelium.

Table 2. Histometric measurements (mean ± standard deviation, μm) of epithelial layer thickness, mucosal fold width, mucosal fold height, and muscular layer thickness of the oropharynx and esophagus in *H. macrolepidota* (n = 10).

Histometric parameter	Oropharynx (μm)	Esophagus (μm)
epithelial layer thickness	679.06 ± 137.79	71.47 ± 6.36
mucosal fold width	2,613.22 ± 93.04	409.39 ± 59.99
mucosal fold height	2,899.77 ± 29.69	609.09 ± 96.41
muscular layer thickness	1,300.34 ± 197.86	809.36 ± 29.42

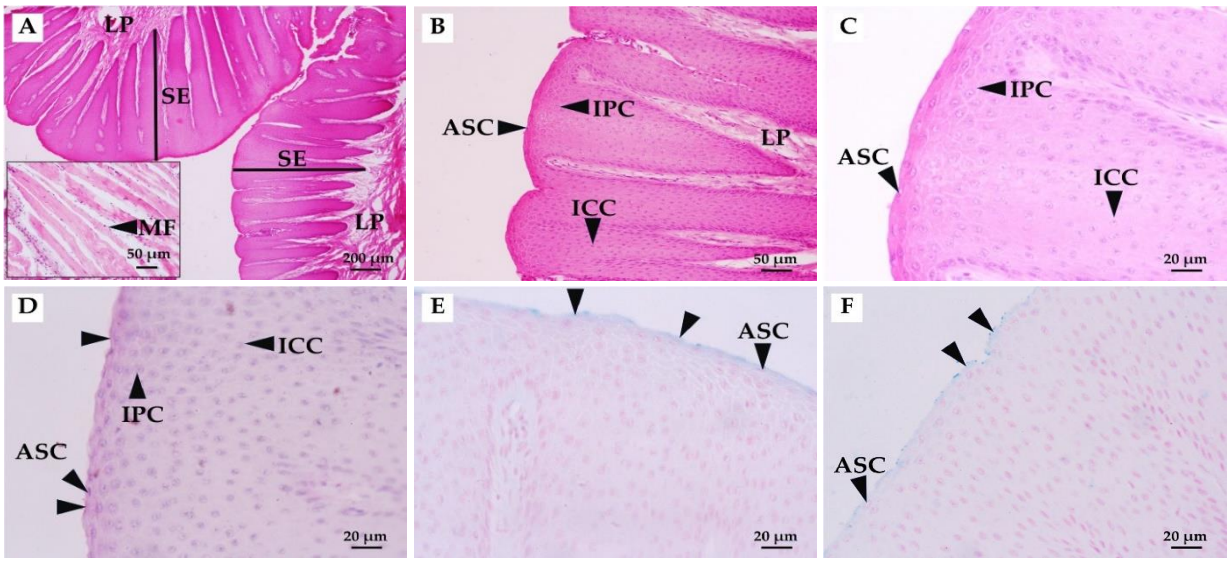


Figure 2. (2A) – (2F) The oropharynx of *H. macrolepidota*. (2A) The mucosal layers, including stratified epithelium (SE) of the mucosal fold, lamina propria (LP), and the box highlighting the muscular layer, consisting of muscular fiber (MF). (2B - 2C). The enlarged image of stratified epithelium of the oropharynx depicts the apical squamous cell (ASC), the intermediate polygonal cell (IPC), and the intermediate cuboidal cell (ICC). (2D - 2F) The apical squamous cell of the oropharynx contains neutral mucins, carboxylated and sulfated acid mucins, respectively. The arrowheads display the positive staining with the respective stains. (2A – 2C, and the box in 2A: H&E), (2D: PAS), (2E: AB pH 2.5), (2F: AB pH 1.0).

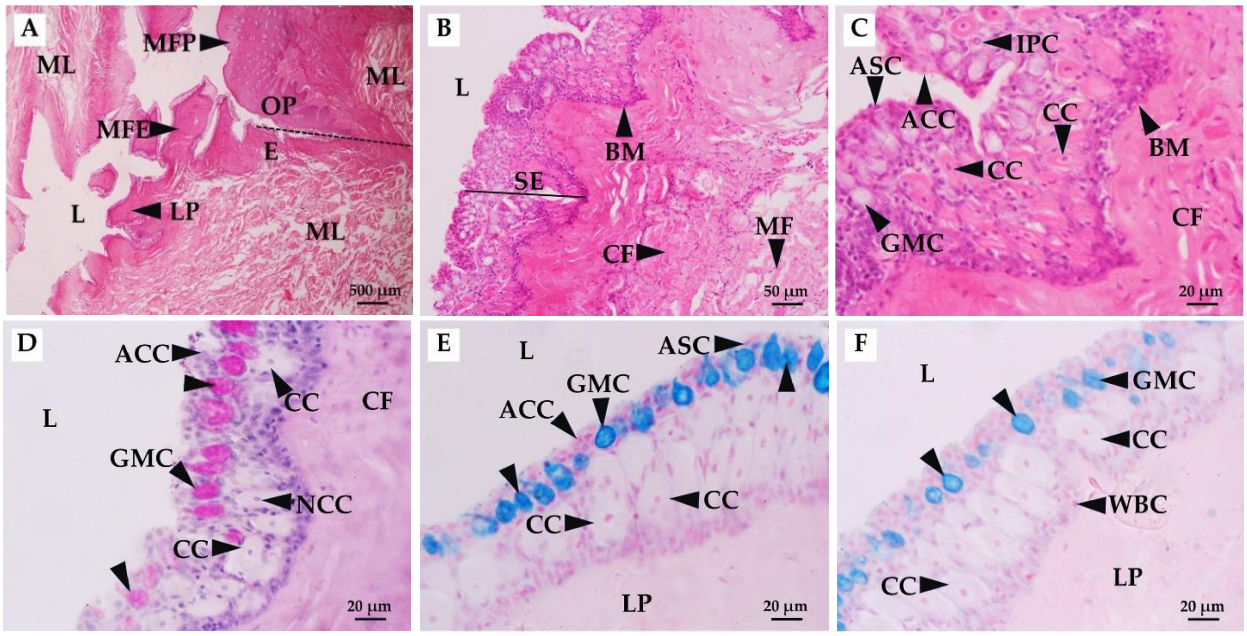


Figure 3. (3A) – (3F) The junction between the oropharynx (OP) and cranial part of esophagus (E) of *H. macrolepidota*. (3A) The dotted line shows the junction between the oropharynx and cranial region of the esophagus and distinct layers, including mucosa and muscular layer (ML). (3B) The stratified epithelium (SE) is located upon the basement membrane (BM) of the mucosal fold. (3C) The epithelium of the cranial region of the esophagus consists of apical squamous cells (ASC), apical cuboidal cells (ACC), intermediate polygonal cells (IPC), globular mucous cells (GMC), and club cells (CC). (2D - 2F) The arrowheads depict the globular mucous cell of the cranial part of the esophagus, containing neutral mucins, carboxylated and sulfated acid mucins, respectively. In contrast, the apical squamous and apical cuboidal cells exhibit negative staining. Collagen fiber (CF), lumen (L), mucosal fold of esophagus (MFE), mucosal fold of oropharynx (MFP), nucleus of club cell (NCC), lamina propria (LP), muscle fiber (MF), white blood cell (WBC). (3A – 3C: H&E), (3D: PAS), (3E: AB pH 2.5), (3F: AB pH 1.0).

3.2.3 Intestine

The transition from the esophagus to the intestine was marked by a muscular sphincter that functioned as a protective barrier against food reflux and contributed to the regulation of food transport. Furthermore, the epithelium changed from stratified squamous in the esophagus to simple columnar in the intestine. The intestine of *H. macrolepidota* could be distinguished into three portions: anterior, middle, and posterior, based on histological characteristics and histometric analyses (Figures 5A – 5L). This three-portion division was according to other fish species such as *S. aurata* [6], *B. altianalis* [9], *L. crocea* [12], *L. calcarifer* [23], *P. boro* [24], *H. forskahlii* [25], and *B. belone* [34], in contrast to those of *X. maculatus*, *X. hellerii* [11], and *O. hepsetus* [22], in which the intestine was subdivided into two portions, anterior and posterior portions. The intestinal wall of all portions comprises four layers: mucosa, submucosa, muscularis, and serosa (Figures 5A, 5F). All portions were filled with villi and lined with simple columnar epithelium (Figures 5A – 5L), corresponding to the works in *P. stoliczkanus* [8], *B. altianalis* [9], *X. maculatus*, *X. hellerii* [11], *O. hepsetus* [22], *P. boro* [24], and *S. porcus* [42]. In addition, the histomorphology of *H. macrolepidota* resembled other carnivorous fish with various features, including blood and lymph vessels in the lamina propria, loose connective tissue in the submucosa, absence of glands and muscularis mucosae, and two muscle sub-layers (inner circular and outer longitudinal layers) (Figures 5A – 5L) [2, 12, 16, 34, 35]. The anterior intestine was lined by simple columnar epithelium, composed of tall cells arranged in a single layer, with a mean epithelial thickness of 46.36 ± 8.27 µm (Table 3). Two cell types were found: enterocytes and goblet cells, among which the enterocytes showed centrally located oval nuclei with apical microvilli (brush border) (Figures 5B – 5E). The goblet cells lacked brush

borders, with basally located nuclei and cytoplasm containing clear mucins on H&E staining (Figure 2B), consistent with studies in *X. maculatus* and *X. hellerii* [11]. In some regions, intraepithelial leukocytes with basophilic, round nuclei were observed near the basement membrane (Figures 5B–5D). The mucosa formed thin folds (villi) with a lamina propria core, some of which branched into secondary folds and showed a slender, sharp-tipped appearance (Figure 5A). The mean villi width and height were 146.20 ± 24.80 μm and 866.40 ± 10.86 μm, respectively (Table 3). Enterocytes were weakly PAS-positive, especially at the base of the brush border (Figure 5C), but were negatively stained with AB at pH 2.5 (Figure 5D) and pH 1.0 (Figure 5E). The cytoplasm of goblet cells was positively stained with PAS, showing magenta (Figure 5C), and with AB at pH 2.5 (Figure 5D) and pH 1.0 (Figure 5E), appearing blue. The lamina propria forming the villus core contained collagen fibers, blood and lymph vessels, and fibroblasts, with more blood vessels near the villus tips (Figures 5B – 5E). Because the muscularis mucosae was absent, the boundary between the lamina propria and submucosa was indistinct. The muscularis consisted of two smooth muscle layers: an inner circular and an outer longitudinal (Figure 5A), with a mean thickness of 202.99 ± 39.15 μm (Table 3). The myenteric nerve plexus was observed between these layers (Figure 5B), corresponding to the observations in *B. altianalis* [9] and *O. hepsetus* [22]. The outermost serosa was lined by mesothelium and contained blood vessels that were embedded in the connective tissue (Figure 5A).

While the middle intestine displayed histological features similar to those of the anterior intestine, except that the epithelium became invaginated, forming crypt-like glands (Figure 5F). This appearance was consistent with that described in other carnivorous fish such as *T. bogotensis* [16]. Ortiz-Ruiz et al. [16], which identified these structures as Lieberkühn's crypts. The mean epithelial thickness of the crypts was 52.22 ± 3.83 μm (Table 3). The epithelium comprised enterocytes and goblet cells (Figures 5F - 5G), with the goblet cells staining positive for PAS (Figure 5G), AB pH 2.5 (Figure 5H), and AB pH 1.0 (Figure 5I). Compared with the anterior intestine, the middle intestine showed a greater number of goblet cells (Figures 5G – 5I). The mean villi width and height were 162.74 ± 14.27 μm and 885.28 ± 70.94 μm, respectively (Table 3). The submucosa, muscularis, and serosa were similar to those of the anterior intestine (Figure 5F). The mean muscular layer thickness was 241.81 ± 28.59 μm (Table 3). Besides, the posterior intestine displayed the histological and histochemical features comparable to those of the anterior and middle intestines (Figures 5J – 5L). The mean epithelial thickness was 37.85 ± 2.50 μm (Table 3), while the mean villi width and height were 87.08 ± 14.24 μm and 609.43 ± 64.14 μm, respectively (Table 3). The goblet cells interspersed among enterocytes positively stained with PAS (Figure 5J), AB pH 2.5 (Figure 5K), and AB pH 1.0 (Figure 5L), and were more numerous than those in the anterior portions (Figures 5J – 5L), with abundant lymphocyte aggregates in the submucosa (Figure 5J). The muscularis and serosa resembled those of the anterior and middle intestines; however, the muscularis of the posterior intestine was the thinnest among the three portions (Figure 5J). The mean muscular layer thickness was 160.39 ± 20.34 μm (Table 3).

Enterocytes in all regions exhibited apical microvilli, whereas the goblet cells were less frequent in the anterior intestine, corresponding to the reports in *X. maculatus*, *X. hellerii* [11], and *O. hepsetus* [22]. The numerous brush borders enhanced the surface area for absorption and interaction with the gut microbiota [49]. The findings suggested that the intestine was a site of enzymatic digestion, especially in the middle intestine, where crypt-like glands were observed. The goblet cells in the anterior, middle, and posterior intestines produced neutral mucins, as well as carboxylated and sulfated acid mucins, according to those observed in *B. altianalis* [9], *L. crocea* [12], *S. nattereri* [13], *O. hepsetus* [22], *L. calcarifer* [23], *P. boro* [24], *T. brasiliensis* [35], and *L. whiffiagonis* [51]. Based on the positive PAS and AB (pH 2.5 and 1.0) staining of globular mucous cells and their mucin secretion, the esophagus, anterior intestine, and middle intestine were considered sites of digestion. These characteristics were similar to those of other agastric fish such as *S. testudineus* [2] and *B. belone* [34]. Consistent with other studies, the goblet cells played a key role in absorption, transport, and the provision of enzymatic cofactors [53]. In addition, the neutral mucins released by the goblet cells of *H. macrolepidota* might also act as the cofactors in enzymatic digestion [12]. Therefore, various mucopolysaccharides may play a crucial role in digestive mechanisms. However, the exact mechanism of digestion in stomachless carnivorous fish has remained unclear [54]. Moreover, despite the evolutionary loss of the stomach, the digestion was not problematic in agastric herbivorous or carnivorous fish [34].

The highest mean epithelial thickness, villi height, and villi width were observed in the middle, anterior, and posterior intestines, respectively, along with the numerous goblet cells and complex crypts of the middle intestine, indicating that the middle intestine played the key roles in the main site for digestion, absorption, and possibly food storage. This observation was similar to that of stomachless fish such as *B. altianalis* [9] and was consistent with Canan et al. [55], who explained that nutrient absorption typically occurs in intestinal regions with complex mucosal structures. Meanwhile, *H. macrolepidota* fed on various invertebrates and fish; therefore, the goblet cells could protect the mucosa from damage caused by large prey, consistent with their secretion of multiple mucin types [53]. The acid mucins secreted by the goblet cells were thought to shield the intestinal mucosa from glycosidase degradation [56]. Furthermore, numerous goblet cells and the smallest mucosal folds were observed in the posterior intestine, consistent with the observations in *P. stoliczkanus* [8], *X. maculatus*, *X. hellerii* [11], *L. crocea* [12], *O. hepsetus* [22], *L. calcarifer* [23], *P. boro* [24], and *H. forskahlii* [25]. These results indicated that the posterior intestine functioned as the site for transporting undigested food. Consistently, the mucins produced by the goblet cells could protect the mucosa during fecal transport. Other studies have reported that acid mucopolysaccharides are important for defense against pathogenic bacteria, immune activation, and protein digestion, and have further noted that goblet cells influence the composition and activity of gut microorganisms [57]. The goblet cells secreted both neutral and acidic mucins, which contained diverse carbohydrates and could serve as a nutrient source for mucin-degrading bacteria [58]. Further studies are required to clarify the correlation between goblet cell number and intestinal function.

Moreover, all intestinal portions lacked muscularis mucosae and glands, consistent with *P. stoliczkanus* [8], *X. maculatus*, *X. hellerii* [11], *L. crocea* [12], and *L. calcarifer* [23]. The mucosa and submucosa were surrounded by two smooth muscle sublayers: the inner circular and the longitudinal layers, as reported in other carnivorous fish [2, 9, 11, 12, 22, 24, 25]. These two layers enhanced the contraction efficiency for mixing food with digestive enzymes and mucus, promoted propulsion, and likely facilitated nutrient absorption and peristalsis [11]. Although fish in the family Cyprinidae are generally regarded as herbivorous or omnivorous, trophic strategies within this family are highly variable and species-specific, ranging from herbivory and omnivory to carnivory depending on ecological niche, prey availability, and morphological adaptations. Accordingly, family-level classification may not accurately reflect the feeding ecology of individual species. In this context, available ecological and dietary evidence suggests that *H. macrolepidota* is more appropriately classified as a carnivorous species despite its placement within a predominantly omnivorous family. The IC of *H. macrolepidota* in the present study was 0.69 (Table 1), which is lower than 1.0 [16] and falls within the range of 0.2–2.5 reported for carnivorous fishes [12], indicating a relatively short intestine adapted for a protein-rich diet. This interpretation is consistent with previous stomach content analyses [29], which reported that *H. macrolepidota* primarily consumes animal prey, including microinvertebrates and small animals such as fish, shrimp, crabs, mollusks, and aquatic insects. In addition, histological characteristics observed in this study, such as the presence of skeletal muscle in the esophagus and diverse mucin secretions along the esophagus and intestines, particularly in the middle intestine, further support the classification of *H. macrolepidota* as a carnivorous species. Furthermore, the IC of *H. macrolepidota* fell within the reported range for carnivorous fish similar to *T. bogotensis* (IC = 0.59) [16], *P. blochii* (IC = 0.93) [37], and *Salminus affinis* (IC = 0.58) [59].

Table 3. Histometric measurements (mean ± standard deviation, μm) of epithelial layer thickness, villi width, villi height, and muscular layer thickness in the anterior, middle, and posterior intestines of *H. macrolepidota* (n = 10). Different superscript letters indicate significant differences among intestinal regions ($p < 0.05$, Duncan's test).

Histometric parameter	Anterior intestine (μm)	Middle intestine (μm)	Posterior intestine (μm)
epithelial layer thickness	46.36 ± 8.27 ^{b}	52.22 ± 3.83^{a}	37.85 ± 2.50^{c}
villi width	146.20 ± 24.80 ^{b}	162.74 ± 14.27 ^{a}	87.08 ± 14.24^{c}
villi height	866.40 ± 10.86 ^{b}	885.28 ± 70.94 ^{a}	609.43 ± 64.14 ^{c}
muscular layer thickness	202.99 ± 39.15 ^{b}	241.81 ± 28.59 ^{a}	160.39 ± 20.34 ^{c}

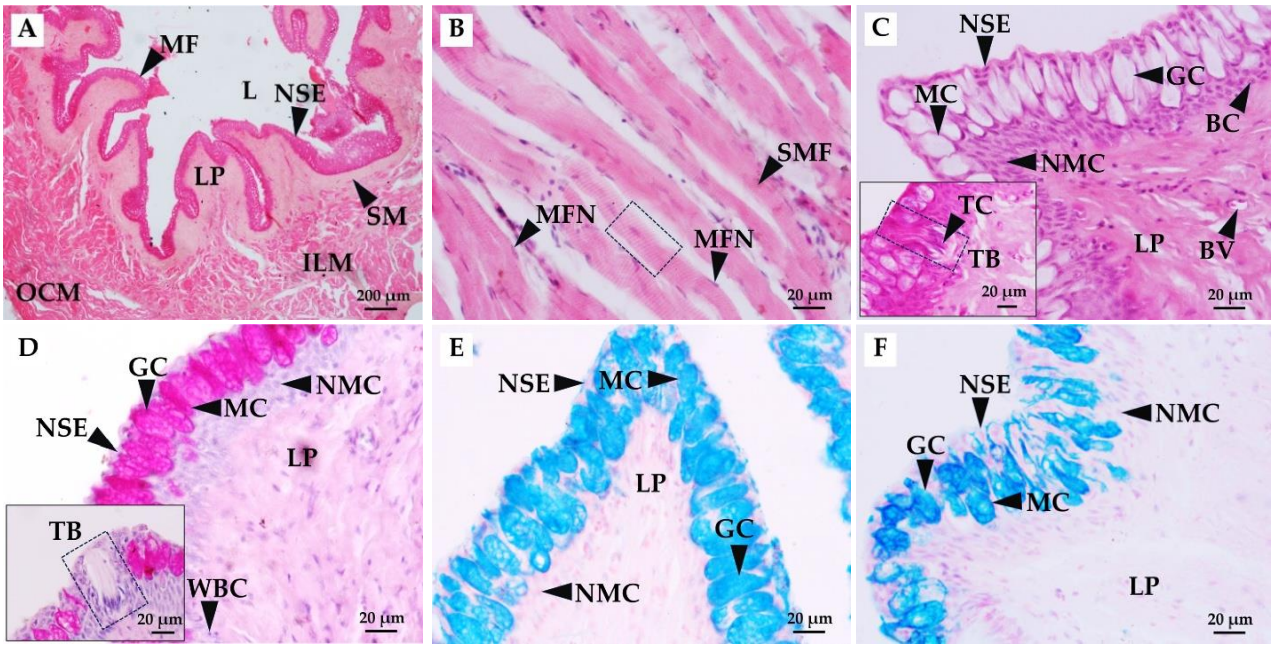


Figure 4. (4A) – (4F) The esophagus of *H. macrolepidota*. (4A): the distinct layers, including non-keratinized stratified epithelium (NSE) of the mucosal fold (MF), lamina propria (LP), submucosa (SM), and muscular layer, where the muscular layer contains two sub-layers of skeletal muscle, namely inner longitudinal muscle (ILM) and outer circular muscle (OCM). (4B) The enlarged picture of the skeletal muscular layer exhibiting the skeletal muscular fiber (SMF), muscular fiber nuclei (MFN). The square-dotted line frame displays the striation of the muscle cell. (4C): the enlarged picture of epithelium, depicting the non-keratinized stratified epithelium cell (NSE), goblet cell (GC), mucous cell (MC), non-mucous cell (NMC), and basal cell (BC). The box in 4C highlights the taste bud (TB), which is embedded in the epithelium and consists of taste cells (TC). (2D - 2F) The goblet cell and mucous cell, containing neutral mucins, carboxylated and sulfated acid mucins, respectively. In contrast, the non-mucous and club cells exhibit negative staining. The box in 4D highlights negative PAS staining of the taste bud. Blood vessel (BV), lumen (L), white blood cell (WBC). (4A – 4C, and the box in 4C: H&E), (4D and the box in 4D: PAS), (4E: AB pH 2.5), (4F: AB pH 1.0).

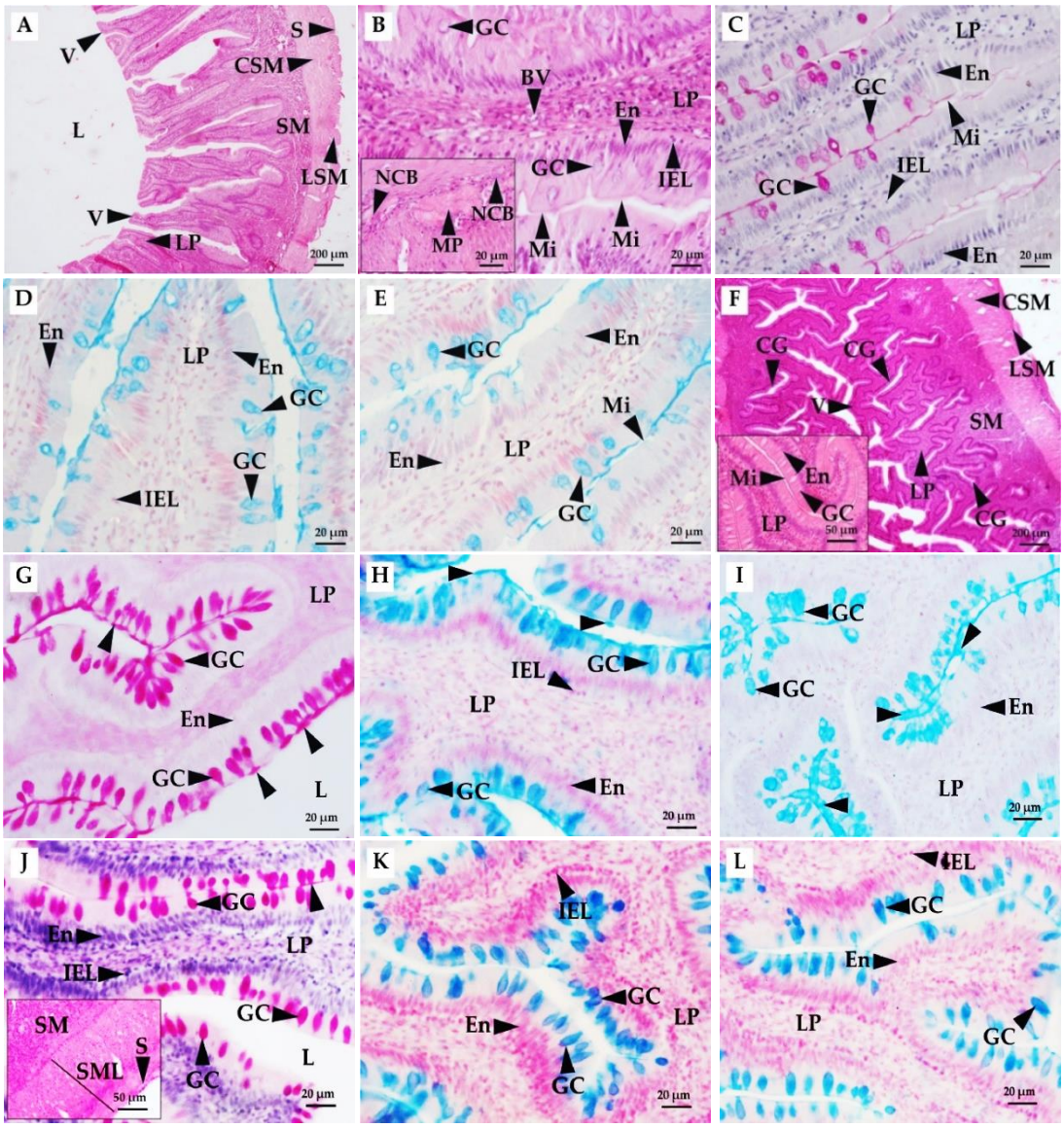


Figure 5. (5A) - (5E) The anterior intestine. (5F) - (5I) The middle intestine. (5J) - (5L) The posterior intestine of *H. macrolepidota*. (5A) The distinct layers of intestine, consisting of mucosa formed by villi (V), submucosa (SM), muscular layer, and serosa (S). The muscular layer is subdivided into two layers: circular smooth muscle (CSM) and longitudinal smooth muscle (LSM). (5B) The villi of the anterior intestine, comprising enterocyte (En), goblet cell (GC), and intraepithelial leukocyte (IEL). The blood vessel (BV) is located in the lamina propria (LP). The box in 5B highlights the myenteric plexus (MP), comprising nerve cell bodies (NCB). (5C) The base of microvilli (Mi) of the enterocyte and goblet cell of the anterior intestine is PAS-positive. (5D) and (5E) AB pH 2.5 and AB pH 1.0 positive goblet cells, respectively. (5F) The distinct layers and villi of the middle intestine, and the box illustrating the enlarged view of the villi. The villi form the crypt-like glands (CG), which display invagination of structures. (5G) The base of microvilli of the enterocyte and goblet cell of the middle intestine with PAS-positive staining. (5H) - (5I) AB pH 2.5 and AB pH 1.0-positive goblet cells, respectively. (5J) The villi of the posterior intestine and the box illustrating the enlarged view of the submucosa, muscular layer, and serosa. The goblet cells are PAS-positively stained. (5K) and (5L) AB pH 2.5 and AB pH 1.0 positive goblet cells, respectively. Lumen (L), smooth muscle layer (SML). The arrowheads demonstrate positive staining of secretion. (5A, 5B, 5F and the box in 5B, 5F and 5J: H&E), (5C, 5G, 5J: PAS), (5D, 5H, 5K: AB pH 2.5), (5E, 5I, 5L: AB pH 1.0).

4. Conclusions

This study provided the first report on the histology and histochemistry of the digestive tract of *H. macrolepidota*. The digestive tract consisted of the oropharynx, esophagus, and intestine, while the stomach was absent, indicating that *H. macrolepidota* was an agastric fish. The oropharyngeal and esophageal epithelia were lined with non-keratinized stratified squamous/cuboidal epithelium, differing in the number of epithelial cell layers. The oropharyngeal epithelial cells were weakly positive-stained for neutral mucopolysaccharides, carboxylated and sulfated acid mucopolysaccharides, whereas the esophageal epithelial cells, especially mucous cells and goblet cells, were strongly positive-stained with all stains. The club cells were observed at the transition junction between the oropharynx and the esophagus, whereas the taste buds were present in the esophagus. In addition, of those portions, the mucosa was surrounded by skeletal muscle. The intestine was divided into three portions, with the mucosa in all regions lined by the simple columnar epithelium containing enterocytes and goblet cells. Enterocytes were PAS-positive and exhibited a brush border, while the goblet cells were positively stained for neutral mucopolysaccharides, carboxylated, and sulfated acid mucopolysaccharides. Comparison among three portions of the intestine showed that the highest values of epithelial layer thickness, villi height and width, and muscular layer thickness were observed in the middle, anterior, and posterior intestines, respectively. Whereas, the mucosa of the middle intestine formed crypt-like glands. Therefore, based on histological and histochemical observations and histometric measurements, although *H. macrolepidota* lacked a stomach, the esophagus and the anterior and middle intestines were identified as the primary sites of digestion, with digestion and nutrient absorption occurring mainly in the middle intestine. Furthermore, the IC value supported a carnivorous feeding habit in *H. macrolepidota*, consistent with the histological and histochemical characteristics and with previous studies on feeding habits and gut contents. The findings enhanced the understanding of the anatomy, microanatomy, and histochemistry of *H. macrolepidota* in relation to its physiology and feeding habits. Future studies may employ additional techniques, such as electron microscopy and immunohistochemistry, to provide deeper insights.

5. Acknowledgements

This research was supported by the National Science, Research and Innovation Fund (NSRF) and Thaksin University (Grant No. FF-2569-213224).

Author Contributions: Conceptualization, A.V. and A.P.; methodology, A.V. and A.P.; validation, A.V. and A.P.; formal analysis, A.V. and A.P.; investigation, A.V. and A.P.; resources, S.I., W.C., and S.K.; data curation, A.P.; writing—original draft preparation, A.V. and A.P.; writing—review and editing, A.V. and A.P.; visualization, A.V. and A.P.; supervision, A.P.; project administration, A.P.; funding acquisition, A.P.

Funding: This research was supported by National Science, Research and Innovation Fund (NSRF) and Thaksin University (Grant No. FF-2569-213224).

Conflicts of Interest: The authors declare no conflict of interest.

References

[1] Al Abdulhadi, H. A. Some comparative histological studies on alimentary tract of tilapia fish (*Tilapia spilurus*) and sea bream (*Mylio cuvieri*). *Egypt. J. Aquat. Res.* **2005**, *31*(1), 387–398.

[2] Fagundes, K. R. C.; Rotundo, M. M.; Mari, R. B. Morphological and histochemical characterization of the digestive tract of the puffer fish *Sphoeroides testudineus* (Linnaeus, 1758) (Tetraodontiformes: Tetraodontidae). *An. Acad. Bras. Cienc.* **2016**, *88*(3), 1615–1624. https://doi.org/10.1590/0001-3765201620150167

[3] Çinar, K.; Senol, N. Histological and histochemical characterization of the mucosa of the digestive tract in flower fish (*Pseudophoxinus antalyae*). *Anat. Histol. Embryol.* **2006**, *35*(3), 147–151. https://doi.org/10.1111/j.1439-0264.2005.00629.x

[4] Okuthe, G. E.; Bhomela, B. Morphology, histology and histochemistry of the digestive tract of the banded tilapia, *Tilapia sparrmanii* (Perciformes: Cichlidae). *Zoologia* **2020**, *37*, e51043. https://doi.org/10.3897/zoologia.37.e51043

[5] Dabrowski, K. R.; Portella, M. C. Feeding plasticity and nutritional physiology in tropical fishes. *Fish Physiol.* **2005**, *21*, 155–224. https://doi.org/10.1097/01.ruq.0000177221.14263.45

[6] Pavelin, T.; Kević, N.; Restović, I.; Bočina, I. Histological and biochemical features of the digestive system in the cage-reared gilthead sea bream (*Sparus aurata*). *Int. J. Biol. Res.* **2018**, *2*(1), 51–56. https://doi.org/10.18689/ijbr-1000108

[7] Genten, F.; Terwinghe, E.; Danguy, A. *Atlas of Fish Histology*, 1st ed.; CRC Press: Boca Raton, FL, 2009.

[8] Senarat, S.; Yenchum, W.; Poolprasert, P. Histological study of the intestine of Stoliczkae's barb *Puntius stoliczkanus* (Day, 1871) (Cypriniformes: Cyprinidae). *Kasetsart J. Nat. Sci.* **2013**, *47*, 247–251.

[9] Aruho, C.; Namulawa, V.; Kato, C. D.; Kisekka, M.; Rutaisire, J.; Bugenyi, F. Histo-morphological description of the digestive system of the rippon barbel *Barbus altianalis* (Boulenger, 1900): A potential species for culture. *Uganda J. Agric. Sci.* **2016**, *17*(2), 197–217. https://doi.org/10.4314/ujas.v17i2.6

[10] Bhat, M. Y.; Channa, A.; Paray, B. A.; Al-Sadoon, M. K.; Rather, I. A. Morphological study of the gastrointestinal tract of the snow trout, *Schizothorax esocinus* (Actinopterygii: Cypriniformes). *Zoologia* **2019**, *36*, e31791. https://doi.org/10.3897/zoologia.36.e31791

[11] Gonçalves, M.; Lopes, C.; Silva, P. Comparative histological description of the intestine in platyfish (*Xiphophorus maculatus*) and swordtail fish (*Xiphophorus helleri*). *Tissue Cell* **2024**, *87*, 102306. https://doi.org/10.1016/j.tice.2024.102306

[12] Kalhoro, H.; Tong, S.; Wang, L.; Hua, Y.; Volatiana, J. A.; Shao, Q. Morphological study of the gastrointestinal tract of *Larimichthys crocea* (Acanthopterygii: Perciformes). *Zoologia* **2018**, *35*, 1–9. https://doi.org/10.3897/zoologia.35.e25171

[13] Raji, A. R.; Norouzi, E. Histological and histochemical study on the alimentary canal in walking catfish (*Clarias batrachus*) and piranha (*Serrasalmus nattereri*). *Iran. J. Vet. Res.* **2010**, *11*(3), 255–261.

[14] Shalaby, W. Comparative morphological and histological studies on the adaptation of esophagus and stomach to the feeding habits in some coral reef fishes at Hurghada, Red Sea, Egypt. *Egypt. J. Aquat. Res.* **2020**, *24* (5), 289–306. https://doi.org/10.21608/ejabf.2020.105059

[15] Evans, D. H.; Claiborne, J. B. *The Physiology of Fishes*, 3rd ed.; CRC Press: Boca Raton, FL, 2006.

[16] Ortiz-Ruiz, M.; López Flórez, C.; Castro Rebolledo, M. I.; Baldisserotto, B.; Gómez Ramírez, E. Anatomy, histology and ultrastructure of the digestive tract in Andean fish (*Trichomycterus bogotensis*) and ecological implications. *Zoomorphology* **2024**, *143*, 433–441. https://doi.org/10.1007/s00435-023-00634-3

[17] Xiong, D.; Zhang, L.; Yu, H.; Xie, C. A study of morphology and histology of the alimentary tract of *Glyptosternum maculatum* (Sisoridae, Siluriformes). *Acta Zool.* **2011**, *92*, 161–169. https://doi.org/10.1111/j.1463-6395.2010.00458.x

[18] Cyrino, J. P. E.; Bureau, D. P.; Kapoor, B. G. *Feeding and Digestive Functions of Fish*, 1st ed.; CRC Press: Boca Raton, FL, 2008.

[19] Yuge, S.; Yamagami, S.; Inoue, K.; Suzuki, N.; Takei, Y. Identification of two functional guanylin receptors in eel: Multiple hormone-receptor system for osmoregulation in fish intestine and kidney. *Gen. Comp. Endocrinol.* **2006**, *149*, 10–20. https://doi.org/10.1016/j.ygcen.2006.04.012

[20] Grosell, M.; Taylor, J. R. Intestinal anion exchange in teleost water balance. *Comp. Biochem. Physiol. A Mol. Integr. Physiol.* **2007**, *148*(1), 14–22. https://doi.org/10.1016/j.cbpa.2006.10.017

[21] Brandtzaeg, P. Mucosal immunity: Induction, dissemination, and effector functions. *Scand. J. Immunol.* **2009**, *70*(6), 505–515. https://doi.org/10.1111/j.1365-3083.2009.02319.x

[22] Vieira-Lopes, D. A.; Pinheiro, N. L.; Sales, A.; Ventura, A.; Araújo, F. G.; Gomes, I. D.; Nascimento, A. A. Immunohistochemical study of the digestive tract of *Oligosarcus hepsetus*. *World J. Gastroenterol.* **2013**, *19*, 1919–1929. https://doi.org/10.3748/wjg.v19.i12.1919

[23] Purushothaman, K.; Lau, D.; Saju, J. M.; Musthaq, S.; Lunny, D. P.; Vij, S.; Orbán, L. Morpho-histological characterisation of the alimentary canal of an important food fish, Asian seabass (*Lates calcarifer*). *PeerJ* **2016**, *4*, e2377. https://doi.org/10.7717/peerj.2377

[24] Na Lampang, P.; Palasai, A.; Senarat, S.; Jiraungkoorskul, W.; Kettratad, J. Observation of gut content and morpho-histology of the digestive system in *Pisodonophis boro* (Hamilton, 1822) from Pranburi River Estuary, Thailand. *Songklanakarin J. Sci. Technol.* **2021**, *43*(2), 496–504.

[25] Kasozi, N.; Iwe, G. D.; Langi, S.; Namulawa, V. T.; Walakira, J. Histological features of the gastrointestinal tract of elongate tigerfish, *Hydrocynus forskahlii* (Cuvier, 1819), from Lake Albert. *J. Basic Appl. Zool.* **2024**, *85*, 11. https://doi.org/10.1186/s41936-024-00364-y

[26] Currie, S.; Evans, D. H. *The Physiology of Fishes*, 5th ed.; CRC Press: Boca Raton, FL, 2021.

[27] Ghosh, S. K.; Chakrabarti, P. Histological and histochemical characterization on stomach of *Mystus cavasius*, *Oreochromis niloticus* and *Gudusia chapra*: Comparative study. *J. Basic Appl. Zool.* **2015**, *70*, 16–24. https://doi.org/10.1016/j.jobaz.2015.04.002

[28] Guillard, J.; Tessier, A.; Beaune, D.; Kue, K.; Cottet, M.; Chanudet, V.; Descloux, S.; Panfili, J. Life History Traits and Exploitation of *Hampala macrolepidota* (Cyprinidae) in a Subtropical Reservoir (Lao PDR). *Cybium* **2019**, *43*(4), 351–365.

[29] Titin, H.; Yustiatia, A.; Nurhayatia, A. Growth Patterns and Reproduction of *Hampala macrolepidota* in Jatigede Reservoir, West Java, Indonesia. *InaJL* **2022**, *3*(2), 66–75. https://doi.org/10.51264/inajl.v3i2.33

[30] Ahmad, A. B. *Hampala macrolepidota*. *The IUCN Red List of Threatened Species* **2019**, e.T181255A1714119. https://doi.org/10.2305/IUCN.UK.2019-2.RLTS.T181255A1714119.en (accessed October 31, 2025).

[31] Risdawati, R.; Dahelmi, D.; Nurdin, J.; Syandri, H. Bioecological Aspects of *Hampala macrolepidota* in Lake Singkarak, West Sumatera, Indonesia. *AACL Bioflux* **2020**, *13*(2), 893–901.

[32] Liu, M. D.; Huang, F. J.; Zhu, J. Z.; Liu, R. C.; Liu, S. P. Reproductive Biology of *Hampala macrolepidota*. *Chin. J. Zool.* **2015**, *50*(3), 405–414.

[33] Bancroft, J. D.; Gamble, M. *Theory and Practice of Histological Techniques*; Churchill Livingstone: London, U.K., 2002.

[34] Bočina, I.; Šantić, Ž.; Restović, I.; Topić, S. Histology of the Digestive System of the Garfish *Belone belone*. *Eur. Zool. J.* **2017**, *81*(1), 89–95.

[35] de Oliveira Ribeiro, C. A.; Fanta, E. Microscopic Morphology and Histochemistry of the Digestive System of *Trichomycterus brasiliensis*. *Rev. Bras. Zool.* **2000**, *17*(4), 953–971. https://doi.org/10.1590/S0101-81752000000400007

[36] Gómez-Ramírez, E.; Tovar, O.; Bulla, M. J. O.; Hurtado, H. Estudio Histológico del Tracto Digestivo del Pez *Ariopsis seemanni*. *Rev. Fac. Cienc. Básicas* **2010**, *6*(2), 216–225.

[37] Beltran, L. G.; Santana, V. D.; Verdugo, M. H.; Gómez-Ramírez, E.; Hurtado-Giraldo, H. Descripción Anatómica e Histológica del Tracto Digestivo de *Pimelodus blochii*. *Orinoquia* **2013**, *17*(1), 102–110. https://doi.org/10.22579/20112629.55

[38] Olaya, C. M.; Ovalle, C. H.; Gómez, E.; Rodríguez, D.; Caldas, M. L.; Hurtado, H. Histología y Morfometría del Sistema Digestivo de *Pimelodus pictus*. *Rev. Fac. Med. Vet. Zootec.* **2007**, *54*, 311–323.

[39] Elliott, D. G. *Integumentary System*; Academic Press: United Kingdom, 2000. https://doi.org/10.1016/B978-012529650-2/50008-1

[40] Mello, G. C. G.; Santos, M. L.; Arantes, F.; Pessali, T. C. Morphological Characterisation of the Digestive Tract of *Lophiosilurus alexandri*. *Acta Zool.* **2017**, 1–10.

[41] Chivers, D. P.; Wisenden, B. D.; Hindman, C. J.; Michalak, T. A.; Kusch, C.; Kaminskyj, S. G. W.; Jack, K. L.; Ferrari, M. C. O.; Pollock, R. J.; Halbgewachs, C. F.; Pollock, M. S.; Alemadi, S.; James, C. T.; Savaloja, R. K.; Goater, C. P.; Corwin, A.; Mirza, R. S.; Kiesecker, J. M.; Brown, G. E.; Adrian, J. C.;

Krone, P. H.; Blaustein, A. R.; Mathis, A. Epidermal Alarm Substance Cells of Fishes Maintained by Non-Alarm Functions. *Proc. R. Soc. B* **2007**, 1–9.

[42] Nazlić, M.; Paladini, A.; Bočina, I. Histology of the Digestive System of *Scorpaena porcus*. *Acta Adriat.* **2014**, *55*(1), 65–74.

[43] Machado, M. R. F.; de Oliveira Souza, H.; de Souza, V. L.; de Azevedo, A.; Goitein, R.; Nobre, A. D. Morphological and Anatomical Characterization of the Digestive Tract of *Centropomus parallelus* and *C. undecimalis*. *Acta Sci.* **2013**, *35*(4), 467–474. https://doi.org/10.4025/actascibiolsci.v35i4.14352

[44] Pewhom, A.; Vanikasampanna, A. Histological Structure and Histochemistry of the Digestive Tract of *Pristolepis fasciata*. *ASEAN J. Sci. Technol. Rep.* **2024**, *27*(4). https://doi.org/10.55164/ajstr.v27i4.253044

[45] Morais, S. The Physiology of Taste in Fish: Potential Implications for Feeding Stimulation and Gut Chemical Sensing. *Rev. Fish. Sci. Aquac.* **2017**, 1–17.

[46] Pedini, V.; Dall'Aglio, C.; Parillo, F.; Scocco, P. A Lectin Histochemical Study of the Oesophagus of Shidrum. *J. Fish Biol.* **2004**, *64*, 625–631. https://doi.org/10.1111/j.1095-8649.2004.00326.x

[47] Abd, E. A.; Hafez, E.; Mokhtar, D.; Abou-Elhamd, A. S. Comparative Histomorphological Studies on Oesophagus of Catfish and Grass Carp. *J. Histol.* **2013**, 1–10. https://doi.org/10.1155/2013/858674

[48] Mittal, R. K.; Holloway, R. H.; Penagini, R.; Blackshaw, L. A.; Dent, J. Transient Lower Esophageal Sphincter Relaxation. *Gastroenterology* **1995**, *109*(2), 601–610. https://doi.org/10.1016/0016-5085(95)90351-8

[49] Wilson, J. M.; Castro, L. F. C. Morphological Diversity of the Gastrointestinal Tract in Fishes. In *Fish Physiology: The Multifunctional Gut of Fish*; Grosell, M.; Farrell, A. P.; Brauner, C. J., Eds.; Academic Press: United States, 2011; pp 1–55.

[50] Sangsawang, A.; Vaniksampanna, A.; Intachai, S.; Pewhom, A. Histological and Histochemical Characteristics of the Digestive Tract of *Mastacembelus favus*. *Trends Sci.* **2025**, *22*(11), 10687. https://doi.org/10.48048/tis.2025.10687

[51] Bebić, M.; Kević, N.; Restović, I.; Šantić, M.; Bočina, I. Histological and Histochemical Studies of Digestive System in *Lepidorhombus whiffiagonis*. *Iran. J. Ichthyol.* **2020**, *7*, 125–135.

[52] Grosell, M.; Farrell, A. P.; Brauner, C. J. *The Multifunctional Gut of Fish*; Academic Press: United States, 2011.

[53] Scocco, R.; Pedini, V. Histochemical Characterisation of Complex Carbohydrates Expressed in the Alimentary Tract of Chickens. *Vet. J.* **2010**, *185*, 228–230. https://doi.org/10.1016/j.tvjl.2009.04.015

[54] Day, R. D.; German, D. P.; Manjakasy, J. M.; Farr, I.; Hansen, M. J.; Tibbetts, I. R. Enzymatic Digestion in Stomachless Fishes. *J. Comp. Physiol. B* **2011**, *181*, 603–613.

[55] Canan, B.; do Nascimento, W. S.; da Silva, N. B.; Chellappa, S. Morphohistology of the Digestive Tract of *Stegastes fuscus*. *Sci. World J.* **2012**, 787316, 1–9. https://doi.org/10.1100/2012/787316

[56] Carrassón, M.; Grau, A.; Dopazo, L. R.; Crespo, S. A Histological, Histochemical and Ultrastructural Study of the Digestive Tract of *Dentex dentex*. *Histol. Histopathol.* **2006**, *21*, 579–593.

[57] Quintana-Hayashi, M. P.; Mahu, M.; De Pauw, N.; Boyen, F.; Pasmans, F.; Martel, A.; Premaratne, P.; Fernandez, H. R.; Teymournejad, O.; Maele, L. V.; Haesebrouck, F.; Lindén, S. K. Binding of *Brachyspira hyodysenteriae* to Porcine Colonic Mucins. *Infect. Immun.* **2015**, *83*(4), 1610–1619. https://doi.org/10.1128/IAI.03073-14

[58] Lu, F.; Li, Y.; Wang, X.; Hu, X.; Liao, X.; Zhang, Y. Early-Life Polyphenol Intake Promotes *Akkermansia* Growth. *Food Res. Int.* **2021**, *149*, 110648. https://doi.org/10.1016/j.foodres.2021.110648

[59] García, A.; Hernández, J.; Pardo, S. C. Descripción Morfológica del Tubo Digestivo de Juveniles de *Salminus affinis*. *Acta Biol. Colomb.* **2008**, *13*, 99–112.

ASEAN
Journal of Scientific and Technological Reports
Online ISSN:2773-8752

Research article

Optimizing Brown Rice Drying With Modified LSU Systems For Energy Efficiency, Carbon Reduction, and 2AP Preservation

Sompot Khomkaew[1], Nattapong Suksabai[2], Tanawat Srirugsa[3, 4], Tawat Chuchit[3, 4], Wiwat Su-hren[3], and Supachai Kaewpoung[3, 4*]

[1] Faculty of Industry and Technology, Rajamangala University of Technology Rattanakosin Wang Klai Kangwon Campus, Prachuap Khiri Khan, 77110, Thailand
[2] Faculty of Engineering at Kamphaeng Saen, Kasetsart University, Kamphaeng Saen, Nakhon Pathom, 73140, Thailand
[3] Faculty of Engineering, Thaksin University, Phatthalung, 93210, Thailand
[4] Center of Excellence for Agricultural Innovation and Bioproducts of Thaksin University, Thaksin University, Phatthalung, 93210, Thailand
* Correspondence: supachai.ka@tsu.ac.th

Citation:
Khomkaew, S., Suksabai, N., Srirugsa, T., Chuchit, T., Su-hren, W., Kaewpoung, S., Optimizing brown rice drying with modified LSU systems for energy efficiency, carbon reduction and 2AP preservation. *ASEAN J. Sci. Tech. Report.* **2026**, *29*(4), e260421. https://doi.org/10.55164/ajstr.v29i4.260421

Article history:
Received: July 19, 2025
Revised: February 3, 2026
Accepted: February 22, 2026
Available online: March 25, 2026

Publisher's Note:
This article is published and distributed under the terms of the Thaksin University.

Abstract: This research examines how the quality of 2AP in Thai fragrant brown rice is affected by non-continuous LSU drying, emphasizing thermal energy management, moisture content, and aroma retention, which exhibit significant interrelationships and nonlinear responses across drying conditions and carbon emissions. The drying system employed an LSU-type dryer, a cyclone hot-air furnace, and a paddle mixer, using 4 tons of coal daily. This is equivalent to 26,680 kWh daily or an average power of 1,112 kW. The experiment took place in two stages: the first used 16,008 kWh/day to bring rice moisture down to 24.3-29.3%, averaging 26.5%, while the second used 10,672 kWh/day to reduce moisture to 10.9-12.4%, averaging 12.0%. During the 33.3% (stage-2 saving), energy use decreased the total system saving by 54.71%. In line with this, CO_2 emissions dropped from 13,337 kg.CO_2/day to 8,003 kg.CO_2/day a decrease of 5,334 kg.CO_2/day. Drying was meticulously controlled, with furnace temperatures maintained below 145°C and hot-air temperatures kept below 120°C. The research, conducted at a commercial rice mill operated by Maejaitana Chotiwat Co., Ltd., documented 2AP levels ranging from 1.83 to 2.67 μg/g, averaging 2.14 μg/g, with a mean drying temperature of 37.8°C. The results suggest that energy management, moisture control, and aroma retention are positively correlated. The study underscores the promise of low-emission, energy-efficient drying methods for improving product quality and promoting sustainability in the agro-industrial sector, with potential applications for crops such as cassava and corn.

Keywords: 2AP; LSU-Type drying system; thermal energy management; carbon emissions reduction; sustainable agro-industry

1. Introduction

Rice processing technology faces critical challenges in balancing product quality, energy efficiency, and environmental sustainability. For aromatic rice varieties, particularly Thai fragrant rice, preserving the distinctive 2-Acetyl-1-Pyrroline (2AP) compound during drying represents a significant technical challenge, as demonstrated by Bryant et al. [1]. Traditional high-temperature drying methods, while efficient for moisture reduction, often compromise the sensory qualities that command premium market prices [2-3]. The Louisiana State University (LSU) drying system has become the industry standard in Thailand, accounting for 64.4% of industrial rice dryers and processing 79.3% of

production volume, according to industry surveys. These systems typically employ continuous recirculation with either rice husk or coal as the primary fuel, achieving substantial throughputs of 41.6 tons per hour during continuous 24-hour operations reported by Soponronnarit [4]. However, conventional operating parameters often subject rice kernels to thermal conditions that accelerate the degradation of volatile aromatic compounds, particularly when combustion chamber temperatures exceed 145°C [5]. Research on 2AP stability has demonstrated that this compound is most stable between 18-60°C, with significant deterioration at elevated temperatures [6]. Paradoxically, some studies indicate that under specific controlled conditions, temperatures between 100-150°C can actually promote 2AP formation, highlighting the complex relationship between thermal treatment and aromatic quality [7]. This suggests that precisely managed drying protocols could potentially enhance rather than degrade sensory attributes.

Current industrial drying systems consume between 3.874 and 4.421 MJ/kg of evaporated water, representing a substantial energy input and corresponding environmental impacts, according to Jittanit et al. [8]. Mathematical modeling by Sarker et al. [9] identified optimal drying parameters for efficiency, including a bed thickness of 10 cm, a specific airflow rate of 0.05 kg/s (corresponding to an air velocity of 2.3 m/s), and carefully controlled residence times. These parameters achieved moisture reduction from 30% to 24.3% (dry basis) with specific electrical energy consumption of 0.48 MJ/kg and thermal energy of 6.15 MJ/kg of evaporated water. The environmental implications of rice processing have received increasing attention, particularly regarding carbon emissions. Standard LSU systems using 4 tons of coal daily generate approximately 13,337 kg of CO_2, contributing significantly to Thailand's agricultural carbon footprint, according to the Thailand National Life Cycle Inventory Database [10]. Research by Lertworasirikul and Prachayawarakorn [11] demonstrated that initial high-temperature treatment at 150°C for 3 minutes, followed by cooling and tempering phases, could reduce moisture from 33% to 16.5% in approximately 53 minutes without compromising yield or appearance. Similarly, experimental data from Treeamnuk et al. [12] indicated that airflow rates of 0.0512 m^3/s achieved optimal moisture extraction with specific energy consumption of 7.25 MJ/kg, while slightly higher airflow (0.0631 m^3/s) maximized head rice yield at 36.84%.

Alternative drying approaches have also demonstrated potential for quality preservation. Research by Kaensup et al. [13] found that high-moisture paddy (initial moisture >24% wet basis) could be effectively reduced to 18% (wet basis) in just 3-4 seconds using hot air at moderately elevated temperatures (50-60°C) without inducing kernel cracking, suggesting opportunities for rapid, gentle moisture removal. Intermittent drying, consisting of alternating drying and tempering phases, has been widely recommended by Jaisut et al. [14] to optimize moisture uniformity while reducing overall processing time. The nutritional implications of drying methods further underscore the importance of optimized processing. Comparative analyses by Moongngarm and Saetung [15] demonstrated that drying temperatures significantly impact essential nutrients, including gamma-aminobutyric acid (GABA) and antioxidant compounds. Low-temperature methods better preserved anthocyanins and γ-oryzanol compared to conventional hot air drying, while high temperatures accelerated anthocyanin degradation and color changes by Tian et al. [16], Somta et al. [17]. Installing a paddle mixer improves the system's uniformity of heat distribution, which increases the heating process' efficiency, according to a study by Phetnamkhiew et al. [18]. Modified drying protocols developed by Meesukchaosumran and Chitsomboon [19] demonstrated the potential to reduce emissions by over 5,000 kg of CO_2 per day while maintaining product quality, aligning with growing industry sustainability goals. Two-stage drying processes have shown particular promise in optimizing both quality and efficiency.

This research aims to investigate optimized drying protocols for LSU systems that preserve 2AP content in Thai fragrant brown rice while reducing energy consumption and carbon emissions. By establishing precise correlations between thermal management, moisture reduction, and aromatic quality, this study seeks to develop commercially viable modifications to existing infrastructure that balance product excellence with environmental and economic sustainability.

2. Materials and Methods

2.1 System Design Modifications to Standard LSU Dryers

The experimental setup modified a commercial-scale LSU dryer at Maejaitana Chotiwat Co., Ltd. (Figure 1) according to the principles established by Soponronnarit [4]. The standard system consisted of four drying chambers with a throughput capacity of 25 tons per hour, operating continuously over 24 hours. We installed a cyclone-type hot air furnace with precise temperature control mechanisms based on the designs of Kaensup et al. [13], and we integrated a paddle mixer to enhance uniformity of heat distribution, as recommended by Phetnamkhiew et al. [18]. Air distribution channels were retrofitted to create a two-stage drying system with separate temperature zones following specifications from Jittanit et al. [8], and adjustable airflow regulators were implemented to maintain optimal velocities between 1-4 m/s as identified by Meesukchaosumran and Chitsomboon [19]. The system used coal as its primary fuel, consuming approximately 4 tons daily (equivalent to 26,680 kWh/day, or an average power of 1,112 kW).



Figure 1. Components for the LSU dryer of Maejaitana Chotiwat Co., Ltd.

The system starts with the intake of paddy rice at the receiving point (No. 1) with an initial moisture content of about 28-30%, as shown in Figure 2, before processing. The first bucket elevator (No. 2) lifts the paddy and sends it into the cleaning process, which consists of two passes through a vibrating sieve unit (No. 3) to remove dust, debris, and other contaminants. The dust collection unit (No. 13) receives these separated materials. After this, the cleaned paddy is conveyed by the second bucket elevator (No. 2) into the first LSU drying chamber (No. 4), where it is subjected to hot air from a husk-fired furnace (No. 8). Husk fuel is delivered from a storage bin (No. 12) through a feed pipe (No. 6), and combustion efficiency is improved by a forced-draft air blower (No. 10). The hot air generated is conveyed via a duct (No. 9) into the LSU dryer. Inside the drying chamber, a hot-air control system (No. 7) ensures efficient heat transfer and uniform contact with the

paddy grains through a two-stage moisture-reduction process. The outlet (No. 5) discharges the paddy that has been partially dried, and it then enters the next LSU dryers (No. 4: second through fourth units) in a continuous stream until its moisture content reaches the target level of about 14%. Once the drying process is finished, the dried paddy is transported by the final bucket elevator (No. 2) to a storage bin (Storage) for either transportation or additional processing.

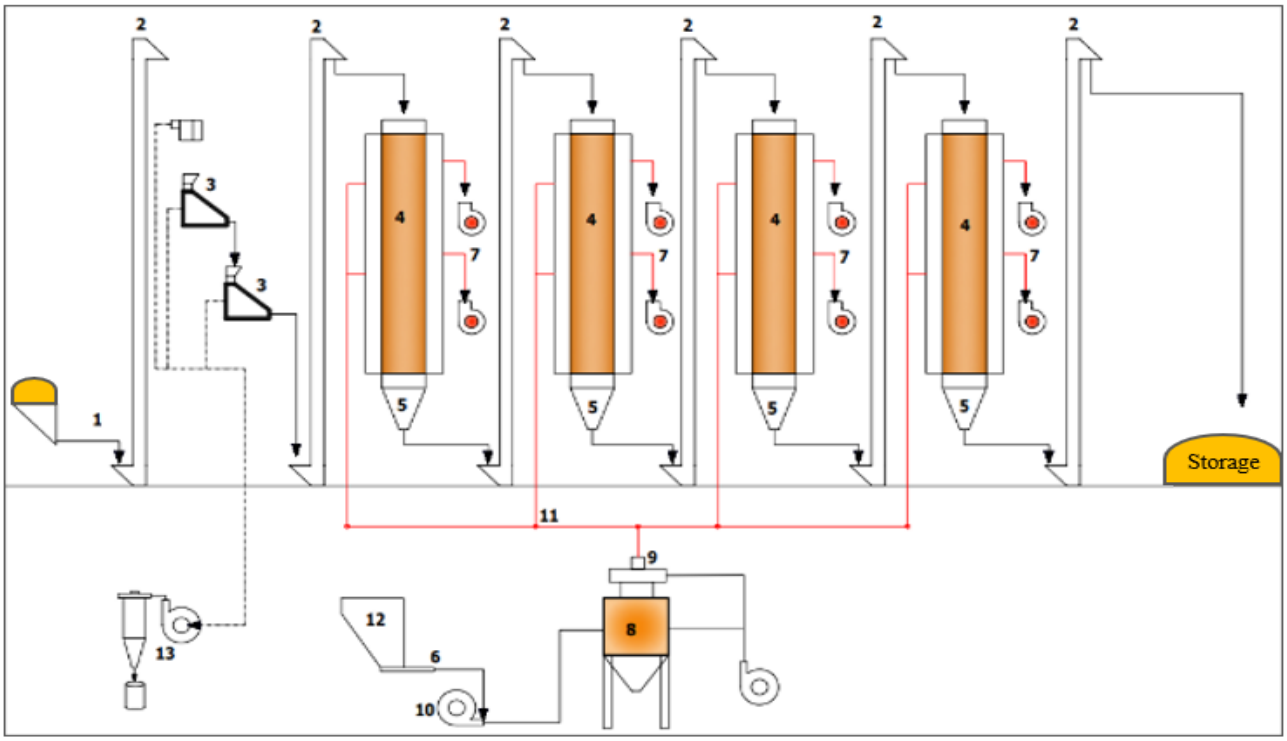


Figure 2. Single-line diagram for the LSU model system.

2.1.1 Replication and Sample Size

Experimental Replication

All drying experiments were conducted with **three independent biological replications (n = 3)**. Each replication consisted of a separate batch of freshly harvested paddy rice (approximately 200 kg per batch) dried on different days under identical operating conditions. **Pre-drying phase:** 5 temperature settings × 3 replications = **15 runs**. **Post-drying phase:** 5 temperature settings × 3 replications = **15 runs**. In total, **30 independent drying batches** were evaluated.

2AP Sample Size

At each sampling time, three subsamples (≈50 g each) were collected from the top, middle, and bottom layers of the dryer. These were pooled and homogenized into a single composite sample per batch, and the composite samples were analyzed in triplicate by GC–MS. Thus, the effective sample size per time point was n = 3 (biological replicates) × 3 (analytical replicates) = 9n. All 2AP data are reported as **mean ± standard deviation**.

2.1.2 Control Experiments (Conventional vs. Modified LSU Dryer)

The conventional and modified LSU dryers were operated **simultaneously** in the same facility under identical conditions, including ambient temperature and humidity, paddy source and harvest date, initial moisture content, airflow rate, and batch size. The systems were installed side-by-side and tested in parallel, ensuring that observed differences were attributable solely to dryer modification.

2.1.3 Statistical Analysis

All statistical analyses were performed using **SPSS version 26.0**. Data normality and homogeneity of variance were assessed using the **Shapiro–Wilk** and **Levene's tests**, respectively. Mean differences among treatments were evaluated by **one-way ANOVA**, followed by **Tukey's HSD** post hoc test at $p < 0.05$. A **multiple linear regression model** was applied to examine the effects of drying temperature, moisture content, and drying phase on 2AP concentration.

2.1.4 Moisture Increase During Pre-Drying

The temporary moisture increase observed in Table 3 (e.g., 25.1% to 28.5%) is attributed to **hygroscopic rewetting** caused by ambient humidity fluctuations during pre-drying, particularly when the burner was inactive, relative humidity exceeded 85%, and grain temperature fell below the ambient dew point. This phenomenon, commonly reported in tropical drying environments (Soponronnarit, 1997; ASABE Standards), reflects environmental moisture exchange rather than system malfunction.

2.2 Multi-Stage Temperature Control Protocols

Grounded in the study by Treeamnuk et al. [12], a temperature control protocol was developed and applied to a drying process divided into two stages. During the first stage (initial drying phase), the furnace temperature was maintained at 145°C, while the temperature in the drying chamber ranged from 36.7 to 39.2°C, averaging 37.8°C. To bring the moisture content down to 24.3-29.3% on a wet basis, the process used an average of 16,008 kilowatt-hours of energy daily. This phase lasted for a duration adjusted to the amount of paddy being dried. During the second stage (final drying phase), the furnace temperature was lowered to 120°C, and the temperature within the drying chamber ranged from 36.7°C to 39.2°C, averaging 37.8°C. Consequently, energy use dropped to 10,672 kilowatt-hours per day, and the moisture content was further reduced into the target range of 10.9-12.4% on a wet basis. To maintain rice quality and improve moisture diffusion efficiency, a tempering period was added, as advised by Jaisut et al. [14].

2.3 Real-Time Monitoring of 2AP and Moisture Content

Quantification of 2-acetyl-1-pyrroline (2AP) was performed using an external calibration curve constructed from authentic 2AP standards (0.1–10 μg/g, $R^2 > 0.995$). 2,4,6-trimethylpyridine was used as the internal standard to correct for injection and matrix effects. The limit of detection (LOD) and limit of quantification (LOQ) were determined at signal-to-noise ratios of 3 and 10, respectively (LOD = 0.03 μg/g; LOQ = 0.10 μg/g). Method validation was performed through triplicate analyses, recovery tests (92–105%), and intra-day and inter-day precision (RSD < 5%). The aroma compounds in brown rice were analyzed using headspace comprehensive two-dimensional gas chromatography-time-of-flight mass spectrometry (HS-GCxGC-TOFMS). The sample preparation process included grinding the rice into flour using a TissueLyser 2 instrument. As outlined by Calingacion et al. (2014) [20], a 1 g sample of rice flour was placed in a sealed vial and incubated at room temperature for at least 12 hours before analysis to allow aroma compounds to equilibrate. The quantification of 2AP was reported in μg/g, based on an analysis conducted with LECO's HS-GCxGC-TOFMS system. The moisture content of rice was determined using traditional methods, with calculations on both wet and dry bases according to the standardized protocol. Using the wet basis method, moisture content is expressed as a percentage of the water weight relative to the total sample weight. According to the 2014 rice seed standard, rice seeds should retain a moisture content of 12-14% after moisture reduction. A seed moisture meter or oven-drying can be used to measure moisture content, with the percentage calculated from the weight or volume loss of water. This study employed the equation proposed by Soponronnarit [4] to calculate moisture content. Hourly rice samples were collected during the drying process, and calibrated thermocouples recorded the rice temperature simultaneously. The sample preparation consisted of the following steps: (i) grinding rice into flour using a Tissue Lyser 2, (ii) placing 1-gram portions of flour into sealed vials to equilibrate at room temperature for at least 12 hours, (iii) analyzing with LECO's HS-GCxGC-TOFMS system, and (iv) recording the quantification of 2AP in μg/g. The moisture content was evaluated using both wet- and dry-basis methods as per ASAE Standards (2002) [21], with calculations derived

from the provided formulas. In equation (1), is used for this calculation. The standard moisture content on a dry basis is calculated as the ratio of the material's moisture content to its dry weight, as shown in equation (2).

$$M_w = \frac{W_w}{W} = \frac{W - W_d}{W} \quad (1)$$

$$M_d = \frac{W_w}{W_d} = \frac{W - W_d}{W_d} \quad (2)$$

When M_w is wet basis (%)

M_d is dry moisture basic (%)

W is mass of material (kg)

W_w is mass of moisture (kg)

W_d is dry mass (kg)

For research by Kaensup et al. [13], it is possible to reduce the moisture content of high-moisture paddy (initial moisture >24% wet basis) to about 18% (wet basis) in only 3-4 seconds using hot air at a temperature of 50-60°C, without resulting in kernel cracking. This approach is appropriate for applications on small-scale farms. Ultimately, tests were carried out with a cyclone-type hot-air furnace using 4 tons of coal per day, with a system comprising four drying chambers that had a throughput of 25 tons per hour and operated continuously for 24 hours (Table 1) compares fuel consumption among nine dryer types.

Table 1. Results on energy consumption of dryers.

Model of dryers	Evaporation capacity ($kg.H_2O/h.m^2$)	Energy consumption ($kJ/kg\ of\ H_2O$)
Tunnel dryer	70/m²-	5,800
Band dryer	60/m²-	4,200
Impingement dryer	50/m²	5,400
Rotary dryer	30-80/m²	5,500
Fluidized bed dryer	30/m²	4,300
Flash air dryer	5-100/m² (Depends on particle size)	4,700
Spray dryer	1-30/m²	10,000
Drum dryer	6-20/m²	6,600
Dryer LSU	40/m²	800 -1,200

2.4 Energy Consumption and Carbon Emission Measurement

Energy consumption was estimated from coal input rather than directly measured. Theoretical analysis of moisture content was performed on a dry-basis and compared with a constant value, denoted as , representing the heat supplied to the air by the heating system. This value corresponds to the difference in the enthalpy flow of the inlet air, as defined in Equation (3).

$$Q_a = M_a(C_a + C_v H_1)(T_1 - T_2)t \quad (3)$$

When Q_a is heat received by the air (kJ)

M_a is mass flow rate (kg_{dryair}/h)

H_1 is the humidity ratio (kg_{water}/kg_{dryair})

C_a is the specific heat of dry air (kJ/kg_{dryair}°C)

C_v is the specific heat of steam (kJ/kg_{water}°C)

T_1 is the air temperature before (°C)
T_2 is the temperature of the air leaving (°C)
t is the drying time (h)

To determine the heat output of the air heating system, psychrometrics are used. With respect to the drying chamber, we can determine the heat required to evaporate water from the material using equation (4).

$$Q_{evap} = W_d (M_i - M_f) h_{fg} \tag{4}$$

When Q_{evap} does it evaporate (kJ)
M_i is moisture before drying (%)
M_f is the moisture content after drying (%)
h_{fg} is the latent heat of water (kJ/kg)

The heat required to raise the drying material's temperature from its initial value to its final value upon leaving the drying machine can be calculated using equation (5).

$$Q_s = W_d C_{pd} (T_{p2} - T_{p1}) + W_d C_{pw} (T_{p2} - T_{p1}) M_i \tag{5}$$

When Q_s is heat raising the material temperature (kJ)
C_{pd} is the specific heat of dry material (kJ/kg°C)
C_{pw} is the specific heat of water (kJ/kg°C)
T_{p1} is the temperature before drying (°C)
T_{p2} is the temperature after drying (°C)

According to equation (5), which calculates the thermal energy involved in drying, it can be used to determine the electrical energy required to convert that thermal energy. This conversion can be carried out with the help of equation (6), which demonstrates how the thermal energy relates to the actual electrical energy used in the system.

$$E_s = \frac{Q_s}{\eta 3600} \tag{6}$$

When E_s is the actual electrical energy used (kWh)
η is the efficiency of the drying system (0 to 1)

Furthermore, the electricity emission factor was replaced with a coal combustion emission factor (~0.95 kg CO_2/kWh) sourced from the Thailand National LCI Database (TIIS–MTEC, NSTDA). The carbon footprint calculation was based on the IPCC 2013 GWP 100a V1.030 method and is consistent with AR5 data, incorporating TGO electricity statistics for the period 2016–2018. The term **retention** is used consistently throughout the manuscript, with **loss** reported only as a secondary metric.

3. Results and Discussion

3.1 Temperature-Moisture-2AP Relationships During Drying

Across both drying phases, drying temperature and moisture content showed clear effects on 2AP concentration. During pre-drying (Table 2), rice held at 30.8–39.5°C and 24.3–29.3% moisture produced 2AP levels of 4.92–5.59 μg/g. In contrast, post-drying at slightly higher temperatures (36.7–39.2°C) but much lower moisture contents (10.9–12.4%) resulted in reduced 2AP levels of 1.83–2.67 μg/g. Temperature control was therefore critical for preserving aroma. The optimal temperature range for 2AP retention during final drying was 36.7–38.0°C (Figure 3), with an average concentration of 2.14 μg/g, corresponding to approximately 41% retention of the original aroma. This agrees with Buttery et al. [2], who reported that 2AP is stable between 18 and 60°C but degrades rapidly at higher temperatures. The temperature–2AP relationship was nonlinear. Although 2AP was 2.15 μg/g at 36.7°C, it decreased to 1.83 μg/g at 38.2°C before rising to 2.67 μg/g at 38.4°C, supporting the findings of Laohakunjit and Noomhorm [3] that certain temperatures can enhance 2AP formation via Maillard reactions. In pre-drying, the highest 2AP concentration (5.59 μg/g) occurred at 39.5°C, suggesting that initial thermal treatment activates aroma precursors, consistent with Bryant et al. [1]. As shown in Figure 4, the moisture-reduction profile indicated multiple critical transition points that significantly impacted the final 2AP content. During the initial drying phase, moisture content decreased from roughly 28.3% to 25.9% over 10 hours, while concentrations of 2AP were only slightly affected (5.30 to 5.59 μg/g). The transition between phases (hours 10-12) coincided with a swift decline in 2AP, from 5.59 to 2.32 μg/g, while moisture fell from 25.9% to 11.6%. It seems that the ideal moisture content for preserving 2AP during final drying is between 12.0 and 12.4%, as concentrations were stabilized in the range of 2.15 to 2.67 μg/g. This range reflects a compromise between adequately removing moisture for storage stability and preserving volatile compounds. Wongpichet and Thongpan [6] reported comparable findings, showing that a moisture content below 12% tends to limit the formation of aromatic compounds. Chungcharoen et al. [5] proposed that a gradual moisture reduction of about 1.2% per hour helps reduce stress on rice kernels and maintain their quality attributes. This recommendation is supported by our data, which shows that periods of more rapid moisture reduction (>2% per hour) were associated with increased 2AP losses.

The 3D response surface model (Figure 5) illustrates the complex relationship between temperature, moisture, and 2AP concentration. Two different areas exhibited the greatest 2AP values (>5.0 μg/g): (1) conditions of low temperature (30.8-34.0°C) and high moisture (24.3-29.3%), and (2) conditions of high temperature (39.5°C) and medium moisture (25.9%). Statistical analysis demonstrated a substantial correlation between drying parameters and 2AP retention ($r^2 = 0.78$, $p < 0.01$). Temperature had a greater impact (partial $r^2 = 0.52$) than moisture content (partial $r^2 = 0.26$), corroborating the findings of Meesukchaosumran and Chitsomboon [19] about the importance of thermal management in aromatic rice processing. The optimal processing window was determined to be 37.0-38.0°C with a moisture content of 11.5-12.5%, resulting in an approximate 40-45% retention of 2AP compared to pre-dried samples. This finding aligns with the work of Lertworasirikul and Prachayawarakorn [11], who suggested similar parameters for optimizing energy efficiency and rice quality. It is worth noting that prolonged exposure to temperatures above 38.5°C resulted in significant degradation of 2AP, independent of moisture levels. This finding corroborates the thermal sensitivity thresholds identified in previous research [14]. The observed increase in 2AP at 38.4°C and 12.4% moisture may be associated with temperature-dependent biochemical reactions. While previous studies suggest that enzymatic activity could influence 2AP formation, this mechanism was not directly evaluated in the present study and therefore remains speculative, as suggested by Laokuldilok and Kanha [7]. Our findings demonstrate that a precise thermal management strategy (36.7-38.0°C) and moisture reduction to 12.0-12.4% provide the best compromise between processing efficiency and aroma preservation in Thai fragrant rice.

Furthermore, the effect of drying time on the moisture rice, rice temperature, and 2AP during drying (pre-control phase), Form in (Table 3), the hourly recorded alterations in moisture content, rice temperature, and concentration of 2AP (measured in μg/g) during the pre-control drying phase are presented. The data reveal significant trends that can be used to evaluate the system's effectiveness before implementing temperature and airflow regulation. Rice exhibited a moisture content range of 24.3% to 29.3% (on a wet basis), averaging 26.5%. Even though it was part of a drying operation, moisture reduction did not show a consistent

downward trend during the first 10 hours. This irregularity may stem from uneven distribution of hot air or instability in temperature control within the drying chamber, leading to inefficient moisture removal. These results highlight potential shortcomings in the drying mechanism during the initial phase of operation. The rice temperature ranged from 30.8°C to 39.5°C, averaging at 33.1°C. It is worth noting that hour 10 recorded the highest temperature, 39.5°C. This hour also coincided with the concentration of 2AP reaching its peak value of 5.59 µg/g. The simultaneous rise suggests a potential link between rising temperatures and increased generation or discharge of 2AP, an important aromatic compound that gives aromatic rice its distinctive scent. Throughout the observation period, the 2AP concentration ranged from 4.92 to 5.59 µg/g, with an average of 5.21 µg/g.

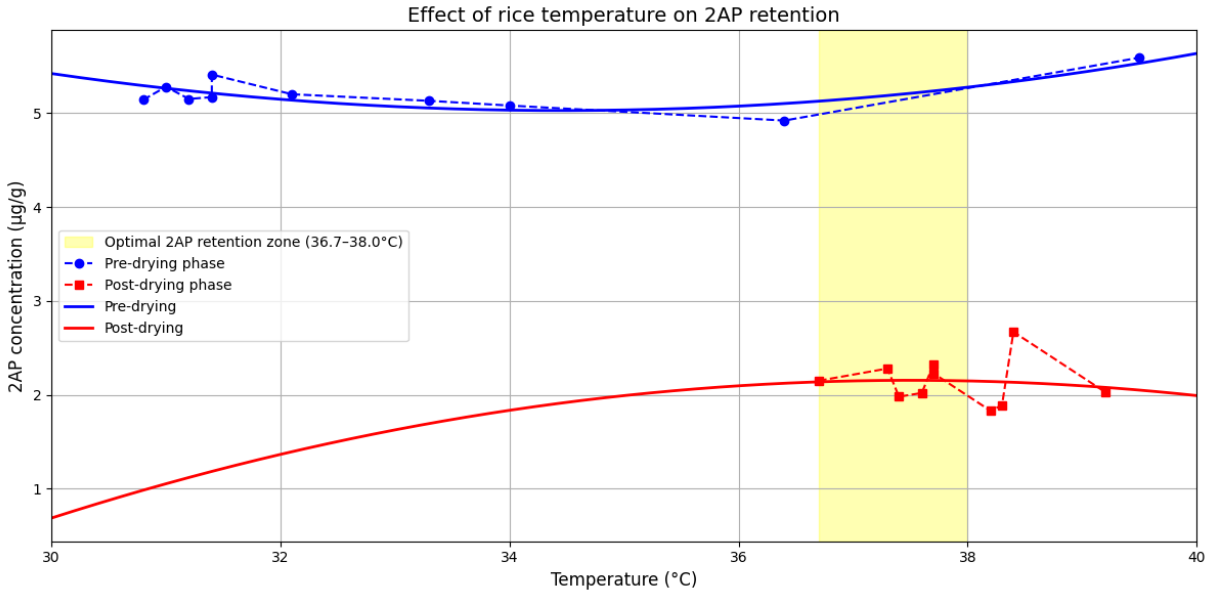


Figure 3. Effect of rice temperature on 2AP retention.

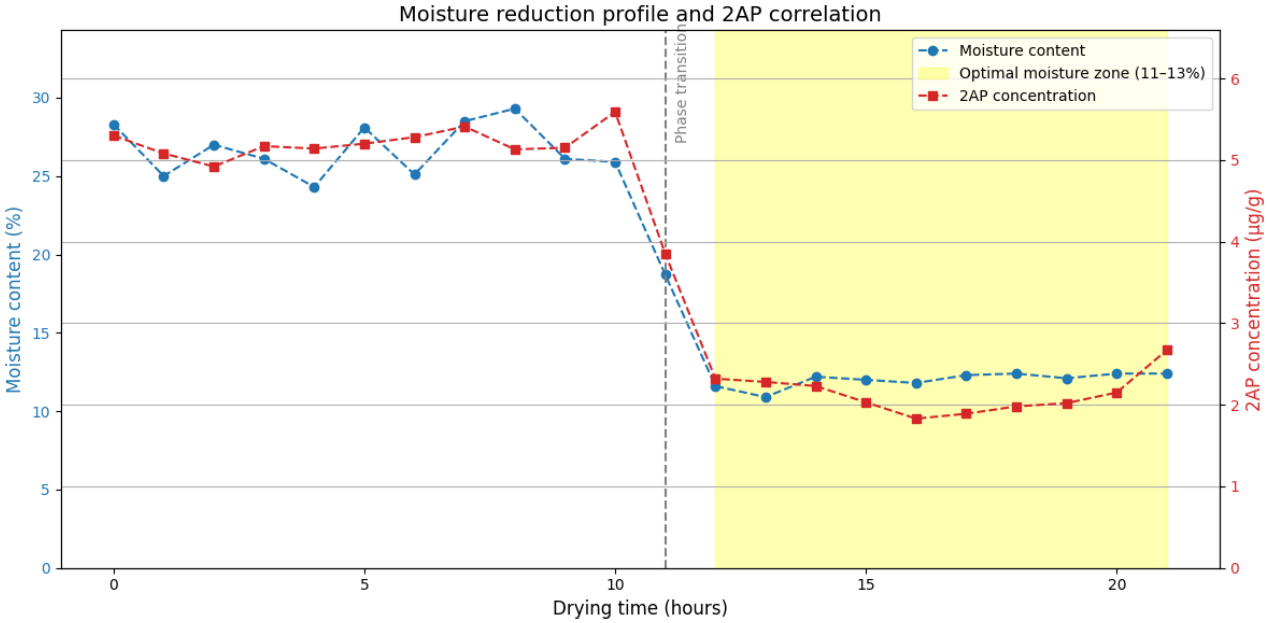


Figure 4. Moisture reduction profile and 2AP correlation.

Table 2. Relationship between temperature, moisture content, and 2AP concentration for two-phase drying.

Drying phase	Temperature range (°C)	Moisture content (%)	2AP concentration (μg/g)	Energy consumption (kWh/day)
Initial (Pre-drying)	30.8-39.5 (avg: 33.1)	24.3-29.3 (avg: 26.5)	4.92-5.59 (avg: 5.21)	16,008
Final (Post-drying)	36.7-39.2 (avg: 37.8)	10.9-12.4 (avg: 12.0)	1.83-2.67 (avg: 2.14)	10,672
Percent change	+14.2%	-54.7%	-58.9%	-33.3%

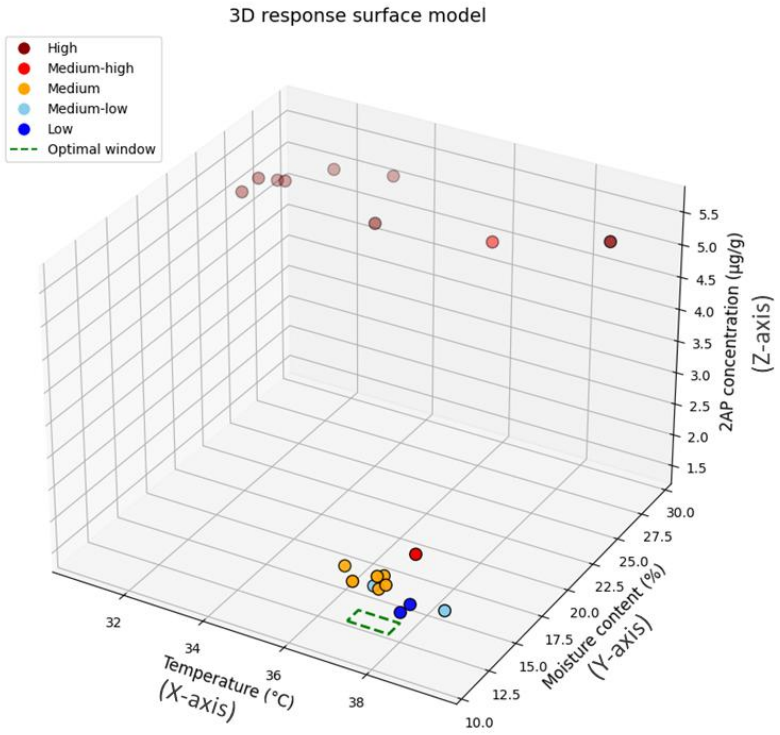
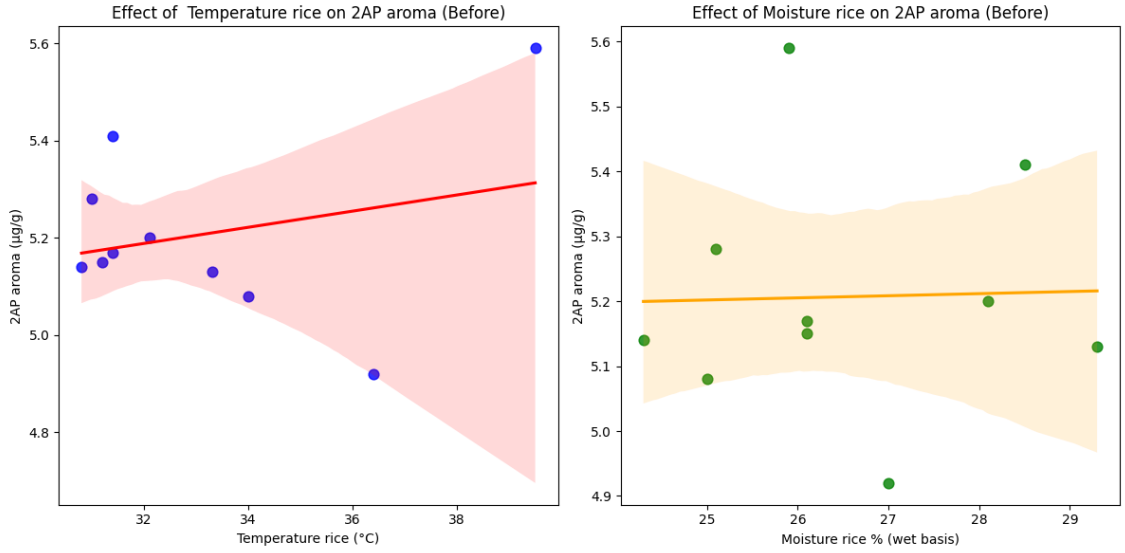


Figure 5. 3D response surface model.

Table 3. Results of the effects of moisture rice, temperature rice, and 2AP aroma during the drying process (Before).

Drying time (h)	Moisture rice % (wet basic)	Temperature rice (°C)	2AP aroma (μg/g)
1	25.0	34.0	5.08
2	27.0	36.4	4.92
3	26.1	31.4	5.17
4	24.3	30.8	5.14
5	28.1	32.1	5.20
6	25.1	31.0	5.28
7	28.5	31.4	5.41
8	29.3	33.3	5.13
9	26.1	31.2	5.15
10	25.9	39.5	5.59
Average	**26.5**	**33.1**	**5.21**

Correlational observations suggest that temperature plays a more significant role than moisture content in influencing 2AP dynamics during the pre-control phase. Although the moisture content did not show a distinct decrease, the gradual rise in rice temperature appeared to promote 2AP accumulation. This highlights the importance of a carefully managed thermal environment to improve aromatic quality during drying. To summarize, the findings show that rice temperature significantly influences 2AP development in the early drying process, while moisture content fluctuated and did not decrease adequately. The results indicate that accurate temperature control could improve aroma compound retention and should be a key consideration in refining drying methods for high-quality aromatic rice production.



(a) (b)

Figure 6. Before the relationship between temperature and 2AP (a), and the moisture of rice and 2AP (b).

As shown in Figure 6, the experimental findings indicate that the temperature of the rice during drying has a major impact on the levels of the aromatic compound 2AP, especially during the first 10 hours of drying. It was discovered that higher temperatures could increase the formation or release of 2AP. Moreover, the hourly analysis showed a weak positive correlation between rice temperature and 2AP concentration. The maximum temperature (39.5°C) coincided with the highest recorded 2AP level (5.59 µg/g), suggesting that increased temperatures could facilitate the formation or release of 2AP. By contrast, moisture content did not show a clear linear correlation with 2AP, though moderate to high aroma levels were frequently associated with values within the 24.3-29.3% moisture range. The average values recorded throughout the monitoring period were as follows: rice moisture content was 26.5%, rice temperature was 33.1°C, and the concentration of 2AP was 5.21 µg/g. The results indicate that keeping drying temperatures in the range of 30.8-39.5°C could aid in preserving aromatic quality. It is advisable to adopt gradual temperature control and to observe the effects of drying for longer than 10 hours. This may provide a better understanding of the impact of prolonged heat exposure and help reduce aroma loss during extended drying.

3.2 Energy Consumption Analysis

Modifying the two-stage drying system yielded considerable improvements in energy efficiency compared with standard LSU operations (Table 4). The total energy consumption decreased from 42,552 kWh/day to 26,680 kWh/day, a 37.3% reduction. The main reason for this efficiency gain was the optimization of thermal management during both processing phases. Energy requirements for phase 1 dropped by 33.3% (from 24,012 to 16,008 kWh/day), whereas phase 2 saw an even more significant 42.4% reduction (from 18,540 to 10,672 kWh/day). The increased efficiency is consistent with the results of Jittanit et al. [8], who found that staged drying methods could save energy by 35–45%. The specific energy consumption (SEC) dropped from 4.42 to 2.76 MJ/kg of water removed, exceeding the benchmark of 3.87 MJ/kg set by Fungpongpan et al. [22] for efficient rice drying. The analysis of energy flow (Figure 7) showed that thermal efficiency rose from 32.4%

to 58.0%, mainly due to reduced heat losses in the furnace (20% compared to 36% in conventional systems) and the exhaust (8% compared to 15%). Mujumdar [23] noted that temperature differentials and airflow regulation have a strong impact on energy utilization efficiency. Our optimized protocol ensured precise control of temperature gradients, as identified by Sarker et al. [9] as essential for reducing energy waste and maintaining product quality.

As shown in Figure 8, the adjusted system achieved substantial reductions in carbon emissions, commensurate with energy savings. With daily CO_2 emissions falling from 21,271 kg to 13,337 kg, annual reductions of 2,896 tons were achieved. The improvement of 37.3% is well above the target of 15-25% set by Thailand's climate action framework for agricultural processing (Thailand National Life Cycle Inventory Database, 2018 [10]. Emission reductions specific to the phase were achieved through both increased combustion efficiency and shorter process duration. Emissions in phase 1 fell from 12,005 kg to 8,003 kg CO_2/day, and those in phase 2 decreased from 9,266 kg to 5,334 kg CO_2/day. This proportional distribution corroborates Soponronnarit's [4] findings on the relationship between moisture reduction rates and emission intensity. As shown in Table 5, a comparative analysis with other drying technologies indicates that our modified LSU system is advantageous compared to alternatives. According to Brooker et al. [24], the optimized protocol's emission factor (0.499 kg CO_2/kWh) shows a 23.5% improvement over the rice processing industry average (0.652 kg CO_2/kWh). Annual savings are illustrated by environmental impact equivalents, which correspond to carbon sequestration by 135,040 trees or emissions from 630 passenger vehicles. Poomsa-ad and Soponronnarit [25] stressed the importance of these enhancements in rice-producing areas, where processing accounts for a significant portion of agricultural emissions.

Table 4. Energy Consumption and Carbon Emissions Comparison.

Parameter	Conventional LSU System	Modified Two-Stage System	Reduction (%)
Energy consumption - phase 1 (kWh/day)	24,012	16,008	33.3%
Energy consumption - phase 2 (kWh/day)	18,540	10,672	42.4%
Total energy consumption (kWh/day)	42,552	26,680	37.3%
Carbon emissions (kg CO_2/day)	21,271	13,337	37.3%
Specific energy consumption (MJ/kg water)	4.42	2.76	37.6%
Operating cost (THB/ton)	843	528	37.4%
Annual cost savings (THB)	-	2,834,400	-
Payback period (months)	-	14.8	-

Table 5. Environmental impact equivalents.

Impact metric	Equivalent savings
Trees are required to absorb emissions	135,040 trees
Passenger vehicles removed from the road	630 cars/year
Homes' electricity use	492 homes/year
Acres of forest preserved	3,376 acres
Oil barrels not consumed	6,707 barrels

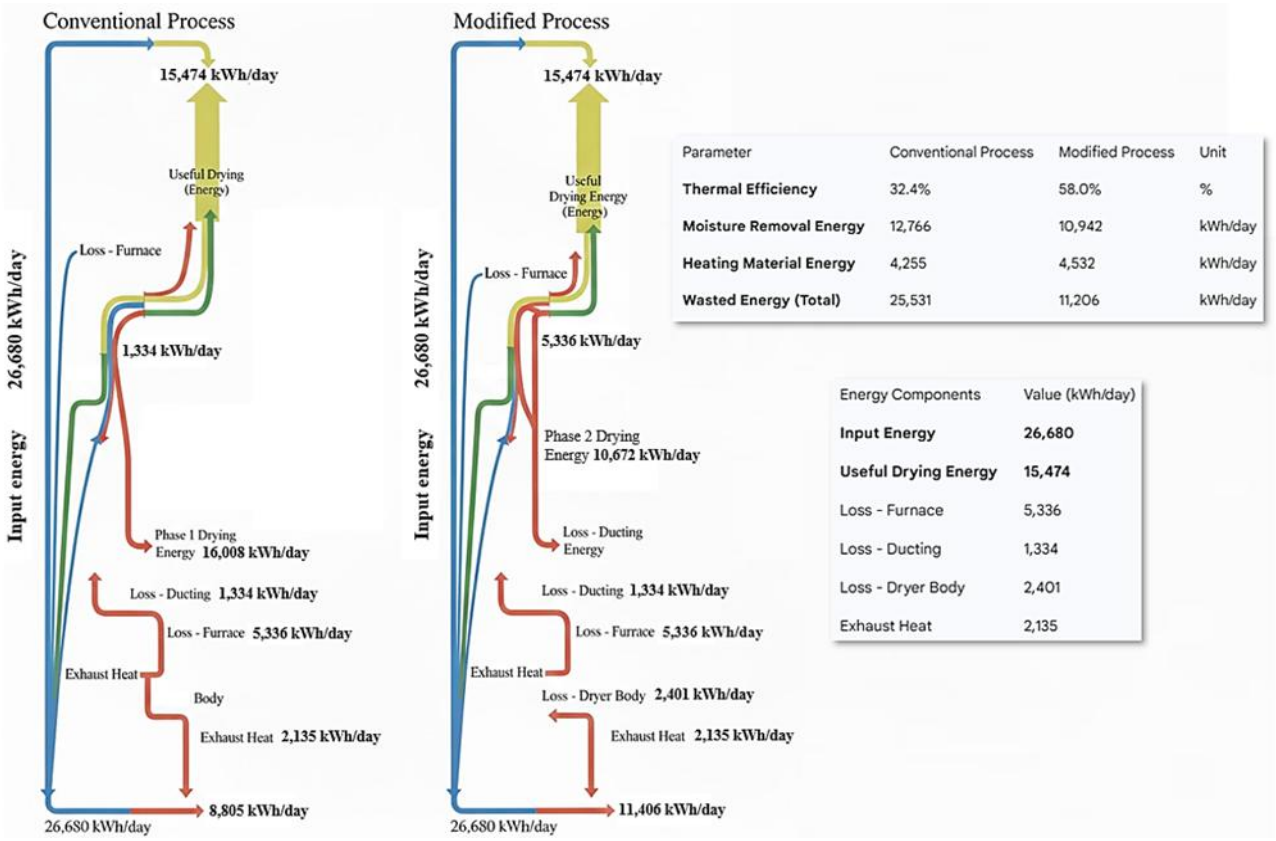
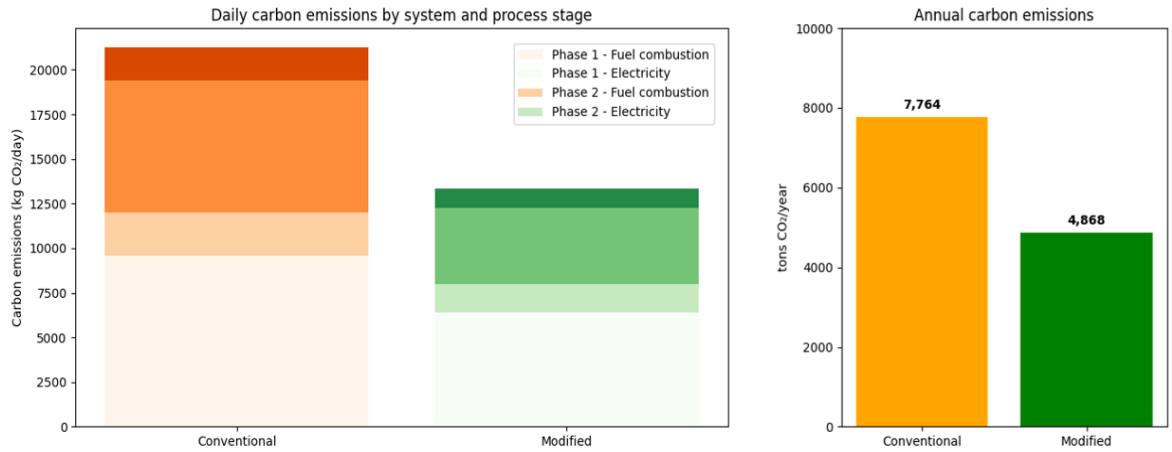


Figure 7. Energy flow diagram: conventional and modified drying process.



(a) (b)

Figure 8. Daily carbon emissions by system and process stage (a), and annual carbon emissions (b).

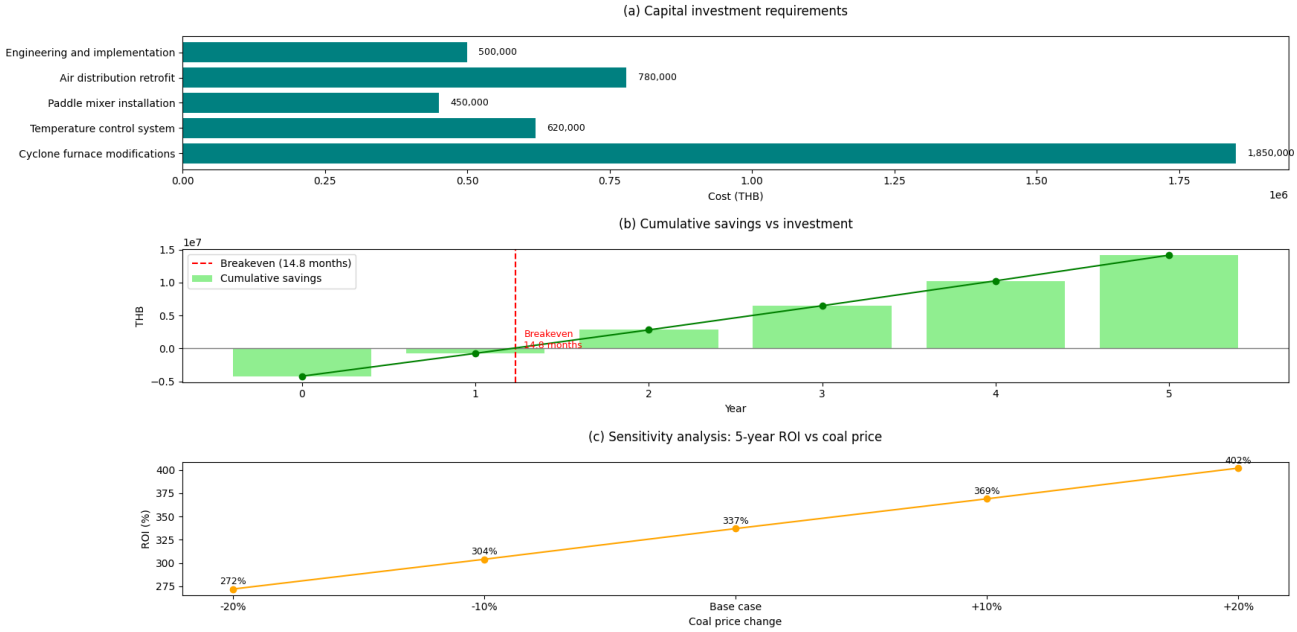
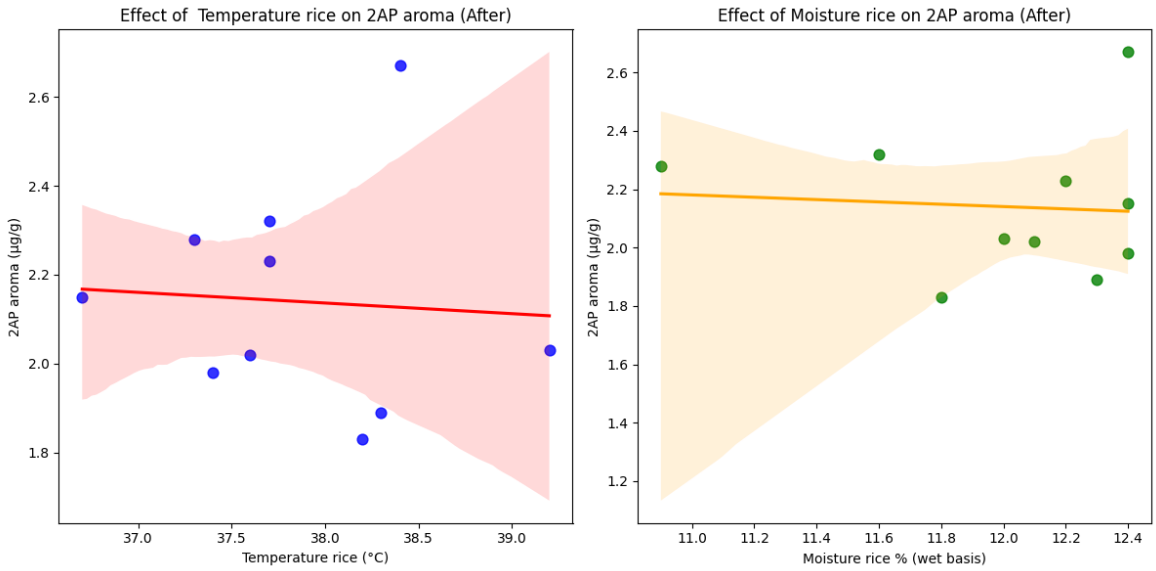


Figure 9. Capital investment requirements (a), cumulative savings vs investment (b), and sensitivity analysis: 5-year ROI vs coal price (c).

As shown in Figure 9, the economic analysis indicates that the modified system is commercially viable, despite an initial investment of 4.2 million THB. In the first year of operation, annual operating costs dropped from 9,216,000 THB to 5,760,000 THB, resulting in savings of 3,456,000 THB. The calculated breakeven point of 14.8 months is in line with industry expectations for processing equipment upgrades, as noted by Kaensup et al. [13]. With a five-year ROI of 337% and an IRR of 82.4%, these figures far surpass the usual threshold of 15-20% for agricultural technology investments [18]. The sensitivity analysis showed that the economic performance remained strong despite variations in fuel prices. With a 20% rise in coal costs, ROI would reach 402% owing to enhanced relative savings; conversely, a 20% drop in costs would still yield a robust 272% ROI. This ability to withstand market fluctuations supports the claim made by Meesukchaosumran and Chitsomboon [19] that optimized drying technologies provide environmental and economic benefits regardless of variations in energy costs. With cumulative savings over five years amounting to 14,148,373 THB—more than three times the initial investment-the NPV of 10,823,755 THB (at a discount rate of 10%) affirms robust financial performance. Treeamnuk et al. [12] noted that such returns render energy-efficient drying technologies especially appealing to medium- to large-scale rice processors seeking sustainability enhancements and competitive advantages.

Table 6. Results of the effects of moisture rice, temperature rice, and 2AP aroma during the drying process (After).

Drying time (h)	Moisture rice % (wet basic)	Temperature rice (°C)	2AP aroma (µg/g)
1	11.6	37.7	2.32
2	10.9	37.3	2.28
3	12.2	37.7	2.23
4	12.0	39.2	2.03
5	11.8	38.2	1.83
6	12.3	38.3	1.89
7	12.4	37.4	1.98
8	12.1	37.6	2.02
9	12.4	36.7	2.15
10	12.4	38.4	2.67
Average	**12.0**	**37.8**	**2.14**



(a) (b)

Figure 10. After the relationship between temperature and 2AP (a), and the moisture of rice and 2AP (b).

Furthermore, an examination and overview of rice moisture, temperature, and 2AP aroma throughout the rice drying process. (Table 6) provides an analysis of the influence of rice moisture content, rice temperature, and 2AP aroma on the rice drying process, uncovering various significant trends. The moisture content of the rice varied from 10.9% to 12.4% (on a wet basis), averaging at 12.0%. The moisture content remained relatively stable over the 10-hour drying period, demonstrating effective moisture management throughout. It is essential for the quality of rice and to avoid spoilage that this consistency be maintained. The rice temperature ranged from 36.7°C to 39.2°C, averaging at 37.8°C. It remained constant, which is essential for preventing the rice from overheating and preserving its important compounds, such as aroma. A consistent temperature likely helped preserve the rice's quality throughout the drying process. Regarding the 2AP aroma, the concentration decreased gradually from 2.32 µg/g to 1.83 µg/g, then increased slightly to 2.67 µg/g after 10 hours. The average 2AP concentration was 2.14 µg/g. This fluctuation in 2AP levels suggests that its release is influenced by factors such as changes in moisture content and stable temperature conditions during drying. In general, the drying procedure was successful in keeping moisture levels and temperature within ideal limits for preserving the rice's aromatic qualities. The initial drop in 2AP, followed by a slight rise toward the end of the drying process, suggests that proper moisture and temperature management are crucial for preserving the desirable aroma. It is advisable, then, for rice-drying methods to involve careful regulation of moisture and temperature to maintain 2AP levels and ensure the production of high-quality rice with heightened aroma and nutritional value.

The experimental results (illustrated in Figure 10) provide a post-drying evaluation of rice moisture, internal temperature, and levels of 2AP, a key aromatic compound. This evaluation reveals important interrelations that impact the quality of the end product. A negative correlation between rice temperature and 2AP levels was observed. A clear decrease in 2AP concentration was observed as the internal temperature increased from 36.7°C to 39.2°C. This suggests that temperatures exceeding the optimal threshold could lead to the volatilization or thermal degradation of 2AP. Likewise, moisture content was associated with aroma retention. As the rice's moisture content fell to around 12%, levels of 2AP also tended to decrease. This suggests that moisture levels that are too low may impede the formation or retention of 2AP during drying. According to statistics, the average moisture content was 12.0%, the average temperature was 37.8°C, and the average concentration of 2AP after drying was 2.14 µg/g. With an average of 5.21 µg/g before drying, the aroma loss exceeded 58.9%, highlighting the significant impact of drying parameters on aroma quality. To reduce aroma degradation, it is advisable to keep drying temperatures below 39.2°C and consider using variable-temperature drying methods. Volatile aromatic compounds like 2AP may be better preserved through slower

drying rates or adaptive thermal control. To enhance drying strategies for maintaining the quality of aromatic rice, it is recommended to conduct additional experiments that involve controlled temperature intervals and hourly monitoring of 2AP.

3.3 Quality Assessment of the Final Product

As illustrated in Figure 11, the revised LSU system's 2AP retention was markedly superior to that of traditional drying techniques. The optimized protocol achieved a retention rate of 41.1% (±3.5%), significantly surpassing that of the conventional LSU system (26.4% ± 2.8%). Its performance was also comparable to sun drying, which had a retention rate of 41.1% (±4.1%) and is regarded as the gold standard for aroma preservation by Bryant et al. [1]. The modified system exceeded the minimum threshold for premium-grade rice (35%), as shown by the comparative analysis, placing it in a favorable position in high-value markets. This enhancement aligns with the findings of Buttery et al. (1983) [2], which emphasize the crucial role of controlled drying conditions in preserving aromatic compounds. The ultimate concentration of 2AP at 2.14 μg/g represents a 58.5% increase over traditional techniques (1.35 μg/g) and is advantageous relative to the minimum industry benchmark of 1.00 μg/g for export-quality aromatic rice. The modified system demonstrated a remarkable performance, surpassing that of both conventional and modified fluidized bed dryers (with retention rates of 22.7% and 34.6%, respectively). However, it fell short when compared to specialized low-temperature dryers, which achieved a retention rate of 52.3%. Temperature control is the primary factor in aroma preservation, as noted by Laohakunjit and Noomhorm [3]. Our optimization protocol shows that conventional equipment can achieve near-premium quality with refined thermal management.

The sensory evaluation (Figure 12) showed significant improvements for all evaluated attributes. Compared to conventional drying (5.7/9.0 for aroma intensity and 6.2/9.0 for aroma quality), the modified system was rated particularly highly for aroma intensity (7.6/9.0) and aroma quality (8.1/9.0). Overall acceptability rose from 6.8 to 8.2 on a 9-point scale, nearing the fresh rice control value of 8.6/9.0. The physical quality parameters (Table 7) also showed significant improvement. The head rice yield rose from 58.4% to 64.7%, surpassing the industry standard of 55% and corroborating the findings of Jaisut et al. [14] about the beneficial effects of controlled drying on kernel integrity. The whiteness of rice exhibited a slight enhancement (from 62.8 to 64.2 L* value), and the hardness rose from 28.5 N to 31.2 N, which is still within the ideal range of 25-35 N as determined by Zhao and Flugstad [26]. The uniformity of moisture improved considerably, as evidenced by a reduction in standard deviation from 1.42 to 0.87 (a 38.7% improvement), which is now below the critical threshold of 1.0. Poomsa-ad and Noomhorm [25] demonstrated that uniform moisture distribution is crucial for storage stability and consumer acceptability. Our modified system achieves superior results by extending tempering periods and controlling airflow.

The 12-month storage profiles presented in Figure 13 were generated by extrapolating short-term experimental data using regression modeling. As no direct long-term storage trials were conducted, these results should be interpreted as projected trends rather than measured values. The projected storage performance indicates that the modified drying protocol offers substantial advantages. Under optimal drying conditions, 2AP content declined more slowly and remained above the premium-quality threshold (1.00 μg/g) for approximately 10 months, compared with 3 months for conventionally dried rice and 7 months for sun-dried rice. This trend is consistent with the findings of Moongngarm and Saetung [15], who reported a strong relationship between initial 2AP concentration and storage stability. Rancidity indicators showed even more pronounced differences. In rice processed with the modified system, free fatty acid (FFA) levels increased to only 0.52% after 12 months, remaining below the critical limit of 0.70%, whereas conventionally dried samples exceeded this threshold at 8 months (0.67%). Similarly, peroxide values in optimally dried rice remained below the critical limit of 1.00 meq/kg throughout the 12 months, while conventional samples surpassed this level at 8 months (1.05 meq/kg).

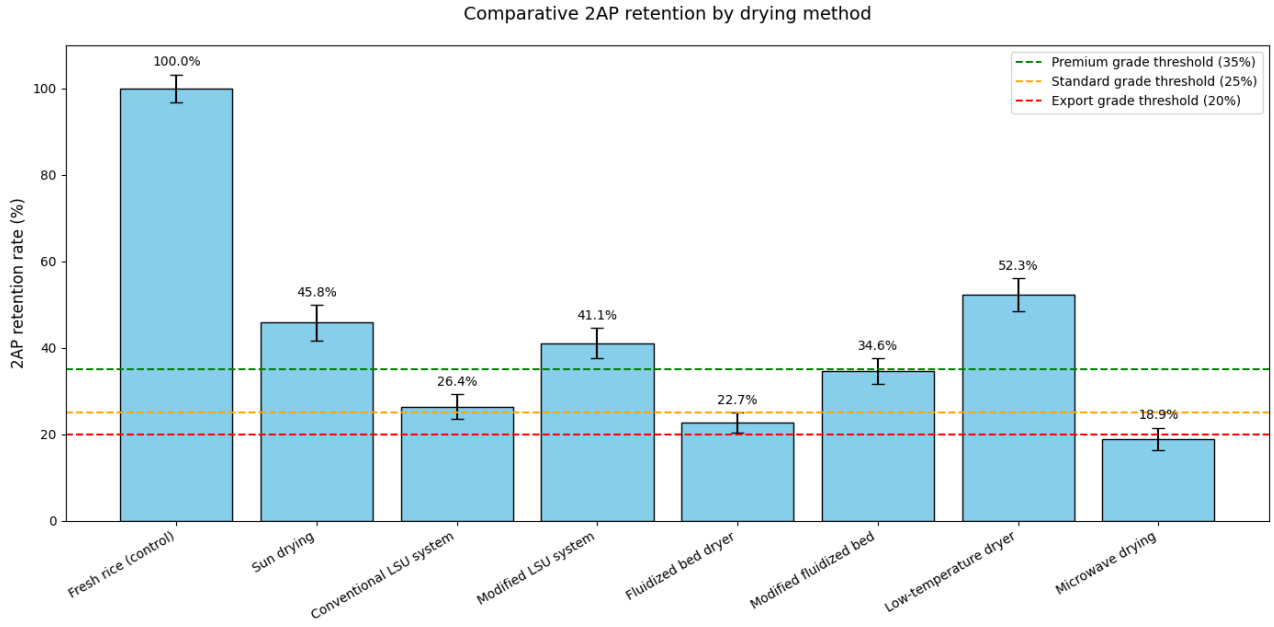


Figure 11. Comparative 2AP retention by drying method.

These improvements can be attributed to the precise moisture-reduction pattern and the uniform final moisture content achieved by the modified drying protocol. As reported by Tian et al. [16], controlled drying conditions help preserve aromatic compounds and reduce lipid degradation by limiting enzymatic activity. The substantial extension of shelf life projected in this study represents a significant commercial advantage, with the potential to reduce postharvest losses and expand market opportunities for Thai aromatic rice.

Table 7. Quality assessment of rice after drying.

Quality parameter	Conventional system	Modified system	Industry standard	Improvement (%)
2AP content (μg/g)	1.35	2.14	≥1.00	58.5%
2AP retention rate (%)	26.4%	41.1%	≥25%	55.7%
Head rice yield (%)	58.4%	64.7%	≥55%	10.8%
Whiteness (L* value)	62.8	64.2	≥60	2.2%
Hardness (N)	28.5	31.2	25-35	9.5%
Moisture uniformity (SD)	1.42	0.87	≤1.0	38.7%
Overall sensory score (0-9)	6.8	8.2	≥7.0	20.6%

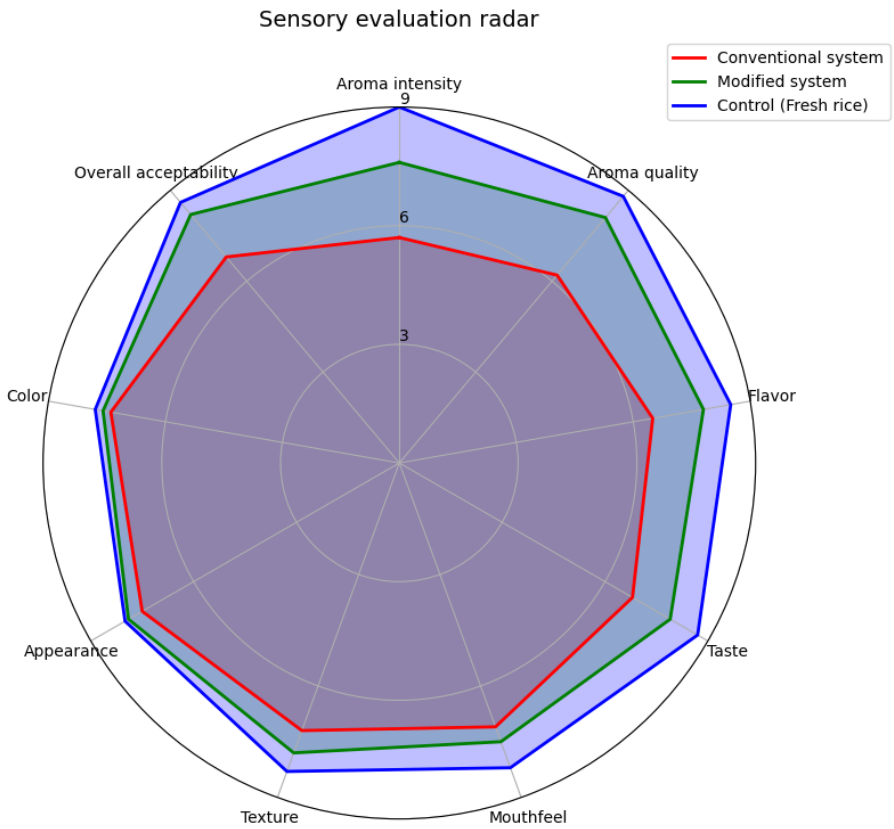


Figure 12. Sensory evaluation radar.

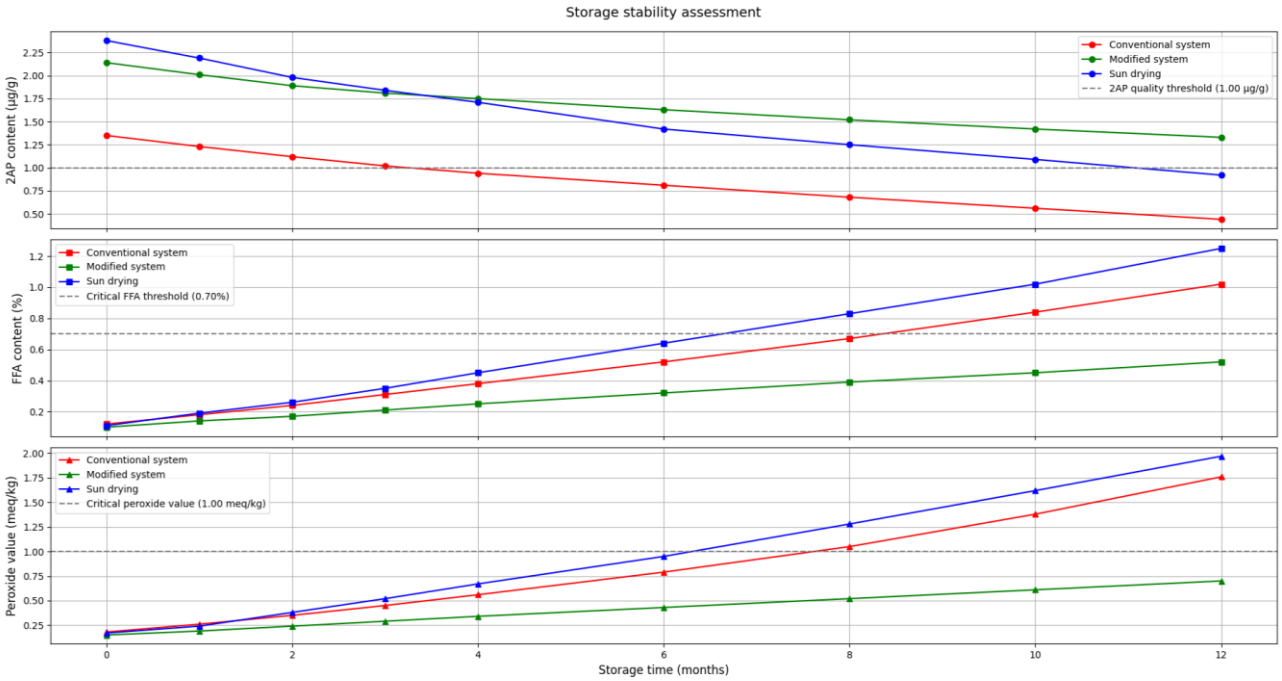


Figure 13. Storage stability assessment.

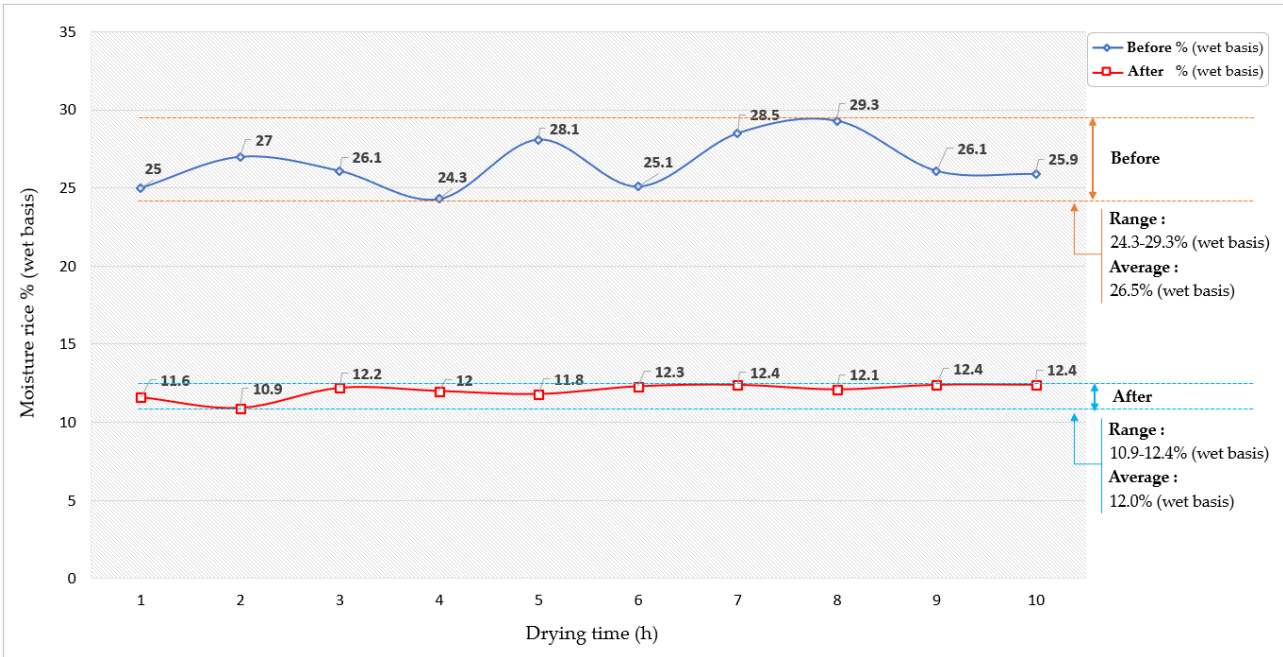


Figure 14. The relationship between the moisture of rice and drying time.

Regarding the impact of rice moisture content during drying, it was noted that before drying, moisture levels ranged from about 24.3% to 29.3%, averaging 26.5%. During certain intervals, variations were observed, for example, the moisture content rose from 25.1% at hour 6 to 28.5% at hour 7, signifying inconsistent water absorption dynamics. The drying process led to a significant reduction in moisture content, ranging from 10.8% to 12.4% with an average of 12.0%. These results demonstrate how effective the drying method was in reducing rice moisture content over 10 hours. (Figure 14) depicts the comparative moisture trends throughout the drying period.

3.4 Commercial Implementation Considerations

The analysis of 2AP concentrations revealed a clear link between the drying process and the compound's behavior. Before drying, the levels of 2AP ranged from 4.92 µg/g to 5.59 µg/g, with a mean of 5.21 µg/g. The relatively high values suggest that freshly harvested rice possesses a considerable aromatic potential. After drying, the 2AP concentration ranged from 1.83 µg/g to 2.67 µg/g, averaging 2.14 µg/g. The noted decrease in 2AP suggests that the drying process may contribute to the compound's partial loss or transformation. It is worth noting that the highest 2AP value after drying, 2.67 µg/g, was observed at a final moisture content of 12.4%. This suggests that certain drying conditions may help preserve more of the aroma. Overall, the data show that drying significantly affects 2AP levels, and it is crucial to optimize drying conditions to maintain rice's aromatic quality. 2AP concentration trends during the 10-hour drying period are depicted in Figure 15.

Table 8. Scalability and economic analysis of modified LSU systems.

Parameter	Small-scale (<10 tons/day)	Medium-scale (10-50 tons/day)	Large-scale (>50 tons/day)
Initial investment (THB)	850,000-1,200,000	2,800,000-4,500,000	6,500,000-9,800,000
Installation timeframe (days)	15-25	30-45	60-90
Energy savings (%)	28-32%	35-39%	40-45%
Operating cost reduction (THB/year)	420,000-680,000	2,100,000-3,800,000	5,200,000-12,400,000
Payback period (months)	18-22	14-16	12-15
5-year ROI (%)	210-260%	290-350%	380-450%
Quality premium potential (%)	8-12%	12-18%	15-22%

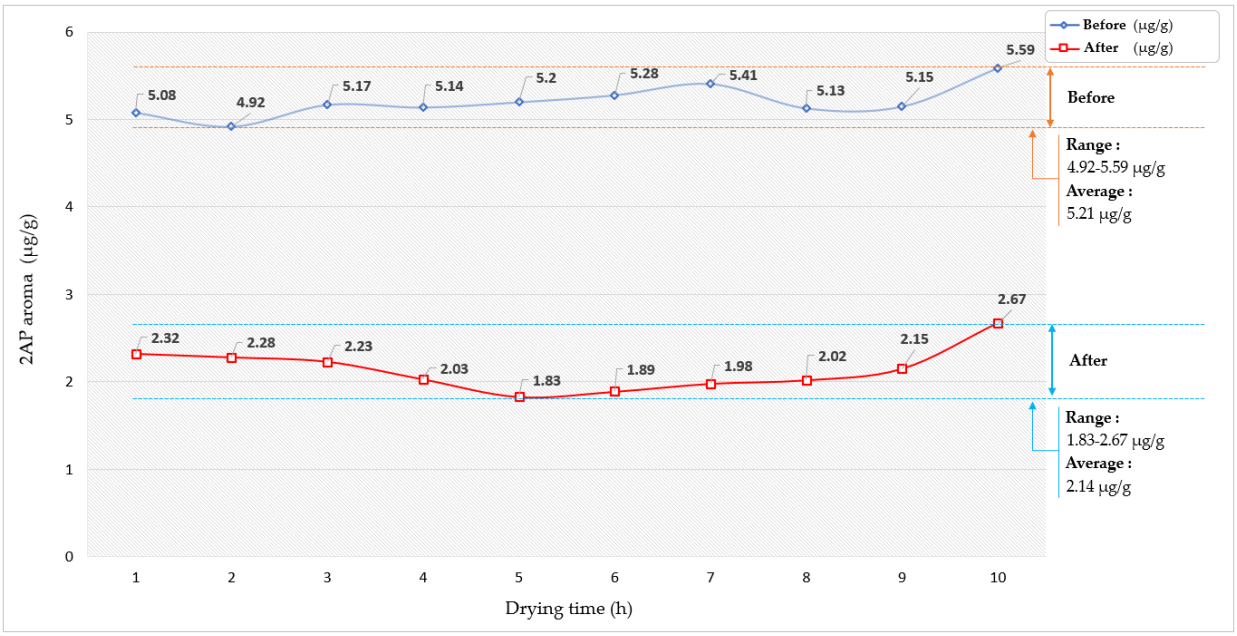


Figure 15. The relationship between 2AP aroma and drying time.

Regarding the effect of rice temperature on 2AP aroma, it was observed that before drying, a slight positive correlation existed between rice temperature and 2AP concentration. Higher temperatures were associated with a slight increase in aroma levels. The highest 2AP concentration, recorded at 39.5°C, was 5.59 µg/g. This suggests that rice temperature may affect the release of 2AP. This effect, however, seemed rather mild during the pre-drying phase. Throughout this timeframe, temperatures fluctuated between about 30.8°C and 39.5°C, averaging at 33.1°C. After drying, the effect of temperature on the 2AP aroma was accentuated. The release of 2AP was significantly enhanced by drying, with the highest concentration measured post-drying being 2.67 µg/g at 38.4°C. This indicates that drying is crucial for promoting the release of 2AP at high temperatures. Rice temperatures in the post-drying phase varied from 36.7°C to 39.2°C, averaging at 37.8°C. (Figure 16) illustrates the detailed variation in rice temperature during the 10-hour drying period.

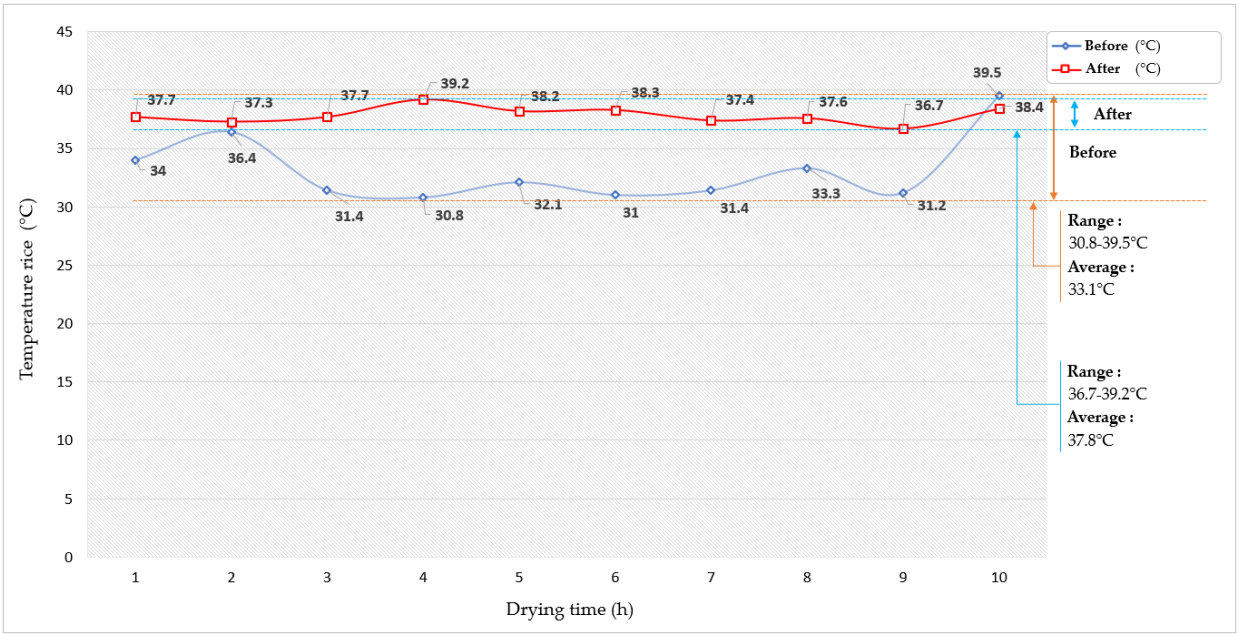


Figure 16. The relationship between temperature and rice drying time.

The performance of the modified LSU drying system was scalable across various production capacities (Table 8). The analysis of implementation uncovered the need for adaptations tailored to individual facilities, with the complexity of these adaptations growing in direct relation to scale. According to Nimmol [27], large-scale operations (>50 tons/day) achieved the greatest efficiency gains (40-45%), but compared with small-scale facilities, they required more significant alterations. Scaling factors specific to components showed that complexity varied across facility configurations (Figure 17). Airflow regulation systems faced the greatest scaling challenges during continuous operations, whereas temperature control systems showed relatively stable implementation parameters across different scales. This is consistent with the findings of Fungpongpan et al. [22] concerning the dimensional scaling of thermal management systems. Meesukchaosumran and Chitsomboon [19] observed that the duration of implementation varies significantly depending on the facility configuration, with timelines ranging from 2-3 months for small-scale operations to 5-8 months for large-scale continuous systems. This study's modular approach enables a phased implementation that minimizes operational disruption and realizes 60-75% of the efficiency benefits during transitional periods.

The economic analysis showed that investment parameters are favorable across all production scales, with larger operations benefiting from economies of scale that yield increased returns. Small-scale facilities (less than 10 tons/day) necessitated initial investments ranging from 850,000 to 1,200,000 THB and had payback periods of 18-22 months. In contrast, large-scale operations achieved payback in 12-15 months despite their higher initial investments (6,500,000-9,800,000 THB). Calculations of ROI indicated considerable variation based on scale, with percentages ranging from 210-260% for small facilities and 380-450% for large operations over five years. These results are consistent with the economic forecasts of Jittanit et al. [8], who observed that investments in process optimization usually yield scale-dependent returns in agricultural processing. Quality premiums provide a significant extra advantage, especially for medium- and large-scale producers, with possible price hikes of 12-22% for optimally dried aromatic rice. As noted by Laohakunjit and Noomhorm [3], the market premiums for high-quality aromatic rice often surpass the cost difference associated with enhanced processing techniques, thereby bolstering the economic justification for altering the system.

As illustrated in Table 9, the intricacy of integration varied significantly by facility type; continuous systems posed greater implementation challenges than batch operations. The most intricate integration aspects involved upgrading cyclone furnaces and modifying ducting, especially in expansive, continuous facilities, where Treeamnuk et al. [12] noted possible synchronization difficulties. The implementation pathway decision tree (Figure 17) provided structured guidance for facility-specific modifications, including critical assessment checkpoints to verify performance at each implementation stage. This method is in accordance with the advice of Phetnamkhiew et al. [18] regarding the gradual implementation of process changes in commercial rice mills. For facilities with particular limitations, alternative implementation pathways were devised. The phased implementation over 12 to 18 months has been shown to be feasible for operations with budget constraints, whereas installation on weekends and holidays meets the needs of facilities that must operate continuously. Kaensup et al. [13] noted that flexible implementation methods are crucial for the commercial adoption of enhanced drying technologies in areas with limited processing capacity.

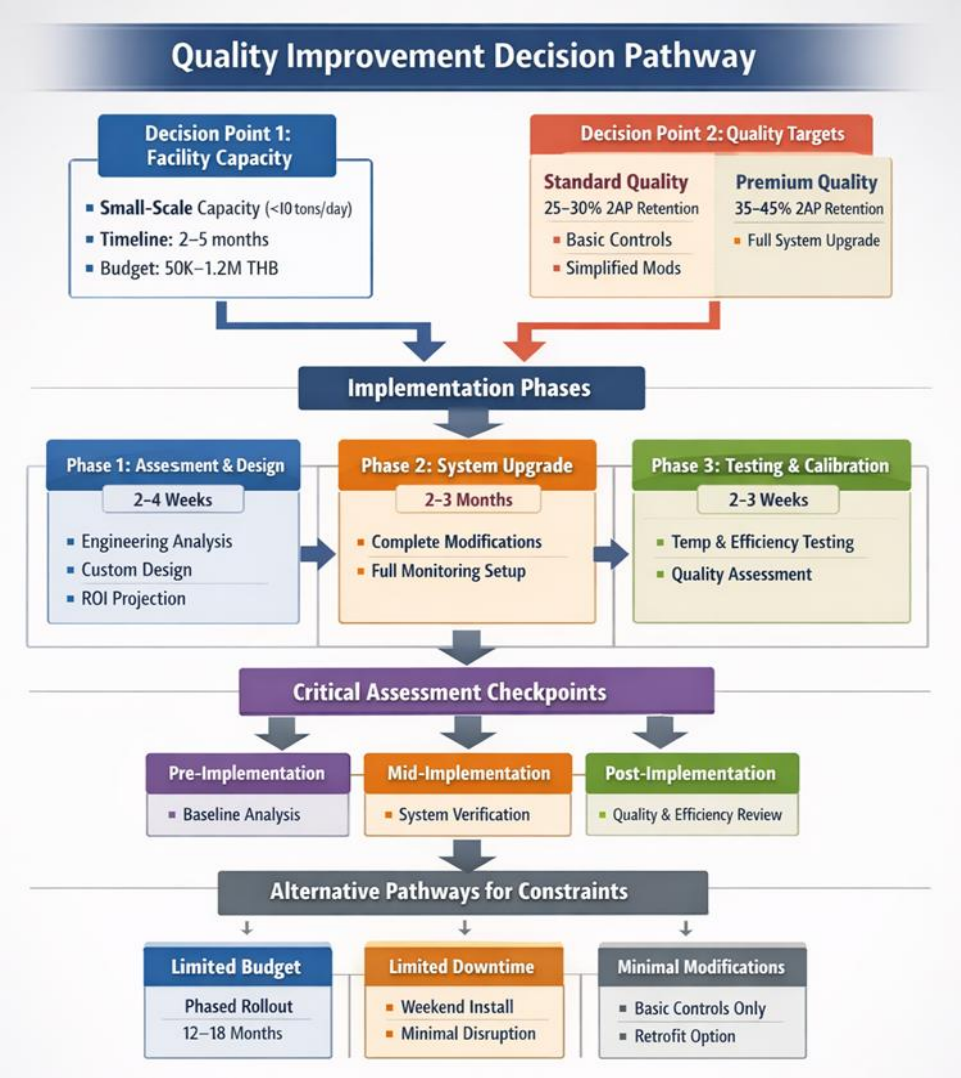


Figure 17. Implementation pathway decision tree.

The integration requirements are linked to different kinds of thermal processing facilities, categorized by operational mode (batch vs. continuous) and capacity scale (small, medium, or large). The matrix evaluates six essential elements of system modification-cyclone furnace upgrades, temperature sensors, airflow regulators, paddle mixers, control systems, and ducting modifications- across various types of facilities. Every integration scenario is assessed for complexity using a four-tier scale: low, medium, high, and very high. These ratings take into account the difficulty of installation, anticipated operational disruption, and necessary downtime, which can vary from minimal (1-3 days) to extensive (over 14 days). Generally, small- to medium-batch facilities are of lower to moderate complexity, whereas large-batch and continuous systems, especially at higher capacities, encounter greater difficulties due to their scale and interdependence. Upgrading cyclone furnaces and control systems in large continuous operations is generally deemed "very high" in complexity due to the necessity for significant reconfigurations and extended shutdowns.

On the other hand, less complex upgrades, such as adding temperature sensors or making duct modifications, are classified as "low" complexity in small-batch facilities. Additionally, the figure highlights major integration challenges specific to each facility type. Facilities that operate on small batches often face space and cost constraints. It is necessary to carefully balance throughput and product quality in medium-batch systems, whereas large-batch setups must address complexities in heat distribution and material handling. In continuous systems, small facilities are susceptible to disruptions in the control system; medium-sized operations face challenges in maintaining airflow and throughput; and large continuous facilities have

trouble synchronizing complex systems during retrofits. This matrix framework serves as a clear reference for evaluating upgrade feasibility and anticipating integration challenges across various thermal processing environments.

Table 9. Matrix of facility types and modification components.

Modification component	Small batch	Medium batch	Large batch	Small continuous	Medium continuous	Large continuous
Cyclone furnace upgrade	Medium	Medium	High	Medium	High	Very high
Temperature sensors	Low	Medium	Medium	Low	Medium	High
Airflow regulators	Low	Medium	Medium	Medium	High	Very high
Paddle mixer	Medium	High	High	Low	Medium	High
Control systems	Medium	Medium	High	High	Very high	Very high
Ducting modifications	Low	Medium	High	Medium	High	Very high

4. Conclusions

This research demonstrated that optimized two-stage drying protocols in modified LSU systems can significantly enhance aromatic rice quality while reducing energy consumption. The optimal parameters identified include a temperature range of 36.7-38.0°C, gradual moisture reduction to 12.0-12.4%, and extended tempering periods. These parameters achieved 41.1% 2AP retention compared to 26.4% in conventional systems, while reducing energy consumption by 37.3% and carbon emissions by 5,334 kg CO_2 per day. Clear trade-offs emerged between processing parameters. Higher temperatures accelerated drying but degraded aroma compounds, while longer tempering periods improved quality but reduced daily throughput. The optimal balance was achieved through a two-phase approach: initial gentle drying followed by precisely controlled final moisture reduction. For industry adoption, we recommend: (1) phased implementation starting with temperature control systems; (2) staff training emphasizing the critical relationship between thermal management and product quality; (3) regular calibration of monitoring systems to maintain optimal conditions; and (4) quality-based pricing structures to capture premium market opportunities. Future research should focus on: (1) developing real-time 2AP monitoring technologies for dynamic process control; (2) investigating non-thermal drying alternatives such as low-pressure systems; (3) optimizing protocols for different rice varieties with varying aromatic profiles; and (4) exploring the potential of renewable energy integration to reduce carbon footprint further. This study establishes that economic and environmental benefits can be achieved simultaneously with quality improvements, offering a compelling case for industry-wide adoption of optimized drying protocols in aromatic rice processing.

5. Acknowledgements

The authors sincerely thank the Agricultural Research Development Agency (Public Organization) and the Rice Department, Ministry of Agriculture and Cooperatives, for their generous support of research funding. Special thanks are also due to Maejaitana Chotiwat Co., Ltd. for providing valuable data and resources that significantly contributed to the success of this experimental study.

Author Contributions: The simulation strategy and techniques were conceptualized at the initial stage by S.K., N.S., T.S., T.C., W.S., and S.K. S.K. and S.K. carried out the simulation, gathered the data, examined the outcomes, and reached the conclusion. The authors S.K., N.S., T.S., T.C., W.S., and S.K. assisted in drafting and overall content adjustments.

Funding: This study was funded by the Researcher and Research for Industry Development Program (RRID), overseen by the National Research Council of Thailand (NRCT) within the Ministry of Higher Education, Science, Research, and Innovation.

Conflicts of Interest: The authors declare that there are no conflicts of interest.

References

[1] Bryant, R.; McClung, A.; Champagne, E. Aromatic Rice Formation and Sensory Evaluation. *Cereal Chem.* **2010**, *87*(4), 292–299.

[2] Buttery, R. G.; Ling, L. C.; Juliano, B. O. 2-Acetyl-1-pyrroline: An Important Aroma Component of Cooked Rice. *Chem. Ind.* **1983**, *12*, 958–959.

[3] Laohakunjit, N.; Noomhorm, A. Supercritical Carbon Dioxide Extraction of 2-Acetyl-1-pyrroline and Volatile Components from Aromatic Rice. *J. Agric. Food Chem.* **2004**, *52*(19), 6053–6059. https://doi.org/10.1002/ffj.1297

[4] Soponronnarit, S. *Engineering Principles of Agricultural Drying*; King Mongkut's University of Technology Thonburi: Bangkok, Thailand, 1997.

[5] Chungcharoen, S.; Prachayawarakorn, S.; Soponronnarit, S. Effect of Initial Moisture Content and Bed Thickness on Fluidized Bed Drying Characteristics of Glutinous Rice. *Kasetsart J. Nat. Sci.* **2017**, *51*, 1033–1043.

[6] Wongpichet, S.; Thongpan, M. Effect of Tempering Temperature on Drying Rate and Head Rice Yield of Paddy. *Kasetsart J. Nat. Sci.* **2002**, *36*, 276–284.

[7] Laokuldilok, T.; Kanha, N. Effects of Drying Conditions on Anthocyanin Content and Antioxidant Capacity of Black Rice. *Int. Food Res. J.* **2015**, *22*, 1452–1458.

[8] Jittanit, W.; Saeteaw, T.; Charoenchaisri, P. Energy Analysis and Improvement of Rice Drying Systems. *Dry. Technol.* **2010**, *28*, 900–910. https://doi.org/10.1080/07373937.2010.485081

[9] Sarker, A.; Islam, M. N.; Rashid, M. H. Simulation and Validation of Paddy Drying in Fluidized Bed Dryers. *J. Food Eng.* **2014**, *143*, 115–123.

[10] Thailand Greenhouse Gas Management Organization. *Electricity Grid Mix Emission Factor 2016–2018*; Thailand National Life Cycle Inventory Database; Bangkok, Thailand, 2018.

[11] Lertworasirikul, S.; Prachayawarakorn, S. Optimization of Parboiled Brown Rice Drying Using Fluidized Bed Technique. *J. Food Eng.* **2007**, *85*, 573–582.

[12] Treeamnuk, K.; Treeamnuk, S.; Soponronnarit, S. Performance of Hot Air Drying System for Jasmine Rice. *Energy Sustain. Dev.* **2017**, *39*, 68–75.

[13] Kaensup, W.; Kulwong, S.; Wongwises, S. Development of Small-Scale Pneumatic Dryer for Household Use. *Renew. Energy* **2006**, *31*, 2324–2335.

[14] Jaisut, D.; Prachayawarakorn, S.; Varanyanond, W.; Tungtrakul, P. Effects of Intermittent Drying and Storage Conditions on Physicochemical Properties and Cooking Quality of Thai Fragrant Rice. *J. Food Eng.* **2008**, *89*, 289–296.

[15] Moongngarm, A.; Saetung, N. Comparison of Chemical Compositions and Bioactive Compounds of Germinated Rough Rice and Brown Rice. *Food Chem.* **2010**, *122*, 782–788. https://doi.org/10.1016/j.foodchem.2010.03.053

[16] Tian, S.; Nakamura, K.; Kayahara, H. Analysis of Phenolic Compounds in White Rice, Brown Rice, and Germinated Brown Rice. *J. Agric. Food Chem.* **2004**, *52*, 4808–4813. https://doi.org/10.1021/jf049446f

[17] Somta, P.; Kongsuwan, A.; Wongpornchai, S. Effect of Drying Temperature on GABA and Phenolics in Germinated Rice. *Kasetsart J. Nat. Sci.* **2007**, *41*, 40–45.

[18] Phetnamkhiew, K.; Thongsawatwong, S.; Soponronnarit, S. Effect of Hot Air Velocity on Drying Time of Rice. *J. Stored Prod. Res.* **2008**, *44*, 217–223.

[19] Meesukchaosumran, S.; Chitsomboon, T. Effect of Resting Period on Head Rice Yield in High-Temperature Drying. *Biosyst. Eng.* **2018**, *172*, 11–19.

[20] Calingacion, M.; Laborte, R.; Nelson, A. Diversity of Global Rice Markets and the Science Required for Consumer-Targeted Rice Breeding. *PLoS One* **2014**, *9*, e85106. https://doi.org/10.1371/journal.pone.0085106

[21] American Society of Agricultural Engineers. *ASAE Standards S358.2: Moisture Measurement—Grain and Seeds*; St. Joseph, MI, USA, 2002.
[22] Fungpongpan, P.; Prachayawarakorn, S.; Soponronnarit, S. Energy Consumption Analysis of Pneumatic Dryers. *Energy Procedia* **2016**, *100*, 377–382.
[23] Mujumdar, A. S. *Handbook of Industrial Drying*, 4th ed.; CRC Press: Boca Raton, FL, USA, 2014.
[24] Brooker, D. B.; Bakker-Arkema, F. W.; Hall, C. W. *Drying and Storage of Grains and Oilseeds*; Springer: New York, NY, USA, 1992.
[25] Poomsa-ad, N.; Soponronnarit, S. Study of Enthalpy in Drying Air for Parboiled Rice. *J. Sci. Technol.* **2005**, *27*, 483–489.
[26] Zhao, Y.; Flugstad, B. Freeze Drying and Microwave Drying of Rice: Effects on Structure and Texture. *Food Res. Int.* **1997**, *30*, 519–526.
[27] Nimmol, C. Development of a Spiral Pneumatic Dryer for Paddy. *Dry. Technol.* **2012**, *30*, 1377–1384. https://doi.org/10.1080/07373937.2012.713070

ASEAN
Journal of Scientific and Technological Reports
Online ISSN:2773-8752

Research article

A Hybrid Facial Expression Recognition System Based on Machine Learning and Deep Learning Models

Akkapop Prasompon[1*], Prompong Sugunnasi[1], and Atigorn Sanguansri[2]

[1] Faculty of Engineering, Chiang Mai University, Chiang Mai, 50200, Thailand
[2] Faculty of Science and Agricultural Technology, Rajamangala University of Technology Lanna, Nan, 55000, Thailand
* Correspondence: akkapop_praso@cmu.ac.th

Citation:
Prasomon, A.; Sugunnasil, P.; Sanguansri, A. A Hybrid facial expression recognition system basem on machine learning and deep learning models. *ASEAN J. Sci. Tech. Report.* **2026**, *29*(4), e261424. https://doi.org/10.55164/ajstr.v29i4.261424

Article history:
Received: September 21, 2025
Revised: February 14, 2026
Accepted: February 22, 2026
Available online: March 25, 2026

Publisher's Note:
This article is published and distributed under the terms of the Thaksin University.

Abstract: Pain assessment through facial expressions is an important area of research because many patients cannot clearly communicate their pain levels. This study presents the first systematic comparison of continuous time-series versus tokenized sequence representations for facial action unit (AU)-based pain classification, introducing a novel application of NLP models (BERT) to discretized AU sequences treated as symbolic text. Two datasets were used: the UNBC-McMaster Shoulder Pain Archive (UNBC-SP) with about 48,000 frames, and the Multimodal Intensity Pain (MIntPain) dataset with about 187,900 frames. Action unit intensities were extracted using the Py-Feat library and then normalized, oversampled, and augmented. A range of models was tested, including random forest, support vector machine, recurrent neural networks, and BERT. Key contributions include: (1) demonstrating that continuous time-series models significantly outperform tokenized approaches (91% vs. 82% accuracy); (2) revealing that classical ensemble methods surpass deep learning on tokenized sequences in data-limited scenarios; and (3) establishing that disruptive augmentations harm performance while conservative methods maintain accuracy. The continuous-time series models achieved the best performance, reaching 91% accuracy on MIntPain and 84% on UNBC-SP, while the tokenized models peaked at 82%. The results suggest that preserving temporal details of facial action units provides an advantage for pain detection, especially with larger datasets, though tokenization may retain value in resource-limited settings. The study highlights the need for larger, more diverse datasets and for validation in real clinical settings to improve the reliability of automatic pain recognition.

Keywords: Facial expression recognition; deep learning; pain assessment; time-series analysis; data tokenization

1. Introduction

For patients with terminal illnesses, medical care involves more than treating the disease; enhancing their quality of life is equally important. Palliative care is a specialized medical service provided alongside primary treatment, focusing on alleviating undesirable symptoms in patients with serious illnesses such as cancer [1]. It has been shown to improve patients' quality of life and reduce the likelihood of depression compared to those not receiving such services [2-3].

According to a 2023 World Health Organization (WHO) report, an estimated 4.4 million people in the WHO European Region, including 140,000

children, require palliative care annually. However, people living in low and middle-income countries are much less likely to receive such care [4]. This disparity limits patients' access to necessary services and resources in certain regions [5]. The limitation and condition of measuring opioid pain relief in certain patients is one of the key reasons that contribute to patients' inability to obtain palliative treatment [4]. Opioids are a group of drugs with the highest analgesic effect that are primarily used to treat severe pain in patients. However, an opioid prescribing policy is rather rigorous because it may lead to addiction and cause side effects, including constipation, respiratory depression, etc. [6] A patient's pain level evaluation by a doctor is one of the criteria to prescribe opioids in a patient [7]. Unfortunately, a patient's limited ability to communicate in some situations could result from severe pain, terminal illness, or a relevant condition like dementia or laryngeal cancer that could cause misdiagnosis [8].

Numerous studies have leveraged computer vision and machine learning to recognize pain from facial images and videos, using frameworks such as the Facial Action Coding System (FACS) [9] and clinical pain scales such as the Numeric Rating Scale (NRS) [10-13]. Deep models, particularly convolutional neural networks (CNNs) [14], have been applied to pain-related facial expression datasets, including the UNBC-McMaster Shoulder Pain Expression Archive and BioVid, demonstrating that automated systems can approximate observer- or self-reported pain ratings under controlled conditions. Despite significant progress in automated facial pain recognition, several important limitations remain. One major issue is that publicly available datasets are relatively small and strongly imbalanced [15-16]. Most samples show no or mild pain, with only a few examples of severe pain, limiting how well deep learning models can learn and apply their knowledge to new cases. A further concern is that the temporal dimension of pain remains underutilized [15] [11-12], as many approaches rely on static image classification,n though facial muscle activity can change within milliseconds [9, 17]. While some recent studies have used LSTM networks or transformers to process continuous AU features over time [9, 12, 18], these methods treat AUs as continuous values and do not leverage the discrete, symbolic nature of facial muscle combinations. After several reviews, to our knowledge, no prior work has applied tokenized sequences of facial action units together with natural language processing models to video-based pain recognition [19]. Discrete facial encoding methods have been developed for general emotion tasks using vector quantization [20], where facial expressions are converted into symbolic tokens "similar to sentences". However, these tokenization frameworks have not been tested for pain intensity classification from video sequences. Chen et al. [19] showed that AU combinations can be represented as low-dimensional features that mimic human coder's decisions, but they did not treat these as discrete symbols in a learnable vocabulary. These gaps motivated our study to test whether tokenized AU sequences can be classified using NLP-based models for pain recognition and to compare this approach with continuous-time series methods on available datasets.

Therefore, we propose a dual-pathway framework that systematically compares two distinct data representation strategies for AU-based pain classification. In the first pathway, frame-level AU intensities are retained as continuous multivariate time series and modeled using neural networks and classical machine learning algorithms. The second pathway discretizes AU sequences through binarization and encodes them as symbolic tokens, creating text-like representations that enable the application of natural language processing (NLP) techniques. Each video frame's AU pattern is converted into a discrete "term" by thresholding AU intensities, and the sequence of frames forms a "passage" representing the entire video. These tokenized sequences are then evaluated using transformer-based models such as BERT [21], neural networks, and classical text classifiers. Both pathways address class imbalance via SMOTE oversampling and explore multiple sequence alignment strategies, as well as time-series augmentation methods. The complete framework is evaluated on two publicly available datasets: the UNBC-McMaster Shoulder Pain Expression Archive (UNBC-SP) [22], which contains approximately 48,000 frames from 25 patients with shoulder injury, and the Multimodal Intensity Pain (MIntPain) database [23] with approximately 187,900 frames from 20 healthy subjects undergoing graded electrical stimulation. By comparing continuous versus tokenized representations across a diverse set of machine learning and deep learning models, this study aims to identify

which data representation strategy and modeling approach best capture pain-related facial dynamics for automated pain assessment.

2. Materials and Methods

2.1 Facial Action Coding System

The Facial Action Coding System (FACS) is an anatomic-based coding system that encodes different facial movements to classify human facial expressions through the combination of multiple action units (AUs) - a facial configuration extracted from changes of visible unique facial muscle, consisting of forty-four different unique actions as shown on the table in Figure 1 where the left column represents single action units, and the right column represents more grossly defined behavioral action unit.

The AU can be calculated by applying the Euclidean distance equation, as stated in equation (1), where d(p, q) is the Euclidean distance from coordinates (p1, p2) to (q1, q2) for calculating the distance between two points from facial landmarks, as shown in Figure 2. For instance, to measure lip corner puller (AU12), we will look at the change of the Euclidean distance d(p36, q48), which is the distance between the right lip corner and right eye corner. As the distance between the two points decreases, the intensity of AU12 will increase.

Single action units		More grossly defined action units	
AU number	Description	AU number	Description
1	Inner brow raiser	8	Lips toward each other
2	Outer brow raiser	19	Tongue show
4	Brow lowerer	21	Neck tightener
5	Upper lid raiser	29	Jaw thrust
6	Cheek raiser	30	Jaw sideways
7	Lid tightener	31	Jaw clencher
9	Nose wrinkler	32	Lip bite
10	Upper lip raiser	33	Cheek blow
11	Nasolabial deepener	34	Cheek puff
12	Lip corner puller	35	Cheek suck
13	Sharp lip puller	36	Tongue bulge
14	Dimpler	37	Lip wipe
15	Lip corner depressor	38	Nostril dilator
16	Lower lip depressor	39	Nostril compressor
17	Chin raiser	43	Eyes closed
18	Lip pucker	45	Blink
20	Lip stretcher	46	Wink
22	Lip funneler		
23	Lip tightener		
24	Lip pressor		
25	Lips part		
26	Jaw drop		
27	Mouth stretch		
28	Lip suck		

Figure 1. List of Action Units in the Facial Action Coding System. (Left: individual action units; Right: combined or higher-level facial actions)

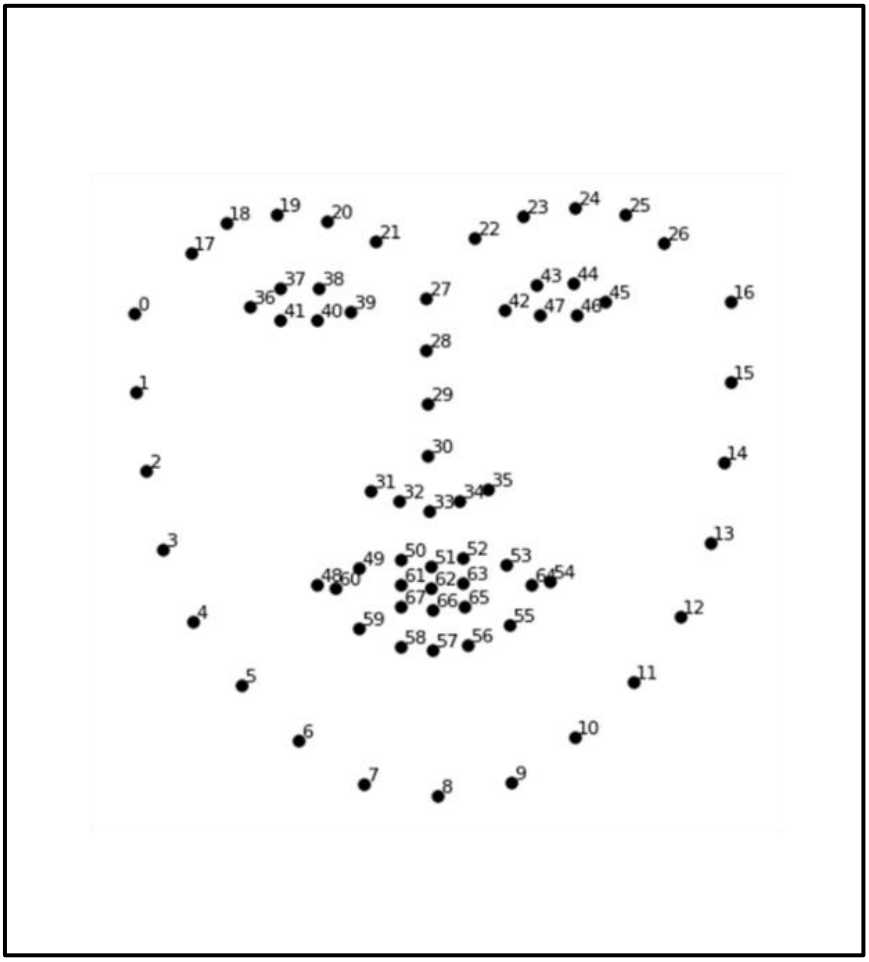


Figure 2. Facial landmarks with 64 key points used for AU intensity calculation

The combination of multiple AUs indicates an individual's expressions. For example, fear expression shows a positive correlation with AU1, AU2, and AU4 [24]. In the clinical context, the use of AU serves as a fundamental indicator for pain assessment through systematic detection of pain-related facial expressions. Prkachin and Solomon established a validated pain measurement framework using four key AUs: AU4 (brow lowering), AU6 or AU7 (narrowing of the eyes), AU9 or AU10 (raising the upper lip), and AU43 (eye closure). This pain measurement method is also known as Prkachin and Solomon Pain Intensity (PSPI) [25]. Facial pain expression can also be assessed using AU25, AU26, and AU27, which collectively represent mouth-opening movements. Research has demonstrated that self-reported pain intensity shows a stronger correlation with these mouth-opening action units than with eye-narrowing and upper-lip-raising movements [26] [27]. Furthermore, studies by Kunz et al. [28] which examined pain-related facial expressions in dementia patients, have identified AU12 (lip corner puller) as a predefined pain-related action unit associated with moderate-to-severe pain levels. Meanwhile, lip movement-related AUs such as AU20 (lip stretcher) and AU24 (lip press) occur more frequently in clinical pain studies than in experimental pain, suggesting that these AUs are more prominent in real-world clinical pain expressions than in brief experimental pain episodes.

However, these AU combinations would be insufficient if subtle changes in facial muscles remain undetectable by the human eye, as facial expressions can change within 350 milliseconds [9]. Therefore, computer vision techniques are essential in identifying pain in videos of recorded facial expressions. In this study, AUs were extracted using the Py-Feat library [24] in Python. The intensity of the extracted AUs ranges from 0.0 to 1.0, with 1.0 representing the most intense AU detected in the image. Extracted Intensity values were subjected to rolling average smoothing over a specific number of sequential frames to reduce noise from detection failures or periods when subjects displayed minimal facial movement. Since a short period of facial micro expression, approximately 1-6 frames at standard video frame rates of 24–30 fps, to evaluate the impact

of temporal smoothing on pain classification performance without fading pain-triggered frames, we compared a 1-frame window (no smoothing) with a 3-frame rolling average before the binarization step in token sequence modeling. We examine the level of pain following AUs, using multiple studies previously mentioned, including AU04, AU06, AU09, AU10, AU12, AU20, AU24, AU25, AU26, AU27, and AU43. These AUs were implemented for the analysis, selected based on their average correlation with the data labeled with pain values.

2.2 Pain Evaluation

There are numerous methods for evaluating patient pain; however, patient self-report is the most common for determining their pain level. The Numeric Rating Scale (NRS), also sometimes called the Visual Analogue Score (VAS) is the optimal indicator for assessing the pain level in a conscious patient for self-report; it consists of discrete values between zero and ten; 0 indicates "no pain at all," and 10 indicates "pain as severe as you can imagine." In this study, pain labels in the UNBC-SP dataset were classified into four classes as no pain, mild, moderate, and severe based on a 0-10 self-report NRS of zero, between 1 and 3, between 4 and 6, and greater than 6 points, respectively [29], since the MIntPain dataset has already been classified. We did not perform any further label classification on this dataset.

2.3. Methodology

This study proposes a dual-pathway framework for automatic facial pain recognition that integrates continuous-time-series modelling with a symbolic, token-based alternative. In this section, we introduce the corpora, describe preprocessing and feature engineering, outline the modelling strategies, and detail the evaluation protocol. All code was written in Python 3.

2.3.1 Dataset

We surveyed publicly available facial expression databases to identify those suitable for video-based pain level classification. Key criteria for inclusion were: (1) the data consist of face videos (or frame sequences) and (2) each sequence has an associated pain intensity label, preferably on a numerical rating scale (NRS). Several candidate datasets were reviewed [11] , and two were selected for our experiments due to their relevance and the availability of AU annotations. In this work we focus on the (1) UNBC-McMaster Shoulder Pain Expression Archive (UNBC-SP) and (2) Multimodal Intensity Pain (MIntPain) which provide both video and frame-level AU information along with numeric pain intensity annotations (VAS/NRS), making them well-suited for our AU-based approach.

UNBC-SP is a widely used dataset of spontaneous pain expressions in adult patients with shoulder injuries. This archive comprises 200 video sequences totaling 48,398 annotated video frames from 25 patients with rotator-cuff injuries performing prescribed arm movements. Each sequence has a self-reported Visual Analogue Scale (VAS, 0–10) rating and an expert Observer Pain Index. Following Prkachin et al., VAS scores were discretized into four ordinal classes: no pain (0), mild (1–3), moderate (4–6), and severe (7–10) to align with clinical practice while mitigating class imbalance.

The MIntPain database contains 187,939 frames from 1,600 stimulus sweeps across 20 healthy participants who received graded electrical-muscle stimulation. Pain level is annotated on a five-point scale (0–4). Only RGB imagery is provided; consequently, all Action Units (AUs) were re-extracted (Section 3.2) to ensure a homogeneous feature space across datasets.

For each corpus, cases were stratified into a 70 % development set and a 30 % hold-out test set. Within the development fold, we executed a stratified three-fold cross-validation (CV): two folds for training and one for validation, cycling through the folds. Stratified splitting was adopted to preserve the class distribution in each fold, which is particularly important given the class imbalance present in pain datasets [30]. Three folds were chosen as a practical compromise between estimation variance and the limited number of sequences available per class. All model hyperparameter tuning was conducted within these inner CV folds using a nested procedure to prevent information leakage from validation data into hyperparameter selection [31]. The final hold-out set was kept separate and was evaluated exactly once for each trained model configuration, to obtain an unbiased performance estimate.

2.3.2 Preprocessing

2.3.2.1 Action-Unit extraction

Frame-wise AU intensity values were computed for each video frame using the Py-Feat toolbox [24] with a face detector and a ResNet-50 backbone for feature extraction. Detected facial landmarks were aligned using img2pose to normalize head pose. To compensate for varying lighting conditions and camera setups, each sequence's AU time series was standardized to a zero mean and unit variance per AU to preserve temporal dynamics while equalizing scale.

2.3.2.2 Time-series representation

We aggregated frame-level AU vectors into time-series representations for each subject video. Since video lengths varied widely across our dataset, we implemented sequence-length normalization to ensure consistent model input dimensions. Three strategies were evaluated: (1) truncation, which reduced all sequences to the shortest length, discarding excess frames from longer videos; (2) average-length adjustment, which set sequences to the dataset's mean length (rounded to the nearest integer) by truncating longer sequences and padding shorter ones with low-variance Gaussian-noise frames to reach the target length; and (3) padding to the longest length, which extended all sequences to the maximum observed length by adding small, zero-centered Gaussian-noise frames to shorter sequences, approximating near-neutral expressions and avoiding constant-zero padding.

After applying one of these normalization methods, each sequence was further standardized (per sequence) to zero mean and unit variance to address residual differences in overall intensity across subjects or recording conditions. We then addressed class imbalance in the training data by oversampling minority classes using the Synthetic Minority Over-sampling Technique (SMOTE) [32]. SMOTE has demonstrated high effectiveness in oversampling for various sequence-based models with imbalanced datasets [33]. In our implementation, each time-series sequence, originally represented as a tensor $x \in \mathbb{R}^{N\times T\times F}$ were processed, where N is the number of samples after oversampling, T is the number of timesteps, and F is the number of features. Each sequence X_i is flattened into a one-dimensional vector $x_i \in \mathbb{R}^{(T\cdot F)}$ SMOTE then generates synthetic samples by interpolating between a minority sample x_i and one of its nearest neighbors x_j using a random number between 0 and 1, represented as δ, according to equation 1. Finally, the synthetic vectors x_{syn} are reshaped back into the three-dimensional form (T, F) for subsequent analyses.

$$x_{syn} = x_i + \delta(x_j - x_i) \quad (1)$$

In addition to oversampling, we applied data augmentation to the AU time series to expand the effective training set and improve generalization. We generated augmented versions of each sequence using several standard time-series augmentation methods [34]: jittering, scaling, permutation, and time warping. These transformations have been used in prior time-series classification research to simulate variations while preserving class characteristics [34]. We also included a "no augmentation" case for baseline comparison. All augmented sequences inherit the original sequence's label. By training on both original and augmented samples, we aim to increase model robustness to variations in facial movement and potential measurement noise.

2.3.2.3 Tokenized AU Sequence Processing

Nie et al. [35] propose segmenting time series into patch "tokens" for a Vision Transformer-like model, markedly improving performance on long sequences [35]. Thus, we also experimented with a novel representation of the AU time series as tokenized "text" sequences, enabling the use of text-based classification techniques. In this approach, each video's AU sequence is converted into a "sequence" of textual tokens by discretizing the AU intensities and treating each frame as a "word". The conversion process involved several steps. We first applied a rolling average size 1 (no smoothing) and 3 frames to smooth intensity values before binarization. As a result, we produced a "sentence-like" structure, where each frame corresponds to a token describing which AUs are present (equation 2), where $\widetilde{AU}_t^{(i)}$ is the averaged intensity of AU i at frame t, and w is the window size. After smoothing, the class imbalance was again addressed by oversampling minority classes.

$$\widetilde{AU}_t^{(i)} = \frac{1}{w} \sum_{j=t-w+1}^{t} \widetilde{AU}_t^{(i)} \quad (2)$$

Converting graded AU outputs into categorical occurrence labels has been used in facial expression analysis [36]. In our study, we binarized AU intensities using relative thresholds on the normalized 0.00–1.00 Py-Feat scale, similar to how manual FACS coding distinguishes between absent and present AUs using discrete intensity levels. AU intensities were binarized using equation 3 with thresholds $\theta \in \{0.25, 0.50\}$, consistent with common AU practices and corresponding to "low-to-moderate" vs "moderate" activation zones.

$$AU_t^{(i)} = \begin{cases} 1 & \text{if } AU_t^{(i)} > \theta \\ 0 & \text{Otherwise} \end{cases} \quad (3)$$

Each binary vector of 11 AUs per frame is then converted into a symbolic representation by formatting each AU value into a binary string and concatenating them into a compact token for that frame. For example, a frame with AU01=1, AU06=0, AU09=1, and so on, is encoded as shown in equation 4, yielding a token such as "10100100011". Tokens from successive frames were joined with whitespace to form a textual sequence for the entire video. Before modeling, a tokenizer was applied, and SMOTE was implemented to address class imbalance.

$$AU_Str_t = AU04_t + AU06_t + \cdots + AU43_t \quad (4)$$

2.3.3 Modeling

Our objective was to classify each video (the AU sequence) into the correct pain level. We pursued two complementary approaches: (1) sequence-based modeling on continuous AU time series, and (2) token-based modeling on discrete AU text sequences.

2.3.3.1 Continuous-sequence models

Six neural architectures were implemented in TensorFlow 2 to evaluate a range of sequence modeling strategies shown to be effective for time-series classification. Recurrent architectures were selected for their capacity to model sequential dependencies. A three-layer 1D CNN was included to capture local temporal patterns through convolutional filters; vanilla LSTMs and GRUs were included as established gated recurrent units designed to capture long-range temporal patterns; and a bidirectional LSTM was used to exploit both forward and backward context. A simple RNN served as a non-gated baseline, and a hybrid CNN + LSTM combined local feature extraction with sequential modeling. Hidden widths were constrained to 50–250 units, and recurrent depth to 2 layers, to limit overfitting. Networks were optimized with Adam under categorical cross-entropy. In parallel, traditional classifiers were trained on flattened sequences to provide a complementary set of non-sequential baselines. These included random forests (RF), extreme gradient boosting (XGB), support vector machines (SVM), decision trees (DT), Gaussian naïve Bayes (NB), k-nearest neighbors (KNN), and a multivariate classifier (MVC). A 30-trial random search was performed within each CV fold to select hyperparameters.

2.3.3.2 Token-sequence models

In this approach, three model families were explored to assess the suitability of different classification paradigms for the tokenized AU representation. (1) BERT, which is a pre-trained transformer-based language model that has achieved state-of-the-art results in numerous NLP sequence classification tasks, was fine-tuned for multi-class sequence classification; maximum token length equaled the longest training sentence. (2) Classical machine learning classifiers were trained on features extracted from the tokenized sequences to evaluate whether established algorithms can exploit the symbolic co-occurrence patterns. These included Multilayer perceptron (MLP), logistic regression (LR), Extra Trees (ET), DT, RF, NB, KNN, SVM, and XGB. Finally, we also experimented with a lightweight parameter-free method (3) called "Low-Resource," which is a parameter-free 5-NN classifier that employsormalized Compression Distance (NCD) as the similarity metric [37].

2.4 Evaluation

Performance was quantified by overall accuracy defined as the proportion of correctly classified samples: Accuracy is equal to (TP + TN) / (TP + TN + FP + FN), where TP, TN, FP, and FN represent true positive, true negative, false positive, and false negative counts, respectively. Accuracy was selected as the primary metric because SMOTE oversampling was applied to balance the class distribution in the training data, thereby reducing bias toward the majority classes that would otherwise make accuracy misleading in imbalanced data. Reported values correspond to the mean ± standard deviation across the three outer CV splits, where the standard deviation provides insight into the stability of model performance across different data partitions. Distributional assumptions were assessed using the Shapiro–Wilk test for normality of the model residuals and Levene's test for homogeneity of variances across groups. Where both assumptions were satisfied, a two-factor mixed ANOVA (alignment strategy × augmentation) was performed to analyze main effects and their interaction. Otherwise, the Kruskal–Wallis test followed by Dunn–Bonferroni post-hoc comparisons was applied. Significance was accepted at p-value < 0.05. Following significant omnibus tests, pairwise comparisons were conducted using Tukey's HSD test for parametric analyses and the Dunn–Bonferroni procedure for non-parametric analyses, both controlling the family-wise error rate. To counteract hyperparameter optimism, the best configuration from each inner CV loop was retrained on the entire development fold before a single evaluation on the holdout data.

3. Results and Discussion

In this section, we present the results of continuous-time series modeling and tokenized sequence modeling, and then discuss their implications. Examination was performed across the UNBC-SP and MIntPain facial pain datasets. The goal of this study was to identify which strategy, and which specific configuration within each strategy, produced the highest classification accuracy for pain detection. Statistical analysis involved mean accuracies from 3-fold cross-validation and, when relevant, subsequent ANOVA or post hoc comparisons. All reported p-values, effect sizes, and confidence intervals stem from these tests.

3.1 Continuous time-series modeling – UNBC-SP dataset

For the continuous-AU strategy, we evaluated three sequence alignment methods (Truncation, Averaging, and Padding) combined with five augmentation schemes (None, Jitter, Scaling, Time Warping, and Permutation). On the UNBC-SP dataset, results indicated that model performance varied significantly by augmentation ($F(4,42)=3.02$, $p=0.027$), although multiple pairwise comparisons did not detect consistently large differences, except for Permutation, which significantly reduced accuracy in several classifiers (e.g., SVM dropped from 79% to 51%). The alignment strategy also approached significance ($p=0.0585$), with truncation and averaging generally outperforming padding. Across all continuous models on the UNBC-SP dataset, the highest accuracy reached about 84% (RF under Averaging with no augmentation). Some deep learning architectures, such as Bi-directional LSTM, achieved around 69% but did not surpass the best classical models. Table 1 summarizes the mean accuracy results for the UNBC-SP dataset on continuous-model experiments under each alignment and augmentation condition.

3.2 Continuous time-series modeling - MIntPain dataset

In contrast, the continuous-model approach on the MIntPain dataset yielded higher peak performance (see Table 2). The top accuracy was approximately 91%, achieved by an SVM classifier with a truncation alignment and three augmentation approaches, including no augmentation, jittering, and scaling method, followed by an RF with a truncation alignment and two augmentation approaches, including no augmentation and jittering, and a GRU-based model with a truncation alignment and scaling augmentation method, that both approached 90%. Statistical tests indicated that alignment ($F(2,42)=6.88$, $p<0.005$) and augmentation ($F(4,42)=4.11$, $p=0.006$) significantly influenced performance on MIntPain. Post-hoc comparisons showed that disruptive augmentations, such as permutation, undermined results on datasets like the UNBC-SP, while less intrusive operations, such as jittering or minor Scaling, introduced no significant detriment compared to no augmentation.

Table 1. Mean accuracy % for continuous time-series modeling using the UNBC-SP dataset with various alignments and augmentation methods

	Truncate					Padding					Average				
	N	**JT**	**SC**	**PM**	**TW**	**N**	**JT**	**SC**	**PM**	**TW**	**N**	**JT**	**SC**	**PM**	**TW**
1DCNN	0.60	0.60	0.64	0.44	0.59	0.42	0.39	0.44	0.29	0.26	0.66	0.63	0.65	0.51	0.43
LSTM	0.44	0.42	0.45	0.30	0.29	0.25	0.25	0.25	0.34	0.25	0.21	0.23	0.28	0.23	0.25
RNN	0.61	0.60	0.61	0.40	0.62	0.31	0.60	0.35	0.25	0.27	0.54	0.51	0.51	0.40	0.52
GRU	0.51	0.51	0.51	0.40	0.54	0.33	0.27	0.36	0.38	0.28	0.38	0.43	0.46	0.29	0.49
Bi LSTM	0.69	0.69	0.65	0.45	0.63	0.59	0.58	0.52	0.31	0.38	0.65	0.67	0.68	0.50	0.60
CNN+LSTM	0.49	0.47	0.54	0.34	0.36	0.28	0.25	0.25	0.25	0.29	0.19	0.35	0.27	0.27	0.26
DT	0.56	0.50	0.47	0.36	0.47	0.63	0.64	0.56	0.47	0.58	0.61	0.57	0.59	0.36	0.59
RF	0.69	0.74	0.71	0.49	0.63	0.72	0.72	0.66	0.56	0.66	**0.84**	0.74	0.72	0.50	0.64
NB	0.60	0.60	0.60	0.40	0.29	0.49	0.49	0.50	0.35	0.48	0.58	0.58	0.57	0.40	0.46
KNN	0.57	0.57	0.56	0.39	0.58	0.70	0.70	0.69	0.52	0.62	0.66	0.66	0.67	0.47	0.55
SVM	**0.79**	**0.79**	0.78	0.51	0.68	0.80	**0.81**	0.79	0.52	0.58	0.83	0.83	0.83	0.52	0.59
XGB	0.66	0.67	0.68	0.44	0.58	0.75	0.74	0.73	0.53	0.69	0.74	0.74	0.75	0.51	0.68
Arima	0.20	0.20	0.20	0.20	0.20	0.20	0.20	0.20	0.20	0.20	0.20	0.20	0.20	0.20	0.20

Table 2. Mean accuracy % for continuous time-series modeling using the MIntPain dataset with various alignments and augmentation methods

	Truncate					Padding					Average				
	N	**JT**	**SC**	**PM**	**TW**	**N**	**JT**	**SC**	**PM**	**TW**	**N**	**JT**	**SC**	**PM**	**TW**
1DCNN	0.84	0.85	0.84	0.51	0.73	0.86	0.85	0.85	0.48	0.33	0.85	0.84	0.84	0.51	0.54
LSTM	0.81	0.82	0.80	0.67	0.77	0.51	0.37	0.34	0.27	0.24	0.68	0.69	0.69	0.55	0.50
RNN	0.84	0.84	0.82	0.54	0.73	0.44	0.48	0.41	0.25	0.25	0.70	0.77	0.78	0.40	0.38
GRU	0.82	0.81	0.90	0.66	0.77	0.69	0.66	0.59	0.49	0.39	0.73	0.76	0.74	0.59	0.58
Bi LSTM	0.85	0.85	0.84	0.59	0.78	0.73	0.72	0.61	0.45	0.54	0.74	0.79	0.77	0.50	0.65
CNN+LSTM	0.84	0.83	0.84	0.66	0.71	0.22	0.23	0.23	0.23	0.22	0.70	0.68	0.68	0.51	0.46
MVC	0.33	0.31	0.29	0.28	0.28	0.33	0.32	0.27	0.25	0.24	0.31	0.31	0.29	0.25	0.23
DT	0.57	0.55	0.52	0.31	0.51	0.56	0.53	0.48	0.32	0.52	0.27	0.55	0.48	0.32	0.53
RF	0.90	0.90	0.89	0.52	0.81	0.89	0.88	0.82	0.53	0.78	0.83	0.89	0.86	0.50	0.79
NB	0.39	0.39	0.39	0.29	0.31	0.27	0.27	0.27	0.21	0.21	0.32	0.32	0.32	0.26	0.23
KNN	0.77	0.77	0.77	0.45	0.76	0.77	0.76	0.76	0.43	0.48	0.77	0.76	0.76	0.43	0.61
SVM	**0.91**	**0.91**	**0.91**	0.56	0.85	0.88	0.88	0.88	0.52	0.45	0.83	0.87	0.87	0.51	0.61
XGB	0.87	0.86	0.85	0.51	0.77	**0.88**	**0.88**	0.85	0.53	0.78	**0.86**	0.87	0.85	0.49	0.77
Arima	0.20	0.20	0.20	0.20	0.20	0.20	0.20	0.20	0.20	0.20	0.20	0.20	0.20	0.20	0.20

3.3 Tokenized sequence modeling – UNBC-SP dataset

For the token-based approach, we focused on two key preprocessing parameters: the smoothing window (1-frame vs. 3-frame averaging) and the binarization threshold (e.g., 0.25 vs. 0.5). A two-way ANOVA revealed a statistically significant effect of smoothing ($F(1,12)=7.92$, $p<0.05$) such that a 3-frame average lowered accuracy for most classifiers. By contrast, the binarized threshold manipulations had little effect on overall performance ($F(1,12)=0.44$, $p=0.52$). Several machine learning models, especially ensemble-based methods such as KNN, ET, and RF, achieved high accuracy (up to 82%). In comparison, the recurrent deep networks and the BERT-based classifiers struggled with tokenized sequences, often performing at chance levels of 20 to 30 percent accuracy for the four-class task. Statistical tests supported a significant performance

gap between classical and deep models on tokenized UNBC-SP data ($p<0.001$), with classical methods outperforming the neural architectures by large margins.

3.4 Tokenized sequence modeling – MIntPain dataset

Tokenized results on the MIntPain dataset were qualitatively similar to those of the UNBC-SP. Sequence data with a 1-frame window yielded better accuracy than 3-frame smoothing, although the smoothing effect did not reach statistical significance (ANOVA, $F(1,12) = 0.36$, $p = 0.56$). The binarization threshold again had no notable impact ($p = 0.56$). The best-performing models on token data were classical ensemble methods, achieving accuracies around 82%, comparable to the UNBC-SP token results. Neural network models (LSTMs, BERT, etc.) generally did not surpass random guessing on tokenized sequences for MIntPain, suggesting difficulty learning from the discrete token representation with limited data. For example, ensemble methods such as KNN, ET, and RF significantly outperformed deep models on token data, such as the UNBC-SP dataset. Table 3 summarizes the token-based modeling accuracies across various settings. It shows the limited influence of threshold choices and the consistently stronger performance of classical algorithms over deep learning in this context.

Table 3. Mean accuracy % for tokenized sequence modeling with UNBC-SP and MIntPain dataset, modeling with each different average window (1-frame and 3-frame) and threshold (0.25, 0.5)

	UNBC-SP				**MIntPain**			
Rolling Average	**1-frame window**		**3-frame window**		**1-frame window**		**3-frame window**	
Threshold	**0.25**	**0.5**	**0.25**	**0.5**	**0.25**	**0.5**	**0.25**	**0.5**
RNN	0.43	0.43	0.43	0.2	0.5	0.5	0.5	0.5
LSTM	0.18	0.18	0.43	0.18	0.5	0.5	0.5	0.5
GRU	0.43	0.18	0.2	0.43	0.5	0.5	0.5	0.5
Bi-LSTM	0.4	0.33	0.3	0.43	0.5	0.5	0.5	0.5
BERT	0.43	0.43	0.43	0.43	0.5	0.5	0.5	0.5
MLP	0.74	0.74	0.68	0.67	0.75	0.72	0.69	0.65
LR	0.3	0.29	0.24	0.31	0.25	0.25	0.24	0.25
ExtraTree	**0.82**	0.81	0.71	0.71	**0.82**	**0.82**	0.73	0.69
DT	0.58	0.58	0.56	0.56	0.58	0.59	0.56	0.55
RF	0.79	0.77	0.69	0.69	0.79	0.8	0.71	0.67
NB	0.23	0.23	0.21	0.22	0.22	0.22	0.21	0.22
KNN	0.78	0.75	0.67	0.66	0.78	0.78	0.69	0.64
SVM	0.68	0.74	0.61	0.68	0.68	0.72	0.62	0.64
XGB	0.67	0.63	0.57	0.59	0.58	0.58	0.55	0.51
Low Resource	0.23	0.23	0.25	0.24	0.2	0.21	0.23	0.21

3.5 Comparison of Continuous vs. Token approaches

A direct comparison between the continuous and tokenized strategies highlights a few important points. On the MIntPain dataset, continuous-time series modeling achieved higher overall accuracy (peak ~91%) than the token-based approach (peak ~82%), and this difference was statistically significant ($p < 0.01$). In contrast, on the smaller UNBC-SP dataset, the top continuous and tokenized accuracies were very similar (~84% vs. 82%) and not significantly different ($p = 0.34$). Classical machine-learning algorithms emerged as strong contenders across both continuous and tokenized pipelines, whereas deep learning architectures were more effective on continuous data and generally less competitive in the tokenized condition. Post hoc Tukey tests confirmed that the permutation augmentation consistently reduced performance across models (in both strategies and datasets), and that smoothing frames before tokenization often lowered accuracy without providing benefits.

3.6 Discussion

The study results show that continuous-time series analysis combined with classical machine learning, and, in some settings, with deep learning, yields higher or at least comparable performance to the sentence tokenization approach on both datasets. Tokenization reduced accuracy across most models, especially in complex deep learning architectures. This pattern likely reflects the small sample size and data imbalance, which favor lower-complexity classifiers. Considering the results together, retaining continuous action-unit dynamics confers a clear advantage over the tokenized-sequence strategy. Notably, classical models such as random forests and ET often matched or surpassed deep learning, which, in some configurations, approached chance. This gap can be interpreted through several factors related to data representation and model capacity. One issue came from the data preprocessing step: the binarization step in the tokenization process removes the graded intensity information from each AU, causing models to lose access to the continuous intensity gradients they rely on for capturing temporal dynamics. The dataset sizes of approximately 200 sequences for UNBC-SP and approximately 1,600 sequences for MIntPain dataset are also the big issue that leading to insufficient for data classification using neural network architecture, especially, BERT, which was designed for large scale language modeling, showed accuracy results close to random chance when trained on these limited tokenized sequences, indicating that the model failed to converge on meaningful representations of the tokenized input. While binarization reduces information content for complex models, this simplification may flatten data patterns, helping tree-based and margin-based classifiers find useful decision boundaries. Models such as RF, ET, and SVM can effectively exploit co-occurrence patterns of binary AU activations without requiring full intensity resolution, which explains their relatively stronger performance on tokenized data. However, the result 82% accuracy with the sentence tokenization method and 91% with the continuous time series method supports the feasibility of using temporal dynamics data, such as facial action units, to assist in classifying facial expression characteristics in human pain, which is consistent with previous research [38] that emphasizes motion cues in pain recognition.

The statistical analysis shows that specific preprocessing choices materially affect outcomes. The truncation and average length alignment generally outperformed padding. The permutation augmentation technique reduced accuracy by disrupting the temporal order. Permutation augmentation strategies result in reduced accuracy because they disrupt temporal order. Simultaneously, although data tested with jittering and scaling augmentation methods may demonstrate higher accuracy in some datasets, statistical tests indicate that outcomes may show minimal or no differences compared to not implementing these methods. For the tokenization process, it was found that 3-frame window smoothing reduces accuracy, and the different thresholds used to binarize AU intensity data in this study do not significantly affect results. This supports the micro-expression principle that AU changes over short time intervals are crucial for pain differentiation, as smoothing these values removes important information from the dataset. Therefore, the results of this study indicate that preserving fine-scale temporal data details and avoiding disturbance or temporal-sequence transformation of data represent an appropriate method for analyzing facial pain from AU data in sequence format.

Finally, this study reflects both the support and limitations of pain classification from facial AU sequences. First, dataset size and quality remain primary factors determining model performance, as this study demonstrates that the MIntPain dataset, with its larger data volume, produces clearly improved results compared to the UNBC-SP dataset. Second, preserving the data sequence, avoiding unnecessary data reduction, and managing data balance are crucial for developing pain-detection systems from facial expressions. Finally, although CV evaluation includes controlled hyperparameter selection and statistical testing, external validation covering diverse data sources, equipment, and populations, along with calibration, will enhance readiness for clinical applications.

4. Conclusion

This study developed a novel dual-pathway system for facial pain recognition by combining continuous time-series analysis of action units with a tokenized sequence approach. Instead of focusing primarily on continuous time-series representations of AU data, this study applied a tokenized AU sequence

approach, treating frame-level binarized AUs as text-like tokens, for facial pain classification using NLP-based models. A systematic comparison between continuous and tokenized representation strategies across multiple classifier families, including traditional machine learning, deep learning, and low-resource methods, was introduced in this study. The classification architecture was tested on two datasets, UNBC-SP and MIntPain, and showed that continuous models yielded the best results, with accuracies of up to 91% on the SVM classifier using the MIntPain dataset and 84% on the RF classifier using the UNBC-SP dataset. Tokenization was less effective overall but still reached about 82% accuracy with classical models on the UNBC-SP dataset, suggesting that it may be useful in certain conditions. Augmentation methods, such as permutation, reduced accuracy, while smoothing did not improve performance for tokenized models. The results also indicate that preserving the temporal sequence of action units is important for accurate pain classification. The findings of this study contribute to the development of non-invasive pain assessment tools for patients in palliative care settings who have limited ability to self-report pain, such as those with dementia, laryngeal cancer, or end-stage illness. Continuous AU monitoring from video can capture micro-expressions that indicate pain at time scales difficult for human observers to detect, which could serve as a decision-support tool for healthcare providers in evaluating pain levels. Importantly, this study clarifies which data representations and model architectures can extract discriminative features from AU data and which cannot. These empirical insights can serve as a reference for future research on facial pain recognition, enabling researchers to select appropriate tools and methods more efficiently and accelerating progress toward practical clinical applications.

The main limitation of this work is the small size and restricted scope of available datasets. The models were tested only on controlled data, and their performance in real-world settings is still uncertain. There was also no independent verification of the pain labels, and only a limited set of preprocessing parameters was examined. Future work should focus on expanding datasets to include a wider range of patients and conditions, as well as testing in natural, uncontrolled environments. It will also be important to include expert review of labels, explore more advanced sequence models such as Transformers, and test how different frame rates affect accuracy. For practical use in clinics, further steps will be needed to address video quality, privacy, and usability. Finally, the most important challenge in pain analysis research for palliative care patients is developing systems capable of identifying background pain or non-stimulus-evoked pain, which would help overcome the communication barriers that currently limit pain assessment and improve quality of life in this patient group. With these improvements, automated facial pain recognition could become a reliable tool to support healthcare providers in monitoring and managing patient pain.

5. Acknowledgement

The author would like to express gratitude to Asst. Prof. Dr. Prompong Sugunnasil for his continued support and guidance throughout this study. The author is also grateful to the dataset owners who provided access to their resources and made this research possible. Finally, the author would like to acknowledge the earlier work of Atigorn Sanguansri, which provided an important inspiration for the direction of this study.

Author Contributions:

Conceptualization:	AP (Akkapop Prasompon), PS (Prompong Sugunnasil), AS (Atigorn Sanguansri)
Methodology:	AP and PS
Software:	AP
Validation:	AP and PS
Formal analysis:	AP
Investigation:	AP
Resources:	AP and PS
Data Curation:	AP
Writing - original draft:	AP
Writing - review & editing:	AP and PS
Visualization:	AP
Supervision:	PS
Project administration:	PS

Funding: This research received no external funding.

Conflicts of Interest: The authors declare no conflict of interest.

References

[1] Miller, K. D.; Leticia, N.; Theresa, D. Cancer Treatment and Survivorship Statistics, 2022. *CA Cancer J. Clin.* **2022**, *5*, 409–436. https://doi.org/10.3322/caac.21731

[2] Parikh, R. B.; Kirch, R. A.; Thomas, J. S. Early Specialty Palliative Care—Translating Data in Oncology into Practice. *N. Engl. J. Med.* **2013**, *24*, 2347–2351. https://doi.org/10.1056/NEJMsb1305469

[3] Laura, A. P. M. Why and How to Integrate Early Palliative Care into Cutting-Edge Personalized Cancer Care. *J. Clin. Oncol. Educ. Book* **2024**.

[4] World Health Organization. *Palliative Care*; World Health Organization: Geneva, Switzerland, 2023; https://www.who.int/europe/news-room/fact-sheets/item/palliative-care (accessed June 1, 2023).

[5] Clark, D.; Nicole, B.; Clelland, E. G. Mapping Levels of Palliative Care Development in 198 Countries: The Situation in 2017. *J. Pain Symptom Manage.* **2020**, 794–807. https://doi.org/10.1016/j.jpainsymman.2019.11.009

[6] Dowell, D.; Ragan, K.; Jones, C. CDC Clinical Practice Guideline for Prescribing Opioids for Pain—United States, 2022. *MMWR Recomm. Rep.* **2022**. https://doi.org/10.15585/mmwr.rr7103a1

[7] Cohen, B.; Leigh, J. R.; Charles, V. P. *Opioid Analgesics*; StatPearls Publishing: Treasure Island, FL, USA, 2017.

[8] De, S.; Gioacchino, D. Using AI to Detect Pain through Facial Expressions: A Review. *Bioengineering* **2023**, 548. https://doi.org/10.3390/bioengineering10050548

[9] Ekman, P.; Friesen, W. V. Facial Action Coding System. *Environ. Psychol. Nonverbal Behav.* **1978**. https://doi.org/10.1037/t27734-000

[10] Safikhani, S.; Gries, K. S.; Trudeau, J. J. Response Scale Selection in Adult Pain Measures: Results from a Literature Review. *J. Patient-Rep. Outcomes* **2018**, *2*, 1–9. https://doi.org/10.1186/s41687-018-0053-6

[11] Fang, R.; Hosseini, E.; Zhang, R. Survey on Pain Detection Using Machine Learning Models: Narrative Review. *JMIR AI* **2025**, *4*, e53026. https://doi.org/10.2196/53026

[12] Wen, C. T.; Du, T.; Teo, J. C. Automated Pain Detection Using Facial Expression in Adult Patients with a Customized Spatial Temporal Attention Long Short-Term Memory (STA-LSTM) Network. *Sci. Rep.* **2025**, *15*, 13429. https://doi.org/10.1038/s41598-025-97885-5

[13] Chen, Z.; Ansari, R.; Wilkie, D. J. Automated Detection of Pain from Facial Expressions: A Rule-Based Approach Using AAM. In *Proceedings of SPIE*; 2012; Vol. 8314, 83143O. https://doi.org/10.1117/12.912537

[14] Takalkar, M. A.; Min, X. Image-Based Facial Micro-Expression Recognition Using Deep Learning on Small Datasets. In *Proceedings of the International Conference on Digital Image Computing: Techniques and Applications (DICTA)*; 2017; pp 1–7. https://doi.org/10.1109/DICTA.2017.8227443

[15] Hassan, T.; Seus, D.; Wollenberg, J.; Weitz, K.; Kunz, M.; Lautenbacher, S.; Garbas, J.-U.; Schmid, U. Automatic Detection of Pain from Facial Expression: A Survey. *IEEE Trans. Pattern Anal. Mach. Intell.* **2021**, *43*, 1815–1831. https://doi.org/10.1109/TPAMI.2019.2958341

[16] Lautenbacher, S.; Hassan, T.; Seuss, D. Automatic Coding of Facial Expressions of Pain: Are We There Yet? *Pain Res. Manag.* **2022**, *2022*. https://doi.org/10.1155/2022/6635496

[17] Chongwen, W.; Wang, Z. Progressive Multi-Scale Vision Transformer for Facial Action Unit Detection. *Front. Neurorobot.* **2022**, *15*. https://doi.org/10.3389/fnbot.2021.824592

[18] Pouromran, F.; Lin, Y.; Kamarthi, S. Personalized Deep Bi-LSTM RNN Based Model for Pain Intensity Classification Using EDA Signal. *Sensors* **2022**, *21*, 8087. https://doi.org/10.3390/s22218087

[19] Chen, Z.; Ansari, R.; Wilkie, D. J. Learning Pain from Action Unit Combinations: A Weakly Supervised Approach via Multiple Instance Learning. *IEEE Trans. Affect. Comput.* **2022**, *31*, 135–146. https://doi.org/10.1109/TAFFC.2019.2949314

[20] Tran, M.; Siniukov, M.; Jin, Z.; Soleymani, M. Discrete Facial Encoding: A Framework for Data-Driven Facial Display Discovery. *arXiv* **2025**, arXiv:2510.01662

[21] Devlin, J.; Chang, M.-W.; Lee, K. BERT: Pre-Training of Deep Bidirectional Transformers for Language Understanding. In *Proceedings of NAACL-HLT*; 2019; pp 4171–4186.

[22] Lucey, P.; Cohn, J. F.; Prkachin, K. M. Painful Data: The UNBC-McMaster Shoulder Pain Expression Archive Database. In *Proceedings of the IEEE Int. Conf. Autom. Face Gesture Recognit. (FG)*; 2011; pp 57–64. https://doi.org/10.1109/FG.2011.5771462

[23] Haque, M. A.; Bautista, R. B.; Noroozi, F. Deep Multimodal Pain Recognition: A Database and Comparison of Spatio-Temporal Visual Modalities. In *Proceedings of the IEEE Int. Conf. Autom. Face Gesture Recognit. (FG 2018)*; 2018; pp 250–257. https://doi.org/10.1109/FG.2018.00044

[24] Cheong, J. H.; Jolly, E.; Xie, T. Py-Feat: Python Facial Expression Analysis Toolbox. *Affect. Sci.* **2023**, 781–796. https://doi.org/10.1007/s42761-023-00191-4

[25] Prkachin, K. M. The Consistency of Facial Expressions of Pain: A Comparison across Modalities. *Pain* **1992**, *51*, 297–306. https://doi.org/10.1016/0304-3959(92)90213-U

[26] Kunz, M.; Meixner, D.; Lautenbacher, S. Facial Muscle Movements Encoding Pain—A Systematic Review. *Pain* **2019**, *160*, 535–549. https://doi.org/10.1097/j.pain.0000000000001424

[27] Dildine, T.; Atlas, L. The Need for Diversity in Research on Facial Expressions of Pain. *Pain* **2019**, *160*, 1901–1902. https://doi.org/10.1097/j.pain.0000000000001593

[28] Atee, M.; Hoti, K.; Chivers, P.; Hughes, J. D. Faces of Pain in Dementia: Learnings from a Real-World Study Using a Technology-Enabled Pain Assessment Tool. *Front. Pain Res.* **2022**, *3*. https://doi.org/10.3389/fpain.2022.827551

[29] Boonstra, A. M.; Stewart, R. E.; Köke, A. J. Cut-Off Points for Mild, Moderate, and Severe Pain on the Numeric Rating Scale for Pain in Patients with Chronic Musculoskeletal Pain: Variability and Influence of Sex and Catastrophizing. *Front. Psychol.* **2016**, *7*, 1466. https://doi.org/10.3389/fpsyg.2016.01466

[30] Kohavi, R. A Study of Cross-Validation and Bootstrap for Accuracy Estimation and Model Selection. In *Proceedings of the Int. Joint Conf. Artif. Intell. (IJCAI)*; 1995; pp 1137–1143.

[31] Cawley, G. C. On Over-Fitting in Model Selection and Subsequent Selection Bias in Performance Evaluation. *J. Mach. Learn. Res.* **2010**, *11*, 2079–2107.

[32] Chawla, N. V.; Bowyer, K. W.; Hall, L. O.; Kegelmeyer, W. P. SMOTE: Synthetic Minority Over-Sampling Technique. *J. Artif. Intell. Res.* **2002**, *16*. https://doi.org/10.1613/jair.953

[33] Mujahid, M.; Kına, E.; Rustam, F.; et al. Data Oversampling and Imbalanced Datasets: An Investigation of Performance for Machine Learning and Feature Engineering. *J. Big Data* **2024**, *11*, 87. https://doi.org/10.1186/s40537-024-00943-4

[34] Brian, K. I.; Seiichi, U. Time Series Data Augmentation. In *Proceedings of the Int. Conf. Pattern Recognit. (ICPR)*; 2020.

[35] Nie, Y.; Nguyen, N. H.; Sinthong, P. A Time Series Is Worth 64 Words: Long-Term Forecasting with Transformers. *arXiv* **2023**, arXiv:2211.14730.

[36] Girard, J. M.; Cohn, J. F.; Torre, F. D. L. Estimating Smile Intensity: A Better Way. *Pattern Recognit. Lett.* **2015**, *16*, 12–21. https://doi.org/10.1016/j.patrec.2014.10.004

[37] Jiang, Z.; Yang, M.; Tsirlin, M.; Tang, R.; Dai, Y.; Lin, J. "Low-Resource" Text Classification: A Parameter-Free Classification Method with Compressors. In *Findings of the Association for Computational Linguistics: ACL 2023*; 2023; pp 6810–6828. https://doi.org/10.18653/v1/2023.findings-acl.426

[38] Broomé, S.; Gleerup, K. B.; Andersen, P. H. Dynamics Are Important for the Recognition of Equine Pain in Video. In *Proceedings of the IEEE/CVF Conf. Comput. Vis. Pattern Recognit. (CVPR)*; 2019; pp 12667–12676. https://doi.org/10.1109/CVPR.2019.01295



ASEAN
Journal of Scientific and Technological Reports
Online ISSN:2773-8752

ASEAN
Journal of Scientific and Technological Reports
Online ISSN: 2773-8752

Article type

Type of the Paper (Article, Review, Communication, etc.) *about 8,000 words maximum*

Title (Palatino Linotype 18 pt, bold)

Firstname Lastname[1], Firstname Lastname[2] and Firstname Lastname[2*]

[1] Affiliation 1; e-mail@e-mail.com
[2] Affiliation 2; e-mail@e-mail.com
* Correspondence: e-mail@e-mail.com; (one corresponding authors, add author initials)

Citation:
Lastname, F.; Lastname, F.; Lastname, F. Title. *ASEAN J. Sci. Tech. Report.* **2023**, *26*(X), xx-xx. https://doi.org/10.55164/ajstr.vxxix.xxxxxx

Article history:
Received: date
Revised: date
Accepted: date
Available online: date

Publisher's Note:
This article is published and distributed under the terms of the Thaksin University.

Abstract: A single paragraph of about 400 words maximum. Self-contained and concisely describe the reason for the work, methodology, results, and conclusions. Uncommon abbreviations should be spelled out at first use. We strongly encourage authors to use the following style of structured abstracts, but without headings: (1) Background: Place the question addressed in a broad context and highlight the purpose of the study; (2) Methods: briefly describe the main methods or treatments applied; (3) Results: summarize the article's main findings; (4) Conclusions: indicate the main conclusions or interpretations.

Keywords: keyword 1; keyword 2; keyword 3 (List three to ten pertinent keywords specific to the article yet reasonably common within the subject discipline.)

1. Introduction

The introduction should briefly place the study in a broad context and highlight why it is crucial. It should define the purpose of the work and its significance. The current state of the research field should be carefully reviewed and critical publications cited. Please highlight controversial and diverging hypotheses when necessary. Finally, briefly mention the main aim of the work. References should be numbered in order of appearance and indicated by a numeral or numerals in square brackets—e.g., [1] or [2, 3], or [4–6]. See the end of the document for further details on references.

2. Materials and Methods

The materials and methods should be described with sufficient details to allow others to replicate and build on the published results. Please note that your manuscript's publication implicates that you must make all materials, data, computer code, and protocols associated with the publication available to readers. Please disclose at the submission stage any restrictions on the availability of materials or information. New methods and protocols should be described in detail, while well-established methods can be briefly described and appropriately cited.

Interventional studies involving animals or humans, and other studies that require ethical approval, must list the authority that provided approval and the corresponding ethical approval code.

2.1 Subsection

2.1.1. Subsubsection

3. Results and Discussion

This section may be divided by subheadings. It should provide a concise and precise description of the experimental results, their interpretation, as well as the experimental conclusions that can be drawn.Authors should discuss the results and how they can be interpreted from previous studies and the working hypotheses. The findings and their implications should be discussed in the broadest context possible. Future research directions may also be highlighted.

3.1. Subsection

3.1.1. Subsubsection

3.2. Figures, Tables, and Schemes

All figures and tables should be cited in the main text as Figure 1, Table 1, etc.



Figure 1. This is a figure. Schemes follow the same formatting.

Table 1. This is a table. Tables should be placed in the main text near the first time they are cited.

Title 1	Title 2	Title 3
entry 1	data	data
entry 2	data	data [1]

[1] Table may have a footer.

3.3. Formatting of Mathematical Components

This is example 1 of an equation:

$$a = 1, \tag{1}$$

The text following an equation need not be a new paragraph. Please punctuate equations as regular text. This is example 2 of an equation:

$$a = b + c + d + e + f + g + h + i + j + k + l + m + n + o + p + q + r + s + t + u \tag{2}$$

The text following an equation need not be a new paragraph. Please punctuate equations as regular text. The text continues here.

4. Conclusions

Concisely restate the hypothesis and most important findings. Summarize the significant findings, contributions to existing knowledge, and limitations. What are the future directions? Conclusions MUST be well stated, linked to original research question & limited to supporting results.

5. Acknowledgements

Should not be used to acknowledge funders – funding will be entered as a separate. As a matter of courtesy, we suggest you inform anyone whom you acknowledge.

Author Contributions: For research articles with several authors, a short paragraph specifying their individual contributions must be provided. The following statements should be used "Conceptualization, X.X. and Y.Y.; methodology, X.X.; software, X.X.; validation, X.X., Y.Y. and Z.Z.; formal analysis, X.X.; investigation, X.X.; resources, X.X.; data curation, X.X.; writing—original draft preparation, X.X.; writing—review and editing, X.X.; visualization, X.X.; supervision, X.X.; project administration, X.X.; funding acquisition, Y.Y. All authors have read and agreed to the published version of the manuscript." Please turn to the CRediT taxonomy for the term explanation. Authorship must be limited to those who have contributed substantially to the work reported.

Funding: Please add: "This research received no external funding" or "This research was funded by NAME OF FUNDER, grant number XXX" and "The APC was funded by XXX". Check carefully that the details given are accurate and use the standard spelling of funding agency names at https://search.crossref.org/funding. Any errors may affect your future funding.

Conflicts of Interest: Declare conflicts of interest or state "The authors declare no conflict of interest." Authors must identify and declare any personal circumstances or interest that may be perceived as inappropriately influencing the representation or interpretation of reported research results. Any role of the funders in the design of the study; in the collection, analyses or interpretation of data; in the writing of the manuscript, or in the decision to publish the results must be declared in this section. If there is no role, please state "The funders had no role in the design of the study; in the collection, analyses, or interpretation of data; in the writing of the manuscript, or in the decision to publish the results".

References

References must be numbered in order of appearance in the text (including citations in tables and legends) and listed individually at the end of the manuscript. We recommend preparing the references with a bibliography software package, such as EndNote, ReferenceManager to avoid typing mistakes and duplicated references. Include the digital object identifier (DOI) for all references where available.

Citations and references in the Supplementary Materials are permitted provided that they also appear in the reference list here.

In the text, reference numbers should be placed in square brackets [ ] and placed before the punctuation; for example [1], [1–3] or [1, 3]. For embedded citations in the text with pagination, use both parentheses and brackets to indicate the reference number and page numbers; for example [5] (p. 100), or [6] (pp. 101–105).

Using the American Chemical Society (ACS) referencing style

[1] Author 1, A.B.; Author 2, C.D. Title of the article. *Abbreviated Journal Name* Year, *Volume*, page range.

[2] Author 1, A.; Author 2, B. Title of the chapter. In *Book Title*, 2nd ed.; Editor 1, A., Editor 2, B., Eds.; Publisher: Publisher Location, Country. **2007**, Volume *3*, pp. 154–196.

[3] Author 1, A.; Author 2, B. *Book Title*, 3rd ed.; Publisher: Publisher Location, Country, **2008**, pp. 154–196.
[4] Author 1, A.B.; Author 2, C. Title of Unpublished Work. *Abbreviated Journal Name* stage of publication (under review; accepted; in press).
[5] Author 1, A.B. (University, City, State, Country); Author 2, C. (Institute, City, State, Country). Personal communication, 2012.
[6] Author 1, A.B.; Author 2, C.D.; Author 3, E.F. Title of Presentation. In Title of the Collected Work (if available), Proceedings of the Name of the Conference, Location of Conference, Country, Date of Conference; Editor 1, Editor 2, Eds. (if available); Publisher: City, Country, Year (if available); Abstract Number (optional), Pagination (optional).
[7] Author 1, A.B. Title of Thesis. Level of Thesis, Degree-Granting University, Location of University, Date of Completion.
[8] Title of Site. Available online: URL (accessed on Day Month Year).

Reviewers sugestion

1. Name, Address, e-mail
2. Name, Address, e-mail
3. Name, Address, e-mail
4. Name, Address, e-mail

URL link:

Notes for Authors >>
https://drive.google.com/file/d/1r0zegnIVeQqe4iLQyT1xDEIinNggINPD/view?usp=sharing
https://drive.google.com/file/d/1r0zegnIVeQqe4iLQyT1xDEIinNggINPD/view?usp=sharing

Online Submissions >> https://ph02.tci-thaijo.org/index.php/tsujournal/user/register

Current Issue >> https://ph02.tci-thaijo.org/index.php/tsujournal/issue/view/16516

AJSTR Publication Ethics and Malpractice >> https://ph02.tci-thaijo.org/index.php/tsujournal/ethics

Journal Title Abbreviations >> http://library.caltech.edu/reference/abbreviations



ASEAN
Journal of Scientific and Technological Reports
Online ISSN:2773-8752



ASEAN
Journal of Scientific and Technological Reports
Online ISSN:2773-8752

ASEAN Journal of Scientific and Technological Reports (AJSTR)
Institute of Research and Innovation, Thaksin University, Phatthalung Campus
222 Moo. 2, Baan Prao Sub-District, Papayom District, Phatthalung, 93210, Thailand
Tel. +668 1540 7304

